Finite element analysis in geotechnical engineering

application

David M Potts and Lidija Zdravkovic

Finite element analysis in geotechnical engineering

Application

David M. Potts and Lidija Zdravković
Imperial College of Science, Technology and Medicine

With contributions from:

Trevor I. Addenbrooke
Kelvin G. Higgins
Nebojša Kovačević

Thomas Telford

Published by Thomas Telford Publishing, Thomas Telford Ltd, 1 Heron Quay, London E14 4JD.
URL: http://www.thomastelford.com

Distributors for Thomas Telford books are
USA: ASCE Press, 1801 Alexander Bell Drive, Reston, VA 20191-4400, USA
Japan: Maruzen Co. Ltd, Book Department, 3–10 Nihonbashi 2-chome, Chuo-ku, Tokyo 103
Australia: DA Books and Journals, 648 Whitehorse Road, Mitcham 3132, Victoria

First published 2001

Also available from Thomas Telford Books
Finite element analysis in geotechnical engineering: theory. ISBN 0 7277 2753 2

A catalogue record for this book is available from the British Library

ISBN: 0 7277 2783 4

Contents

Preface

While the finite element method has been used in many fields of engineering practice for over thirty years, it is only relatively recently that it has begun to be widely used for analysing geotechnical problems. This is probably because there are many complex issues which are specific to geotechnical engineering and which have only been resolved relatively recently. Perhaps this explains why there are few books which cover the application of the finite element method to geotechnical engineering.

For over twenty years we, at Imperial College, have been working at the leading edge of the application of the finite element method to the analysis of practical geotechnical problems. Consequently, we have gained enormous experience of this type of work and have shown that, when properly used, this method can produce realistic results which are of value to practical engineering problems. Because we have written all our own computer code, we also have an in-depth understanding of the relevant theory.

Based on this experience we believe that, to perform useful geotechnical finite element analysis, an engineer requires specialist knowledge in a range of subjects. Firstly, a sound understanding of soil mechanics and finite element theory is required. Secondly, an in-depth understanding and appreciation of the limitations of the various constitutive models that are currently available is needed. Lastly, users must be fully conversant with the manner in which the software they are using works. Unfortunately, it is not easy for a geotechnical engineer to gain all these skills, as it is vary rare for all of them to be part of a single undergraduate or postgraduate degree course. It is perhaps, therefore, not surprising that many engineers, who carry out such analyses and/or use the results from such analyses, are not aware of the potential restrictions and pitfalls involved.

This problem was highlighted four years ago when we gave a four day course on numerical analysis in geotechnical engineering. Although the course was a great success, attracting many participants from both industry and academia, it did highlight the difficulty that engineers have in obtaining the necessary skills required to perform good numerical analysis. In fact, it was the delegates on this course who urged us, and provided the inspiration, to write this book.

The overall objective of the book is to provide the reader with an insight into the use of the finite element method in geotechnical engineering. More specific aims are:

- To present the theory, assumptions and approximations involved in finite element analysis;
- To describe some of the more popular constitutive models currently available and explore their strengths and weaknesses;
- To provide sufficient information so that readers can assess and compare the capabilities of available commercial software;
- To provide sufficient information so that readers can make judgements as to the credibility of numerical results that they may obtain, or review, in the future;
- To show, by means of practical examples, the restrictions, pitfalls, advantages and disadvantages of numerical analysis.

The book is primarily aimed at users of commercial finite element software both in industry and in academia. However, it will also be of use to students in their final years of an undergraduate course, or those on a postgraduate course in geotechnical engineering. A prime objective has been to present the material in the simplest possible way and in manner understandable to most engineers. Consequently, we have refrained from using tensor notation and have presented all theory in terms of conventional matrix algebra.

When we first considered writing this book, it became clear that we could not cover all aspects of numerical analysis relevant to geotechnical engineering. We reached this conclusion for two reasons. Firstly, the subject area is so vast that to adequately cover it would take many volumes and, secondly, we did not have experience with all the different aspects. Consequently, we decided only to include material which we felt we had adequate experience of and that was useful to a practising engineer. As a result we have concentrated on static behaviour and have not considered dynamic effects. Even so, we soon found that the material we wished to include would not sensibly fit into a single volume. The material has therefore been divided into theory and application, each presented in a separate volume.

Volume 1 concentrates on the theory behind the finite element method and on the various constitutive models currently available. This is essential reading for any user of a finite element package as it clearly outlines the assumptions and limitations involved. Volume 2 concentrates on the application of the method to real geotechnical problems, highlighting how the method can be applied, its advantages and disadvantages, and some of the pitfalls. This is also essential reading for a user of a software package and for any engineer who is commissioning and/or reviewing the results of finite element analyses.

Volume 1 of this book consists of twelve chapters. Chapter 1 considers the general requirements of any form of geotechnical analysis and provides a framework for assessing the relevant merits of the different methods of analysis currently used in geotechnical design. This enables the reader to gain an insight into the potential advantage of numerical analysis over the more 'conventional' approaches currently in use. The basic finite element theory for linear material behaviour is described in Chapter 2. Emphasis is placed on highlighting the

assumptions and limitations. Chapter 3 then presents the modifications and additions that are required to enable geotechnical analysis to be performed.

The main limitation of the basic finite element theory is that it is based on the assumption of linear material behaviour. Soils do not behave in such a manner and Chapter 4 highlights the important facets of soil behaviour that ideally should be accounted for by a constitutive model. Unfortunately, a constitutive model which can account for all these facets of behaviour, and at the same time be defined by a realistic number of input parameters which can readily be determined from simple laboratory tests, does not exist. Nonlinear elastic constitutive models are presented in Chapter 5 and although these are an improvement over the linear elastic models that were used in the early days of finite element analyses, they suffer severe limitations. The majority of constitutive models currently in use are based on the framework of elasto-plasticity and this is described in Chapter 6. Simple elasto-plastic models are then presented in Chapter 7 and more complex models in Chapter 8.

To use these nonlinear constitutive models in finite element analysis requires an extension of the theory presented in Chapter 2. This is described in Chapter 9 where some of the most popular nonlinear solution strategies are considered. It is shown that some of these can result in large errors unless extreme care is exercised by the user. The procedures required to obtain accurate solutions are discussed.

Chapter 10 presents the finite element theory for analysing coupled problems involving both deformation and pore fluid flow. This enables time dependent consolidation problems to be analysed.

Three dimensional problems are considered in Chapter 11. Such problems require large amounts of computer resources and methods for reducing these are discussed. In particular the use of iterative equation solvers is considered. While these have been used successfully in other branches of engineering, it is shown that, with present computer hardware, they are unlikely to be economical for the majority of geotechnical problems.

The theory behind Fourier Series Aided Finite Element Analysis is described in Chapter 12. Such analysis can be applied to three dimensional problems which possess an axi-symmetric geometry but a non axi-symmetric distribution of material properties and/or loading. It is shown that analyses based on this approach can give accurate results with up to an order of magnitude saving in computer resources, compared to equivalent analyses performed with a conventional three dimensional finite element formulation.

This volume of the book (i.e Volume 2) builds on the material given in Volume 1. However, the emphasis is less on theory and more on the application of the finite element method in engineering practice. It consists of nine chapters.

Chapter 1 considers the problems involved in obtaining geotechnical parameters. These are necessary to define the constitutive models and initial conditions for an analysis. The relative merits of laboratory and field testing are discussed and the parameters that can be obtained from the various tests examined.

The analyses of tunnel construction is considered in Chapter 2. Emphasis is

placed on simulating the construction process and how this can be achieved in a two dimensional analysis. Modelling of the tunnel lining, the choice of an appropriate constitutive model for the soil and the selection of appropriate hydraulic boundary conditions are considered.

Chapter 3 considers the analysis of earth retaining structures. In particular the analysis of gravity, embedded and reinforced/anchored walls are examined. Emphasis is placed on modelling the structural elements, choosing appropriate constitutive models and simulating construction.

Cut slopes are considered in Chapter 4. The concepts behind progressive failure are introduced. Its role in slope stability is then examined and in particular its interaction with the long term dissipation of excess pore water pressures.

The analysis of embankments is discussed in Chapter 5. Embankments built of earthfill and rockfill and those built on weak and strong foundations are considered. The choice of appropriate constitutive models is discussed at some length as are the appropriate hydraulic boundary conditions and the role of progressive failure. For embankments on soft ground, single and multi-staged construction and the benefits of reinforcement are examined.

Chapter 6 considers shallow foundations. To begin with, simple surface foundations are considered and comparisons with the classical bearing capacity solutions made. The ability of numerical analysis to advance the current state of the art is then demonstrated by considering some of the weaknesses in current bearing capacity theory. For example, the effect of self weight on drained bearing capacity, the effect of foundation shape and its depth below the soil surface are considered. The effects of anisotropic soil strength and of pre-loading on bearing capacity are also examined. The analysis of tall towers and the difference between bearing capacity failure and leaning instability is discussed. Analysis of the leaning Tower of Pisa is then used to demonstrate the power of numerical analysis.

Deep foundations are considered in Chapter 7. The analyses of single piles and pile groups subjected to combined vertical, lateral and moment loading are considered. The behaviour of suction caissons and the possible detrimental effects of neglecting anisotropic soil strength are discussed.

Benchmarking and validation of numerical analyses are discussed in Chapter 8. The various options, their deficiencies and results from some recent benchmarking exercises are described.

Chapter 9 describes many of the restrictions and pitfalls that the authors have experienced. In particular, restrictions implicit in modelling problems as plane strain, problems associated with initial conditions and pitfalls associated with the use of some of the more common constitutive models are discussed.

Emphasis throughout this volume of the book is placed on explaining how the finite element method should be applied and what are the restrictions and pitfalls. In particular, the choice of suitable constitutive models for the various geotechnical boundary value problems is discussed at some length. To illustrate the material presented, examples from the authors experiences with practical geotechnical problems are used.

All the numerical examples presented in both this volume and Volume 1 of this book have been obtained using the Authors' own computer code. This software is not available commercially and therefore the results presented are unbiased. As commercial software has not been used, the reader must consider what implications the results may have on the use of such software.

London
March 2001

David M. Potts
Lidija Zdravković

Authorship

This volume has been edited and much of its content written by David Potts and Lidija Zdravković. Several of the chapters involve contributions from colleagues at Imperial College and the Geotechnical Consulting Group (GCG). In particular:

Dr Trevor Addenbrooke (Imperial College) wrote a large part of Chapter 2 (Tunnels);

Mr Kelvin Higgins (GCG) wrote Chapter 8 (Benchmarking) and contributed to Chapter 3 (Earth retaining structures);

Dr Nebojša Kovačević (GCG) wrote large parts of Chapter 4 (Cut slopes) and Chapter 5 (Embankments).

Acknowledgements

We would like to acknowledge our colleagues Professors John Burland and Peter Vaughan and all the past and present research students at Imperial College, without whose interest and involvement this book would not have been possible. In particular we would like to acknowledge Dr Dennis Ganendra whose PhD work on pile groups (supervised by David Potts) forms part of Chapter 7 (Deep foundations).

David Potts
Lidija Zdravković

1. Obtaining geotechnical parameters

1.1 Synopsis

One of the essential ingredients for a successful finite element analysis of a geotechnical problem is an appropriate soil constitutive model. As explained in Volume 1 of this book, there is not a single constitutive model currently available which can reproduce all aspects of real soil behaviour. It is therefore important to recognise in the analysis what aspects of the problem are of major interest and to choose a model accordingly. However, to employ a particular soil model in an analysis, appropriate laboratory and/or field tests are required from which to derive the necessary model parameters. This chapter describes the standard laboratory and field experiments used in geotechnical practice and the parameters that can be obtained from each of them.

1.2 Introduction

Since none of the currently available soil constitutive models can reproduce all of the aspects of real soil behaviour, it is necessary to decide which soil features govern the behaviour of a particular geotechnical problem (e.g. stiffness, deformation, strength, dilation, anisotropy, etc.) and choose a constitutive model that can best capture these features. Another factor that governs the choice of soil models for finite element analysis is the availability of appropriate soil data from which to derive the necessary model parameters. This often limits the use of sophisticated soil models in practice, because their parameters cannot be readily derived from standard laboratory or field tests.

The aim of this chapter is to give a brief description of standard and special laboratory and field tests and to review the soil parameters that can be derived from each of them. Due to restrictions on space it is not possible to give a detailed account of how the parameters are deduced from the raw laboratory and/or field data. For this information the reader is referred to the specialist texts on this subject. It is recognised that a good site investigation should combine the strengths of both laboratory and field testing.

1.3 Laboratory tests

1.3.1 Introduction

A laboratory investigation is a key feature of almost all geotechnical projects. The activities in the laboratory can be divided into several groups:

- Soil profiling, which involves soil fabric studies, index tests (e.g. water content, grading, Atterberg limits), chemical and organic content, mineralogy, etc.;
- Element testing to characterise the mechanical behaviour of the soils (e.g. stress-strain properties, yield, strength, creep, permeability, etc.);
- Derivation of parameters for empirical design methods (e.g. CBR for road pavements);
- Physical modelling (e.g. centrifuge tests, calibration chamber tests, shaking table tests)

For the purpose of deriving parameters for constitutive models, element testing is the most appropriate investigation. However, limited use is also made of the results from soil profiling. The aim of these element tests is to measure, as accurately as possible and in a controlled manner, the response of a soil element to imposed changes in stresses, strains and/or pore pressures. This ability of accurate control and measurement of soil response is the main advantage of laboratory over field testing. On the other hand, the main disadvantage of laboratory element testing is the difficulty in obtaining undisturbed samples (i.e. samples with preserved initial fabric and state). However, this can be overcome, to some extent, by the use of advanced sampling techniques (e.g. Laval samplers, Hight (1993))). Difficulties, however, still remain if sandy and weakly bonded soils are to be sampled.

The essential requirement for element testing is to simulate field conditions as closely as possible. This involves simulation of:

- Initial stresses (e.g. state of consolidation);
- Imposed stress changes;
- Sequence and rate of changes;
- Field drainage conditions.

If a natural material is tested, experiments are normally performed on a set of soil samples from different depths across a particular site, so that a full range of soil response parameters can be collected. In a similar manner, if reconstituted soil is tested, a group of samples is normally prepared with an identical set-up procedure and tested at different initial stress levels so that again a full range of material response parameters can be obtained.

The following paragraphs of this section will describe the majority of soil laboratory equipment currently available and the experiments that can be performed in it.

1.3.2 Oedometer test

A standard oedometer apparatus (see Figure 1.1) consists of a circular metal ring containing a soil sample which is usually 70mm in diameter and 20mm high. Porous discs are placed at the top and bottom end of the sample, thus allowing free drainage of the sample in the vertical direction. Radial drainage is not possible because the metal ring is impermeable. The sample is loaded only in the vertical direction, via the top platen, by applying increments of load until a desired stress level is reached. After each load increment is applied sufficient time is usually allowed for full dissipation of any excess pore water pressures.

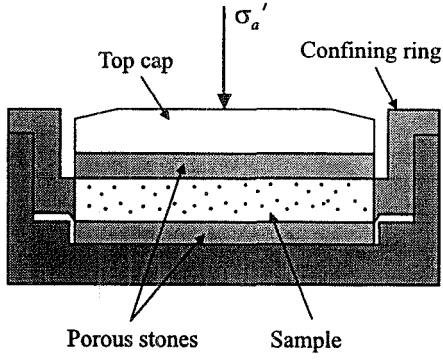

Figure 1.1: Schematic presentation of an oedometer apparatus

The complete stress state of a sample in the oedometer apparatus is not known. The only known stress is the axial total stress, σ_a. Radial stress and pore water pressure are not normally measured in the standard oedometer. Regarding strains, the axial strain ε_a is measured as the displacement of the top cap divided by the sample height, while the lateral deformation does not exist because of the confinement imposed by the metal ring (i.e. ε_r=0). Therefore the total volumetric strain of the sample equals the axial strain (i.e. ε_v=ε_a). Due to these constraints samples are said to undergo one dimensional compression.

Results from oedometer tests on clay soils are normally presented in the form of a void ratio-axial effective stress (i.e. e-logσ_a') diagram, see Figure 1.2. As noted above, sufficient time is allowed after the application of each increment of load to ensure full dissipation of any excess pore water pressures. Consequently, at this stage σ_a'=σ_a. With increasing axial effective stress the volume of a sample (i.e. its void ratio) reduces and the loading curve from the initial sample conditions follows the path 'abcd', see Figure 1.2. This path is usually assumed to become straight once the pre-consolidation pressure is exceeded (i.e. σ_a'>$(\sigma_a')_b$) and is called the virgin compression line. The slope of this line is known as the compression index C_c, which is calculated as:

$$C_c = \frac{\Delta e}{\Delta(\log \sigma_a')} \tag{1.1}$$

To examine the swelling potential of a soil, the oedometric sample can be unloaded axially, which causes an increase in the void ratio (i.e. path 'ce' in Figure 1.2). In the same e-logσ_a' diagram this line is called a swelling line and again is usually assumed to be straight, with a gradient C_s which is called the swelling index.

The pre-consolidation pressure is usually associated with the maximum previous vertical effective stress that the sample has ever been subjected to. Hence the original overconsolidation ratio of the sample, *OCR*, can be calculated by dividing $(\sigma_a')_b$ by the vertical effective stress existing in the field at the location the sample was taken from. It should be noted that for structured soils this approach may lead to an overestimate of *OCR*, as the process of ageing has the effect of increasing the stress associated with point 'b'.

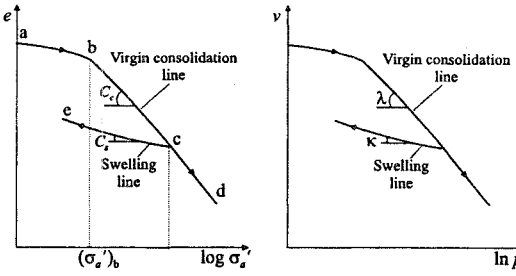

Figure 1.2: Typical results from an oedometer test on clay soil

To be able to use the oedometer data in general stress space, its is necessary to express the gradients of the compression and swelling lines in terms of invariants. By knowing the ratio of the radial to axial effective stress in one dimensional compression (i.e. $K_o = \sigma_r'/\sigma_a'$), it is possible to estimate the mean effective stress p' $(=(\sigma_a'+2K_o\,\sigma_a')/3)$ and replot compression and swelling behaviour in terms of specific volume, v $(=1+e)$, and mean effective stress, p'(i.e. v-lnp' diagram). The gradient of the virgin compression line is then usually denoted as λ and is calculated as:

$$\lambda = \frac{\Delta v}{\Delta(\ln p')} \tag{1.2}$$

The slope of the swelling line, κ, in the same diagram is calculated in a similar manner. These two parameters, λ and κ, are essential for critical state type models, such as modified Cam clay, bounding surface plasticity and bubble models (see Chapters 7 and 8 of Volume 1).

The difficulty is estimating the value of K_o which is not measured in the standard oedometer test. When the soil is on the virgin compression line it is termed normally consolidated and it is often assumed that $K_o=K_o^{NC}=(1-\sin\varphi')$ (i.e. Jaky's formula), where φ' is the angle of shearing resistance. If φ' is known, then K_o and hence p' can be estimated. As K_o^{NC} is approximately constant along the virgin compression line, then if this line is straight in e-logσ_a' space it will also be straight in v-lnp' space. In fact, it can be easily shown that $C_c=2.3\lambda$. However, on a swelling line K_o is not constant but increases as the sample is unloaded. While there are some empirical equations describing how K_o^{OC} varies, there is no universally accepted expression. Consequently it is difficult to calculate p' on a swelling line. In addition, if K_o^{OC} varies and the swelling line is straight in e-logσ_a' space, then it will not be straight in v-lnp' space and vice versa. Clearly the determination of κ from an oedometer test is therefore difficult and considerable judgement is required.

The third parameter, which is needed to define the position of the virgin compression and swelling curves in a v-lnp' diagram, is the value of the specific volume at unit mean effective stress or, for the MIT models, at p'=100kPa. Care must be exercised here as usually this parameter is required for the virgin compression line obtained under conditions of isotropic compression (i.e. no deviatoric stress). As noted above in the oedometer test the horizontal and vertical stresses are unlikely to be equal (i.e. $K_o \neq 1$), consequently the virgin consolidation line, although parallel to the equivalent line obtained under isotropic conditions, will be shifted towards the origin of the v-lnp' diagram. For most constitutive models it is possible to transform the values of the specific volume on the oedometer virgin consolidation line to the appropriate values on the isotropic virgin consolidation line.

To complicate matters even further some of the more advanced constitutive models plot isotropic consolidation data in ln$v$-lnp' space and assume that the virgin consolidation and swelling lines are straight in this space, for example the AlTabbaa and Wood model described in Section 8.9 of Volume 1 of this book.

The results from the oedometer test can also be used to estimate the coefficient of permeability in the vertical direction, k_v. If, after each increment of load is applied, the change in sample height is monitored with time this data can be combined with one dimensional consolidation theory to estimate k_v (Head (1994)).

For sands the behaviour in the oedometer test is more complex, as the initial density of the sample affects its behaviour. If two samples of the same sand are placed in an oedometer, one in a loose and one in a dense state, their behaviour under increased vertical loading might be as indicated in Figure 1.3. As the samples have different initial densities they will have different initial voids ratios. With increasing vertical effective stress the samples will initially follow different normal compression lines. At some point these normal compression lines will merge with a unique virgin compression line, see Figure 1.3. This will happen at a lower vertical effective stress the looser the sample. The magnitude of the vertical effective stress at which the virgin compression line is reached is much higher than for clay soils and is often considerably larger than the stress levels experienced in many practical situations. If unloaded at any time the sample will follow a swelling/reloading line. Behaviour is therefore characterised either as being on a normal compression line, on the virgin compression line or on a swelling/reloading line. These lines are often assumed to be straight in either e-logσ_a', v-lnp' or ln$v$-lnp' space.

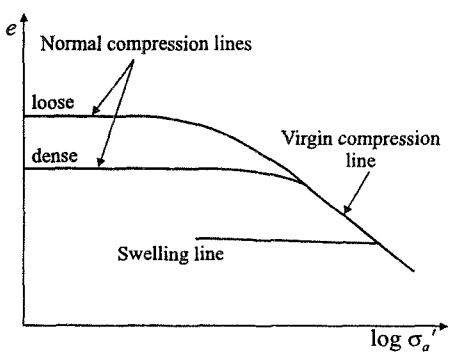

Figure 1.3: Typical result from an oedometer test on sand soil

The data from the oedometer test can also be used to calculate the constrained modulus as:

$$E_c = \frac{\Delta\sigma'_a}{\Delta\varepsilon_a} \tag{1.3}$$

If the soil is assumed to be isotropic elastic, this can be equated to the one dimensional modulus to give:

$$E_c = \frac{E(1-\mu)}{(1-\mu-\mu^2)} \tag{1.4}$$

If a value for the Poisson's ratio μ is assumed, it is possible to estimate the Young's modulus E from E_c.

1.3.3 Triaxial test

The triaxial apparatus is the most widely used piece of laboratory equipment for soil testing. It is described in detail by Bishop and Henkel (1962) in their standard text book on triaxial testing of soil. A more advanced version of the triaxial apparatus is the stress path cell described by Bishop and Wesley (1975).

A conventional triaxial apparatus (Figure 1.4) incorporates a cylindrical soil sample which has a diameter of either 38mm or 100mm. The larger diameter apparatus is usually employed for testing natural clays, because of the fissuring that is often present in these materials. With a smaller diameter sample this feature might be missed. The sample is enclosed in a thin rubber membrane which is sealed at the top and bottom platens by rubber O-ring seals. The membrane gives flexibility to radial deformation of the sample. It also separates pore pressures generated inside the sample from total radial stresses applied to the outside of the sample.

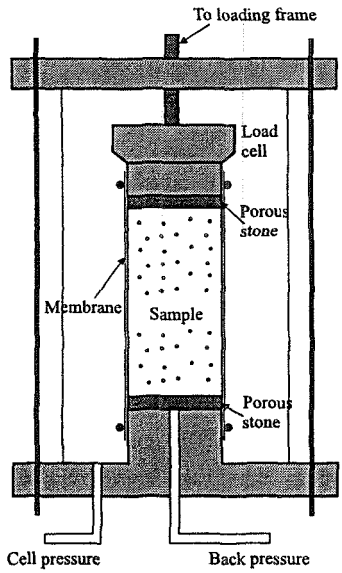

Figure 1.4: Schematic presentation of a triaxial apparatus

The sealed sample is placed on a pedestal in a water-filled cell. An all-around cell pressure, σ_c, applies radial total stress, σ_r, to the vertical sides of the sample and a uniform vertical stress to the top rigid platen, see Figure 1.5. An additional axial force, F_a, is applied to the top platen via a loading frame. If the cross-sectional area of the sample is A, then the total axial stress on the sample is:

$$\sigma_a = \sigma_c + F_a / A \tag{1.5}$$

It is important to note that the force in the loading frame is not equivalent to the axial stress, but to the stress equal to $(\sigma_a - \sigma_r)$, which is known as the deviator stress, q. The pore water pressures can be measured in the triaxial sample and therefore effective axial and radial stresses can be evaluated:

$$\sigma'_a = \sigma_a - p_f$$
$$\sigma'_r = \sigma_r - p_f \qquad (1.6)$$

Pore pressure can be measured in the end platens adjacent to the bottom and/or top end of the sample, or by a probe placed at approximately mid-height of the sample.

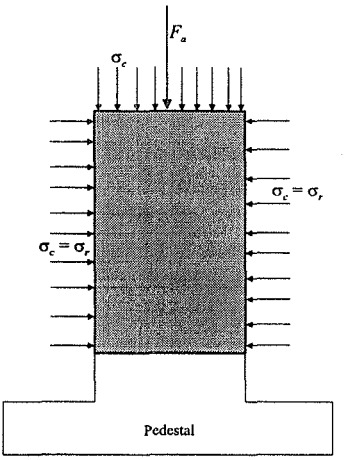

Figure 1.5: Stresses acting on a triaxial sample

Originally axial strains were deduced from measurements of axial displacements made with dial gauges positioned outside the triaxial cell and therefore remote from the sample. However, strain measurement has advanced in the last twenty years so that it is now possible to attach instruments on the sample itself. This avoids errors associated with the compliance of the testing system. Both axial and radial strains can be measured in this way.

Triaxial apparatus can be used to perform several different tests. Some of the more common tests are:

- If σ_a and σ_r are increased together such that the radial strain ε_r=0, the sample will deform in one dimensional compression, similar to oedometer conditions. The advantage over the oedometer test is that, by measuring pore water pressure and radial stress, effective stresses can be calculated and the coefficient of earth pressure at rest, K_o^{NC}, estimated as:

$$K_o^{NC} = \sigma'_r / \sigma'_a \qquad (1.7)$$

  In a similar manner, if σ_a and σ_r are reduced together such that ε_r=0, the coefficient of earth pressure in overconsolidation, K_o^{OC}, can be estimated for different *OCR*s. The results of such one dimensional compression and swelling tests can be plotted in a e-logσ_a' diagram and parameters C_c and C_s estimated as in Equation (1.1). The total volumetric strain, ε_v, in both cases equals the axial strain, ε_a. It should be noted that these values can only be related to in-situ conditions if the *OCR* is known. An alternative procedure for estimating the value of K_o from undisturbed sample is discussed subsequently.
- If the loading frame is locked such that it is not in contact with the top platen of the sample and the sample is loaded only with an all-around cell pressure (i.e. σ_a=σ_r), it is deforming under isotropic compression. If the all-around cell pressure is reduced, the sample is said to undergo isotropic swelling. The

results of such tests can be plotted in a v-lnp' diagram and used to obtain values for the parameters λ and κ, see Equation (1.2).

- After initial isotropic or anisotropic compression to a certain stress level, samples can be subjected to either drained or undrained shearing. In this case the total radial stress is held constant, while the axial stress is either increased or decreased. If $\sigma_a > \sigma_r$ the sample is undergoing triaxial compression and in this case $\sigma_a = \sigma_1$ and $\sigma_r = \sigma_\theta = \sigma_2 = \sigma_3$. The parameter b $(=(\sigma_2 - \sigma_3)/(\sigma_1 - \sigma_3))$, which accounts for the effect of the intermediate principal stress, is therefore zero. On the other hand, if the sample is axially unloaded, such that $\sigma_a < \sigma_r$, it undergoes triaxial extension and in this case $\sigma_a = \sigma_3$ and $\sigma_r = \sigma_\theta = \sigma_1 = \sigma_2$, resulting in $b = 1.0$. In Volume 1 of this book the Lode's angle θ was used to express the relative magnitude of the intermediate principal stress. Using Equation (5.3) of Volume 1 it can be shown that $\theta = \tan^{-1}[(2b-1)/\sqrt{3}]$ and consequently in triaxial compression $b = 0$ and $\theta = -30°$ and in triaxial extension $b = 1$ and $\theta = 30°$.

The results from both drained and undrained triaxial shearing are normally plotted in terms of stress-strain diagrams (q-ε_a) and stress path diagrams (q-p' or t-s', where $t = (\sigma_a' - \sigma_r')/2$ and $s' = (\sigma_a' + \sigma_r')/2$), see Figure 1.6. In addition, for undrained shearing the change in pore water pressure, p_f, is usually plotted against axial strain, ε_a, whereas for drained shearing the volumetric strain, ε_{vol}, is plotted against axial strain, ε_a. Both clay and sand soils may experience peak deviatoric stress, before softening towards a constant deviatoric stress which doesn't change with further straining. This state is known as the *critical state* for a particular material. Parameters of importance for modelling and design are values of the angle of shearing resistance at peak, φ_p', and at critical state, φ_{cs}', and they can be different in triaxial compression and triaxial extension. They are calculated from the known stress state at peak and critical state as:

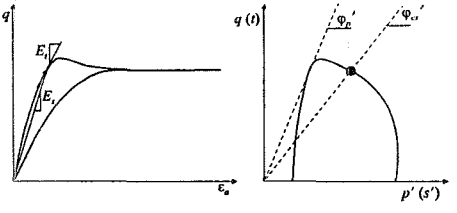

Figure 1.6: Schematic presentation of stress paths and stress-strain curves from a triaxial test

$$\varphi' = \sin^{-1}\left(\frac{\sigma_1' - \sigma_3'}{\sigma_1' + \sigma_3'}\right) \tag{1.8}$$

Another parameter of interest in geotechnical practice is the stiffness of the soil. From triaxial tests both drained, E', and undrained, E_u, Young's moduli can be estimated in both triaxial compression and extension. From stress-stain curves these parameters can be calculated as either secant or tangent values, see Figure 1.6:

$$E' = \frac{\Delta\sigma_a'}{\Delta\varepsilon_a} \quad ; \quad E_u = \frac{\Delta\sigma_a}{\Delta\varepsilon_a} \tag{1.9}$$

The triaxial test provides a complete history of the degradation of soil stiffness with increase in strain level, as shown in Figure 1.7. If the resolution of the local strain instrumentation is sufficiently high so that it can detect the initial elastic behaviour of a material, the stiffness curve will have an initial horizontal plateau associated with the maximum stiffness value. This small strain behaviour is an essential part of constitutive modelling if soil deformations are of interest in the analysis, because soil stiffness is much higher in the early stages of deformation than it is at large strains. Ignoring this can result in the prediction of patterns of movement considerably different to those observed in the field, see Chapters 2 and 3.

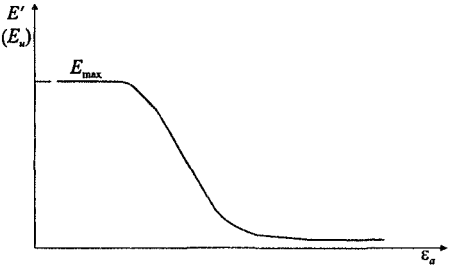

Figure 1.7: Soil stiffness curve

If the small strain Young's modulus, E'_{max}, can be obtained, the other elastic parameter that can be calculated from a drained triaxial compression test is Poisson's ratio μ_{ar}' for straining in the radial direction due to changes in axial stress, which is calculated as:

$$\mu'_{ar} = -\frac{\Delta\varepsilon_r}{\Delta\varepsilon_a} \tag{1.10}$$

The ability to measure the radial strain to a very high resolution is essential for this parameter to be estimated.

However, instead of using parameters E' and μ, soil elasticity can be expressed in terms of shear modulus G and bulk modulus K, see Section 5.5 of Volume 1. Both can be calculated from triaxial compression or extension tests, although K only from a drained test:

$$G = \frac{\Delta J}{\Delta E_d} \tag{1.11}$$

where: ΔJ is the incremental invariant deviatoric stress:

$$\Delta J = \tfrac{1}{\sqrt{6}}\sqrt{(\sigma_1' - \sigma_2')^2 + (\sigma_2' - \sigma_3')^2 + (\sigma_1' - \sigma_3')^2} = \tfrac{1}{\sqrt{3}}(\sigma_a' - \sigma_r') = q/\sqrt{3}$$

ΔE_d is the incremental invariant deviatoric strain:

$$\Delta E_d = \tfrac{2}{\sqrt{6}}\sqrt{(\varepsilon_1 - \varepsilon_2)^2 + (\varepsilon_2 - \varepsilon_3)^2 + (\varepsilon_1 - \varepsilon_3)^2} = \tfrac{2}{\sqrt{3}}(\varepsilon_a - \varepsilon_r)$$

and

$$K = \frac{\Delta p'}{\Delta\varepsilon_v} \tag{1.12}$$

where: $\Delta p'$ is the incrmental mean effective stress and

$$\Delta p' = (\Delta\sigma_1' + 2\Delta\sigma_3')/3 = (\Delta\sigma_a' + 2\Delta\sigma_r')/3$$

$\Delta\varepsilon_v$ is the incremental volumetric strain and

$$\Delta\varepsilon_v = \Delta\varepsilon_1 + 2\Delta\varepsilon_3 = \Delta\varepsilon_a + 2\Delta\varepsilon_r$$

Again, the complete degradation of shear and bulk stiffness from small to large strains can be obtained from a triaxial test.

It is worth noting that it is not possible to obtain many anisotropic stiffness parameters from a triaxial test. For example, if the parameters for the linear transversely isotropic model were required, see Section 5.6 of Volume 1, then only the values of the axial Young's modulus, $E_a=\Delta\sigma_a'/\Delta\varepsilon_a$ and Poisson's ratio $\mu_{ar}=\Delta\varepsilon_r/\Delta\varepsilon_a$ can be obtained from the standard tests described above. If dynamic probes such as bender elements, see Section 1.3.10, are mounted on the sides and ends of the sample it is possible to obtain estimates of a further two parameters, but it is still not possible to obtain a value for the fifth parameter.

The angle of shearing resistance and stiffness parameters are essential for nearly all of the currently existing constitutive models.

Although not common, the triaxial cell can be used to obtain an estimate of in-situ values of K_o in clay soils. Usually, when soil samples are taken during a site investigation, they are immediately sealed to ensure no transfer of water from or to the sample. This seal is only broken when a smaller test sample is required for testing. If it is assumed that during the whole sampling and storage process, from extraction from the ground until placement in the triaxial cell, the sample remains undrained, then the sample will retain its mean effective stress, p_k'. The sample on placement in the triaxial cell will have a zero mean total stress applied to it and consequently the initial pore water suction will be equal to p_k'. If a cell pressure (i.e. σ_r) is then applied to the sample until a positive pore water pressure is recorded, (note that most pore water pressure transducers used for triaxial testing cannot measure suction), the initial p_k' can be calculated as the difference between the applied cell pressure and measured pore water pressure. This can then be used to determine the in-situ value of K_o using Equation (1.13) (see Burland and Maswoswe (1982)):

$$K_o = \frac{p_k' / \sigma_v' - A_s}{1 - A_s} \tag{1.13}$$

where A_s accounts for the change in pore water pressure due to the reduction in deviatoric stress which occurs during sampling in the field. A value of A_s=1/3 corresponds to an isotropic elastic material, whereas a stiff clay (e.g. London clay) typically has a value of approximately 1/2; σ_v' is the original vertical effective stress in the sample in-situ and can be estimated knowing the depth of the sample, the bulk unit weights of the overlying materials and the pore water pressure.

Accurate estimates of K_o from this approach require that the sample remains undrained at all times. On setting up the sample in the triaxial cell care must be exercised so that it does not come into contact with water. This can be difficult as it is usual practice to saturate the porous stones at the top and bottom of the sample and consequently special testing techniques are required, see Burland and

Maswoswe (1982). The approach also neglects any changes in pore water pressure that occur when the sample is forced into and out of the sampling tube in which it is stored.

The triaxial cell can also be used to obtain estimates of permeability. A sample can be subjected to a cell pressure, σ_r, and then a difference in pressure applied between the drainage lines at the top and bottom platens. This will promote flow of water through the sample. By knowing this pressure difference and measuring the quantity of water flowing through the sample in a set time, once steady state conditions have been reached, enables the permeability to be estimated using Darcy's law. By performing a series of permeability tests at different cell pressures enables a relationship between permeability and voids ratio (or mean effective stress) to be determined. As the time required for these tests depends on the drainage path length, which in turn is related to the sample height, short stubby samples are usually used.

For soils with a low permeability (i.e $K_o<10^{-7}$m/sec) it is also possible to estimate the permeability k from a dissipation stage of a triaxial test. This involves applying a change in cell pressure quickly and then allowing consolidation during which time the decay in excess pore water pressure with time is monitored. One dimensional consolidation theory can then be used to estimate k.

1.3.4 True triaxial test

In contrast to a conventional triaxial apparatus, the true triaxial equipment tests a cubical soil sample. The difference between the two experiments is that in the true triaxial equipment all three principal stresses, σ_1, σ_2 and σ_3, can be applied and controlled independently, see Figure 1.8, while in a conventional triaxial cell two principal stresses are always equal (i.e. $\sigma_r=\sigma_\theta$).

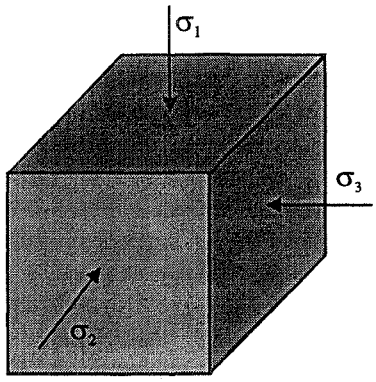

Figure 1.8: Stresses controlled in a true triaxial apparatus

The advantage of this experiment is that the values of the angle of shearing resistance, φ', can be obtained for the full range of b between 0 and 1, while conventional triaxial tests with a cylindrical sample can only have b=0 (triaxial compression) or b=1(triaxial extension). This is useful if the value of φ' is needed for conditions in the ground other than triaxial (for example plane strain, for which $0.2<b<0.4$, depending on soil type).

It is also possible to measure the soil stiffness in three directions. For example it is possible to obtain estimates of four of the five parameters necessary to define the linear transversely anisotropic model. If dynamic probes (i.e. bender elements)

are installed in the sample it is also possible to obtain an estimate for the fifth parameter.

While clearly an advantage over the conventional triaxial equipment, it is not easy to obtain and set up the samples. Consequently true triaxial apparatus are rarely used for commercial testing. Only a limited number of apparatus exist and these are mainly located in universities.

1.3.5 Direct shear test

The direct shear test is performed in the shear box apparatus, schematically illustrated in Figure 1.9. The sample is typically 60x60mm in plane and about 25mm high. It is placed between rigid and rough top and bottom platens, in a square box which is split horizontally. Vertical load is applied via the top cap and is normally kept constant during the test. A horizontal force is applied to the top half of the box with the bottom half fixed, thus forcing the two halves of the box to move horizontally relative to each other. Rough top and bottom platens transfer shear stress into the soil. The main purpose of the test is to examine soil strength. It is unsuitable for measuring soil stiffness because of the non-uniformities imposed in the sample by the loading arrangement.

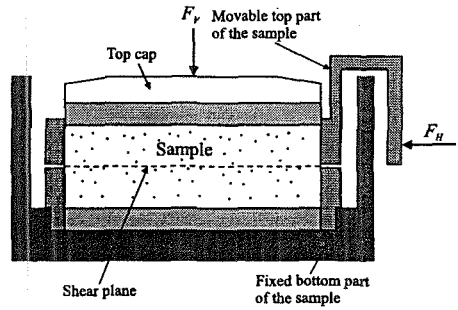

Figure 1.9: Schematic presentation of a direct shear box apparatus

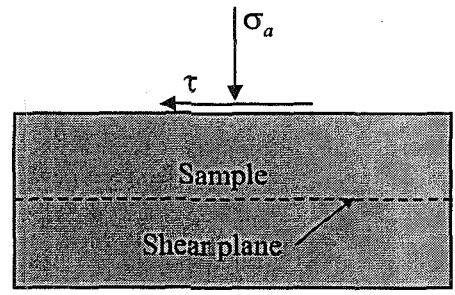

Figure 1.10: Stresses acting on a sample in a direct shear box

The only known stresses on the sample are the average vertical stress and the average shear stress, see Figure 1.10. The application of a shear stress causes the major principal stress, σ_1, to rotate continually away from the vertical, but there is no means of measuring this rotation. Because the sample is confined in a box, it is subjected to significant stress and strain non-uniformities during shearing.

Interpretation of the direct shear box is based on assuming that the deformation of the sample conforms to that of ideal simple shear, see Potts *et al.* (1987). Such an idealised condition is indicated in Figure 1.11 which shows the top boundary of a layer of soil displaced parallel to the bottom boundary, under plane strain

conditions. The behaviour of a typical element is indicated. The soil is subjected to a prescribed shear strain γ_{xy} and is constrained to have zero direct strain in the x direction (ε_x=0). As a result of these prescribed boundary conditions, the soil is subjected to a shear stress τ_{xy}, a direct strain ε_y and a change in stress in the x direction ($\Delta\sigma_x \neq 0$). Because horizontal planes remain horizontal and are inextensible (ε_x=0), at ultimate plastic failure these planes are a set of velocity characteristics (Davis (1968)). Such planes are inclined at $\pm(45°-\nu/2)$ to the direction of the major principal plastic strain increment. In an isotropic elasto-plastic material the directions of the principal stresses and the principal plastic strain increments coincide. Consequently at failure, when all deformation is plastic, any horizontal plane is a velocity characteristic and is inclined at $\pm(45°-\nu/2)$ to the direction of the major principal stress σ_1 and hence is inclined at $\pm(45°+\nu/2)$ to the plane on which σ_1 acts. The Mohr circle of stress for this state is shown in Figure 1.12. Point P is the pole of the circle and point H represents the stresses $(\tau_{xy})_f$ and σ_y' which act on the horizontal plane. From the geometry of the circle it can be shown that:

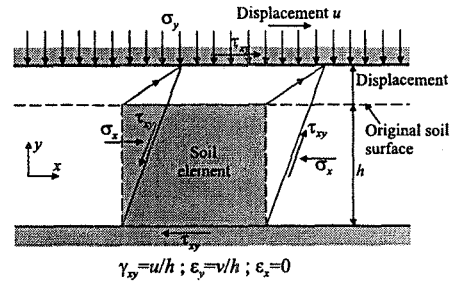

Figure 1.11: Simple shear conditions

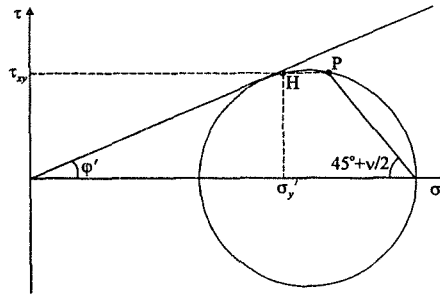

Figure 1.12: Mohr's circle of stress at ultimate conditions

$$\left(\frac{\tau_{xy}}{\sigma_y'}\right)_f = \frac{\sin\varphi'\cos\nu}{1-\sin\varphi'\sin\nu} \qquad (1.14)$$

which reduces to $(\tau_{xy}/\sigma_y')_f=\sin\varphi'$ when ν=0 and $(\tau_{xy}/\sigma_y')_f=\tan\varphi'$ when $\nu=\varphi'$. It should be noted that $(\tau_{xy}/\sigma_y')_f=\sin\varphi'$ is the interpretation advocated by Hill (1950), whereas $(\tau_{xy}/\sigma_y')_f=\tan\varphi'$ is the more common interpretation. In reality, due to the non-uniformities inherent in the direct shear box test, it is unlikely that the condition of idealised simple shear exists throughout much of the sample.

The usual presentation of direct shear results is in terms of a shear stress-horizontal displacement diagram (i.e. τ-d), see Figure 1.13. The shear stress normally increases up to a peak value during the early stages of horizontal displacement, and then gradually decreases until reaching a residual value after a large horizontal displacement of the shear box. From this test both peak and residual angles of shearing resistance can be evaluated, although to obtain the latter

several reversals of loading may be necessary. Residual strength can be very important in some boundary value problems involving high plasticity clays, see Chapter 4. Because clay particles are elongated and, in their natural condition, oriented in some structure, after large deformations they can become aligned with the direction of shearing. Such a situation could occur, for example, during a landslide. Low plasticity clays and granular materials have a less pronounced drop from critical state to residual strength.

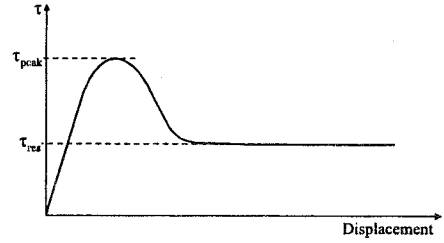

Figure 1.13: Typical shear stress-displacement diagram from direct shear box test

The direct shear box apparatus is also used for interface shear testing. In this situation soil is sheared against some other material (e.g. concrete, steel, etc.) in order to examine the angle of friction, δ, at the interface of the two materials. This parameter is used, for example, in pile or retaining wall analysis, where it is necessary to know the maximum value of the angle of friction between the pile or wall material (concrete or steel) and soil (Jardine and Chow (1996), Day and Potts (1998)). For such investigations the interface between the soil and the material against which it is to be sheared is positioned at the split between the upper and lower halves of the shear box.

1.3.6 Simple shear test

The simple shear apparatus works on a similar principle to the direct shear box in that the top platen is moved horizontally with respect to the bottom platen. However, the apparatus is designed so that the sample is allowed to deform more uniformly. There are currently two designs of simple shear apparatus: one developed at Cambridge University and the other at the Norwegian Geotechnical Institute (NGI) in Oslo. The NGI device is the more common design and can be found in many laboratories, both academic and commercial, around the world.

The NGI device is schematically drawn in Figure 1.14a. It has a cylindrical sample, 80mm in diameter and about 10mm thick, contained within a wire-reinforced rubber membrane. This membrane maintains a constant sample circumference, but allows uniform vertical deformation and rotation of the vertical sides of the sample. The whole sample is placed between top and bottom platens. Axial and shear forces are applied via the top platen. Usually the axial force is kept constant, while the shear force increases during the test, similar to the direct shear box test. The vertical and shear strains of a sample can be measured by observing the vertical and horizontal displacement of the top platen. Although the pore pressure can be measured, the full stress and strain states of the sample are not known in the NGI device and again the results are interpreted assuming ideal simple shear conditions, as discussed above in Section 1.3.5.

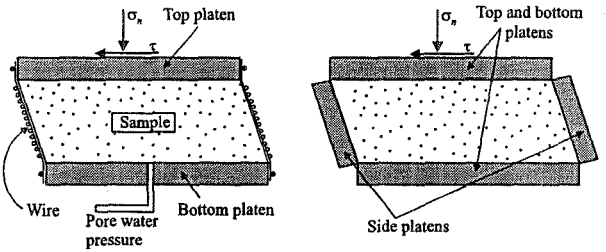

Figure 1.14: Schematic presentation of a) NGI and b) Cambridge simple shear devices

The Cambridge University device is schematically presented in Figure 1.14b. The sample here is a rectangular prism, 100 by 100mm in plan and about 20mm thick. It is placed within rough rigid top and bottom platens which allow vertical deformation and rotation of the side platens. From the measurements of these external deformations it is possible to estimate the average strains within the sample. As the side platens are designed to allow vertical movement (i.e. they are smooth) they do not provide complementary shear stresses on the vertical boundaries of the sample. Consequently the stress and strain state is not uniform within the sample. Usually normal and shear stress transducers are placed in the platens and stresses are measured over the middle third of the sample. As it is more difficult to obtain, test and instrument these prismatic samples only a few pieces of equipment of this type exist.

Both types of simple shear apparatus are mainly used for measuring soil strength (i.e. undrained strength or angle of shearing resistance). Due to the more uniform behaviour of the sample in the Cambridge apparatus, it can also be used to obtain pre-failure stress strain data.

1.3.7 Ring shear test

The ring shear apparatus is another device suitable only for measuring soil strength. The principle of operation is similar to the direct shear box apparatus, except that the sample has the shape of a squat hollow cylinder and the top half of the box is rotated with respect to the bottom. The sample, about 100mm in outer diameter, about 20mm thick and of 15mm wall thickness (see Figure 1.15), is placed within rough top and bottom platens in a horizontally split metal ring. Constant vertical load is applied via the top platen, while the bottom part of the ring is rotated with respect to the top part, thus applying a horizontal shear stress and creating a horizontal slip surface in the sample. No other stresses or strains can be measured in the standard ring shear apparatus and consequently interpretation of the results is difficult.

The results from a ring shear test are normally plotted in terms of shear stress versus displacement (i.e. τ-d) diagram, as for the direct shear box, see Figure 1.13.

The shear stress can experience a peak value (i.e. associated with φ_p'), after which the soil strength drops and reaches a residual value (i.e. φ_{res}'). Again strength parameters are determined assuming behaviour is similar to ideal simple shear. The difference between this test and shear box test is that much larger displacements can be achieved in a ring shear device (e.g. several metres) and therefore a better estimate of the residual strength can be obtained. Another advantage of the ring shear apparatus is that it can be used to examine the effects of very high rates of shearing on residual strength, which is useful when investigating soil behaviour under earthquake loading.

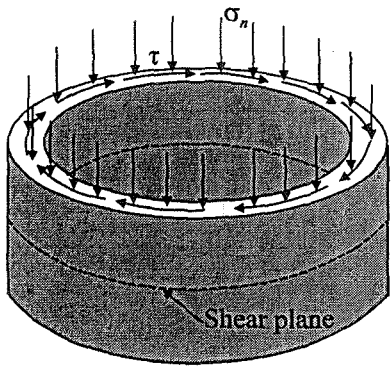

Figure 1.15: Schematic presentation of a ring shear apparatus

The ring shear apparatus can also be used for interface testing.

1.3.8 Hollow cylinder test

From the previous discussion it can be concluded that in the oedometer, triaxial and true triaxial apparatus the principal stress and strain directions applied to the sample are parallel with the sample boundaries. It is only possible for the relative magnitudes of the principal stresses and strains to change. Their directions are fixed. In contrast the direct, simple and ring shear apparatus allow rotation of the principal stress and strain directions, but because not all of the stress components can be measured it is not possible to measure the magnitude of the principal stresses, or more importantly control their directions. The only exception might be a highly instrumented Cambridge type simple shear apparatus, where sufficient load cells are used to enable sufficient stress components to be measured to calculate the principal effective stresses, however, it is still not possible to control or alter the direction of the principal stresses, as this is implicitly set by the manner in which the apparatus works.

The hollow cylinder apparatus does not suffer from the above shortcomings, as it allows full control of both the magnitude and the rotation of principal stresses. It is therefore extremely suitable for investigating soil anisotropy. The sample is a hollow cylinder (see Figure 1.16) which can have various dimensions. For example, the large and small hollow cylinder apparatus in the Imperial College laboratory test samples with the following dimensions: the large one is 25cm high, 25cm outer diameter and 2.5cm wall thickness; the smaller device is 19cm high, 10cm outer diameter and 1.5cm wall thickness.

Four independent loads can be applied to a hollow cylindrical sample (see Figure 1.16), as opposed to only the one, two or three that can be applied to

samples in the other laboratory devices. These loads are the inner cell pressure, p_i , the outer cell pressure, p_o , the vertical load, W, and the torque, M_T. This combination of loads allows control of four component stresses, namely the normal stresses σ_z , σ_r and σ_θ and the torsional shear stress $\tau_{z\theta}$ (note the remaining shear stresses τ_{rz} and $\tau_{r\theta}$ are zero). This then permits control over the magnitudes and directions α of the principal stresses. Because all three major stresses can be controlled, it is also possible to independently control the parameter b. So, with a well designed hollow cylinder apparatus it is possible to perform a set of shear tests with a constant value of b while changing α, and vice versa, with a constant value of α while changing b, thus enabling an independent evaluation of the effects of each of these two parameters on soil strength, stiffness, yielding, etc.

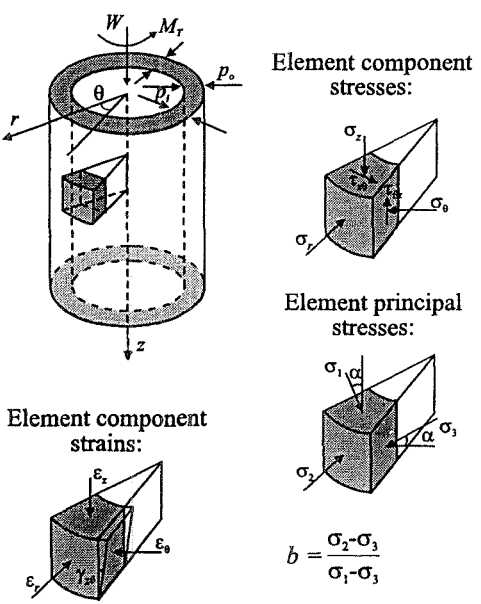

Figure 1.16: Stresses and strains in a hollow cylinder apparatus

All component strains can be measured locally in a hollow cylinder device: the three normal strains ε_z, ε_r and ε_θ and the torsional shear strain $\gamma_{z\theta}$, so that the strain state in the sample is completely known (note γ_{rz}=$\gamma_{r\theta}$=0).

Because of the flexibility of a hollow cylinder apparatus, a variety of stress paths can be applied to soil samples. However, for design purposes its use is usually most valuable for investigating initial soil anisotropy, where samples are initially K_o consolidated to a certain stress level (thus simulating initial green-field conditions in the ground after the sedimentation/erosion process) and then sheared with different orientations of the major principal stress (i.e. a set of samples where each sample is sheared with a different α value in the range from 0° to 90°). The results from these tests are normally plotted in terms of stress-strain (J-E_d) and stress path (J-p') diagrams, the latter being a two dimensional projections of the three dimensional J-p'-α stress space, see Figure 1.17. This figure shows results from a typical series of hollow cylinder tests performed on a granular soil (see Zdravković and Jardine (2000)). In particular, the results show how the peak deviator stress reduces with an increase of α. Typical results derived from such a set of experiments gives the variation of both drained, φ_p', and undrained, S_u, soil strength with α, shown in Figure 1.18. These results clearly indicate a degree of soil anisotropy.

excavation inducing a lengthening of the vertical diameter and shortening of the horizontal diameter. It is clear that the closer the two tunnels, the greater the induced distortion. For all the analyses, the lengthening of the vertical diameter is greater than the associated shortening of the horizontal diameter, and the induced distortions are never as severe as those for side-by-side tunnels at the same pillar dimension (the curves for side-by-side tunnels are reproduced from Figure 2.42). Sensible extrapolations of the numerical predictions for the distortion to the upper tunnel on passage of the lower tunnel are in good agreement with the field data from Kimmance *et al.* (1996). Not surprisingly this construction sequence causes more distortion than the alternative of the second tunnel passing above the existing tunnel. Indeed, it is clear that there is very little influence when the second tunnel passes above the existing tunnel, and for pillar depths greater than 3 diameters the influence is effectively zero.

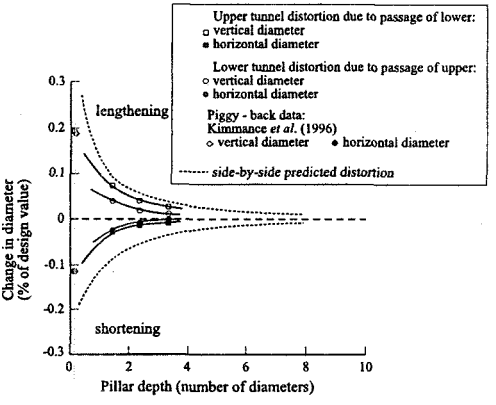

Figure 2.43: Deformation of 1st tunnel in response to 2nd tunnel for piggy back geometry

The results presented here demonstrate that the relative position (above, below, or to the side) and the physical spacing of the tunnels has a significant effect on the tunnel lining response. The results presented quantify the expected distortion induced in an existing tunnel lining when an adjacent tunnel is excavated. Addenbrooke and Potts (2001) draw further conclusions with respect to the surface settlement profiles expected above twin tunnel projects, and the influence of the rest period between construction of the two tunnels.

2.8 Summary

1. Tunnel construction is a three dimensional engineering process. If restricted to two dimensional analysis, then one must consider either plane strain or axially symmetric representations, depending on what the analysis aims to achieve.
2. Methods of simulating tunnel construction in plane strain require at least one assumption: the volume loss to be expected; the percentage of load removal prior to lining construction; or the actual displacement of the tunnel boundary.
3. If severe distortions of the tunnel lining are expected (i.e. in response to the passage of an adjacent tunnel in close proximity) then a model can be used which allows segmental linings to open or rotate at their joints, or allows sprayed concrete linings to crack.
4. The recognition of permeability's dependence on stress level has led to nonlinear models for permeability. Using such a model in place of a linear

alternative will alter the long term pore water pressure regime, for the same hydraulic boundary conditions. This will alter the ground response during consolidation and swelling.

5. The intermediate and long term behaviour is governed by many factors. In particular, whether the tunnel acts as a drain or is impermeable, and whether the initial pore water pressure profile is close to hydrostatic or not. It is important to be aware of the dependencies, and so to view any prediction of intermediate and long term behaviour with a critical eye.
6. It is important to select constitutive models capable of reproducing field behaviour. For example, in a situation where pre-yield behaviour dominates the ground response, it is essential to model the nonlinear elasticity at small strains.
7. Devices for improving settlement predictions can be developed. These questions must be asked: What is the influence of this adjustment on the soil behaviour? What are the knock on effects? For example, if one is adopting a device to match a surface settlement profile, how does this alter any prediction of sub-surface movement, the pore pressure response, or the lining stresses and deformations.
8 The finite element method can be used to quickly assess the impact of different influences on tunnelling-induced ground movements. Parametric studies can prove extremely useful in the development of design charts and interaction diagrams.
9. One of the great benefits of numerical analysis to the tunnel engineer is that an analysis can incorporate adjacent influences. For example existing surface structures, or existing tunnels. It is also possible to reproduce the effects of compensation grouting to protect surface structures during tunnelling projects. This chapter has demonstrated the power of the finite element method in this respect.

3. Earth retaining structures

3.1 Synopsis

This chapter discusses the analysis of earth retaining structures of various forms. It draws heavily on issues that have to be considered when analysing real structures. After a brief description of the main types of retaining structures in current use, general considerations, such as choice of constitutive model, construction method, ground water control and support systems, are discussed. Attention is then focussed on the specific analysis of gravity, embedded and reinforced/anchored retaining walls.

3.2 Introduction

The purpose of an earth retaining structure is, generally, to withstand the lateral forces exerted by a vertical or near vertical surface in natural ground or fill. The structural system usually includes a wall, which may be supported by other structural members such as props, floor slabs, ground anchors or reinforcing strips. Alternatively, or additionally, the wall may be supported by ground at its base or into which it penetrates. In most situations the soil provides both the activating and resisting forces, with the wall and its structural support providing a transfer mechanism.

The design engineer must assess the forces imposed on the wall and other structural members, and the likely movements of both the structure and retained material. Usually these have to be determined under working and ultimate load conditions, see Chapter 1 of Volume 1 of this book. In addition, estimates of the magnitude and extent of potential ground movements arising from construction of the structure, both in the short term and in the long term as drainage within the ground occurs, are required. This may be because of the effect construction may have on existing, or planned, services or structures (buildings, tunnels, foundations, etc.) in close proximity. Potential damage could occur which has to be assessed and methods of construction considered which minimise these effects.

Design of retaining walls has traditionally been carried out using simplified methods of analysis (e.g. limit equilibrium, stress fields) or empirical approaches. Simplified methods have been developed for free standing gravity walls, embedded cantilever walls, or embedded walls with a single prop or anchor. Some of these are described in BS 8002 (1994) and Padfield and Mair (1984). Because of the

statically indeterminate nature of multiple propped (or anchored) walls, these have often been dealt with using empirical approaches such as those suggested by Peck (1969). Simplified methods of analysis are also available for reinforced/anchored earth, for example see BS 8006 (1995).

Because all of these traditional design methods are based on simplified analysis or empirical rules, they cannot, and do not, provide the engineer with all the desired design information. In particular, they often only provide very limited indications of soil movements and no information on the interaction with adjacent structures.

The introduction of inexpensive, but sophisticated, computer hardware and numerical software has resulted in considerable advances in the analysis and design of retaining structures over the past ten years. Much progress has been made in attempting to model the behaviour of retaining structures in service and to investigate the mechanisms of soil-structure interaction. This chapter will review some of these advances and discuss some of the important issues that must be addressed when performing numerical analysis of earth retaining structures. It begins by describing the different types of retaining structure and the general issues which must be considered before starting an analysis. It then goes on to consider the three main categories of retaining structures (i.e. gravity, embedded and reinforced/anchored earth walls) in more detail.

3.3 Types of retaining structure

3.3.1 Introduction

The complexity and uncertainty involved in design and analysis increase with the degree of soil-structure interaction and thus depend on the type of retaining structure to be employed. It is therefore appropriate to categorise the types of retaining structure on the basis of the soil structure interaction problems that arise in design. In Figure 3.1 the main wall types are shown in order of increasing complexity of soil-structure interaction.

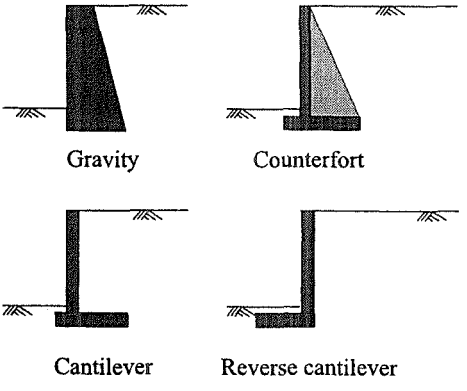

Figure 3.1: Types of retaining structure (cont...)

3.3.2 Gravity walls

Gravity, counterfort and cantilever walls are stiff structures for which the soil-structure interaction is relatively simple. For overall stability, the earth forces on the back of a wall have to be balanced by normal and shear stresses at its base. The magnitudes of these resisting forces are, to a large extent, controlled by the weight of the

structure, hence the term gravity wall. Such walls can be formed of mass concrete, reinforced concrete, or pre-cast units such as crib walls or gabions. Movement arising from deformation of the ground beneath the wall is often negligibly small, but exceptions occur if the wall and backfill are constructed on a deep layer of compressible soil.

3.3.3 Reinforced/anchored earth walls

Reinforced earth walls and walls involving soil nails essentially act as large gravity walls. However, their internal stability relies on a complex interaction between the soil and the reinforcing elements (or nails). These walls generally have non-structural membrane facing units which are intended to prevent erosion, or are purely aesthetic. The membrane has to be designed to resist any bending moments and forces that occur, but this is not the primary method of earth retention. The resistance to ground movement is provided by soil nails, anchors and ties of various forms (not ground anchors) or strips of metal or geo-fabric.

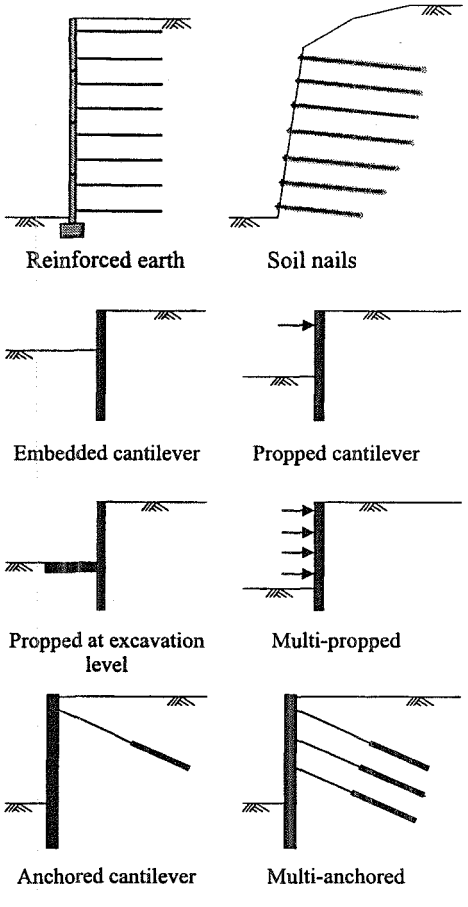

Figure 3.1: (...cont) Types of retaining structure

3.3.4 Embedded walls

When soil movements are important and/or construction space is limited, embedded cantilever walls may be used, with or without props or anchors. Sheet pile walls, diaphragm walls, contiguous bored pile walls and secant pile walls are all examples of this type of wall. To maintain stability the walls rely on the resistance of the ground below excavation level and on the resistance forces provided by any props or anchors. The flexibility of embedded walls vary within a wide range and this has considerable effect on the distribution of earth pressures. The more flexible walls often have smaller bending moments in the structural elements, but may lead to larger deformations, particularly for embedded cantilevers with no props or anchors. The complexity of soil-structure interaction

increases with the number of levels of props and/or anchors and hence the structural redundancy.

3.4 General considerations

3.4.1 Introduction

Before starting any numerical analysis it is important to address a number of issues to ensure that the most appropriate methods of modelling the soil and structure are used. It is also important that the correct boundary conditions (e.g. displacements, pore water pressures, loads, etc.) are applied in any analysis. This section briefly outlines some of the more important issues. A number of these are discussed in greater detail in subsequent sections.

3.4.2 Symmetry

In reality all geotechnical problems involving retaining structures are three dimensional and, ideally, three dimensional analyses, fully representing the structure's geometry, loading conditions and variations in ground conditions across the site, should be undertaken. With current computer hardware this is not a practical proposition for all, but a number of very limited and extremely simple cases. To analyse any structure it is therefore necessary to make a number of simplifying assumptions. Most commonly two dimensional plane strain or axi-symmetric analyses are undertaken, see Chapter 1 of Volume 1 of this book.

For two dimensional and axi-symmetric analysis the assumption is frequently made that there is an axis of symmetry about the centre line of an excavation and that only a 'half section' needs to be modelled. In the case of a three dimensional analysis two planes of symmetry are often assumed and a 'quarter section' is considered. For example, Figure 3.2 shows a plane strain excavation supported by two parallel walls propped near to the ground surface. If there is symmetry about the vertical line passing through the centre of the excavation, it is only necessary to analyse half the problem, either that half of the problem to the right of the plane of symmetry or that half to the left. This clearly reduces the size of the problem and the number of finite elements needed to represent it. However, for such an analysis to be truly representative there must be complete symmetry about the centre line of the excavation. This symmetry includes geometry, construction sequence, soil properties and ground conditions. In practice it is rarely the case that all of these have symmetry and therefore analyses using a 'half section' usually imply further approximations.

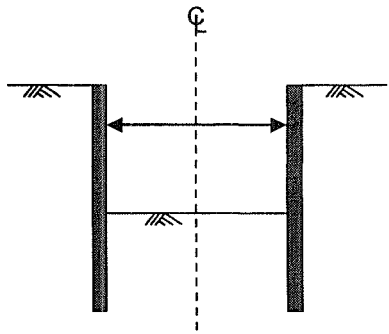

Figure 3.2: Example of axi-symmetric geometry

As an example consider the situation shown in Figure 3.3. This shows the cross section of a road tunnel forming part of a road improvement scheme. The tunnel is formed of two secant pile retaining walls, a roof slab which is connected to the outer walls by a full moment connection, a base slab which is not connected to the walls and a central wall that also provides support to the roof slab. The central piles support the central wall, but neither are connected to the base slab.

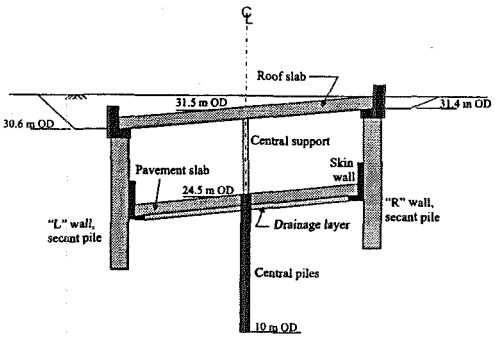

Figure 3.3: Cross-section of a road tunnel

The road alignment at the location of the tunnel is on a bend and consequently the tunnel roof and base slab are inclined to the horizontal. However, the fall across the structure does not appear great, less than 1m across the excavation which is between 25 to 26m wide. Consequently, it is tempting to simplify the analysis by ignoring the fall across the structure and assuming symmetry about its centre. Only a 'half section' would then need to be considered in any analysis.

To investigate whether such an approximation is reasonable, a finite element analysis was undertaken considering the full cross section of the tunnel as shown in Figure 3.3. Figure 3.4 shows the predicted displaced shape of the two retaining walls at an exaggerated scale (solid profile; the undeformed profile of the walls, as represented in the finite element mesh, is shown as a dotted line). It is apparent that there is some sway of the tunnel structure and wall displacements are not the same on either side of the excavation. The top of the right hand wall of the tunnel is pushed back into the soil behind it.

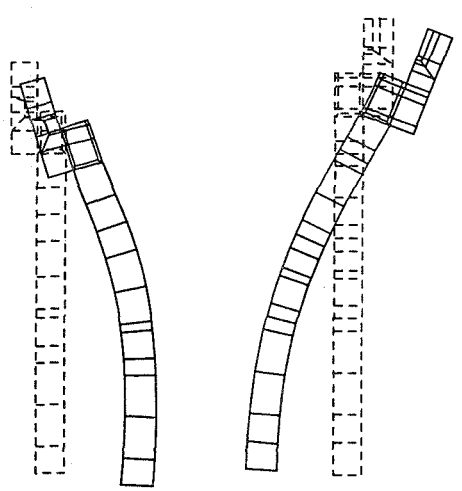

Figure 3.4: Displaced shape of walls of road tunnel

An analysis of a 'half section' would not have predicted this asymmetrical behaviour. It would have predicted that both walls move symmetrically inwards towards the centre of the excavation. Because the displaced shape of one, or both, walls was not correct, the predicted bending moments and forces in the walls would also have been incorrectly predicted.

Obviously, no analysis can model geometry in detail, or for that matter every construction activity, but this example illustrates the care that must be taken when making simplifying assumptions of any form.

3.4.3 Geometry of the finite element model

Another decision that arises when performing a numerical analysis is the choice of the depth and lateral extent of the finite element mesh. For example, when considering the simple excavation problem shown in Figure 3.5, a decision must be made as to the depth of the mesh below the ground surface and the lateral extent of the right hand boundary of the mesh. As, in this case, the excavation is symmetric, the position of the left hand boundary of the mesh is fixed.

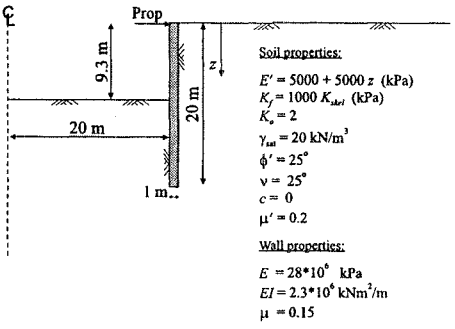

Figure 3.5: Propped retaining wall

When considering the bottom boundary of the mesh, the soil stratigraphy often provides an obvious location. For example, the occurrence of a very stiff and strong layer (e.g. rock) at depth provides an ideal location for the bottom boundary of the mesh. Also, because soil strength and stiffness usually increase with depth, analyses are not so sensitive to the location of the bottom boundary as long as it is not unreasonably close to the bottom of the wall. The location of the far field vertical (i.e. the right hand) boundary is more problematic and will, in part, depend on the constitutive model employed to represent soil behaviour.

To illustrate these points analyses have been performed for the excavation problem shown in Figure 3.5. A typical mesh is shown in Figure 3.6. Also shown are the displacement boundary conditions imposed on the bottom and vertical boundaries of the mesh. Both the soil and the wall are modelled using eight noded isoparametric elements. Wider meshes were obtained by adding elements to the right side of the mesh shown in Figure 3.6. Shallower meshes were obtained by deleting elements from the bottom of the mesh. In the vicinity of the excavation all meshes were similar.

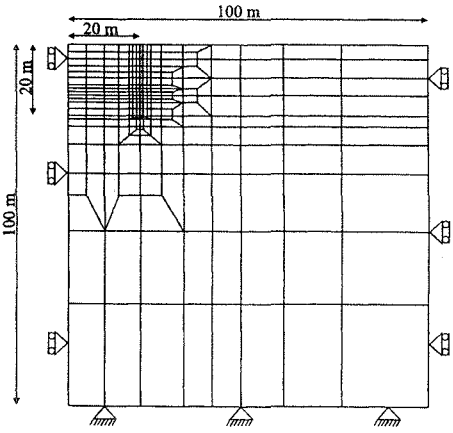

Figure 3.6: Typical finite element mesh for excavation problem

In the first set of analyses the soil was represented by a linear elastic Mohr-Coulomb constitutive model in which the soil stiffness increased with depth. The parameters used are shown on Figure 3.5. The procedure and boundary conditions for all the analyses were the same. Only the dimensions of the mesh varied with boundaries of differing depths and distances from the rear of the wall. This set of analyses was then repeated modelling the soil with the same strength parameters, but with the linear elasticity replaced by the small strain stiffness model described in Section 5.7.5 of Volume 1. The parameters for the small strain stiffness model are given in Table 3.1. In both sets of analyses the soil parameters are typical of the same stiff clay and are therefore consistent with each other. All analyses simulated undrained excavation to a depth of 9.3m, with a rigid prop at the top of the wall.

The surface settlement troughs behind the wall predicted by analyses with a lateral extent of 100m (five times the half width of the excavation) and with depths of 36m, 52m and 100m (1.8, 2.6 and 5 times the half width of the excavation) are presented in Figure 3.7. The results of the analyses using linear elastic pre-yield behaviour of the soil shown in Figure 3.7a indicate that the depth of the mesh has a significant effect on the predictions. In contrast, the analyses with the pre-yield small strain soil behaviour show a much smaller dependency on the mesh depth (Figure 3.7b).

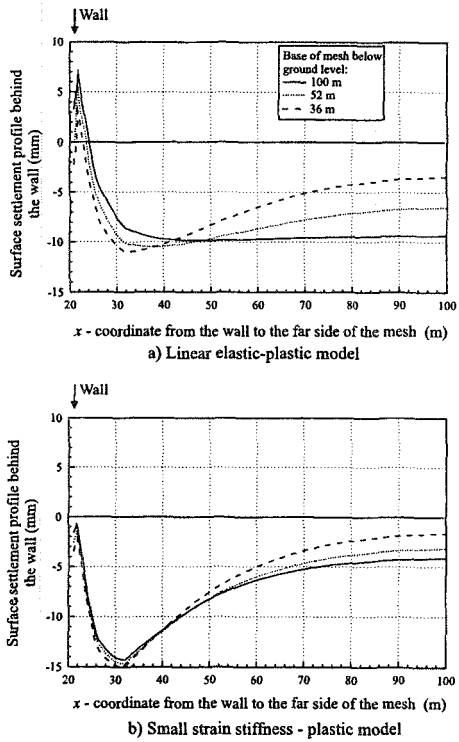

Figure 3.7: Effect of the depth of the mesh on the surface settlement trough

The surface settlement troughs behind the wall predicted by analyses with a depth of 100m and with lateral extents if 100m, 180m and 340m (5, 9 and 17 times the half width of the excavation) are presented in Figure 3.8. These predictions indicate that for the analyses performed using the small strain stiffness model, see Figure 3.8b, there is little difference between the surface settlement troughs predicted by the analyses using meshes with 180m and 340m lateral extent. However, for the analyses employing linear elastic behaviour pre-yield, see Figure 3.8a, but with stiffness increasing with depth, the predicted surface settlement troughs differ in all three analyses. These results therefore indicate that if the small strain stiffness model is being used to represent elastic behaviour, the mesh with a lateral extent of 180m is sufficient. However, if the elastic behaviour is linear then a much wider mesh must be used.

Table 3.1: Small strain stiffness parameters

Parameter	$G/p'=A+B\cos[\alpha(\log_{10}(E/(\sqrt{3}C)))^{\gamma}]$	Parameter	$K/p'=R+S\cos[\delta(\log_{10}(\lvert\varepsilon_v\rvert/T))^{\mu}]$
A	466.6	R	686.0
B	423.3	S	633.0
C (%)	$1*10^{-4}$	T (%)	$1*10^{-3}$
α	1.335	δ	2.069
γ	0.617	μ	0.420
E_{min} (%)	$8.66025*10^{-4}$	$\varepsilon_{v,min}$ (%)	$5*10^{3}$
E_{max} (%)	0.69282	$\varepsilon_{v,max}$ (%)	0.15
G_{min}	2666.7	K_{min}	5000.0

Clearly it is not possible to make a general statement as to the appropriate vertical and lateral extent of the finite element mesh. This will depend on the problem being analysed, the constitutive models employed and what facet of behaviour is under investigation. In practice it is therefore sensible to experiment with meshes of different size, unless experience has already been gained of analysing a similar problem in the past.

Another decision that must be made when performing the finite element analysis is the nature of the boundary conditions to be applied to the boundaries of the mesh. In the above analyses, zero horizontal displacements and zero vertical forces were applied to the vertical boundaries of the mesh. While this is the correct boundary condition to model the axis of symmetry represented by the left hand vertical boundary, the alternative of fixing both vertical and horizontal

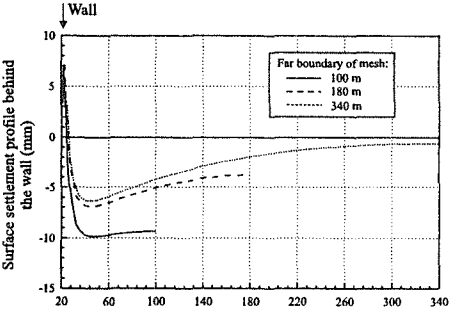

a) Linear elastic-plastic model

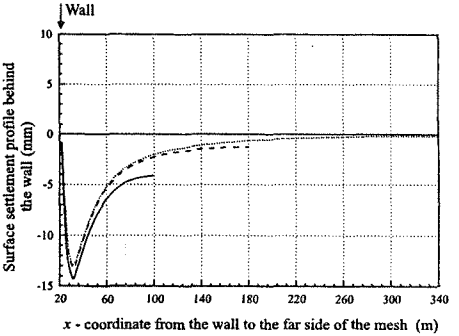

b) Small strain stiffness - plastic model

Figure 3.8: Effect of the lateral extent of the mesh on the surface settlement trough

displacements to zero on the far field vertical right hand boundary is equally valid. Likewise, for the bottom boundary, fixing either the vertical displacement or both the vertical and horizontal displacements is equally valid. Whether or not the choice affects the results depends on the lateral and vertical extent of the mesh and, in particular, how far they are from the excavation.

To investigate the influence of the boundary condition applied to the right hand side of the mesh, the analysis presented above, using the mesh 180m wide and 100m deep, was repeated, fixing both the vertical and horizontal incremental displacements on the far field vertical right hand boundary of the mesh (i.e. $\Delta u = \Delta v = 0$). The predicted surface settlement troughs are shown in Figure 3.9. Also shown, for comparison, are the results from the analysis in which only the horizontal displacement on the right hand boundary was fixed ($\Delta u = 0$). It can be seen that in the vicinity of the excavation the surface settlements are not affected by the choice of boundary condition. It is only near to the vertical right hand boundary that the surface settlement trough is influenced by the choice of boundary condition.

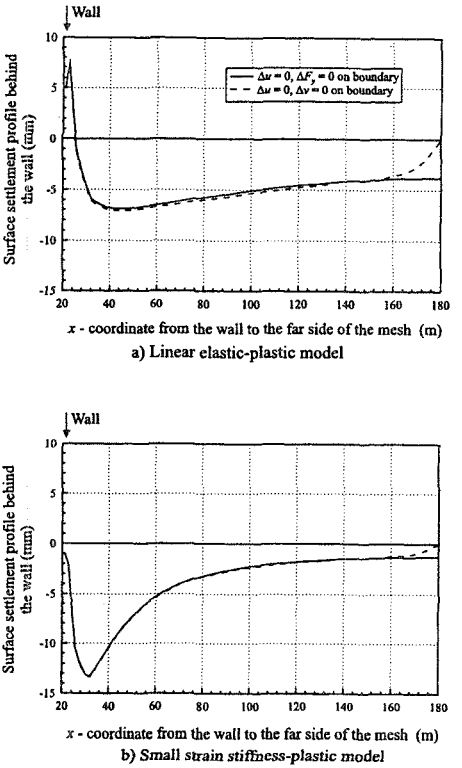

Figure 3.9: Effect of displacement boundary conditions on the far boundary of the mesh on the surface settlement trough

3.4.4 Support systems

The methods of supporting walls, or any other earth retaining structure, also need to be addressed (details of any props, ties, anchors, berms, etc.). The details of any connections between structural members need to be examined to ensure that in the analysis the structure is modelled adequately.

These differing methods of supporting the structure act in different ways and can therefore have a considerable influence on the behaviour of the structure. Propping systems (struts, slabs, etc.) provide passive resistance to movement, the resistance to movement is intrinsic. On the contrary, ties, anchors and soil reinforcement rely on stresses within the ground being mobilised to retain the structure. Changing ground conditions, such as drainage, can reduce the effectiveness of the support.

When horizontal props are used to support a wall, see Figure 3.10, analyses are often undertaken in which the props are either assumed to be rigid, with the wall restrained from any horizontal movement at the position of the prop, or represented by springs suitably grounded (i.e. fixed in space) at some distance from the wall, see Figure 3.10. Such assumptions imply symmetry in geometry and loading conditions and therefore that an identical retaining structure exists as a mirror image to that being analysed. Such a condition rarely exists in practice as soil and loading conditions are likely to vary. However, even if such a situation did exist, the construction process is unlikely to be carried out in a symmetrical manner. For example, the walls themselves are likely to be constructed sequentially, the wall one side of the excavation may be constructed before the other, thus imposing non-symmetric conditions which are likely to affect subsequent behaviour, Finno *et al.* (1991).

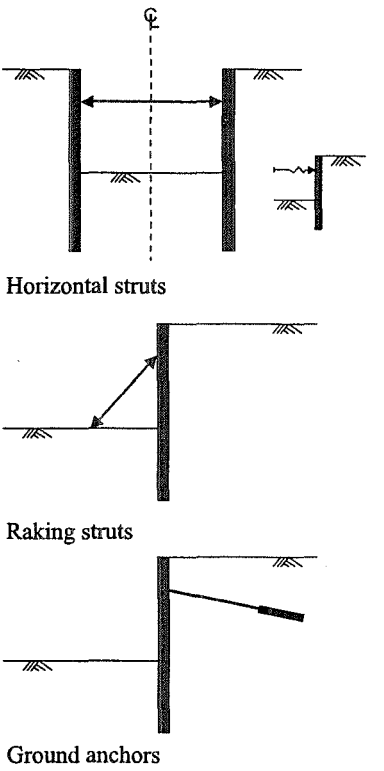

Figure 3.10: Types of structural support

Raking props, see Figure 3.10, also promote complex soil structure interaction. Part of the load from the retained soil is transferred via the prop to be resisted by soil at formation level. The magnitude of the prop load is therefore dependent on the interaction between the walls and the soil behind and at formation level. Depending on the position of the raking props, additional soil pressures may be generated on the front of the wall and resistance to movement will be dictated by soil behaviour.

Ground anchors, see Figure 3.10, involve a complex system of soil interaction, as both the load in, and resistance of, the anchor are derived from the retained soil. Consequently, the behaviour of an anchored wall is likely to be different to that of a propped wall.

The type of connection between wall and support can also affect behaviour and increase the complexity of any design analysis. Three types of connection are shown in Figure 3.11. Most current design procedures often implicitly assume a 'simple' connection, whereas in reality most connections are either 'pin-jointed', 'full moment' or somewhere in between.

These details can have an enormous influence on bending moments, forces and displacements. Any propping system must move with the structure unless it is anchored independently. Most propping systems prevent differential movement

and not absolute movement and it is important to draw this distinction. This was illustrated by the example given in section 3.4.2 above, the roof slab influenced the differential movement of the walls relative to each other, but did not prevent the sway of the structure.

Alternative ways to model the different types of support connection, shown in Figure 3.11, and to model props and ground anchors, are discussed in Chapter 9.

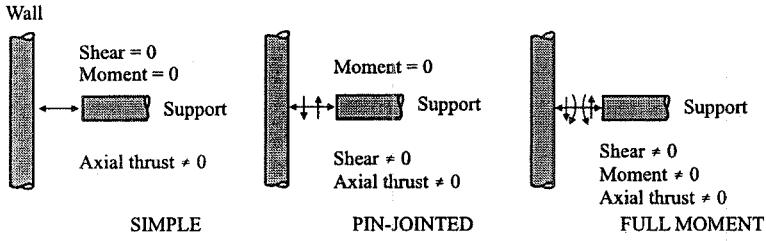

Figure 3.11: Types of wall-support connection

3.4.5 Choice of constitutive models

It is obviously important that in any analysis realistic, and appropriate, constitutive models are used to represent the behaviour of the structural components and the behaviour of the ground.

3.4.5.1 Structural components

When modelling structural components the assumption is frequently made that these elements behave linear elastically and that tensile stresses can be accommodated. In many situations such an idealisation is perfectly adequate. The structure may be designed to sustain these forces. However, under certain circumstances, particularly the case of unreinforced (mass) concrete structures, the analysis may have to account for the structure having limiting tensile and/or compressive strengths. Likewise, when modelling props it may be necessary to restrict their tensile capacity if in practice they have insufficient fixity to resist tensile loads. For such situations a constitutive model with limiting tensile and compressive strengths will have to be employed.

Because most analyses of retaining structures assume plane strain or axi-symmetric conditions (i.e. a two dimensional idealisation), structural members will have to be represented in the same way, even though their geometry may be clearly three dimensional. For example a line of discrete props, each with a circular cross section, will have to be modelled as a continuous slab of constant thickness in the out of plane direction, see Figure 3.12. For structural elements modelled in this manner an equivalent stiffness in bending, compression or tension has to be used. Further details can be found in Chapter 9.

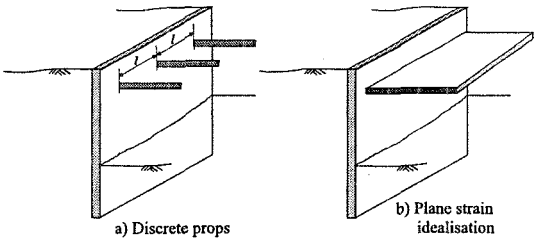

Figure 3.12: Plane strain idealisation of discrete props

3.4.5.2 Soil

Regarding the properties of the soil, it is important to use realistic constitutive models to represent the soil's behaviour. Appropriate methods of modelling soil behaviour are discussed in detail in Chapters 5 to 8 of Volume 1, and obtaining the relevant soil properties has been discussed in Chapter 1 of this book.

Two categories of soil can be identified, those soils which are used as backfill material, and those that are found in-situ. While the latter category of soils is present in all retaining structure problems, the former category is only relevant to a limited set of structures. The significance of the behaviour of each category depends on the type of retaining structure. For example, backfill will have a dominant effect on gravity and reinforced earth walls, whereas in-situ soils will dominate the behaviour of excavations supported by embedded and nailed walls.

Soils used for backfill purposes are usually free draining sands or gravels. However, occasionally clays are used. These soils are often modelled using either an elastic Mohr-Coulomb model, or a model of the Lade type (see Chapters 7 and 8 of Volume 1). If the former constitutive model is used, the elastic part of the model should preferable be nonlinear, with both bulk and shear stiffness dependent on stress and strain level (see Chapter 5 of Volume 1).

In-situ soils should be modelled using the most appropriate constitutive model that is available and that can be justified from the site investigation data. Ideally, this model should account for both nonlinearity at small strains and soil plasticity. The former being required to enable realistic predictions of displacements and the latter to limit the magnitudes of the active and passive earth pressures.

In cases where a relatively large amount of field data has been collected concerning movements around retained excavations, such as in London (e.g. Burland and Kalra (1986)), empirical correlations have been derived for soil stiffness. These are often obtained by back analysis. However, these relationships are usually linear elastic and are based on observations of movements made around deep excavations during construction and for only a very limited period after completion. Consequently, such relationships are not necessarily relevant to other ground conditions, the construction of other types of retaining structure or to long term conditions.

When long term performance is important, or where there is insufficient field data available to derive empirical relationships, such as those derived by Burland and Kalra (1986), then the only option is to rely on laboratory experiments on soil samples and in-situ field tests to derive suitable parameters for use in analysis. In most practical cases this is the situation facing the design engineer. For example, the coefficients and limits needed for the small strain model described in Section 5.7.5 of Volume 1 can all be derived from high quality triaxial tests which are now commonly undertaken by commercial laboratories. Alternatively, in the absence of such laboratory tests, these parameters can be derived from self boring pressuremeter tests, see Chapter 1.

Regarding the relative performance of the differing categories of constitutive model, the following points should be considered:

- It is apparent that in the overwhelming majority of cases simple, linear elastic analyses, using either isotropic or anisotropic constitutive models, are entirely inappropriate and can be misleading. In such analyses there is no restriction on the tensile stresses that can develop within the soil, nor the magnitude of the active and passive earth pressures.

  Considering a simple embedded cantilever wall with an excavation in front of it, tension in the soil behind the top of the wall will tend to hold the wall back. The displacement profile of the wall will be affected and consequently bending moments and forces induced in the structure. There is also no limit on the passive resistance that may develop in front of the wall.

  This can be illustrated by considering the example of the embedded cantilever wall shown in Figure 3.13. For simplicity the water table is assumed to be at considerable depth below the bottom of the wall and the soil is assumed to behave in a drained manner. Two analyses have been performed using the finite element mesh shown in Figure 3.6, one with an elasto-plastic (Mohr-Coulomb) and the other with a purely elastic constitutive model. The parameters for both analyses are given on Figure 3.13. In both analyses the elastic properties were identical.

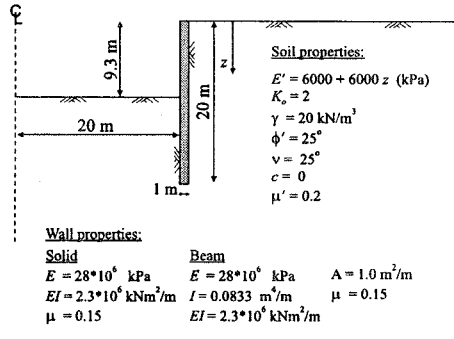

Figure 3.13: Embedded cantilever wall

  Excavation was carried out to a depth of 9.3m and the predicted horizontal displacement of, and bending moments in, the wall are shown in Figures 3.14a and 3.14b respectively. Clearly, there are large differences in the predictions from the two analyses, with the elastic analyses predicting unrealistic behaviour. The reason for this can be, partly, seen from Figure 3.15 which shows the predicted earth pressure distributions acting on the back and front of

the wall. The elastic analysis predicts tensile horizontal pressures and pressures below the active limit on the back of the wall, while on the front of the wall, just below excavation level, the predicted pressures greatly exceed the passive limit. The results from the elastic analysis would have been even worse if the elastic stiffness had been constant and not increased with depth.

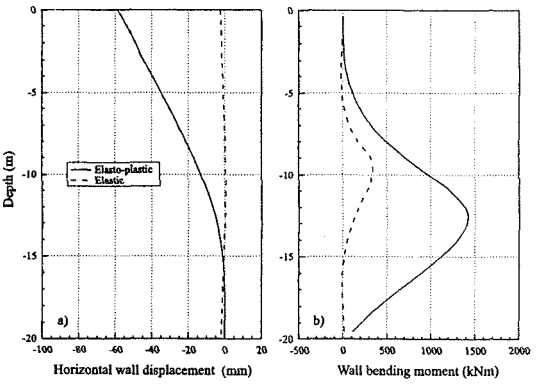

Figure 3.14: Comparison of elastic and elasto-plastic analysis of cantilever wall

- Linear-elastic perfectly plastic constitutive models do limit the tensile stresses in the soil and the active and passive pressures that can develop. However, they generally give poor predictions of both the extent and the distribution of ground movements adjacent to the structure under construction.

Beyond the zones immediately adjacent to the earth retaining structure where active and passive earth pressures may develop (the soil starts to behave plastically), or where loading causes the soil to yield, the soil's response is entirely elastic and reasonably uniform displacements are obtained. This is illustrated in Figures 3.7a and 3.8a where it can be seen that the use of linear elastic behaviour pre-yield, albeit with stiffness increasing with depth, results in surface settlement troughs behind the wall that are of a large and unrealistic extent. As noted in Chapter 4 of Volume 1, it is generally recognised that soil stiffness changes with varying levels of stress and strain, but these models take no account of such effects.

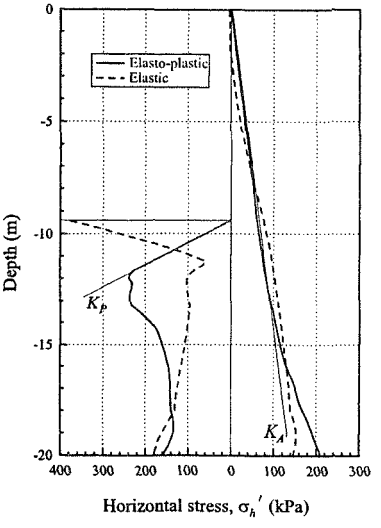

Figure 3.15: Earth pressures predicted by elastic and elasto-plastic analyses of a cantilever wall

- The use of nonlinear elastic perfectly plastic or strain hardening/softening plastic constitutive models generally gives much better predictions of

movements around retaining structures. Many of the constitutive models described in Volume 1 account for the variations in soil stiffness due to varying levels of both stress and strain.

Such models generally give much more realistic distributions of movements around retaining structures than the other two categories of models discussed above, because the extent of movement is limited. This is important when considering issues such as potential building damage of adjacent structures. It is the shape of the displacement profile, as much as the magnitude of displacements, that dictates the strains induced within the structure in question.

Predictions from such a constitutive model are shown in Figures 3.7b and 3.8b. The settlement troughs shown are much more realistic than those obtained from a constitutive model assuming linear elastic behaviour pre-yield.

3.4.6 Initial ground conditions

3.4.6.1 General

With the exception of embankments retained by reinforced earth walls or gravity walls, there is usually some excavation associated with the construction of earth retaining structures. Because the loading of the structure depends, in part, upon stress changes associated with this process, it is important that these stresses are estimated reasonably accurately.

Even if there is no excavation associated with construction of the structure, the initial stresses in the ground are important. For a simple gravity structure constructed on the ground surface the performance of the foundation, and consequently the structure, will be influenced by these stresses.

It is important to know the state of stress in the ground if any form of nonlinear constitutive model is being used to model soil behaviour. This includes linear elastic perfectly plastic models.

3.4.6.2 'Greenfield' conditions

'Greenfield' conditions are the un-modified initial stresses that exist within the ground, arising from the various geological processes that it has been subjected to. These stresses have not been modified by construction or any other man made activity. The earth retaining structure may have to resist these stresses either in whole or in part (some stress may be partially relieved before the structure is formed).

The geological processes that the soil has been subjected to will determine the ratio of the horizontal to vertical effective stress (i.e. the value of K_o). This ratio can have an enormous influence on the soil behaviour and consequently the performance of any structure within it, as demonstrated by Potts and Fourie (1986).

Consider an element of soil with an effective vertical stress of 400kPa. Points A, B and C on Figure 3.16 show the position in effective stress space for K_o values of 1.0, 1.5 and 2.0 respectively. The stress paths shown on this figure are those associated with a reduction of effective vertical stress under one dimensional conditions.

Considering the soil beneath an excavation and in front of an embedded wall, there is likely to be a greater extent of soil that has failed in passive stress relief, because if K_o is high then less straining is required for the soil to yield than if K_o was lower (i.e. in Figure 3.16 point C is closer to the failure envelope than point A). This has important implications for the long term performance of the structure and the short term behaviour if the rate of excavation is slow and rates of drainage are high. These effects will be discussed in subsequent sections.

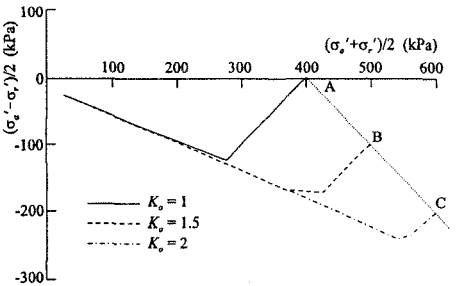

Figure 3.16: Stress paths for the swelling of clay from different K_o values

3.4.6.3 Modified initial soil stresses

The presence of adjacent structures (e.g. existing tunnels, deep basements, ground bearing or piled foundations, etc.) will inevitably modify the state of stress within the ground and these effects must be accounted for in any analysis. Such effects may influence the loads that the retaining structure has to carry. Before the earth retaining structure is formed, another structure may have loaded the soil or in the case of a tunnel there may have been some unloading.

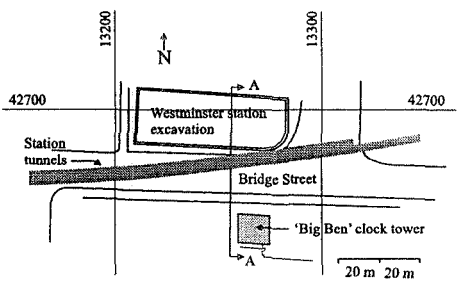

Figure 3.17: Plan of the site for the Jubilee Line station at Westminster

To illustrate this point, consider the example of the Jubilee Line Extension underground station at Westminster (Higgins *et al.* (1996)). Figures 3.17 and 3.18 show a plan and a cross section through the site respectively. The excavation for the station is 37m deep and is supported by 1m thick diaphragm walls, which in turn are supported by a series of temporary and permanent props. Close to the excavation are two tunnels. Also in very close proximity is the Big Ben clock tower, a historic structure of great significance.

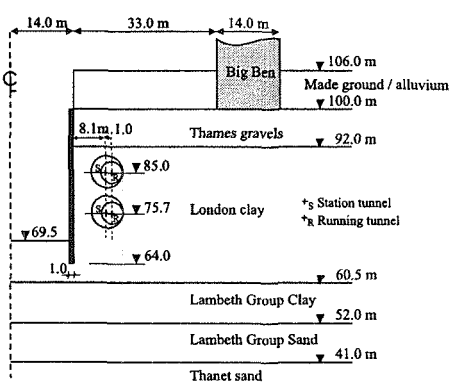

Figure 3.18: Cross-section AA of the Westminster site

A series of analyses were undertaken which modelled the construction of both the tunnels and the station box. A second series of analyses were also undertaken which modelled the construction of the station box alone. Figure 3.19 shows contours of stress level within the ground before and after tunnel construction. The stress level is a dimensionless measure of the available shear strength mobilised at a particular mean effective stress. It is defined in Appendix III.1. A stress level of zero corresponds to a state of stress in which $\sigma_1=\sigma_2=\sigma_3$ and a value of unity corresponds to a stress state on the failure envelope. The small excavation evident in the top left hand corner of the plots in Figure 3.19 is a temporary excavation performed prior to tunnel construction and is not the main excavation for the station box.

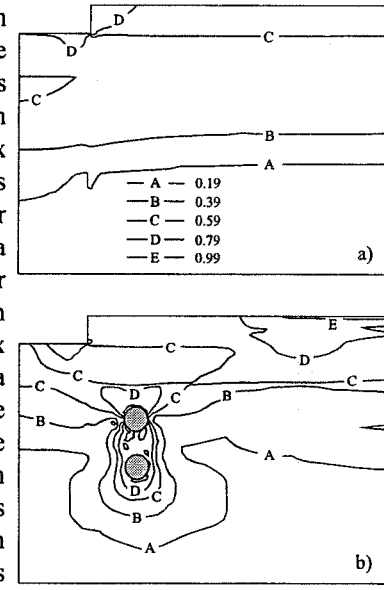

Figure 3.19: Contours of stress level a) before and b) after tunnel construction

Inspection of Figure 3.19 clearly shows that construction of the tunnels has modified the stresses within the ground close to the position where the main walls for the station box are to be constructed (at this stage these walls are not present in the analysis). The soil in this location has been unloaded and consequently the loads imposed on the walls when they are constructed will be affected.

Figure 3.20 shows the wall displacements for comparable analyses with and without the tunnels present. These correspond to the condition where construction of the station box is complete. It is apparent that the presence of the tunnels affects the wall displacements. This is not an uncommon situation in a dense urban environment such as London, with an extensive underground system. This example demonstrates the importance of modelling the complete pre-construction history.

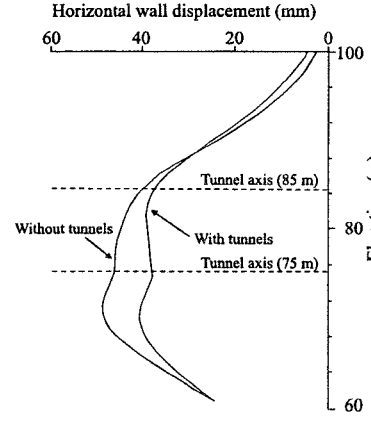

Figure 3.20: Horizontal displacements of station box walls with and without tunnels in analysis

Groundwater conditions may also have been modified as a result of the presence of an adjacent structure. There may be seepage around an impermeable basement wall, there may be a tunnel which is not watertight and tends to drain the

surrounding ground, or there may even be a supply of water from some source. These effects also have to be considered, particularly when using the more complex constitutive soil models.

3.4.7 Construction method and programme

3.4.7.1 General

Consideration must be given to how the structure is to be constructed (temporary as well as permanent works) and the time taken to construct it. Different sequences of construction mean that soil may experience differing stress paths, yield may occur in soil elements at differing times or be suppressed completely. As a consequence additional forces, such as swelling pressures, might be imposed on the structure. Further, if construction is slow some drainage may occur within the ground, which might reduce long term effects. However, if significant drainage does occur there may be some implications for the design of temporary works.

3.4.7.2 Construction method

In order to illustrate the effect of differing methods of construction, the example of the road tunnel, shown in Figure 3.3, is considered. Analyses have been performed in which the tunnel has been built in two ways, firstly by 'top down' and secondly by 'bottom up' construction. In both types of construction the walls were constructed first. For the top down construction excavation to a level just below the underside of the roof slab was performed, the roof slab was then constructed before further excavation. In the bottom up construction excavation to the underside of the road slab was performed and the road slab cast with some temporary propping provided. The roof slab was then cast and then the temporary propping removed.

The different methods of construction necessitated differing methods of supporting the walls. In the analysis with the bottom up method there was actually a discontinuous temporary prop (a series of tubular steel sections along the length of the tunnel) between the walls during excavation, with a nominal stiffness approximately 10 times less than that of the roof slab.

Table 3.2 summarises the predicted bending moments in the walls for both methods of construction at the stage in the analyses where the structure has been completed, but drainage in the soil has yet to occur. Even for this relatively simple problem, a relatively shallow excavation of between 8 to 10 m depth with a single prop for the walls, there is a variation in bending moments of up to 20% attributable to differing construction methods. Without the temporary prop the differences would have been even greater.

The analysis of the George Green cut and cover tunnel (Potts and Knights (1985)) is another good example of how the construction method influenced the form of the analysis. Figure 3.21 shows a cross section through the tunnel. The geometry of the tunnel is approximately symmetrical about the centre line of the tunnel and, as with the example discussed in Section 3.4.2, it is very tempting to model this as a 'half section'. Doing so would have been a very serious mistake.

Table 3.2: Summary of bending moments for alternative methods of construction

Method of construction	Wall	Bending moment (kNm/m)	
		Max.	Min.
Top down	Left	1226	-18
Bottom up	Left	1484	-14
Top down	Right	6	-1322
Bottom up	Right	6	-1452

Although the geometry was symmetric, the method of construction was not. The embedded walls were installed first. There was a preliminary excavation to allow the roof slab to be constructed, but soil was then excavated out to the underside of the base slab to form one half of the tunnel. The base slab for this half of the tunnel was then cast before excavation started for the other half of the tunnel. The effect of this construction procedure on the central wall is shown in Figure 3.22. An analysis of only half the section would have suggested that there was no bending or lateral displacement of this wall.

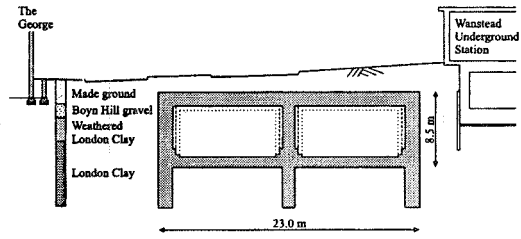

Figure 3.21: Cross-section of the George Green Tunnel

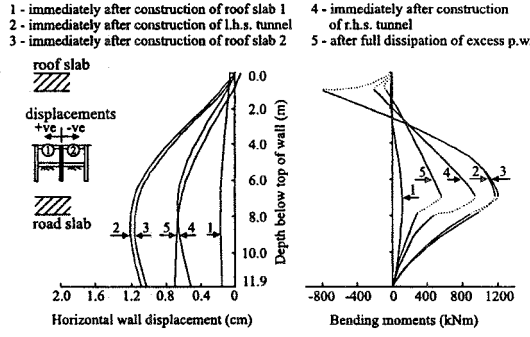

Figure 3.22: Bending moments and displacements for the central wall

3.4.7.3 Time related movements

To make an assessment of time related movements, analysis need to be time related and therefore an analysis with fully coupled consolidation is generally required, see Chapter 10 of Volume 1. For such analysis it is necessary to specify pore water pressure and/or

flow boundary conditions in addition to displacements and/or forces. In addition, the permeability of the soil has to be known in order to make a reasonable estimate of how much drainage may occur during construction. Unfortunately, this is a notoriously difficult parameter to measure and therefore it is normally prudent to consider a range of values and perform a small parametric study.

Not only must the magnitude of the permeabilities be correct, but also their distribution, particularly where under-drainage exists. The permeability distribution has to be consistent with the initial steady state pore water pressure profile. Otherwise, during the course of the analysis drainage will occur as the pore water pressures try to come into equilibrium with the boundary conditions. This problem is discussed in greater detail in Chapter 9.

3.4.7.4 Ground water control

Measures taken for groundwater control, during construction and in the long term, are also an important consideration. De-watering may be necessary to form an excavation. For example, consider the case shown in Figure 3.23 in which an excavation is to be made at a site in which clay overlies sand and the water table is near to the ground surface. Unless the sand within the excavation is de-watered, a base heave failure will occur during the excavation process, when the total vertical stress imposed by the remaining clay equals the pore water pressure in the sand at the sand-clay interface. Such de-watering must also be simulated in any analysis.

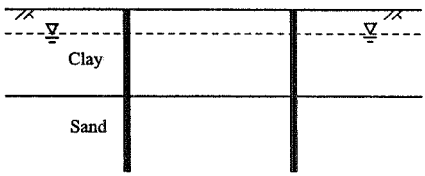

Figure 3.23: An example of the necessity for de-watering

Once construction is complete, measures may need to be taken to minimise the effects of long term heave beneath a structure. Voids may be left beneath ground slabs to allow for the ground to swell without imposing any load on the structure. In such situations water would have to be pumped from the void. Alternatively pumping or drainage systems may be installed to minimise pore water pressure changes and the consequent loading on the structure.

Another important consideration is the boundary condition applied to excavated surfaces. Is there a supply of water which will help promote swelling within the soil, or do excavated surfaces remain impermeable? In such situations the precipitation boundary condition described in Section 10.6.6 of Volume 1 may be more appropriate than either a pore water pressure or no-flow boundary condition.

3.5 Gravity walls

3.5.1 Introduction

When the retained height is not large, typically less then 5m, soil movements are not important and construction space is not limited, gravity type retaining walls are

often used. There is a variety of forms of gravity wall and some examples are given in Figure 3.1. To maintain stability this category of retaining walls relies on the weight of the wall (and any enclosed soil) and the shear resistance between the base of the wall and underlying soil to resist the earth pressures generated by the retained ground.

During design these walls should be checked for overall stability, sliding, overturning and bearing capacity failure, see Figure 3.24. As this type of structure is not usually used where there are adjacent structures and/or services which are sensitive to ground movements, displacements are not usually explicitly calculated. In many design codes it is often implicitly assumed that if there is a sufficient margin of safety against instability, then movements will be acceptable. If movements are of concern it may be better to use a different form of retaining structure, such as an embedded wall, see Figure 3.1.

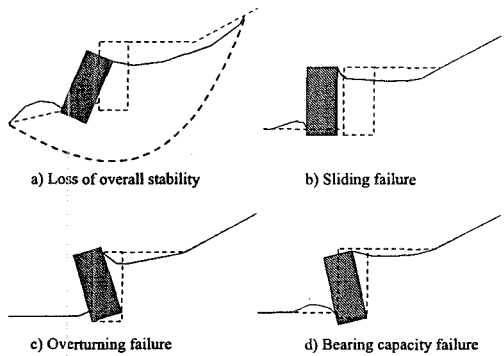

Figure 3.24: Limit states for gravity walls

As there exists considerable experience with the design of this type of wall, and as movements are not usually of concern, numerical analysis is rarely performed for standard gravity wall types. However, there may be situations where movements are of concern, or where the soil conditions are unusual or the structure has dimensions outside current experience. In such cases numerical analysis can be used. Such analyses can investigate all the potential instabilities shown in Figure 3.24, as well as provide an estimate of movements.

The rest of this section will consider some of the important issues concerned with the numerical analysis of gravity retaining walls. Although reinforced earth and nailed walls are gravity walls, they have additional complications associated with internal stability. Consequently, this type of retaining structure is discussed separately in Section 3.6.

3.5.2 Earth pressure due to compaction

In many situations gravity walls are built on a foundation, with backfill placed behind them. Therefore it is necessary to consider not only the properties of the structure and the behaviour of the foundation (as noted in Figure 3.24 bearing capacity may be an issue), but also the nature of the backfill. As most backfills are compacted in layers, stresses will be imposed on the retaining wall due to the compaction process. However, there are very few reliable measurements of these stresses from which suitable values may be deduced.

Although numerical procedures do exist for estimating compaction stresses (e.g. Duncan and Seed (1986)), these are generally quite complicated and may be problematic with highly nonlinear soil models. Because of the lack of reliable field data, validating these procedures is also difficult. It is much simpler to specify the horizontal stresses in layers of fill, as a proportion of the vertical stress, as they are constructed during an analysis, see Section 3.7.9 of Volume1.

In practice the backfill may be constructed in many layers. Simplifications will therefore often have to be made in an analysis and much fewer layers used. A discussion on the problems of selecting the number of layers and choosing the horizontal stress ratio is given in Section 5.3.4 in relation to embankment construction.

3.5.3 Finite element analysis

The main issues involved with the numerical analysis, apart from selecting appropriate constitutive models for the structure, foundation and backfill, are the simulation of the construction procedure and the modelling of the interface between the soil and structure.

As noted above, the stability of a gravity wall is mainly derived from the shear stresses mobilised along its base. This in turn is a function of the vertical force on the base and the cohesion and angle of interface friction between the base and the underlying soil. The vertical force is derived from the weight of the wall (including any inclosed soil) and the vertical shear force imposed on its back by the retained soil. The latter force is dependent on the cohesion and angle of interface friction between the back of the wall and the retained soil. Clearly, the interface properties between the wall and the soil, both foundation and retained, can have a dominating effect and must be accurately modelled in any analysis. The most appropriate way of doing this is to include interface elements within the mesh, see Figure 3.25. However, there are drawbacks and limitations associated with the use of such elements. These are discussed further in Chapter 9.

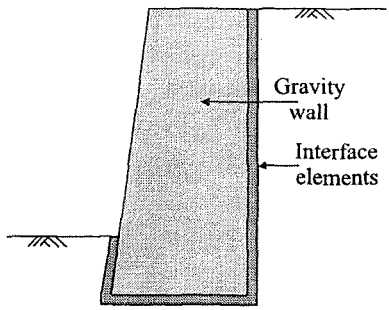

Figure 3.25: Position of interface elements in gravity wall analysis

Once the construction procedure has been established, and in particular the number of layers to be used in backfill construction, the finite element mesh can be developed. Clearly, each layer of backfill must consist of a finite set of elements (i.e. elements cannot span more than one construction layer). During the analysis problems are often encountered due to inadmissible stresses arising in elements that have just been constructed. This is usually a consequence of the elements 'hanging' on the wall during the construction process resulting in tensile stresses. This problem, and some solutions, are discussed further in Chapter 9.

Gravity walls may be constructed in cuttings. Certainly this was a common technique before modern plant enabled alternative methods of construction to be developed (e.g. diaphragm walls, etc.). In this instance the analysis must model the cutting which may be backfilled completely behind the wall or only partially, see Figure 3.26. Depending on the time that the cutting has to stand, there may be some drainage within the foundation and softening towards the base of the slope. This may affect the subsequent performance of the structure.

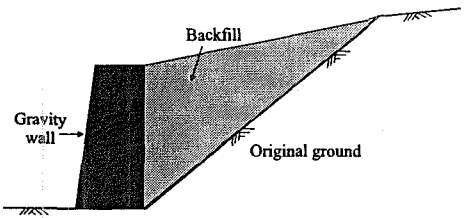

Figure 3.26: Cutting behind the gravity wall

On occasions these walls can have piled foundations simply to resist a large overturning moment. An example is a quay wall, where piles may be installed to increase the capacity of the quay to resists forces from ship impact and mooring lines. Other measures to increase capacity, such as anchors, may be included for a variety of reasons. Again these piles or additional means of support have to be modelled realistically.

3.6 Reinforced earth walls

3.6.1 Introduction

Following its first modern applications in France in the 1960's, reinforced earth has become an increasingly popular alternative to gravity retaining walls. The method has been shown to be significantly more economic in many situations, due to the efficient use of material and its favourable distribution of load on soft foundations. The mechanical properties of the soil are supplemented by the addition of reinforcement with a tensile capacity, to allow the soil mass to become self supporting.

Reinforced earth walls generally have a facing membrane which is normally non-structural and reasonably flexible, its purpose being to prevent local unravelling of soil. In their original format reinforced walls were constructed by backfilling in layers, see Figure 3.27. A typical situation might be as shown in Figure 3.28. A membrane unit is placed on a purposely built foundation and is temporarily supported while a layer of soil is backfilled behind it. When this layer reaches mid-height of the membrane unit, a reinforcing strip is

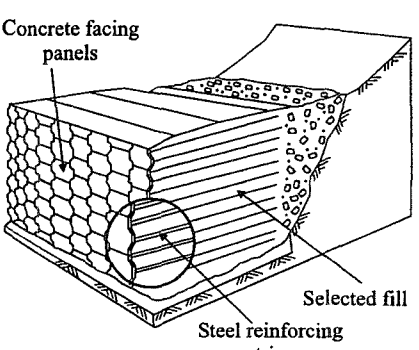

Figure 3.27: Typical construction details of a reinforced earth wall

placed on top of it and is connected to the membrane unit. Further backfill is placed until it reaches the top of the membrane unit. The temporary support to the unit is then removed and used to support the next membrane unit, which is positioned on the top of the previous one. The process is repeated until the desired wall height is achieved. In practice there have been many variations on this basic construction process.

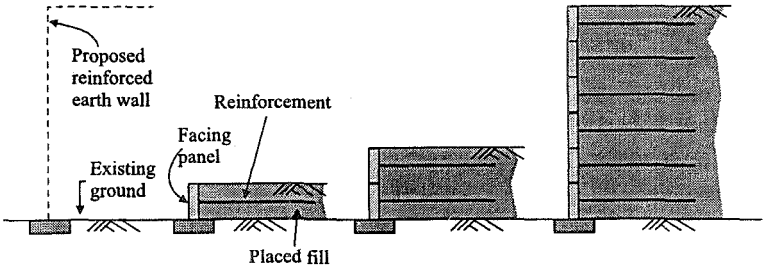

Figure 3.28: Typical construction procedure for a reinforced earth wall

Originally the reinforcement consisted of thin strips of metal which were connected to the facing membrane and run back 5m to 10m into the backfill. These strips are typically 100mm to 400 mm wide and are not continuous in the out of plane direction. They rely on interface friction for their pull-out resistance. Nowadays sheets of geotextile are sometimes used. These are continuous in the out of plane direction. The same sheets can also be used to form the facing membrane, see Figure 3.29. Some of these geotextiles have a mesh like appearance and their pull out capacity is a function of both interface friction between the fabric and the soil and bearing capacity failure of the soil in front of the individual components making up the edges of the holes in the geotextile, see Figure 3.30.

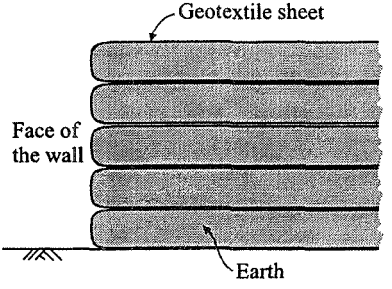

Figure 3.29: Geotextile used as facing membrane

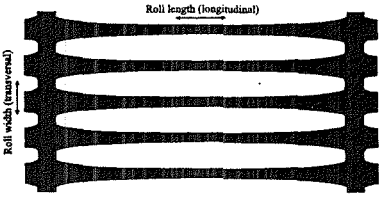

Figure 3.30: Example of geotextile membrane

Further developments have been to replace the reinforcing strips or sheets by discrete anchors (Harris *et al.* (1993)), see Figure 3.31. The anchors can be made from bent steel bars, blocks of concrete or even old car or lorry tyres. The anchor cables can be

metal or some form of rope material (e.g. Paraweb). The reinforcing effect is now derived from the pull out resistance of the anchor blocks.

Both the reinforced and anchored walls described above are constructed using back fill. An alternative approach sometimes used to form a reinforced wall in-situ is to use soil nails. This technique involves excavating a shallow depth in front of the wall (typically 1 to 2m), applying a layer of shotcrete over a reinforcing mesh and installing a row of soil nails. The wall is formed from the top downwards by a sequence of such steps, see Figure 3.32. The spacing and type of nails used are dependent on the nature of the soil and the size and geometry of the structure. There are different types of nails available: bored and grouted, jet-grouted, driven and more recently ballistically fired steel rods. Grouted nails have been used most extensively for retaining wall construction, as they provide a greater surface area for mobilisation of friction and can be installed to a greater distance into the soil mass than driven or fired nails. They are usually angled slightly downwards to facilitate grouting operations.

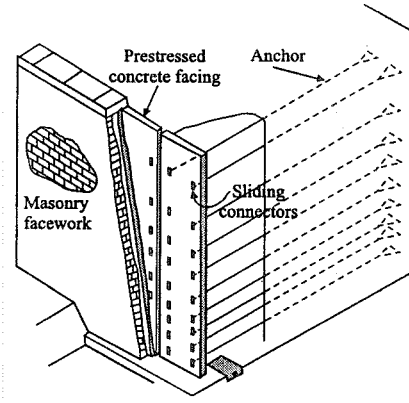

Figure 3.31: Example of a anchored earth wall

Reinforced soil walls can fail by a number of mechanisms, see Figure 3.33. Assuming that the reinforced earth mass is suitably reinforced, failure can occur as a result of global instability, in much the same way as discussed above for gravity walls.

In addition, failure can occur as a result of internal instability. For example, the reinforcement itself can rupture resulting in a loss of tensile strength and possibly triggering a global failure of the reinforced earth wall. Alternatively, as the integrity of the reinforced soil mass is dependent on the stress transfer between the soil and the reinforcement, contact failure can result in pull-out of the reinforcement or block sliding of the soil along the planes of reinforcement, if the reinforcement forms continuous sheets.

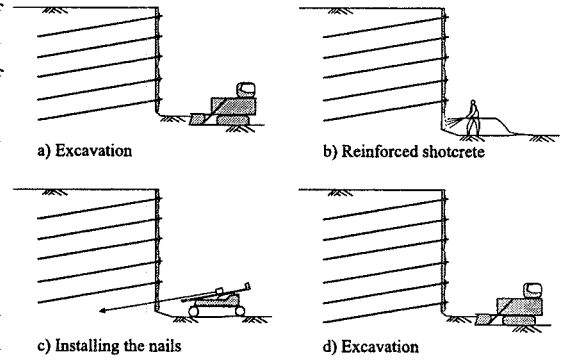

Figure 3.32: Construction sequence for a reinforced wall using soil nailing

A further mechanism induced within the reinforced mass is caused by the use of reinforcement of insufficient stiffness. In this situation, if sufficient strains have accumulated within the soil mass before full strength of the reinforcement has been mobilised, a displacement induced failure can occur. This mechanism is particularly important when considering the long term effects of plastic creep in geotextile reinforcement. An example of this type of failure for a reinforced embankment is given in Section 5.5.6.

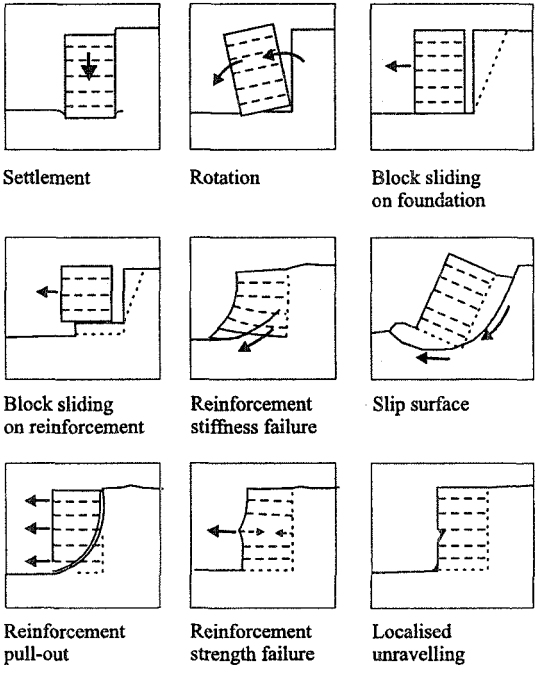

Figure 3.33: Possible failure mechanisms for reinforced soil wall

3.6.2 Finite element analysis

From the above discussion it is clear that reinforced earth walls come in many different forms, each of which will have its own particular modelling problems. Within this text it is not possible to discuss all the issues involved. They are very complex and would probably justify a text on their own. Instead, finite element analysis of a conventional reinforced earth wall will be discussed in detail. Many of the modelling problems associated with this type of structure will also be applicable to other forms of reinforced earth walls. Some of the more important issues with these other wall types will then be discussed. A plane strain situation is assumed.

Figure 3.34 shows part of a finite element mesh used to analyse a reinforced earth wall with a maximum height of 13m. The figure shows the detailed part of the mesh in the vicinity of the wall. The complete mesh extended further in both the lateral direction and with depth. The reinforcing elements extended 7m into the backfill and had 1m vertical spacing. Consequently there is only a single row of solid elements between each reinforcing level. While this is acceptable for the present demonstration, in practice it is advisable to use more than one row of elements.

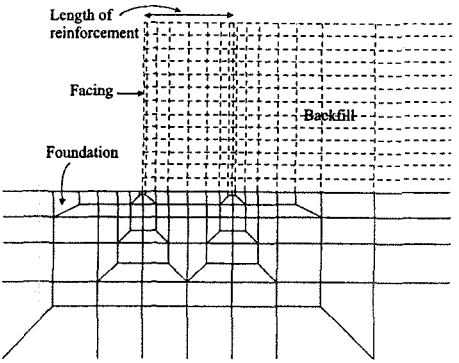

Figure 3.34: Finite element mesh for a reinforced earth wall

The reinforcing layers were simulated using membrane elements which had a capacity to resist only tensile forces. The facing membrane was modelled using discrete Mindlin beam elements, while the interfaces between them and the soil, and between the membrane elements and the soil were modelled using zero thickness interface elements, see Figure 3.35. It should be noted that the beam elements representing the facing units were not continuous but were discrete, in this example a single element for each facing unit. It is often necessary to use beam elements as opposed to membrane elements to model the facing units, as these elements can be given some bending and shear stiffness to resist the local unravelling of the soil immediately adjacent to the facing unit.

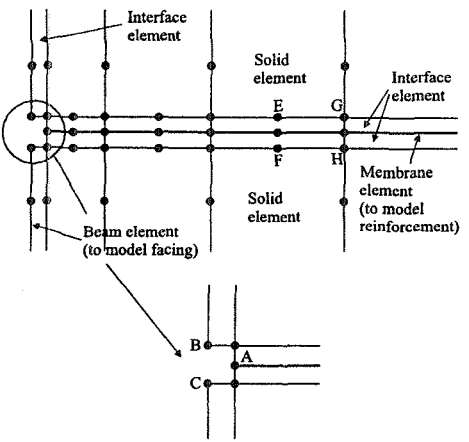

Figure 3.35: Modelling details of reinforcing layer and facing membrane

The stability of a reinforced earth wall is dependent on the mobilisation of the reinforcing element strength. This can only be achieved once the reinforcement is in a position to withstand tensile forces which do not occur until it is attached to the facing units and has normal stresses applied along its length. Consequently, there is a stage of the construction process during which the uppermost soil layer is unsupported and in the absence of cohesive strength will suffer local failure unless temporary support is provided.

To avoid this local instability the following construction procedure could be employed, see Figure 3.36:

- The first soil layer along with the beam, membrane and interface elements, representing the facing unit, and the first layer of reinforcing are constructed, see Section 3.7.9 of Volume 1. During this process zero horizontal displacement boundary conditions are applied to the nodes of the beam element representing the facing unit to provide temporary support. To simulate the connection between the reinforcing strip and the facing unit the horizontal displacements of the node on the membrane element nearest to the facing unit, (i.e. node A in Figure 3.35) are tied to those of the nearest node on the facing unit (i.e. node B). The vertical displacements of these nodes are also tied.

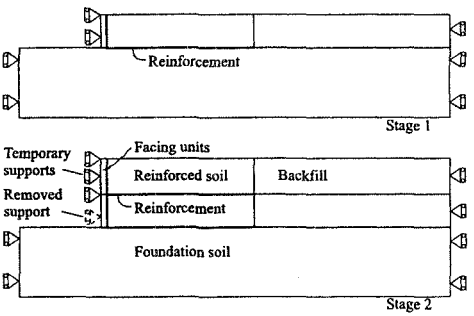

Figure 3.36: Finite element modelling of construction sequence

- The next layer of backfill along with the beam, membrane and interface elements representing the second facing unit and the second layer of reinforcing are then constructed. Zero horizontal displacement boundary conditions are applied to the nodes of the beam element representing the new facing unit to provide temporary support. The displacement boundary conditions that were imposed on the first facing unit are removed. This involves turning this boundary condition off and removing the nodal reactions that were created in the previous stage at these nodes.
- This process is repeated for the additional layers of backfill. However, it should be noted that to model the connection between the reinforcing strips and the facing units, the horizontal displacements at nodes A, B and C (see Figure 3.35) should be tied for each reinforcing strip. Similarly, so should the vertical displacements at these same nodes. It should be noted that as the facing elements are not connected to each other and as their rotations are not tied, they cannot directly transmit moments to each other. Clearly these tied boundary conditions might change depending on the finer details of the construction process and the connection between reinforcing and facing unit.

Specifying the material properties for the membrane and interface elements is also problematic. If the reinforcement is a geotextile, it is usually continuous in the out of plane direction and therefore compatible with the plane strain assumption. However, as noted previously, its pull out resistance is derived from friction generated on the soil-reinforcement boundary and the in plane bearing capacity of the soil within the holes of the geotextile, see Figure 3.30. As these holes are not

modelled by the combination of membrane and interface elements, an approximation has to be made. There are several empirical methods for accounting for both components. A convenient method is to assume that the maximum shear stress that can be mobilised in the interface elements is given by:

$$\tau = \sigma_n' \mu \tan\varphi' \tag{3.1}$$

where φ' is the angle of shearing resistance of the backfill and μ accounts for both bearing and frictional effects. μ can be found from shear box interface tests performed on the reinforcement and can have values greater than unity.

If the reinforcement is steel strips then its pull out resistance is mobilised from interface friction with the soil. However, as the reinforcement is not continuous in the out of plane direction, it is not consistent with the plane strain assumption and again an approximation has to be made.

One approach to the problem is to model the interface elements as having equivalent frictional contact strength, by considering the relative areas and μ values of the soil to soil and soil to reinforcement interfaces. However this approach does not provide logical results. For example, if the width of the strip increases the proportion of soil to reinforcement surface area (μ<1) increases relative to the soil to soil surface area (μ=1) and there is a corresponding drop in the effective contact strength.

In addition, failure of the interface elements will result in block sliding as noted in Figure 3.33. This does not accurately represent pull-out failure as it disregards the soil to soil connectivity in the discontinuities between the reinforcement elements in the horizontal out of plane direction.

A possible solution to the problem is to tie adjacent nodes of the soil elements together across the reinforcement. For example, the vertical displacement of nodes such as E and G in Figure 3.35 are tied to nodes F and H respectively. Likewise the horizontal displacements of these nodes are also tied. This approach has the advantage of modelling the soil continuity while still allowing failure along the soil-reinforcement interface.

A better solution to the problem would be to perform three dimensional analyses. If the wall satisfies most of the assumptions of plane strain, apart from

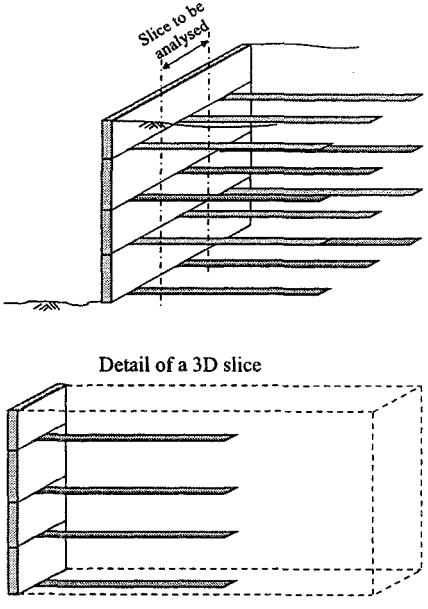

Figure 3.37: 3D modelling of a reinforced earth wall

the reinforcement not being continuous in the out of plane direction, then use can be made of planes of symmetry and only a three dimensional slice of the wall needs to be analysed, see Figure 3.37.

If the wall is reinforced with anchors as shown in Figure 3.31, plane strain conditions are again not really appropriate and in principle full three dimensional analyses are required. However, with present computer hardware this is not practical and further assumptions are made to model the anchors. This problem and some of the solutions available are discussed further in Chapter 9.

Additional problems arise with nailed walls. Not only are the nails not really applicable to a plane strain assumption, but problems also arise because at the start of the analysis they have not been installed. For example, consider the situation shown in Figure 3.38. At the beginning of the analysis the membrane (or beam) and interface elements are not present in the mesh. Consequently, there are slots (holes) in the mesh at the nail positions. Clearly it would be unwise to perform analysis with these holes in the mesh. To get around the problem, the adjacent nodes on either side of a slot must have their displacements tied. These ties are removed once the membrane (or beam) and interface elements representing the anchor are constructed.

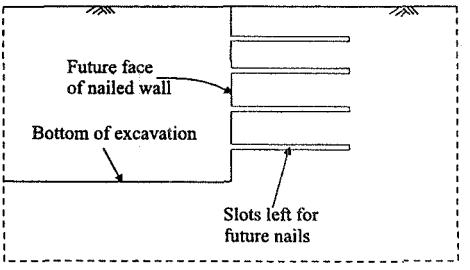

Figure 3.38: Difficulties in modelling soil nails

3.7 Embedded walls

3.7.1 Introduction

The most common use of concrete embedded walls (such as diaphragm, secant pile and contiguous pile walls, see Figure 3.39) is to support the sides of deep excavations, or tunnels which are formed by various means (cut and cover, top down, etc). While steel sheet piles can be, and are, used for this purpose, concrete walls are also used to form bridge abutments and quay walls.

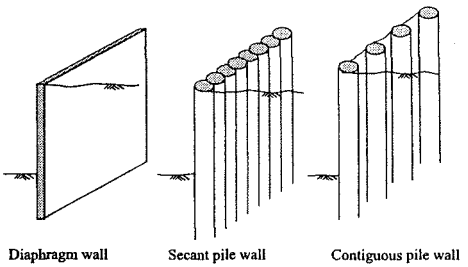

Figure 3.39: Types of embedded wall

Under some circumstances these walls may also be used to limit ground movements within another structure such as an embankment or cutting, or to control groundwater (slurry walls to cut off water flow into an excavation or cutting). However, the following discussion is aimed solely at the first category.

3.7.2 Installation effects

3.7.2.1 General

This is an extremely complex issue which is generally ignored in most numerical analyses. In most instances the walls are 'wished in place'. This is the term usually used to indicate that installation effects have been ignored and implies the assumption that there is no increase or reduction in stresses associated with installation of the walls.

In reality, concrete piled walls are constructed as a series of individual bored piles and diaphragm walls are constructed as a series of individual panels. During construction the holes in which the piles or diaphragm wall panels are concreted maybe supported temporarily (e.g. by bentonite slurry). This is obviously a very three dimensional process and not easily approximated by a two dimensional analysis. There is some stress redistribution around these individual elements, both horizontally and vertically (Huder (1972), Davies and Henkel (1982)).

Likewise the installation of steel sheet piles will alter the stresses within the adjacent ground.

3.7.2.2 Field measurements

Intuitively it can be expected that wall installation will cause some change in the stresses within the ground surrounding walls, and some stress changes associated with this process have been measured for concrete walls (Symons and Carder (1993)). Despite this work the significance of these stress changes is difficult to quantify.

Symons and Carder (1993) suggest that total stress reductions of up to 10% may occur close to bored piles in a stiff over-consolidated clay, whereas for a diaphragm wall this may be as high as 20%. A value of 30% was inferred from measurements at the Bell Common tunnel (Tedd *et al.* (1984)), but there are some doubts concerning the reliability of these particular observations.

Current evidence is that, with reasonable workmanship, installation effects are reasonably localised. Inevitably on some occasions effects are more widespread, particularly when there are significant losses of fluid supporting the excavation for a pile or panel to the surrounding ground.

One example of where significant movements, and presumably corresponding stress changes, associated with wall installation did occur, was presented by Davies and Henkel (1980). The diaphragm walls were intended to support the sides of an excavation for Chater Station in Hong Kong. During installation of the panels settlements of up to 78mm were observed adjacent to the wall. By the time the wall was completed movements were detected at up to 50 m away from the wall (the panels were up to 37m deep). The conclusion was that:

> "Horizontal movement adjacent to individual panels was a result of swelling of the decomposed granite which created a compressible zone around the diaphragm wall panel. On construction of adjacent panels, the arching around the compressible zone broke down and re-compression occurred as the earth

pressures built up. This caused horizontal ground movements to extend back from the diaphragm wall, which resulted in large displacements".

Obviously this is a very complex mechanism and very difficult to reproduce in any analysis. Such large movements were not expected before construction started, but to try to minimise these effects subsequently panel lengths were reduced and slurry pressures increased.

There is little field information available concerning displacements and stress changes associated with the installation of sheet piling.

3.7.2.3 Analysis

The issue is whether or not installation effects should be represented in any analyses, or should it be assumed that measures will be taken during construction to mitigate such influences. It should be remembered that in many situations embedded walls are being used because movements are critical and therefore every effort will be made to minimise movements during wall installation. As stress changes within the soil only occur if movements are allowed, minimising the latter will also limit the former.

A number of researchers have tried to analyse these effects (for example Higgins (1983), Ng (1992), Gunn *et al.* (1993) and De Moor (1994)). Unfortunately none of these approaches has been entirely satisfactory because they have not realistically considered three dimensional effects, see St John *et al.* (1995)).

More recently some results of three dimensional analyses involving wall installation have been published (e.g. Schweiger and Freiseder (1994) and Gourvenec (1998)), but these analyses have generally used very simple constitutive models and very crude meshes. Such simplifications were necessary because, as noted in Chapter 11 of Volume 1, very large computer resources are needed to perform full three dimensional analyses. It is therefore questionable how realistic were the predictions of remote movements associated with wall installation. Since the purpose of trying to model wall installation is normally to assess remote movements, and because allowing soil stresses to relax is generally not conservative as far as the design of structures is concerned, it is questionable how valuable these studies were. To get a better understanding of the process more sophistication is required.

One example where this issue had to be addressed was the design of a pin-joint connection between an inclined road slab and a contiguous bored pile wall for an underpass (Higgins *et al.* (1999)). The connection between the slab and the wall was a pre-cast concrete hinge with a rounded stainless steel bearing, see Figure 3.40.

The designers were extremely concerned about the ratio of the horizontal to vertical thrust in this joint under long term conditions and they placed a limit on this 'thrust ratio'. Assuming that the wall was 'wished in place' would allow no stress relief during installation. For any given assumption concerning the

coefficient of earth pressure at rest, K_o, it was considered necessary to examine what reduction in horizontal stress may occur by installation of the bored pile wall. This was considered likely to affect the thrust ratio.

To make an assessment of these effects, a series of plane strain finite element analyses were undertaken, which modelled the complete construction sequence and long term conditions. These analyses started with the finite elements representing the wall being excavated and simultaneously replaced by a fluid pressure equivalent to wet concrete. This allowed some relaxation of the stresses within the soil and enabled the 'thrust ratio' to be evaluated. Because these analyses were two dimensional plane strain analyses they actually represented the excavation of an infinitely long slot. Since this method is likely to overestimate the effects of installation, it was actually a conservative approach providing a bound to the problem. The other bound came from an analyses in which the piles were 'wished in place'.

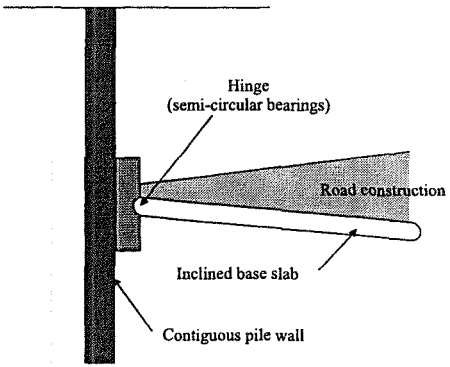

Figure 3.40: Cross-section of an underpass

3.7.2.4 Comments

To model wall installation realistically a fully three dimensional approach is required. Even then the sequence of pile or panel installation will need to be known, in order to correctly account for the effects such as arching around the individual excavations (piles or panels).

This is apparent from the Chater Station case history described above. If it had been possible to analyse construction of the wall realistically (i.e. a fully three dimensional analysis, a representative soil model and realistic boundary conditions), then some indication of the problems might have been obtained. Relatively simpler procedures, such as those currently proposed, are unlikely to have been of much assistance.

Each case has to be considered on its merits. If it is necessary to account for installation effects, care must be taken in any analysis to ensure that the results are not simply a consequence of the applied boundary conditions, as discussed by St John *et al.* (1995). Care must be taken to ensure that these effects are not over-estimated, since this could have serious implications for the design of the structure. A cautious approach is required.

3.7.3 Modelling of walls

3.7.3.1 Element type

A major concern when modelling embedded walls is the choice of finite element type to represent the wall itself. If the wall is a diaphragm, secant pile or contiguous pile wall, see Figure 3.39, then it is relatively thick (usually greater than 0.8m) and solid elements are probably appropriate. However, if the wall is made from steel sheet piles, then the use of beam (or shell) elements is more appropriate. However, in either case solid or beam (or shell) elements can be used.

As noted in Chapter 3 of Volume 1, beam (or shell) elements provide an efficient but approximate way of modelling structural members. They are approximate in the sense that they reduce one dimension of the structural member to zero. For example, if used to model an embedded retaining wall, the wall is essentially modelled as having zero thickness. At first sight this approximation may seem reasonable and consequently the approximation is often overlooked in practice. However, the approximation can have a significant effect on the analysis of an embedded retaining wall.

As an example consider the embedded cantilever wall shown in Figure 3.13. The wall is 1m thick and 20m deep and is made of concrete. The properties of both the soil and wall are given on Figure 3.13. To simplify matters the water table is assumed to be at depth below the base of the wall.

Analyses have been performed in which the wall was modelled using a single column of solid elements, with the finite element mesh shown in Figure 3.6. Two analyses have been performed, one with $K_o = 2.0$ and the other with $K_o = 0.5$. The analyses have also been repeated with a similar mesh, but with Mindlin beam elements used to model the wall. The predicted horizontal wall displacements and associated bending moments for the analyses with $K_o = 2.0$ are given in Figure 3.41. These predictions correspond to an excavation depth of 9.3m. Corresponding results from the analyses with $K_o = 0.5$ are given in Figure 3.42.

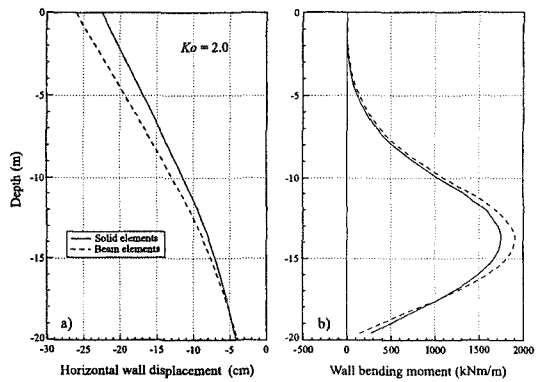

Figure 3.41: Effect of wall element type in a $K_o = 2.0$ soil

For both K_o values the use of beam elements to represent the wall results in larger horizontal movements and bending moments. This is particularly so for the analyses with $K_o = 0.5$ were the maximum wall displacement and the maximum bending moment are 33% and 20% respectively greater for the analysis using beam elements compared to the analysis using solid elements to represent the wall. The differences are smaller for the analyses with $K_o = 2$.

The reason why there are differences between the analyses modelling the wall with solid and beam elements is due to the vertical shear stresses mobilised on the back of the wall. For the analyses using solid elements, these shear stresses act downward at a distance of 0.5m (half the wall thickness) from the neutral axis of the wall. They therefore provide a clockwise moment which partially offsets the anticlockwise moment generated by the horizontal stresses acting on the back of the wall. While these same shear stresses are mobilised on the wall in the analyses using beam elements to represent the wall, the wall has no thickness and therefore there is no lever arm and no clockwise moment. Hence the difference in results.

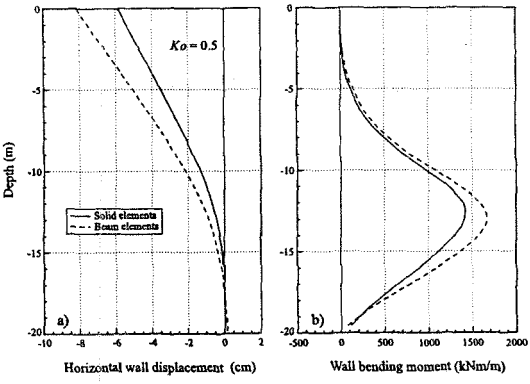

Figure 3.42: Effect of wall element type in a $K_o = 0.5$ soil

The same potential error is likely to arise when modelling sheet pile walls using beam elements. Although the steel sheet piles are made of relatively thin steel sheet, the shape of the sections in plan gives the wall an equivalent thickness, see Figure 3.43.

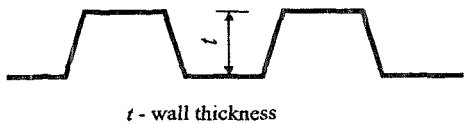

Figure 3.43: Detail of a sheet pile wall

Clearly care must be exercised when using beam (or shell) elements. As noted above, the relative magnitude of the effect depends on the value of K_o. It will also depend on the interface properties between the back of the wall and the soil and on the number of props or anchors. The effect is likely to be smaller if the wall is propped.

Another source of approximation concerns the shape of the wall in plan. A simple diaphragm wall usually has a constant thickness and therefore its properties may be constant along the wall. However, sheet pile walls (see Figure 3.43), secant pile, contiguous pile and T-shaped diaphragm walls

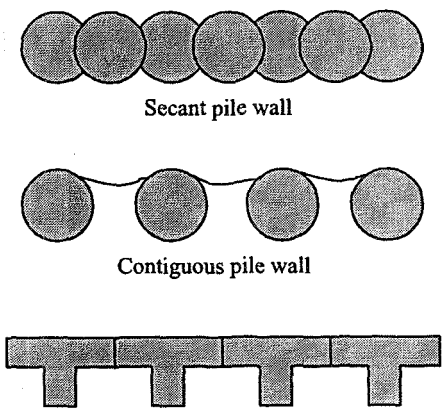

Figure 3.44: Different wall cross-sections

(see Figure 3.44) do not have a constant cross section in plan. Such geometries violate the basic assumption of plane strain conditions and consequently further approximations are involved when performing plane strain analyses. This problem is discussed further in Chapter 9.

3.7.3.2 *Wall stiffness*

The effective stiffness of the wall is obviously an important consideration for short and long term conditions. It is common practice to assume that there is a reduction in stiffness in the long term for concrete walls, due to factors such as creep and cracking. Some structural engineers suggest that the stiffness should be reduced by 50% to account for this. In a finite element analysis this can be modelled by changing the stiffness of the concrete after construction and prior to simulation of long term pore water pressure equilisation.

Potts and Day (1990) undertook a detailed study of the effects of a variation in wall stiffness. They performed a series of plane strain finite element analyses of three schemes: Bell Common tunnel, the George Green tunnel and the House of Commons car park. Figure 3.45 shows cross sections through these structures. The Bell Common tunnel is propped at roof level only, the George Green tunnel is propped at both roof and road level and the House of Commons car peak has seven levels of support.

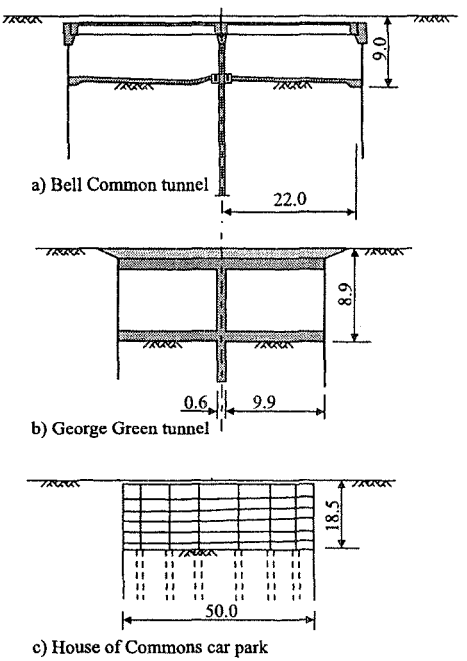

Figure 3.45: Cross-sections of three structures with different support

Each of these schemes was analysed with retaining walls of varying stiffness. For each scheme and for each wall they looked at the maximum horizontal displacement and the maximum bending moment in the wall in the short term and in the long term. Because ground conditions and the propping arrangements vary between schemes they could not define unique relationships. The results of this study are summarised in Figures 3.46 and 3.47, where for each scheme the results are normalised by those predicted for the stiffest wall section (i.e. the 1m thick concrete wall). They show that the bending moments in the wall are highly dependent on the wall stiffness, see Figure 3.46. There was a fivefold reduction in bending moment when the wall stiffness was reduced from that of a 1m wide concrete section to that of a Frodingham 1N

sheet pile. This occurred for all three schemes. This clearly has implications on the design of the wall.

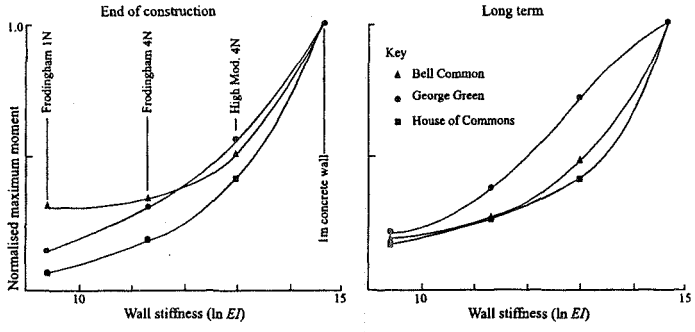

Figure 3.46: Variation of bending moment with stiffness for the three schemes

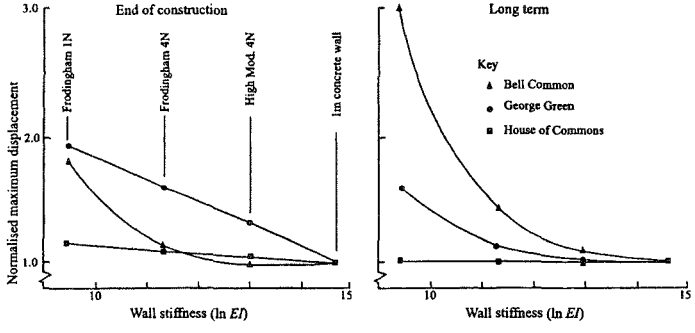

Figure 3.47: Variation of lateral wall displacement with stiffness for the three schemes

In contrast, the lateral wall displacements increased as the stiffness of the wall reduced. The magnitude of the increase in displacement depended on the scheme. For the Bell Common tunnel, which had a single prop, the maximum displacement increased by as much as a factor of three in the long term. However, as the number of propping levels increased, the increase in displacement reduced. For the House of Commons car park there was only a very small increase in the maximum wall displacement as the stiffness of the wall reduced.

Hight and Higgins (1994) undertook a much simpler study of a hypothetical scheme thought to be reasonably typical of deep excavations in central London. When looking at wall stiffness, they only considered short term effects. Figure 3.48 shows a cross section of the problem they analysed. Their results are shown in Figure 3.49. The wall was 1m wide and in the standard case the Young's modulus, E, of the section was 28GPa. Two other cases were also considered, one with E

reduced by a factor of 10 and one with it increased by a factor of 10. The results show that reducing the stiffness of the wall by a factor of 100 led to a doubling of the maximum wall movement. There were also important changes in the displaced shape of the wall. Vertical displacements and the curvature of the settlement trough behind the wall were affected, but not far field settlements.

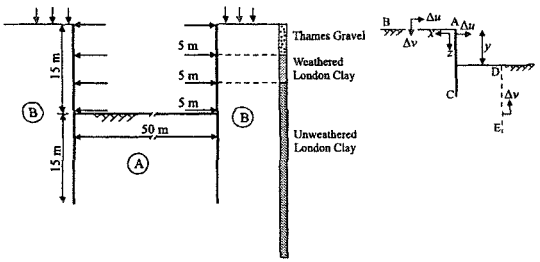

Figure 3.48: Cross-section of a typical excavation and notation for results

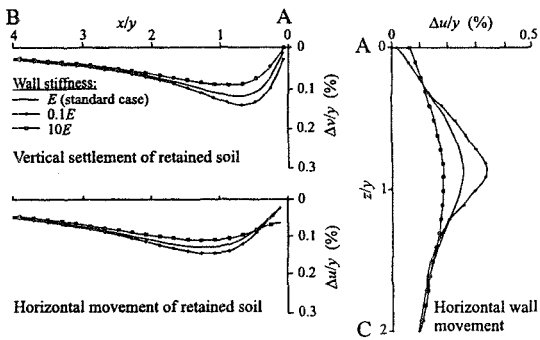

Figure 3.49: Predicted displacements for different wall stiffness

3.7.3.3 Interface behaviour

To model the interface behaviour between the soil and the wall, interface elements can be placed around the wall. Day and Potts (1998) have shown that the zero interface elements described in Section 3.6 of Volume 1 work well in this situation. They also show that results are not too sensitive to the stiffness used for the interface elements. This is good news, as interface stiffness is difficult to determine accurately. However, they do show that the angle of dilation of the interface elements can have a significant effect on soil movements.

3.7.3.4 Wall permeability

One important consideration which is often overlooked is the relative permeability of the wall in relation to the surrounding ground. Obviously, some walls are likely to be more permeable than others and measures can be taken to minimise seepage through the wall.

An assessment of the effectiveness of the wall needs to be made and appropriate boundary conditions applied in any analysis. The wall may be treated as being completely impermeable, completely permeable, or even given some finite permeability.

Solid elements representing the wall can easily model any of these conditions, but if beam (or shell) elements are used more care must be taken. If elements with zero thickness are used no distinction is made between nodes on either side of the wall. The wall is therefore permeable. To make the wall impermeable a distinction

must be made between nodes on either side of the wall. This can be done by introducing interface elements between the soil and the wall. However, a beam element cannot be used to model a wall of finite permeability. This problem is discussed in more detail in Chapter 9.

3.7.4 Support systems

3.7.4.1 Introduction

Section 3.4.4 discussed support systems in general terms. Embedded walls can be supported in a variety of ways. Different methods might be chosen to support walls during construction to those methods adopted for the permanent condition. The permanent support system may be used to support walls during construction, but measures such as berms, anchors, grillages or props might be used which are removed as the permanent system is installed. Generally, these temporary measures are necessary to provide greater working space or more flexibility in the method of working.

At the design stage uncertainties will exist over:

- The effective stiffness of the support system;
- The time between excavation and the installation of supports;
- The level of prestress applied to the props or anchors.

All these factors need to be considered in any analysis.

3.7.4.2 Support stiffness

The effective stiffness of the support systems can be significantly reduced by effects such as temperature, creep, bedding, concrete shrinkage, openings in floor slabs, packing between the prop and the wall, etc. These effects are discussed by St John (1975).

At the Bell Common tunnel, see Figure 3.50, a 'Kork' packing was placed between the roof slab and the walls to reduce thermal effects. It was concluded by Higgins *et al.* (1993), based on finite element analyses of the tunnel, that the roof slab would provide some support to the walls during the later stages of construction and in the long term. These analyses used stiffness values obtained from laboratory tests performed by the manufacturer of the 'Kork' packing. However, field monitoring indicates that even four years after construction little support is being provided by the roof slab. This

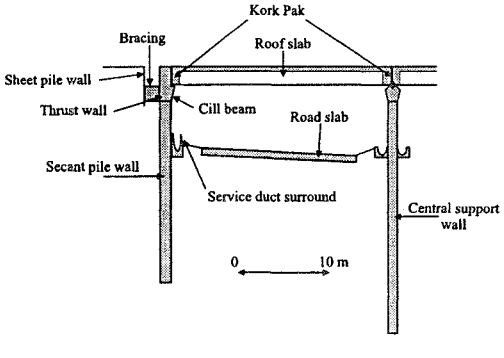

Figure 3.50: Cross-section of the Bell Common tunnel

is due to the much higher compressibility of the packing in the field which has significantly reduced the effective stiffness of the support to the wall. This example demonstrates the difficulties in determining appropriate support stiffness.

The simple study of a typical deep basement undertaken by Hight and Higgins (1994), see Figure 3.48, considered the effect of variations in prop stiffness on wall and ground displacements during construction. An initial analyses was performed with a prop stiffness K=50 MN/m/m. This value is typical of that provided by a concrete slab. The analysis was then repeated with prop stiffness values of $0.2K$, $5K$ and $10K$. The results are shown in Figure 3.51. It is apparent that there is a very nonlinear relationship between stiffness of the props and the predicted displacements. Because the displaced shape of the wall was modified, there was a consequential effect on the bending moments in it.

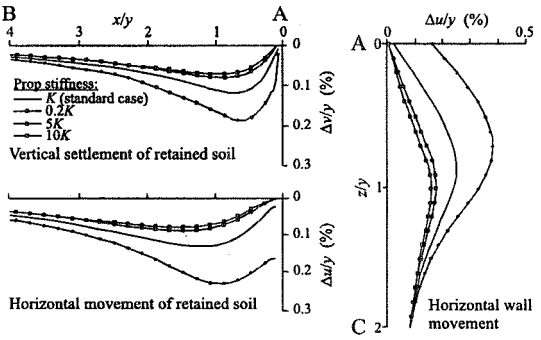

Figure 3.51: Predicted displacements for differing prop stiffness

It is apparent that the effective stiffness of the support system can have a significant influence on the observed and predicted behaviour of walls. Care must be taken not to over-estimate the effectiveness of this support. However, in some instances struts are pre-stressed in order to minimise problems associated with bedding effects, thereby maximising the effectiveness of the support. This pre-stressing can, and should, be modelled in any analysis.

3.7.4.3 Connection details

The way in which structural components are joined together influences how forces and moments are transmitted between them. They also influence how the structure can distort and therefore the behaviour of the ground. Three alternative types of wall-support connection are shown in Figure 3.11. The various options for modelling these in numerical analyses are discussed in Chapter 9.

However, to illustrate the importance of the connection consider the example shown in Figure 3.3. Figure 3.52 shows displaced shapes of the walls and roof slab with two different connection details between walls and the roof slab. In one analysis there was a full moment connection between the roof slab and the walls, but in the second analysis relative rotation between the walls and the roof slab was allowed (i.e. pin-jointed connection).

Figure 3.53 shows a comparison between the bending moments in the left wall. There is a significant effect due solely to the anticipated connection detail. It is apparent that such issues need very careful attention in any analysis.

The ability of the connections between supports and a wall to withstand tension must also be considered. It may be that if a support is simply resting against the wall then there can be no tension and the analysis must not allow this to develop. Therefore some form of 'cut-off' has to be used which prevents tensile forces from developing. While this is possible if the support is represented by finite elements (e.g. solid, bar or beam elements), it is not so easy if it is represented by a displacement or spring boundary condition.

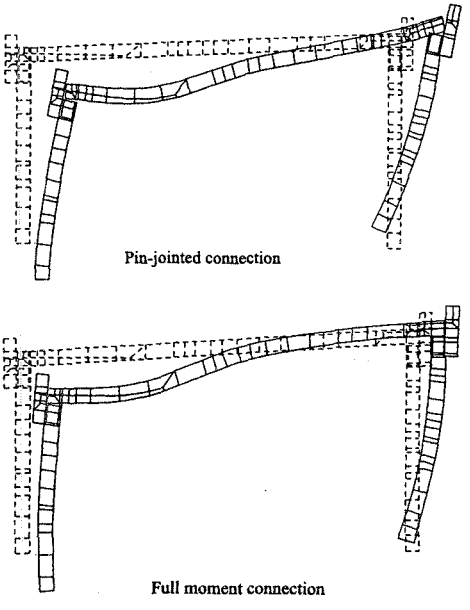

Figure 3.52: Displaced shapes of walls for different connection details

3.7.4.4 Active support systems

In order to control ground movements, active propping systems are installed on occasions. During construction ground movements are monitored and if they exceed set 'trigger levels' the supports are loaded to prevent any further distortion or at least minimise it. Either a specified load is applied to the support or load is continually adjusted to prevent movement. Obviously, if such an active system is being considered, then any analysis has to reproduce these effects and the details of the controls (i.e. 'trigger levels') have to be known.

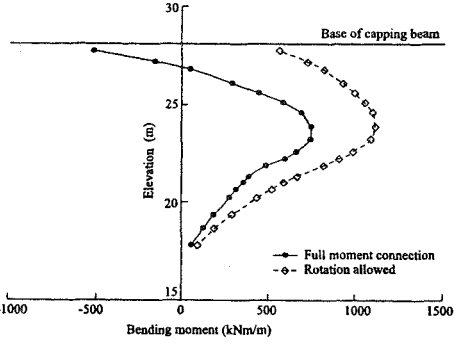

Figure 3.53: Bending moments in left wall for different connection details

If the specified method of supporting the wall is that a constant load is maintained in a prop or a series of props (i.e. load control system), then the forces that result in the support will have to be continually assessed and additional forces continually applied, or removed, throughout the analysis to maintain this load. Alternatively, if in a specification there is a limit on the maximum displacement of the wall (displacement controlled system), then when this limit is reached a displacement boundary condition can be applied to 'lock off' any further movement. However,

the correct boundary condition must be applied and the possibility that the wall will want to move away (displacements falling below the specified maximum level) must be considered.

The most complicated situation of all is where the loads applied to the props are controlled entirely by the displacement of a remote point such as a building. In anything other than a simple structure there are obviously many different combinations of loading that could be applied to the system.

Unless a finite element (or finite difference) program has an 'automatic' method of modelling these systems, they can be extremely difficult to analyse.

3.7.4.5 Berms

Potts *et al.* (1993) described a study of the use of berms to provide temporary support for retaining walls which considered variations in the geometry of the berms. They related 'displacement efficiency' and 'normalised bending moment' to the volume of the berm. There were a number of interesting results from this study concerning the influence of the berm's geometry and the effectiveness of berms. However, one of their conclusions was that:

> "The horizontal resistance provided by the berm has a substantial effect on wall behaviour. It is therefore not accurate to use an equivalent surcharge load to model the effect of a berm. If such an approach is used, the effectiveness of the berm is likely to be under estimated."

Berms are comparatively easy to model, although their stability, as drainage occurs during construction, may need to be considered. There is also an issue concerning the correct pore water pressure boundary conditions that should be applied to their surface if they are left to stand for some time, see Section 3.4.7.4.

Problems can arise when berms are removed and a permanent support is installed. The berm may be removed in sections and replaced with another form of support, such as a slab cast in sections on the floor of the excavation. This procedure is very difficult to model in a two dimensional plane strain analysis and therefore approximate methods have to be considered. This may involve partial berm excavation before installing the other form of support or, considering a worst case scenario, complete removal of the berm without another means of support.

3.7.4.6 Ground anchors

Ground anchors may be modelled in several different ways and this is discussed in some detail in Chapter 9. However, in order to model the anchor it is necessary to consider how the components that form the anchor act.

Generally, there is a fixed length and a free length of the anchor. Over the fixed length shear stresses develop between the anchor and the soil, whereas over the free length there is no frictional component. It is therefore necessary not to overestimate the frictional forces that might develop between the soil and the anchor as movement occurs.

The most successful method of modelling an anchor is to use a combination of beam elements and interface elements to model the fixed length. A limit placed on the friction that can develop along the interface ensures that the influence of the anchor is not overestimated and the elastic extension of the tendon is represented by the beam element. To model the free length, a beam, bar or spring may be used, but this should be disconnected from the soil in order to ensure that no friction develops.

Clearly, anchors have a three dimensional geometry. Modelling them in a plane strain analysis therefore involves severe approximations, see Chapter 9.

3.7.4.7 Relieving slabs

Relieving slabs may also be used to support a wall and these are quite easily modelled as long as the soil behaviour is realistically represented. These slabs may be placed either in front of a wall or behind it. In some circumstances slabs on both sides of the wall may be used.

St John *et al.* (1993) described a design study for a cantilever bored pile wall with relieving slabs in front of the wall and behind it. Figure 3.54 shows the effect of the relieving slab behind the wall on bending moments and wall displacements. The beneficial effect of the rear slab is in creating a restoring moment to the wall prior to excavation, which reduces the peak bending moment and pulls back the head of the wall. Both short and long term stability is enhanced. Figure 3.55 shows the effect of a slab in front of the wall on the long term behaviour. Since the front relieving slab can only be installed after excavation is completed, it can only have an effect on long term behaviour. The benefit is again in reducing the maximum wall bending moment.

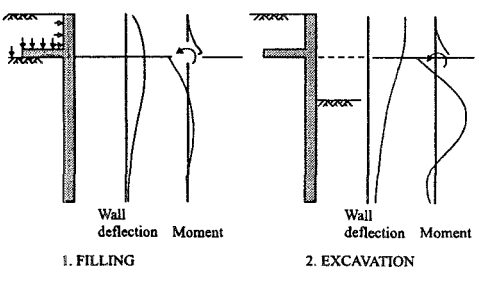

Figure 3.54: Effect of rear relieving slab

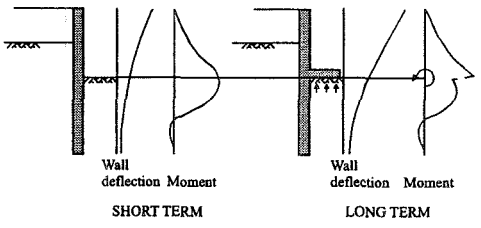

Figure 3.55: Effect of front relieving slab

The cross section used for St John *et al.*'s study is shown in Figure 3.56 and the effect of these slabs on horizontal wall displacements is summarised in Figure 3.57. Run 5 considered a cantilever wall with no relieving slabs, in Run 2 there was a slab behind the wall, while in Run 7.1 only a slab in front of the wall was constructed. The stages of analyses, marked on Figure 3.57, correspond to:

A - Construction of bored pile wall (i.e. 'wished in place');
B - Construction of slab behind the wall (where appropriate);
C - Construction of fill behind the wall;
D - Application of bridge loads on the wall;
E - Excavation to El. +19.7m;
F - Ground drainage in front of the wall;
G - Construction of front relieving slab (where appropriate);
H - Long term dissipation.

Clearly the slabs, especially the one at the rear of the wall, substantially reduce wall movements.

A structure of this form can only be analysed using a full numerical approach.

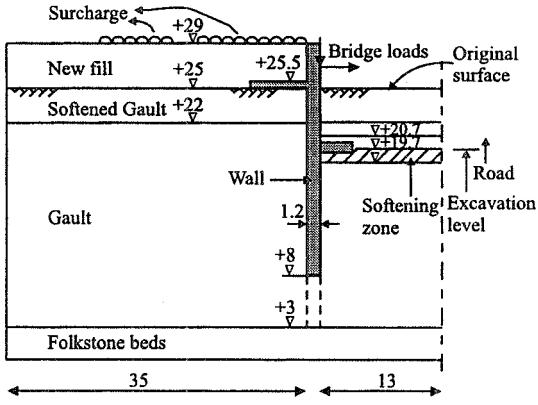

Figure 3.56: Cross-section analysed for the design study

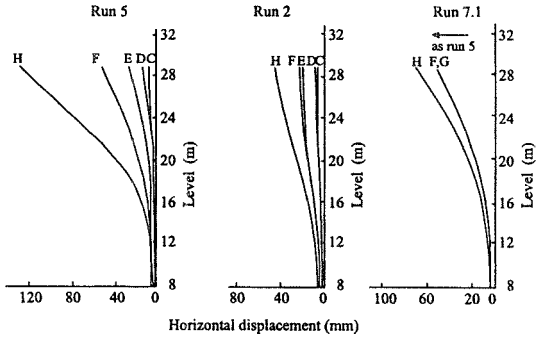

Figure 3.57: Horizontal wall displacements

3.7.5 Long term behaviour and post construction effects

In stiff over consolidated clays, such as London Clay, long term effects can be significant and can dominate the behaviour of a structure taking many years to occur. London Clay is a relatively well understood soil (emphasis should be placed on the word *relatively*), but even so there are few case records with measurements of long term heave against which the predictive capability of constitutive models can be assessed.

In any design possible long term effects need careful consideration and measures taken to mitigate them or to cope with them. If construction is slow, some drainage will occur during this period and this will tend to reduce post-construction effects.

Apart from changes in earth pressures that act on a wall as drainage occurs and excess pore water pressures dissipate, one of the most significant long term effects is the swelling of clays beneath deep excavations. Figure 3.58 shows measurements of swelling in oedometer tests on London Clay, together with two predictions. One of these predictions is based on a linear elastic-plastic constitutive model. The other has the same plastic behaviour but the elasticity is based on the small strain model described in Section 5.7.5 of Volume 1. It is apparent that at low effective stress the test data indicate that large volumetric strains occur and that large vertical displacements result. The predictions based on the linear elastic-plastic constitutive behaviour are unable to reproduce this behaviour. However, reasonable predictions are obtained from the small strain model.

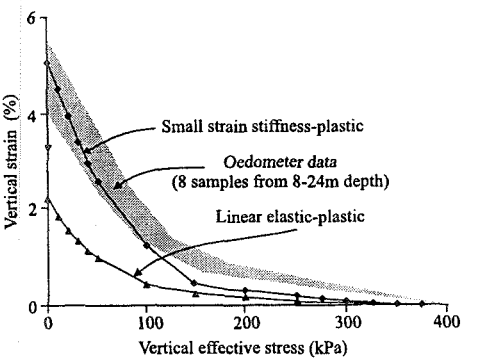

Figure 3.58: Predictions and measurements of swelling behaviour of London Clay

To minimise the effects of these large volumetric strains and pore water pressure changes, the swelling potential of the clays may need to be controlled by drainage, or by other means. Alternatively, a void may be left beneath a basement to allow heave to occur without imposing any stresses on the base slab of a structure. Modelling of this is reasonably straightforward, but the depth of the void needs to be known before the analysis is performed. Throughout the analysis the heave is monitored at nodes along the soil surface beneath the base slab until the displacement of the soil equals the depth of the void. Subsequently, displacements at nodes along the soil surface become linked (i.e. tied) to the corresponding nodes on the slab (this is not a zero displacement boundary condition, see Section 3.7.4 of Volume 1), and forces transferred from the soil to the structure. Unfortunately, this will not occur evenly across the base of an excavation due to the non-uniformity of stress conditions.

An alternative solution may be to disconnect the base slab from the walls and the rest of the structure and allow it to move freely with the soil. In this case care needs to be taken to ensure that the correct connection detail is modelled. It is all too easy to have a mesh that implies a full moment connection, in which case the base slab will not move freely as the soil swells but will resist movement and transfer forces to the rest of the structure.

As in the example of the road tunnel shown in Figure 3.3, there may be piles beneath the base of the structure. These will inhibit vertical heave due to swelling. However, these piles have a three dimensional geometry and consequently, when modelled in a plane strain analysis, assumptions are necessary, see Chapter 9. It is important that the frictional effects between the ground and the pile are not overestimated, equally they should not be underestimated.

Even in fast draining soils post-construction effects may be significant. It may be necessary to de-water the ground, or certain strata within it, in order to form an excavation, see Section 3.4.7.4. Completion of the structure and turning off of the de-watering system may subject the structure to significant pressures which have to be accommodated. The analysis of a deep excavation at Langley Point, Eastbourne, was reported by Fernie *et al.* (1996). Figure 3.59 shows a cross section through this excavation. The base slab was restrained by deep piles which restricted its movement.

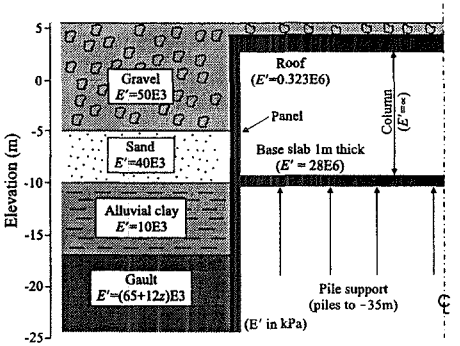

Figure 3.59: Cross-section for the marine treatment works at Langley Point

During excavation a de-watering system was installed to reduce pore water pressures within the area of excavation. When the de-watering system was turned off, after construction was complete, the soil beneath the base slab swelled and pushed the walls back (the authors termed this the 'balloon effect'). This had the effect of increasing the maximum bending moment in the walls by 50% and subjecting the connection between base slab and walls to tensile forces. In these analyses very careful consideration had to be given to the modelling of the connection between the base slab and the walls.

3.7.6 Adjacent structures

One of the main reasons for undertaking a soil-structure interaction analysis is to make an assessment of the effect of construction of a particular scheme on adjacent structures and/or services. As discussed in Section 3.4.6, the presence of such structures may have influenced ground conditions and the subsequent behaviour of it.

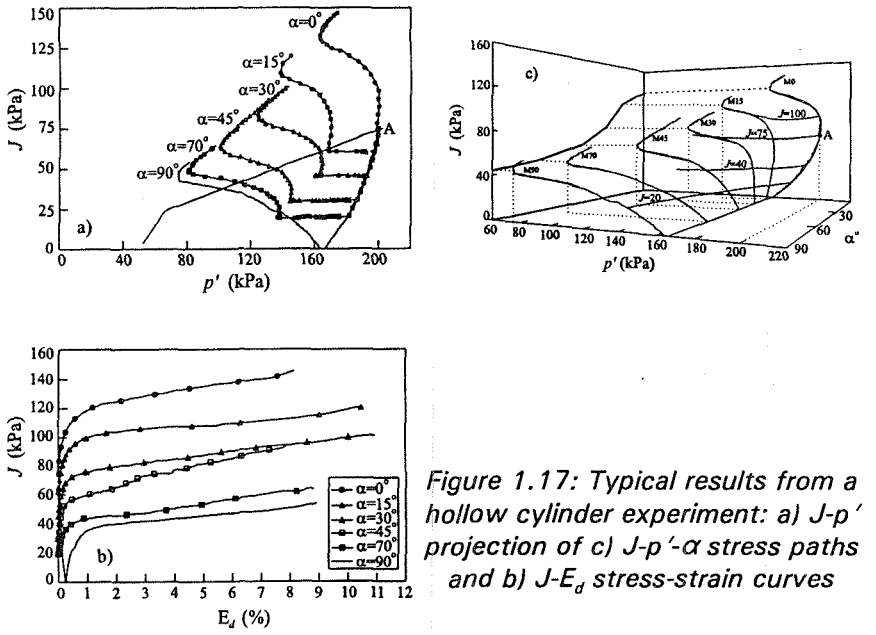

Figure 1.17: Typical results from a hollow cylinder experiment: a) J-p′ projection of c) J-p′-α stress paths and b) J-E_d stress-strain curves

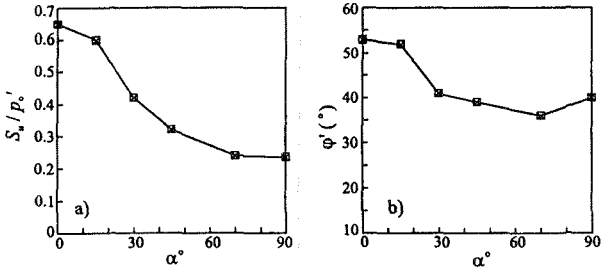

Figure 1.18: Anisotropy of a) undrained and b) drained strength

In addition to information on soil strength, hollow cylinder experiments provide information on the directional variation of soil stiffness, i.e. stiffness anisotropy. For example, Figure 1.19 shows results comparing the stiffness of samples sheared in drained conditions by changing only the vertical effective stress ($E_v'=E_z'=\Delta\sigma_z'/\Delta\varepsilon_z$), the horizontal effective stress ($E_h'=E_\theta'=\Delta\sigma_\theta'/\Delta\varepsilon_\theta$), or the torsional shear stress ($G_{vh}=G_{z\theta}=\Delta\tau_{z\theta}/\Delta\gamma_{z\theta}$), see Zdravković and Jardine (1997).

Drained directional shearing can also be used for estimating Poisson's ratios. From a drained test where only the vertical effective stress is changing, the Poisson's ratio μ_{vh}' (horizontal straining due to a vertical direct stress) can be calculated as:

$$\mu'_{vh} = \mu'_{zr} = -\frac{\varepsilon_r}{\varepsilon_z} \quad \text{or}$$
$$\mu'_{vh} = \mu'_{z\theta} = -\frac{\varepsilon_\theta}{\varepsilon_z} \tag{1.15}$$

From a drained test where only the horizontal effective stress is changing, Poisson's ratios v_{hv}' (vertical straining due to horizontal stress) and v_{hh}' (horizontal straining due to horizontal stress) can be calculated as:

$$\mu'_{hv} = \mu'_{\theta r} = -\frac{\varepsilon_z}{\varepsilon_\theta} \quad \text{and}$$
$$\mu'_{hh} = \mu'_{\theta r} = -\frac{\varepsilon_r}{\varepsilon_\theta} \tag{1.16}$$

From these results the anisotropic compliance matrix can be constructed:

$$\begin{Bmatrix} \Delta\varepsilon_z \\ \Delta\varepsilon_r \\ \Delta\varepsilon_\theta \\ \Delta\gamma_{z\theta} \end{Bmatrix} = \begin{bmatrix} \frac{1}{E'_z} & -\frac{\mu'_{\theta r}}{E'_\theta} & -\frac{\mu'_{\theta r}}{E'_\theta} & 0 \\ -\frac{\mu'_{z\theta}}{E'_z} & \frac{1}{E'_\theta} & -\frac{\mu'_{\theta r}}{E'_\theta} & 0 \\ -\frac{\mu'_{\theta r}}{E'_\theta} & -\frac{\mu'_{\theta r}}{E'_\theta} & \frac{1}{E'_\theta} & 0 \\ 0 & 0 & 0 & \frac{1}{G_{z\theta}} \end{bmatrix} \begin{Bmatrix} \Delta\sigma_z \\ \Delta\sigma_r \\ \Delta\sigma_\theta \\ \Delta\tau_{z\theta} \end{Bmatrix} \tag{1.17}$$

This compliance matrix is symmetric in the linear elastic region (i.e. elastic plateau) of soil behaviour and in that case:

$$\frac{\mu'_{z\theta}}{E'_z} = \frac{\mu'_{\theta r}}{E'_\theta} \tag{1.18}$$

However, at larger strains, but still within the small strain region, nonlinear parameters do not necessarily produce a symmetric compliance matrix (see Zdravković and Jardine (1997)).

Hollow cylinder testing is highly desirable if anisotropic soil behaviour is to be simulated through models such as MIT-E3.

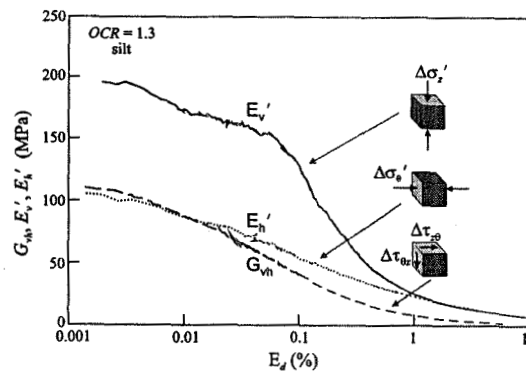

Figure 1.19: Stiffness anisotropy obtained from a hollow cylinder test

1.3.9 Directional shear cell

The directional shear cell (DSC) is an example of a piece of specialist equipment capable of investigating soil anisotropy. It was developed at University College London (UCL) by Arthur and Menzies (1972) for testing samples under plane strain conditions. The plane strain conditions are imposed on two opposite faces of a cubical sample by end platens. On the other four sides both direct and shear stresses are applied via flexible membranes and pressure bags (see Figure 1.20) so that the direction of the major principal stress can be rotated in a controlled manner. The UCL version of the DSC is capable of testing only dry samples, whereas the MIT version (Germaine (1982)) has been developed to conduct undrained tests too.

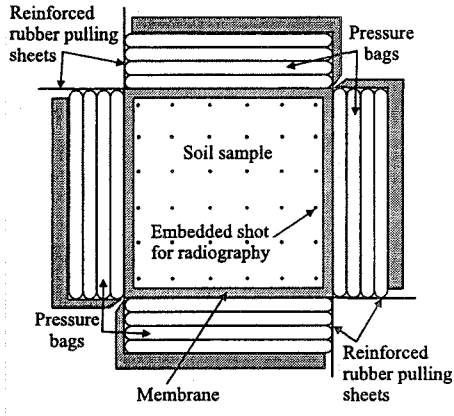

Figure 1.20: Schematic presentation of a directional shear cell

Strain measurement is normally performed via photometry and/or radiography, which is a labourious process and prevents the testing from being conducted using servo-control. Because the apparatus is restricted to testing samples under plane strain conditions it is not as a flexible as the hollow cylinder apparatus.

As with the hollow cylinder apparatus tests performed in this apparatus provide information on both the anisotropic stiffness and strength of the soil samples.

1.3.10 Geophysical techniques

Recently the bender element technique has been developed for very small strain (i.e. on the elastic plateau) shear stiffness measurements in the laboratory. Bender elements are plates made of a piezoelectric material which has the capability to either convert an applied electric voltage into mechanical motion, or convert an applied mechanical motion into an electric voltage. These plates are placed onto two opposite sides of a sample: one plate acts as a transmitter that generates a shear wave which propagates through the soil until it reaches the other plate which acts as a receiver. From the measured time that it takes for the shear wave to traverse the sample and the distance between the bender plates it is possible to calculate the velocity of the shear wave and hence estimate the value of the elastic shear modulus G_{max} ($=\rho V^2$, where ρ is the material density).

Schultheiss (1981) was the first to install bender elements in triaxial and oedometer cells, and others then followed suite (e.g. Lo Presti *et al.* (1993), Jamiolkowki *et al.* (1994), Viggiani (1992), Porović (1995), Jovičić and Coop (1998), Kuwano (1999)). The use of bender elements in a conventional triaxial test

allows three different shear moduli to be determined. For triaxial samples with bedding planes positioned horizontally, the shear modulus G_{vh} can be measured by propagating, from the top of the sample, a vertical shear wave which oscillates in the horizontal direction, Figure 1.21a. The other two moduli, G_{hv} and G_{hh}, can be measured by placing two more pairs of bender elements on radially opposite sides of the sample, see Figure 1.21b, or by trimming a sample such that the bedding planes are vertical and placing it in two positions relative to the axial bender elements, as shown in Figure 1.21c.

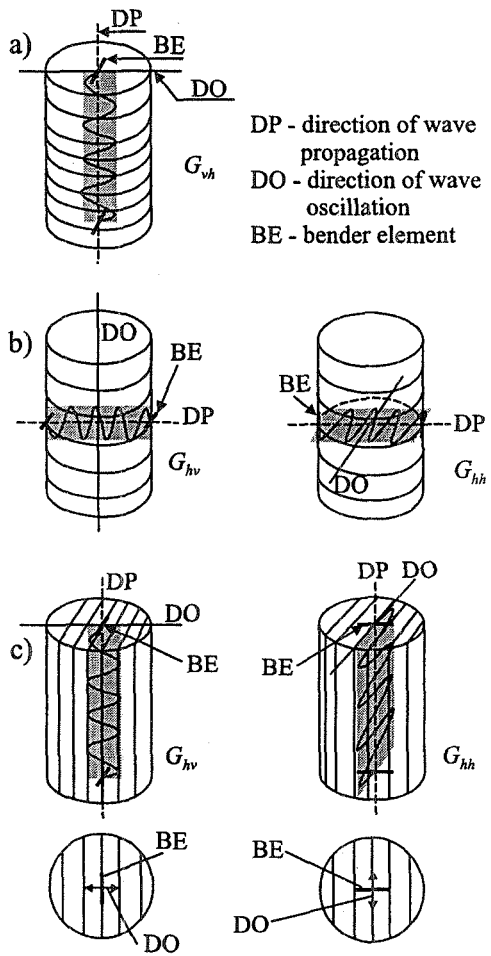

Figure 1.21: Small strain stiffness measurements using bender elements

1.3.11 Permeameters

The most common means of measuring permeability in the laboratory is to use a permeameter. However, because of the very large range of permeability in soils, no simple piece of equipment is suitable for all cases. The types of equipment most generally used are:

- The constant head permeameter, for permeabilities, k, down to about 10^{-4}m/sec, and
- The falling head permeameter, for values of k between 10^{-4} and 10^{-7}m/sec.

Below about 10^{-7}m/sec permeability can generally only be measured by indirect means in a consolidation test in the oedometer, or in a dissipation test in the triaxial apparatus.

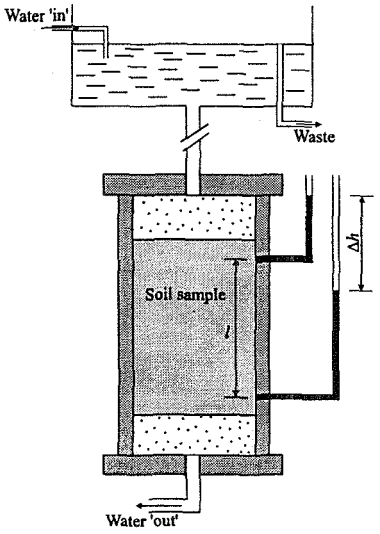

Figure 1.22: Schematic presentation of a constant head permeameter

The constant head permeameter

This apparatus is illustrated diagrammatically in Figure 1.22. A constant head of water is maintained across the sample during the test. Once steady state conditions are reached, the rate of flow is measured. From the measurements of flow rate and the hydraulic gradient, $\Delta h/l$, it is possible to use Darcy's law to determine the permeability, k.

The falling head permeameter

When the rate of flow through the sample is too small to be accurately measured in the constant head permeameter, the falling head apparatus is used, see Figure 1.23. In this case the water flows through the sample from a standpipe, and the head across the sample at any moment is taken to be the difference between levels in the standpipe and in the container surrounding the sample. Noting the rate of drop of the water level in the standpipe and using Darcy's law enables the permeability to be estimated.

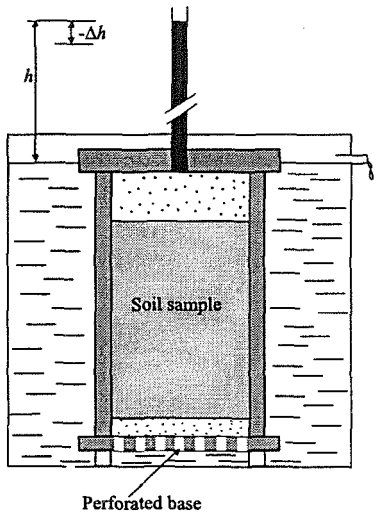

Figure 1.23: Schematic presentation of a falling head permeameter

1.4 In-situ tests

1.4.1 Introduction

In-situ soil testing offers complementary capabilities to laboratory testing by providing information about current conditions in the ground (e.g. piezometric levels, strength variation with depth, soil description, etc.). The principal advantage of in-situ tests is that they assess soil behaviour in its natural condition, thus avoiding sample disturbance. They can also be more economical than laboratory tests and in some cases can provide more representative results through a higher density of data collection.

However, the disadvantage of in-situ testing is that most geotechnical parameters (e.g. strength, stiffness, etc.) are estimated from empirical correlations, rather than from direct measurement. Also, in-situ tests load the ground in different ways to conventional laboratory tests. Because soil properties are nonlinear, anisotropic and rate dependent a wide range of results can be obtained from similar tests in the same deposit. Therefore great care is required in test preparation.

In many practical situations the only information that exists about a particular site comes from in-situ testing. This often restricts any finite element analysis to the use of simple constitutive models.

This section describes the most common in-situ equipment and procedures for soil investigation and the modelling parameters that can be obtained from them.

1.4.2 Standard penetration test (SPT)

The standard penetration test (SPT) is performed at the bottom of a pre-drilled borehole, by driving a standard sampling tool through a prescribed distance (450 mm), with a hammer of known weight (63.5 kg). The hammer is dropped from a fixed height of 760 mm onto an anvil placed on the top of the drilling rods and the number of blows required for it to penetrate 450mm recorded. The drilling rods are connected to the back of the sampler and transfer the driving energy from the hammer to the sampler. The borehole diameter is normally within the 65 to 115mm recommended in most guidelines, because it is known that larger boreholes result in lower blow counts. Another recommendation is that the SPT test is performed in a water filled borehole.

The number of hammer blows required to drive the sampler through the first 150mm is normally discarded (as being affected by drilling disturbance). The number of hammer blows required to drive the sampler through the last 300mm is taken as the blow count, *N*. Penetration and blow-counting continues until the desired depth of the borehole is reached and a typical borehole log is shown in Figure 1.24.

The SPT is mainly used in granular soils because of the difficulties associated with taking undisturbed samples for laboratory testing. However, it is also used for testing clays. It is a simple and cheap test, but not easy to interpret. The reason for this is the variety of sampling tools, anvils, hammers and methods of hammer release that exist. They all affect the energy transmitted from the hammer into the

sampler and consequently affect the blow count. Skempton (1986) suggested that the N values measured by a particular method should be normalised using a standard procedure. If the hammer energy, E_r, delivered into the rod stem can be expressed as a ratio of the theoretical free-fall energy, E_x, such that:

$$E_r = (ER_r)E_x \qquad (1.19)$$

where ER_r is the 'rod energy ratio', and if the standard ER_r is adopted to be 60%, then the N values measured with a known or estimated ER_r value can be normalised to this standard by the conversion:

$$N_{60} = N\frac{ER_r}{60} \qquad (1.20)$$

where N_{60} is the normalised blow count.

Stroud (1989) summarised the existing correlations between N_{60} and soil density, strength and stiffness, derived for both clays and sands. Some of his findings are outlined below.

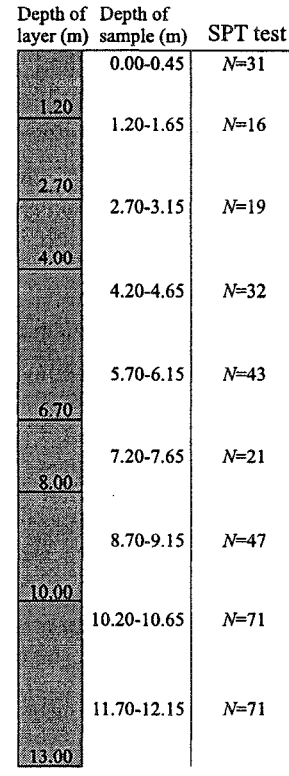

Figure 1.24: Typical SPT log

Sand - strength

Skempton (1986) suggested that Terzaghi and Peck's (1948) correlation between blow count, N, and relative density, D_r, should be corrected for the above normalisation. The new expression then becomes:

$$\frac{N_{60}}{D_r^2} = a + b\sigma_v' \qquad (1.21)$$

where a and b are material constants and σ_v' is the effective overburden pressure. He further suggested that it was convenient to normalise the blow count in the above expression to a standard effective overburden pressure of 100 kPa (i.e. 1kg/cm^2):

$$\frac{(N_1)_{60}}{D_r^2} = a + b \qquad (1.22)$$

where $(N_1)_{60}=C_N N_{60}$ and C_N is a correction factor for overburden pressure, given in Figure 1.25.

He then derived the relationship between relative density, D_r, and standardised SPT value, $(N_1)_{60}$, for sands shown in Figure 1.26. Bolton (1986) introduced the critical state value of the angle of shearing resistance, φ_{cs}', into the correlation and, on the basis of data collected for different sands, drew a revised relationship.

Stroud (1989) then replotted all the available data to obtain the variation of φ' vs. $(N_1)_{60}$ and $(N_1)_{60}$ vs. D_r for different OCRs and different φ_{cv}', as shown in Figure 1.27.

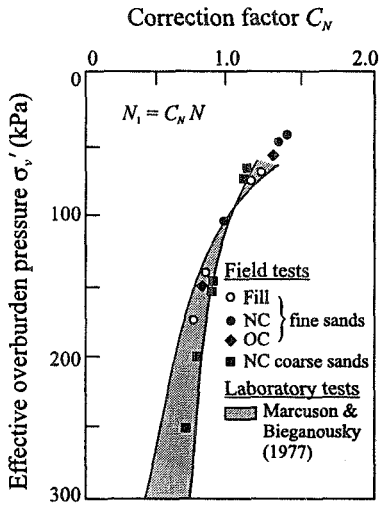

Figure 1.25: Correction for effective overburden pressure (after Skempton (1986))

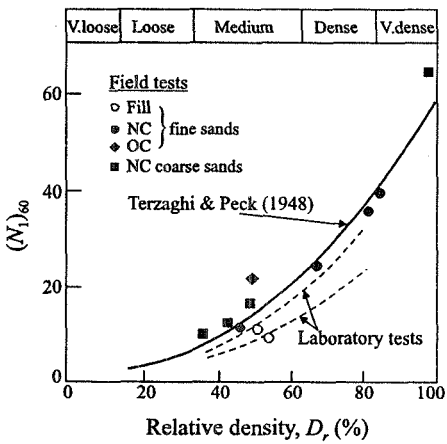

Figure 1.26: Effect of relative density, based on field data (after Skempton (1986))

Sand - stiffness

It is now widely accepted that soil stiffness is strain level dependent, i.e. it gradually reduces as strains increase. To accurately predict movements of structures in the ground (e.g. footings, retaining walls, tunnels etc.) it is necessary to obtain a good estimate of the stiffness of the ground.

Vesić (1973) performed tests with a loaded foundation of a constant breadth in sands of varying density. He found a unique relationship between settlement, ρ, and the degree of loading, q/q_{ult}, expressed as a ratio of the design load, q, to the ultimate load, q_{ult}. This suggested that q/q_{ult} could be used as an indirect measure of shear strain and therefore linked to the average stiffness E' (expressed in terms of Young's modulus).

For this purpose data from a wide range of strip footings, raft foundations and plate tests on both normally and overconsolidated sands have been collected (Stroud (1989)). They have been taken from case histories where SPT tests have been carried out and a correlation, shown in Figure 1.28, has been derived between the E'/N_{60} and q/q_{ult} values. Knowing the design loading and estimating the ultimate bearing capacity, it is possible to use this graph to estimate the average ground stiffness at working load on the basis of SPT blow counts.

Clays - strength

The undrained shear strength, S_u, of overconsolidated clays can be related to SPT blow counts using the simple correlation proposed by Stroud (1974):

$$S_u = f_1 N_{60} \tag{1.23}$$

where the variation of f_1 with plasticity index is shown in Figure 1.29.

Clay - stiffness

The drained stiffness, E', again expressed in terms of Young's modulus, of overconsolidated clays in vertical loading can be estimated from case histories, in a similar manner as for sands. Figure 1.30 shows such data plotted as E'/N_{60} against q/q_{ult}. Again, a trend of decreasing stiffness with increasing degree of loading (i.e. increasing strain level) is evident.

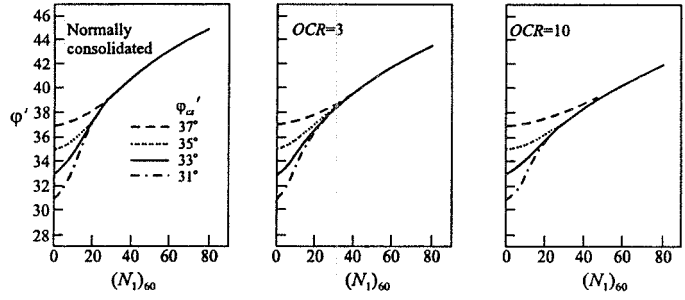

Figure 1.27a: Variation of ϕ' and $(N_1)_{60}$ with ϕ_{cs}' and OCR (after Stroud (1989))

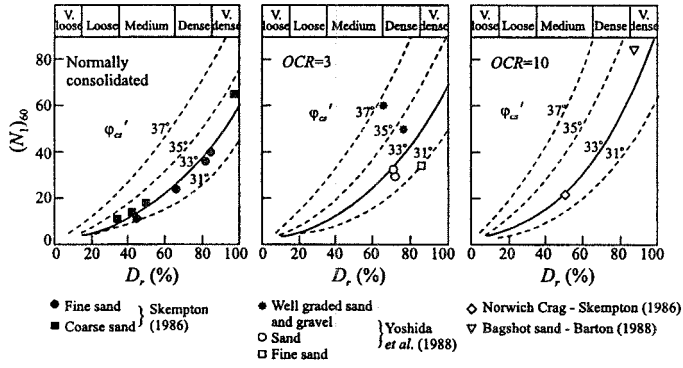

Figure 1.27b: Variation of $(N_1)_{60}$ and D_r with ϕ_{cs}' and OCR (after Stroud (1989))

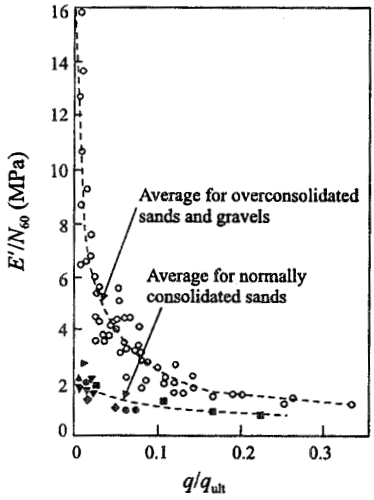

Figure 1.28: Stiffness vs. degree of loading for sand (after Stroud (1989))

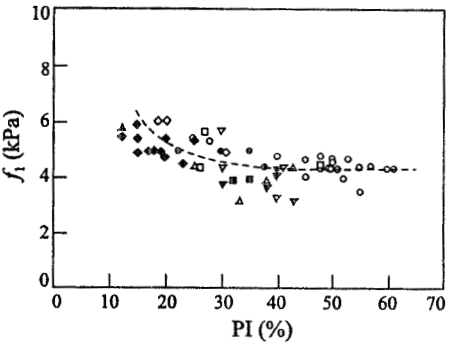

Figure 1.29: Variation of f_1 with plasticity index (after Stroud (1989))

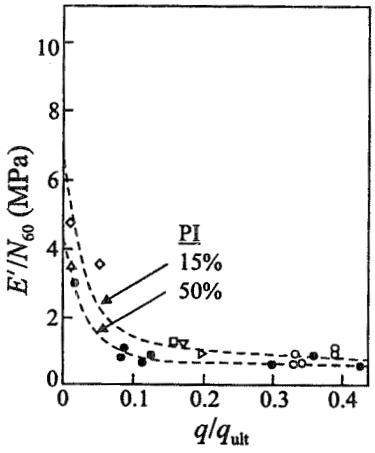

Figure 1.30: Stiffness vs. degree of loading for clays (after Stroud (1989))

1.4.3 Cone penetration test (CPT)

The cone penetration test (CPT) consists of pushing into the ground a series of cylindrical rods with a cone at the base. During the push the penetration resistance,

q_c, and, if required, the frictional resistance on the side (sleeve) of the cone, f_s, are recorded at depth intervals. A typical CPT result is shown in Figure 1.31. The ratio f_s/q_c is termed the friction ratio.

Empirical correlations are available between these measured quantities and the angle of shearing resistance and relative density for sands and undrained shear strength for clays. These correlations should be used with care because they may only apply to a particular set of conditions (e.g. penetrometer dimensions, penetration rate, soil type).

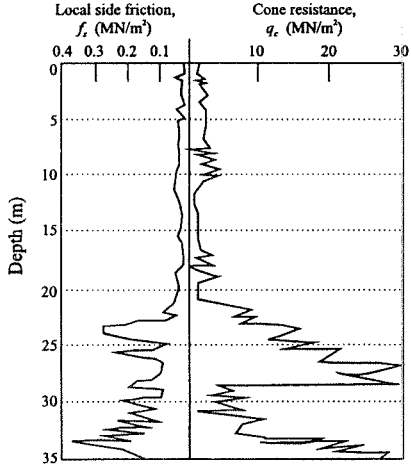

Figure 1.31: Typical CPT log

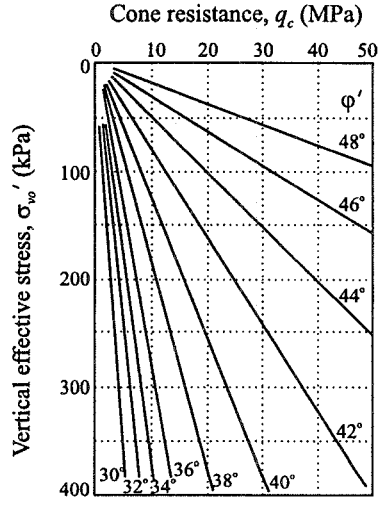

Figure 1.32:Cone resistance vs. peak ϕ' for sand (after Robertson and Campanella (1983))

Sand

The existing correlations of cone resistance with φ', E and G have been derived from tests performed in a calibration chamber.

Robertson and Campanella (1983) presented relationships between q_c and peak φ' for normally consolidated quartz sands at increasing vertical effective stress, see Figure 1.32. The angles of shearing resistance were obtained from triaxial tests performed at confining stresses approximately equal to the horizontal effective stress in the calibration chamber prior to cone penetration. Using the relationships given in Figure 1.32 for overconsolidated sands will tend to slightly overestimate φ'.

Robertson and Campanella (1983) also presented relationships between cone resistance, q_c, and Young's and shear moduli at increasing vertical effective stress levels, see Figure 1.33.

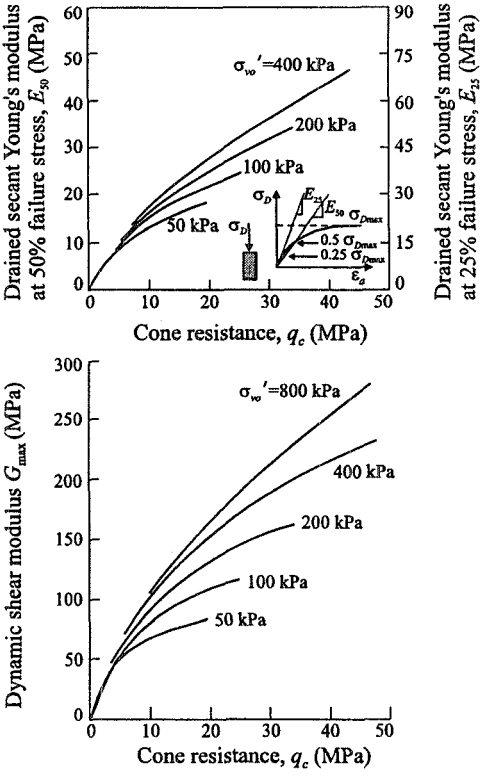

Figure 1.33: Cone resistance vs. Young's and shear moduli for sand (after Robertson and Campanella (1983))

Clays

The measurement of clay properties using the CPT is highly dependent on the rate of cone penetration, because of the build up of excess pore water pressures. The CPT in clays is principally used to estimate the undrained shear strength, S_u, and the relationship with q_c is expressed as:

$$q_c = N_k S_u + \sigma_{vo} \tag{1.24}$$

where: σ_{vo} is the total overburden stress;
N_k is the 'cone factor' analogous to the bearing capacity factor N_c, see Chapter 6.

N_k is established using empirical correlations, with shear strength measured using other techniques. Lunne and Kleven (1981) found that for normally consolidated clays N_k was independent of plasticity index and suggested an average value of 15, with the majority of data being between 11 and 19.

For overconsolidated clays Marsland and Quarterman (1982) presented cone factors based on the undrained shear strength from plate loading tests and showed that for stiff fissured marine clays the cone factor was as high as 30, with an average of about 27.

1.4.4 Pressuremeter testing

The pressuremeter is a device that applies a uniform pressure to the walls of a borehole and measures stress and deformation of the wall, which is then used for interpretation of soil properties. Although there are three types of pressuremeter device (i.e. Menard (MPM), self-boring (SBP) and cone (CPM)) the basic concept consists of a deformable, cylindrical, rubber membrane which inflates laterally to radially deform the soil (see Figure 1.34).

Interpretation of pressuremeter test results is based on cavity expansion theory. It consists of: (i) an elastic phase, during which soil deformation is considered to be isotropic elastic, and (ii) a plastic phase, during which soil behaviour is assumed to be perfectly plastic. From measurements taken during the elastic phase estimates of the shear modulus can be made, while during the plastic phase the measurements can be used to evaluate the shear strength.

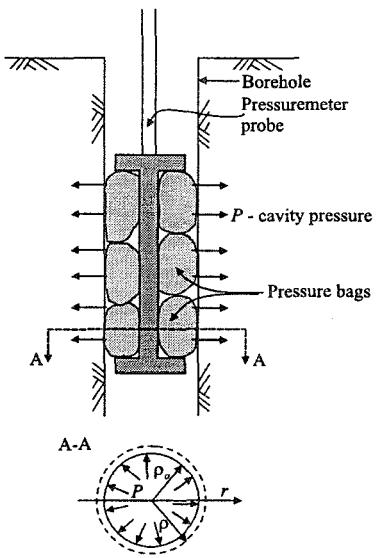

Figure 1.34: Schematic presentation of Menard pressuremeter

Elastic expansion

The main parameters and variables for membrane expansion are shown in Figure 1.34. The radius of the cavity, when the cavity pressure P is equal to the initial horizontal stress in the soil, σ_{ho}, is marked as ρ_o. When $P>\sigma_{ho}$, the cavity will deform, having a new radius ρ. The cavity strain, ε_c, is then given by:

$$\varepsilon_c = \frac{\rho - \rho_o}{\rho_o} \tag{1.25}$$

The pressuremeter tangent shear modulus of the soil is then calculated as:

$$G_p = \frac{1}{2}\left(\frac{\rho}{\rho_o}\right)\left(\frac{\Delta P}{\Delta \varepsilon_c}\right) \tag{1.26}$$

For most practical purposes $\rho/\rho_o \approx 1$, which simplifies Equation (1.26).

However, G_p is not the secant modulus of the soil, G_s, which is the parameter normally used for analysis in geotechnics. It can, however, be related to it through

the following expression:

$$G_s = G_p + \varepsilon_c \frac{\Delta G_p}{\Delta \varepsilon_c} \tag{1.27}$$

Estimates of a single (average) value of G_s can be made from the initial portion of the pressuremeter P-ε_c curve or from unload-reload loops.

Jardine (1992) compared triaxial G_s-ε_s curves, where ε_s is the shear strain (=2/3(ε_a-ε_r)), with pressuremeter G_p-ε_c curves and derived an empirical relationship between ε_s and ε_c by comparing the strain values at identical shear moduli levels:

$$\frac{\varepsilon_s}{\varepsilon_c} = 1.2 + 0.8 \log_{10}\left(\frac{\varepsilon_c}{10^{-5}}\right) \tag{1.28}$$

With the above expression pressuremeter G_p-ε_c curves can be transformed into triaxial G_s-ε_s curves, which are normally used in geotechnical design. For example, such curves can be used to obtain parameters for the small strain models described in Chapter 5 of Volume 1.

When using the pressuremeter in sands it should be noted that the shear modulus is likely to be stress level dependent. As the stress level in the sand adjacent to the pressuremeter decreases with distance, the value determined from the pressuremeter test represents an average value.

It is not possible to obtain estimates of the bulk modulus, K, or Poisson's ratio, μ, from pressuremeter tests.

Plastic expansion

If the soil behaves as a Tresca material, yielding will occur when the shear stress in the cavity wall reaches the undrained shear strength of the soil:

$$P = \sigma_{ho} + S_u \tag{1.29}$$

If the cavity pressure increases above this yield value, an annulus of plastic soil will develop around the cavity, while the soil further away from the cavity will continue to behave elastically. The cavity pressure can then be expressed in the following form:

$$P = \sigma_{ho} + S_u\left[1 + \ln\left(\frac{G}{S_u}\right)\right] + S_u\left[\ln\left(\frac{\Delta V}{V}\right)\right] \tag{1.30}$$

where V is the volume of the cavity occupied by the inflatable membrane.

With further loading a limit condition will be reached where the cavity expands with no change in pressure, at which stage $\Delta V/V \approx 1$ and the limiting cavity pressure, P_L, becomes:

$$P_L = \sigma_{ho} + S_u\left[1 + \ln\left(\frac{G}{S_u}\right)\right] \tag{1.31}$$

The current cavity pressure, P, given by Equation 1.30 can therefore be re-expressed as:

$$P = P_L + S_u \ln\left(\frac{\Delta V}{V}\right) \tag{1.32}$$

If the cavity pressure P is plotted against $\ln(\Delta V/V)$ for the duration of the pressuremeter test, it should give a straight line with a gradient equal to the undrained strength S_u during the later stages of the test, see Figure 1.35. Undrained strengths determined from pressuremeter tests are often significantly larger than values obtained by other means and therefore should be used with caution.

While it is theoretically possible to obtain estimates of the angles of shearing resistance, φ', and dilation, ν, from a pressuremeter test in sand, it is difficult in practice due to the disturbance involved in installing the instrument in the ground, see Mair and Wood (1987).

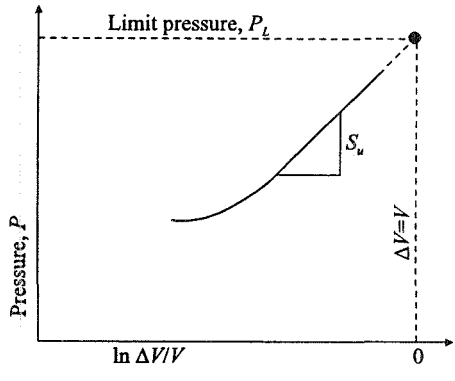

Figure 1.35: Cavity pressure vs. volume change during a pressuremeter test

Coefficient of earth pressure at rest

As noted above, under ideal circumstances, the radius of the cavity will only begin to deform when the pressure P equals the in-situ horizontal stress σ_{ho}. If this pressure is noted along with the in-situ pore water pressure, then it is possible to estimate the coefficient of earth pressure at rest, K_o, in the ground. In practice such measurements are only usually possible with the self boring types of pressuremeter.

1.4.5 The plate loading test

The plate loading test provides a direct measurement of the compressibility and bearing capacity of soils. A plate (0.3m to 1.0m in diameter) is loaded, via a reaction system (see Figure 1.36), and a loading test is performed in one of two possible ways:

- Maintained load test, where load is applied in increments of about 1/5th the design load and held at that level until the rate of settlement reduces to less than 0.004 mm/min over a one hour period. The test continues until either the soil fails in shear, or the bearing pressure reaches 2 to 3 times the design pressure. The results are usually plotted as time vs. settlement and load vs. settlement curves (see Figure 1.37).

- Constant rate of penetration test, where load is applied in a continuous manner, to give a plate penetration of 2.5 mm/min. The ultimate bearing capacity is then defined as the load required to produce a settlement equal to 15% if the plate diameter. This test is less common.

The interpretation of deformation properties is usually made using isotropic elastic theory or empirical correlations.

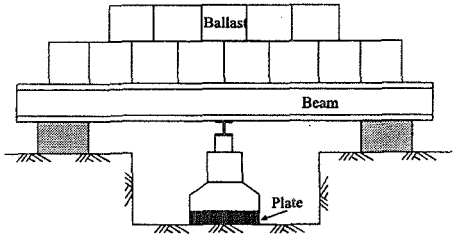

Figure 1.36: Schematic layout for a plate loading test

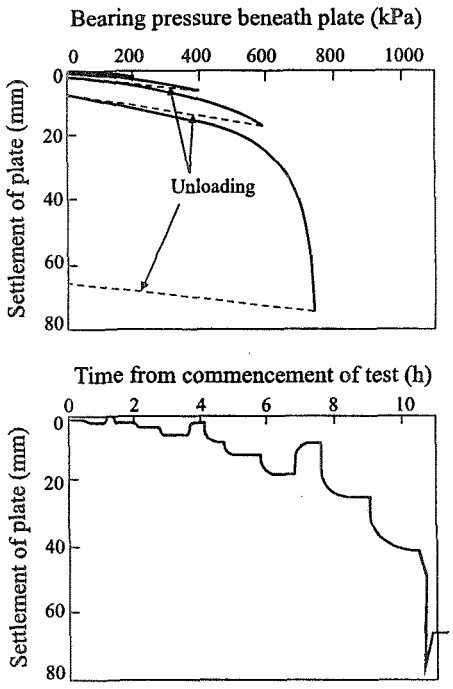

Figure 1.37: Typical presentation of results from a plate loading test

Sand test

Using elastic theory the settlement of a rigid surface plate of diameter B, with a uniform load q applied on a semi-infinite isotropic soil characterised by Young's modulus E and Poisson's ratio μ, is given by:

$$\rho = \frac{\pi q B}{4E}\left(1-\mu^2\right) \tag{1.33}$$

Terzaghi and Peck (1948) observed that elastic theory tends to overestimate settlements on sands and proposed that the settlement ρ_B of a footing of with B was better represented by the following correction:

$$\rho_B = \rho_1\left(\frac{2B}{B+1}\right)^2 \tag{1.34}$$

where ρ_1 is the elastic settlement (i.e. Equation (1.33)) of a one foot plate (i.e. B=0.3m).

Clay test - settlement

Marsland and Easom (1973) highlighted the fact that the settlement of a loaded plate on clay deviates more from the isotropic elastic theory than the equivalent plate on sand.

The test can be performed either on the surface of the clay or in a borehole. The borehole test, where D is the borehole diameter, is shown in Figure 1.38. Elastic theory predicts that the settlement of a fully buried rigid plate is equal to half of the settlement of the equivalent surface plate. However, in a borehole the plate is not fully buried and Burland (1969) showed that a correction factor of 0.7 should be applied. When B/D<0.6, where B is the plate diameter, the surface analysis applies.

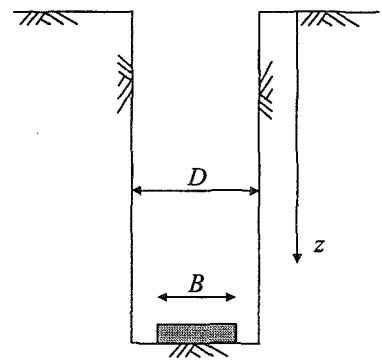

Figure 1.38: Plate loading test in a borehole

Clay test - undrained strength

The undrained strength of clays can be calculated using bearing capacity theory:

$$q_f = N_c S_u + p_o \tag{1.35}$$

where: q_f is load at failure, measured in a test;
p_o is the overburden pressure;
N_c is a bearing capacity factor, see Chapter 6.

1.4.6 Pumping tests

Because of the limited size of the samples that can be tested in the laboratory, they may not provide a representative value of the in-situ permeability. For example, the sample may not contain a thin seam of more porous material that may exist in-situ. In addition, samples of granular soil have to be reconstituted in the laboratory. For these reasons in-situ measurements of permeability are generally more reliable than laboratory tests. However, they are usually considerably more expensive.

In the field the permeability of a stratum of soil is most commonly determined by measuring the discharge from a well. A well (borehole) is sunk into the stratum, and water is pumped from it at a constant rate. This pumping lowers the piezometric level in the vicinity of the well, and the resulting hydraulic gradient causes water to flow towards the well. The piezometric level may be determined by sinking observation boreholes at various distances from the well, and by measuring the height at which the water stands in each, once a steady state has been established. From this data and using Darcy's law an estimate of the average permeability can be determined.

While pumping tests are applicable to relatively permeable soils, they are not necessarily appropriate for some clays. In these cases a borehole can be sunk into the clay and sealed over its length in contact with overlying soils. If left water will flow from the clay into the borehole. By measuring the rate of increase in the height of the water level in the borehole and again using Darcy's law it is possible to estimate the permeability. Alternatively, the borehole can be filled to the ground surface with water and the rate of reduction in level noted. Coupled with Darcy's law this allows an estimate of k to be made.

1.5 Summary

1. Both laboratory and field tests are available from which soil parameters can be derived. Both types of testing have their strengths and weaknesses and ideally most soil investigations should contain a combination of tests.
2. The aim of laboratory tests is to measure as accurately as possible and in a controlled manner the response of a soil element to changes in stresses, strains and/or pore water pressures.
3. Oedometer tests can be performed to provide information on overconsolidation ratio, OCR, the compression index, C_c, and the swelling index, C_s. With an appropriate assumption for K_o it is also possible to estimate the gradients of the virgin consolidation line, λ, and swelling lines, κ, in v-lnp' space. It is also possible to obtain estimates of the constrained modulus, E_c, and the coefficient of permeability, k.
4. The conventional triaxial apparatus can be used to estimate K_o values, strength values c', φ' or S_u and stiffness values E and μ (or K and G). It can also be used to estimate permeability. However, it is restricted to testing samples under triaxial compression (b=0) or triaxial extension (b=1) conditions and therefore cannot conveniently be used to investigate the effect of varying b or for investigating anisotropic behaviour.

5. The true triaxial apparatus is an improvement over the conventional apparatus, enabling stiffness to be determined in three independent directions and strength values under various b values. It is, however, not possible to vary the orientation of the principal stresses in a controlled manner. It is also cumbersome to use and therefore few exist.
6. Direct shear box tests can be used to estimate strength values. Due to the non-uniformities induced in the sample they are not normally used to estimate stiffness parameters.
7. Simple shear tests, while potentially an improvement over direct shear box tests, also induce non-uniformities in the sample and consequently are usually only used to estimate strength parameters.
8. Ring shear tests suffer from all the weaknesses associated with the direct and simple shear tests, but allow samples to be sheared to very large displacements. They are used to estimate residual strength.
9. The hollow cylinder apparatus overcomes many of the shortcomings of the above apparatus, allowing control over both the magnitude and direction of the principal stresses. Both stiffness and strength parameters can be estimated from tests performed in this apparatus. Such tests are ideal for investigating the anisotropic behaviour of soil.
10. The directional shear cell can also be used to investigate anisotropic soil behaviour. However, tests are usually restricted to plane strain conditions. As very few apparatus exist such tests are not common.
11. Incorporation of bender elements into the soil samples in the above apparatus enables geophysical techniques to be used to estimate stiffness parameters. Their use therefore provides a welcome addition to standard laboratory tests.
12. Permeameters, both constant and falling head types, are used to measure soil permeability in the laboratory. However, for very low permeabilities, $k<10^{-7}$ m/sec, indirect methods (i.e. consolidation and/or dissipation tests) are often employed to determine k.
13. Field tests come in many forms, but usually involve testing soil under non-uniform conditions (i.e. many tests are essentially boundary value problems). In addition, many of the geotechnical parameters are estimated from empirical correlations, which have often been calibrated against laboratory tests.
14. The standard penetration test (SPT) is probably the most common form of in-situ test. It is simple to perform, but all geotechnical parameters must be estimated from empirical correlations. Such correlations exist between the measured SPT blow count and strength parameters c', φ' and S_u, and Young's modulus E.
15. The cone penetration test, while an improvement over the SPT, still relies on empirical correlations to obtain geotechnical parameters. Again, it is possible to estimate values of S_u, φ' and E. Such tests also provide good profiling tools.
16. Pressuremeter tests can be used to estimate strength parameters S_u and φ', the coefficient of earth pressure at rest K_o and the elastic shear stiffness G. The

interpretation is based on theory related to the expansion of an infinitely long cylinder. As such, the estimated parameters are very sensitive to the disturbance caused during installation of the pressuremeter. This is particularly so for tests performed in sandy soils.

17. Plate loading tests can be used to provide estimates of both soil stiffness and strength. To obtain stiffness parameters the interpretation is based on the assumption that the soil is isotropic linear elastic, whereas the soil is assumed to be linear elastic perfectly plastic when estimating strength parameters.
18. Pumping tests can be performed to obtain estimates of the average in-situ permeability.

2. Tunnels

2.1 Synopsis

This chapter presents the application of numerical methods to the analysis of tunnel construction, with emphasis on soft ground tunnelling. First, different methods of tunnel excavation are presented, some of which have application in rock and soil. The simulation of this excavation process is then discussed, with particular reference to plane strain analysis, followed by the ways of modelling tunnel linings. The chapter then focuses on the modelling of time dependent behaviour and on constitutive models appropriate to the modelling of soft ground tunnelling. The final section presents examples of analyses of tunnelling in stiff clay. These examples include the analyses of case studies and parametric studies, covering greenfield tunnelling, tunnelling beneath buildings, and tunnelling adjacent to existing tunnels.

2.2 Introduction

In this chapter some of the numerical techniques presented in Volume 1 are applied to the analysis of tunnel construction. Attention is restricted to bored tunnels. Tunnels formed by the cut and cover construction technique are covered in Chapter 3. The Authors' experience and expertise is in the area of tunnelling in soils and soft rocks modelled as continuum materials, where structural features, such as faults and joints, are not represented. This chapter therefore deals with soft ground tunnelling.

The first question to be asked of anyone advocating the application of numerical methods to tunnelling is surely "why use numerical methods to analyse tunnel construction?" There are non-numerical ways of obtaining good predictions of the likely ground response to tunnelling, and the likely loads in a tunnel lining. These conventional design tools are arguably cheaper and quicker to use. But they are characteristically uncoupled, i.e. the loads are determined by one technique (usually an elastic solution), and movements by another (usually empirical), the two not being linked together. Furthermore, the information gained from conventional analysis is often limited. For example, empirical predictions are limited to greenfield situations, where there is no existing surface or sub surface structure to influence the pattern, or magnitude of ground displacement. In a real tunnel, however, the different facets are clearly coupled and the problem is

complex, involving pore pressure changes, plasticity, lining deformations and existing structures. Numerical procedures, such as the finite element technique, lend themselves to the analysis of such complex problems. The finite element method can:

- simulate the construction sequence;
- deal with complex ground conditions;
- model realistic soil behaviour;
- handle complex hydraulic conditions;
- deal with ground treatment (e.g. compensation grouting);
- account for adjacent services and structures;
- simulate intermediate and long term conditions;
- deal with multiple tunnels.

This establishes a strong case for using numerical methods. It also focuses the mind on the type of problem for which one might consider the use of numerical methods. This chapter deals with all aspects of the above list: the construction sequence and its simulation (excavation and lining); the choice of an appropriate soil model (stress-strain-strength and permeability); the modelling of hydraulic boundaries; and examples of analyses of tunnelling beneath buildings and alongside existing tunnels.

2.3 Tunnel construction

2.3.1 Introduction

Historically soft ground tunnels were excavated by hand, using spades for cutting clayey soils and picks for breaking up granular soils and weak rocks. Openings would be supported by timbering and subsequently lined in brick. The first use of a tunnelling shield was for construction of Brunel's Thames Tunnel between 1825-1843 (Skempton and Chrimes (1994)). The men excavating the face were protected from falls by a large shield within which they worked. The advent of pneumatic spades and picks clearly enabled more rapid hand excavation. Hand excavation is still in use today on short lengths of tunnel, or where access for mechanical means is restricted.

Civil engineering construction starts the 21st Century with many alternative mechanical methods for creating underground openings. The engineer can design the most remarkable tunnel excavations, cathedral like in proportion and complex in shape. The decision as to which method to adopt is based on knowledge of the geology and the size and shape of the opening required. This section briefly introduces three of the most common tunnel excavation techniques, highlighting some of the key features which have an implication for numerical modelling.

Temporary support is today provided by a number of means - shield support, compressed air, slurry machine, earth pressure balance machine (EPB), or shotcrete. Permanent support is also provided by various means, including wedge-block precast concrete and cast iron, bolted cast iron lining, reinforced shotcrete,

or cast in-situ reinforced concrete. Section 2.4.5 of the chapter deals with modelling the tunnel lining.

2.3.2 Open faced shield tunnelling

Tunnel shields are designed to protect against falls of ground, see Figure 2.1. They do not provide permanent support, and a lining is usually constructed within or just behind the shield. The shield itself is jacked forwards through reaction against the completed lining. The face is unsupported, but can be partially supported by face jacks, face plates, or compressed air working. Compressed air can be used to control squeezing of soft clays or flow of water and loss of fines in sandy soils. During down time the face can be fully supported by timbering or shotcrete.

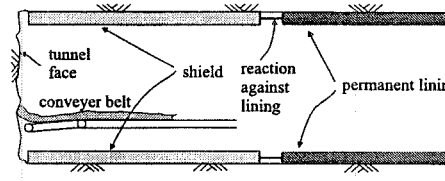

Figure 2.1: Schematic view of shielding during tunnel excavation

The method of excavation of the open face within the shield can vary. Hand excavation has already been mentioned. Mechanical alternatives are hydraulic backhoe excavators, or roadheaders mounted within the shield.

2.3.3 Tunnel Boring Machines (TBM), including slurry shield and Earth Pressure Balance (EPB) tunnelling

TBMs are closed face systems which advance through the ground by rotation of a cutting head, propelled by reaction against the constructed lining, see Figure 2.2 (in rock applications the TBM can propel itself by reaction against the rock.) Such tunnelling has traditionally been restricted to single bore circular section tunnels. Recent technological developments in Japan have led to the creation of quite remarkable multiple faced TBMs (e.g. Kuzuno *et al.* (1996)). Face support is provided through controlling the applied thrust and the rate of removal of excavated material.

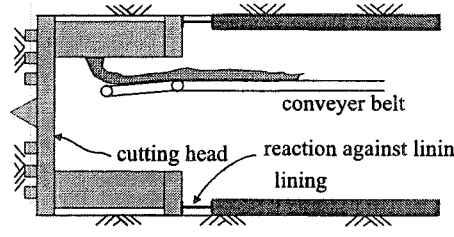

Figure 2.2: Schematic view of the TBM

Tunnel headings may be additionally supported through application of slurry or EPB machines. These TBMs pressurize the face. A slurry machine uses a bentonite slurry pressurised within the cutting bulkhead. An EPB machine controls the pressure of the excavated material itself against the face within the bulkhead, so balancing the earth pressures in the ground.

2.3.4 The sprayed concrete lining (SCL) method

The SCL method is a soft ground application of the New Austrian Tunnelling Method (NATM), see Figure 2.3. As well as standard circular section tunnelling, SCL can be used in competent ground to create large non-circular openings. The method of excavation is usually by independent track or wheel mounted hydraulic excavators. Support is provided as soon as possible by the application of sprayed concrete (shotcrete). This is often reinforced by a steel mesh or a series of steel hoops or arches installed before concreting. A permanent reinforced lining is usually created at a later date, either by the application of further shotcrete, or in-situ concreting. The current trend is, however, towards using a single shotcrete lining, adequately reinforced.

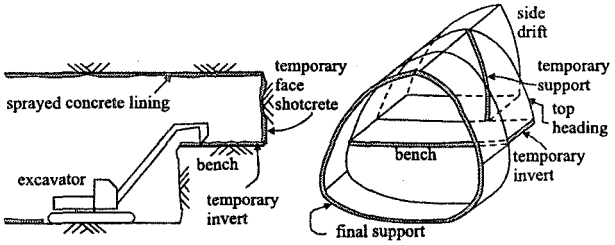

Figure 2.3: Schematic view of SCL method

For large openings using SCL it is always the case that the tunnel is created by the method of advanced headings. This can involve excavation of the crown first, leaving a temporary invert, or the use of left and right side drifts, or a combination depending on the ground quality and the size of opening. In all cases the advanced heading is fully lined by shotcrete before the following drift commences.

2.3.5 Ground response to tunnel construction

Excavation in the ground induces stress relief which causes soil movement towards the opening. If there were no closure of the ground into the opening, the volume of soil excavated would exactly equal the volume of tunnel created. Because ground does however close into the opening, extra soil over and above the volume of final tunnel created must be excavated. This excess soil is termed the ground loss, and is often quoted as a percentage of the theoretical tunnel volume, the

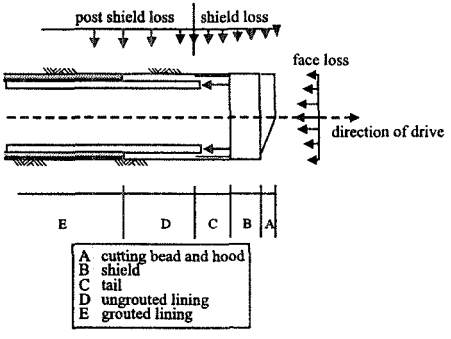

Figure 2.4: Sources of volume loss (example of the TBM)

percentage volume loss. During the driving of a tunnel there are various distinct causes of loss of ground into the excavation. Figure 2.4 shows, as an example, a conventional shield tunnelling machine geometry and highlights the sources of short-term volume loss discussed here:

Face loss: Loss first occurs into the face of the excavation, causing ground settlements to appear at the surface ahead of the tunnel. These losses can be reduced through the use of a closed face TBM, compressed air, slurry shield or EPB machine.

Shield loss: Soil will relax radially towards the shield after the cutting bead has passed, filling the bead width void if the deformations are large enough. Any over-excavation will contribute to increase this radial loss. The shield drives itself forward by pushing off the last ring of lining segments to be erected. If the soil deformations are large enough to fill the bead width void, then the tail to the shield provides support to the cut perimeter of the soil. Another source of shield loss occurs if the shield does not move forward with its axis coincident with the axis of the tunnel, see Figure 2.5. In such a situation the size of the excavated hole is larger than the final lining. This behaviour is often referred to as *pitching* and occurs due to bad steering, or when tunnelling on a curved alignment.

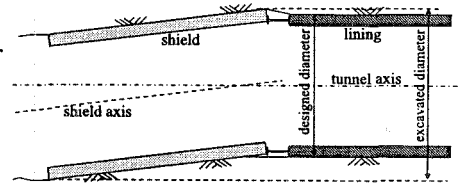

Figure 2.5: Schematic view of pitching

Post shield loss: If the lining is erected behind, rather than within the shield, then there will be a length of unsupported soil between the back of the tail to the shield and the erected liner, over which radial deformation can occur. Once the lining is in place, whether constructed within or behind the tail to the shield, ground will continue to squeeze into the excavation if a void exists behind the lining. It is common practice therefore to grout up any voids between liners and the exposed soil surface. Expanded concrete liners are theoretically expanded against the soil leaving no void.

These three aspects form the major contribution to the short term volume loss. If excavation is taking place in a low permeability clay soil, then rapid construction progress may result in a no volume change, undrained ground response. Thus the volume loss at the tunnel will be exactly reflected at the surface in the settlement trough. This statement will only hold rigorously true if there are no other boundaries which can deform in response to the volume of soil moving into the new excavation, such as open excavations. In a clay soil, after the tunnel has been constructed and the lining installed, ground displacements are likely to be seen to continue at the surface. This is due to the consolidation movements of the clay as pore water pressures equilibrate to the new steady state regime, dictated by the

presence of the tunnel. The tunnel lining may also deform as the earth pressures act on it, causing ground displacements.

2.4 Simulation of the construction process

2.4.1 Introduction

Tunnel excavation is a three dimensional engineering process. Whilst recognising that three dimensional analysis is becoming possible in the work place, it is still two dimensional modelling that dominates. This is because there are practical limits on cost and computer resource which, when performing analyses sufficiently sophisticated to handle all the complexities outlined in Section 2.2, restrict us to two dimensional modelling. If multiple shallow tunnels are to be analysed, or if the ground surface response is key to the analysis, then a plane strain representation of the transverse section is required (e.g. to study effects on structures, Figure 2.6). If a single deep tunnel is to be investigated, and surface effects are not of prime interest, then an axially symmetric approximation may be appropriate and heading advance can be studied, all be it within a simplified stress regime (Figure 2.7).

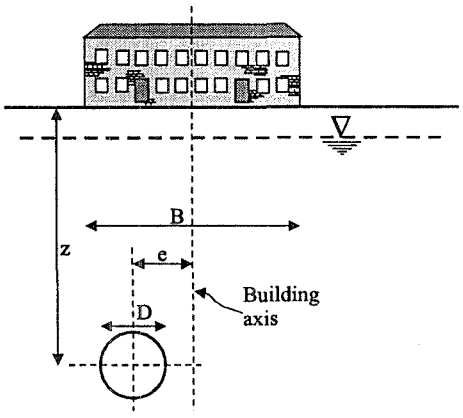

Figure 2.6: Plane strain geometry

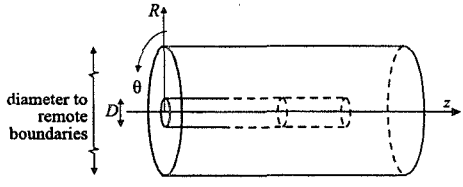

Figure 2.7: Axi-symmetric geometry

More recently three dimensional analyses have been carried out using the Fourier series aided finite element method (FSAFEM), applied to an axially symmetric geometry to analyse the advance of a single tunnel heading (Shin (2000)). FSAFEM is covered in detail in Chapter 12 of Volume 1. Such an approach allows the material properties, initial stresses and boundary conditions to vary with θ (Figure 2.8), so introducing the ground surface whilst maintaining the 2 dimensional simplification for the finite element mesh. This still demands substantial computer time and restricts the analyst to considering one tunnel, but is a significant advance for research into tunnel heading behaviour.

When modelling in plane strain at least one assumption must be made, i.e. something must be prescribed, rather than predicted. There are various accepted assumptions which are addressed in Section 2.4.4 of this chapter. The reader might

also find useful the excellent summary by Clough and Leca (1989) of work done, up to 1989, using the finite element method as a means to analyse soft ground tunnels.

2.4.2 Setting up the initial conditions

Following the generation of a suitable finite element mesh, before the effects of tunnelling activities can be analysed, the initial conditions in the ground must be established. This can be achieved by modelling the complete geological history of the site, if it is known. If it is not known, then the initial conditions can be achieved in two stages. First, the conditions appropriate to a greenfield site are input into the analysis. Commonly, the engineer directly specifies the distributions of vertical and horizontal effective stress in the ground prior to any construction activity (by means of the material unit weight, the pore water pressure profile and the coefficient of earth pressure at rest, K_o). Depending on the constitutive models to be used, it might also be necessary to specify the initial void ratio and any hardening parameters required to model the soil behaviour. The second stage involves simulating any previous construction activities that have occurred at the site. These could consist of demolition or construction of buildings, excavation of deep basements, construction of services, or any other tunnels. This usually involves several increments of analysis. For tunnels constructed in a greenfield site, or where previous construction activities have caused minimal disturbance to the in-situ soil conditions, stage two may be omitted.

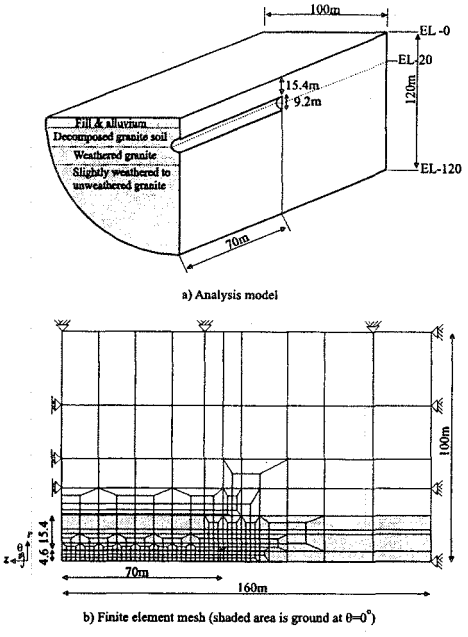

Figure 2.8: FSAFEM geometry

It is noteworthy that if stage two is to be included, then the elements representing the soil to be excavated for the tunnel must be included within the mesh, and removed at the relevant construction stage. This is also true if staged multiple tunnel analysis is to be modelled.

Having established the initial conditions, the analysis goes on to model tunnel excavation, for which there are various accepted methods. A recommended way of dealing with excavation during an analysis is to remove all the elements to be excavated at the beginning of the relevant construction stage. In doing this the mesh boundary is redefined excluding the excavated elements, so permitting the specification of necessary boundary conditions (load/displacement and pore

pressure/flow conditions). In addition, computer resources are saved because when an element is excavated it makes no contribution to the global stiffness matrix.

2.4.3 Important boundary conditions

A number of boundary conditions are required to model tunnel construction. They include the boundary displacement conditions, required to represent the far field conditions or any symmetry of the problem; any surface traction; the excavation of solid soil elements; the construction of structural shell elements; and the hydraulic conditions at the far field boundaries, the soil strata interfaces (if an interface is between consolidating and non-consolidating elements) and the tunnel lining itself.

Loading and flow boundary conditions affect the right hand side of the global equilibrium equations, whilst displacement and pore water pressure boundary conditions affect the vectors of nodal displacements and pore pressures on the left hand side of these equations, see Section 2.8 of Volume 1. Sufficient displacement conditions must be prescribed in order to retain any rigid body modes, such as rotations or translations of the complete mesh.

Analysis of tunnelling in drained granular materials will require careful consideration of the hydraulic boundary condition, both during and after excavation. In contrast, excavation in clay is usually rapid enough to be treated as an undrained process, so the tunnel perimeter may remain impermeable until after excavation is complete. Section 2.5.3 considers the hydraulic boundary condition in more detail.

2.4.4 Modelling tunnel excavation

The 'gap' method

This method was introduced by Rowe *et al.* (1983). A predefined void is introduced into the finite element mesh which represents the total ground loss expected. In this way the out of plane and in plane ground losses are incorporated together with additional losses to allow for miss-alignment of the shield, the quality of workmanship, and the volume change due to soil remoulding. It is clear therefore how one can account for the different tunnel construction methods outlined above by varying the size of the void. For example, if modelling an EPB machine, the out of plane component of the total ground loss could be reduced.

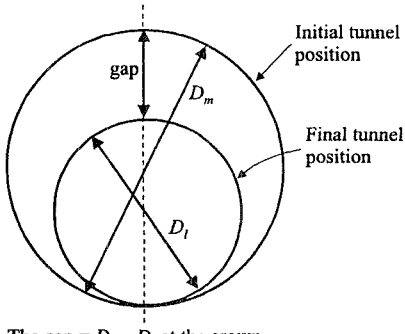

Figure 2.9: The gap method for modelling tunnel excavation

The void is placed around the final tunnel position and so locates the soil boundary prior to excavation (Figure 2.9). This is achieved by resting the invert of the tunnel on the underlying soil and prescribing the *gap parameter* at the crown. The gap parameter is the vertical distance between the crown of the tunnel and the initial position before tunnelling. The analysis proceeds by removing boundary tractions at the perimeter of the opening and monitoring the resulting nodal displacements. When the displacement of a node indicates that the void has been closed and the soil is in contact with the predefined lining position, soil/lining interaction is activated at that node. The soil and the lining are actually treated as separate bodies, related only by nodal forces (Rowe *et al.* (1978)).

The 'convergence-confinement' method

Another approach to modelling excavation is the λ or *convergence-confinement* method (Panet and Guenot (1982)), in which the proportion of unloading before lining construction is prescribed, so volume loss is a predicted value. An internal force vector, $(1-\lambda)\{F_o\}$, is applied at the nodes on the tunnel boundary ($\{F_o\}$ being equivalent to the initial soil stresses $\{\sigma_o\}$). λ is initially equal to 0 and is then progressively increased to 1 to model the excavation process. At a prescribed value λ_d the lining is installed, at which point the stress reduction at the boundary is $\lambda_d\{\sigma_o\}$. The remainder of the stress reduction is applied to create the lining stress. The stress reduction with the lining in place is then $(1-\lambda_d)\{\sigma_o\}$, see Figure 2.10.

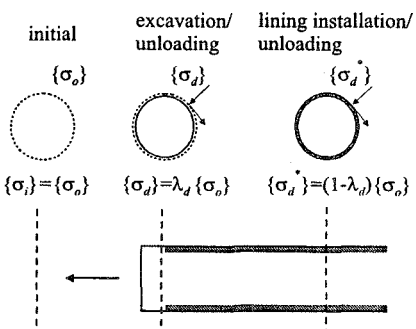

Figure 2.10: Convergence-confinement method

The 'progressive softening' method

A method termed *progressive softening* was developed for the modelling of NATM (or sprayed concrete) tunnelling, Swoboda (1979). The soil within the heading is softened by multiplying the soil stiffness by a reduction factor β. The effects of the softening are evident when excavation forces are applied to the boundary of the future tunnel. As with the convergence-confinement method, the lining is installed before the modelled excavation is complete, see Figure 2.11. If the tunnel is constructed with a bench and heading, then the above procedure can be applied to each of them sequentially. The same methodology could be applied to an analysis with side drifts.

The 'volume loss control' method

This method is similar to the convergence-confinement method, but instead of prescribing the proportion of unloading prior to lining construction, the analyst

prescribes the volume loss that will result on completion of excavation, see Figure 2.12. This method is therefore applicable to predictive analyses of excavation in soil types for which the expected volume loss can be confidently (and conservatively) determined for the given tunnelling method. It is also invaluable for worthwhile back analysis of excavations for which measurements of volume loss have been made.

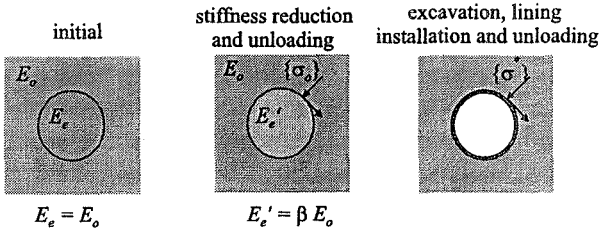

Figure 2.11: Progressive softening method

With the λ method, the outward support pressure on what is to be the tunnel boundary is progressively reduced. An alternative is for the program to calculate the value of $\{F_o\}$, the equivalent nodal forces which represent the pressure exerted, on what is to be the tunnel boundary, by the soil to be excavated. This is linearly apportioned to the number of increments, n, over which the excavation is to take place, to give $\{\Delta F\}=\{F_o\}/n$. The equal and opposite force vector $\{-\Delta F\}$ is then applied at the excavation boundary for each of the n increments of excavation (Figure 2.13). The volume loss induced by each increment of boundary loading can be monitored (given by displacement normal to the tunnel perimeter, or by the surface settlement profile in an undrained greenfield excavation) and the tunnel lining constructed on the increment at which the desired volume loss is achieved. After lining construction, the loading boundary condition, $\{-\Delta F\}$, is still applied to the excavation perimeter for the remainder of the n increments, thus introducing an initial stresses into the lining.

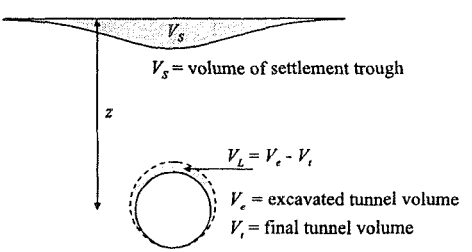

Figure 2.12: Volume loss method

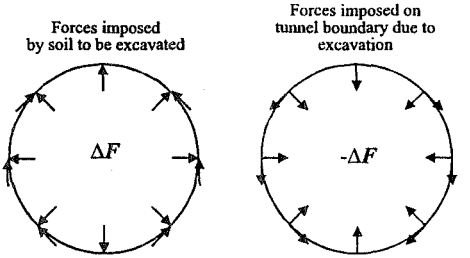

Figure 2.13: Modelling excavation of solid elements

Depending on the stiffness of the lining further volume loss can occur during the latter process. It may therefore be necessary to install the lining at an increment which has a smaller volume loss than that desired, so that after full excavation the desired volume loss is achieved.

Problems associated with soft clay

When modelling tunnelling in soft clay, problems may occur. When a lining is constructed during excavation, the subsequent unloading within the lining results in a desire for the complete tunnel to move upwards, with a corresponding reduction in ground surface settlement. In a soft clay, this upward movement may be so significant as to cancel out all the ground surface settlement occurring before lining construction. Analysis of tunnelling in soft clay may therefore require the application of support pressures within the tunnel during excavation. Tunnelling in Singapore has been analysed at Imperial College (Ong (1996) and Ong (1997)). The very soft marine clay was modelled using a modified Cam clay model. The incremental nodal forces, $\{-\Delta F\}$, were applied at the tunnel boundary, and simultaneously an isotropic radial support force (akin to a compressed air working pressure) was prescribed at each node in the opposite direction to the excavation boundary force. The support force was adjusted to give the desired volume loss on completion of excavation. The lining was not constructed until excavation was complete. The sum of the incremental support forces accumulated during the excavation gave the magnitude of the final support force. The removal of this final support force required the application of an equal and opposite radial force at each boundary node. This introduces initial stresses into the lining.

The application of an isotropic outward pressure on the tunnel boundary can be used to represent working under compressed air conditions. A similar approach was adopted recently in association with the λ method (Bernat (1996)). Bernat was reproducing the effect of grout injection behind the tunnel lining.

2.4.5 Modelling the tunnel lining

In the previous section it was apparent that insertion of a lining is required to control movements. It might be possible in a soil with sufficient undrained strength to complete excavation of a plane strain tunnel with no lining support. The ground movements predicted will however be significant, as plane strain analysis fails to recognise the support from the lining already constructed behind the face, into which the stresses arch.

Construction of an element can only usually take place if it existed within the initial mesh. Elements which are to be constructed at some point during an analysis (such as a tunnel lining) must therefore have been generated within the mesh at the outset. Many software packages have a special facility permitting initial excavation of these elements without the application of any loads at the commencement of any analysis. Construction can be executed over a number of increments, or in a single increment. With the volume loss control and convergence-confinement approaches

to modelling tunnel excavation, the lining is constructed in a single specified increment.

The use of solid elements

Using solid elements to represent a tunnel lining allows the analyst a very wide range of constitutive models. A significant drawback is the need to maintain an acceptable element shape (defined by the aspect ratio of length to width). A tunnel lining is likely to be very thin relative to the tunnel diameter and boundary distance. The consequence of maintaining an acceptable aspect ratio is the need for a large number of elements.

The use of shell elements

Using zero thickness curved shell elements to model a tunnel lining removes the problem of aspect ratio control mentioned above. (Mindlin beam elements used in plane strain or axial symmetry are effectively shell elements, and such elements are covered in Chapter 3 of Volume 1.) Their use therefore allows more flexibility in the mesh definition, but such elements do introduce numerical problems which can be overcome by using selective reduced integration. It is additionally advantageous that the solution for shell elements is of a structural nature, i.e. shear force, hoop force, and bending moment. Special constitutive models can be coded for shell elements to model cracking or crushing.

Modelling the connections between lining segments

Many tunnel linings are jointed. This introduces particular modelling requirements. Probably the simplest way to model these tunnel linings is to use shell elements and leave a gap at the positions of the joints between lining segments, see Figure 2.14a. Tied freedom boundary conditions, see Section 3.7.4 of Volume 1, can then be applied between the two nodes representing the ends of adjacent segments (i.e. nodes A and B on Figure 2.14a). The two nodes can be tied so that their displacements are the same, but their rotations left untied. This will result in a joint that is free to rotate (i.e. cannot sustain a moment), but will be able to transmit axial thrusts and shear forces. Clearly, this is a simplification as most segmented linings will be able to transmit some moments across the their joints.

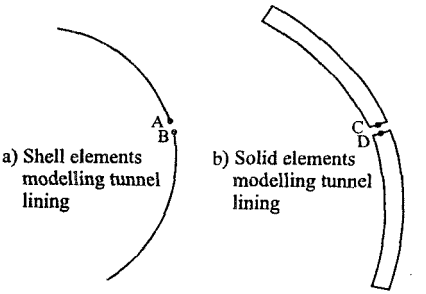

Figure 2.14: Modelling segment connection as a moment-free joint

A similar procedure could be applied if solid elements were used to represent the tunnel segments, see Figure 2.14b. In this case the displacements of the mid-side nodes C and D would be tied.

The drawback with this approach is that problems can arise with the elements representing the soil adjacent to the joint. For example, consider the situation shown in Figure 2.15 where shell elements have been used to represent the lining segments. Although the lining is discontinuous at the joint, the soil is not, consequently at least one soil element must span the joint region. In Figure 2.15 the mesh generation has resulted in two soil elements which span the joint and the nodes E, F and G are not supported by the lining. If the soil is modelled with a finite strength (i.e. not linear elastic), then during the analysis the two soil elements adjacent to the joint are likely to fail due to the lack of radial support and the soil will be squeezed through the gap between the lining elements. At the very least, this is likely to give rise to numerical instability, but it could also represent a legitimate failure mechanism, albeit an unrealistic one. This problem also arises if solid elements are used to represent the lining.

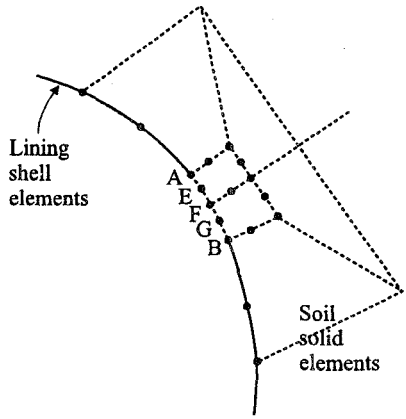

Figure 2.15: Problems associated with the moment-free joint

To overcome this problem one solution would be to tie the displacements of nodes E, F and G to those of nodes A and B. However, experience indicates that such an approach is likely to result in numerical instability due to the very large gradients of stress and strain that such constraints place in the soil elements adjacent to the joint. Another solution, but not one that is recommended, is to make the two soil elements adjacent to the joint linear elastic.

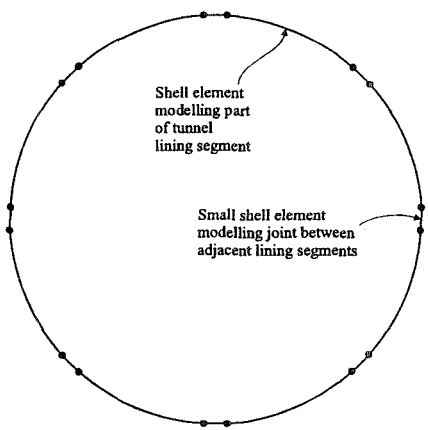

Figure 2.16: Modelling segment connection using small shell elements

An alternative approach to modelling the joints between tunnel segments is to place a small shell element between those representing the segments (Figure 2.16). A special constitutive model which simulates rotation at the joints between tunnel segments can be used for these elements. In this way more accurate bending moment distributions can be predicted in situations of significant distortion. The model requires the specification of the maximum compressive stress permissible across the joint, σ_f, and the position of the neutral axis within the lining section (see Figure 2.17a). The bending moment,

M, and hoop force, N, developed at each joint between two lining segments can be represented by the normal force, N, acting at an eccentricity, e, such that $eN=M$ (Figure 2.17b). As the induced bending moment increases during lining deformation, the normal force translates across the joint, see Figure 2.17c. The two limiting moment values, M_e and M_i, above which the joint will open on the intrados or extrados, are set by the model based on the defined position of the neutral axis and the maximum compressive stress:

$$M_e = N\left(y_e - \frac{N}{2\sigma_f}\right)$$
$$M_i = N\left(y_i - \frac{N}{2\sigma_f}\right) \qquad (2.1)$$

If M_e or M_i is exceeded at any joint, the joint will rotate and open, allowing the extra moments to redistribute through the lining, maintaining the limiting value at the joint. Two further conditions are that if N is tensile the joint will open, and if N is such that the maximum compressive stress is violated across the entire joint, failure due to crushing will occur.

In some circumstances it may also be necessary to apply restrictions to the shear forces that can be developed. For example, a simple, but appropriate assumption, is that the maximum shear force, S_{max}, is related to the normal force, N, via the angle of friction, δ, between the lining segments (i.e. $S_{max} = N \tan\delta$).

To use this model in an analysis it is necessary to construct a finite element mesh in which the lining is represented by a continuous series of shell elements. The small elements at the positions of the joints are assigned the special constitutive model described above, while those representing the tunnel segments are assigned appropriate structural properties.

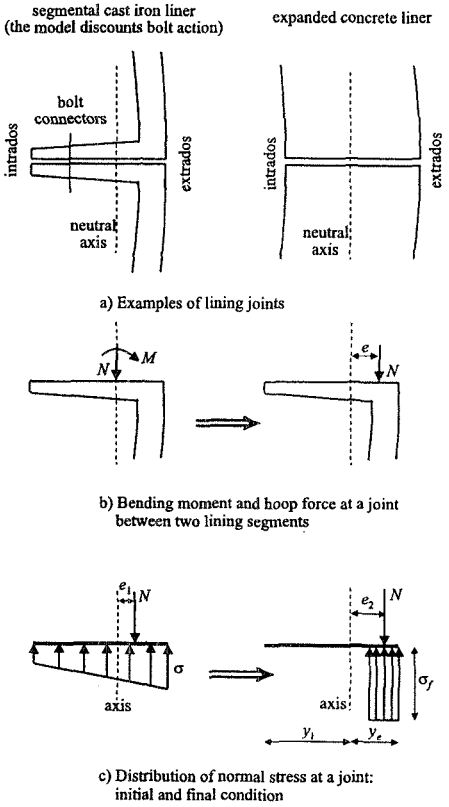

Figure 2.17: Modelling tunnel lining joints

In a plane strain analysis the idealisation shown in Figure 2.16 represents a tunnel with an *unrolled* lining, as shown in Figure 2.18a. If in reality the lining segments are *rolled*, see Figure 2.18b, the above model may not be appropriate.

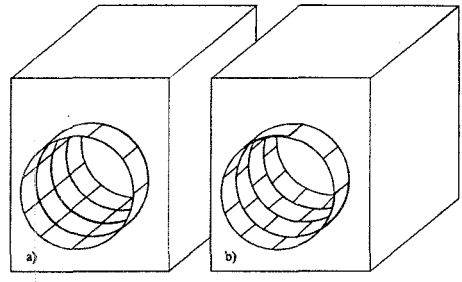

Figure 2.18: a) Unrolled and b) rolled tunnel lining

Modelling sprayed concrete linings

The lining model presented in the previous section can also be applied to the modelling of sprayed concrete linings. In such linings there are no segments and joints, but the entire lining uses this special model, so cracking is permitted to develop at any location around the lining. If solid elements are being used to represent a sprayed concrete lining, then a limiting tensile strength yield criterion would be an appropriate plastic model to incorporate in conjunction with a crushing model. A suitable double yield surface model is presented in Section 8.3 of Volume 1.

The behaviour of fresh sprayed concrete is also time dependent. Both its strength and stiffness increase rapidly during the construction period. This behaviour should be accounted for in any analysis. This problem is recently discussed in depth by Shin (2000) and Shin and Potts (2001).

2.5 Modelling time dependent behaviour

2.5.1 Introduction

It is often important to model the consolidation behaviour of a soil during and after excavation of a tunnel. To reliably study the time variant behaviour of the ground and the tunnel, coupled consolidation analysis must be carried out. For coupled consolidation analyses the hydraulic boundary conditions must clearly be correct and representative of the field, as must the permeability of the continuum. A crucial, and often ill considered, hydraulic boundary condition is that controlling flow around the newly constructed tunnel. This section discusses such considerations.

2.5.2 Setting up the initial conditions

It is useful when modelling time dependent behaviour to use software with the flexibility to handle consolidating and non-consolidating elements in the same mesh. A consolidating element will have both displacement and pore pressure nodal degrees of freedom. A discourse on such elements and the choice of the function to define pore pressure variation across an element can be found in Section 10.4 of Volume 1. It is clear that having both displacement and pore

pressure degrees of freedom at every node in a mesh will significantly increase the computer resource and time demand on that analysis. In a mixed situation the engineer benefits therefore from being able to treat granular strata as free draining, whilst only considering the consolidation behaviour of silty or clayey strata.

Any consolidating elements will require a model to define the permeability (see Section 2.5.4). It is important to prescribe an initial pore water pressure distribution which is in agreement with field measurements from the site. Reliable measurements of permeability are less likely to have been made, but reasonable judgement should be used when defining the permeability profile. The initial stresses which prescribe the pore pressure profile at the outset of the analysis must be consistent with the material permeability distribution. In the simple case of a linear initial pore pressure profile, combined with a homogeneous permeability, there is no problem (these will always be compatible). Modelling a nonlinear initial pore pressure distribution, in combination with a more realistic inhomogeneous permeability model, needs more care. Such a situation exists in London, and the following example serves as a useful guide to approaching such situations, see also Chapter 9.

Under-drained pore pressures in London

Historically water has been pumped from a deep aquifer beneath London. Although now ceased, this action has induced under-drained pore pressure profiles through the low permeability London Clay. Recent pore water pressure measurements at Waterloo (Hight *et al.* (1992)) clearly show the sub-hydrostatic profile plotted in Figure 2.19. Also shown is a data point of Skempton and Henkel (1957). Such a steady state profile can be achieved numerically with a model in which permeability reduces with increasing depth, or reduces with increasing mean effective stress (see Section 2.5.4 below). The numerically predicted profile shown through the data in Figure 2.19 was achieved using the latter.

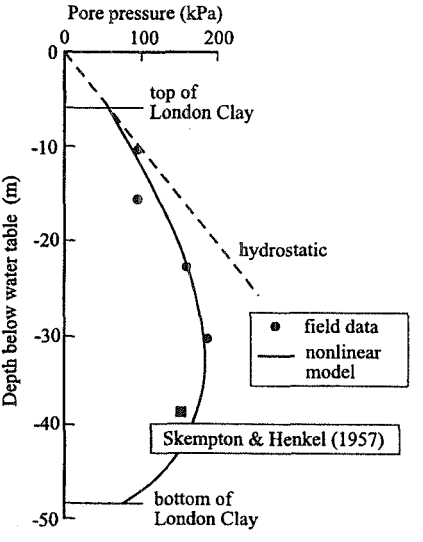

Figure 2.19: Under-drained pore water pressure profile for Waterloo, London

A useful approach to establishing compatible pore water pressures and permeability in such circumstances is a unit width column of consolidating elements. Displacement boundary conditions appropriate to a one dimensional analysis are specified and an initial hydrostatic pore pressure profile prescribed. Figure 2.20 shows the column in comparison with

the actual boundary value problem to be analysed. The elements in the column are given the stress-strain and permeability constitutive models that will be used in the full analysis and the desired steady state pore pressures at the top and bottom are prescribed as boundary conditions. Taking the analysis to the long term (through the use of sufficient time step increments) gives a prediction of the steady state pore pressure profile. This prediction can be compared with the data, and if the match is not acceptable the parameters in the permeability model can be adjusted and the analysis repeated. Using a unit width column for this exercise, rather than the full mesh developed for the boundary value problem, is quicker. Once an acceptable pore pressure profile has been obtained, this can be included in the full analysis in the initial stresses, in the knowledge that it is compatible with the soil permeability.

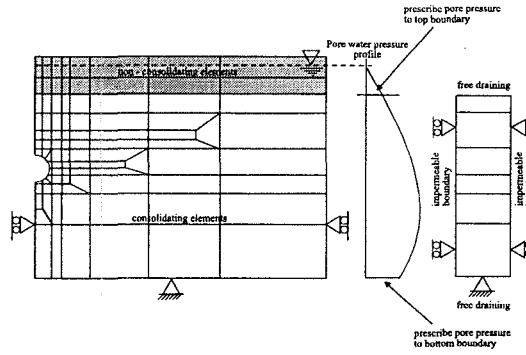

Figure 2.20: Column method for predicting steady state pore water pressure profile

The example analyses in Section 2.5.5 demonstrate the influence of an under-drained pore pressure profile on long term ground movement predictions, through comparison with a hydrostatic scenario.

2.5.3 Hydraulic boundary conditions

Subsequently, during an analysis, representative flow or pore pressure conditions must be stipulated at the borders of consolidating layers, be they mesh boundaries or material interfaces. Many hydraulic boundary conditions are introduced in Section 10.6 of Volume 1. Typically for tunnel analysis free draining and no-flow boundaries are necessary: a boundary which is free draining is dictated by no change from the initial pore water pressure condition; a mesh boundary which represents a line of symmetry must be a no flow boundary, and the pore water pressures must be permitted to change accordingly. The tunnel boundary itself poses more of a problem. From the outset of tunnel excavation the tunnel perimeter is a mesh boundary. During rapid excavation in low permeability clay the tunnel boundary can be considered to be a no flow boundary. During consolidation however the tunnel lining can be treated as either free draining or impermeable. This decision must be based on knowledge of whether the completed and fully lined tunnel will act as a drain or not. The example analyses in Section 2.5.5 show how significant this decision can be with respect to ground movement predictions.

If it is decided that the tunnel will act as drain, the pore pressure condition to be applied on the tunnel boundary is logically zero (or equal to whatever positive

outward pressure is being applied to represent compressed air working, etc.). Soil adjacent to a tunnel excavation might develop tensile pore pressures (suctions) during excavation. This will arise if the reduction in pore water pressure due to unloading is greater than the initial pore water pressure around the tunnel. In this case, if a zero (or positive) pore pressure boundary condition is prescribed, the soil will draw water across the tunnel boundary. This is clearly unrepresentative of reality, as a new tunnel is not a source of water. A more sophisticated boundary condition is therefore required.

The application of a precipitation boundary condition to a tunnel lining is presented in Section 10.6.6 of Volume 1. When using such a condition, the program monitors the pore water pressures at the boundary nodes. If, at any time, at any node, the soil pore water pressure is tensile with respect to the boundary pressure, then a no flow condition is maintained at that node to prevent flow from the tunnel into the soil; if however it is compressive, then the boundary pressure is prescribed and free flow at that boundary node is permitted. In this way, in the intermediate term, the swelling soil is forced to take water from surrounding soil and not across the boundary, but the long term steady state is a flow regime towards the new tunnel. As the condition is applied node by node it is possible at some stage in an analysis to have flow across the tunnel boundary (into the tunnel) in places, whilst still forcing a no flow condition in other places.

2.5.4 Permeability models

Coupled consolidation analyses require the material permeability, k, to be defined. Most software packages permit simple linear isotropic permeability to be defined, or anisotropic permeability, both having the option to vary k spatially (inhomogeneity). Alternatively, nonlinear permeability can be defined. With a nonlinear model the permeability varies during an analysis, the variation depending on void ratio or mean effective stress. A number of alternatives are presented in Section 10.7 of Volume 1.

As noted above, if initial pore pressure profiles are nonlinear then an inhomogeneous model must be adopted. It is also the case that different permeability models will lead to different long term pore pressure conditions after completion of tunnelling. Figure 2.21 exemplifies this through presentation of the numerically generated long term pore pressure profiles down the centre line above a 34m deep, 4m diameter tunnel in London Clay, which acts as a drain. The initial pore water

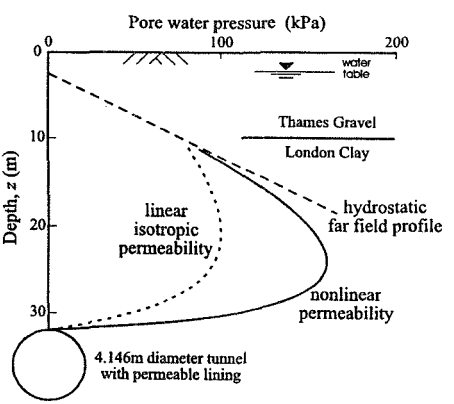

Figure 2.21: Long term pore water pressure profiles

pressure profile was hydrostatic. Two permeability models were used and the analyses taken to the long term. The first model was a linear, isotropic, inhomogeneous permeability (reducing with depth). The second model was a nonlinear model of the form presented below in Equation (2.2), in which permeability varies with mean effective stress and is continually updated during the analysis. The hydraulic boundaries in the long term are hydrostatic pressure at the top of the London Clay (defined by the water table in the gravel) and zero pore pressure at the permeable tunnel boundary. Figure 2.21 shows that the nonlinear permeability model predicts a near hydrostatic profile down to within 10 m of the crown, below which a rapid fall off of pore pressure is evident. The linear permeability model however predicts a pore pressure profile significantly below hydrostatic. If a back analysis is to be carried out, and piezometer readings have shown the pore pressures to be near hydrostatic above the tunnel in spite of the fact that the tunnel is acting as a drain, then clearly the nonlinear model is more appropriate.

If the decision is made to use a nonlinear model for a tunnel analysis, then it is noteworthy that the necessary data on which to base the parameters for such a model are unlikely to have been obtained during a standard site investigation. Hence the need to have reliable pore water pressure measurements which can be matched, as outlined in Section 2.5.2. It is also noteworthy that a model in which k depends on mean effective stress implicitly assumes something about the volume change behaviour of the soil. Observations of seepage pressures in fills and in-situ soils have shown that measured pore water pressures are generally very different from those predicted using conventional theory, hence the development of more sophisticated models for analysis (Vaughan (1989)). It is known that permeability varies with void ratio, often by several orders of magnitude over the range of possible void ratios for a given soil. Void ratio itself varies with effective stress, and effective stress is dependent on pore pressures, so the problem is nonlinear. To model London Clay a logarithmic law, relating permeability to mean effective stress, has been adopted:

$$k = k_o \, e^{-ap'} \tag{2.2}$$

where k_o is the permeability at zero effective stress, a is a constant incorporating the initial void ratio at zero effective stress and the coefficient of volume compressibility, m_v, and p' is the mean effective stress. The derivation of this logarithmic law therefore requires the assumption that m_v is constant. This is a useful assumption for many soil types, including London Clay (Vaughan (1989)). An alternative model assumes that the compression index, C_c, remains constant, as for one dimensional normal consolidation of wet clays, and leads to a power law relating permeability and mean effective stress. If soil yields during an analysis, there is clearly a question over the validity of the constant m_v or C_c assumptions. Additionally, if the plasticity model adopted allows for dilation on yielding, the mean effective stress can increase dramatically, so reducing the permeability of the yielding soil to unreasonably low values.

2.5.5 A parametric study of the effect of permeable and impermeable tunnel linings

The analyses presented here, carried out by the Geotechnical Consulting Group (1993), considered many factors which influence the intermediate and long term behaviour of tunnelled ground. All the analyses employed the coupled consolidation solution technique to analyse the time dependent consolidation settlement above railway tunnels excavated in London Clay. The study considered the three different tunnels in the profile shown in Figure 2.22. Only single tunnels were modelled in any one analysis. Two 6.5m diameter running tunnels (R) were analysed for axis depths below ground level of z = 15m and 25m. One 12m diameter station tunnel (S) was analysed at z = 25m. The water table was maintained at the top of the London Clay (z = 5m), but two alternative initial pore water pressure profiles were considered, under-drained (U) and hydrostatic (H), which are also indicated in Figure 2.22. The initial pore water pressure profile was in equilibrium with the spatially varying linear anisotropic permeability profile specified. The final far field equilibrium pore water pressure profile was the same as that prescribed initially, i.e. U or H. The pore water pressures in the Thames Gravel (a non-consolidating material) was maintained as zero. On the remote vertical boundaries, at some distance from the centre line, and at the interface between the Lambeth Group Clay and Sand, it was assumed that a source of water maintained the pore water pressure at its initial value throughout the analysis. On any boundary representing a line of symmetry, a no flow boundary condition was prescribed. The near field long term pore water pressure profile was governed by the drainage boundary condition prescribed at the excavated tunnel perimeter during consolidation. The two alternatives investigated were: a fully permeable lining (P) using the special control boundary condition introduced in Section 2.5.3; or a completely impermeable lining (I) modelled as a no flow boundary.

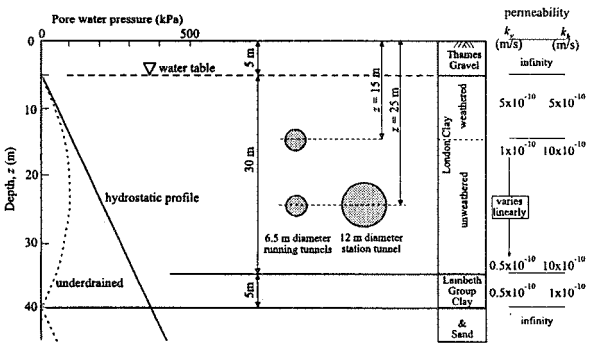

Figure 2.22: Soil profile and pore water pressure profiles for GCG parametric study

The volume loss control method was used with a target value of between 1.7 and 2.0% (see Section 2.4.4). The soil was represented by combining the pre-yield small strain stiffness model (see Section 5.7.5 of Volume 1) with a Mohr-Coulomb plasticity model (see Section 7.5 of Volume 1). The permeability data was based on field measurements reported by Burland and Hancock (1977) in the Westminster area of London. The Thames Gravel and Lambeth Group Sand were modelled as fully drained throughout the analyses. The profiles of permeability

(reducing with depth) in the clay are depicted on Figure 2.22.

Figure 2.23 shows the influence of tunnel diameter (R or S) on the time dependent surface settlements above a tunnel at a fixed depth (z = 25m) with a permeable lining. Both H and U analyses are presented. The diameter has little effect on the hydrostatic analyses, with RH and SH showing trends of increasing maximum settlement, S_{max}, over a 5 to 10 year period in the order of 30 to 35mm. This is clearly a greater percentage of the short term settlement for RH than for SH. The trend is reversed with the under-drained profile, as S_{max} is seen to reduce over a 5 to 10 year period. The reduction for RU is only 3mm, whilst that for SU is 20mm.

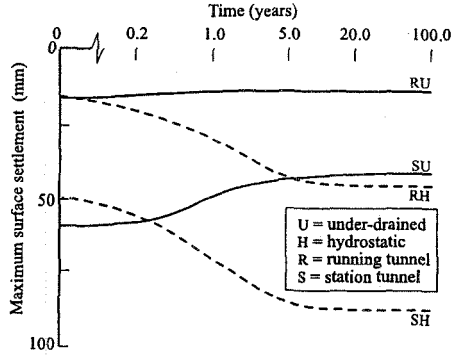

Figure 2.23: Effect of tunnel diameter

Figure 2.24 isolates the influence of depth (15 or 25m) on the time dependent surface settlements above a running tunnel with a permeable lining. During consolidation, S_{max} increases by 18mm for 15H and 30mm for 25H. Similarly there is an increase of 8mm for 15U. In contrast S_{max} reduces by 3mm for 25U. This opposite trend between 25U and 15U is a result of the pore water pressure values at those depths relative to hydrostatic. From Figure 2.22 it can be noted that a tunnel located at 15m is at a depth where the under-drained pore water pressures are near hydrostatic. The surface response in the intermediate period is therefore the same as for the hydrostatic analyses. All movements essentially cease within 10 years.

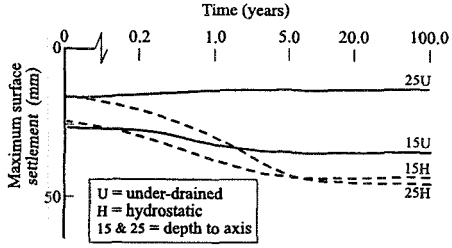

Figure 2.24: Effect of tunnel depth

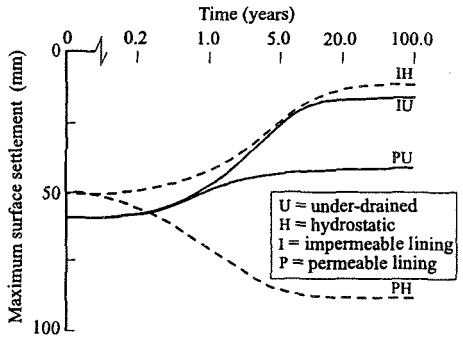

Figure 2.25: Effect of lining permeability

Figure 2.25 presents the influence of the lining permeability (P or I) on the time dependent surface settlements above a large diameter station tunnel at a depth of

25m. There is an increase in S_{max} of 35mm for PH, but a decrease of 20mm for PU. These movements are complete within 5 to 10 years. With an impermeable lining the surface heaves by 45mm for IU, and by 40mm for IH. The drainage path lengths in the consolidating clay are longer if the lining is impermeable, and this is reflected in the increase in time taken for the movements to cease from within 10 years to 20 years.

During the consolidation period after construction (the intermediate period) the predicted ground surface response depends on many factors: the equilibrium pore pressure profile and the tunnel depth within this profile, the tunnel lining drainage condition, and the tunnel diameter.

2.6 Choice of soil model

2.6.1 Introduction

The task of choosing an appropriate soil model for the analysis of tunnelling is a specific, not a general one. Volume 1 deals with many of the available constitutive models, and the particularities of them. This section aims, through example, to show that the choice of soil model can be of great importance in tunnel modelling. Some studies recently completed at Imperial College tested a number of pre-yield constitutive models against each other through the comparison with field measurements of surface and subsurface ground movements induced by tunnelling (Addenbrooke (1996), Addenbrooke *et al.* (1997)). Results from these studies are presented in Section 2.6.2. When modelling tunnelling in an overconsolidated clay, adopting a valid soil model is not necessarily going to give good predictions of ground movements when plane strain geometry is used. Section 2.6.3 discusses a couple of devices for improving predictions of ground movement.

2.6.2 Results from a parametric study

This section presents the results from analyses of tunnelling 34m beneath Regent's Park, 29m beneath Green Park and 30m beneath St. James's Park, in London Clay overlain by Thames Gravel and made ground. All three sites are on the Jubilee Line, the first two from stage I (constructed in the 1970s) and the last one from stage II (Jubilee Line Extension opened in 1999). Being in parks, the ground movements at these sites were not influenced by surface structures, and in each case the first tunnel to be excavated was analysed so there could be no question of sub-surface interaction effects (covered in Section 2.7.3). Each site was analysed in plane strain, the soil was elastic perfectly plastic, and the excavation was modelled

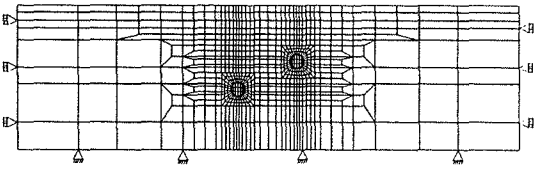

Figure 2.26: Finite element mesh for St. James's Park analysis

as undrained. The mesh for St. James's Park is presented in Figure 2.26 as an example (only the deeper tunnel is considered here). Volume loss controlled excavation was used, with a target of between 1.3% and 1.5% for Regents Park and Green Park and 3.3% for St. James's Park (based on field measurement). The initial stresses prescribed a pore pressure profile considered to be representative at each site, and employed an initial stress ratio, K_o, of 1.5 in the London Clay. In each case linear isotropic, linear anisotropic, and nonlinear elastic constitutive models were alternatively adopted for the pre-yield behaviour. All three cases had stiffness increasing with depth. Plastic behaviour was modelled using the non-associated Mohr-Coulomb model.

Linear isotropic, linear anisotropic and nonlinear elastic constitutive models are introduced in Sections 5.5, 5.6 and 5.7 of Volume 1 respectively. The use of a nonlinear pre-yield model recognises the nonlinear nature of real soil behaviour in the elastic region. One of the models which reproduces nonlinear behaviour at small strains is outlined in Section 5.7.5 of Volume 1. Figure 2.27 shows the secant shear modulus (normalised by mean effective stress p') decay with shear strain, predicted by the model with appropriate parameters for London Clay. This is compared with laboratory data for undrained triaxial compression and extension (samples consolidated anisotropically).

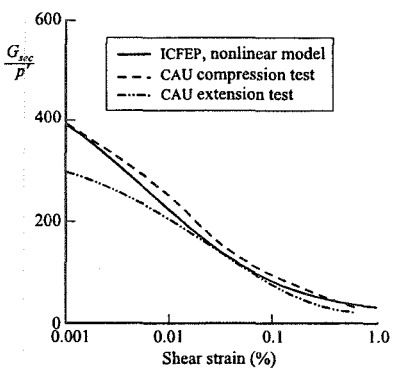

Figure 2.27: Small strain stiffness curves from triaxial tests

The surface settlement profiles presented in Figures 2.28a to c reveal a number of interesting points. First, it is noteworthy how much more precise the settlement monitoring was in the 1990s (Figure 2.28c) compared with the 1970s (Figures 2.28a and b). A full description of the state-of-the-art instrumentation used and the data obtained on the more recent project is presented in Nyren (1998). Secondly, linear elastic models, both isotropic and anisotropic, are wholly ineffective. In all three cases the settlement profiles are too shallow and too wide when compared with the field data, and the isotropic analyses predict profiles of the wrong shape. Thirdly, the introduction of a more representative nonlinear elastic model significantly improves the predictions, see also Addenbrooke *et al.* (1997). The same improvement in prediction with the nonlinear elastic model can be demonstrated for sub-surface ground movements.

2.6.3 Devices for improving the surface settlement prediction

The analyses in Section 2.6.2 were plane strain and the initial stresses prescribed prior to tunnel excavation were the at rest stresses (based on $K_o > 1$). Axially

symmetric and three dimensional analyses have revealed that, as a tunnel heading approaches and passes a plane in space, the effective stress ratio reduces to the side and increases above and below the tunnel. The introduction of a stress scenario such as this in advance of the plane strain excavation may be considered a logical assumption to represent stress changes ahead of the tunnel face. In this section the results of analyses with a local zone of reduced K_o (equal to 0.5) within the London Clay with a much higher global K_o of 1.5 are presented. This zone extended vertically between the crown and the invert of the tunnel, and horizontally a distance, a, of approximately three times the radius of excavation (Figure 2.29). The Jubilee Line tunnels were re-analysed with the reduced K_o approach. Figures 2.30a to c show the improvement in the predicted surface settlement profiles.

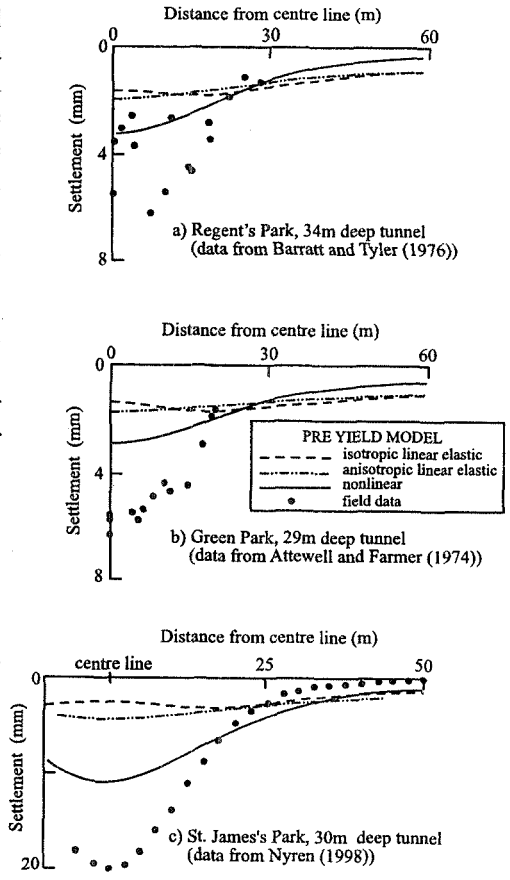

Figure 2.28: Effect of a pre-yield model on predicted settlement profile

Another device for obtaining improved surface settlement profiles is to employ an anisotropic nonlinear pre-yield soil model. If the soil is cross anisotropic then five parameters must be defined: the vertical Young's modulus, E_v', the horizontal Young's modulus, E_h', the Poisson's ratio for the influence of increments of vertical effective stress on horizontal strain, μ_{vh}', the Poisson's ratio for the influence of increments of horizontal effective stress on the horizontal strain in the orthogonal

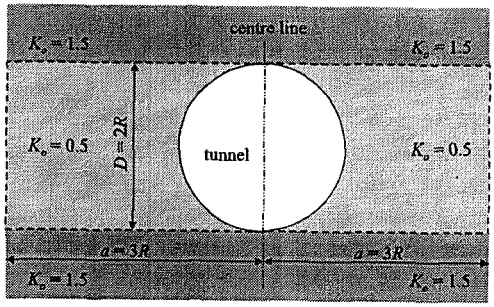

Figure 2.29: Local zone of reduced K_o

horizontal direction, μ_{hh}', and the shear modulus in the vertical plane, G_{vh} (the independent shear modulus). In a linear anisotropic model these parameters are defined directly. The Authors have adapted the nonlinear model from Section 5.7.5 of Volume 1 to investigate the advantages given by combining nonlinearity and anisotropy. The model defines the variation of shear and bulk moduli G and K, from which the modulus E' and a Poisson's ratio μ' can be calculated and so the isotropic elastic stiffness matrix is defined. In the adapted model the anisotropic elastic stiffness matrix is obtained from constant, user defined ratios of μ_{vh}'/μ', μ_{hh}'/μ', E_h'/E, n' $(=E_v'/E_h')$ and m' $(=G_{vh}/E_v')$. The most influential of these ratios was found to be m'. There are two analyses presented here, for both of which $n'=0.625$. For the first analysis $m'=0.444$ (from Burland and Kalra (1986)). Based on laboratory and field data for London Clay, the initial G_{vho} has been determined by Simpson *et al.* (1996) to be $0.65G_{hho}$ (where G_{hh} is the shear modulus in a horizontal plane, dependent on E_h'). With $\mu'=0.2$ and $n'=0.625$, this gives $m'=0.433$. This is very similar to the value adopted here, $m'=0.444$. It is not known how G_{vh} decays with strain, so it is an assumption that it varies along the same function as E'. For the second analysis a very soft independent shear modulus was defined by $m'=0.2$. The initial stresses maintain the $K_o>1$

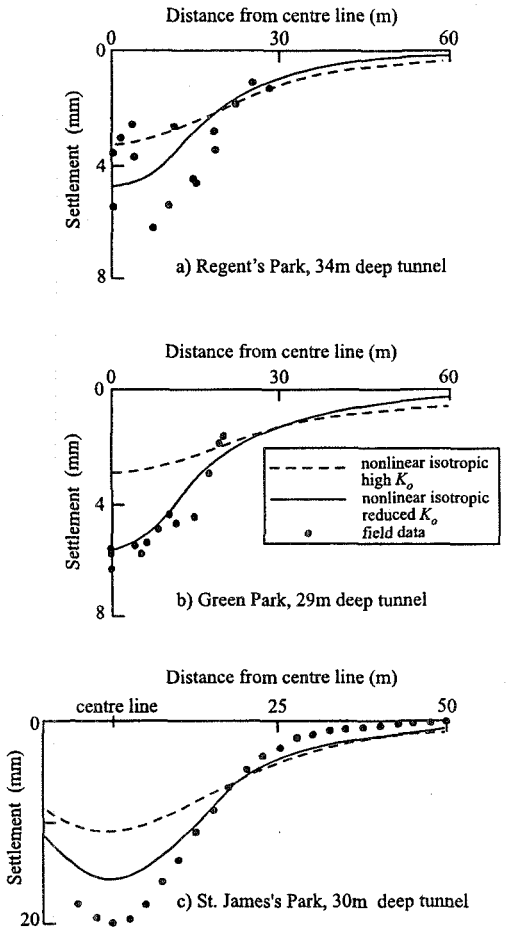

Figure 2.30: Effect of zone of reduced K_o on predicted settlement profiles

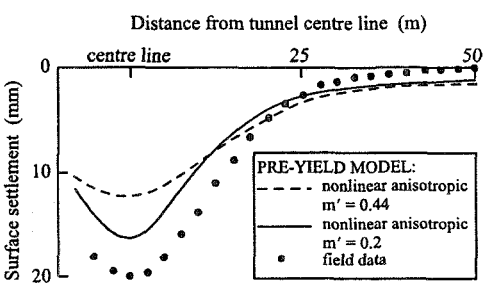

Figure 2.31: Soft shear modulus effect

condition in the London Clay. Figure 2.31 shows the predicted surface settlement above the St. James's Park tunnel in comparison with the field data. The introduction of an independent shear modulus based on field and laboratory data gives little improvement over the isotropic model. A desirable improvement is however achieved through the use of a very soft independent shear modulus.

The reason for using the term 'devices' for these adjustments which improve the surface settlement profiles predicted by the finite element analysis, is that they cannot at present be supported as representative of field conditions. Using a reduced K_o on the premise that there have been stress changes ahead of the tunnel is inconsistent with adopting a nonlinear small strain stiffness which assumes that no straining has taken place ahead of the tunnel. The effect of reducing K_o to the sides of the tunnel is to cause plastic zones to develop in these areas early on in the incremental excavation procedure. This is in contrast to the high K_o analyses in which plastic zones develop above and below the tunnel.

The effect of softening the anisotropic shear modulus in a nonlinear model is to modify the pattern of ground movement close to the tunnel. It also increases the horizontal component of displacement across the whole finite element mesh. There is no laboratory or field evidence for such a soft initial shear modulus G_{vho} for London Clay. It may be that softening the soil in this way represents softening of the soil due to straining ahead of the tunnel face. A major drawback with a nonlinear anisotropic model is that there is no information on how G_{vh} varies with strain level.

With both devices the percentage unloading to achieve the controlled volume loss is reduced from the analyses in Section 2.6.2. This has an effect on the subsequent soil and lining behaviour. If a lining is constructed early in an analysis, then the growth of any zones of developing soil plasticity will be arrested, which in a dilatant soil will reduce the magnitude of any pore water pressure reductions around the tunnel. Also, the sooner the lining is constructed the greater the loads transferred into the lining by the end of excavation.

2.7 Interaction analyses

2.7.1 The influence of building stiffness on tunnel-induced ground movements

As mentioned in Section 2.2 above, empirical methods for the determination of tunnelling-induced settlements are based on measurements at greenfield sites. This is considered inappropriate to the urban situation where tunnels pass beneath existing buildings. Potts and Addenbrooke (1997) applied the finite element method to the analysis of this soil/structure interaction problem. They presented the results of over 100 finite element analyses of tunnel excavation in stiff clay beneath an existing building. Figure 2.6 shows the geometry represented by their analyses. D, z, B and eccentricity e were all varied, as were the bending stiffness (EI) and axial stiffness (EA) of the buildings. The soil was again modelled as nonlinear elastic perfectly plastic. The buildings were represented by shell elements (Mindlin

beam elements in plane strain). The results were synthesised into simple building distortion assessment charts. These new charts allow the engineer to take account of building stiffness when assessing the likely distortion and damage expected from tunnelling-induced ground movements in an urban environment. Two new soil/structure relative stiffness parameters were defined. The relative bending stiffness, ρ^* (with units m^{-1}), and relative axial stiffness, α^*:

$$\rho^* = \frac{E\,I}{E_s\,H^4}$$
$$\alpha^* = \frac{E\,A}{E_s\,H} \tag{2.3}$$

where E_s is a representative soil stiffness, being the secant stiffness at 0.1% axial strain from a triaxial compression test of a sample taken from a depth $z/2$, and H is the building half width, $B/2$.

Each analysis gave a building settlement profile and building horizontal displacement profile. Examples for 60m wide buildings with zero eccentricity above a 20m deep tunnel are shown in Figures 2.32 and 2.33 respectively. These were interpreted in terms of building distortion parameters: a sagging deflection ratio (DR_{sag}) combined with a compressive horizontal strain (ε_{hc}) , and a hogging deflection ratio (DR_{hog}) combined with a tensile horizontal strain (ε_{ht}) for the building. These parameters are often related to limiting tensile strain in a building in order to predict the expected damage due to such a combination of distortions (Burland and Wroth (1974)).

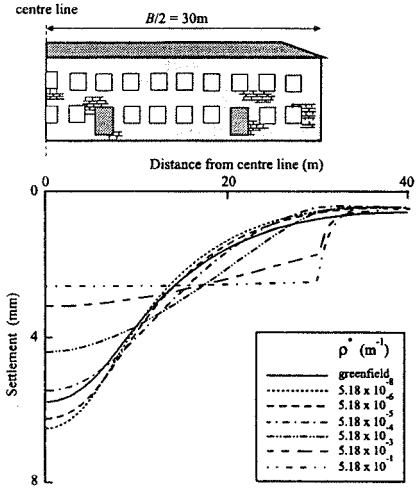

Figure 2.32: The effect of ρ^* on surface settlement profile

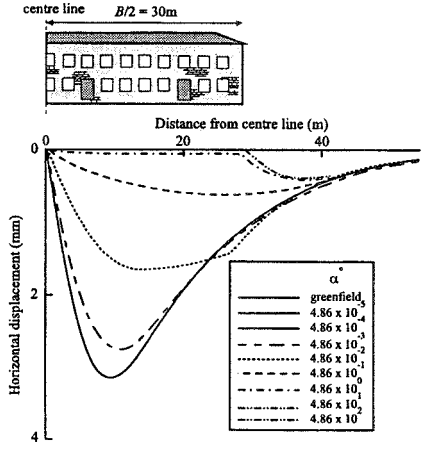

Figure 2.33: The effect of α^* on horizontal surface displacement

In association with these analyses the greenfield situations were analysed for comparison. Greenfield settlement and horizontal displacement are commonly used for damage assessment, and it is relatively cheap and simple to acquire such predictions empirically. For each building size and location (B and e respectively), the greenfield ground surface movements were used to obtain greenfield values for deflection ratio and horizontal strain. These represent the distortion parameters for a completely flexible building. Potts and Addenbrooke (1997) therefore investigated the degree of modification that buildings with different relative stiffness (ρ^* and α^*) and relative position (e/B) make to the greenfield values of distortion. Modification factors, M, were defined which gave a quantitative measure of the degree of modification for a given building. The sagging deflection ratio for an analysis with a building was divided by the equivalent distortion parameter from the greenfield analyses, giving the modification factor M^{DR}_{sag}. Similarly, the horizontal compressive strain for an analysis with a building was divided by the equivalent distortion parameter from the greenfield analysis, giving modification factor M^{ε}_{hc}. For those buildings which lay in part or in total in the hogging region the modification factors for hogging deflection ratio, M^{DR}_{hog}, and tensile horizontal strain, M^{ε}_{ht}, were obtained in the same way.

It was determined that in the likely range of true building stiffness the relative bending stiffness controlled the degree of modification to the deflection ratio (i.e. vertical settlement profile); and the relative axial stiffness controlled the degree of modification to the horizontal strain (i.e. the horizontal displacement). Potts and Addenbrooke (1997) therefore plotted the modification factors for deflection ratio in both sagging and hogging forms, M^{DR}_{sag} and M^{DR}_{hog}, against ρ^* for each e/B. The modification factors for horizontal strain (ε_h) in compression and tension, M^{ε}_{hc} and M^{ε}_{ht}, were plotted against α^* for each e/B. Empirical design curves were fitted through the data and these are reproduced in Figure 2.34.

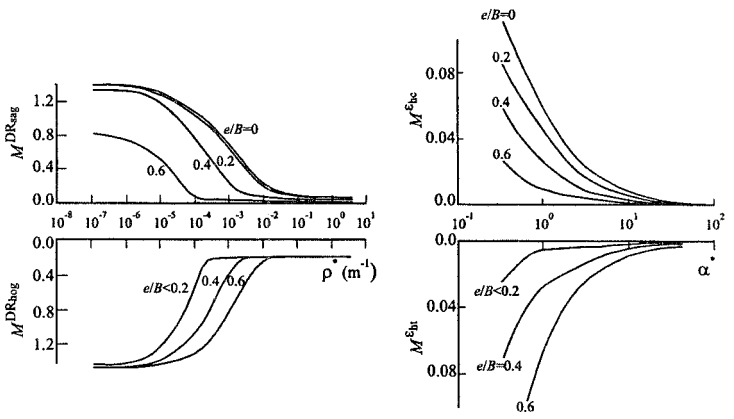

a) Design curves to determine deflection ratio

b) Design curves to determine horizontal strain

Figure 2.34: Design curves to determine a) deflection ratio and b) horizontal strain

The new modified empirical damage assessment procedure for a given building therefore requires:

- The relative bending and axial stiffness for the building in question. As a first estimate the engineer could consider the contribution to stiffness of the foundation alone, before considering the independent or coupled contributions to bending and axial stiffness of slabs, beams, columns and load-bearing walls.
- The modification factors read off the design chart in Figure 2.34. These clearly depend on the relative stiffness and the eccentricity ratio.
- The greenfield distortion parameters for the ground at foundation level, assuming no building were present.
- The multiplication of the greenfield parameters by the relevant modification factors.

These modified parameters give the likely distortion to the building, taking account of the building stiffness.

2.7.2 The Treasury building - a case study

The parametric study presented in Section 2.7.1 dealt with arbitrary buildings above typical tunnels. This section presents the results from the finite element analysis of one particularly sensitive building affected by construction of the Jubilee Line Extension in London - the Treasury building at Westminster. The building had been monitored during the project. Results are given here from those analyses that were performed to model the tunnelling-induced response of the building. To mitigate the effects of tunnel construction an extensive programme of compensation grouting was implemented at the site and this too has been analysed. Only a summarised description of the analyses and the results are included here, further details are given in Standing *et al.* (1998).

The Treasury is a massive stone-clad brick-masonry structure, approximately 210 m long and 100 m wide with four storeys above ground and two basement levels. The foundations consist of strips and pads connected by an unreinforced concrete slab founded in the Terrace Gravels which overlie London Clay. The top of the foundation is approximately 6 m below ground level. As part of the Jubilee Line Extension project, two running tunnels were excavated under one corner of the building (shown in plan on Figure 2.35). The westbound tunnel was the first to be excavated. Following this there was a rest period before compensation grouting and excavation of the eastbound tunnel. Compensation grouting was implemented after driving the westbound tunnel and

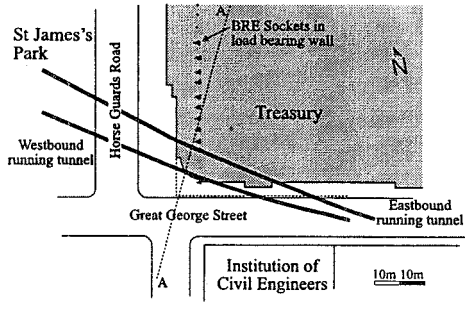

Figure 2.35: Plan of Treasury site

during construction of the eastbound tunnel. The level of the tubes-á-manchette (TAMs) used for this work was roughly 16m below ground level, see Figure 2.36, extending beneath the basement between the tunnels and the foundation slab. The analysis followed the construction activities and associated durations recorded during the works. Both tunnels are 4.95m in diameter, the westbound is 34m below and the eastbound 24m below ground level, both in the London Clay. Concrete segments form the linings and these were placed and expanded immediately behind the shield.

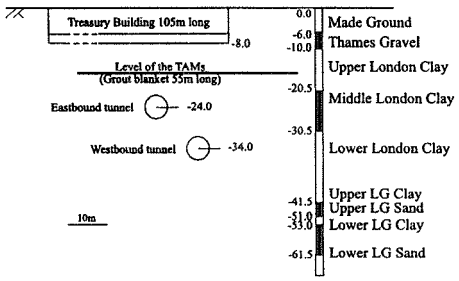

Figure 2.36: Cross-section AA

Plane strain conditions were assumed and the cross-section AA shown on Figures 2.35 and 2.36 was analysed. A section of the finite element mesh is shown in Figure 2.37. For clarity only the detailed part of the mesh in the vicinity of the tunnels is shown. The soil stratigraphy was obtained from the site investigation and different strata were modelled as nonlinear elastic perfectly plastic. The small strain stiffness model described in Section 5.7.5 of Volume 1 was used to represent pre-yield behaviour and a Mohr-Coulomb yield and plastic potential were used to model the plastic behaviour. The permeability was modelled as linear anisotropic inhomogeneous in order to reproduce the under-drained pore pressure profile at the site. Table 2.1 summaries the coefficients for the small strain stiffness model.

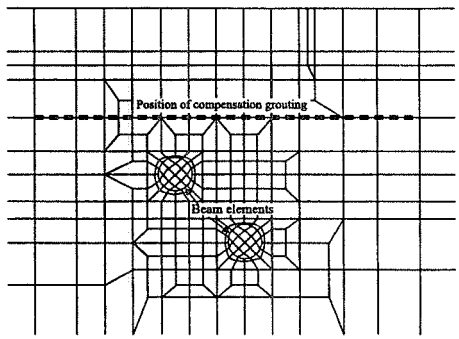

Figure 2.37: Section of finite element mesh

An equivalent elastic raft of 3m thickness was used to model the Treasury foundation (Young's modulus $E = 28\text{x}10^6$ kPa, Poisson's ratio $\mu = 0.15$). The tunnel linings were modelled with elastic shell elements (Mindlin beam elements in plane strain), with Young's modulus $E = 15\text{x}10^6$ kPa, Poisson's ratio, $\mu = 0.15$, thickness of $0.2\text{m}^2/\text{m}$ and second moment of area of $6.67\text{x}10^{-4}$ m^4/m.

Compensation grouting was modelled by applying a pressure within a horizontal slot in the finite element mesh, at the location of the TAM's, see Figures 2.37 and 2.38. This slot was created by including interface elements in the mesh generation, but excavating them prior to the beginning of the analysis. When compensation grouting was not taking place during the analysis, the displacements (both vertical and horizontal) of adjacent nodes on opposite sides of the slit were

tied, see Figure 2.38a and Section 3.7.4 of Volume 1. During an increment of the analysis in which compensation grouting was being modelled, these ties were removed and a pressure was applied to the boundary of the slot, see Figure 2.38b. For all increments the pore pressure degrees of freedom of adjacent nodes on opposite sides of the slit were tied.

The volume loss control method was used for excavation, with the target volume loss based on field measurements from a green field monitoring station at St. James's park.

The results presented here focus on movements after construction of the westbound tunnel and movements 18 weeks after the compensation grouting works and the construction of the eastbound tunnel. Figure 2.39 shows the settlement troughs after excavation of the westbound tunnel (i.e. the first tunnel to be constructed). Field measurements at ground surface from St. James's Park (greenfield) and at foundation level for the Treasury are presented. Comparison of the observations from these two sites indicates the influence of the building. It reduces the maximum settlement, but increases the width of the settlement trough. The maximum settlement beneath the Treasury is beneath its corner, slightly offset from the tunnel centre-line. Also shown is the finite element prediction. The agreement between the prediction and the field observations is excellent. Figure 2.40 presents settlement troughs at foundation level for the Treasury, 18 weeks after construction of the eastbound tunnel. Both observations and finite element predictions are presented. The agreement between prediction and observation is again excellent.

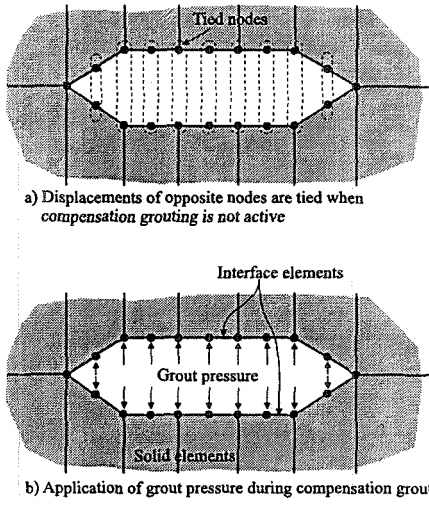

Figure 2.38: Modelling compensation grouting

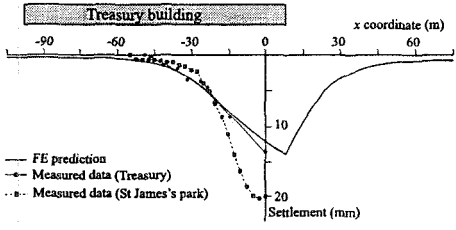

Figure 2.39: Settlement trough after WB tunnel excavation

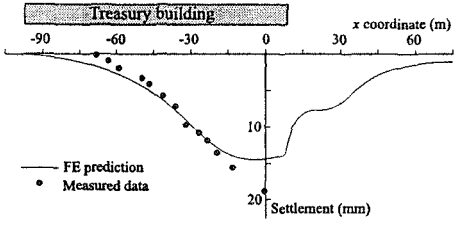

Figure 2.40: Settlement trough 18 weeks after EB tunnel construction

Table 2.1: Coefficients for elastic shear modulus

Strata	A	B	$C \times 10^{-4}$ (%)	α	γ	$E_{d,\min} \times 10^{-4}$ (%)	$E_{d,\max}$ (%)	$G_{\min}$ (kPa)
Made Ground	Isotropic linear elastic: $G = 2083$ kPa							
Thames Gravel	1104	1035	5	0.974	0.940	8.8335	0.3464	2000
Upper LC	1120	1016	1	1.335	0.617	8.6602	0.6928	2333
Middle LC	1400	1270	1	1.335	0.617	8.6602	0.6928	2667
Lower LC	1400	1270	1	1.335	0.617	8.6602	0.6928	2667
Upper Lambeth Group Clay	1000	1045	5	1.344	0.591	13.856	0.3810	2667
Upper Lambeth Group Sand	1300	1380	1	1.220	0.649	1.9053	0.1300	1000
Lower Lambeth Group Clay	1000	1045	5	1.344	0.591	13.856	0.3810	2667
Lower Lambeth Group Sand	1300	1380	1	1.220	0.649	1.9053	0.1300	1000

Table 2.1 (cont.): Coefficients for elastic bulk modulus

Strata	R	S	$T \times 10^{-3}$ (%)	δ	η	$\varepsilon_{v,\min} \times 10^{-3}$ (%)	$\varepsilon_{v,\max}$ (%)	$K_{\min}$ (kPa)
Made Ground	Isotropic linear elastic: $K = 2778$ kPa							
Thames Gravel	275	225	2	0.9798	1.044	2.1	0.2	5000
Upper LC	514	475	1	2.069	0.420	5.0	0.15	4000
Middle LC	686	633	1	2.069	0.420	5.0	0.15	5000
Lower LC	686	633	1	2.069	0.420	5.0	0.15	5000
Upper Lambeth bed Clay	530	460	0.5	1.492	0.678	1.5	0.16	5000
Upper Lambeth Group Sand	275	235	1	1.658	0.535	5.1	0.30	3000
Lower Lambeth Group Clay	530	460	0.5	1.492	0.678	1.5	0.16	5000
Lower Lambeth Group Sand	275	235	1	1.658	0.535	5.1	0.30	3000

Table 2.1 (cont): Other properties

Strata	γ (kN/m^3)	K_0	c'	φ'	υ	k_x (m/sec)	k_y (m/sec)
Made Ground	19	0.5	0.0	25	0	---------	---------
Thames Gravel	19/20	0.5	0.0	35	17.5	---------	---------
Upper LC	20	1.4	5.0	23	12.5	$0.5\text{x}10^{-9}$	$0.25\text{x}10^{-9}$
Middle LC	20	1.4-1.1	5.0	23	12.5	$0.5\text{x}10^{-8}$ to $0.5\text{x}10^{-10}$	$0.5\text{x}10^{-9}$ to $0.25\text{x}10^{-10}$
Lower LC	20	1.1	5.0	23	12.5	$0.5\text{x}10^{-10}$	$0.25\text{x}10^{-10}$
Upper Lambeth Group Clay	20	1.1	0.0	27	13.5	$1.0\text{x}10^{-11}$	$0.5\text{x}10^{-11}$
Upper Lambeth Group Sand	20	1.1	0.0	34	17.0	$0.5\text{x}10^{-6}$	$0.5\text{x}10^{-6}$
Lower Lambeth Group Clay	20	1.1	0.0	27	13.5	$1.0\text{x}10^{-11}$	$0.5\text{x}10^{-11}$
Lower Lambeth Group Sand	20	1	0.0	34	0	$0.5\text{x}10^{-6}$	$0.5\text{x}10^{-6}$

2.7.3 Twin tunnel interaction

Modern metro construction in congested urban environments often involves the excavation of new tunnels in close proximity to each other. In addition, improvement to existing networks requires new construction adjacent to existing tunnels. The finite element method is an appropriate analysis tool for considering more than one tunnel excavation in a given project. At the design stage it is important to address the interaction of the tunnels and their effects on overall ground response. Current design practice, which is based on zero interaction assumptions, rules of thumb, and linear analyses gives little guidance in this respect.

Addenbrooke and Potts (2001) have used the plane strain finite element method to produce interaction diagrams that establish the likely degree of interaction between two tunnels constructed in stiff clay. They have assessed the surface settlement effects and the subsurface lining interactions under various conditions. At each stage any available field data has been used to validate the finite element predictions. They used a coupled consolidation formulation and a nonlinear elastic perfectly plastic soil model. The nonlinear pre-yield model was that of Puzrin and Burland (1998). As published the model was restricted to conventional triaxial stress space. Addenbrooke *et al.* (1997) used an extended version of the model valid for use in general stress space. The extended formulation is presented in Section 5.7.6 of Volume 1. As well as reproducing the expected decay in stiffness with strain level, the model reproduces the kinematic nature of soil behaviour by

responding to changes in stress path direction. The non-associated Mohr-Coulomb model was used to describe post-yield behaviour. The tunnels were lined with elastic shell elements (Mindlin beam elements in plane strain). There were two sets of analyses, the first modelled two tunnels running parallel side-by-side, and the second one above the other (piggy-back), see Figure 2.41. The spacing between the tunnels was varied so as to ascertain the zones of influence, and the time between the construction of the two tunnels was varied to establish the influence of prolonged consolidation or swelling.

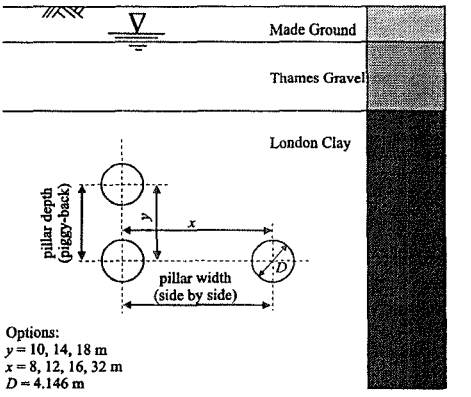

Figure 2.41: Side by side and piggy back geometry

Consider first two tunnels constructed side-by-side, the first completed 3 weeks before the second. Figure 2.42 shows the influence of the excavation of a second tunnel on the lining to the first. The existing lining is pulled toward the new excavation and a squatting deformation is induced. The figure shows the lengthening of the horizontal diameter and shortening of the vertical diameter (as a percentage of the design diameter) and how these distortions reduce with increasing pillar width (extrados to extrados tunnel spacing divided by diameter). Field data is included for comparison: the average deformation from three sets of closely spaced twin tunnels on the Victoria Line in London (Ward (1969)); and recent data from three sites of the Jubilee Line Extension in London (Kimmance *et al.* (1996)). The numerical analyses are in good agreement with the data. The analyses indicate that sub-surface tunnel interaction can be considered negligible for pillar widths greater than 7 diameters.

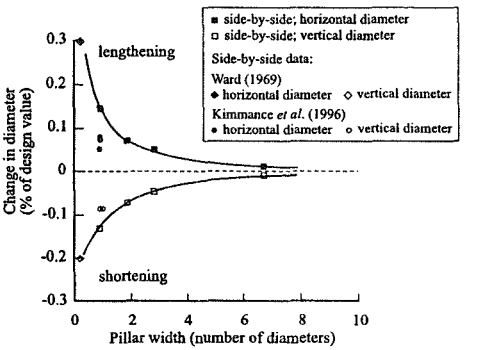

Figure 2.42: Deformation of 1st tunnel in response to 2nd tunnel for side by side geometry

When considering piggy-back tunnels, there are two construction sequence options - upper tunnel first and lower tunnel first. Figure 2.43 shows the deformations induced in the existing lining in response to the second excavation for both construction sequences. The change in diameter, as a percentage of the design diameter, is plotted against pillar depth (extrados to extrados spacing divided by diameter). Again the existing lining is pulled towards the new

Figure 3.18 shows a cross section through the site of the new Jubilee Line Extension (JLE) station at Westminster which was completed in 2000. Very close to the station excavation are two underground tunnels and the Big Ben clock tower. There was obvious concern over the potential movements of the clock tower. Although this is a rather special case, it is not an uncommon situation in a crowded city such as London.

Quite often developments are proposed which are close to other buildings and/or services. It is therefore necessary to make an assessment of potential damage or distortion. The distortion of a tunnel may prevent an underground train from running, or at least mean that speed restrictions have to be imposed, since tolerances are generally quite tight. In some instances they may be no more than a few millimetres. In addition, there may be machinery, such as an escalator, close by which is very sensitive to movement. If distortions become too large certain parts can fracture in a brittle manner and suddenly jam the escalator, potentially causing loss of life.

There are a number of methods of assessing building damage (e.g. Boscardin and Cording (1989), Burland (1995)), but to make an assessment it is necessary to know how a structure will distort. Therefore in any analysis only soil models which are capable of making reasonable predictions of the magnitude and pattern of movement should be used. This normally rules out any constitutive model which incorporates linear elasticity (including linear elastic perfectly plastic models), see Section 3.4.5.

To make an assessment of the movement of an adjacent structure, this structure has to be modelled in an appropriate way and in sufficient detail. For example, if the object of the analysis is to estimate the potential distortion of an adjacent segmental tunnel, it is pointless modelling the tunnel as a stiff ring. Equally, if the tunnel is modelled as fully flexible then the predicted distortions may be excessive and unrealistic. In order to be able to make reasonable predictions, special techniques have been developed to allow rotation of joints between lining segments once limiting conditions are exceeded, see Section 2.4.5. This may be a limiting stress or some other criteria.

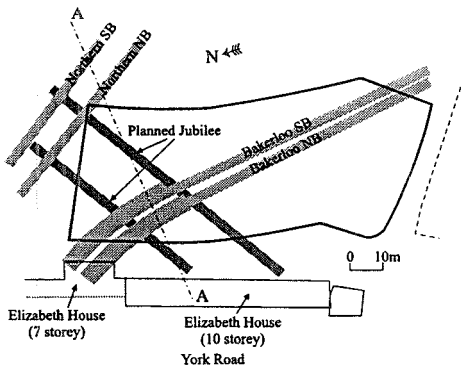

Figure 3.60: Plan of the site for the Waterloo International Terminal

Hight *et al.* (1993) present a good case history of where accurate predictions of tunnel distortions were necessary. Figure 3.60 shows in plan the site of the Waterloo International Terminal in London. Beneath the basement are two Bakerloo Line Underground tunnels and to the side of the excavation are two

Northern Line Underground tunnels. Also at the side of the excavation is an existing structure, Elizabeth House, and to complicate matters further an additional two JLE tunnels were planned (now constructed) beneath the site, see Figure 3.61. The scheme that was originally proposed had a deeper basement than the scheme that was actually built, which made the base of the excavation come to within less than 2m of the crown of one of the tunnels. Plane strain finite element analyses were used to develop methods of construction which limited the distortion of the tunnels and to prove to third parties that there were unlikely to be any adverse effects. If movements had been excessive, at the very least restrictions would have been imposed on trains running in the tunnels.

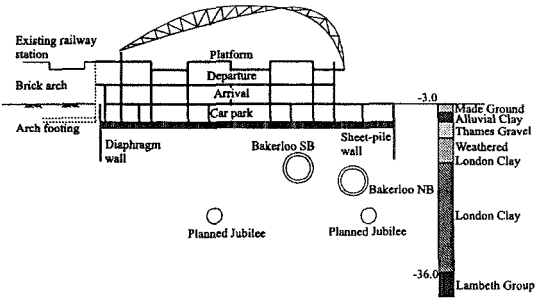

Figure 3.61: Cross-section of the site for the Waterloo International Terminal

As an example of the results from this study, predicted deformations of the station and running tunnels of the Bakerloo Line are shown in Figure 3.62. These predictions were made before construction. However, during construction the deformations of the tunnels were monitored, the recorded movements are also shown on Figure 3.62. Overall, there is excellent agreement between the predictions and the measurements.

There are a number of other examples, mostly unpublished, were such detailed modelling has been necessary. These are truly soil-structure interaction analyses.

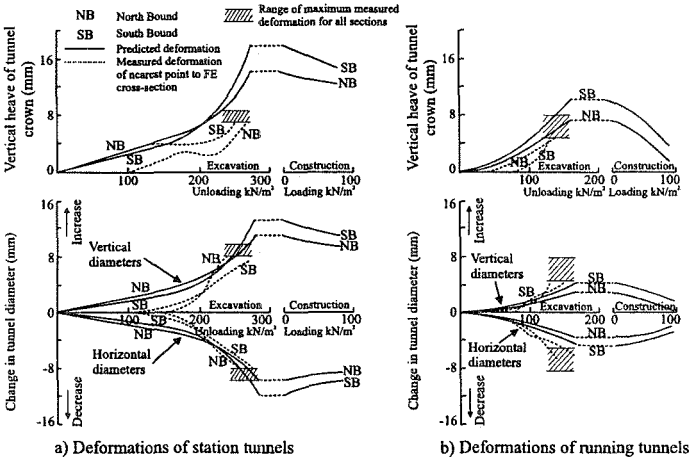

Figure 3.62: Predicted and measured deformations of station and running tunnels of the Bakerloo Line

3.8 Summary

1. The design of retaining walls involves the assessment of forces imposed in the wall and other structural members and the likely movements of both the retaining wall and retained soil.
2. The design of retaining walls has traditionally been carried out using simplified methods of analysis (limit equilibrium, stress fields) or empirical approaches. However, such approaches cannot, and do not, provide all the desired design information.
3. Numerical methods provide a viable alternative and have the advantage that they provide all of the desired design information in a consistent manner.
4. In reality, all geotechnical problems involving retaining structures are three dimensional. However, at present, due to insufficient computing resources, simplifications usually have to be made and two dimensional plane strain or axi-symmetric analyses undertaken.
5. Care must be taken when assuming planes of symmetry. It is often tempting to only analyse a 'half section'. This is only valid if the geometry, soil conditions, construction sequence and loading conditions are all symmetric. In practice this is rarely the case.
6. The lateral and vertical extent of a finite element mesh can have a significant effect on predictions, if they are not large enough. Consequently, it is important to insure that these boundaries are placed at a sufficient distance to have a negligible influence. Unfortunately, it is not possible to give general recommendations for the appropriate lateral and vertical extent of a mesh because they will depend on the problem being analysed, the constitutive models used for the soil and the facet of behaviour under investigation. In practice it is therefore sensible to experiment with meshes of different size, unless experience has already been gained of analysing a similar problem in the past. It is always sensible to add some large elements to the sides and bottom of a mesh. Relatively few of these elements are needed to expand the mesh considerably and consequently they do not add a large overhead to the analysis.
7. The methods of supporting walls have to be addressed (e.g. details of props, ties, anchors, berms, etc.), as they can have a significant influence on behaviour. In particular the type of connection between support and wall (e.g. simple, pin-jointed or full moment) can have a large effect on displacements and structural forces.
8. It is important to use realistic constitutive models to represent soil behaviour. In this respect it is usually necessary to use models that can account for both nonlinearity at small strains and soil plasticity.
9. The initial stresses within the ground before construction of the retaining wall can have a significant influence on wall behaviour. The presence of adjacent structures (e.g. existing tunnels, deep basements, etc.) will inevitably modify the state of stress within the ground and these effects must be accounted for in any analysis.

10. Consideration must be given to how the retaining wall is to be constructed and the time taken to do so. Different sequences of construction could result in the soil experiencing different stress paths. As a consequence additional forces might be imposed on the wall.
11. Any measures taken to control groundwater are an important consideration and must be accurately simulated in any analysis.
12. Gravity walls are not usually used where there are adjacent structures and /or services which are sensitive to ground movements. Consequently, displacements are not explicitly calculated and simple design methods are adequate. However, if movements are of concern, or in situations where the soil conditions are unusual, or where the structure has dimensions outside current practice, numerical analysis provides an ideal design tool.
13. A key feature of any numerical analysis of a gravity wall is the modelling of the interface between the soil and the structure. Consequently, interface elements combined with an appropriate constitutive model for the interface should be used.
14. The behaviour of reinforced earth walls is extremely complex. Numerical analysis provides an ideal tool to analyse this behaviour. However, such analysis is not simple and involves the application of complex boundary conditions.
15. Embedded retaining walls come in many forms and sizes. They are usually used in situations where ground movements are critical. They also often have several rows of props or anchors and are therefore difficult to analyse using simple structural methods. Consequently, numerical analysis is widely used to investigate the behaviour of such structures.
16. Embedded walls can be modelled using either solid or beam (or shell) elements. However, the use of the latter type of element which has a zero thickness implies further approximations. For example, for embedded cantilever walls the use of beam elements results in larger lateral wall displacements and higher bending moments.
17. If the wall is impermeable or has a finite permeability and a coupled analysis is being undertaken, then the use of beam (or shell) elements to model the wall can be problematic and special steps must be taken.
18. Anchors have three dimensional geometries and are therefore difficult to model in plane strain analyses.

Appendix III.1: Stress level

The stress level S is defined as (see Figure III.1):

$$S = \frac{J}{J_f} \tag{III.1}$$

where: J is the current value of the deviatoric stress;

J_f is the value of J on the failure surface at the current value of p' and θ.

For the Mohr-Coulomb constitutive model, see Section 7.5 of Volume 1:

$$J_f = (a + p')\, g(\theta) = \left(\frac{c'}{\tan\varphi'} + p' \right) g(\theta) \qquad \text{(III.2)}$$

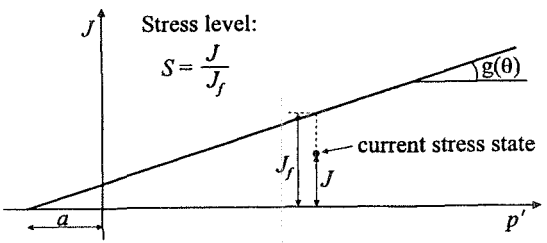

Figure III.1: Definition of the stress level, S

4. Cut slopes

4.1 Synopsis

This chapter describes the application of the finite element method to the analysis of 'man-made' cut slopes (slopes which are formed by geological processes are not considered here). To perform any meaningful finite element analysis of a cutting, it is necessary to model the process of soil excavation (see Section 3.7.10 of Volume 1). This is true even when any other geotechnical structure (tunnel, embankment, foundation, etc.) in the vicinity of a slope is analysed. In such cases, to establish initial stresses in the ground, the modelling of slope formation by excavation is essential.

Cut slopes can be formed in both granular and clayey soils. Granular soils, which have a high permeability, behave in a drained manner, both during excavation and subsequently. Consequently, they are much easier to analyse. An exception is, however, when they are subjected to earthquake loading, when the granular material may respond in an undrained manner. The superficial stability and/or modelling of the various drainage measures are often the only problems associated with slopes cut in granular soils. Clay slopes have proved to be more elusive, and therefore most of this chapter is devoted to the problems encountered with the finite element analyses of slopes cut in these materials.

4.2 Introduction

An excavation in clays of low permeability is likely to be undrained. However, in some normally or lightly overconsolidated soft clays, excavation may almost be drained (Chandler (1984a)). These clays are often of moderate thickness and are likely to have sandy or silty drainage layers which accelerate pore pressure equilisation, despite their relatively low permeability.

Generally, the excavation process unloads the soil and pore water pressures become depressed, both beneath and adjacent to the excavation. With time the soil swells as the pore water pressures equilibrate to the long term steady state seepage regime, imposed by the 'new' hydraulic boundary conditions on the excavation slopes. With swelling and equilibration, mean effective stresses reduce and the stress state approaches failure. The stability of the slope therefore reduces with time. A detailed discussion of this process is given by Bishop and Bjerrum (1960).

One of the fundamental distinctions made in limit equilibrium slope stability

analysis is that between short and long term conditions. It is usually assumed that undrained conditions prevail in the short term. Given that it is not easy to predict the pore water pressure changes immediately after slope excavation, stability analysis in terms of total stresses ($\varphi_u = 0°$ analysis) is often undertaken, in which the undrained soil strength is assumed to be that existing prior to the formation of the slope. In the long-term all excess pore water pressures generated during excavation have dissipated, and the pore water pressures assumed to be in equilibrium with the newly established hydraulic boundary conditions can be determined. Consequently, an effective stress analysis can be undertaken.

Intermediate term situations cover the period between short and long term. Unfortunately, the pore water pressure distribution during this transition period cannot easily be calculated, and it is therefore difficult to carry out effective stress stability analysis by the limit equilibrium method. However, finite element analyses, which incorporate coupled consolidation/swelling, readily predict these pore water pressures, and this is one reason (among others) why the finite element method is particularly suited for this type of boundary value problem.

When analysing clay slopes, it is important to distinguish between the different types of clay in which a slope is cut. The choice of constitutive model will largely depend on the clay type. For example, stiff plastic clays are brittle and prone to progressive failure. The mechanism of progressive failure is complex and impossible to analyse without the incorporation of strain-softening in the analysis. On the other hand, low plasticity tills do not usually soften to a significant extent, and 'simpler' elastic-perfectly plastic constitutive models may well be employed in analyses of slopes cut in this type of material. Soft normally to lightly over-consolidated clays usually undergo a substantial amount of plastic straining during the process of excavation. Then a constitutive model which incorporates plastic behaviour pre-peak may be essential.

In this chapter examples of finite element analyses of slopes cut in the various clay types are presented. Being more straightforward, the analyses of 'non-softening' clays are discussed first. 'Softening' analyses require a substantial amount of computing effort, and they will be outlined later, after the mechanism of progressive failure has been discussed in some detail.

4.3 'Non-softening' analyses

4.3.1 Introduction

The finite element method has only recently become a powerful alternative to the limit equilibrium method of slope stability analysis. The recent papers by Griffiths and Lane (1999) and Naylor (1999) outline the various techniques involved in the analyses of slopes, and summarise many advantages of the finite element method in conjunction with an elastic-perfectly plastic soil model of the Mohr-Coulomb type.

Finite element analyses of this kind have been used here to shed further light on the mechanisms taking place inside a slope since its formation. As it will be

seen later (Section 4.5), these mechanisms can be extremely complex in cut slopes formed in strain-softening materials. Thus 'non-softening' analyses provide a useful reference point against which more complex slope behaviour can be judged.

4.3.2 Cut slope in stiff 'non-softening' clay

4.3.2.1 Introduction

Finite element analyses of a hypothetical cut slope in a stiff 'non-softening' clay were carried out to verify the method of analysis subsequently employed (Section 4.5) in the analyses of slopes cut in stiff plastic 'strain-softening' clays.

4.3.2.2 Soil parameters

A nonlinear elastic-perfectly plastic soil model incorporating a Mohr-Coulomb yield criterion given by the cohesion intercept, c', the angle of shearing resistance, φ', and the angle of dilation, v, was used in the analyses. The model requires the specification of a Young's modulus, E, a Poisson's ratio, μ, the (peak) strength parameters, φ_p' and c_p', and the angle of dilation, v. The analyses were of a coupled nature, and therefore it was also necessary to specify the coefficient of permeability, k.

Detailed discussion of the derivation of the material properties is given in Section 4.5.4.2. The model parameters are listed in Table 4.1.

4.3.2.3 Finite element analyses

'Non-softening' analyses were performed on a 10m high, 2:1 slope. Note that analyses of 3:1 and 2.5:1 slopes, 10m high, were also performed with a non-softening soil, but collapse was not predicted. The finite element mesh was similar to the mesh shown in Figure 4.33, where a 3:1 slope is modelled. No horizontal displacement was allowed on the vertical boundaries, whereas the bottom boundary was completely fixed in both the vertical and horizontal direction. The initial pore pressure was assumed to be hydrostatic, with a surface boundary value of p_{fh}=−10kPa, this being the average surface value indicated by field measurements in the U.K. (Vaughan (1994)).

Excavation was simulated by removing layers of elements at a uniform rate. For a 10m high cutting, excavation was complete in an overall time of 3 months. There was no significant swelling during excavation.

After excavation, swelling was allowed with a surface boundary suction of p_{fh}=−10kPa maintained at the excavated slope, and on the original ground surface. Seasonal fluctuations in surface boundary conditions were not modelled. The vertical and bottom boundaries of the mesh were assumed to be impermeable. Swelling was simulated in the finite element analyses by applying increments of time, Δt, with no change to the other boundary conditions. The first time step after excavation was Δt=0.25years, the second Δt=0.5years. The subsequent steps were Δt=1year until collapse was approached, when the time step had to be reduced substantially.

Two sets of analyses were performed. In the first set, the angle of dilation was assumed to be v=0°, and the initial in-situ stresses were assumed to be given by the coefficient of earth pressure at rest K_o=1.0, 1.5 and 2.0. The second set of analyses was similar to the first set, except that the angle of dilation was $v = \varphi'$.

Table 4.1: Properties of London Clay assumed in the analyses

Property	In-situ clay	Compacted fill
Bulk unit weight, γ (kN/m^3)	18.8	18.8
Peak strength (intact)	c_p'=14kPa, φ_p'=20°	c_p'=12kPa, φ_p'=20°
Discontinuity strength	c_s'=0kPa, φ_s'=20°	no discontinuities
Bulk peak strength	c_p'=7kPa, φ_p'=20°	as peak intact
Residual strength	c_r'=2kPa, φ_r'=13°	c_r'=2kPa, φ_r'=13°
Plastic strain at peak	$(E_d^p)_p$ = 0 - 5%	as in-situ clay
Plastic strain at residual	$(E_d^p)_r$ = 20%	$(E_d^p)_r$ = 50%
Poisson's ratio, μ	0.20	0.30
Young's modulus, E (kPa) (mean effective stress p′ in kPa)	2500·(p'+100)/100 (min. 4000)	1000·(p'+100)/100 (min. 2000)
Angle of dilatation, v (°)	0 (or 20)	0
Permeability, k (m/s)	varies (see Figure 4.30)	1.5 x 10^{-10}
Coeff. of earth pressure at rest, K_o	varies	not relevant

4.3.2.4 Results of analyses

In the first set of analyses collapse was predicted during the swelling process, with a well defined rupture zone of the same shape in each analysis. Figure 4.1a shows the change with time of the predicted average pore water pressure on this rupture

surface, expressed as the pore pressure ratio, $r_u^* = p_f/\sigma_v$, where p_f is pore water pressure, and σ_v is the predicted vertical stress on the rupture surface. This definition differs slightly from the conventional one, $r_u = p_f/(\gamma h)$, where γh is an overburden pressure. $\overline{r_u}^*$ is the average value along the rupture surface. All three analyses gave $\overline{r_u}^* = 0.235$ at collapse. Also shown on this figure is the equilibrium value of $\overline{r_u}^* = 0.3$. This is the value that would have been obtained after a very long time, if collapse had not occurred. It was calculated by performing a separate long-term steady state seepage analysis. The associated change with time of the mid-slope horizontal displacement, δ_h, is given in Figure 4.1b. It is evident from these plots that collapse occurs suddenly, after a delay which depends on the value of K_o.

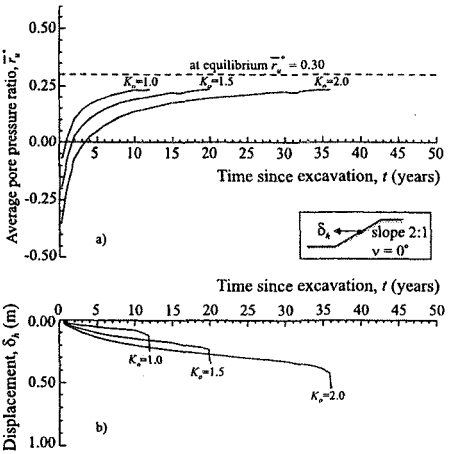

Figure 4.1: Non-softening clay with $\nu = 0°$; development of a) $\bar{r}_u^*$ on the rupture surface and b) mid-slope displacement, δ_h, with time

The results from the second set of analyses are shown in Figure 4.2. Well defined rupture surfaces were again predicted, of the same shape in each analysis, but of different shape to that predicted with $\nu = 0$. This is why there is a slight difference between the steady state equilibrium values of $\overline{r_u}^*$ in Figures 4.1a and 4.2a. The final values of the average pore water pressure at collapse were all $\overline{r_u}^* = 0.25$, which is slightly higher than for the first set of analyses.

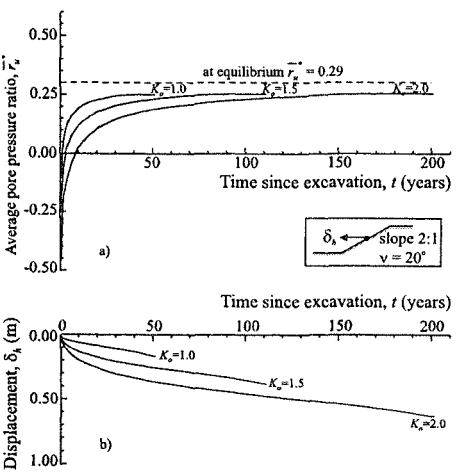

Figure 4.2: Non-softening clay with $\nu = \phi'$; development of a) $\bar{r}_u^*$ on the rupture surface and b) mid-slope displacement, δ_h, with time

Figure 4.2b shows the change of mid-slope horizontal displacement with time. When rupture develops and the average pore water pressures become constant, the displacements do not accelerate as in Figure 4.1b. Instead, there is a gradual increase in displacement with time. This is due to two compensating effects. During swelling pore water pressures are generally

increasing with time, whereas in the thin rupture zone the soil is dilating and the pore water pressures are reducing. At collapse the rate of decrease in pore water pressure in the rupture zone is exactly matched by the increase due to swelling. The generation of negative pore water pressure is controlled by the permeability of the clay and the thickness of the rupture zone. This accounts for the gradual increase in displacement, which is predicted with $\nu = \varphi'$ once a rupture surface has formed, and for the higher average pore water pressure at collapse. To check the validity of the latter statement, an attempt was made to restart these analyses but with the angle of dilation, ν, reduced to zero. In each case it was not possible to maintain equilibrium of the solution and very large displacements occurred. The pore water pressures generated by dilation essentially act as a partial brake on post rupture movements. This effect is of great practical significance, since it helps to prevent rapid post-collapse movement of slides in strain-softening clays (Vaughan (1994)).

In reality, dilation would be restricted in the field to a much thinner rupture zone than that predicted by the analyses, where the rupture surface is approximately half an element thick (typically 0.5m for the current mesh). Equilibration of pore water pressure would occur more rapidly in the field. Thus, if it is assumed that dilation occurs post-peak and only on thin shear surfaces, as occurs in laboratory tests (Sandroni (1977)), the analyses in which $\nu=0°$ are likely to give a better representation of undrained effects in clay in which discontinuities develop post-peak, unless an unrealistically large number of elements are used to allow a thin rupture zone to develop. Consequently, as it will be seen later, for analyses involving strain-softening, an angle of dilation $\nu=0°$ was adopted.

The angle of dilation also affects the position of the rupture surface predicted and the stresses acting on it. The angles which the predicted rupture surfaces (velocity characteristics) make with the plane on which the major principal stress acts are $\pm(45°+\nu/2)$. The shear stresses acting on these rupture surfaces are given by:

$$\tau_f = \frac{c' \cos\varphi' \cos\nu + \sigma_n' \sin\varphi' \cos\nu}{1 - \sin\varphi' \sin\nu} \tag{4.1}$$

When $\nu=\varphi'$, Equation (4.1) reduces to the Coulomb failure criterion, namely:

$$\tau_f = c' + \sigma_n' \tan\varphi' \tag{4.2}$$

If $\nu \neq \varphi'$, the strength on the rupture surface from Equation (4.1) does not reduce to the Coulomb criterion. For instance, if $\nu=0°$, Equation (4.1) reduces to:

$$\tau_f = c' \cos\varphi' + \sigma_n' \sin\varphi' \tag{4.3}$$

For clays, the differences are small, but they need to be taken into account when comparisons are made between the results of finite element analyses and limit equilibrium calculations in which the Coulomb equation is adopted (see Potts *et al.* (1990)). If the rupture surface is kinematically constrained, then the differences are likely to be mainly in the strength on the rupture surface. If the rupture surface is not constrained, the differences are likely to be mainly in the location of the rupture surface itself.

As noted previously, the rupture surfaces predicted by the non-softening finite element analyses depend on v. The two surfaces predicted for $v=\varphi'$ and $v=0°$ are shown in Figure 4.3. Also shown is the critical circular slip surface obtained from a limit equilibrium calculation using the Bishop rigorous method of slices (Bishop (1955)). In the cut slope problem there is little kinematic restraint on the position of the rupture surface, and it is therefore not surprising that the rupture surfaces from the finite element analyses are dependent on v. It may be noted that at the soil surface the major principal effective stress is vertical and the rupture surfaces should be inclined at an angle of $(45° - v/2)$ to the vertical. Inspection of Figure 4.3 shows this to be so.

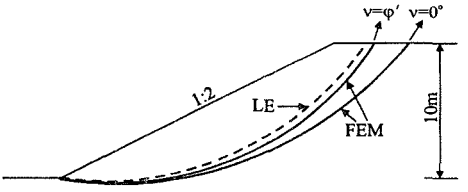

Figure 4.3: Comparison of predicted rupture surfaces from 'non-softening' analyses

From the limit equilibrium analysis the average pore water pressure ratio on the slip surface was $\overline{r_u}^* = 0.233$ at collapse. This is in good agreement with the finite element results ($\overline{r_u}^* \approx 0.235$ for $v=0°$ and $\overline{r_u}^* \approx 0.25$ for $v=\varphi'$). The average values of the shear and normal stress acting on the rupture surfaces at failure are plotted in Figure 4.4 along with Equations 4.2 and 4.3. As would be expected, the results from the finite element analyses with $v=0°$ agree with Equation 4.3, whereas the analyses with $v=\varphi'$ and the limit equilibrium analysis agree with Equation 4.2.

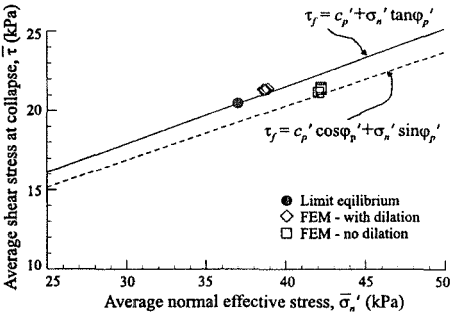

Figure 4.4: Average shear stress at collapse predicted by 'non-softening' FE analyses and limit equilibrium analysis

In the softening analyses reported later, Equation 4.3 is used. Since there is little apparent kinematic constraint on the rupture surfaces, and $v=0°$ is assumed, a small difference between the predicted rupture surfaces and those in the field is likely.

4.3.3 Cut slope in soft clay

4.3.3.1 Introduction

In spite of the limited evidence for depressed pore water pressures following excavation, it is generally accepted that an excavation in stiff, heavily over-consolidated clay with low in-situ permeability is undrained. The situation is less clear with soft, normally or lightly-overconsolidated clays. As mentioned above,

slopes cut in these materials may achieve long-term pore water pressures either during excavation or within a few months after excavation. The time required for the pore water pressures to equilibrate to the steady-state condition is important when designing a cut slope. Given that stability of a slope reduces with time, it may be wise to either measure the pore water pressures during excavation, or design slopes in soft clays on the basis of long-term conditions, even when the slope is only temporary.

It has been appreciated for some time (Tavenas and Leroueil (1980)) that partial drainage can play a significant role in short term problems involving embankments on soft clays, where the measured pore water pressures during the early stages of relatively rapid loading fell short of those expected for undrained conditions. However, while Chandler (1984a) has argued that soft clays are often of moderate thickness and are likely to have sandy or silty drainage layers, which accelerate pore water pressure equalization despite their relative low permeability, Tavenas and Leroueil (1980) concluded that these phenomena may be due to 'nonlinear consolidation'. Namely, soft clays have high initial shear and bulk stiffnesses when loaded (or, in the case of cuttings, unloaded) from their in-situ conditions. Although these stiffnesses reduce rapidly as strains grow, the operational 'linear' equivalent consolidation (swelling) coefficients would have been very high initially as construction (excavation) proceeds, and when a significant factor of safety operates in soft clays (further away from 'yield').

To investigate the possible effects of a high soil stiffness at small strains on the time required for the pore water pressure equilibration, a series of finite element analyses of a hypothetical slope cut in a soft clay was undertaken.

4.3.3.2 Soil parameters

A form of the modified Cam clay model (see Chapter 7 of Volume 1), which had a Mohr-Coulomb hexagon and a circle for the shapes of the yield and plastic potential surface in the deviatoric plane respectively, was used to represent the soft clay (and its weathered crust). The elastic behaviour was modelled in two ways. In the first approach, the basic critical state formulation, in which both bulk and shear moduli are derived from the slope of swelling lines, κ, assuming a constant value of Poisson's ratio, μ, was utilised. In the second approach the nonlinear elastic behaviour proposed by Jardine *et al.* (1986) (see Section 5.7.5 of Volume 1) was used. As this model is able to capture the high soil stiffness at small strains for stress states inside the yield surface, it is more realistic.

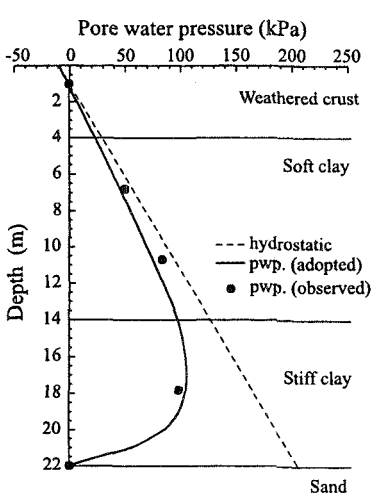

Figure 4.5: Observed and adopted pore water pressure profile

The soil profile used in the analyses is presented in Figure 4.5, together with the ground water conditions. It consists of four distinctive layers: (i) a weathered crust extending to 4m depth, (ii) a 10m thick layer of soft clay, (iii) stiff clay extending from 14 to 22m, overlying (iv) a sand layer (not modelled in the analyses).

Model parameters for the soft clay were derived on the basis of a comprehensive set of both field and laboratory investigations on the soft Bangkok Clay (Shibuya (1999)). They are listed in Tables 4.2 and 4.3 for the soft and stiff clays respectively. The derived small strain stiffness parameters are presented in Table 4.4 and they generate the small strain stiffness curves shown in Figure 4.6.

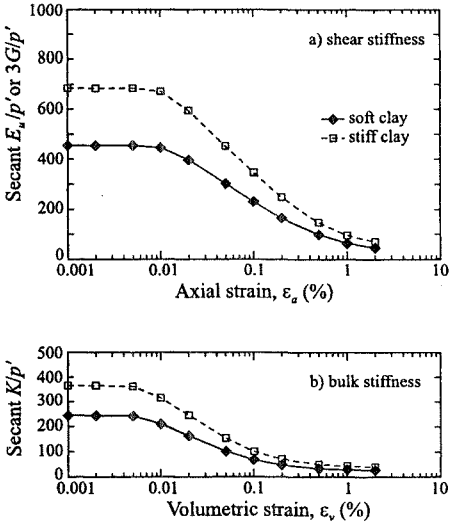

Figure 4.6: Adopted non-linear elastic small strain secant a) shear and b) bulk stiffness

Single element tests have been performed to predict the behaviour of the soft Bangkok Clay in triaxial compression and extension (Figure 4.7) and oedometer loading and unloading (Figures 4.8). For the latter test a prediction is also made using the standard critical state formulation for the elastic component of the model (Figure 4.9). The observed response in laboratory oedometer tests on three samples from different depths is superimposed in plots of the vertical effective stress, σ_v', versus volumetric strain, ε_v. The match with the finite element predictions is reasonable.

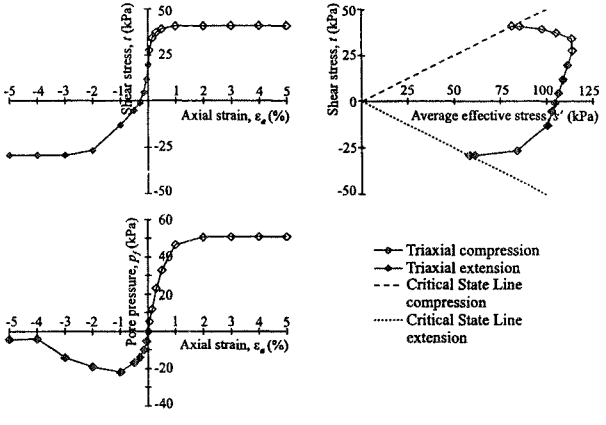

Figure 4.7: Predicted response of soft Bangkok Clay in triaxial compression and extension tests (small strain stiffness used)

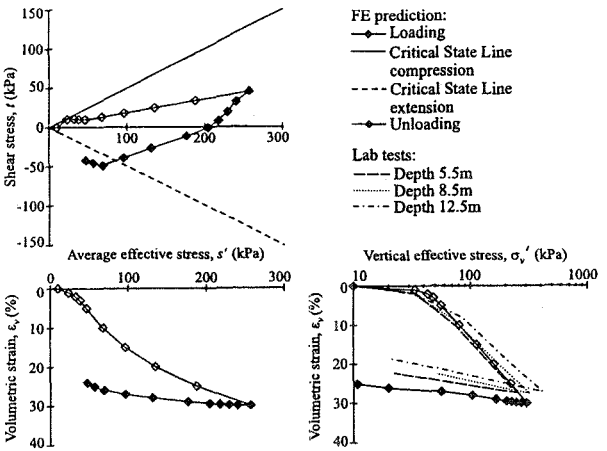

Figure 4.8: Predicted and observed response of soft Bangkok Clay in oedometer test (small strain stiffness used)

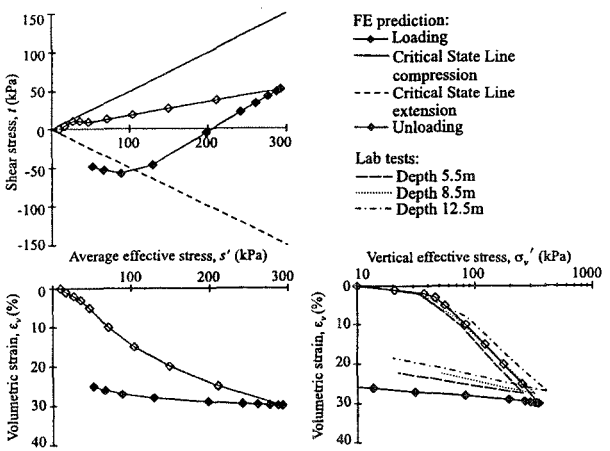

Figure 4.9: Predicted and observed response of soft Bangkok Clay in oedometer test ('standard' modified Cam clay model used)

The most critical issue when dealing with the modelling of soft clays is usually their undrained shear strength, S_u. While the undrained shear strength is not an input parameter to the modified Cam clay model, it can be calculated from the input parameters and the initial stress conditions (see Section 7.9.3 of Volume 1). The model parameters listed in Tables 4.2 and 4.4, in combination with the profiles

of the overconsolidation ratio, *OCR*, (Figure 4.10) and the coefficient of earth pressure at rest, K_o, (Figure 4.11) have generated the undrained strength profiles given in Figure 4.12. It can be seen that predictions depend not only on the type of the test modelled (triaxial compression or plane strain), but also on the elastic component of the model used in the analysis. However, the trend observed in both field (vane tests) and laboratory (triaxial compression tests) is reasonably captured.

Table 4.2: Soil properties assumed for soft clay (modified Cam clay)

Property	Value
Bulk unit weight, γ* (kN/m^3)	16.0
Specific volume at unit pressure, v_1	4.0
Slope of VCL, λ	0.33
Slopes of swelling lines, κ**	0.066
Poisson's ratio, μ**	0.20
Angle of shearing resistance, φ' (deg)	30
Coefficient of earth pressure at rest, K_o	$K_o = (1-\sin\varphi')\mathrm{OCR}^{\sin\varphi'}$
(*) - for weathered crust γ = 18.0 kN/m^3 (**) - small strain stiffness parameters listed in Table 4.4 used	

Table 4.3: Soil properties assumed for stiff clay (Mohr-Coulomb)

Property	Value
Unit weight, γ (kN/m^3)	17.0
Effective cohesion, c' (kN/m^2)	5.0
Angle of shearing resistance, φ' (deg)	26
Angle of dilation, v (deg)	13
Coefficient of earth pressure at rest, K_o	1.0
Young's modulus, E (MN/m^2)	Small strain stiffness parameters used, see Table 4.4
Poisson's ratio, μ	

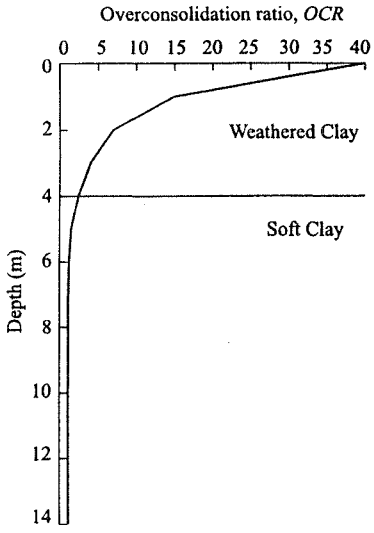

Figure 4.10: Adopted OCR profile in soft clay

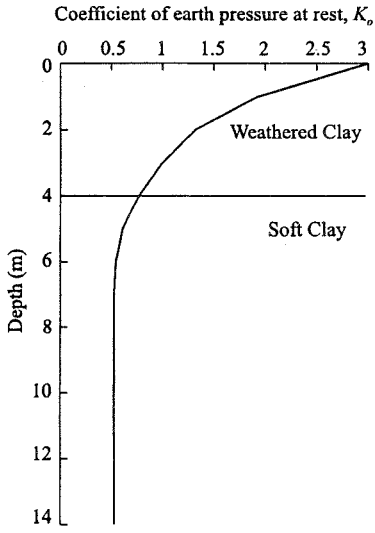

Figure 4.11: Adopted K_o profile in soft clay

4.3.3.3 Finite element analyses

The finite element analyses were of the coupled consolidation/swelling type, and therefore it was necessary to specify the permeability of the soils involved. It can be seen from Figure 4.5 that the observed pore water pressure profile is underdrained. To model underdrainage, it is necessary to adopt a permeability model in which permeabilities decrease with depth (see Chapter 9). The non-linear model used here, which relates the permeability, k, to the mean effective stress, p', is given by the following relationship (Section 10.7 of Volume 1):

$$k = k_o \, e^{(-ap')} \tag{4.4}$$

where k_o is the coefficient of permeability at $p'=0$ and a is a material parameter. The value of a=0.0125m^2/kPa was deduced in order to match the observed underdrained pore water pressure profile (see Figure 4.5). The permeabilities obtained from site investigations at three different depths are presented in Figure 4.13. Also shown is the permeability profile calculated using the above equation adopting the value of $k_o = 1.2 \times 10^{-9}$ m/s . Better matching is possible, but then the observed underdrained permeability profile could no longer be recovered. Note that the same nonlinear permeability model parameters, k_o and a, were used for both soft and stiff clays. The sudden drop in permeability predicted when entering the stiff clay layer is due to the higher adopted value of K_o in this material.

The finite element mesh used to model a 1:1 cut in the soft Bangkok Clay is shown in Figure 4.14, together with the displacement and pore water pressure boundary conditions. Excavation has been modelled by removing soil in 1m thick

horizontal layers, with short time steps to ensure an undrained soil response. One analysis increment per layer was typically employed initially when a significant factor of safety operated in the slope. When collapse was approaching it was necessary to use more increments (typically ten) per layer in order to catch the critical depth of 'undrained' excavation.

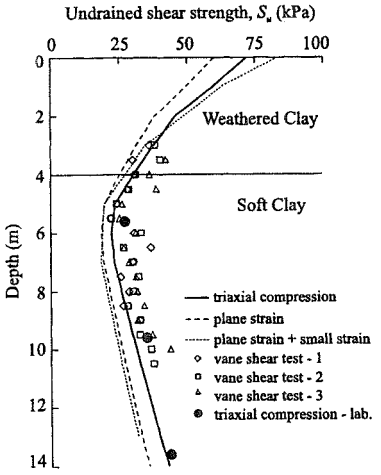

Figure 4.12: Measured and predicted S_u profiles in soft clay

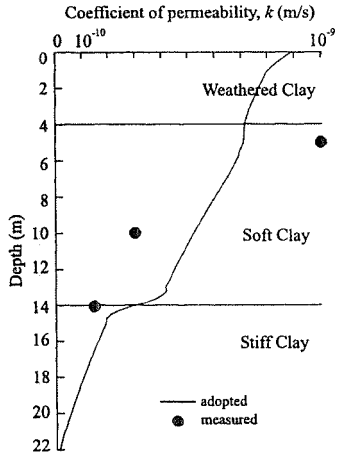

Figure 4.13: Measured and adopted permeability profiles

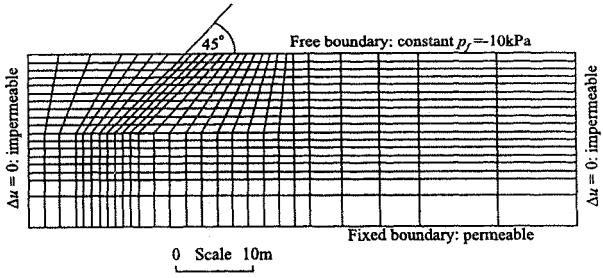

Figure 4.14: Finite element mesh and boundary conditions

Undrained excavation in soft clay slopes causes a substantial amount of shearing, particularly in the later stages of excavation when failure conditions are approached. Consequently, the influence of the stiffness at small strains on subsequent times for equilisation of pore water pressures depressed by excavation may well be diminished. To check the influence of small strain stiffness on swelling times after 'undrained' excavation, it was necessary to ensure a small

'disturbance' of the ground due to excavation, i.e. a shallow depth of excavation. Then the swelling was modelled in ever-increasing time increments until the long term steady-state seepage condition was established. This condition was imposed by a surface boundary suction of p_{fh}=−10kPa at the excavated slope and on the original ground surface. Underdrainage at the bottom of the mesh was maintained throughout the analyses.

4.3.3.4 Results of analyses

Figures 4.15a and 4.15b show the development of horizontal and vertical movements of the crest of the slope during excavation. A critical depth of 7m was predicted by the analysis employing the small strain stiffness model. The 'standard' modified Cam clay model, in which the elastic stiffness at small strains was not included, recovered a slightly shallower critical depth (d_c=6.7m). The reason for this can be found in Figure 4.12, where it can be seen that the introduction of the greater stiffness at small strains in the modified Cam clay model leads to the prediction of a higher undrained shear strength, S_u, at least in the first 5m of the profile. Also, it is of interest to note that due to this higher stiffness smaller horizontal displacements of the crest are predicted, particularly during the early stages of excavation, when no significant yielding occurs in the slope. Surprisingly, the crest movements in the vertical direction are almost the same.

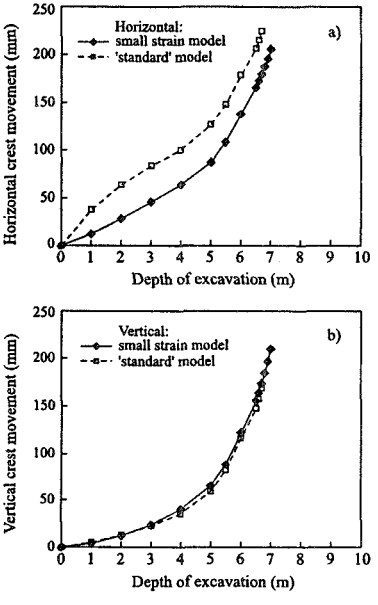

Figure 4.15: a) Horizontal and b) vertical movements of slope crest against depth of excavation

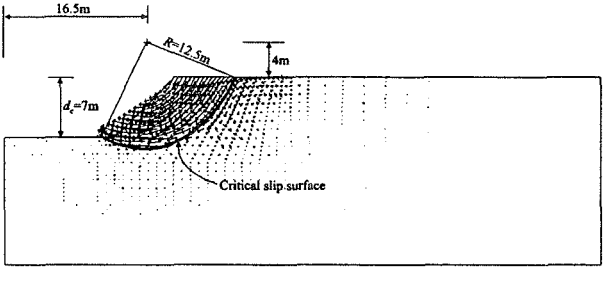

Figure 4.16: Critical slip surface and vectors of incremental displacements just prior to collapse

The position of the critical slip surface, predicted by the finite element analysis in which the elastic small strain stiffness model had been used, is shown in Figure 4.16, together with incremental displacement vectors at the 'end' of excavation, just before collapse. The vectors show the current mechanism of movement, and their absolute values are of no significance.

Table 4.4a: Coefficients and limits for nonlinear elastic secant shear modulus expression

Stratum	A	B	C (%)	α	γ	$E_{d,\min}$ (%)	$E_{d,\max}$ (%)	$G_{\min}$ (kPa)
Soft Clay	575	575	5.0×10^{-4}	1.348	0.58	1.21×10^{-2}	0.866	1000
Stiff Clay	862	862	5.0×10^{-4}	1.348	0.58	1.21×10^{-2}	0.866	1000

Table 4.4b: Coefficients and limits for nonlinear elastic secant bulk modulus expression

Strata	R	S	T (%)	δ	λ	$\varepsilon_{v,\min}$ (%)	$\varepsilon_{v,\max}$ (%)	$K_{\min}$ (kPa)
Soft Clay	250	210	8.0×10^{-4}	1.462	0.77	4.0×10^{-3}	0.2	1000
Stiff Clay	375	315	8.0×10^{-4}	1.462	0.77	4.0×10^{-3}	0.2	1000

Development of the average pore water pressure ratio, $\overline{r_u}^*$, along this slip surface (the critical slip surface after 7m of excavation) with time is shown in Figure 4.17, for an analysis in which excavation stopped after only 3m of the soft clay had been excavated. Figure 4.18 shows the contours of stress level, S, at this stage of the analysis. The stress level, S, is a measure of the current strength mobilised, and its reciprocal value can be considered as a local factor of safety, see Appendix III.1. A reasonable (global) factor of safety still operates in the slope. For the permeability profile adopted in Figure

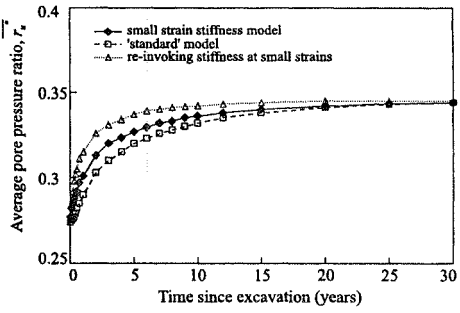

Figure 4.17: Average pore pressure ratio against time

4.13, a time period in excess of 20 years is necessary for nearly complete equilisation of the depressed pore water pressures caused by a 3m deep excavation. Also shown on Figure 4.17 are results from a similar analysis, but with the 'standard' modified Cam clay elastic parameters. It is apparent that, although the small strain stiffness model speeds up the process of swelling for some time after excavation (when strains are small), the time for complete equilisation is largely unaffected.

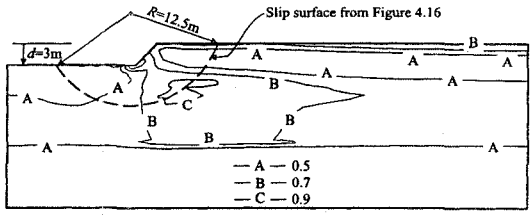

Figure 4.18: Contours of stress level, S

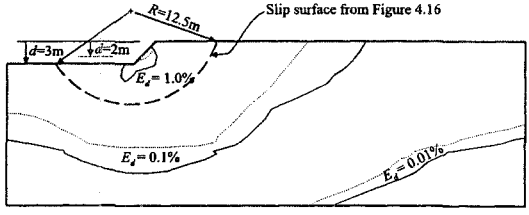

Figure 4.19: Contours of deviatoric strain, E_d, at 2m and 3m of excavation

To investigate this matter further, an additional analysis has been carried out in which the high soil stiffness at small strains has been re-invoked (the shear strains have been 'zeroed') immediately after excavation. Because small time steps have been used during excavation to ensure an undrained soil response, the volumetric strains are already zero. It can be argued that at the start of swelling (after undrained excavation has been carried out) the stress path (or strain path) changes direction, at least in a large part of the mesh. This is associated with an increased soil stiffness response (see e.g. Jardine (1994)). Then, the assumption of zeroing strains in order to account for an increased soil stiffness may well be justified. Also, a 3m deep excavation in soft Bangkok Clay causes a reasonable amount of straining (see Figure 4.19), and therefore partially eliminates the influence of the small strain stiffness on the time for swelling. Thus, the analysis with 'zeroing' the strains immediately after excavation may also indicate the response that may be expected after excavation to a shallower depth, when the amount of straining is smaller (Figure 4.19) and consequently soil stiffness higher.

Results from such an analysis are also presented in Figure 4.17. It can be seen that in this case a much quicker pore water pressure response has been predicted for all times after undrained excavation. Again this is particularly so during the initial stages of swelling when smaller strains operate in the slope. It seems that *partial* drainage can occur in the short term when excavating in soft clays. However, for excavations in soft Bangkok Clay at least, the soil response is not likely to be *completely* drained. For this to happen, a soft clay must be of higher permeability and/or possess sandy or silty drainage layers which accelerate pore water pressure equalization.

4.4 Progressive failure

The term progressive failure is best explained by considering the simple example of a beam of elastic material sliding on a rough surface with a brittle shear stress displacement characteristic (see Figure 4.20). The normal stress acting on the rough surface due to the weight of the beam is σ_n, the friction angle between the beam and the rough surface is μ and the relative displacement between the beam and the surface is δ.

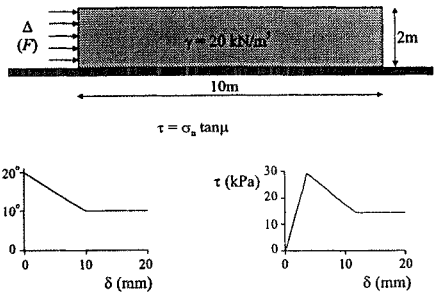

Figure 4.20: Progressive failure of a beam

As noted on Figure 4.20, the friction angle drops with further displacement, after a peak value has been mobilised, to a constant lower residual value. The relationship between the shear stress, τ, generated between beam and surface, and the relative displacement, δ, is also shown on Figure 4.20. It can be seen that initially the shear stress increases with increase in relative displacement until a peak value is mobilised. With further displacement the shear stress drops until a residual value is reached. It then remains constant at this residual value. This is brittle behaviour.

The beam is loaded at its left hand end by a force F, giving rise to an associated displacement, Δ. Two scenarios will now be considered. In the first the beam is assumed to be rigid, whereas in the second it is assumed to have a finite stiffness.

Consider first the case when the beam is rigid. The beam is loaded at its left hand end by progressively increasing the displacement Δ. The resulting behaviour is shown in Figures 4.21a to 4.21f. Each of these figures refer to a different stage of loading (i.e. to a different value of Δ). Several diagrams are shown on each figure. The top diagram indicates the distribution of relative displacement, δ, along the beam. The dots on this diagram represent the displacement, δ, at equi-spaced positions along the beam. In a similar manner the bottom diagram shows the distribution of interface shear stress, τ, along the interface. Also marked on this diagram are the peak, τ_p, and residual, τ_r, shear stresses. These are evaluated from σ_n, which remains constant along the beam, and μ_p and μ_r respectively. The three small diagrams in the centre of each figure are used to track the shear stress-relative displacement relationship as it is mobilised at three positions along the beam/surface interface. The centre diagram is for the middle of the beam. The two end diagrams represent positions just in from the ends of the beam. The thin line in these diagrams indicate the shear stress-relative displacement curves that will be followed as the beam is loaded (i.e displaced).

Initially (see Figure 4.21a), the beam is not loaded and both the relative displacement and shear stress are zero. The situation after the left hand side of the beam has been displaced by 2mm is shown in Figure 4.21b. Not surprisingly, as the beam is rigid, behaviour along the beam is everywhere the same. This uniform

behaviour continues as the beam is loaded (i.e. displaced) further. Figure 4.21c shows the situation when peak shear stress is mobilised everywhere along the beam. With further displacement (see Figure 4.21d) the shear stress drops from peak towards residual. Once enough displacement is applied to reach residual conditions (see Figure 4.21e), the stresses remain at this value with further loading (see Figure 4.21f).

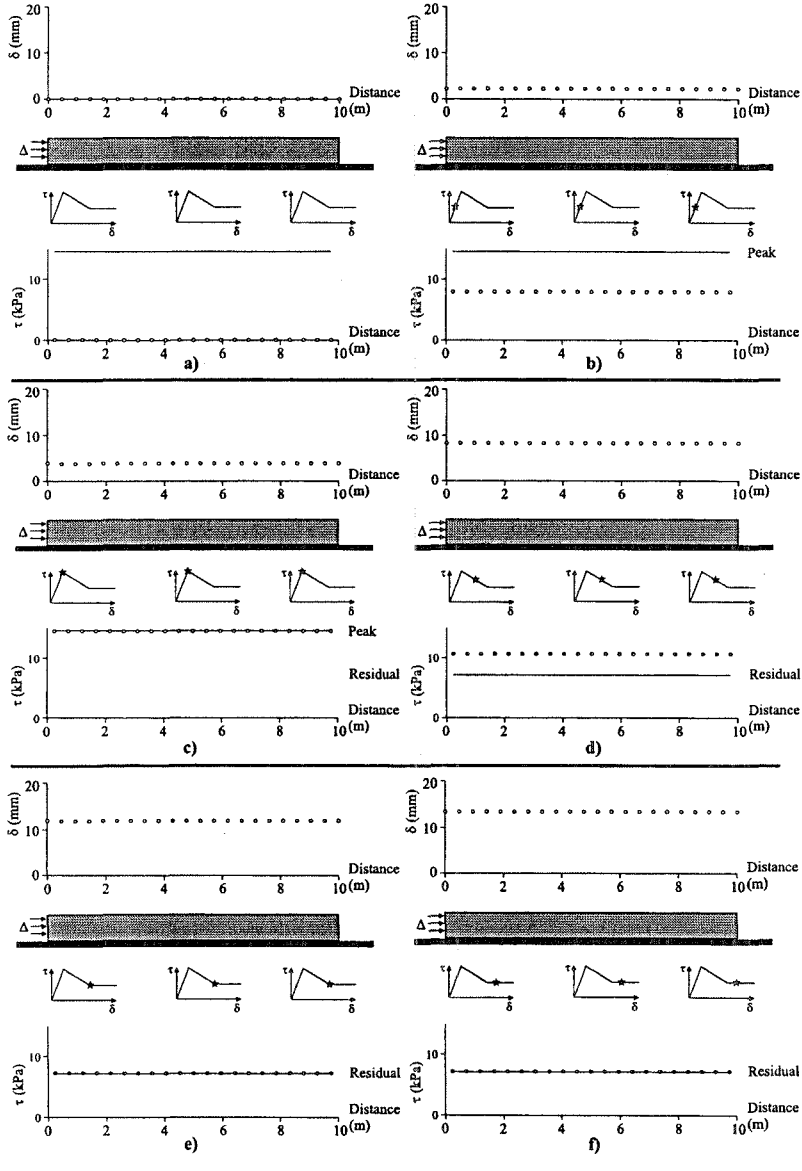

Figure 4.21: Progressive failure of a rigid beam

The relationship between the force F and the displacement Δ of the loaded end of the beam (i.e. the left hand end) is shown in Figure 4.22. The behaviour mirrors the shear stress, τ, versus relative displacement, δ, behaviour at the interface. The maximum resistance, F_{max}, is simply the peak shear stress multiplied by the area of contact.

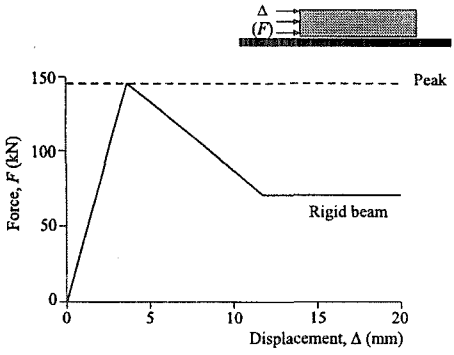

Figure 4.22: F-Δ relationship for rigid beam

If the same loading exercise is now repeated with a beam of finite stiffness, the results are as shown in Figures 4.23a to 4.23f. These figures are in a similar format to those shown in Figure 4.21 and discussed above. Before loading is applied, conditions are the same as for the rigid beam shown in Figure 4.21a. The situation after the left hand end of the beam has been displaced by 2mm is shown in Figure 4.23a, and can be directly compared with the results for the rigid beam given in Figure 4.21b. The displacement and shear stress are no longer uniform along the beam. They are both larger at the left hand end of the beam and decrease with distance along the beam.

As loading continues, non-uniformity develops further (see Figure 4.23b). Figure 4.23c shows the situation when the shear stress at the left hand end of the beam has reached peak and has begun to soften towards residual. In the lower diagram of Figure 4.23c it can be seen that the two dots nearest the left hand of the beam are on the softening branch of the shear stress-relative displacement curve. The third dot has just reached peak shear stress and the dots remaining are still on the initial (hardening) branch of the shear stress-relative displacement curve. With further loading the resistance at the left hand end of the beam reduces, whereas it increases along the rest of the beam (see Figure 4.23d). Eventually (see Figure 4.23e), all of the beam-surface interface is operating on the softening branch of the shear stress - relative displacement curve. After large displacements all positions along the beam reach and maintain a residual condition (see Figure 4.23f).

At no time is there more than one position along the beam which is mobilising peak shear stress at the beam-surface interface. Hence the term progressive failure. In contrast to the rigid beam, the maximum total resistance, F_{max}, must be less than the peak shear stress multiplied by the contact area. The total resistance, F, is plotted against displacement, Δ, of the left hand end of the beam in Figure 4.24. Also shown in this figure is the result for the rigid beam. Compared to the rigid beam it may be noted that: (i) the behaviour has become nonlinear, (ii) the maximum resistance, F_{max}, has been reduced, and (iii) more displacement is required to mobilise the maximum resistance.

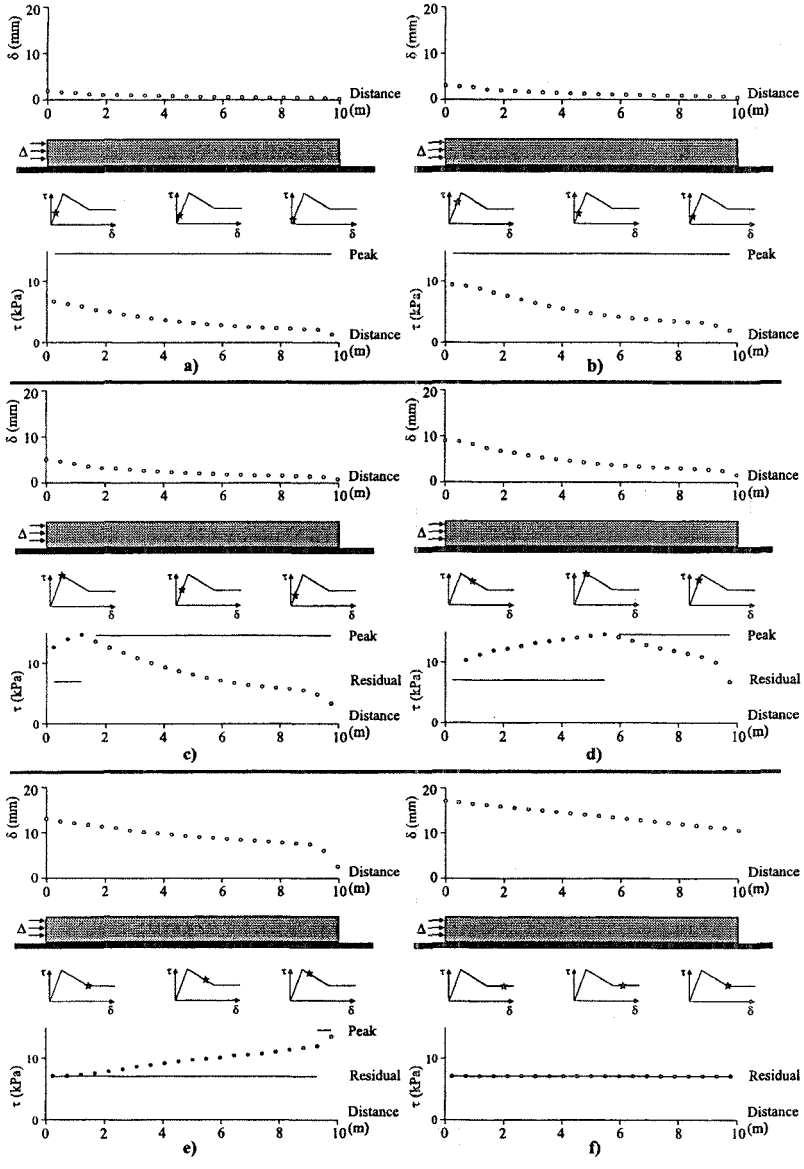

Figure 4.23: Progressive failure of a compressible beam

The data in Figure 4.24 is replotted in Figure 4.25 with the force F divided by the contact area between the beam and surface to give a plot of average shear resistance against displacement Δ. Also shown on this figure are two further results. One is for the same compressible beam as above, but loaded at its centre instead of at its end (see inset in Figure 4.25a). The other is for a similar

compressible beam of twice the length of the one considered above, but still loaded at its left hand end (see inset in Figure 4.25b). For the beam loaded at its centre the maximum force, F_{max}, is greater and the response stiffer than for the case discussed above. Clearly, the way in which the beam is loaded affects the amount of progressive failure, and consequently the maximum resistance. For the longer beam the response is softer, and the maximum average shear stress, τ_{max}^{av} is lower. Thus, increasing the size of the beam increases the amount of progressive failure and reduces the maximum resistance.

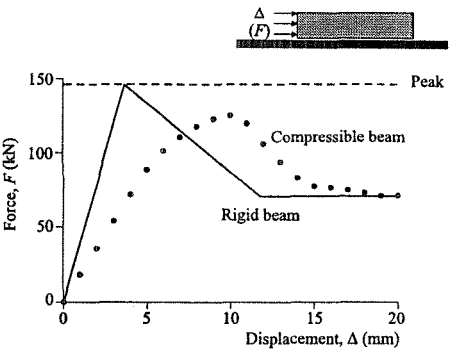

Figure 4.24: F-Δ relationship for compressible beam

This simple example shows that for progressive failure to occur: (i) the material must be brittle, (ii) a stress concentration must exist (i.e. the interface in the above example), and (iii) the loading must be non-uniform. The example also shows that the amount of progressive failure is influenced by: (i) the relative stiffness of the materials involved, (ii) the nature of the loading, and (iii) the scale of the shearing surface. Consequently, it is not surprising that progressive failure cannot be analysed using simple methods.

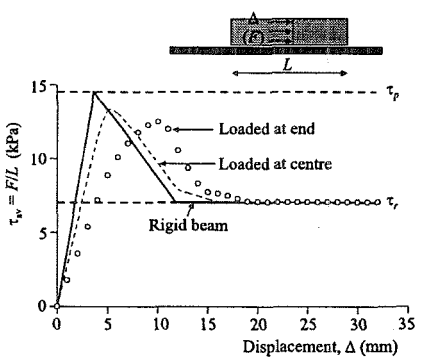

Figure 4.25a: τ_{av}-Δ relationship for a single length beam

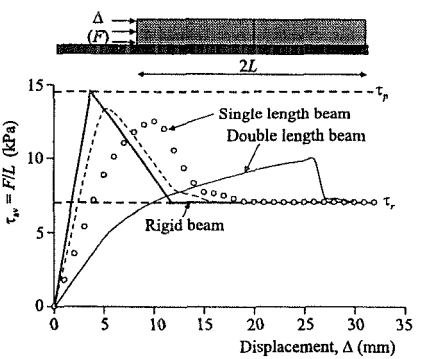

Figure 4.25b: τ_{av}-Δ relationship for a double length beam

4.5 'Softening' analyses

4.5.1 Introduction

The delayed collapse of old British railway cutting slopes in stiff plastic clays, by the formation of deep-seated slides, has been studied extensively (see e.g.

Skempton (1977)). Collapse is delayed primarily by slow swelling and pore pressure equilibration (Vaughan and Walbancke (1973)). However, the average drained strength operating at collapse is considerably less than the peak strength measured in the laboratory. The clays involved are brittle, and the discrepancy between the strengths has often been attributed to progressive failure.

Recent enhancement to the finite element code at Imperial College has enabled both strain-softening and coupled consolidation/swelling to be included in an analysis. Using these developments Potts *et al.* (1997) were able to disclose the role of progressive failure and explain most of the phenomena associated with the delayed failures of slopes composed of strain-softening clays. These analyses, together with parametric studies into the effects of the initial in-situ stresses, the surface hydraulic boundary conditions and the slope geometry, will be presented first and the results compared with field data. In an attempt to model the commonly observed sliding in the superficial soil layers of a slope, a higher permeability layer due to deterioration of the surface clay was introduced and the results of some of these analyses are presented. Finally, the effects of subsequent changes to slope geometry, such as those frequently employed to widen the existing motorway network in Britain, are examined in some detail and the possible consequences discussed.

4.5.2 Choice of constitutive model

For progressive failure to play a role in the delayed collapse of cut slopes, the soil must exhibit brittle properties and nonlinear strains must be mobilised along any potential rupture surface (see Section 4.4). Simple methods of analysis, such as limit equilibrium, are incapable of dealing which such complexities, and therefore little progress has been made theoretically in quantifying the possible effects of progressive failure. The use of the finite element method to analyse the recent end-of-construction slip in the Carsington embankment (see Section 5.4.4 of this volume) has shown that progressive failure can be accurately reproduced and quantified. However, those studies involved large embankments which were subjected to loading and consolidation. Here the same techniques have been applied to cuttings which involve unloading and swelling. In addition, the analyses include coupled consolidation which enable the history of swelling and, in particular, the time to collapse to be predicted.

The constitutive model employed to model soil strain-softening behaviour has been described in Section 7.8 of Volume 1. This is an elasto-plastic model of the Mohr-Coulomb type in which softening behaviour is accounted for by

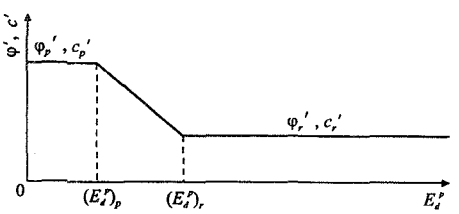

Figure 4.26: Variation of ϕ' and c' with the deviatoric plastic strain invariant, E_d^p (Potts et al. (1990))

allowing the angle of shearing resistance, φ', and/or the cohesion intercept, c', to vary with the deviatoric plastic strain invariant, E_d^p, as shown in Figure 4.26. The incremental deviatoric plastic strain invariant, ΔE_d^p, is defined as:

$$\Delta E_d^p = \frac{2}{\sqrt{6}}\sqrt{(\Delta\varepsilon_1^p - \Delta\varepsilon_2^p)^2 + (\Delta\varepsilon_2^p - \Delta\varepsilon_3^p)^2 + (\Delta\varepsilon_3^p - \Delta\varepsilon_1^p)^2} \qquad (4.5)$$

The model requires the specification of peak (φ_p', c_p') and residual (φ_r', c_r') strength, the angle of dilation, v, pre-peak stiffness, E, stiffness in unloading, E_u, and the rate at which strength is lost with strain ($(E_d^p)_p$, $(E_d^p)_r$). As the analysis involves swelling, it is also necessary to specify a permeability, k.

The stiffness prior to failure is given by a simple elastic model in which Poisson's ratio, μ, is constant, and Young's modulus, E, varies with mean effective stress, p', but not with shear stress level. No distinction is made between unloading and loading. Consolidation and swelling behaviour indicate approximately the same modulus in stiff clays, and therefore the Young's modulus used in the present analysis is based on the appropriate swelling modulus. The parameters used are listed in Table 4.1.

4.5.3 Implications for convergence

Monitoring of convergence is difficult for analyses involving strain-softening. The norms (see Section 9.6 of Volume 1) of the iterative nodal displacements, loads, flows and pore water pressures were all kept less than one percent of the norms of the associated incremental values. However, this procedure alone was not adequate and, in addition, the residual stresses at all integration points were monitored and kept small. For the early stages of an analysis, residual stresses were kept below 2 kPa. However, when collapse was approached more stringent conditions were introduced and stresses were kept below 0.1 kPa. To achieve this level of accuracy, small time steps (typically 0.0025 years) and a large number of iterations (typically 200) were required towards the end of an analysis. The time at collapse was deduced by plotting horizontal mid-slope displacement against time. Once the collapse time was exceeded, the solution became unstable, since the slope could not then be in equilibrium. This was always confirmed by running the final increment for a small time step of 0.0025 years and a large number of iterations (typically 400). Instability was indicated when deformations increased according to the number of iterations, without an improvement in convergence (Kovačević (1994)).

4.5.4 Cut slopes in London Clay

4.5.4.1 Introduction

The delayed sliding of slopes cut in stiff plastic clays has been the subject of considerable soil mechanics interest for a number of years (see e.g. Terzaghi and Peck (1948)). In Britain, most of the data concerns slopes and soil properties for

Brown London Clay (see e.g. Skempton (1977)), and that is why slopes in this material have been chosen for this study.

4.5.4.2 Soil parameters

As analyses of progressive failure are complex, it is essential to pay great attention to the derivation of the model parameters for the materials involved. As an example, the determination of the properties for Brown London Clay is now briefly presented.

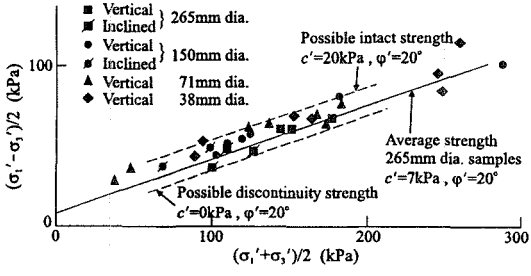

Figure 4.27: Peak strength of fissured Brown London Clay in terms of effective stress (Sandroni (1977))

Peak strength

Figure 4.27 shows the data from undrained triaxial compression tests on soil samples of different diameter. The tests on larger samples give a peak strength envelope, according to Mohr-Coulomb, of c_p'=7kPa and φ_p'= 20°, which is considered to be representative of the fissured clay structure.

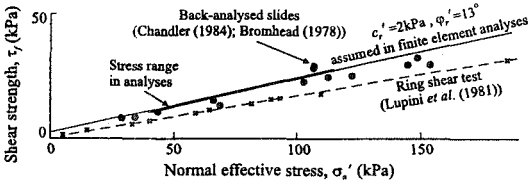

Figure 4.28: Drained residual strength of Brown London Clay

Residual strength

Measurements of residual strength are summarised in Figure 4.28. Both ring shear and field data are shown. The strength back-calculated from field slips is slightly higher, probably due to the less planar shear surfaces usually formed in the field. The field strength of c_r'=2kPa and φ_r'=13° is adopted.

Stiffness

The clay in a slope swells with time, and the strains and strain-softening are strongly influenced by the strain energy released by swelling. Very little experimental data is available for

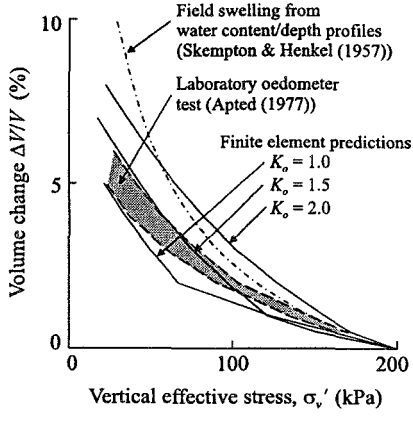

Figure 4.29: Observed and predicted swelling of Brown London Clay

swelling along different stress paths. Some swelling data from oedometer tests (Apted (1977)) are shown in Figure 4.29. Also shown is the swelling curve obtained by plotting depth-water content profiles (Skempton and Henkel (1957)). The swelling lines predicted by the simple elasto-plastic constitutive model adopted are also shown.

Permeability

The coefficient of permeability was assumed to vary with depth as shown in Figure 4.30, where field data for both the Upper Lias Clay and the London Clay are also shown. This permeability, together with the swelling modulus from Figure 4.29 for K_o=1.5, gives a coefficient of swelling c_s=2.7m^2/year at 5 m depth. Walbancke (1976) quotes field rates of swelling equivalent to c_s=3.2m^2/year for the Brown London Clay.

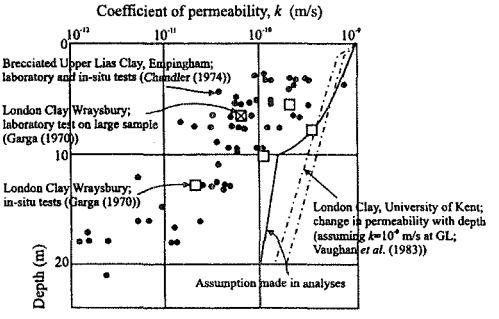

Figure 4.30: Variation of permeability with depth - assumed in the analyses and laboratory data

Rate of softening

The rate at which a clay strain-softens post-peak is difficult to establish. A reasonable assumption was made based on precedent from other analyses. Parametric studies, performed as part of the present investigation, have shown that this property, when varied over a realistic range, does not have a major influence on the results obtained (Kovačević (1994)). One or more shear surfaces are likely to form as peak strength is mobilised in real plastic clays, and loss of strength post-peak occurs as a consequence of sliding on these surfaces. Such thin discontinuities are not reproduced in the finite element analysis, in which the minimum thickness of a rupture surface is approximately half the thickness of an element. This must be taken into account when specifying the rate at which strength is lost post-peak. The shear stress-displacement plot for a shear zone of thickness T in simple shear is shown in Figure 4.31.

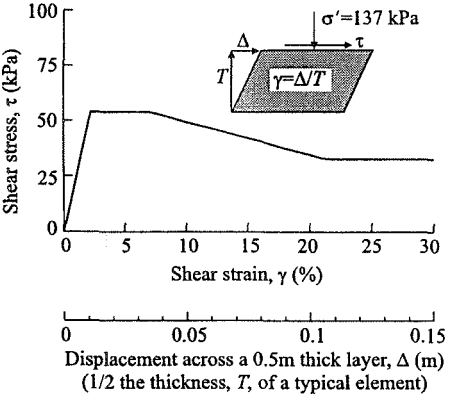

Figure 4.31: Assumed stress-strain and stress-displacement relationship in simple shear

Typically, in the present investigation, half an element is 0.5m thick. A displacement scale equivalent to this is also shown in the figure.

Figure 4.32 shows a comparison between the stress-strain behaviour observed in two unconsolidated undrained triaxial tests on 265 mm diameter samples of Brown London Clay (Sandroni (1977)) and the predictions made from the model adopted. The comparison is reasonable, although the generation of pore water pressure during shear is underestimated.

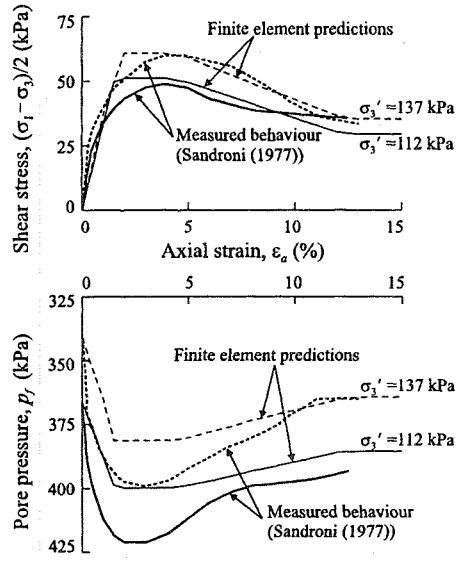

Figure 4.32: Measured and predicted behaviour of Brown London Clay in triaxial tests

4.5.4.3 Finite element analyses

A typical finite element mesh for a 10m high, 3:1 slope is shown in Figure 4.33. The boundary conditions and method of analysis were the same as in the 'non-softening' analyses presented in Section 4.3.2. However, greater care had to be exercised when collapse was approached in the 'softening' analyses, as discussed in Section 4.5.3.

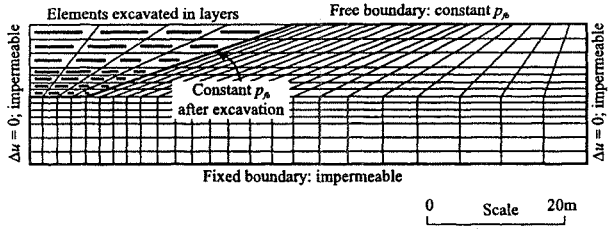

Figure 4.33: Typical finite element mesh

4.5.4.4 Results of a typical analysis

Results are now shown from a typical analysis of a 10m high, 3:1 slope, with a value of the initial coefficient of earth pressure at rest, K_o=1.5. This slope has a conventional long-term factor of safety of 1.4, based on a limit equilibrium calculation with peak soil strengths (c_p'=7kPa and φ_p'=20°).

Figure 4.34 shows predicted vectors of current (incremental) displacement 9 years after excavation, and 14.5 years after excavation, just before collapse is predicted. The vectors show the current mechanism of movement and indicate the eventual collapse mechanism. The absolute values of the displacements are of no

significance. The figures show that the outer part of the slip surface has developed after 9 years, and that the complete slip has developed after 14.5 years.

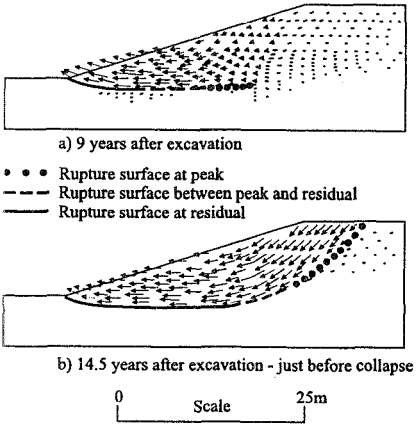

Figure 4.34: Vectors of incremental displacements

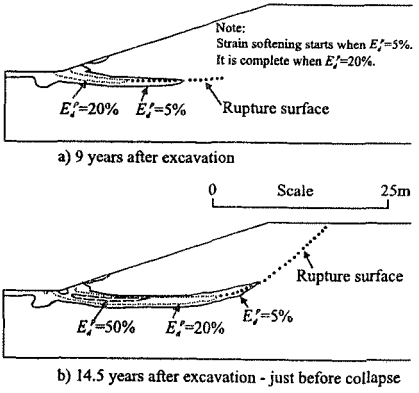

Figure 4.35: Contours of accumulated deviatoric plastic strain, E_d^p

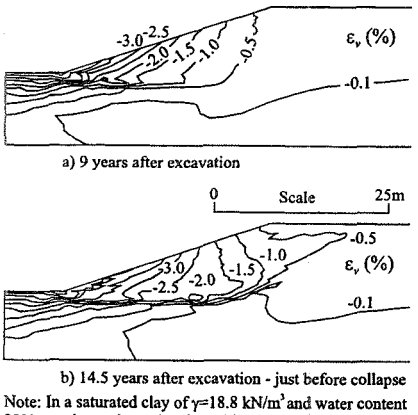

Figure 4.36: Contours of volumetric strain, ε_v

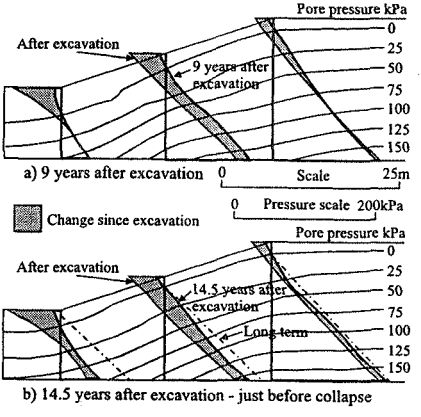

Figure 4.37: Contours of pore water pressure

Contours of deviatoric plastic strain, E_d^p (see Equation 4.5) are given in Figure 4.35. The 5% and 20% contours represent the start and end of strain softening. A horizontal shear zone propagates from just below the toe of the slope, in a manner similar to that observed in the field by Burland *et al.* (1977). The strength acting on this base shear rapidly drops from peak to residual as the rupture zone develops.

Figure 4.36 shows the volumetric strains which develop due to swelling. The strains within the slip are quite large, and are equivalent to a change in water content at the toe of the slope before collapse of the order of 1-2%. The analysis predicts an abrupt change in volumetric strains across the rupture surface.

Pore water pressure development is shown by contours in Figure 4.37, with some vertical profiles on which both changes towards equilibrium and equilibrium pressures are shown. In the middle of the slope, pore water pressure changes due to excavation are almost constant with depth. For this value of K_o they change by an amount almost equal to the weight of soil removed from the slope above. At the crest of the slope the reduction is nearly linear with depth. It varies from 20kPa to 30kPa due to lateral stress relief, although there is no removal of weight at this section. Below the toe of the slope, high lateral stresses remain after excavation. The reduction in mean total stress is less, and the reduction in pore water pressure is significantly less than the weight of soil removed. The interaction between changes in total stress and pore water pressure is clear. After 9 years, the pore water pressures at depth have reduced due to undrained unloading, as the slope deforms outwards and releases the locked-in lateral stresses, rather than increased due to swelling.

Residual strength has been reached along the complete horizontal part of the rupture zone (see Figure 4.35). The amount of progressive failure is substantial, with the residual factor R=0.623, i.e. the average strength has dropped 62.3% of the way from peak to residual. The residual factor R is a measure of the difference between the average field strength at collapse and the strengths measured in the laboratory: $R=(\overline{\tau}_p-\overline{\tau})/(\overline{\tau}_p-\overline{\tau}_r)$, where $\overline{\tau}$ is the average shear stress at collapse and $\overline{\tau}_p$ and $\overline{\tau}_r$ are the average peak and residual strengths at the current normal effective stress along the eventual rupture surface (Skempton (1964)). The average operational strength along the eventual rupture surface at collapse is given by $\overline{\tau}/\overline{\sigma}_n'$=0.328, which is equivalent to c'=0, φ'=18.2°. The average pore water pressure ratio on the final rupture surface has increased from $\overline{r}_u^*$=0.06 after excavation, to $\overline{r}_u^*$=0.247 at collapse. The long-term equilibrium pore water pressure is equivalent to $\overline{r}_u^*$=0.375. Thus, on the rupture surface, the average pore water pressure has changed 60% of the way towards final equilibrium.

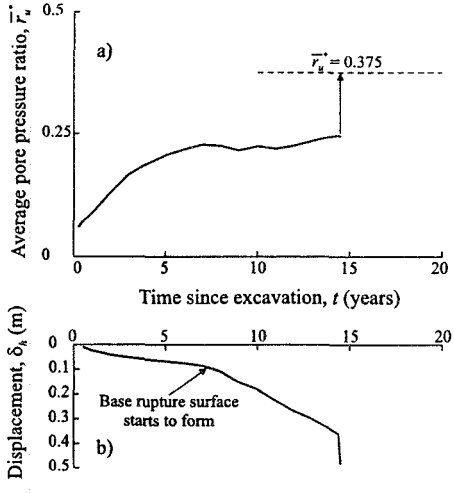

Figure 4.38: Softening clay; development of a) $\overline{r}_u^*$ on the rupture surface and b) mid-slope displacement, δ_h, with time

Figures 4.38a and 4.38b show the change with time of the predicted

average pore water pressure ratio on the rupture surface, $\overline{r_u}^*$, and the horizontal displacement at mid-height of the slope, δ_h. The average pore water pressure has got close to the value at collapse, before the rupture surface at the base of the slide starts to form. The mid-height displacement then starts to accelerate. Swelling then involves reducing lateral total stress, rather than increasing pore water pressure. The coupled effect of the reducing lateral total stress causes a small decrease in average pore water pressure, although the clay is continuing to swell. There is only a relatively small increase in pore water pressure in the five years preceding collapse. Thus the analysis implies that the measurement of pore pressure in the field is a poor way of monitoring risk of collapse. Final collapse is quite abrupt, without significant warning from accelerating displacement.

The predicted deformations are consistent with the limited precedents from field observation of London Clay slopes. The best recorded data are of the Kensal Green retaining wall (Skempton (1977)), which moved nearly 0.5 m before failing some 29 years after its construction. The movements were about 100mm after 26 years.

4.5.4.5 *Effect of coefficient of earth pressure at rest*

In order to study this effect, 6 analyses were performed for a 10m high, 3:1 slope, varying the value of K_o (=1.0, 1.25, 1.5, 1.75, 2.0 and 2.15, the last value is approximately equal to K_p, the passive coefficient of earth pressure). The variations of average pore water pressure ratio and mid-height horizontal displacement with time from these analyses are plotted in Figure 4.39. It may be noted that the 'ultimate' equilibrium pore water pressure ratios shown on this plot are from the same steady state seepage solution, but differ because the rupture surface for each analysis is different. This plot shows that the time to collapse is strongly dependent on K_o and reaches a minimum of about 13 years when K_o is about 1.25. Maximum pore water pressure ratios at collapse are similar, ranging from $\overline{r_u}^*$=0.225 to $\overline{r_u}^*$=0.275. However, two types of behaviour can be seen. First, when $K_o \leq 1.25$, pore water pressures reach close to their maximum values soon after excavation. Second, when $K_o \geq 1.5$, there is a rapid equilibration of pore water pressures over about 5 years, followed by a much slower increase until collapse.

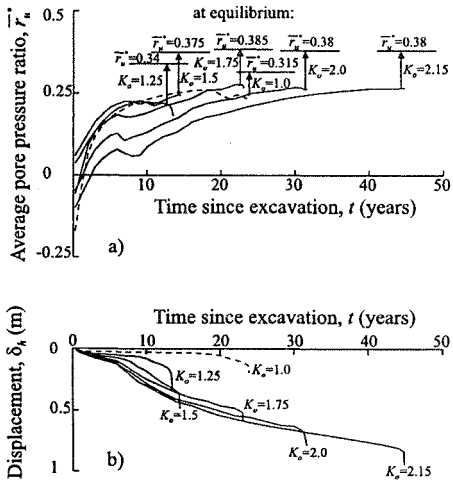

Figure 4.39: Effect of K_o: development of a) $\overline{r_u}^*$ on the rupture surface and b) mid-slope displacement, δ_h, with time

This slow increase is accompanied by an initially increasing rate of displacement, which then slows down. Rates of displacement only accelerate again a few months before collapse. There is little warning of collapse from observations of either pore water pressure or movement. Collapse is predicted when pore water pressures are significantly lower than the final long term equilibrium values.

The shapes of the rupture surface and the residual factor, R, for each analysis are shown in Figure 4.40. The rupture surfaces are strongly influenced by the value of K_o. They become deeper as K_o increases from 1.0 to 1.75. As K_o increases further, the back of the slip moves out towards the slope. In all cases only a short length of the rupture surface is at a strength between peak and residual. The rupture surface at the crest of the slip forms after the collapse event when K_o is low. The rupture surfaces are compared with each other and with field surfaces in Figure 4.41. The field surfaces have been geometrically scaled to the same slope and height as the analyses. The predicted and observed rupture surfaces are in broad agreement.

The amounts of progressive failure, as expressed by the residual factor R, predicted from all the analyses are similar. However, the influence of progressive failure changes as K_o exceeds 1.75, as shown by the values of R in Figure 4.42. Initially the influence increases with K_o, then it decreases, finally it increases again. The reason for this is shown in Figure 4.40. The length of the horizontal rupture surface which develops from the toe of the slope increases with K_o. With high values of K_o it extends beyond the crest of the slope. Then the back of the final rupture surface

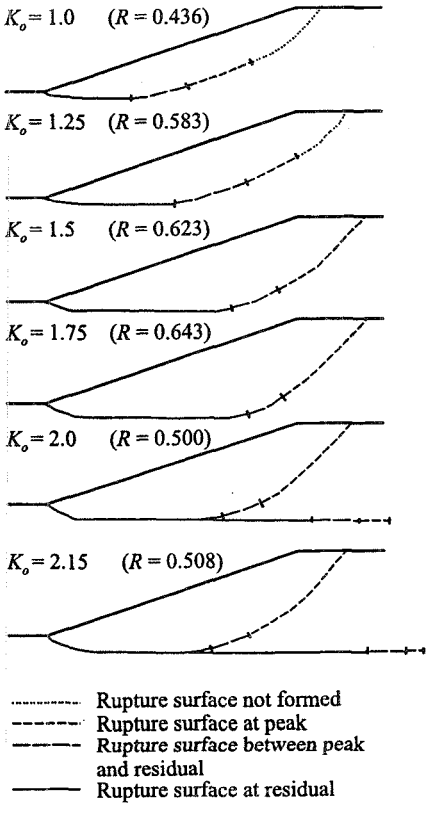

Figure 4.40: Rupture surfaces predicted for varying K_o

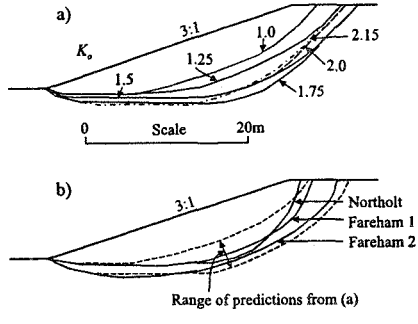

Figure 4.41: a) Predicted rupture surfaces; b) comparison with field observations in London Clay

develops subsequently closer to the slope, and the inner part of the horizontal rupture surface is not incorporated in the final rupture surface. As a consequence, part of the horizontal stress in the zone in which the back of the slip finally develops is relieved before collapse, and the amount of progressive failure is reduced.

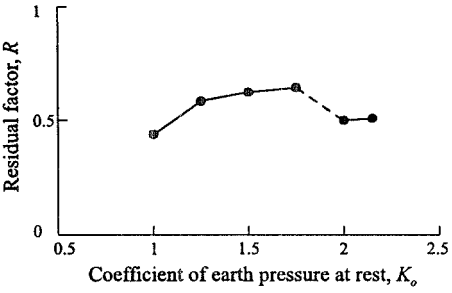

Figure 4.42: Change in residual factor with the initial K_o

4.5.4.6 Effect of surface boundary suction

Analysis of a 3:1 slope, 10m high, with a K_o=2 and with the surface suction raised to p_{fb}=−20kPa was performed. Such an increase in suction might be produced by the management of slope vegetation. The results may be compared directly with the analysis in which p_{fb}=−10kPa. Figure 4.43 shows how the average pore water pressure ratio on the rupture surface and the horizontal displacement at mid-height develop in the two analyses. Collapse with the increased boundary suction occurs after 100 years. Also shown are results from an analysis in which no strain softening was modelled. No collapse occurred, and the changes in behaviour as the base shear develops about 5 years after excavation were eliminated.

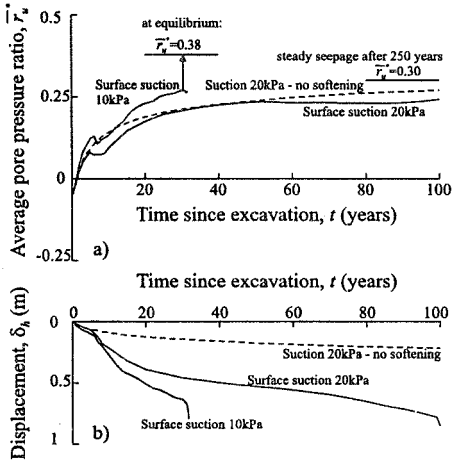

Figure 4.43: Effect of surface suction; development of a) $\bar{r}_u^*$ on the rupture surface and b) mid-slope displacement, δ_h, with time

The rupture surface for the analysis with p_{fb}=−20 kPa was slightly deeper than that for the analysis with p_{fb}=−10 kPa. Also, the average pore water pressure ratio at collapse on the rupture surface was lower and, to compensate, the amount of progressive failure was higher. However, in spite of more progressive failure, the small increase in boundary suction (from p_{fb}=−10kPa to p_{fb}=−20 kPa) improves stability substantially. Extrapolation indicates that a further increase in boundary suction to p_{fb}=−30 kPa would be just sufficient to prevent collapse.

4.5.4.7 Effect of slope geometry

Two analyses were performed to examine the stability of 2:1 and 2.5:1 slopes, 10m high, with K_o=2.0 and p_{fb}=−10kPa. Results may be compared with the

corresponding analysis of the 3:1 slope. The development of pore water pressure and deformation with time are shown in Figure 4.44. Both slopes fail in less than 10 years, with relatively low average pore water pressure ratios on their rupture surfaces. There was slightly more progressive failure than for the 3:1 slope.

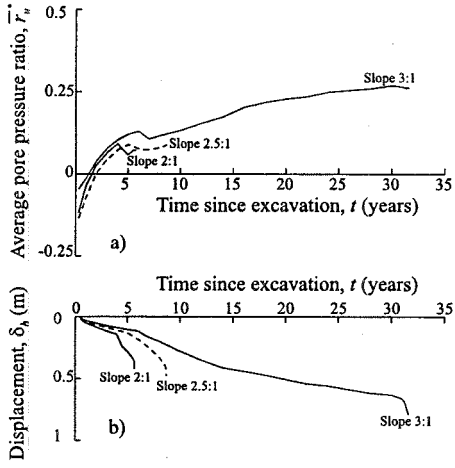

Figure 4.44: Effect of slope inclination; development of a) $\bar{r}_u^*$ on the rupture surface and b) mid-slope displacement, δ_h, with time

Analyses of a 4:1 slope with high K_o showed similar behaviour to the 3:1 slope. They indicated that a 4:1 slope was nearly stable when 10m high, even in the very long-term, but a 15m high slope failed with pore water pressures some way from the predicted equilibrium values. While predicted times to collapse are very long (i.e. greater than 100 years), such that the eventual collapse may be considered rather academic, such slopes may be vulnerable if geological features, such as sand or silt layers, within the slope lead to more rapid swelling.

Analyses of 6m high slopes were more stable. While the 3:1 slope was just stable in the long-term, the behaviour of the 2:5 and 2:1 slopes was similar to that of the 3:1 slope, 10m high. Equilibrium long-term pore pressures were decreased and the amount of progressive failure was slightly reduced.

4.5.4.8 Effect of surface cracking

Shallow slides have been commonly observed on both road cuttings and embankment slopes (Perry (1989)). No such slides were reproduced by analyses of cutting slopes with constant surface boundary conditions and soil properties. Surface effects can involve cyclic shrinkage and swelling with down-slope movement due to non-recoverable strain, cracking and, possibly, loss of strength.

Calculations made by limit equilibrium methods of analysis for embankment slopes which include high pore water pressures, such as those generated in a saturated cracked zone (Crabb and Atkinson (1991)), have shown that slipping can only be explained if the operational strength is much lower than the peak strength of the fill. Analyses are presented here which examine whether this strength reduction could occur due to progressive failure. The analyses were similar to those described above, with the exception that a higher permeability zone due to cracking was incorporated on the slope surface.

Analyses were performed on 3:1 cutting slopes, 10m high, with a high permeability zone approximately 2m thick (three rows of finite elements, see

Figure 4.33). Both high and low values of K_o (2.0 and 1.0) were examined, with surface boundary suctions of p_{fb}=−10kPa and zero.

The permeability adopted for the 'cracked' layer was k=10^{-9}m/s. This is the same as the permeability of the 'uncracked' clay at the top of the slope, and is seven times higher than the 'uncracked' clay at the bottom of the slope. The layer only produces a discontinuity in the pore water pressure distribution during swelling.

Nearly all analyses showed deep-seated sliding, similar to that shown by the equivalent analyses without the 'cracked' zone. Collapse was significantly accelerated by the permeable surface layer, which promoted swelling. A slight increase in progressive failure due to the less uniform seepage pressure distribution induced by the permeable layer was also observed.

Only the analysis with K_o=1.0 and zero boundary suction developed a shallow slip shortly after excavation. Figures 4.45 and 4.46 show the development of the slip with time. It can be seen that a thin superficial layer swells quite quickly and fails by progressive failure from the bottom up. It seems that this mechanism is inhibited by a high initial value of K_o, apparently because of the early formation of a deep-seated rupture surface and the stress relief associated with it. It reduces subsequent swelling and the potential for progressive failure in a superficial layer.

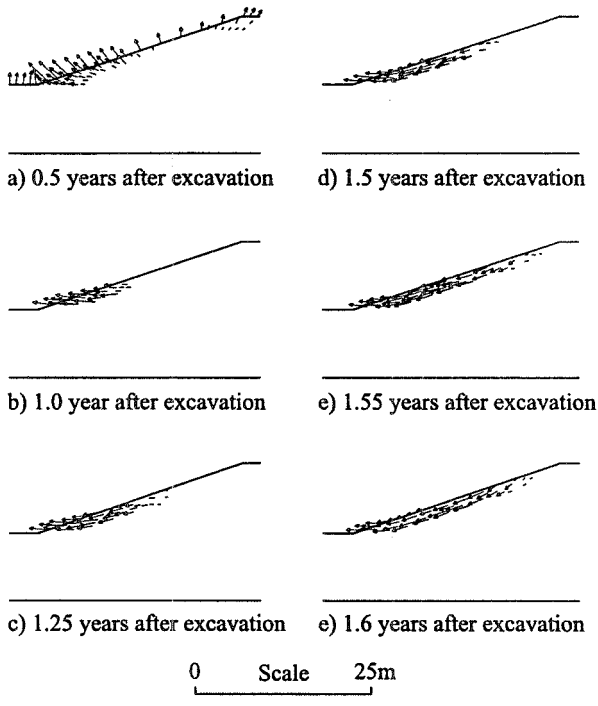

Figure 4.45: Incremental displacement vectors showing the development of the superficial slip

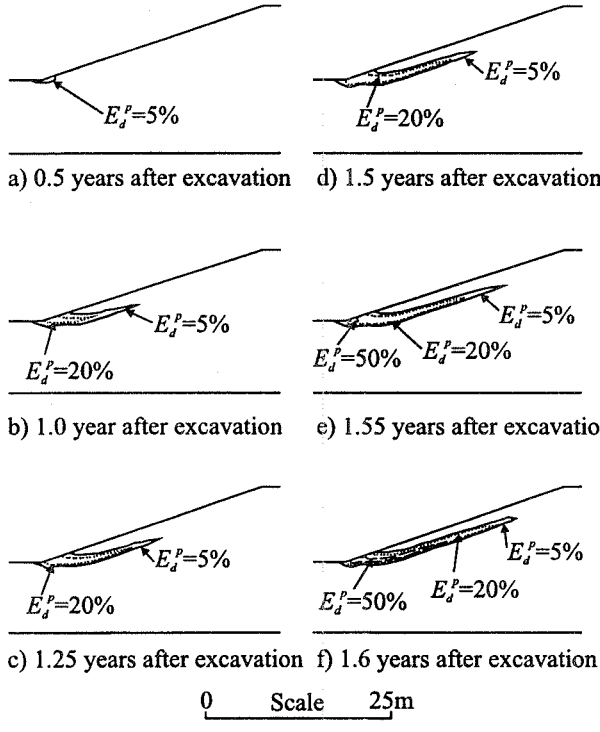

Figure 4.46: Contours of accumulated deviatoric plastic strain, E_d^p, showing the development of the superficial slip

The predicted time-scale for the shallow slip to develop (i.e. 1.6 years) is shorter than is usually observed in the field. However, the prediction involves a monotonic swelling process with zero boundary pore pressure (equivalent to winter conditions), with cracks already developed. The time scale in the field may be controlled by the time taken for cracks to develop, and by the delay before the slope is subjected to a long 'wet' winter.

4.5.4.9 Effect of subsequent changes to slope geometry

Increases in motorway traffic often require widening of existing motorways. In the case of a motorway cutting, this is usually achieved by removing its toes and thus forming steeper overall slopes. Such an approach is attractive because no extra land is required. The local stability at the toe is often provided by a form of gravity retaining wall. Walls formed of reinforced earth have become increasingly popular.

The effect of widening a motorway cutting in Brown London Clay by removing the toe of a 4:1, 10m high slope, to form a 3:1 slope overall, at different times after initial construction, has been examined (see Figure 4.47). The typical finite element mesh shown in Figure 4.33 has been modified in order to account for

excavation of the toe and formation of a concrete gravity wall. No attempt has been made to model formation of the more widely used reinforced earth type retaining wall. Such modelling is complex and in this case not justified, because it would not have a significant impact on the results of the analyses. An initial in-situ value of K_o=1.5 was assumed in all analyses. A surface boundary suction of p_{fb}=−10 kPa was assumed initially, although the influence of an increasing surface suction due to the management of slope vegetation was also investigated. An efficient drainage system behind and beneath the retaining wall is needed, particularly when constructing clay filled reinforced soil slopes. In the analyses described here it was assumed that the concrete retaining wall will drain the surrounding soil. This was achieved by specifying a zero pore water pressure condition at the wall-soil interface.

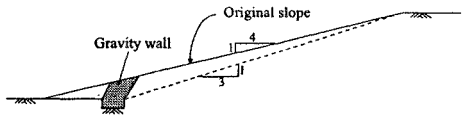

Figure 4.47: Scheme for motorway widening

The results of the analyses are presented as before, in terms of the change with time of the predicted average pore water pressure ratio, $\overline{r_u}^*$, and the associated mid-slope horizontal displacement, δ_h (see Figure 4.48). Wall installation was modelled at four different times after slope formation: (i) immediately after excavation, (ii) 15 years after excavation, (iii) 50 years after excavation, and (iv) after a steady state condition is reached. Widening greatly accelerates delayed failure (a 4:1, 10m high slope without widening is nearly stable, see Section 4.5.4.7) and may lead to immediate failure, if done 50 years or more after initial excavation. However, the amount of progressive failure as quantified by the residual factor, R, remains about the same as before.

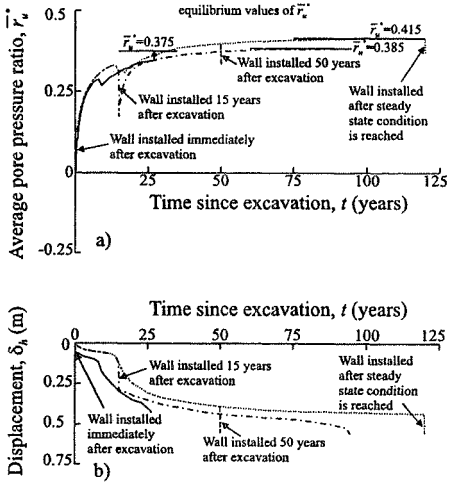

Figure 4.48: Effect of widening; development of a) $\overline{r_u}^*$ on the rupture surface and b) mid-slope displacement, δ_h, with time

If widening is done a short time after excavation (e.g. 15 years), stability may improve to some extent as a result of the additional depression in pore water pressures due to toe excavation (the immediate increase in pore water pressure due to wall construction is localised and negligible). However, eventual failure is inevitable. It can be suppressed if the surface suction produced by, for example, management of slope vegetation is increased (see Figure 4.49). The increased

surface suction at the slope behind the wall will also eliminate delayed failure when the wall is installed immediately after slope excavation (see Figure 4.50). Note that no increase in suction in front of the wall has been modelled in the analyses. The increasing surface boundary suction reduces the equilibrium values of the average pore water pressure ratio in the slope and the amount of slope movement during swelling. Although difficult to achieve in practice, high values of the average surface boundary suction (in excess of 30kPa) may eliminate the base shear formation, if not completely, then for a substantial period of time (see Figure 4.50a).

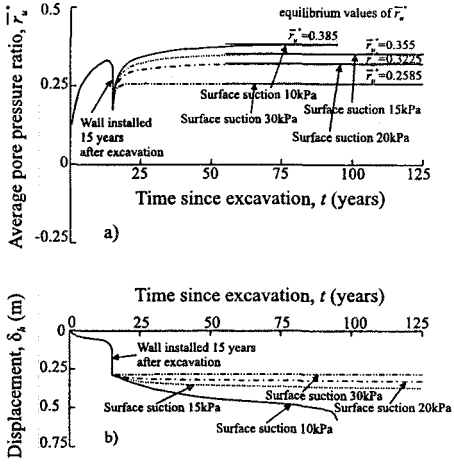

Figure 4.49: Wall installed after 15 years; development of a) $\bar{r}_u^*$ on the rupture surface and b) mid-slope displacement, δ_h, with time

4.5.4.10 Further discussion

The delay predicted for collapse and the average pore water pressure ratio, $\overline{r_u}^*$, on the rupture surface at collapse, for the various analyses performed, are shown in Figure 4.51. Also shown on this figure are field observations (Chandler (1984a), (1984b)). The agreement between the finite element predictions and field measurements is good. Considering the difficulties in estimating the coefficient of permeability, k, on which the time to collapse directly depends, the times to collapse predicted by the analyses are consistent with field observations, particularly when higher K_o values (which are likely to be more representative of stiff clay) are assumed.

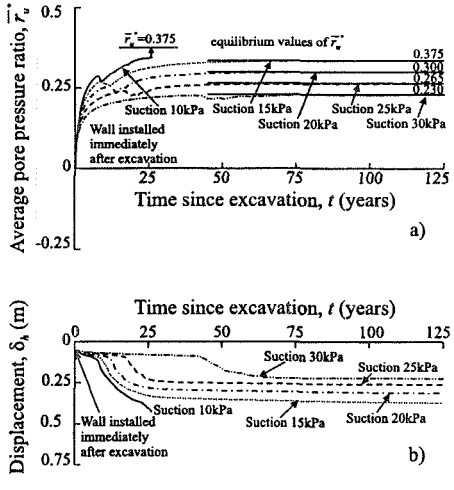

Figure 4.50: Wall installed immediately; development of a) $\bar{r}_u^*$ on the rupture surface and b) mid-slope displacement, δ_h, with time

The average strength at collapse predicted by the analyses is shown in Figure 4.52, together with the peak and residual strengths. Also shown are the operational strengths deduced from back analysis (using limit equilibrium method)

of slips by Chandler and Skempton (1974). The strengths from the finite element analyses are generally lower than those of Chandler and Skempton (1974). However, the finite element analyses typically predict deeper rupture surfaces than the critical surfaces predicted by limit equilibrium analyses. As the rupture surface becomes deeper, the amount of progressive failure increases, and the average strength, expressed as a stress ratio, decreases. At low values of K_o the relatively shallow rupture surfaces approximate to the critical surfaces predicted by limit equilibrium analyses. Then the average strengths predicted by the finite element analyses agree with those obtained by limit equilibrium back-analysis.

Figure 4.53 shows values of $\overline{r_u}^*$ on the eventual rupture surface, after excavation, at collapse and after full equilibration (steady state), for all the analyses, plotted against slope inclination. The pore water pressures required for collapse increase with decreasing slope angle, but so do the equilibrium pore water pressures. The analyses show that collapse is sensitive to the magnitude of the pore water pressures in the slope, and thus to the equilibrium pore water pressures to which these pressures tend. This plot could be used to assess the effectiveness of any remedial drainage measures. For example, the effect of increasing the surface boundary suction from p_{fb}=−10kPa to p_{fb}=−20 kPa for a 3:1 slope, 10m high, is to reduce the long term steady state value of $\overline{r_u}^*$ to just above the 'collapse' range (see Figure 4.53).

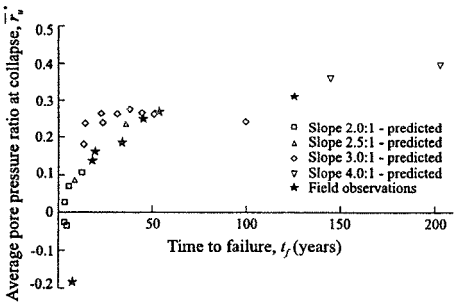

Figure 4.51: Predicted average pore pressure ratio on the rupture surface vs. time to collapse, and field observations

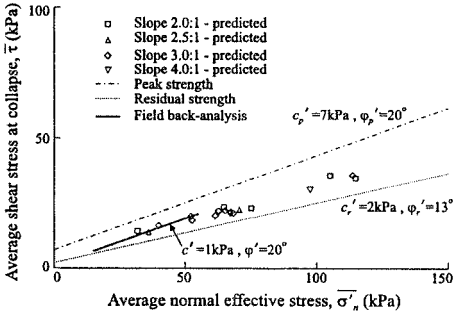

Figure 4.52: Average operational strength at collapse predicted by FE analyses and limit equilibrium analysis

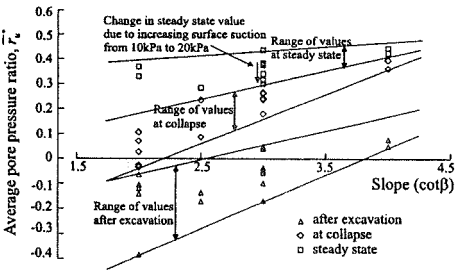

Figure 4.53: Variation of average pore pressure ratio on the rupture surface with slope inclination

This implies that, although the time to collapse would increase, collapse would still occur (see Section 4.5.4.6). For collapse to be prevented, the surface suction would have to be increased still further, so that the long-term value of $\overline{r_u}^*$ fell below the 'collapse' range indicated in Figure 4.53.

Figure 4.36 shows a sharp discontinuity in volumetric strain across the horizontal rupture surface of 2-3%, equivalent to a change of water content of 1-2%. Such a discontinuity could be detected by site investigation. This would be a potential way of examining the stability of old slopes. As can be seen from Figure 4.35a, the basal part of the rupture surface forms quite early on. Its formation does not indicate that collapse will eventually occur, but its presence with continuing movement on it (which could be monitored) indicates decreasing stability. The absence of movement would indicate stability.

Figure 4.54 shows a section through a slip on the M11 near Loughton in Essex, in a slope 18 years old. Results from tests on samples taken from just above and below the rupture surface are given on the figure. There is nearly a 4% change in water content and a two fold change in remoulded undrained strength across the rupture surface. This observation is consistent with the numerical analysis.

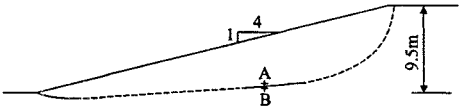

	Water content	Liquid limit	Plastic limit	Remoulded quick undrained shear strngth
	W %	W_L %	W_P %	S_u kPa
Sample A	33.2	70	33	26
Sample B	29.4	75	32	62

Figure 4.54: Slip on the east side of the M11 near Loughton, Essex (1993)

4.6 Construction of cut slopes under water

Excavation of cut slopes underwater can be problematic. For example, consider the situation shown in Figure 4.55a, where a trench is to be excavated in the sea bed. At the beginning of the analysis, the initial stresses and pore water pressures in the soil are in equilibrium with the sea level (the mean sea level is often assumed, but its fluctuation can, in principle, be accounted for). Excavation is then simulated by sequentially removing rows (or blocks) of elements. However, care must be taken to properly account for the water pressures applied to the newly excavated soil surface.

When excavating the first row (row 1) of elements shown in Figure 4.55b, the process essentially also removes the water pressure acting on the original ground surface between points A and H. It is therefore necessary to simultaneously (i.e. over the same increments as excavation occurs) apply a boundary stress over the newly excavated soil surface ABGH, to represent the water pressure acting on it. This process must be repeated as each row of elements is removed.

Although the process described above is logical, it is cumbersome and often difficult to achieve with some computer software. This arises as many programs

do not correctly account for the stresses applied along the previous excavated soil surface when further elements are removed. For example, when excavating row 2 in Figure 4.55c, the software must specifically remove the nodal forces associated with points B and G, which are due to the boundary stresses representing the water acting over the surface BG, as well as simulating excavation of the elements in row 2 and the boundary stress associated with the water acting over the newly excavated surface BCFG. Note that it is not necessary to specifically remove the nodal forces due to the boundary stress representing the water acting over the old excavation surface BG at any other nodes between B and G, as these are implicitly accounted for in the simulation of the excavation of the elements in row 2. The reason why the nodes at points B and G require special consideration is that part of the nodal force due to the water pressure is applied to soil which is not to be removed. This process requires complex book keeping and consequently many software packages neglect to account for this. The error involved increases with the depth of water above the original ground surface.

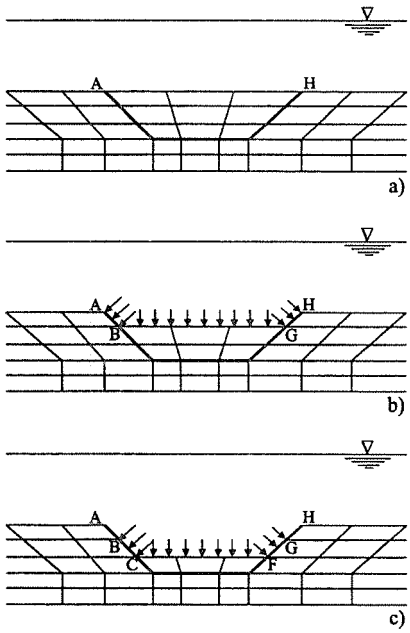

Figure 4.55: Scheme for excavation under water

4.7 Summary

1. When analysing cut slopes, it is important to distinguish between different types of materials in which they are cut. Granular soils behave in a drained manner. Clays of low permeability are largely undrained during excavation. Coupled consolidation/swelling is necessary for intermediate and long term situations. The choice of constitutive model depends on the material type.
2. The analyses of 2:1 cut slopes, 10m high in stiff 'non-softening' clay all show well defined rupture surfaces at collapse. The average pore water pressures on the rupture surface at collapse, $\overline{r_u}^*$, were independent of K_o. They are influenced slightly by any dilation that occurs when the soil fails. The depression in pore water pressures due to dilation acts as a partial brake on the rate of post-collapse movement on the slip surface.
3. The values of $\overline{r_u}^*$ at collapse predicted by the analyses with zero dilation are in good agreement with those obtained from limit equilibrium analysis assuming a circular rupture surface. However, the position of the rupture surface predicted by the numerical analysis differs from the critical slip circle.

4. The time to collapse increases with K_o.
5. Partial drainage can occur in the short term when excavating in soft clays. For shallow excavations this may well be due to high initial stiffness. Partial drainage can also operate in deeper excavations, when soft clays are of relatively higher permeability and/or of moderate thickness, due to the presence of sandy or silty layers which accelerate pore pressure equilisation.
6. Progressive failure refers to the non-uniform mobilisation of shear strength along a potential rupture surface. If a brittle soil is loaded non-uniformly, some elements of soil will reach peak strength before others and a rupture surface will begin to develop. With further loading, the post-peak strains along the rupture surface increase, and the strength reduces from peak towards residual. At collapse, part of the rupture surface has formed and lost strength post-peak, and a part has not yet formed. Thus the average strength of the soil mass at failure must be smaller than the peak strength and greater than the residual strength.
7. The parametric studies of the 3:1 slope, 10m high in stiff 'softening' soil, such as London Clay, show that the probability of collapse is relatively insensitive to the value of K_o assumed. The value of K_o strongly influences the location of the shear surface and the time to collapse. There is a slight increase in the amount of progressive failure with increasing K_o up to a critical value, after which the base rupture surface extends beyond the final inclined rupture surface, which relieves the stress in the slip prior to its final formation and reduces the amount of progressive failure.
8. The rupture surface has four parts, namely: (i) the horizontal base shear, which forms early and reaches residual well before collapse; (ii) a short transition length between peak and residual; (iii) an inclined back surface, in which rupture has occurred but where strains are not sufficient for strain-softening to start; and (iv), when K_o is low, an inclined section near the original ground surface on which rupture only occurs post-collapse.
9. The deep-seated nature of slips predicted at the high values of K_o, usually present in in-situ London Clay, is typical of field experience. The analyses show that, at the higher values of K_o, the rupture surface is developed by progressive failure at a greater depth than the critical surface which would be determined by limit equilibrium analysis. As a consequence, the predicted operational strength on the rupture surface is less than that which would be determined for the same slope with the same pore water pressures by limit equilibrium analysis, using a search technique to find the critical surface.
10. There is considerable variability in the predicted time to collapse of the slopes analysed, bearing in mind that a constant permeability is assumed. The parametric studies on the 3:1 slope predict time to failure between 11 and 45 years. The steeper slopes fail in less than a decade. The flatter ones may fail after more than 100 years. The field experience also shows considerable variability in time to collapse. There will be seasonal variation in superficial pore water pressures, not represented in the analyses, superimposed on the

general trend. Thus collapse will tend to occur in winter, when surface suction is zero (see e.g. Chandler (1984b)).

11. The surface hydraulic boundary condition has a strong effect on stability. The analyses show that an increase in surface suction from 10kPa to 20kPa goes more than half way to stabilise the 3:1 slope. Surface pore water pressures can be reduced by increasing evapo-transpiration through the controlled use of vegetation, or by surface drainage which reduces pore water pressures below the depth of the drains.
12. The analyses show, beyond reasonable doubt, that the mechanism causing deep-seated delayed slips in these slopes is progressive failure promoted by swelling. They enable the importance of the controlling variables to be established, and the effect of possible stabilising measures to be evaluated. The new and sophisticated techniques of numerical analysis have an encouraging ability to reproduce observed behaviour, provided that realistic input data is used. No assumptions need then be made about behaviour mechanisms, as these are established by the analysis.
13. No shallow slips were predicted in the analysis in which uniform soil properties were assumed. However, shallow slides can be reproduced by differential strains and progressive failure at the base of a superficial layer of clay of higher permeability due to shrinkage cracks, although this is not the only possible reason for such slides. This mechanism was inhibited by high initial values of K_o, when early formation of a horizontal rupture surface probably reduced the strain energy stored in the superficial 'cracked' layer.
14. Care should be exercised when widening a motorway cutting by removing the toe. The analyses show that widening greatly accelerates delayed failure, although the amount of progressive failure remains about the same. The increasing surface boundary suction produced by management of slope vegetation, or surface drainage which reduces pore water pressures below the depth of drains, may halt development of slips in the longer term.

5. Embankments

5.1 Synopsis

Many attempts have been made to predict the behaviour of various types of embankments. The finite element method is a powerful tool for such predictions. This chapter deals with applications of the finite element method in the analyses of this type of structure. Examples of modelling are presented and discussed.

5.2 Introduction

Geometrically, embankments are very simple structures. However, the materials involved may vary widely, involving construction on foundations ranging from soft clays to hard rocks and fills ranging from compacted clays to rockfills.

They are often used to retain water, varying from simple flood protection embankments to large embankment dams, hundreds of metres high and involving tens of millions of cubic metres of fill. They also may be used to support structures, like roads and railways.

Embankments are usually placed by earth-moving plant, in layers of varying degrees of mechanical compaction, although they may be loose dumped or even placed hydraulically. Quite often embankments of compacted fill are used to retain hydraulic fills as in land reclamation and waste disposal.

The mechanisms involved in the embankment behaviour can be quite simple, as in a non-water retaining embankment of permeable granular fill on a 'strong' foundation. On the other hand, they can also be much more complicated, as in the case of low permeability fills being placed on a 'weak' foundation, where pore pressure changes are generated by total stress changes (short-term undrained events) and by equilibration during the processes of consolidation and seepage in the longer term.

It is apparent that the finite element analysis of stresses and deformations in embankments is an exceedingly complex problem. Obviously, all types of embankments cannot be covered here, neither can all the various mechanisms involved. Thus a selection has been made to present examples of finite element analysis of various types of rockfill dams, earth embankments and embankments on soft ground.

5.3 Finite element analysis of rockfill dams

5.3.1 Introduction

According to the nature and position of the watertight element, there are two main types of rockfill dam: (i) that containing a relatively impervious internal earth core, either wide or narrow, central or inclined, and (ii) that with an upstream impervious membrane, made either of concrete or asphalt. Usually rockfill and clayey fill are involved in the former and just rockfill in the latter.

Being derived from rockfill only, dams with an upstream impervious membrane are simpler to analyse and therefore an example of finite element analysis of this type of dam will be presented first. This membrane is usually thin and flexible and has little bearing on rockfill deformation during first reservoir impounding and subsequent operation. First, some general features involved in embankment dam modelling will be briefly discussed.

5.3.2 Typical stress paths

A great variety of stress paths occurs in embankment dams (and their foundations). They are often accompanied by a large rotation of principal stresses and may be particularly complex during first reservoir impounding and subsequent operation. It is difficult to reproduce all these real stress paths, even using sophisticated laboratory equipment such as the hollow cylinder or true triaxial apparatus. Nevertheless, it is common to describe the behaviour of fills using standard laboratory tests. This is particularly so for rockfills. Because of their coarse nature, the tests have to be performed on large samples and are therefore expensive and labourious. Consequently, their number and types are limited. Sometimes both large triaxial and oedometer tests are performed for rockfills, but quite often only results from one of these two tests are available. Therefore, it is necessary to establish which of these is more representative to simulate rockfill behaviour in an embankment dam.

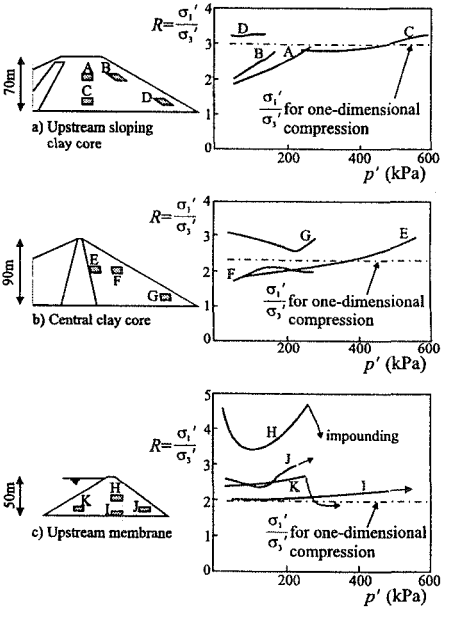

Figure 5.1: Stress paths for three types of rockfill dam (after Charles (1976))

It can be argued that the oedometer test, providing a constant stress ratio path, $R = \sigma_1'/\sigma_3' = 1/K_o$, can better capture fill behaviour, at least during the construction stage. Although the principal stress ratio, R,

is not ideally constant during dam construction, in most cases its value changes within a relatively narrow limit and usually around the assumed $R = 1/K_o$ value (Figure 5.1). That is why oedometer tests, with R typically between 2.0 and 3.0, give a reasonable prediction of overall rockfill dam behaviour during construction. However, in spite of this, triaxial tests should not be neglected. Apart from defining the rockfill strength envelope, these tests provide a useful insight into the stress-strain properties of rockfills too. Also, due to lateral yield, the stress paths in the dam shoulders deviate from the K_o line towards the strength envelope and can approach those imposed by standard triaxial testing (Figure 5.2). It seems that, if rotation of principal stresses is ignored, the typical stress path during dam construction is somewhere between those imposed by oedometer and standard triaxial testing. Ideally, any constitutive model should predict the observed rockfill behaviour in both oedometer and standard triaxial tests (if both types of test are available). Then, it is reasonable to assume that the rockfill behaviour may be captured for any stress path in between. How well the available constitutive models can achieve this is, however, another question!

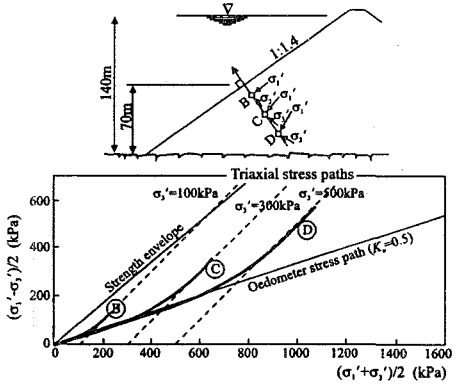

Figure 5.2: Stress paths for three points along a line normal to the concrete face of a hypothetical rockfill dam (after Mori and Pinto (1988))

5.3.3 Choice of constitutive models

It has been repeatedly shown (see e.g. Duncan (1992)) that the most influential factor in the finite element analysis of embankment dams is the modelling of the stress-strain behaviour of the fill by an appropriate constitutive law. However, in spite of the diversity of the stress-strain relationships being used, reasonable agreement has usually been found when the results of finite element analyses (typically movements) have been compared with field observations. This is not surprising bearing in mind the fact that most of the analyses were done after the field measurements had been made, resulting in after-the-event or so called 'Class C1' predictions (according to Lambe (1973)).

A review of different constitutive laws used in the numerical analysis of embankment dams can be found in publications by Naylor (1991a) and Duncan (1992). Both elastic and elasto-plastic formulations are available. In the following the most representative models will be reviewed briefly, with emphasis on their validity and parameter derivation. Some of them have already been described in Chapters 5 and 7 of Volume 1 of this book.

5.3.3.1 Linear elastic analysis

Soils are far from being either linear or elastic (see Chapter 4 of Volume 1). Nevertheless, because of simplicity, geotechnical engineers have often characterized the behaviour of real soil using idealized models of linear isotropic elasticity. Reasonable results can only be obtained for conditions far away from failure, when a significant factor of safety operates. These conditions usually prevail in rockfill dams, and thus it is not surprising that linear elastic analyses have been successful in a number of cases.

Only two elastic constants are needed to characterise the stress-strain behaviour of isotropic linear elastic materials. They are usually Young's modulus, E, and Poisson's ratio, μ. In order to obtain reasonable values of stresses and particularly displacements, it is essential to find the most suitable values of the above elastic constants. A 'constant equivalent compressibility' method for determination of Young's modulus using data from oedometer tests, was proposed by Penman *et al.* (1971). They showed that the internal distribution of vertical displacement during construction of a thick, broad layer (one dimensional condition) possessing self weight, can be predicted with little error by the use of constant Young's modulus determined to give the correct final displacement of a point half-way up the complete layer.

5.3.3.2 'Power law' models

These models were developed in an attempt to fit the data from the oedometer test, which is sometimes the only available test for fills (e.g. rockfill). For granular materials, the relationship between volumetric strain, ε_v, and axial stress, σ_a', in a one dimensional compression test can be described by a power law of the form (Rowe (1971)):

$$\varepsilon_v = C(\sigma_a' / p_a)^D \tag{5.1}$$

where p_a is atmospheric pressure in the same units as σ_a', C and D are dimensionless parameters. Skinner (1975) used the above relationship to derive the closed form solution for the settlement profile on the centre line of an embankment of height H constructed of rockfill of bulk unit weight γ:

$$s = \frac{C_1 \gamma^D}{D+1}[H^{D+1} - (H-h)^{D+1} - h^{D+1}] \tag{5.2}$$

where s is the settlement of a marker placed at a height h above the foundation and $C_1 = C/p_a^D$. Settlements in this case are treated as one dimensional and vertical effective stress is presumed to be equal to the overburden pressure (pore pressure is zero). The former results in an underestimate of settlements, the latter in an overestimate. The two effects are likely to be relatively small and compensating.

By differentiating Equation (5.1), the expression for the tangential constrained modulus, E_c', can be obtained. The tangential Young's modulus, E_t, can be derived using the value of Poisson's ratio, μ, estimated from the K_o value (i.e. $\mu = K_o/(1+K_o)$) from elastic theory, where K_o is related to the angle of shearing

resistance φ' according to $K_o = 1 - \sin\varphi'$, or determined directly from the oedometer test as $K_o = \sigma_r'/\sigma_a'$, by measuring the radial stress σ_r'. If a constant K_o value is assumed (a frequently made assumption for soils), at least three model parameters are required to represent loading conditions. Additional parameters are needed to model unloading (see e.g. Naylor (1991a)).

5.3.3.3 Hyperbolic model

As described in Section 5.7.4 of Volume 1, this model is based on a hyperbolic function which approximates the stress-strain curve in a conventional triaxial compression test. Various modifications have been made to the original formulation. Using a Mohr-Coulomb failure criterion, the following expression for the drained tangential Young's modulus, E_t, can be derived:

$$E_t = \left[1 - \frac{R_f(1-\sin\varphi')(\sigma_1' - \sigma_3')}{2c'\cos\varphi' + 2\sigma_3'\sin\varphi'}\right]^2 M_l p_a \left(\frac{\sigma_3'}{p_a}\right)^n \tag{5.3}$$

where R_f is the stress ratio at failure with a value always less than unity, p_a is atmospheric pressure, M_l is a modulus number, and n is an exponent determining the rate of variation of the initial tangential modulus, E_i, with confining stress, σ_3'.

The curved nature of the failure envelope for granular materials ($c'=0$) can be accounted for by using the following logarithmic expression for φ':

$$\varphi' = \varphi_o' - \Delta\varphi' \log(\sigma_3' / p_a) \tag{5.4}$$

where φ_o' is the angle of shearing resistance for a confining stress $\sigma_3' = p_a$ and $\Delta\varphi'$ is the reduction in φ' for a tenfold increase in σ_3'.

Instead of modelling the tangential Poisson's ratio, μ_t, Duncan *et al.* (1980) preferred to model the volume change behaviour of soils by an exponentional relationship between the bulk tangent modulus, K_t, and confining pressure, σ_3':

$$K_t = M_B p_a (\sigma_3' / p_a)^m \tag{5.5}$$

where M_B and m are dimensionless model parameters with a similar function as M_l and n in Equation (5.3).

It can be noted that seven parameters are required to characterize the model. If a stiffer response on unloading is to be modelled, the additional parameter M_u (an increased value of M_l) can be employed. All parameters can be evaluated using data from conventional triaxial tests.

The hyperbolic model has been used extensively in the finite element analyses of different geotechnical problems, particularly embankments. Consequently, considerable experience with the model has been accumulated and this has enabled Duncan *et al.* (1980) to compile parameter values for different fills taking into account relative density (compaction), grading, particle shape and mineral composition. This has been the main advantage of the model, especially when applied to the analyses of rockfill dams, given the difficulties associated with the laboratory testing of rockfills.

A nonlinear elastic model, similar in formulation to the above hyperbolic model, has been used at Imperial College for numerical analyses of a number of embankment dams (Hamza (1976), Dounias (1987), Kovačević (1994)). The drained elastic parameters vary according to the following expressions:

$$E = E_i \frac{1 - ABS}{1 + BS} \tag{5.6}$$

$$E_i = E_o \left(\frac{p' + p_a}{p_a} \right)^C \tag{5.7}$$

$$\mu = \left[I - L \log \left(\frac{p' + p_a}{p_a} \right) \right] (1 - S) + 0.49 S \tag{5.8}$$

$$E_u = H E_i \tag{5.9}$$

where E and E_u are the drained Young's moduli on first loading and unloading/reloading respectively, μ is the Poisson's ratio, p_a is atmospheric pressure, and E_o, A, B, C, H, I, L are model parameters. The stress level, S, represents the proportion of the shear strength mobilised at the current mean effective stress, p', and varies from zero, when the state of stress is on the hydrostatic axis, to unity, when it is on the failure envelope given by cohesion, c', and angle of shearing resistance, φ' (see Appendix III.1).

Problems can be experienced with this type of model when deriving the model parameters to satisfy both oedometer and triaxial test data. It is often not possible to accurately model results from both types of test. Bearing in mind the above discussion about typical stress paths, emphasis is often placed on fitting the oedometer stress-strain curve. When results of analyses are compared against field measurements, it emerges that the predicted settlements are in reasonable agreement with the measured ones, but horizontal displacements are overpredicted (see e.g. Potts *et al.* (1990), Kovačević (1994)).

5.3.3.4 K-G model

It was recognized a long time ago that modelling of soils in terms of the bulk modulus, K, and the shear modulus, G, had some advantages over the use of Young's modulus, E, and Poisson's ratio, μ. A particular form of this model has been described in some detail in Section 5.7.3 of Volume 1.

In comparison with the hyperbolic model this model is simpler. Only five parameters are required. For unloading an additional parameter is needed. However, their derivation is somewhat 'messy' (Naylor (1991a)). As with the hyperbolic model discussed above, it seems that a good fit to both oedometer and triaxial test data cannot be obtained. This is in agreement with the previous experience gained at Imperial College using Equations 5.6 to 5.9.

5.3.3.5 Elasto-plastic models

It is well known that elasto-plastic stress-strain relationships are capable of modelling the behaviour of real soils more closely. Taking into account the

influence of stress path on soil behaviour, elasto-plastic finite element analyses should provide a better prediction of stresses and especially movements in embankment dams. Unfortunately, in spite of the existence of different elasto-plastic constitutive models, these have not been widely used in practice. One reason might be the considerable complexity of such analyses. Another can be found in the difficulties connected with the testing of fill materials, especially rockfills.

Nevertheless, there have been attempts in the past to characterize the behaviour of rockfill using elasto-plastic stress-strain relationships. The use of various elastic perfectly plastic models gave, essentially, an elastic solution as no (or only small) zones of plastic yielding were discovered. Significant factors of safety usually operate in rockfill dams and the modelling of plastic behaviour at peak and post-peak, even with the inclusion of hardening or softening behaviour, is unnecessary. Modelling such behaviour is only of importance in special circumstances when a shear failure surface develops (see e.g. Potts *et al.* (1990)).

The inclusion of plasticity pre-peak has usually been associated with the modelling of dilatancy, i.e. the tendency of well compacted granular fills to increase, or soft clayey fills to decrease, their volume on shearing. There is both laboratory and field evidence that suggests dilatancy is unlikely to occur widely in rockfill dams. Thus, the use of a complex elasto-plastic model to account for dilatancy alone is not warranted. However, the modelling of the plastic behaviour pre-peak has another, more subtle advantage which concerns the pattern of deformation during yielding. Namely, in contrast to the elastic strains which are dependent on the stress increment only, the plastic strains depend on the accumulated stress as well. The implications of this was clearly demonstrated by Naylor (1975) who analysed the behaviour during construction of a clay core embankment dam using two different constitutive models: 'variable' elastic and critical state elasto-plastic. He showed that the deformation behaviour was sensitive to the type of model being used even though both models produce similar triaxial test stress-strain curves.

There exist a large variety of elasto-plastic models that have been proposed in order to characterize the stress-strain and strength behaviour of soils. Most of them have been conceived from the concept of critical state soil mechanics. The Cam clay model and its various modifications have been increasingly used in the finite element analysis of various dams and embankments. Unfortunately, most of these applications were associated with embankments on soft ground where the overall behaviour is usually governed by the soft materials present in the foundation (see Duncan (1992), (1994)). Very few examples of the application of the critical state models to predict the behaviour of rockfill dams have been reported.

However, the suitability of critical state models to predict the behaviour of fill materials is questionable. These models were originally developed for sedimentary clays. Compacted fills have a behaviour pattern similar to that of sands. Thus, the elasto-plastic constitutive models originally proposed for sands can better capture the behaviour of compacted fills, even of clays. Rockfill can be considered as an extreme granular material.

Elasto-plastic models for sands usually separate the effects of consolidation and shearing. During consolidation deformations are governed mainly by crushing and yielding of interparticle contacts. During shearing to high stress ratios deformations develop also due to sliding and rolling. To account for different plastic deformations during consolidation and shearing, so-called 'double hardening' models have been proposed. A double hardening model of the form proposed by Lade (1977) has been described in Section 8.5 of Volume 1.

5.3.4 Layered analysis, stiffness of the simulated layer and compaction stresses

Embankments are built up in relatively thin horizontal layers. Consequently, there will be a large number of layers during the construction of a large dam. The limitations of computer modelling require relatively thick layers to be used in the idealization (Figure 5.3).

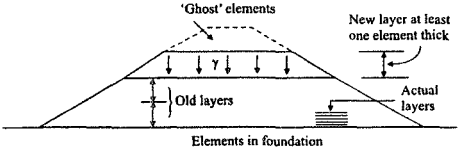

Figure 5.3: Finite element modelling of fill construction

In the past, to provide an insight into the errors involved, the closed form solution of the incremental analysis was usually compared to the finite element 'layered' analysis using a one dimensional model which represents either a soil column or a fill of large lateral extent. It was concluded that as few as five layers is usually sufficient in embankment dam analyses if a nonlinear elastic constitutive model is employed (see e.g. Naylor (1991b)). However, the implication of this finding if an elasto-plastic model is employed has not been considered. It will be shown below that significant errors can occur if the layers are too thick when the effects of compaction are modelled, even in the case of elastic constitutive models (linear or nonlinear).

The effect of compaction is to increase horizontal stresses in a layer as further fill is placed. This effect typically becomes insignificant when 3 to 5m of fill has been placed. To model this, the technique described in Section 3.7.9 of Volume 1 has been used. Construction of a new layer is essentially performed by a gravity 'turn-on' analysis. For a broad fill, the vertical stresses are equal to the overburden pressure, whereas the horizontal stresses are determined by the value of K_o input by the user.

To provide an insight into the effect of modelling compaction stresses in a 'newly' constructed layer on the settlement profile during dam construction, a finite element 'layered' analysis using a one dimensional model (no lateral strain) can been performed. A 50m high soil column is constructed in four, ten and twenty layers respectively. The fill is modelled using the Lade's double hardening model with the parameter values derived for the Winscar sandstone rockfill (Kovačević (1994)). In the first set of analyses the horizontal stresses in a 'newly' constructed layer were determined by the value of Poisson's ratio $\mu = 0.45$ leading to $K_o =$

$\mu/(1-\mu)\approx 0.80$. In the second set of analyses the horizontal stresses were reduced to be equal to $K_o = 0.25$ times the calculated vertical stresses, where K_o=0.25 is a typical K_o value predicted by the idealised, single element oedometer test on the sandstone rockfill using the Lade's double hardening model (Kovačević (1994)).

The results of this exercise are presented in Figure 5.4. It can be seen that the second set of analyses (broken lines with open symbols) predicts settlement profiles which are nearly independent of the number of construction layers used. This is not so when the higher horizontal stresses due to compaction were modelled as in the first set of analyses (full lines with shaded symbols). However, the larger the number of layers employed, the more the settlement profile approaches to that predicted by the second set of analyses.

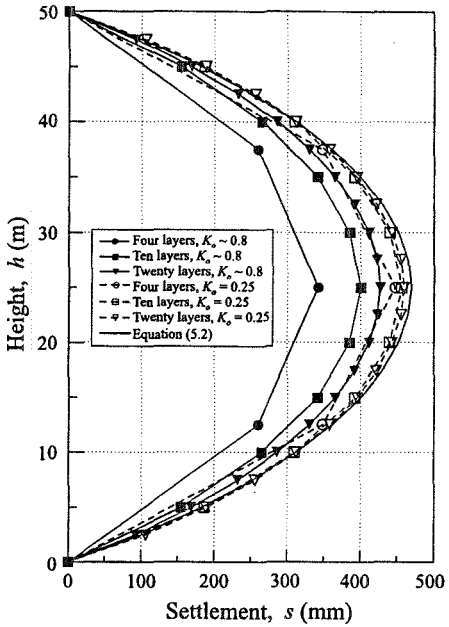

Figure 5.4: Effect of number of layers and compaction stresses on settlement of a soil column

Although the one dimensional model (no lateral strain) is a good approximation of dam construction (at least in the central portion of the dam), and therefore is very useful in determining the optimum number of layers in the finite element analysis, it is important to recognise the particular influence of the stiffness of the new layer in two dimensional analysis. This is due to the difference in bending between one 'thick' simulated layer in the finite element analysis when gravity is suddenly applied, and progressively occurring bending of several 'thin' layers in the field. It was recognised that some stiffness between zero and the full in-place stiffness would make the finite element layer equivalent to the real situation, and some work has been done in this respect for both linear and nonlinear elastic materials (see Naylor (1991b)). Bearing in mind the complexity associated with modelling of compaction stresses (and, in the case of clayey fills, initial suctions), no attempt has been made to include these considerations in the examples reported here. Consequently, a negligible stiffness assigned to the layer of elements during construction (see Section 3.7.9 of Volume 1) results in an overestimate of deformation in the underlying layers. The effect of this when fills are modelled as elasto-plastic materials is unknown, but is likely to be small.

5.3.5 Example: Analysis of Roadford dam

5.3.5.1 Introduction

Roadford dam is a 41m high rockfill dam with an upstream membrane of asphaltic concrete, constructed in the South West of the United Kingdom. A typical cross section of the embankment is shown in Figure 5.5a. The rockfill is composed of mudstone, siltstone and sandstone. Details of the design of the dam and of the properties of the rockfill are given by Wilson and Evans (1990).

An important design detail of the dam is the junction of the asphaltic membrane and the concrete inspection gallery at the upstream toe. To minimise differential movements in this region a zone of stiffer fill (sand waste) was used immediately against the inspection gallery (see Figure 5.5b). A grout curtain approximately 40m deep is located below the inspection gallery.

Instrumentation to measure vertical settlements and lateral displacements of the dam, and to measure the movement of the asphaltic membrane in the vicinity of the inspection gallery, was installed during construction of the dam. The location of some of this instrumentation is also shown in Figure 5.5.

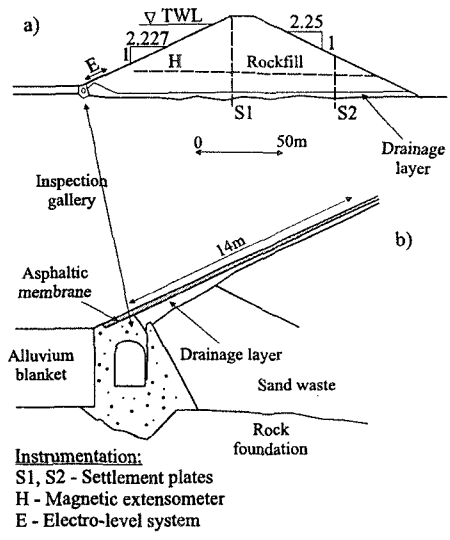

Figure 5.5: Roadford dam: a) Cross-section showing location of instrumentation and b) Detail of the upstream toe

5.3.5.2 Material parameters

Analyses of Roadford dam have been performed using two different constitutive models. One of these was a 'simple' nonlinear elastic perfectly plastic model. It incorporated a Mohr-Coulomb failure criterion (c' and φ') as a yield surface. Non-associated plasticity was assumed with a value of the angle of dilation $v = \varphi'/4$. However, the actual value adopted was of little significance since none of the fill in the dam reached failure. Thus essentially only the nonlinear elastic part of the model is active and the model is referred to as non-linear elastic. The elastic parameters are defined in Equations (5.6) to (5.9). The other model was a 'complex' work hardening/softening elasto-plastic model of the Lade's type, with two intersecting yield surfaces (see Section 8.5 of Volume 1).

Large scale laboratory tests were carried out at the Building Research Establishment (BRE) to determine the relevant properties of the low grade rockfill

and sand waste material (Charles and Watts (1985)). These included investigations of compressibility in 1m diameter oedometer tests and strength (and compressibility) in 0.23m diameter triaxial compression tests. The data from these tests have been used to derive the parameters for the two constitutive models (see Tables 5.1 and 5.2) to give the best fit.

Comparison of predictions from the two constitutive models with results from triaxial and oedometer laboratory tests for the rockfill are shown in Figure 5.6. Inspection of this figure indicates that the fit from the Lade's model is good for both the triaxial and oedometer tests. The fit for the nonlinear elastic perfectly plastic model is not so good but is still satisfactory, especially at low stress levels.

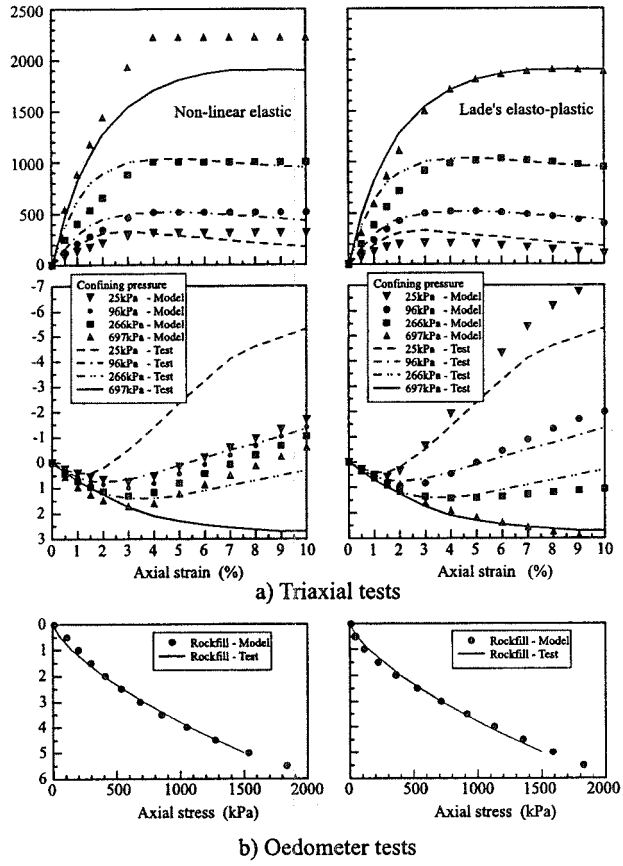

Figure 5.6: Comparison of predicted and measured behaviour in laboratory tests

Table 5.1: Nonlinear elastic model parameters for Roadford rockfill and sand waste fill

Parameter	Rockfill	Sand waste
Modulus number, E_o	30000.0	65000.0
Modulus constant, A	0.05	2.90
Modulus constant, B	6.0	0.3
Modulus exponent, C	1.00	1.15
Unloading model parameter, H	1.0	1.0
Poisson's ratio constant, I	0.25	0.25
Poisson's ratio constant, L	0.5	0.0
Cohesion, c'	50	5
Angle of shearing resistance, φ'	36	40
Angle of dilation, v	9	10

5.3.5.3 Finite element analyses

The finite element mesh is shown in Figure 5.7a. The mesh was refined at the upstream embankment toe, since particular attention was paid to the deflections of the asphaltic concrete membrane during reservoir impounding.

The foundation material and the concrete of the inspection gallery were modelled as linear elastic materials with Young's moduli of 225MPa and 30GPa and Poisson's ratios of 0.2 and 0.15 respectively. No specific laboratory test data or field observations were available for the drainage layer located below the asphaltic membrane and the foundation drainage layer. These materials have only a small influence on deformation and, for convenience, their properties were assumed to be the same as those of the sand waste fill. Only the lower part of the asphaltic

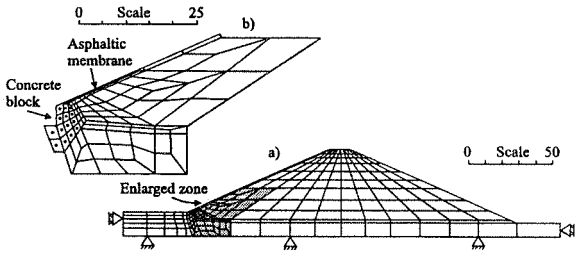

Figure 5.7: Roadford dam: a) Finite element mesh and boundary conditions and b) Mesh detail at the upstream embankment toe

concrete membrane was modelled as a separate zone (see Figure 5.7b). Because of the very high viscosity of bitumen, the asphaltic concrete of the membrane was modelled as an undrained granular soil in terms of effective stresses, assuming the properties of the sand waste fill and the drainage materials (K_e = 100 K_{skel}, see Section 3.4 of Volume 1).

Table 5.2: Double hardening model parameters for Roadford rockfill and sand waste fill

Parameter	Rockfill	Sand waste	Component
Modulus number, M_l (*)	400.0	1200.0	Elastic
Exponent, n (*)	0.70	0.60	Elastic
Poisson's ratio, μ	0.25	0.20	Elastic
Collapse modulus, C	0.000450	0.000020	Cap
Collapse exponent, p	1.00	1.35	Cap
Failure constant, $\acute{\eta}_1$	260.0	35.5	Failure
Failure exponent, m	0.65	0.0	Failure
Plastic potent. const., ρ	0.35	0.45	Conical
Plastic potent. const., R	0.0	0.0	Conical
Plastic potent. Const., t	12.0	0.0	Conical
Work hard. const., α	2.6	3.0	Conical
Work hard. const., β	0.0	0.0	Conical
Work hard. const., P	0.11	0.15	Conical
Work-hard. expnt, l	1.05	1.15	Conical
(*)-Young's modulus $E = M_l p_a (\sigma_3'/p_a)^n$, where p_a is atmospheric pressure			

Construction of the dam was simulated by building in nine layers, each horizontal layer of elements being treated as a construction layer. The foundation drainage layer and sand waste fill at the upstream toe of the embankment were constructed together with the first layer of rockfill material. The layer of drainage material on the upstream face and asphaltic concrete membrane were placed after the embankment had been built.

Reservoir impounding was simulated by applying water pressures to both the upstream slope and upstream foundation (see Figure 5.8). During this process

drained conditions were assumed in the fill material. While a static water pressure, consistent with a water table, was maintained at foundation level behind the grout curtain, an increase in water pressure in front of the grout curtain due to impounding was modelled.

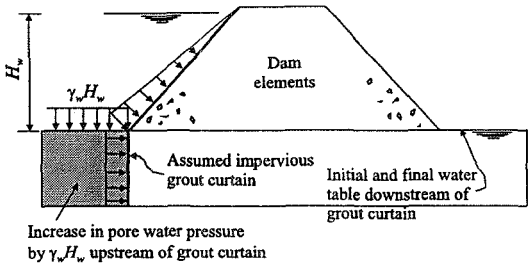

Figure 5.8: Simulation of reservoir loading during impounding

5.3.5.4 Comparison with observations

Vertical movement of the embankment fill was measured with an array of settlement plates at two locations within the dam, S1 and S2, and the lateral displacement with an extensometer at location H (see Figure 5.5a). A comparison of the predicted and measured movements at these locations after dam construction is shown in Figures 5.9 and 5.10.

Inspection of these figures indicates that the analysis using the Lade's model is in much better agreement with the field data. The analysis with the nonlinear elastic model predicts settlements reasonably, but overpredicts horizontal movements severely. These predictions could be improved by adjusting the nonlinear elastic model parameters, but then the laboratory test data could no longer be recovered.

During impounding of the reservoir the deflections of the lower part of the upstream slope of the embankment were measured using a series of electro levels. The location of

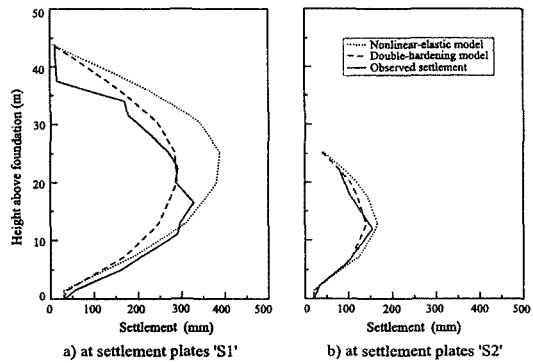

Figure 5.9: Comparison of predicted and measured settlements after construction

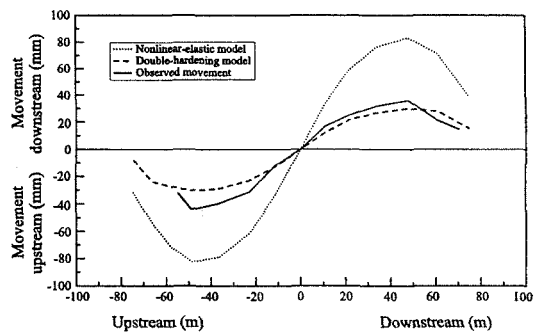

Figure 5.10: Comparison of predicted and measured lateral movements at extensometer 'H'

these gauges is marked as E in Figure 5.5a. A comparison of the predicted and measured deflections are given in Figure 5.11 for three different levels of reservoir impounding. Both models predicted the magnitude of the movements normal to the membrane reasonably well.

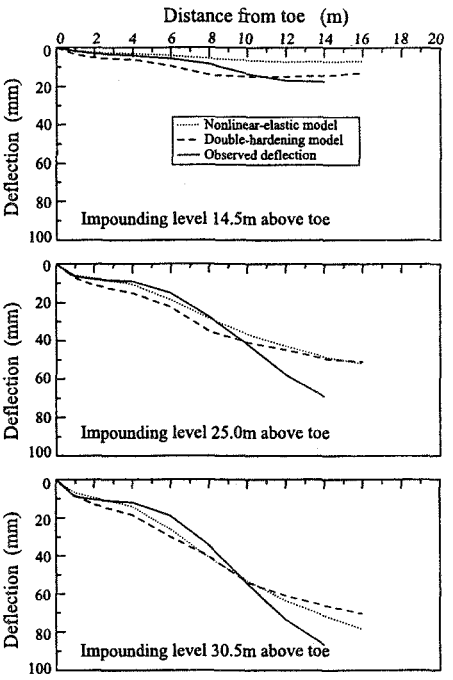

Figure 5.11: Comparison of predicted and measured deflections of asphaltic concrete membrane

5.3.6 Example: Analysis of old puddle clay core dams

5.3.6.1 Introduction

A large number of embankment dams with central cores of puddle clay were built in Great Britain in the 19th century. As the puddle clay was expensive, the cores were made as thin as possible. This made the cores vulnerable to cracking by hydraulic fracture if they were subjected to full reservoir pressure on their upstream boundary, where the seepage pressure may exceed the normal total stress by an amount greater than the tensile strength (which is usually negligible).

It has been deduced that hydraulic fracture of the core was the most probable cause of the failure of the Dale Dyke dam at the end of first impounding (Binnie (1978)). Dounias *et al.* (1996) have performed finite element analyses of the construction and first impounding of this dam to see whether this mode of failure could be recovered. Their findings will be briefly presented in the first part of this section.

There is little information of how these old dams were built. In particular, shoulder fill was often variable and placed in rather thick layers with little compaction. This, in combination with extremely soft puddle cores, may give rise to significant crest settlements as a result of operational cycles of drawdown and re-filling (Tedd *et al.* (1994)). Kovačević *et al.* (1997) have analysed the movements of four embankment sections to examine whether these measured movements could be recovered, and their implications for long term stability. Results for one section (Ramsden dam) will be briefly discussed.

5.3.6.2 Dale Dyke dam

The collapse of the Dale Dyke embankment in 1864 provoked considerable professional discussion and caused changes in the design of old British dams. The changes typically included the use of concrete-filled rather than puddle-filled cut-off trenches, and the adoption of slightly wider cores and zones of compacted finer-grained fill on either side of the core.

The cross-section analysed, together with the finite element mesh and assumed boundary conditions, is shown in Figure 5.12. The puddle clay core, the fill and the top 3m of the foundation were modelled in terms of effective stresses using the elasto-plastic constitutive model described in Section 4.5. The foundation below 3m was assumed rigid. The undrained strength of puddle clay was of the order of 12 kN/m^2. A small amount of strain softening (as a result of dilation) was modelled only in the fill and the foundation, though the strength properties of the fill and the foundation had little influence on the results.

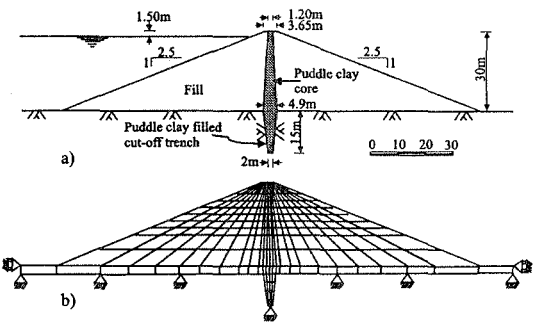

Figure 5.12: Assumed section, FE mesh and boundary conditions (Dale Dyke)

The fill and the foundation were assumed to be fully drained, i.e. no construction pore pressures were generated. Analyses were not 'coupled' so the effects of consolidation in the core were considered by changing the pore water pressure at the various stages of the analysis according to a simplified one dimensional consolidation analysis carried out 'externally'. For example Figure 5.13 shows contours of pore water pressure in the core, immediately after construction, based on these simple one dimensional calculations.

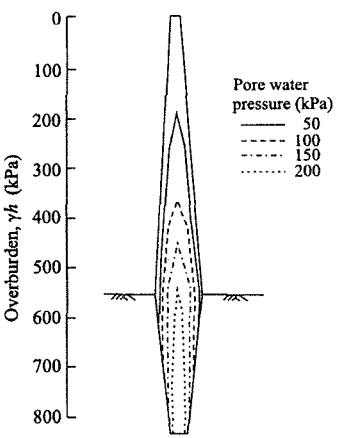

Figure 5.13: Pore water pressures in the core at the end of construction (Dale Dyke)

During impounding the water load was simulated as an external pressure on the upstream slope of the dam plus an increase in pore water pressure throughout the upstream shoulder. Collapse settlement has not been modelled in the analyses. It was considered that it would have only a minor influence on the behaviour of old British dams built in wet upland areas. This comes from the consideration that

collapse settlement primarily occurs in poorly compacted and 'unsaturated' rockfill when particle strength is reduced by wetting due to inundation in the first reservoir impounding, or rain infiltration, leading to additional crushing at particle contacts. The full reservoir pressure was assumed to act at the upstream core boundary, since the fill was very permeable. The water level was raised in increments and one dimensional consolidation calculations were performed after each increment to define the pore water pressure response in the dam core. An example of the changing pore pressures in the puddle clay core at one particular level is shown in Figure 5.14.

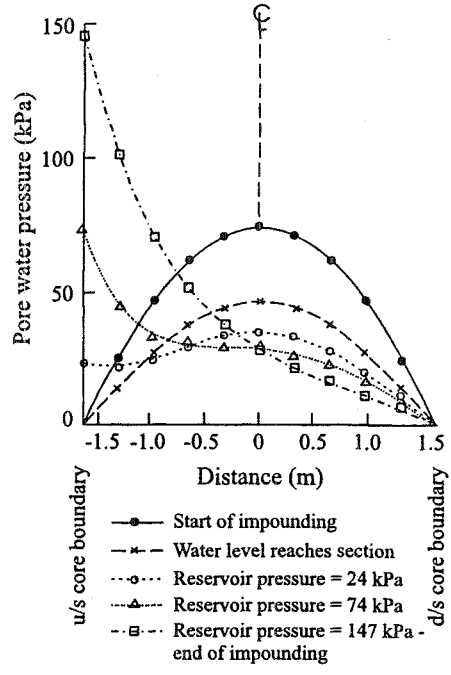

Figure 5.14: Pore water pressure distribution along a horizontal section of the core, 17m below crest level, during impounding (Dale Dyke)

The hydraulic fracture potential at the end of impounding is examined in Figure 5.15. Minimum total stresses are plotted at the upstream core boundary and at a small distance inside the boundary. A comparison of these minimum stresses with the reservoir pressure shows that in the cut-off trench cracking by hydraulic fracture of the puddle clay is almost inevitable. In reality, it is likely that failure is prevented by the non-erodible nature of a rock foundation, which prevents the enlargement of an erosion channel. In the core, the reservoir pressure is lower than the minimum stresses at the upstream boundary, but is almost equal to the minimum stresses acting a small distance inside the boundary.

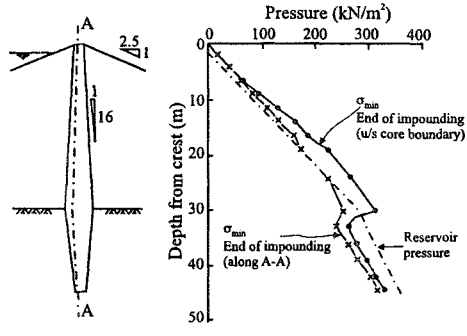

Figure 5.15: Minimum total stress near the upstream boundary of the core after drained impounding (Dale Dyke)

In the analyses presented above it was assumed that the impounding was relatively slow and carried out at a constant rate. The Dale Dyke dam

collapsed during a heavy storm, and it is quite likely that the last few metres were filled rapidly. This scenario was investigated in a further analysis where the last 7.5m was filled quickly, assuming that the core behaved in an undrained manner. The results are presented in Figure 5.16. It can be seen that minimum total stresses at the upstream core boundary are equal to the reservoir pressure at a depth between 7 and 12m below the crest. At a small distance inside the boundary they are lower than the reservoir pressure almost along the whole length of the core. It seems that the rapid undrained final impounding may induce hydraulic fracture around a depth of 10m from the crest. Once formed, it will propagate rapidly downstream, where the total stresses are lower, as an undrained fracture.

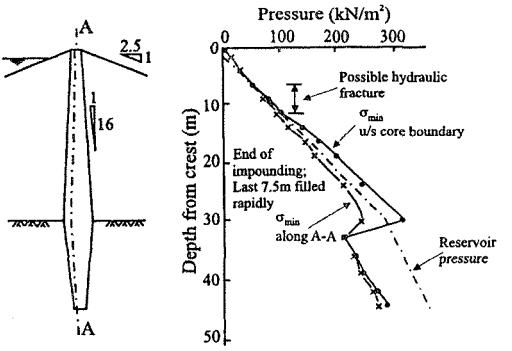

Figure 5.16: Minimum total stress near the upstream boundary of the core, effect of undrained impounding (Dale Dyke)

5.3.6.3 Ramsden dam

Ramsden dam in Derbyshire, England, built between 1879 and 1883, has a central puddle clay core and a concrete filled cut-off trench (not modelled in the analysis, see Figure 5.17). With time it has shown signs of significant settlements, and the crest had to be reconstructed at least twice prior to 1988, when the reservoir was almost emptied (16.5 m drawdown). It was drawn down by 6 m in 1989. The ongoing settlements have given rise to considerable concern, and therefore detailed observations have been made during two drawdowns in 1988 and 1989 (Tedd *et al.* (1990)).

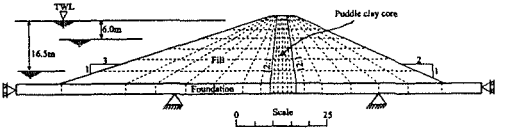

Figure 5.17: Ramsden dam: Finite element mesh

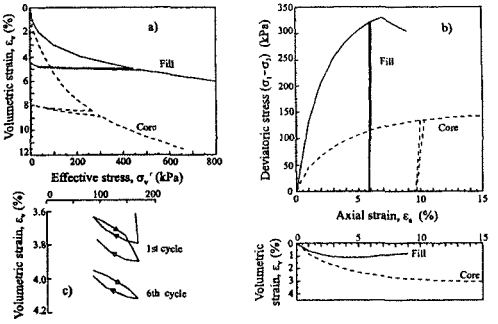

Figure 5.18: Material properties: a) assumed 1D compression, b) assumed triaxial compression, c) cyclic1D loading (Tedd et al., 1994)

The material properties adopted for the shoulder fill and the puddle core are shown, as

predictions for conventional laboratory soil tests, on Figures 5.18a and b. The core was simulated using a model based on modified Cam clay (see Section 7.9 of Volume 1) and the fill by Lade's single hardening model (Lade and Kim (1988)). This model is different from the Lade's double hardening model used in the analysis of Roadford dam and briefly described in Chapter 8 of Volume1. Plastic yield before failure is still accounted for with this model, but this time utilising only one yield surface. The results of a cyclic oedometer test on a typical fill from a mudrock are shown on Figure 5.18c (Tedd *et al.* (1994)).

The load-unload properties adopted, which dominate predictions during reservoir operation, were based on this test. The irrecoverable deformations during operational cycles of drawdown and re-filling are due to the different elastic stiffnesses adopted during unloading and reloading, not due to plastic straining.

The analyses were performed in terms of effective stress. The shoulder fill and the foundation were assumed to be free-draining. Coupled consolidation/swelling was adopted for the puddle clay core, with either a constant permeability or one varying with the mean effective stress, p' (see Section 10.7.5 of Volume 1):

$$k = k_o \, e^{(-ap')} \tag{5.10}$$

where $k_o = 10^{-8}$ m/s is the coefficient of permeability at zero mean effective stress and $a = 0.03$ m^2/kN is a material constant. The analysis using Equation 5.10 gave a nearly perfect fit with the observations (see Figure 5.19). The degree of consolidation in the clay core controlled by coupling of volumetric strain and permeability enabled the time dependent response to load changes to be modelled in real time. No separate approximate consolidation calculations were needed for these analyses.

The purpose of the analyses was to examine behaviour during operation of the reservoir only. Thus a simplified construction history was simulated, involving construction in layers, full consolidation of the core, impounding and the establishment of steady seepage, prior to the impositions of the drawdown and re-impounding cycles.

The observations and predictions of crest movement are shown in Figure 5.20. Small adjustments to the elastic properties shown in Figure 5.18 were made to recover the difference in movement observed between the core and the shoulders. There is no doubt that better agreement between prediction and observation could have been obtained by further adjustments to the assumptions made. However, the reality is unknown and there is a limitation on what can be achieved without a detailed site investigation.

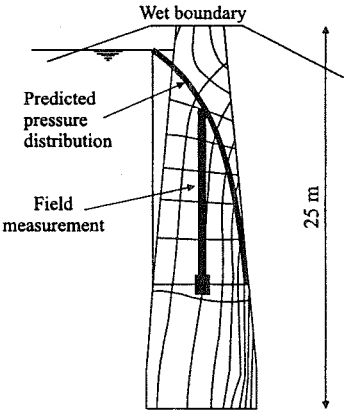

Figure 5.19: Seepage pressure through a narrow core (Vaughan (1994))

Although the analyses cannot predict the extent of the observed irrecoverable deformation towards downstream of the whole embankment crest due to a drawdown cycle, they show that the large and irrecoverable deformations observed can be reproduced by assuming soil parameters which are consistent with the actual materials. The average local factor of safety (the ratio of strength mobilised to strength available at the current stress level) at the end of major drawdown is quite high (about 1.8). Thus large irrecoverable deformations occur despite a substantial factor of safety against overall slope stability, and such large movements do not necessarily indicate incipient instability. In the analyses the irrecoverability arises through the difference in elastic properties assumed in unloading and reloading, not through plastic strains. Thus irrecoverability is predicted for the second smaller drawdown. Large drawdowns do not eliminate irrecoverable movements during subsequent smaller drawdowns.

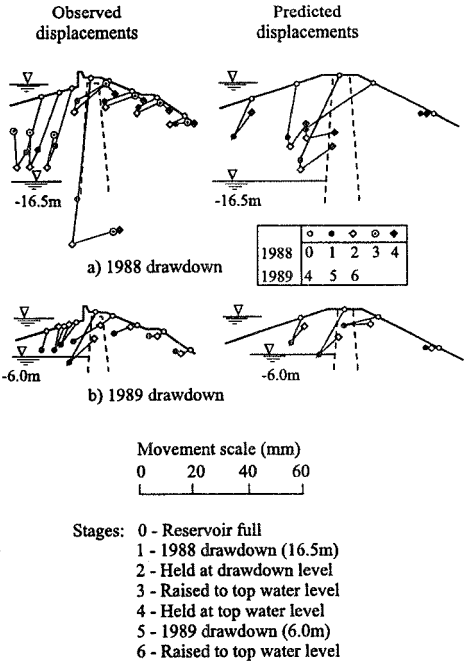

Figure 5.20: Ramsden dam: Observed and predicted displacements during two reservoir drawdowns

5.4 Finite element analysis of earth embankments

5.4.1 Introduction

Finite element analysis of earth embankments is potentially more difficult than that of rockfill dams, as an earth embankment is usually derived from clayey fill only and may sit on a foundation of varying strength and permeability which will affect its performance. The extreme condition of an embankment placed on a soft clay will be presented in Section 5.5. Here, only embankments sitting on a relatively 'stronger' foundation will be considered. The first example is a typical road embankment derived from a stiff clay on a stiff clay foundation, where behaviour of the embankment is mostly governed by the undrained shear strength of the foundation material due to changes in pore water pressure near the surface. The second example is of a large embankment dam founded on a competent foundation covered by a plastic clay deposit which was left in place below the embankment, enabling the embankment to fail progressively during its construction.

5.4.2 Modelling of earthfill

During construction it is usually assumed that the earthfill is saturated and will behave largely undrained. Because of simplicity, analyses of undrained saturated fill in terms of total stresses is quite common (see e.g. Section 5.4.4). However, the pore pressures could then only be estimated from the total stresses.

Analyses in terms of effective stresses are more tempting because they predict undrained pore water pressures directly. Besides, in clay fills it is often necessary to model initial suctions (negative tensile pore pressures). To do this, after the element has been constructed, the mean effective stress p' can be reset to be equal to an appropriate initial suction p_{fo}, and the pore water pressure is reset to $p_f = p_{fo}+p_o'$, where p_o' is the mean effective stress (equal to the mean total stress, p_o) after construction of the element. By essentially resetting the mean effective stress p', it is possible to control the undrained shear strength, S_u, of the clay fill material. It is worth noting that, by changing both mean effective stress and pore water pressure, total stresses remain constant and equilibrium of forces is maintained.

In spite of their low permeability, real earthfills are partly drained at the end of construction, at least at the outer boundaries of the dam. To model this time dependent behaviour in terms of dissipation of construction generated excess pore water pressures, 'coupled' approaches which consider the interaction between the soil skeleton and the pore water are needed. The problem is solved on the basis of equilibrium and the constitutive relationships of the soil skeleton together with the water continuity equation (see Section 10.3 of Volume 1). This approach has been used in some of the examples presented here (see Sections 5.3.6 and 5.4.3).

In the above approach it is assumed that (i) water completely fills all soil voids (the so called 'coupled saturated' approach) and (ii) water is incompressible. Nevertheless, these are reasonable assumptions for fine grained fills placed in a wet compaction state, such as a typical British clay fill derived from a saturated borrow pit.

In order to model the actual soil compressibility in unsaturated conditions, it is necessary to use the 'coupled unsaturated' approaches (see, for example, Pagano (1998)) which consider the actual multiphase character of earthfills (soil skeleton, pore air, pore water). The problem is then solved on the basis of (i) equilibrium equations, (ii) water continuity equation, (iii) air continuity equation, (iv) soil skeleton constitutive equations, and (v) water retention characteristic curve. By assuming the air pressure to be equal to the atmospheric value, the air continuity equation can be eliminated from the set of governing equations.

5.4.3 Example: Road embankments on London Clay

5.4.3.1 Introduction

Foundations for a typical road embankment may vary from an undrained clay to a drained granular material. During embankment construction on a saturated low permeability clay, such as stiff plastic London Clay, excess positive pore pressures are generated. As these pore pressures dissipate, stability should then improve with

time. Undrained stability in the short-term may be of a concern, and clearly it will depend on the undrained shear strength of the clay in the foundation. Regarding the fill material, placement and compaction of clay fills may generate quite high pore water suctions, particularly in more plastic clays. Thus in plastic clay fills of modest height, typical of road works, long-term equilibrium pore pressures are likely to be higher than those at the end of construction. The strength of the fill may then decrease with time as the pore pressures equilibrate and there is a risk of delayed slides.

Undrained shear strength of stiff plastic clays depends more on effective stress rather than water content. There is a seasonal variation of pore water pressure in the surface of a typical British clay stratum as shown in Figure 5.21, and therefore the undrained shear strength will also vary seasonally. Examples of short-term behaviour of embankments derived from London Clay and constructed on London Clay foundations in either summer or winter weather conditions will be now presented (Vaughan (1994)).

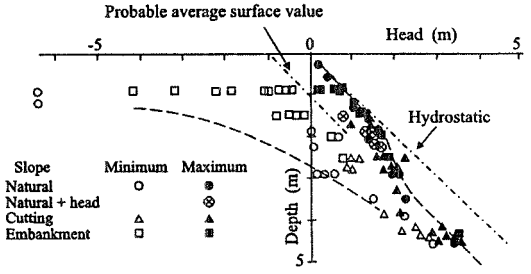

Figure 5.21: Pore water pressures near the surface of the ground: slopes in clay in the UK (Walbancke (1976), Vaughan (1994))

5.4.3.2 Material properties

Soil properties for the in-situ weathered London Clay were the same as those used in the analyses of slopes cut in this material (see Chapter 4). The assumed properties for the fill derived from London Clay are also listed in Table 4.1. The higher value of c'=12kPa, compared to c'=7kPa adopted for the in-situ Brown London Clay, reflects the absence of fissures in the fill. Also, a reduced pre-peak stiffness and an increased post-peak straining to reduce strength from peak to residual have been assumed for the fill. The fill was simulated as a saturated clay with an initial suction as placed to give an undrained shear strength of S_u=60 kPa, typical of a slightly

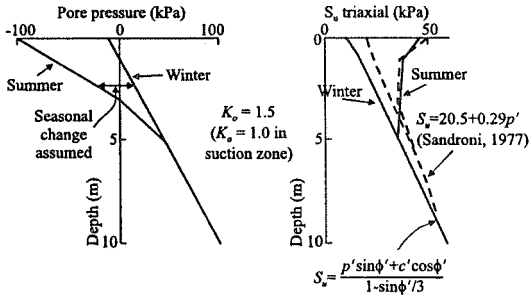

Figure 5.22: Changes in undrained strength of stiff plastic clay due to changes in pore water pressure near to the surface of the ground

wet fill. The permeability of plastic clay fill is low, and a constant value of the coefficient of permeability of k=1.5x10^{-10} m/s has been adopted to match, with the stiffness assumed, typical field deduced values for the coefficient of consolidation/swelling in the range of c_v = 0.5-2.0 m^2/year.

The predicted peak undrained strengths (the soil model described in Section 4.5 has been used in these predictions and subsequent analyses), as would be measured in a triaxial compression test on a saturated sample obtained from the ground without a change in mean effective stress, are shown in Figure 5.22. It can be seen that there is a significant difference between the winter and summer strengths, the former being much lower. Also shown on this figure are strength profiles based on empirical relations proposed by Sandroni (1977). The implication of this with respect to stability will be briefly discussed.

5.4.3.3 Finite element analyses

A typical finite element mesh, with appropriate boundary conditions, used in the analyses is shown in Figure 5.23. It was intended to build a 10 m high embankment with an external slope 2.5 to 1 (horizontal to vertical). The embankment was constructed in layers, with the weight of each layer increased in several increments so that the height at which the embankment collapses can be determined accurately. Analyses were of the coupled consolidation/swelling type, although the London Clay response, with the permeability assumed and time steps used, was nearly undrained.

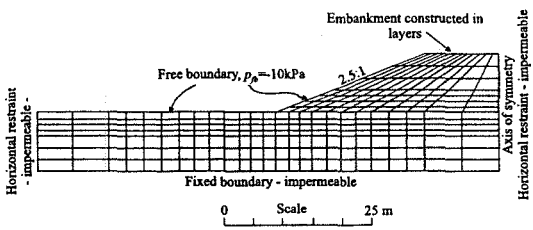

Figure 5.23: Mesh for analysis of 10m high embankment

Figure 5.24 shows the displacement vectors just before collapse when the embankment was built on the clay foundation with undrained strengths based on pore water pressures at the end of winter. A rupture surface developed in the weakest clay just below the level to which consolidation has penetrated. The strength along this rupture surface is between peak and residual. The final rupture surface through the fill has not formed when the embankment collapses. This is a consequence of progressive failure. Collapse is predicted when the embankment reaches a height of 6.2m.

Figure 5.25 shows results from a similar analysis with the foundation strength profile at the end of summer. A deeper rupture surface is predicted this time. It penetrates to just below the level where the strength has been increased by the suctions induced by summer weather. Collapse is now predicted when the embankment reaches a height of 10.4 m. The importance of the initial pore water pressures assumed in the analyses (and thus the time of the year when an embankment is constructed) is clearly demonstrated.

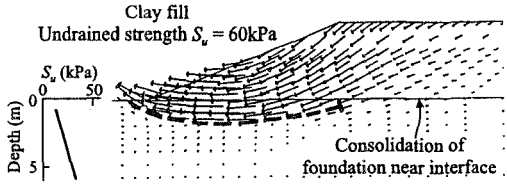

Figure 5.24: Collapse with pore pressures at the end of winter; critical height 6.2m

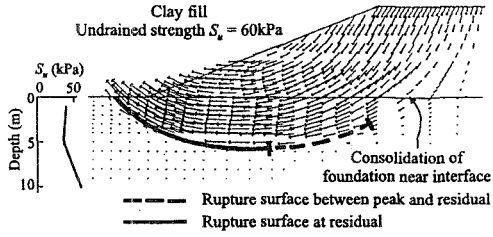

Figure 5.25: Collapse with pore pressures at the end of summer; critical height 10.4m

5.4.4 Example: Failure of Carsington embankment

5.4.4.1 Introduction

The failure of the upstream side of Carsington embankment just prior to its completion in 1984 has been reported in the literature (Skempton and Coats (1985), Skempton (1985)). The detailed investigations into the failure showed that an analysis by conventional limit equilibrium methods gave a safety factor at the time of the collapse significantly greater than one. Since the soils involved were brittle, this discrepancy could be attributed to progressive failure. As an attempt to provide an independent demonstration of this, methods of nonlinear finite element analysis involving the modelling of strain softening and brittleness were developed (see Section 4.5 of this volume) and analyses of the failure were then performed (Dounias (1987), Potts *et al.* (1990)). The failure of the embankment was recovered realistically, assuming soil properties consistent with laboratory and field test data, and the significant role of progressive failure in the collapse was confirmed.

This example briefly considers the various material parameters used in the analyses, describes the finite element analyses performed on the original Carsington section, and discuses some findings deduced from the analyses carried

out subsequently on embankment geometries which are variants of the original Carsington section.

5.4.4.2 Material parameters and soil model used

The cross section of the Carsington embankment used for analyses, with the various materials involved, is depicted in Figure 5.26. Although some analyses were performed as part of a parametric study in which material properties were varied, the most probable material properties are summarised in Table 5.3. Most parameters have been derived from test data, others largely assumed. Their derivation has been discussed in detail by Potts *et al.* (1990). The core has been assumed to be undrained and was modelled using total stress parameters. The foundation and the shoulder materials were assumed to be fully drained.

A generalised nonlinear elastic strain-softening plastic Mohr-Coulomb model of the form already described in Section 4.5 of this volume was adopted for all materials other than the core. The undrained and saturated core reached yield early on in the analyses and consequently was assumed to be linear elastic before peak undrained shear strength was reached. Strain-softening was modelled as a reduction of undrained strength with increasing plastic strain.

Table 5.3: Material properties assumed in the Carsington dam analysis

Property	Foundation	Yellow Clay	Zone I Fill	Zone II Fill	Core
Unit weight γ (kN/m^3)	-	20.0	20.6	22.0	18.5
Peak strength	-	c_p'=6kPa φ_p'=19°	c_p'=10kPa φ_p'=22°	c_p'=13.5kPa φ_p'=26.5°	c_p'=42kPa φ_p'=0°
Residual strength	-	c_r'=0kPa, φ_r'=12°	c_r'=0kPa, φ_r'=14.5°	c_r'=0kPa, φ_r'=15°	c_r'=30kPa, φ_r'=0°
Plastic strn. to residual	-	ε_{Dr}^p=70%	ε_{Dr}^p=160%	ε_{Dr}^p=160%	ε_{Dr}^p=35%
Poisson's ratio, μ	0.35	0.26(1-S)+ +0.49S	0.08(1-S)+ +0.49S	0.08(1-S)+ +0.49S	0.46
Young's modulus E (kPa)	30p'	20p'	600(p')$^{0.75}$. (1-0.9S)/(1-S)	600(p')$^{0.75}$. (1-0.9S)/(1-S)	5000

5.4.4.3 Finite element analyses

The finite element mesh used in the analyses is shown in Figure 5.27. The dam was built in stages as shown in Figure 5.27. It was constructed until it failed and could not be raised any further. As failure was approached, smaller load increments were adopted, typically equivalent to 0.1 m of fill. The failure height was deduced by plotting typical lateral deformations against height. If the embankment had not failed when the last layer had been placed, the crest was surcharged with a vertical pressure, in a manner shown on Figure 5.27, until failure occurred.

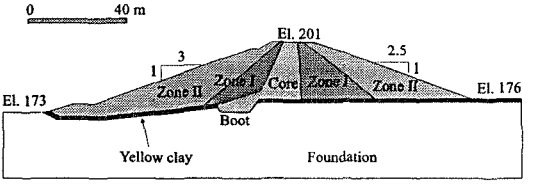

Figure 5.26: Carsington embankment: Cross-section analysed

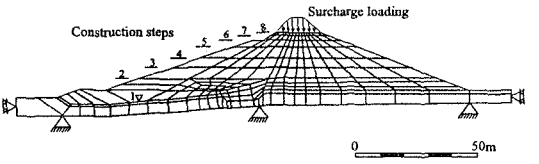

Figure 5.27: Mesh and boundary conditions used in analysis

Once the failure height was exceeded the solution became unstable, since the embankment could not then be in equilibrium. However, it was necessary to be sure that this was not due to a failure of the numerical techniques employed. As in the analyses of progressive failure in cut slopes (Chapter 4), the failure was confirmed by running the final solution for a given number of iterations. Instability was indicated when the deformations increased according to the number of iterations without an improvement in convergence.

5.4.4.4 Original Carsington section

The results obtained at the section through the initial failure are shown in Figure 5.28. The failure (Figure 5.28a) occurred through the core and core extension (the 'boot'), which were of relatively weak clay and which were undrained during construction, and along a layer of clay on top of the foundation (the 'yellow' clay), which was fully consolidated throughout construction. Figures 5.28b and 5.28c show the computed situation at the moment of collapse.

The analysis showed that at collapse (the recovered crest elevation was 200.9m, as compared with actual collapse elevation of 201.0 m) loss of strength had occurred through strain softening in the core (A), and in the inner part of the clay foundation (B) as the failure surface propagated along it. This propagation started when the constructed level was some 5 m lower than at collapse, yet the measured and predicted movements of the dam remained small and gave no warning of collapse (see Figure 5.31). Near the toe of the dam (C), where the final rupture surface developed post-collapse, the strength was not fully mobilised. This can also

be seen from Figure 5.29 which shows the proportion of the available strength mobilised, *S*, for the whole embankment just prior to failure. Corresponding deviatoric strains are shown in Figure 5.30. A concentrated shear zone has developed in the core and boot and in the yellow clay near the boot.

Figure 5.31 shows the horizontal displacements for two characteristic points, one on the upstream slope just above the small added berm and the other at the toe of the boot. The measured displacements at a peg near point B are also shown. The agreement between measurements and predictions is reasonably good, although the creep during the winter shutdown is not modelled in the analysis.

The average mobilised shear stress along the yellow clay upstream at failure was 73kN/m^2 and the residual factor, *R*, was 0.52 (see Section 4.5.4.4). The equivalent values for the fill in the boot and core were 37kN/m^2 and 0.42. The ratio τ_p/τ_{mob} was 1.32 and 1.14 respectively for the two materials through which failure occurred. The factor of safety in terms of peak strength would have been approximately equal to 1.25. According to the analysis, progressive failure was therefore responsible for lowering the factor of safety by 20%.

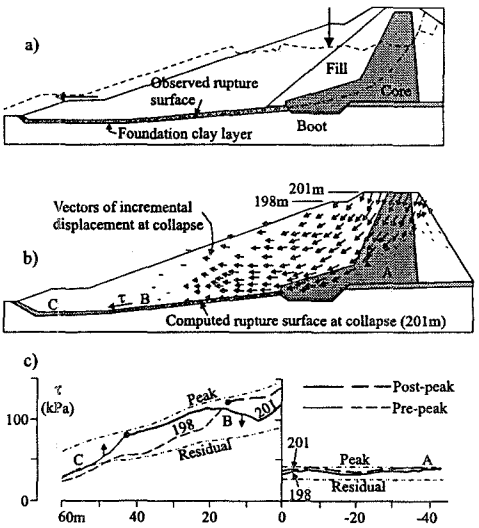

Figure 5.28: The failure of Carsington embankment

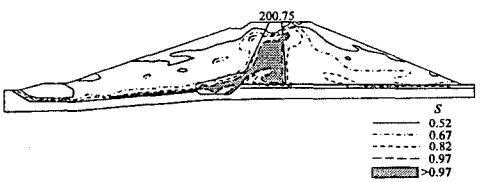

Figure 5.29: Representative analysis: proportion, S, of current strength mobilised just before failure

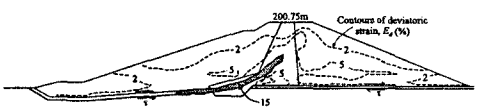

Figure 5.30: Representative analysis: strains in the embankment just before failure

5.4.4.5 Effect of the core geometry on progressive failure

There is no doubt that the stress concentration at the transition from the weak undrained boot to the strong drained foundation, which can be seen in Figure 5.28c, promoted progressive failure. The nature of this stress concentration was

examined by performing analyses of the Carsington section with the same soil properties, but with different core configurations (Dounias *et al.* (1989)). The geometries consisted of a wide core, a narrow core and an inclined core. These analyses are summarised on Figures 5.32a to 5.32d.

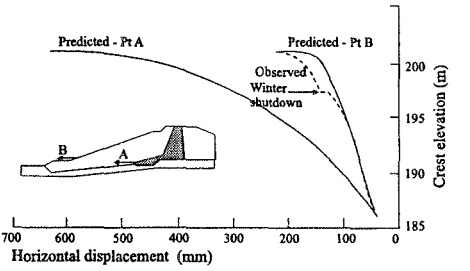

Figure 5.31: Observed and predicted pre-failure movements

The collapse heights and the stress concentration effects are virtually the same for the wide and inclined cores. With the narrow core the embankment could not be built high enough to cause failure through the foundation. However, Figure 5.32e shows that a stress concentration was developing in the foundation near the core at the highest crest height which could be reached (local instability near the crest due to applying surcharge loading did not allow an eventual failure height to be determined).

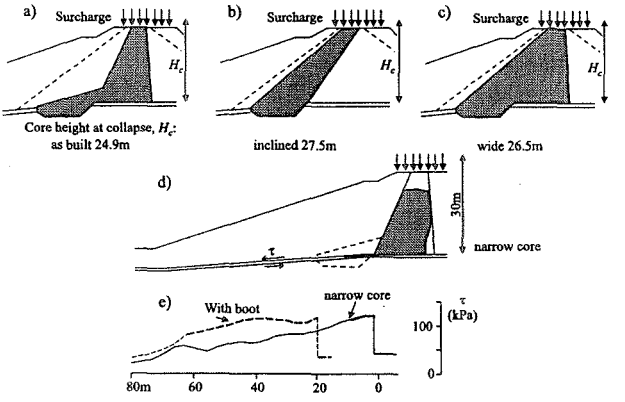

Figure 5.32: Geometries of the Carsington section considered in analyses

It seems that, given the same width, the influence of the core geometry (core and boot, wide core, inclined core) is small, although the core and boot of the original section give slightly worse stability than the other sections. While the section with the narrow central core shows signs of eventual progressive failure, the overall stability along the rupture surface through the core and the yellow clay is much higher than for the other sections.

5.4.4.6 Effect of a berm in improving the stability

An obvious way to improve the stability of a slope such as that at Carsington would be to add a berm at the toe. To investigate the significance of this, simple

analyses of the toe of the embankment were made (Dounias *et al.* (1989), Vaughan (1994)).

In order to save computer time a wedge was analysed, modelling the slope of the embankment. The geometry of the upstream slope of the original Carsington section upstream from the toe of the boot was initially considered (see Figure 5.33a). Two further geometries were analysed: one with a berm added as in Figure 5.33b, and another where a volume equal to the added berm was used to create a uniform slope (see Figure 5.33c). The height of the vertical face was the same for all three analyses.

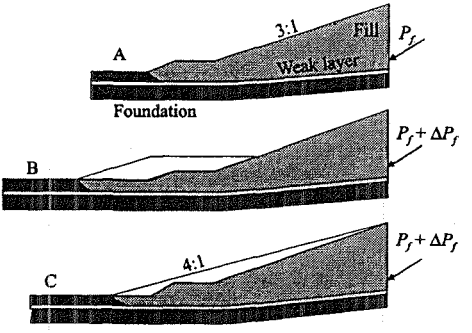

Analysis	$(P_f + \Delta P_f)/P_f$	
	Limit equilibrium	Finite element analysis
A. Original	1.0	1.0
B. First berm	1.3	1.02
C. Second berm	1.3	1.15

Figure 5.33: Effect on stability of adding a berm on Carsington slope

The material properties of the foundation, the weak yellow clay layer and the shoulder fill were the same as those assumed for the initial analyses (see Table 5.3). The wedges were constructed in stages with the vertical face restrained horizontally. The wedge was then loaded by triangular horizontal and shear stress distributions on the vertical face. The resultant thrust had an inclination of 10° to the horizontal. The thrust was applied in increments with decreasing size as failure was approached. All three sections showed similar failure patterns. A yield zone initiated at the vertical face and propagated along the weak zone.

According to limit equilibrium calculations, the resistance of sections (b) and (c) should be equal, and 30 % greater than the resistance of section (a). However, when the effects of progressive failure are included, section (b) has a resistance 2% greater then section (a), and section (c) has a resistance 14 % greater. It is clear that the addition of a berm to stabilise a slope has a reduced effect when the slope is subject to progressive failure. Indeed, the degree of progressive failure can increase so much that the effect of the berm may be negligible. The best result is obtained if the additional fill is used to make the wedge stiffer as well as heavier.

5.5 Finite element analysis of embankments on soft clay

5.5.1 Introduction

Earth embankments are often built on soft clay foundations. Such soils usually occur adjacent to river estuaries and, typically, the embankments are used for flood protection or for carrying roads or railways. As the soft clays are weak, embankments can usually only be built to a height of approximately 3m to 4m.

However, higher embankments are often needed, for example for grade separated junctions and flood protection, and consequently special construction measures are required. Examples of such measures include the use of light weight embankment fill, the provision of reinforcement in the bottom of the embankment and/or stagged construction.

In the latter approach the embankment is constructed in stages. After each stage a rest period is allowed for dissipation of excess pore water pressures in the soft clay. Such dissipation is accompanied by consolidation and a gain in soil strength. This in turn enables the embankment to be raised to a greater height in the next stage of construction. Clearly, the amount of gain in soil strength during the rest periods governs the height to which the embankment can be raised in the next construction stage. Consequently, staged construction is often accompanied by the provision of drainage in the soft clay to increase the amount of pore water pressure dissipation during the rest periods.

Soft clays are often anisotropic, having both stiffness and strength dependent on the orientation of the major principal stress. This complicates any analysis and as sufficient data is not often available to define the magnitude of the anisotropy, empirical factors are introduced into conventional design procedures (Hight *et al.* (1987)).

5.5.2 Typical soil conditions

Soft clays have not usually been subjected to much erosion and therefore have not experienced greater vertical stresses in the past. Consequently, they are normally or very lightly overconsolidated and in principle they should therefore have an undrained strength profile of the form shown in Figure 5.34. This distribution is based on a ground water level 2m below the ground surface and an overconsolidation ratio of 1.0. Note that pore water suctions (hydrostatic) are assumed to occur in the clay above the water table.

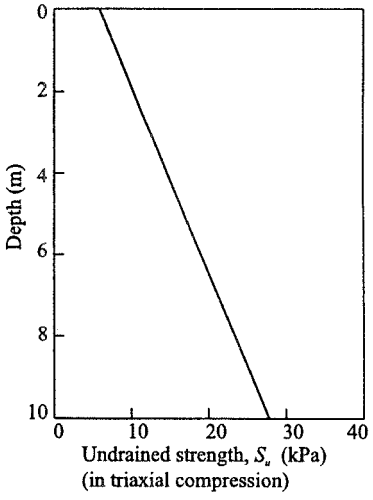

Figure 5.34: Distribution of undrained strength with depth for normally consolidated clay

However, in most, but not all, locations the surface layer of the clay has been subjected to wetting and drying due to fluctuations in the ground water level. This process results in the clay having a surface crust of a higher strength than that indicated in Figure 5.34. A typical strength profile for a soft clay site is shown in Figure 5.35 (Mair *et al.* (1992)). The surface crust extends down to a depth of approximately 2m and below this level the strength is similar to that indicated in Figure 5.34.

The surface crust can have higher undrained strengths than would be associated with a lightly overconsolidated soil. In addition, the stiffness of the crust can be larger than that of the material below it. This strength and stiffness and their distributions with depth can have a significant effect on the stability and deformation of any embankment.

Most embankments built on soft clay foundations are constructed from fill material that is much stronger than the soft clay. A granular fill is often used. Consequently, stability of the embankment fill is not usually the main concern.

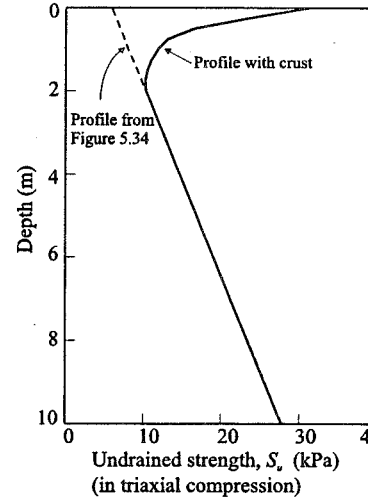

Figure 5.35: Typical distribution of undrained strength with depth for a soft clay

5.5.3 Choice of constitutive model

The most critical issue with embankments on soft clay is usually the strength of the clay. As the embankments are constructed relatively quickly compared to the time required for any significant consolidation, it is the undrained strength of the clay that is important. As noted above, this strength can vary significantly with depth and any crust can have a marked effect on the behaviour of an embankment.

As much of the clay is lightly overconsolidated and as critical state models are reasonably good at reproducing the behaviour of such soils, this type of model is often employed to represent the behaviour of the foundation. These models also have the ability to predict changes in undrained strength with consolidation. It should be noted that a Tresca model cannot reproduce this behaviour. However, there are two potential difficulties when using conventional critical state models.

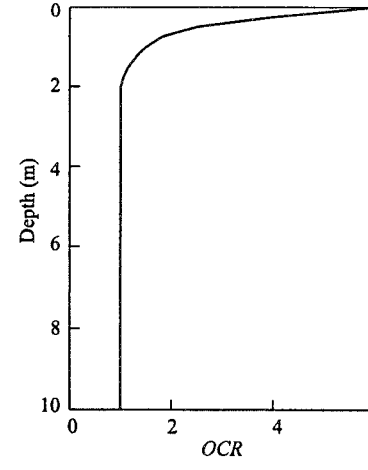

Figure 5.36: Distribution of OCR to give undrained strength in Figure 5.35

The first difficulty is that the undrained strength is not an input parameter to the model. It can, however, be calculated from the input parameters and the initial stress conditions as described in Section 7.9.3

of Volume 1. The required undrained strength profile can then be obtained by adjusting the overconsolidation ratio (*OCR*). For example, to obtain the distribution of undrained strength shown in Figure 5.35, using a form of the modified Cam clay model which has a Mohr-Coulomb hexagon and a circle for the shapes of the yield and plastic potential surfaces in the deviatoric plane respectively, and the parameters given in Table 5.4, requires the distribution of *OCR* shown in Figure 5.36. Clearly, inputting such a distribution of initial *OCR* and its associated K_o distribution may be problematic with some computer programs. This problem is discussed further in Chapter 9.

Table 5.4: Properties for soft clay

Property	Value
Bulk unit weight, γ_{sat}	17 kN/m^3
Void ratio on VCL at p'=1, v_1	3.0
Slope of VCL, λ	0.22
Slope of swelling lines, κ	0.022
Elastic shear modulus, G	1700 kN/m^2
Angle of shearing resistance, φ'	32°
Coefficient of earth pressure at rest, K_o	$K_o = (1-\sin\varphi')\ OCR^{\sin\varphi'}$
Pore fluid modulus, K_e	$K_e = 1000K_{skel}$

It should also be noted that the undrained strength depends on the shapes adopted for both the yield and plastic potential surfaces in the deviatoric plane. For example, the undrained strengths shown in Figures 5.34 and 5.35 are appropriate to triaxial compression conditions. For plane strain conditions the constitutive model, using exactly the same input parameters, will produce smaller undrained strengths. In this case the plane strain strengths will be 0.82 times the triaxial compression strengths.

The second difficulty is that the majority of critical state models assume the soil to be isotropic. For soft clays this is not necessarily correct and both strength and stiffness may be anisotropic and depend on the orientation of the major principal stress. If a clay does exhibit strong anisotropy, then either properties representing some average strength and stiffness must be input into an isotropic model or, preferably, a constitutive model such as MIT-E3 (see Section 8.6 of Volume 1), which can reproduce anisotropic behaviour, should be used. An example of the use of such a model is given in Section 5.5.8.

As noted above, the embankment fill material is usually much stronger and

stiffer than the soft clay and is not therefore critical. However, if stability is to be modelled in the analysis, the constitutive model used to represent fill behaviour must simulate yield and ultimate strength. Consequently, a simple Mohr-Coulomb model is often used. Sometimes the elastic properties are assumed to be stress level dependent. More recently models of the Lade type (see Section 8.5 of Volume 1) have been used.

5.5.4 Modelling soil reinforcement

As noted in Section 5.5.1, reinforcement layers, in the form of sheets of geotextile, are sometimes added to the base of an embankment, see Figure 5.37. The effect of such reinforcement is discussed further in Section 5.5.6. To model the reinforcement, membrane elements (or beam elements with low bending and shear stiffness), see Section 3.5.5 of Volume 1, can be used to represent the geotextile. These elements must then be sandwiched between interface elements (see Figure 5.41), so that the interaction between the soil and the geotextile can be realistically modelled. While the stiffness and strength of the geotextile can be obtained from the supplier or manufacturer, obtaining appropriate interface properties is more difficult.

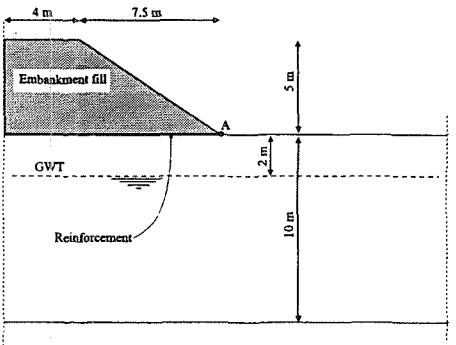

Figure 5.37: Example of an embankment on soft clay

Another complication arises as the behaviour of geotextiles is often time dependent and consequently it may be necessary to include the effects of creep. Whereas, in principle, it is not difficult to include such effects into a constitutive model, it is not so easy to obtain the necessary parameters.

5.5.5 Example: Effect of a surface crust

5.5.5.1 Introduction

To illustrate the effect of a surface crust, two plane strain finite element analyses have been performed for the embankment geometry shown in Figure 5.37. In one example the distribution of soil strength with depth shown in Figure 5.34 was simulated, whereas in the second example the strength profile shown in Figure 5.35 was matched.

5.5.5.2 Soil conditions

A form of the modified Cam clay model, which had a Mohr-Coulomb hexagon and a circle for the shapes of the yield and plastic potential surfaces in the deviatoric plane respectively, and the parameters given in Table 5.4, was used to represent the

soft clay in both analyses. To represent the strength profile shown in Figure 5.34 the *OCR* was assumed to remain constant with depth and have a value of 1.0. To obtain the undrained strength profile shown in Figure 5.35 the distribution of OCR with depth shown in Figure 5.36 was used. It should be noted that in this analysis the K_o value also varied with depth in accordance with the equation given in Table 5.4. Soil suctions (hydrostatic) were assumed to exist in the clay above the water table. Consequently, there were finite vertical effective stresses at the soil surface and hence non zero undrained strengths, see Chapter 9.

In both analyses the embankment was unreinforced and assumed to be constructed of a granular fill. The fill was modelled using a simple linear elastic Mohr-Coulomb model with the properties given in Table 5.5. During the analyses the embankment behaved in a drained manner (i.e. $K_e = 0$), whereas the soft clay behaved undrained (i.e. $K_e = 1000K_{skel}$).

Table 5.5:Properties for embankment fill

Property	Value
Bulk unit weight, γ_{sat}	20kN/m^3
Young's modulus, E	20MN/m^2
Poisson's ratio, μ	0.2
Cohesion, c'	0
Angle of shearing resistance, φ'	40°
Angle of dilation, v	0°
Pore fluid modulus, K_e	0.0

5.5.5.3 Finite element analysis

The finite element mesh used for both analyses is shown in Figure 5.38 and consists of 360 eight noded quadrilateral elements. The embankment was constructed in layers until failure occurred.

Obtaining the failure height was not straightforward. As failure is approached, each layer of elements must be constructed over several increments. Failure is then likely to occur during the construction of a layer of elements. The increment at which this occurs indicates the proportion of the layer that causes the onset of instability. The equivalent

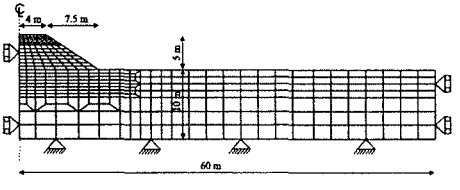

Figure 5.38: Finite element mesh for embankment on soft clay

height of constructed material can then be obtained. Failure is identified when the solution fails to converge and displacements continue to develop without further addition of fill. At this stage equilibrium cannot be maintained. To obtain an accurate estimate of the collapse height several restarts, each with progressively more increments to construct the last construction layer, are necessary. Alternatively, an automatic incrementation algorithm can be used (see for example Abbo and Sloan (1996)).

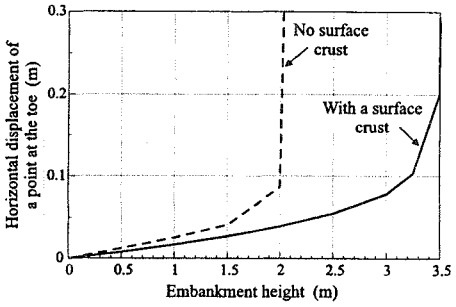

Figure 5.39: Horizontal displacement of embankment toe with increase in embankment height

5.5.5.4 Results

The variation of the lateral movement of the toe of the embankment (point A on Figure 5.37) with height of the embankment for both analyses is shown in Figure 5.39. The surface crust has the effect of increasing the embankment height at failure from 2m to 3.5m.

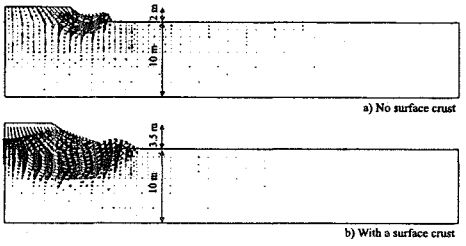

Figure 5.40: Vectors of incremental displacement just before failure

Vectors of incremental displacement during the last increment of each analysis are presented in Figure 5.40. These vectors represent the magnitude and direction of the incremental displacements. It is the relative magnitudes of the displacements and their directions that are of interest and not their absolute values. In both analyses these vectors clearly identify the failure surface. For the analysis with a surface crust the failure surface is deeper and wider, passing through the centre line of the embankment.

5.5.6 Example: Effect of reinforcement

5.5.6.1 Introduction

To examine the effect of reinforcement in the bottom of the embankment, a small parametric study was performed on the example embankment geometry shown in Figure 5.37. In this study both the stiffness and the strength of the reinforcing layer were varied.

The reinforcement was assumed to be a layer of geotextile placed on the surface of the soft clay prior to embankment construction. This was modelled by a layer

of membrane elements sandwiched between two layers of interface elements, see Figure 5.41. These elements were added to the mesh shown in Figure 5.38. Plane strain finite element analyses were performed.

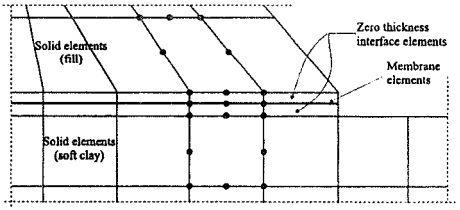

Figure 5.41: Connection between membrane, interface and solid elements

5.5.6.2 Soil conditions

The embankment fill and the soft clay were modelled in the same manner as for the previous example. The soft clay had a surface crust obtained by adopting the *OCR* profile given in Figure 5.36. The interface elements were assigned the properties given in Table 5.6. The membrane elements had a Poisson's ratio of 0.1, a thickness of 0.8mm and were assumed incapable of sustaining compressive forces. The Young's modulus and tensile strength were varied in the study.

Table 5.6: Properties of interface between reinforcement and soil

Property	Value
Shear stiffness, K_s	10^4 kN/m
Normal Stiffness, K_n	10^6 kN/m
Interface cohesion, c_w	0.0
Angle of interface friction, δ	40°
Angle of interface dilation, v_w	20°

5.5.6.3 Results

As shown in the previous section, with no reinforcement the embankment can be built to a height of 3.5m. When reinforcement is added, the embankment can be constructed to a greater height. This can be seen in Figures 5.42 and 5.43 which show the variation of the maximum embankment height with increase in reinforcement strength and stiffness respectively.

Figure 5.42 shows results from a series of analyses in which the stiffness of the reinforcement was 1.5×10^6 kN/m^2/m (a typical value for a geotextile) and its tensile strength was varied. Increasing the tensile strength to 75 kN/m increased the height of the embankment from 3.5m to 4m. Any further increase in the tensile strength of the reinforcement produced an insignificant increase in the embankment height. The results therefore indicate that for a reinforcement stiffness of 1.5×10^6 kN/m^2/m the maximum height of embankment is 4m and, to achieve this, the reinforcement must have a tensile strength greater than 75kN/m. If greater tensile strengths are

used the embankment still fails at 4m and, although the greater tensile strength will enhance the stability, the extra force available is so small compared to the disturbing force that it does not result in any significant increase in embankment height.

Figure 5.43 shows results from a series of analyses in which the tensile strength of the reinforcement was 200kN/m (a typical value for a geotextile) and its stiffness was varied. As the reinforcement stiffness increases so does the height to which the embankment can be constructed. For example, when the stiffness is 10^7kN/m^2/m the embankment can be constructed to a height of 4.75m. However, for this analysis the tensile capacity of the reinforcement is fully mobilised. The results also indicate that any further increase in the stiffness of the reinforcement fails to increase the embankment height as the full tensile capacity of the reinforcement is mobilised at a height of 4.75m.

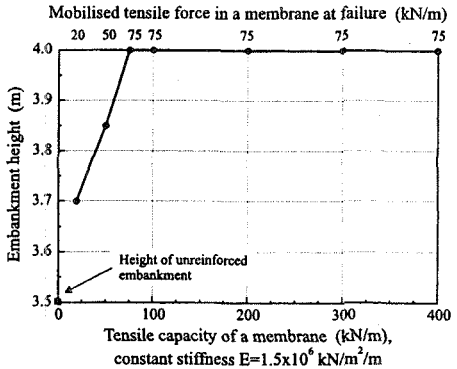

Figure 5.42: Variation of embankment height with strength of reinforcement

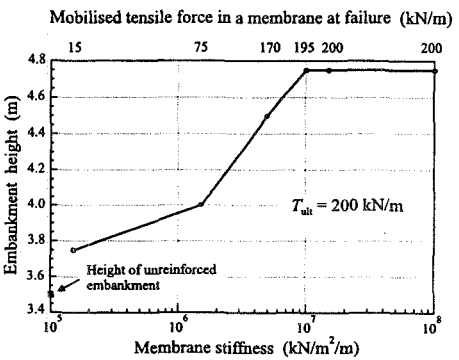

Figure 5.43: Variation of embankment height with stiffness of reinforcement

These results clearly show that it is a combination of both the stiffness and strength of the reinforcement that enables the embankment height to be increased. It is probably impossible to include both of these effects in any simplified analyses and therefore this example demonstrates the advantages of numerical analysis. The results also indicate that it is possible to increase the height of an embankment by 35% by adding reinforcement. However, it should be noted that the analysis presented above do not account for large displacement effects.

5.5.7 Example: Staged construction

5.5.7.1 Introduction

As an example of an embankment on soft clay constructed in stages consider the example shown in Figure 5.44. This road embankment is approximately 8m high and was constructed in the west of the United Kingdom. The foundation consists

of a thick deposit of soft clay overlying sand. The depth of the soft clay is not constant but varies across the site. Because it is not possible to construct an embankment 8m high on the soft clay in a single lift, a staged construction approach is required.

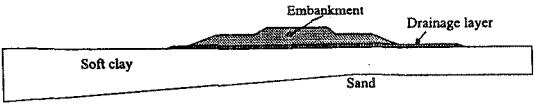

Figure 5.44: Example of a stage constructed embankment

At the design stage it was therefore necessary to decide on the number and timing of the construction stages and the number and position of the drains that must be provided in the foundation. As part of the design process, a series of plane strain finite element analyses were carried out. One of these analysis will briefly be described here.

For calculation purposes the sand below the soft clay was assumed to be rigid and therefore the bottom of the soft clay provided a lower boundary to the finite element mesh. As the depth of the soft clay varied and as the geometry of the embankment was not symmetric (see Figure 5.44), the complete cross section had to be modelled in the analysis.

5.5.7.2 Soil conditions

The soft clay was again modelled using a form of modified Cam clay which used a Mohr-Coulomb hexagon and a circle for the shapes of the yield surface and the plastic potential in the deviatoric plane respectively. A Hvorslev surface was employed for stress states dry of critical, see Section 7.10 in Volume 1. The material properties are given in Table 5.7. The Hvorslev surface had a slope half that of the critical state line. The water table was 0.5m below the ground surface.

Table 5.7: Properties for soft clay for staged construction example

Property	Value
Bulk unit weight, γ_{sat}	17 kN/m^3
Specific volume on VCL at p'=1, v_1	5.2
Slope of VCL, λ	0.5
Slope of swelling lines, κ	0.075
Elastic shear modulus, G	3000 kN/m^2
Angle of shearing resistance, φ'	25.5°
Coefficient of earth pressure at rest, K_o	$K_o = (1-\sin\varphi')OCR^{\sin\varphi'}$
Pore fluid modulus, K_e	$K_e = 1000K_{skel}$

The initial distribution of *OCR* is shown in Figure 5.45. Combining this with the material properties given in Table 5.7 enables the initial distribution of undrained strength with depth to be calculated. The distribution is compared with the design profile in Figure 5.46. The values plotted are for triaxial compression. To obtain values appropriate to plane strain conditions these values should be reduced by 0.86. Clearly, the undrained strength will change during the consolidation stages of embankment construction.

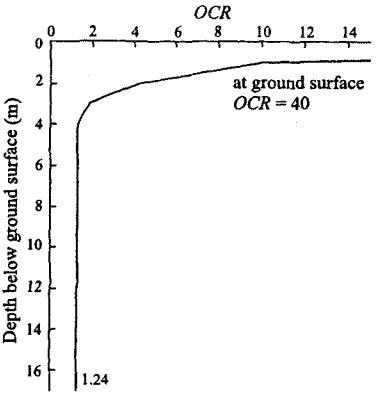

Figure 5.45: Variation of OCR with depth

The drainage blanket was modelled as a simple elasto-plastic Mohr-Coulomb material. The following parameters were adopted: γ_{sat}=20kN/m^3, E=25MN/m^2, μ=0.3, c'=0, φ'=35° and ν=0°. The embankment fill was also modelled using the same model and the same parameters, except that the Young's modulus was different for material in each construction lift. For lifts 2, 3 and 4 the Young's moduli were 21.8, 16.5 and 7MN/m^2 respectively.

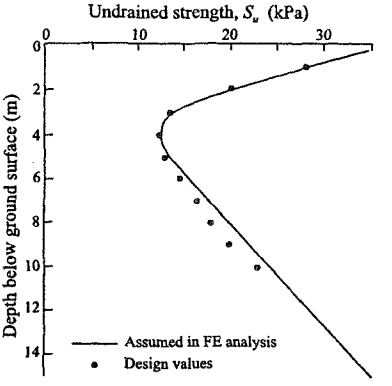

Figure 5.46: Distribution of undrained strength prior to embankment construction

5.5.7.3 Finite element analysis

The finite element mesh is shown in Figure 5.47. By today's standards this mesh is rather coarse. However, the analyses were carried out in 1983 when computer resources were limited. The calculation process involved four stages of construction, each separated by a period of consolidation. The material involved in each of the construction lifts is indicated in Figure 5.48 and the main calculation steps are summarised below:

a) Set initial stresses in the foundation soil;
b) Construct drainage blanket (lift 1);
c) Apply a traffic surcharge of 10kPa to surface of newly constructed material;
d) Remove surcharge of 10kPa;
e) Dissipate all excess pore water pressures;
f) Construct lift 2;
g) Apply a traffic surcharge of 10kPa to surface of newly constructed material;
h) Remove surcharge of 10kPa;

i) Dissipate 90% of accumulated excess pore water pressures;
j) Construct lift 3;
k) Apply a traffic surcharge of 10kPa to surface of newly constructed material;
l) Remove surcharge of 10kPa;
m) Dissipate 90% of accumulated excess pore water pressures;
n) Construct lift 4;
o) Apply a surcharge equivalent to 0.5m and 0.75m of fill to side berms and top of embankment respectively;
p) Apply a traffic surcharge of 10kPa to surface of newly constructed material;
q) Remove surcharge of 10kPa;
r) Dissipate all accumulated excess pore water pressures.

Throughout the analysis the embankment and drainage blanket were assumed to behave in a drained manner. The soft clay was only assumed to behave in a drained manner during the dissipation stages of the analyses. During construction and application and removal of surcharge loading undrained conditions were assumed. A coupled consolidation analysis was not undertaken. It was assumed that enough drains and enough time was available for the dissipation stages to be fully effective. If the analysis were to be carried out today, a coupled analysis would probably be undertaken and the drains modelled using the approach of Hird *et al.* (1990).

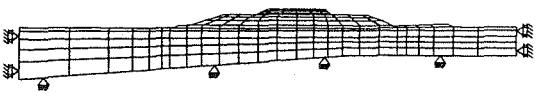

Figure 5.47: Finite element mesh for stage constructed embankment

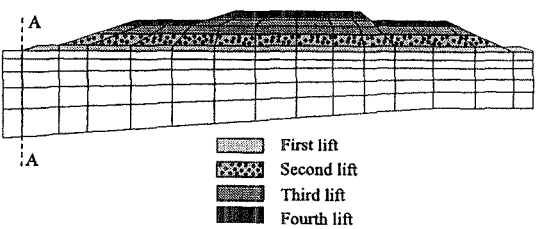

Figure 5.48: Construction sequence

5.5.7.4 Results

Lateral movements of the vertical line AA through the toe of the embankment (see Figure 5.48) are presented in Figure 5.49. Settlements of the original ground surface below the left hand side of the embankment are presented in Figure 5.50. On both figures results are presented for calculation steps 'q' and 'r'.

From Figure 5.50 it can be seen that after construction (step 'q') the original ground surface has settled nearly 2m. This increases to 2.5m in the long term after dissipation of all excess pore water pressures (step 'r'). Such large settlements are often associated with embankments on soft ground.

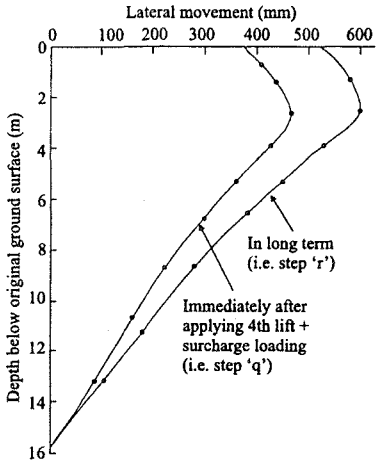

Figure 5.49: Lateral movement of vertical line AA through toe of embankment

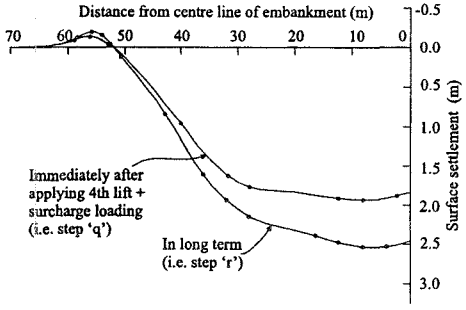

Figure 5.50: Settlement of original ground surface

5.5.8 Example: Effect of anisotropic soil behaviour

5.5.8.1 Introduction

The Champlain clay covers a large part of a densely populated region of Eastern Canada. Construction of the road infrastructure requires numerous overpasses containing embankments approximately 5 m in height. As the clay is only lightly overconsolidated, it is soft and weak and it is therefore difficult to design and construct embankments to the required height.

For this reason the geotechnical group of Laval University decided in 1972 to undertake a research programme involving the construction of test embankments on soft Champlain deposits. The objective of this project was to investigate the failure conditions of fills built on soft, sensitive foundations and also to study the magnitude and rate of settlement of such structures. Four embankments were constructed on instrumented clay foundations at the Saint-Alban site in the Province of Quebec: the first one, which is the subject of this study, was built until failure occurred; three others were built to a smaller height and with different side slopes in order to study settlement behaviour.

Test embankment A, described by La Rochelle *et al.* (1974), was the subject of finite element analyses (Zdravković *et al.*, 2002), with the objective of investigating the effect of anisotropic soil behaviour on embankment height.

5.5.8.2 Geometry

The geometry of this boundary value problem is presented in Figure 5.51. One side of the embankment has a slope of 2:1 (horizontal to vertical) inclination. The

stability of this slope is enhanced by the presence of a 1.5 m high berm, so that any failure is forced onto the other side of the embankment, where the slope is steeper, with 1.5:1 inclination. The predicted height of the embankment, based on conventional analysis, was 4.6 m.

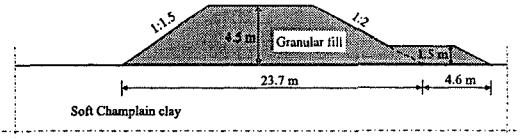

Figure 5.51: Geometry of the designed embankment at St. Alban

The construction sequence was such that the first 0.6m of embankment was lifted in a day, followed by 0.3m per day until a height of 1.5m was reached. After that two 0.3m layers were lifted per day, until failure occurred at about an embankment height of 4 m, which was less than the predicted 4.6m.

5.5.8.3 Soil conditions

A detailed geotechnical investigation was carried out at the Saint-Alban site, with a substantial number of boreholes and both in-situ and laboratory experiments on Champlain clay samples. Details of the results of these tests are given by Tavenas and Chapeau (1973), Sarrailh and Tavenas (1972).

In general, the soil profile on the site has a weathered clay crust extending down to ~2.0m below the ground surface, followed by a soft silty marine clay deposit down to ~13.7m. Beneath this clay layer there is a layer of a dense, fine to medium sand, followed by bedrock. The ground water level is at 0.7m below the ground surface.

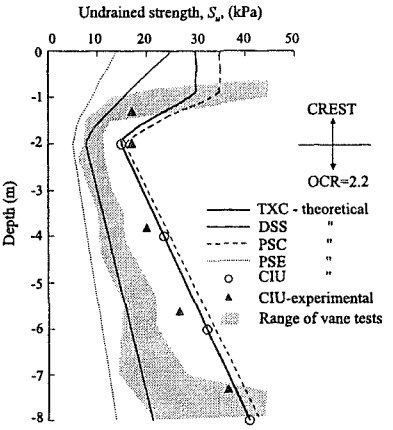

Figure 5.52: Distribution of undrained strength profiles with depth

Clay below the crust is in an overconsolidated state, with $OCR = 2.2$. The permeability of the clay is estimated to be about 10^{-8} m/sec, which implies that with the construction rate applied, failure occurred under undrained conditions. Stress-strain curves from triaxial tests showed substantial strain softening after the clay had reached peak strength (Leroueil (1977)). A summary of undrained strength profiles obtained from vane tests and CIU tests is shown in Figure 5.52 (after Leroueil (1977)).

The embankment fill is granular, with $\varphi' = 44°$.

5.5.8.4 Finite element analyses

For the finite element analyses, these soil conditions were modelled using both MIT-E3 soil model (to simulate anisotropic soil strength) and the modified Cam

clay soil model, MCC (to simulate isotropic soil strength). The parameters necessary to describe both models are summarised in Tables 5.8 and 5.9 respectively. It should be noted that for the MIT-E3 model the effect of the bounding surface plasticity within the state boundary surface was switched off. Consequently, no values for the parameters γ and h are given in Table 5.8.

The undrained strength variation with depth for different loading conditions, simulated by the MIT-E3 model, is presented in Figure 5.52. It can be seen from this figure that the predicted direct simple shear strength (DSS) matches, on average, the strength obtained from vane tests. Also, the simulated CIU strengths match closely the experimental CIU strengths. It can therefore be concluded that the observed anisotropic strength has been modelled very well with the MIT-E3 model. Also presented in Figure 5.52 are the profiles of plane strain compression (PSC) and plane strain extension (PSE) undrained strength.

For the isotropic analyses, the undrained strength in triaxial compression was adopted and the modified Cam clay model was used to simulate the triaxial compression strength profile (TXC) in plane strain, as predicted by the MIT-E3 model in Figure 5.52.

5.5.8.5 Results

The finite element mesh for the embankment analysis is presented in Figure 5.53 and the problem was analysed as plane strain. The same construction sequence and rate were simulated as those implemented on site, such that failure occurred under undrained conditions.

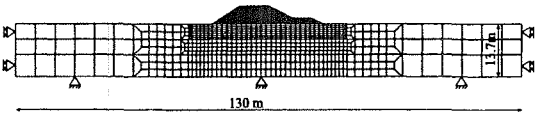

Figure 5.53: Finite element mesh for embankment analysis

Figure 5.54 shows the development of horizontal displacement, u, of the embankment toe with the embankment height. This horizontal displacement is normalised by the maximum horizontal displacement, u_{max}, predicted just before the slope failed.

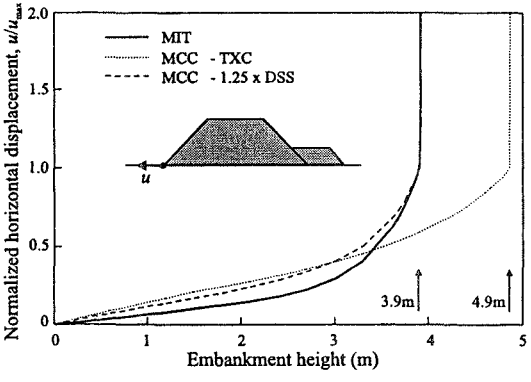

Figure 5.54: Maximum embankment height from different soil models

The analysis performed using the MIT-E3 soil model, which simulated the anisotropic soil strength as depicted in Figure 5.52, predicted failure at an embankment height of 3.9m, which is very close to the 4m observed on site. For

the same embankment, but now analysed with the MCC model with an isotropic undrained strength corresponding to the triaxial compression profile in Figure 5.52, the failure height is grossly overestimated at 4.9m. Back analysis using the MCC model to achieve a failure height of 3.9m with an isotropic strength resulted in the necessary strength being 1.25 times the DSS strength. Analysis with the isotropic strength being equal to the DSS profile, which is what some design practice suggests, is largely conservative, predicting failure at only 3.3m embankment height.

Table 5.8: MIT-E3 parameters for soft Champlain clay

Parameter	Description	Value
v_{100}	Specific volume for a K_o normally consolidated sample at p'=100 kPa	2.65
K_o^{NC}	Normally consolidated coefficient of earth pressure at rest	0.49
φ_{TC}'	Critical state angle of shearing resistance in triaxial compression	27°
φ_{TE}'	Critical state angle of shearing resistance in triaxial extension	25°
c	Ratio of the semi-axes of the bounding surface ellipsoid	0.7
ψ	Parameter affecting rotation of bounding surface	100
λ	Slope of the VCL in v - lnp' space	0.565
κ_0	Initial slope of the swelling line in v - lnp' space	0.03
μ	Poisson's ratio	0.3
S_t	Parameter affecting the degree of strain softening	10.0
C	Parameter affecting the hysteretic elasticity	1.0
n	Parameter affecting the hysteretic elasticity	1.5
ω	Parameter affecting the hysteretic elasticity	0.5

A further set of analyses was performed, where the embankment geometry was altered to have berms on both sides of the embankment, see Figure 5.55. Again both anisotropic and isotropic analyses were performed and the results are presented in Figure 5.56, as normalised horizontal displacement of the embankment toe versus embankment height.

Table 5.9: Modified Cam clay parameters for soft Champlain clay

Property	Value
Bulk unit weight, γ_{sat}	16 kN/m^3
Specific volume on VCL at p'=1 kPa, v_1	3.2
Angle of shearing resistance, φ_{cs}'	27°
Slope of the VCL, λ	0.565
Slope of swelling lines, κ	0.03
Poisson's ratio, μ	0.3

An analysis using the MIT-E3 model predicted that, with the help of a berm, the embankment could now be erected to 4.4m. The same embankment was then analysed with the MCC model, with the isotropic strength back-calculated from the previous set of analyses (i.e. 1.25 times the DSS strength, see Figure 5.54). This analysis predicted an embankment height at failure of 4.9m and therefore overestimated that obtained by the analysis with the MIT-E3 model. To obtain the same failure height as the MIT-E3 analysis, the MCC analysis needed a strength of only 1.15 times the DSS strength.

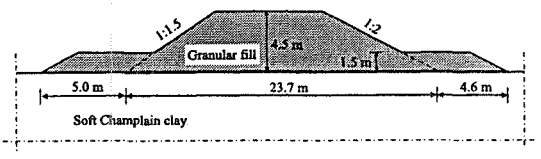

Figure 5.55: Geometry of the embankment at St. Alban with new berm

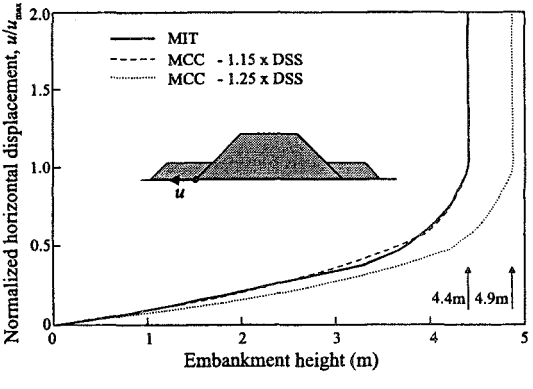

Figure 5.56: Predicted height of the new embankment with different soil models

Several conclusions can be drawn from this embankment study:

- An analysis which assumes isotropic soil behaviour and takes either the triaxial compression strength profile or the DSS strength profile will either overestimate or underestimate the embankment height, respectively;

- Taking account of soil anisotropy, observed through laboratory and field experiments, enables a more accurate prediction of embankment height;
- If an isotropic strength profile is back-calculated from the observed behaviour of a certain embankment geometry, it is not necessarily appropriate if the embankment geometry becomes slightly altered.

5.6 Summary

1. 'Variable' elastic models were widely used in the past to predict behaviour of embankment dams, primarily because of their simplicity and ability to model nonlinear and stress dependent behaviour of fill materials.
2. A great variety of stress paths, accompanied by a rotation of principal stresses, occurs in embankment dams during construction, and subsequent impounding in particular. 'Variable' elastic constitutive models cannot account for stress path dependency which is caused by nonelastic components of soil behaviour.
3. Compacted fills have a behaviour pattern similar to that of granular materials. The double hardening elasto-plastic constitutive model of the Lade's type accounts for pre-peak plasticity and is able to capture several important characteristics of the stress-strain and strength behaviour of fill materials, especially rockfills.
4. The limitations of computer modelling require relatively thick layers to be used in the idealization of dam construction. However, significant errors can occur if the layers are too thick, particularly when the effects of compaction are to be modelled.
5. Comparison of the predictions with the observed behaviour during construction of Roadford dam indicated that the predictions using the Lade's double hardening model were in reasonable agreement with the field data. The analysis using the nonlinear elastic model severely overpredicted lateral movements. This prediction could be improved by adjusting the nonlinear elastic model parameters, but then the laboratory test data could no longer be recovered.
6. The analyses of old puddle clay core dams, which involved construction in layers, impounding, development of seepage pressures, and cyclic drawdowns, with soils behaving drained, undrained and partly consolidated, demonstrated that the behaviour of these water retaining structures can be fully modelled using the finite element method.
7. Cracking by hydraulic fracture of puddle clay in a cut-off trench seems almost inevitable. Narrow puddle clay cores have stresses after construction and during impounding which are close to those allowing hydraulic fracture. The failure of Dale Dyke dam was recovered when rapid undrained final impounding was modelled.
8. The analysis of Ramsden dam has shown that quite large and non-recoverable movements can occur during operational cycles of drawdown and re-impounding, even though the factor of safety against an overall shear failure

is rather high. The combination of accurate field measurements with sophisticated numerical analyses provides a useful tool for assessing the safety of old embankment dams.

9. Finite element analyses of earth embankments are more complex because they are usually derived from clayey fill only and may sit on a foundation of varying strength and permeability. The short-term behaviour of a typical road embankment derived from London Clay and constructed on a London Clay foundation depends on the initial pore pressures assumed in the analyses, and thus the time of the year when an embankment is built.
10. Finite element analyses of the original Carsington Dam section reproduced the progressive development of the actual failure surface and were in reasonable agreement with the field observations. The role of progressive failure in the collapse was confirmed independently and the method of analysis was shown to be effective in predicting it.
11. Progressive failure develops when the centre of an embankment is of weak fill and imposes a substantial increase in active force on the shoulder fill as the embankment is completed. The exact geometry of the core (narrow with wide base, wide or inclined) has little influence, provided the total trust is the same.
12. The addition of berms under drained conditions to the above embankment slope increases the amount of progressive failure, and the improvement in stability is much less than that indicated by limit equilibrium calculations.
13. Embankments constructed on soft clay can usually be built to a height of approximately 3m to 4m without special measures. For higher embankments special construction techniques are required, such as providing reinforcement and/or staged construction.
14. Soft clays are usually lightly overconsolidated but often have a surface crust of higher strength and stiffness.
15. Critical state constitutive models, such as modified Cam clay, are often used to model soft clay. However, care must be taken to ensure that the model gives a realistic undrained strength profile.
16. The surface crust can have a significant influence on the height to which an embankment can be constructed and on the shape and location of the final failure mechanism. In the example considered the effect of the crust was to increase the maximum embankment height by 75%.
17. The provision of reinforcement in the base of an embankment can significantly increase the height to which the embankment can be constructed. Both the stiffness and strength of the reinforcement affect the maximum embankment height.
18. Staged construction allows embankments to be constructed to significant heights. However, any analyses must use a constitutive model for the soft clay that can account for changes in undrained strength during the consolidation periods.
19. Large settlements, greater then 1m, are to be expected when constructing embankments on soft clay.

20. Anisotropic soil behaviour has a significant effect on embankment behaviour. Accounting for anisotropy observed in laboratory and field experiments enables a more accurate prediction of embankment behaviour. Complex constitutive models, such as MIT-E3, must be used to represent anisotropic behaviour.
21. If an isotropic strength is back calculated from the observed behaviour of a certain embankment geometry, it is not necessarily appropriate if the embankment geometry becomes slightly altered.

6. Shallow foundations

6.1 Synopsis

This chapter considers the analysis of shallow foundations. It begins by defining shallow foundations and categorising them into two groups, those that are founded at the ground surface and those that are founded at shallow depth. Each category is then considered separately and the implications for numerical analysis discussed. Issues such as the bearing capacity of pre-loaded foundations, the effect of anisotropic strength on bearing capacity and instability due to insufficient soil stiffness are discussed. Examples are given, where ever possible, to help clarify some of the issues raised. The chapter ends by describing some of the analyses performed for the stabilisation of the leaning Tower of Pisa.

6.2 Introduction

In terms of complexity, shallow foundations are probably the simplest of geotechnical structures. The loads applied to them are often well defined and their purpose is to transfer these loads to the soil. This is in contrast to slopes and /or retaining wall problems, where the soil provides both the activating and resisting forces and there is therefore a complex interaction between the two.

Shallow foundations come in many shapes and sizes and this chapter begins by categorising them as either surface or shallow foundations. Each category is then considered in turn and the implications for finite element analysis are discussed. Examples are given, where possible, to help clarify some of the issues raised. These include the analysis of different shaped footings, the bearing capacity of pre-loaded foundations, the effect of anisotropic strength and instability due to insufficient soil stiffness. Many of these examples are yet to be published and have been selected to demonstrate the ability of the finite element method to provide accurate solutions to conventional problems and also insights into novel problems.

For all analyses an accelerated modified Newton-Raphson scheme, with a sub-stepping stress point algorithm, was employed to solve the nonlinear finite element equations, see Chapter 9 of Volume 1. For the plane strain, axi-symmetric and Fourier Series Aided finite element analysis, 8 noded isoparametric elements were used, with reduced (2x2) integration. For full three dimensional analysis 20 noded isoparametric elements were used, with reduced (2x2x2) integration.

6.3 Foundation types

Shallow foundations may be broadly categorised into one of the following two types.

6.3.1 Surface foundations

These are foundations which are placed on, or very near to, the soil surface. They can come in many shapes and sizes, but are often categorized as either strip, circular or rectangular footings, see Figure 6.1.

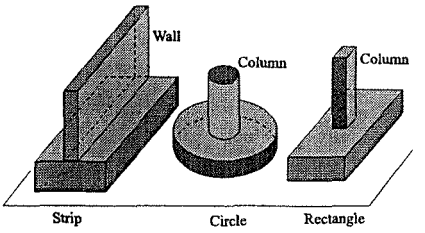

Figure 6.1: Types of surface foundations

6.3.2 Shallow foundations

Shallow foundations are similar to surface foundations, except that they are embedded below the soil surface, see Figure 6.2. For economic reasons their depth below the surface is usually not great, hence the term shallow. Again, they are often categorized as either strip, circular or rectangular.

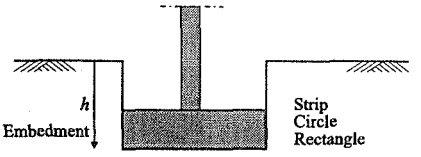

Figure 6.2: Shallow foundations

6.4 Choice of soil model

Conventional foundation design considers bearing capacity and deformations separately. Using these approaches it is not possible to establish the complete load-displacements curve. It is only possible to provide estimates of the ultimate foundation load and of the initial gradient of the load-displacement curve, see Figure 6.3.

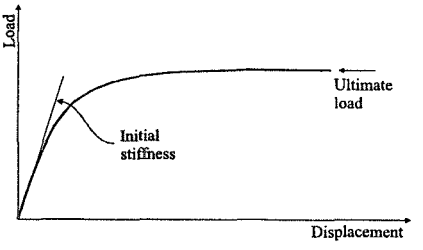

Figure 6.3: Typical load-displacement curve

The calculation of bearing capacity is based on stress field solutions and/or limit analysis, combined with some empirical correlations. The soil is essentially assumed to behave as an elastic Tresca material, if undrained bearing capacity is being considered, and as an elastic Mohr-Coulomb material, if drained bearing capacity is under investigation. Such simple constitutive models can also be used in numerical analysis and it can be shown, see below, that numerical analysis can recover the analytical bearing capacity solutions where they are available. However, while the conventional bearing capacity solutions are only

available for simple foundations resting on one soil type, with either a constant strength or a strength that varies linearly with depth, numerical analysis can consider complex foundation geometries resting on inhomogeneous foundations. Numerical analysis can also cope with complex loading combinations (e.g. vertical, horizontal and moment loading).

Conventional bearing capacity solutions are restricted to either undrained soil or fully drained soil. They do not therefore provide information on the variation of bearing capacity with time. This may be important for foundations constructed on clay soils. Using a coupled numerical approach, see Chapter 10 of Volume 1, it is possible to simulate such time dependent behaviour, as long as a realistic constitutive model is used to represent the soil. In this respect the use of a Tresca model is not appropriate, as the strength of the soil remains constant. Although, in principle, a Mohr-Coulomb model could be used, this is not advisable as unrealistic predictions of bearing capacity can be obtained under undrained and partially drained conditions, see Chapter 9. To obtain realistic predictions it is necessary to use a strain hardening/softening model of at least the complexity of a simple critical state model (e.g. modified Cam Clay).

Conventionally, foundation displacements are predicted using elastic theory. Several approaches are available and they differ in the manner in which the stiffness parameters are derived. Some assume the soil is linear elastic, others obtain the stiffness from an oedometer test. While these approaches appear to give reasonable predictions of average foundation settlement, they do not provide accurate predictions of differential settlements, deformations under combined loading, or movements in the soil adjacent to the foundation. This is perhaps not surprising as the stiffness of the foundation is usually ignored, with the foundation assumed to apply a uniform pressure to the soil. Numerical analyses have the ability to deal with a range of constitutive models and can therefore produce more realistic predictions.

In principle, a soil model that accurately simulates the behaviour of the soils supporting the foundation under investigation should be used. If the foundation consists of layered soils, then several soil models might be used. If bearing capacity is of interest, then clearly the soil model should accurately simulate the soil strength. If deformations are of concern, and in particular those adjacent to the foundation, then it is advisable to use a constitutive model that can accurately represent the nonlinear behaviour of the soil under small strains.

6.5 Finite element analysis of surface foundations

6.5.1 Introduction

If the foundations are subjected to vertical loading only, then a strip footing can be idealised as plane strain, a circular footing as axi-symmetric, but a rectangular footing remains a three dimensional problem. Consequently, while it is relatively straight forward to analyse strip and circular footings under vertical loading, as they can be reduced to two dimensions, considerably more computer resources are

required to analyse rectangular footings which involve a full three dimensional analysis, although account can often be taken of the two vertical planes of symmetry to reduce the complexities of the analysis, see Figure 6.4 (i.e. in this case only a quarter of the full geometry needs to be considered).

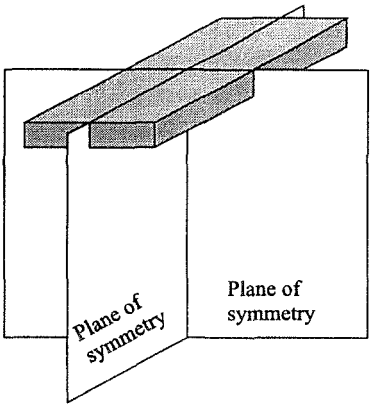

Figure 6.4: Vertical planes of symmetry in 3D analysis of a rectangular footing

If the loading is not vertical but inclined, and the inclination is in the plane perpendicular to the length of the footing, plane strain analysis can still be performed for a strip footing. Otherwise, and for both the circular and rectangular footings, a three dimensional analysis is required. For the circular footing this analysis can be performed using either a full three dimensional, or a Fourier series aided approach. A conventional three dimensional analysis will be required for the rectangular footing.

In general, it is necessary to discretise both the soil and the foundation into finite elements, see Figure 6.5. This enables the correct stiffness of the foundation to be included in the analyses. Interface elements can also be positioned between the underside of the foundation and the soil, so that the correct interface behaviour can be modelled. However, as the foundation is often very stiff compared to the soil, numerical problems can arise due to the large difference in stiffness between adjacent elements on each side of the interface. Although these numerical instabilities are not so much of a problem with modern computers, where it is possible to use increased numerical precision (e.g. double or quadruple precision), surface foundations are often analysed using one of two extreme assumptions (i.e. a perfectly flexible or rigid foundation). Such assumptions are also used in conventional soil mechanics practice. If one of these assumptions is made, then there is no need to include the foundation itself in the analysis.

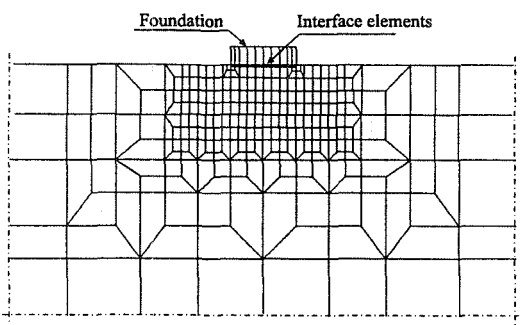

Figure 6.5: Finite element discretisation of both soil and foundation

6.5.2 Flexible foundations

If the footing is assumed to be flexible, then it is possible to simulate its behaviour in a finite element analysis as shown in Figure 6.6. As the footing is flexible, it is assumed that any loading is uniform and can be represented by a surface surcharge pressure applied to the surface of the soil immediately below the position of the footing. As noted in Chapter 3 of Volume 1, such a uniform surcharge load can be converted to give equivalent nodal forces, ΔF_y. In fact, most computer programs do this automatically for the user.

If the footing is smooth, then the other boundary condition that must be applied to the nodes under the footing is that the horizontal nodal forces are zero (i.e. ΔF_x=0). Most computer programs assume that ΔF_x=0 if no boundary condition is specified in the x direction for a particular node.

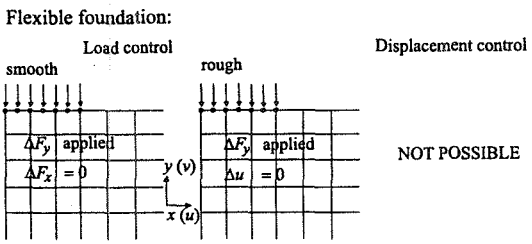

Figure 6.6: Boundary condition options for flexible footing

Alternatively, if the footing is rough, then the horizontal displacement (Δu) of the nodes on the soil surface below the position of the footing must be restricted and therefore set to zero (Δu =0), see Figure 6.6.

It is not possible to apply displacements to the footing and perform the analysis in *displacement* control. Consequently, care must be taken when approaching the collapse load of the foundation, as the application of too much load will cause unlimited displacements. This will probably manifest itself as a convergence problem in the nonlinear solution algorithm. Some finite element programs have facilities for automatically controlling the size of the incremental loads. This is particularly useful for load control problems and can result in accurate estimates of limit loads.

6.5.3 Rigid foundations

If the footing is rigid, analyses can be performed under either *load* or *displacement* control. The various alternatives for the boundary conditions to be applied to the soil surface below the position of the footing are given in Figure 6.7. As noted in this figure, for load control it is necessary to tie the vertical displacements of the nodes below the position of the footing, see Section 3.7.4 of Volume 1. This will ensure that all the nodes move vertically by the same amount. As the vertical displacements are tied, the load can be applied as a uniform pressure over the width of the footing, or as a single point load at the node on the centre line of the footing. In addition, as with flexible foundations, care must be taken when approaching the collapse load of the foundation if the analysis is being performed under load control.

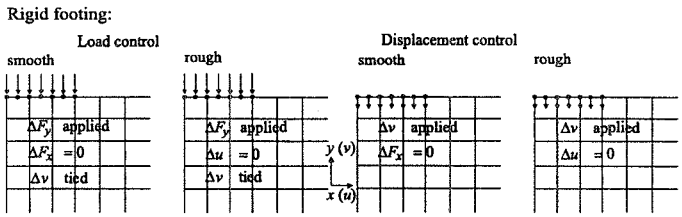

Figure 6.7: Boundary condition options for rigid footing

If the analysis is performed under displacement control, with vertical displacements applied to the soil surface below the position of the footing, then the footing load is obtained from summing the vertical reactions of the nodes which have been subjected to this displacement. In a nonlinear finite element analysis, these nodal reactions are best calculated from the total stresses in the elements connected to the displaced nodes, using:

$$\{\boldsymbol{R}\} = \int_{Vol} [\boldsymbol{B}]^{\mathrm{T}}(\{\sigma\} - \{\sigma_i\})\,\mathrm{d}Vol \tag{6.1}$$

where $\{\boldsymbol{R}\}$ is the vector of reactions in the coordinate directions, $[\boldsymbol{B}]$ is the strain matrix (see Section 2.6 of Volume 1), $\{\sigma\}$ is the vector of current total stresses, $\{\sigma_i\}$ is the vector of total stresses existing prior to displacing the footing, and the volume integration is performed for all soil elements connected to the displaced nodes. Most finite element software have facilities for obtaining such values.

6.5.4 Examples of vertical loading

6.5.4.1 Introduction

As a simple example of the application of numerical analysis, the problem of a vertically loaded surface footing resting on either an undrained clay or a drained soil (clay or sand) is considered. To be consistent with conventional foundation design, the undrained clay and drained soil are modelled using a linear elastic Tresca and a linear elastic Mohr-Coulomb model respectively. The results of these analyses are compared with the conventional bearing capacity solutions.

6.5.4.2 Strip footings on undrained clay

Analyses have been performed to obtain the load-displacement curves for rigid strip surface footings. The soil was assumed to be elasto-plastic, with a Tresca yield surface and properties: E=100MPa, μ = 0.49 and S_u = 100kPa. The mesh shown in Figure 6.8 was used. The two vertical sides of the mesh have been restrained in the horizontal direction, while the base of the mesh was not allowed to move in either the vertical or horizontal direction. Loading was simulated by applying increments of vertical displacement to the soil surface below the position of the footing, as described above.

Load-displacement curves for the strip footing are shown in Figure 6.9. In conventional design the bearing capacity of a vertically loaded strip footing on undrained clay is expressed as:

$$Q_{max} = A N_c S_u \qquad (6.2)$$

where Q_{max} is the maximum vertical load applied to the footing, A its area and N_c the bearing capacity factor. In Figure 6.9 the load is therefore expressed in terms of the mobilised bearing capacity factor N_c^{mob} (= $Q/(A S_u)$), where Q is the load on the footing. The displacement is normalised by B, where B is the half width of the footing. Results from three analyses are given. One of these modelled a smooth footing and the other two a rough footing. The difference between the two analyses modelling a rough footing is that in one analysis a row of interface elements was added between the soil surface and the underside of the footing, see Figure 6.10. In the other analysis and in the analysis modelling a smooth footing, these interface elements were not present. The interface elements were given a shear strength of 100kPa and shear and normal stiffness values of K_s=K_n=10^5kN/m^3 (note that these stiffness values do not have a major influence on the results). It can be seen that the three analyses give slightly different load-displacement curves and slightly different N_c values at failure. These values are quoted on Figure 6.9.

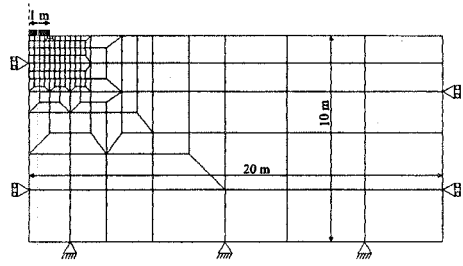

Figure 6.8: Finite element mesh for strip and circular footing analyses

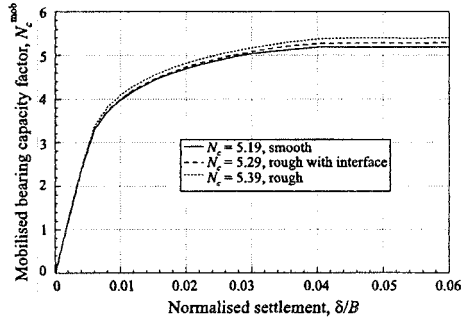

Figure 6.9: Load-displacement curves for strip footing

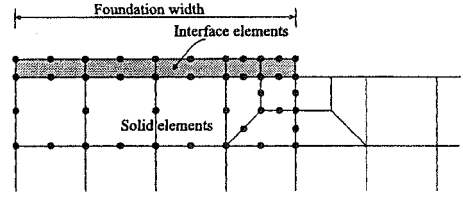

Figure 6.10: Detail of mesh with interface elements

Conventional bearing capacity theory indicates that, for a strip footing resting on undrained clay with a constant strength, the bearing capacity factor N_c should be 5.1416 (= 2+π), for both smooth and rough footings. This solution can be obtained from limit analysis (i.e. both upper (unsafe) and lower (safe) bound solutions) and from a closed form plasticity solution (i.e. combination of stress and

velocity field solutions). It is therefore theoretically exact. The finite element analyses give values of 5.19, 5.39 and 5.29 for the analyses with smooth, rough and rough with interface elements footings respectively. Compared to the analytical solution, the numerical analyses are in error by 0.94%, 4.6% and 2.8% respectively. Clearly, the error is larger for the rough footing analyses, and in particular is larger for the analysis with no interface elements. The reason for this is partly explained in Figure 6.11, which shows the vectors of incremental displacement for the last increment of each analysis (i.e. at failure). The orientation of these vectors indicates the direction of movement and their length the magnitude of movement. As it is the orientation of the vectors and their relative magnitude that indicates the failure mechanism, the absolute magnitude of the incremental displacements is irrelevant and consequently no magnitude scale is given on the figure.

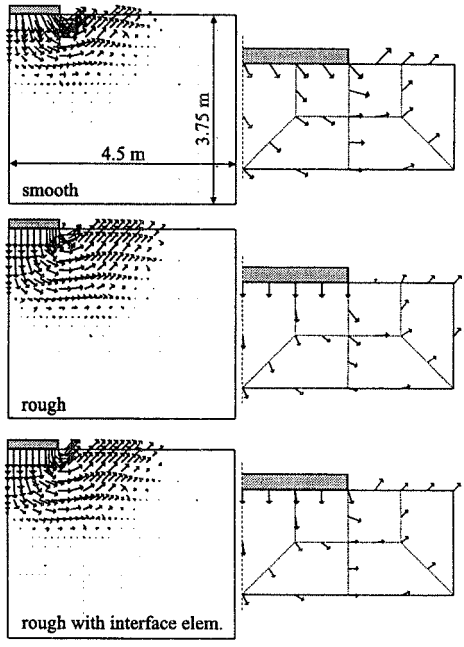

Figure 6.11: Vectors of incremental displacements at failure for three different soil-footing interfaces

Inspection of these failure mechanisms indicates that some horizontal movement occurs at the soil surface immediately below the smooth footing. For the rough footing this is not possible due to the boundary conditions. Consequently, the failure mechanism for the rough footing is slightly deeper and wider than that for the smooth footing. This in turn implies a larger area to the slip surface which, when combined with a constant S_u, leads to a greater ultimate footing load and hence N_c.

The error for all three analyses arises because of the nature of the finite element mesh immediately below and adjacent to the footing. As shown in the insets on Figure 6.11, the vectors of displacement adjacent to the edge of the rough footing change direction very abruptly, from vertically downwards under the corner of the footing to an angle of 45° to the horizontal in an upward direction, on the soil surface adjacent to the footing. This change occurs over the single element positioned at the corner. The accuracy of the solution will therefore depend on the ability of this single element to accommodate this rapid change in displacement. The rapid change in displacement at the edge of the footing is less pronounced in the smooth footing analyses and in the analysis where interface elements have been

used. It can be seen from the inset on Figure 6.11 that for the latter analysis some horizontal movement of the soil surface immediately under the edge of the footing occurs. This is possible because the interface elements in this vicinity are plastic and although the tops of these elements are constrained to move vertically downward, the bottoms can have a horizontal component of movement (note the displacements of the tops of the interface elements are not shown on Figure 6.11).

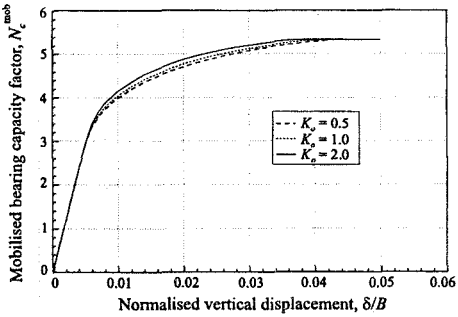

Figure 6.12: Effect of K_o on load-displacement behaviour

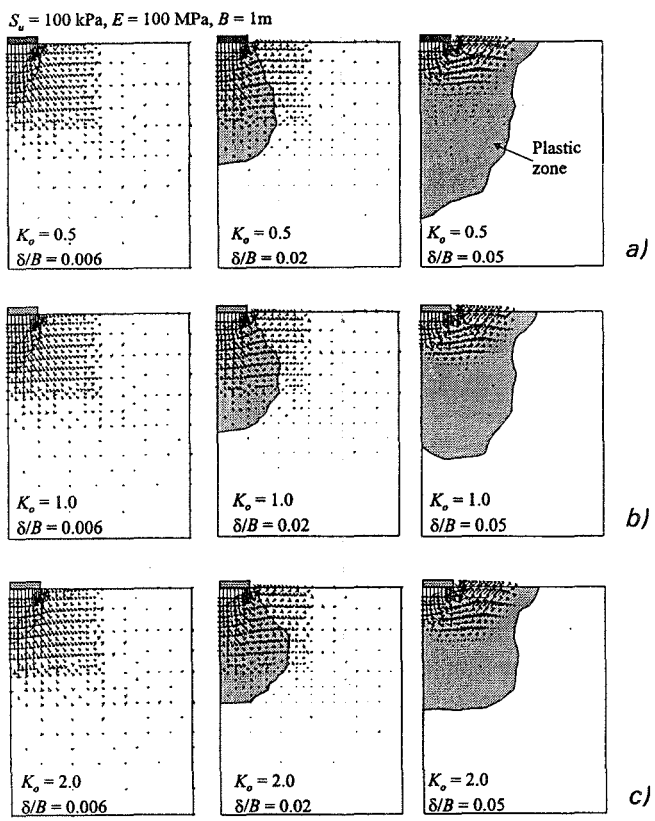

Figure 6.13: Effect of K_o on failure mechanism and plastic zone beneath the footing

As shown in Chapter 9 and by Day and Potts (2000), more accurate solutions can be obtained by using smaller elements around the edge of the footing. However, these solutions involve larger computational times because of the singularity at the edge of the footing. Hence, for the work described in this chapter the mesh shown in Figure 6.8 has been retained. The qualitative comparisons that are made are therefore likely to be correct, but it should be remarked that more accurate quantitative results could have been obtained by using a more refined mesh.

The effects of different initial stress conditions in the ground are shown in Figures 6.12 and 6.13. Results from analyses with K_o values of 0.5, 1.0 and 2.0 are shown. All analyses had the same soil properties (i.e. same stiffness and strength), and had a saturated bulk unit weight of 20kN/m^3 and a ground water table at the soil surface. The load-displacement curves shown in Figure 6.12 indicate that K_o has only a minor influence on the behaviour of the foundation.

Figure 6.13 shows vectors of incremental displacement at three stages, δ/B = 0.006, 0.02 and 0.05, for each analysis, where δ is vertical displacement and B is the half width of the footing. Also shown on these plots are the zones of soil which have become plastic. All three analyses indicate that at δ/B=0.02 the vectors of incremental displacement show significant relative movements at depth below the footing. This is accompanied by an extensive zone of plastic soil. However, at failure the pattern of displacements have changed and the final failure mechanism involves quite shallow movements. There is some indication that the zones of yielded soil extended further laterally and less vertically as K_o increases.

6.5.4.3 *Effect of footing shape on the bearing capacity of undrained clay*

Further analyses have been performed to obtain the load-displacement curves for rigid circular and square surface foundations. The same soil properties, as used for the strip foundations, were adopted. For the circular footing, the mesh of 8 noded elements shown in Figure 6.8 was used, while for the square footing the mesh of 20 noded elements shown in Figure 6.14 was used. As can be seen from Figure 6.14b, the aspect ratios of the elements at depth below the edge of the footing are not ideal. However, as they are a considerable distance from the footing, they did not appear to adversely affect the results. Horizontal movements on the vertical boundaries of the mesh were restrained, while the base of the mesh was not allowed to move in either horizontal or vertical

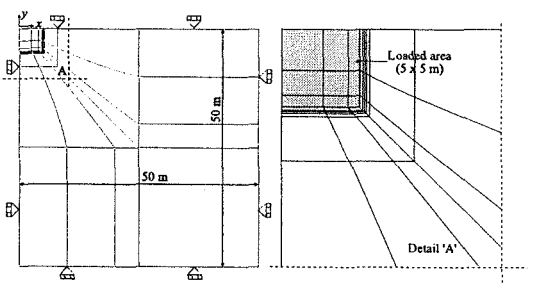

Figure 6.14a: Horizontal cross-section of a 3D mesh for square footing analysis

directions. Loading of the footing was again simulated by imposing vertical displacements to the soil surface below the position of the footing.

A comparison of the load-displacement curves for strip, circular and square footings is shown in Figures 6.15 and 6.16 for smooth and rough footings respectively. Again, the load is expressed in terms of the mobilised bearing capacity factor $N_c^{mob}(=Q/(AS_u))$, and the displacement is normalised by B, where B is the half width of the footing, for the strip and square foundations, and the radius for the circular foundation. It should be noted that, while there is an analytical solution for the ultimate bearing capacity factor for the strip foundation (i.e. $N_c = 5.14$) and a semi-analytical/numerical solution for the circular foundation (i.e. $N_c = 5.69$ and 6.2 for smooth and rough footing respectively), there is no such solution for the square foundation. However, it is commonly assumed that circular and square footings have the same bearing capacity, although there is no theoretical justification for this assumption. The finite element results indicate that the bearing capacity of a square foundation is, in fact, less than that of a circular foundation.

Analyses have also been performed for rectangular footings with length to breadth ratios, L/B, of 2 and 4. These were performed with meshes similar to that used for the square footing, but with additional elements added to account for the increase in length of the footing. The resulting load-displacement curves are presented in the form of mobilised bearing capacity factor, N_c^{mob}, versus

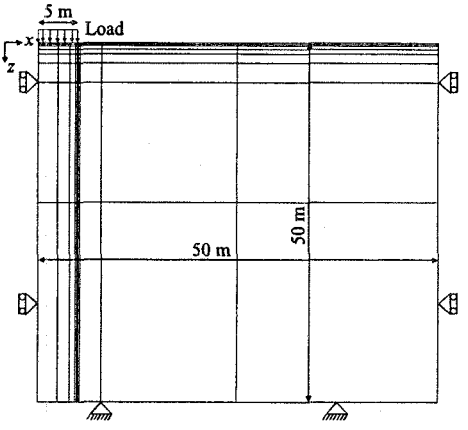

Figure 6.14b: Vertical cross-section of a 3D mesh for square footing analysis

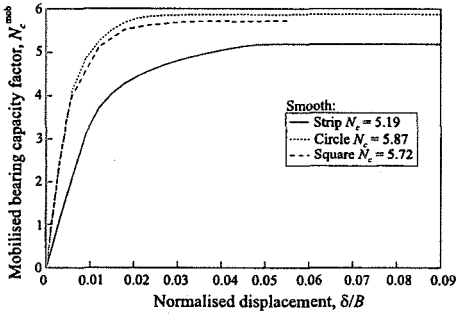

Figure 6.15: Load-displacement curves for smooth strip, circular and square footings

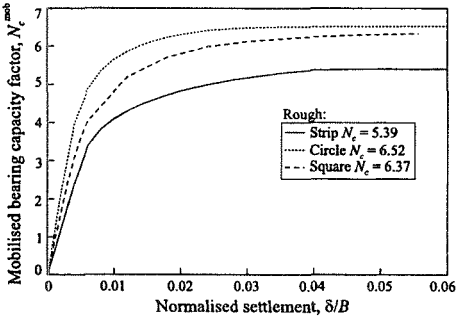

Figure 6.16: Load-displacement curves for rough strip, circular and square footings

vertical normalised displacement of the footing, δ/B, in Figures 6.17 and 6.18, for smooth and rough footings respectively.

Conventionally, the undrained bearing capacity, Q_{max} , of a rectangular surface footing resting on a clay soil is expressed in terms of the ultimate bearing capacity factor of a strip footing, N_c^{strip}, and a shape factor, s_c, by the following equation:

$$Q_{max} = A s_c N_c^{strip} S_u \qquad (6.3)$$

The shape factor s_c depends on the L/B ratio of the footing and is usually determined from the following *empirical* relationship (Skempton 1951):

$$s_c = 1 + 0.2\ B/L \qquad (6.4)$$

This relationship does not distinguish between rough and smooth footings. The results presented in Figures 6.17 and 6.18 can be used to calculate values of s_c for rectangular footings, with L/B values of 1, 2 and 4. These are compared with Equation (6.4) in Figure 6.19.

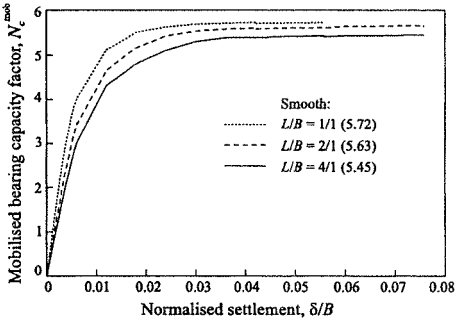

Figure 6.17: Load-displacement curves for smooth rectangular footings

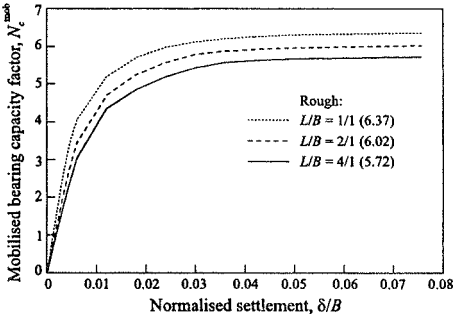

Figure 6.18: Load-displacement curves for rough rectangular footings

6.5.4.4 Strip footings on weightless drained soil

In conventional design the bearing capacity of a vertically loaded strip footing on a drained soil (i.e. sand) is expressed as:

$$Q_{max} / A = c' N_c + q' N_q + \gamma' B N_\gamma \qquad (6.5)$$

where B is the half width of the footing, q' is the magnitude of any surcharge pressure existing on the ground surface adjacent to the

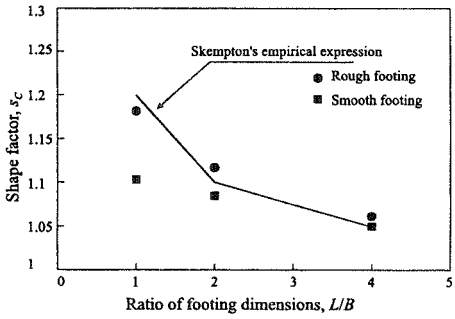

Figure 6.19: Variation of shape factor with L/B

footing, see Figure 6.20, and N_c, N_q and N_γ are bearing capacity factors. The factors N_c and N_q are derived theoretically assuming the soil is weightless, while N_γ is found from an approximate calculation assuming the soil has weight, but no cohesion or surcharge. Superposition is then assumed to give Equation (6.5).

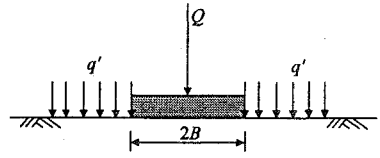

Figure 6.20: Strip footing with surface surcharge

Analytical stress field solutions have been used to obtain the following expressions for N_q and N_c (Prandtl (1920)):

$$N_q = \frac{1+\sin\varphi'}{1-\sin\varphi'} e^{\pi \tan\varphi'} \tag{6.6}$$

$$N_c = (N_q - 1)\cot\varphi' \tag{6.7}$$

For the situation where the angle of dilation equals the angle of shearing resistance (i.e. $v = \varphi'$), it is possible to show that a compatible displacement mechanism is associated with these stress fields. It is also possible to extend the stress fields throughout the soil mass, satisfying equilibrium and without violating the yield condition. The solutions expressed by Equations (6.6) and (6.7) are therefore theoretically exact, see Chapter 1 of Volume 1. The solutions can also be shown to be applicable to both smooth and rough footings. If the angle of dilation, v, does not equal the angle of shearing resistance, φ', then the above solutions are only approximate.

To assess the ability of numerical analysis to predict these results, finite element analyses have been performed using the geometry and finite element mesh shown in Figure 6.8. The Mohr-Coulomb model was used to model soil behaviour, see Section 7.5 of Volume 1. The soil was assumed to be weightless ($\gamma = 0$) and cohesionless ($c' = 0$), with an angle of shearing resistance, φ', of 25°, a Young's modulus, E', of 100MPa and a Poisson's ratio, μ, of 0.3. Four analyses were performed with a surcharge, q', of 100kPa and one analysis with $q' = 10$kPa. The four analyses with $q' = 100$kPa differed in that different combinations of the angle of dilation and roughness of the footing were assumed. For the analysis with $q' = 10$kPa the footing was smooth and the angle of dilation was zero. For the analyses with rough footings interface elements were positioned between the footing and the soil, see Figure 6.10. These were given the same values of φ' and v as the soil, and stiffness values $K_s = K_n = 10^5$ kN/m^3.

The predicted load-displacement curves are shown in Figure 6.21. The load is expressed as the mobilised bearing capacity coefficient, N_q^{mob} ($=Q/(Aq')$). This figure shows that there is little effect of the footing roughness, but that the angle of dilation affects both the shape of the load-displacement curve and the ultimate value of N_q. The magnitude of the surcharge load, q', affects the amount of displacement required to reach failure. However, it does not affect the ultimate value of N_q.

For φ'=25° Equation (6.6) gives a value of N_q = 10.7. The ultimate (failure) values of N_q for each analysis are listed in Table 6.1. As noted above, Equation (6.6) is theoretically exact for a soil with an angle of dilation equal to the angle of shearing resistance and is valid for both smooth and rough footings. The analyses in which v = 25° can therefore be directly compared with the analytical value and the errors are 0.9% and 3%, for the smooth and rough footing respectively. As with the analyses for undrained clay, the numerical predictions are improved if a finer mesh is used in the vicinity of the edge of the footing. The three analyses with a dilation angle of zero give a value of N_q of approximately 10.0. This is some 7% lower than value given by Equation (6.6).

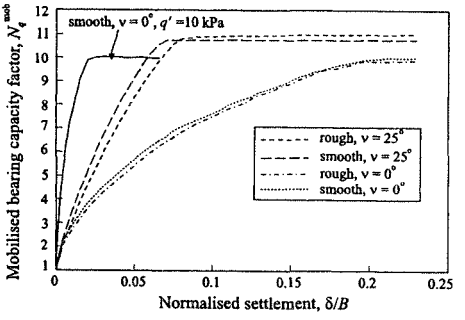

Figure 6.21: Load-displacement curves for strip footings on weightless soil (effect of roughness, dilation and surcharge)

Vectors of incremental displacement at failure for the four analyses with q'=100kPa are shown in Figure 6.22. These show that for all four analyses the failure mechanism is deep seated and has a wide lateral extent.

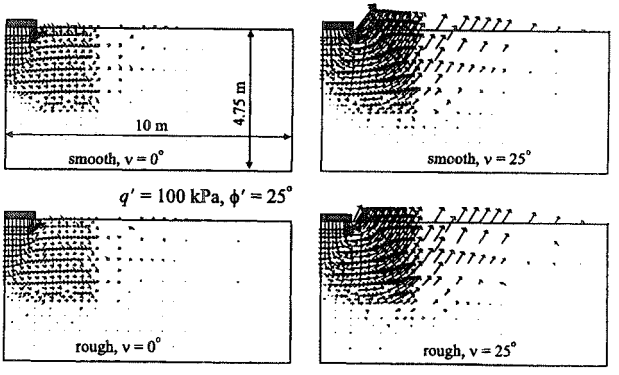

Figure 6.22: Effect of roughness and dilation on the failure mechanism for a strip footing on weightless soil

6.5.4.5 Strip footings on a drained soil

If the soil is cohesionless, has no surcharge but has weight, then only the third term in Equation (6.5) is non-zero. As noted in Section 1.9.2 of Volume 1, it is rarely possible to obtain analytical stress field solutions for a frictional soil (i.e.

$\varphi'>0$) which has weight, due to the complexity of the governing hyperbolic partial differential equations. Consequently, there is no theoretically exact expression for N_γ. In fact, several alternative expressions can be found in the literature. One of the most popular is that by Hansen (1970):

$$N_\gamma = 1.5(N_q - 1)\tan\varphi' \tag{6.8}$$

This equation, as with many of the alternatives, is often used for both rough and smooth footings. However recent work by Bolton and Lau (1993) has shown that footing roughness affects the magnitude of N_γ. Their results are based on numerical integration of the stress field equations and are therefore, again, approximate.

Results from four finite element analyses, using the mesh shown in Figure 6.8 and with the properties given above for the N_q analyses, are shown in Figure 6.23. Dry conditions were assumed and the soil had a bulk unit weight of 18kN/m^3 and K_o=0.577 (i.e.1-sinφ'). A different combination of footing roughness and angle of soil dilation was used in each analysis. The results are expressed as graphs of mobilised N_γ^{mob} against normalised footing displacement, δ/B. In contrast to the analyses presented above for N_q, the final value of N_γ is dependent on footing roughness, but not on the magnitude of the angle of dilation. The final values of N_γ are tabulated in Table 6.2, where they are also compared with values from Bolton and Lau (1993) and from Equation (6.8). It can be noted that for smooth footings the finite element results are in agreement with those of Bolton and Lau (1993). However, for the rough footings the numerical analyses are in much better agreement with Equation (6.8).

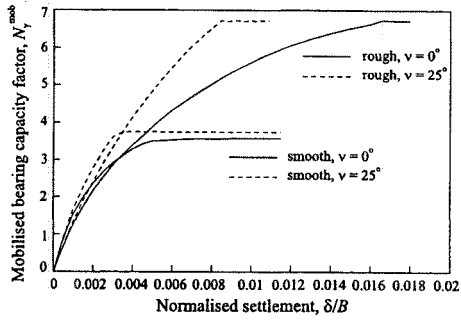

Figure 6.23: Load-displacement curves for a strip footing on cohesionless soil (effect of roughness and dilation)

The vectors of incremental displacement at failure are shown in Figure 6.24. The smooth footings have much shallower failure mechanisms and the difference between these and those for the rough

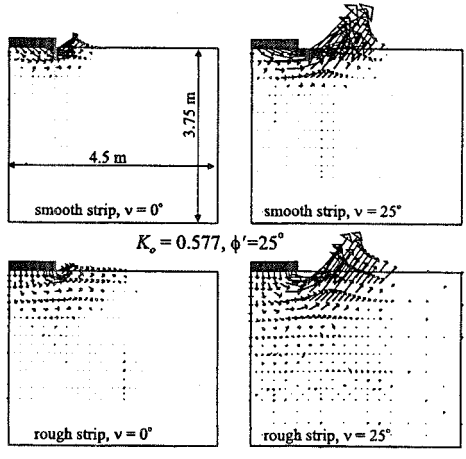

Figure 6.24: Failure mechanism for a strip footing on cohesionless soil (effect of roughness and dilation)

footings explains the difference in the N_γ values.

Vectors of incremental displacement at three different stages of loading for the analysis with a smooth footing and with a zero dilation angle are shown in Figure 6.25. Also shown on these figures are the zones of plasticity. As for the undrained analyses described above, the mode of deformation changes as loading proceeds. The zone of plasticity is much more extensive than the final failure mechanism.

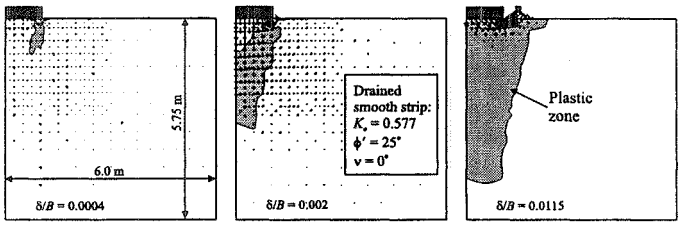

Figure 6.25: Development of failure beneath a smooth strip footing on cohesionless soil

In all of the N_γ analyses presented above $K_o = 0.577$. To investigate the effect of K_o, the analysis with a smooth footing and zero dilation was repeated with K_o values of 1.0 and 2.0. The resulting load-displacement curves are shown in Figure 6.26. The value of K_o has an effect on the load-displacement curve prior to failure, but does not affect the ultimate value of N_γ. The vectors of incremental displacement at failure for each analysis are compared in Figure 6.27. Also shown on this figure are the plastic zones at failure. While the failure mechanism is independent of K_o, the size of the plastic zone is not.

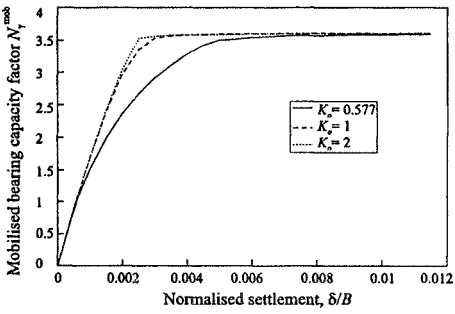

Figure 6.26: Effect of K_o on load-displacement behaviour

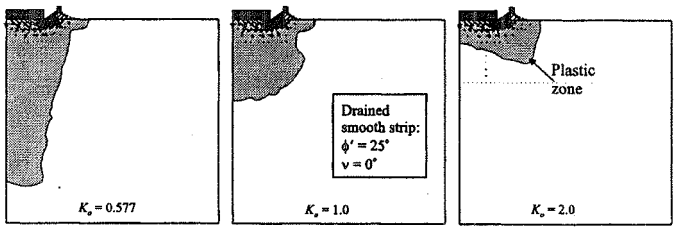

Figure 6.27: Effect of K_o on failure mechanism and development of plastic zone

If a surcharge loading exists on the soil surface adjacent to the foundation and the soil has weight, then both the N_q and N_γ terms of Equation (6.5) are non-zero. As noted above, this equation assumes that the effects of soil weight, γ, and surcharge, q', can be superimposed. To investigate this hypothesis the analysis presented above for a rough footing on sand with an angle of dilation $v = 25°$ was repeated with a surcharge $q' = 10$kPa. This analysis gave an ultimate load on the footing $Q_{max} = 556$ kN/m. Based on $N_q = 11.03$ (see Table 6.1) and $N_\gamma = 6.72$ (see Table 6.2), Equation (6.5) predicts an ultimate load of 463 kN/m. Comparing these values indicates that the superposition assumption implied in Equation (6.5) is conservative. In this particular case by 17%.

One reason why the superposition assumption is not valid is that the failure mechanisms associated with N_q and N_γ differ. This can be seen by comparing the failure mechanisms shown in Figures 6.22 and 6.24. The failure mechanism for N_q is deeper and wider than that for N_γ.

It should also be noted that the magnitudes of the footing settlements required to mobilise full N_q and N_γ values differ (see Figures 6.21 and 6.23). In addition, the settlement required to mobilise the ultimate N_q value depends on the magnitude of the surcharge, q'. Conventional design procedures do not explicitly account for this. However, in practice this could have significant implications, especially in situations where the soil strength degrades (i.e. φ' reduces) with straining. For example, at ultimate load the average strength associated with the first mechanism to form (i.e. N_γ) is likely to have decreased from its peak value, while that associated with the second mechanism (i.e. N_q) is unlikely to have reached its peak value. In such a case Equation (6.5) may not be conservative (see Chapter 4 for a detailed discussion on progressive failure).

6.5.4.6 Circular footings on a weightless drained soil

To evaluate the bearing capacity for a vertically loaded circular footing on a drained soil Equation (6.5) is again used in conventional design. However, the bearing capacity coefficients N_q, N_c and N_γ are modified to account for the circular shape of the footing. This can be done by using different values for N_q, N_c and N_γ, or by maintaining the values associated with a strip footing, but introducing shape factors s_q, s_c and s_γ in a similar manner as shown in Equation (6.3) for undrained clay.

In contrast to the strip footing, where the expressions given by Equations (6.6) and (6.7) for N_q and N_c are theoretically exact, for a circular footing all of the bearing capacity factors used in conventional design are approximate. To quantify the effect of footing shape on N_q the finite element analyses, presented above in Section 6.5.4.4 for weightless sand with q'=100kPa, were repeated with a circular footing.

The predicted load-displacement curves are shown in Figure 6.28 and these can be compared with those for the strip footing given in Figure 6.21. In contrast to the strip footing analyses, which indicate that the footing roughness does not affect the ultimate value of N_q, the circular footing analyses indicate that the rougher the

footing the larger the ultimate N_q value. In addition, and again in contrast to the results for the strip footing, the angle of dilation has only a minor influence on the ultimate value of N_q.

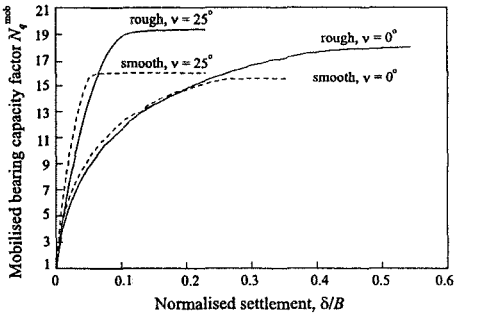

Figure 6.28: Load-displacement curves for a circular footing on weightless soil (effect of roughness and dilation)

One of the reasons for the differences outlined above can be seen in Figure 6.29, which shows vectors of incremental displacement at failure. These vectors indicate that the failure mechanisms for the smooth circular footings are shallower and of a smaller lateral extent than those for the rough circular footings. Comparison of these failure mechanisms with those for the strip footings shown in Figure 6.22 indicates that even for the rough circular footings the failure mechanisms are smaller both laterally and vertically than for the strip footings.

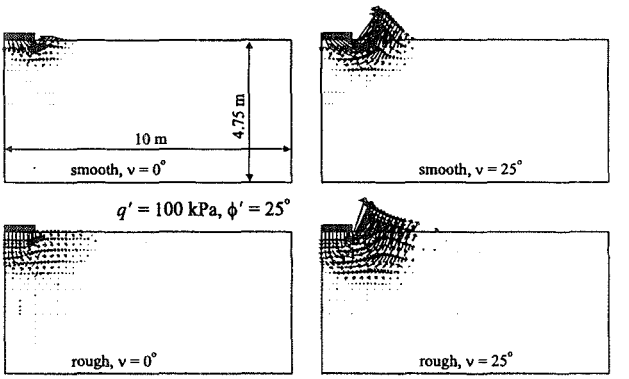

Figure 6.29: Failure mechanism for a circular footing on weightless soil (effect of roughness and dilation)

The ultimate values of N_q are listed in Table 6.1, where they are compared with the equivalent values from the strip footing analyses. The values for the circular footings are substantially larger than those for the equivalent strip footings. This is in agreement with conventional design practice which, depending on the actual design code or advice manual, suggests a shape factor of between 1.2 and 1.5 to be applied to the N_q value for a strip footing.

Table 6.1: Bearing capacity factor N_q

Analysis	N_q at failure	
	Strip footing	Circular footing
Smooth footing, q' = 100kPa, v = 0°	10.03	15.57
Smooth footing, q' = 100kPa, v = 25°	10.8	16.01
Rough footing, q' = 100kPa, v = 0°	9.92	18
Rough footing, q' = 100kPa, v = 25°	11.03	19.42
Smooth footing, q' = 10kPa, v = 0°	10	

6.5.4.7 Circular footings on a drained soil

To investigate the effect of foundation shape on the N_γ term in Equation (6.5) the analyses presented in Section 6.5.4.5 were repeated using an axi-symmetric, as opposed to a plane strain, idealisation. The resulting load-displacement curves are shown in Figure 6.30 and can be compared to those from the equivalent strip footing analyses presented in Figure 6.23. The two sets of analyses show similar behaviour, with the exception that the ultimate N_γ values are smaller for the circular footings. This is in contrast to the N_q analyses, which showed that higher values were obtained for circular footings.

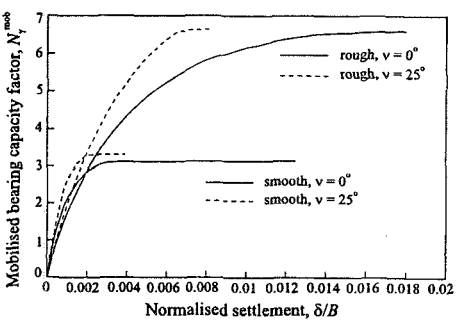

Figure 6.30: Load-displacement curves for a circular footing on cohesionless soil (effect of roughness and dilation)

The ultimate values of N_γ are listed in Table 6.2, where they are compared to those from the strip footing analyses and also to those obtained by Bolton and Lau (1993). Comparing the values obtained from the finite element analyses, the ratios of circular to strip footing N_γ values are 0.88 and 0.98, for the smooth and rough footings respectively. Compared to the values given by Bolton and Lau (1993), the smooth footing results are in reasonable agreement, whereas the rough footing results are not. In fact, Bolton and Lau give values of N_γ for rough circular footings which are substantially larger than for the equivalent strip footing. This is not predicted by the finite element analyses and is also not in agreement with conventional design practice, where shape factors of between 0.6 to 0.9 are recommended (Sieffert and Bay-Gress (2000)).

Table 6.2: Bearing capacity factor N_γ

Analysis	Bolton & Lau		Equation (6.8)		Finite elements	
	Strip	Circle	Strip	Circle	Strip	Circle
Smooth, $v = 0°$	3.51	3	6.76	-	3.59	3.14
Smooth, $v = 25°$	3.51	3	6.76	-	3.74	3.31
Rough, $v = 0°$	11.6	13.5	6.76	-	6.74	6.62
Rough, $v = 25°$	11.6	13.5	6.76	-	6.72	6.64

The vectors of incremental displacements at failure are shown in Figure 6.31. Comparing these with those for the equivalent strip footings given in Figure 6.24, indicates that for circular footings the failure mechanisms are much shallower and of smaller lateral extent.

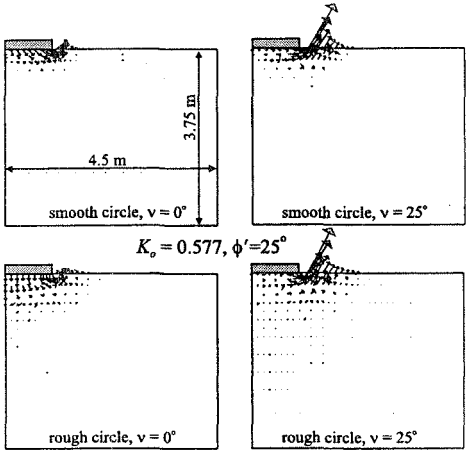

Figure 6.31: Failure mechanism for a circular footing on cohesionless soil (effect of roughness and dilation)

6.5.5. Undrained bearing capacity of non-homogeneous clay

6.5.5.1 Introduction

In Sections 6.5.4.2 and 6.5.4.3 discussing the undrained bearing capacity of clay, the strength was assumed to remain constant with depth. In many field situations this is not a realistic assumption. For some simple linear and bi-linear strength variations with depth, approximate analytical solutions are available (Davis and Booker (1973)), however for more general situations such solutions do not exist.

6.5.5.2 Constitutive model

Accounting for a variation in undrained strength with depth is relatively easy in a finite element analysis. A Tresca model could be employed, in which the undrained strength is allowed to vary spatially across the finite element mesh. The analysis could then be carried out as described above.

However, in anticipation of the content of Section 6.5.6 of this chapter, and to illustrate the use of a more complex constitutive model, a form of the modified Cam Clay model will be used here. In this model the shapes of the yield and plastic potential surfaces are given by a Mohr-Coulomb hexagon and a circle respectively (see Sections 7.9.2 and 7.12 of Volume 1). Both stiff and soft clay soils are considered and the parameters, listed in Table 6.3, have been selected to represent real soil types. It may be noted that these parameters are essentially effective stress parameters. It is not possible to input directly the undrained strength or its change with effective stress. However, as shown in Appendix VII.4 of Volume 1, the undrained strength can be derived from the basic parameters and is given by the following equation:

$$\frac{S_u}{\sigma'_{vi}} = g(\theta)\cos\theta\frac{OCR}{6}(1+2K_o^{NC})[1+B^2]\left[\frac{2(1+2K_o^{OC})}{(1+2K_o^{NC})OCR[1+B^2]}\right]^{\frac{\kappa}{\lambda}} \qquad (6.9)$$

where:
$$g(\theta) = \frac{\sin\varphi'}{\cos\theta + \frac{\sin\theta\sin\varphi'}{\sqrt{3}}}$$

$$B = \frac{\sqrt{3}(1-K_o^{NC})}{g(\theta)(1+2K_o^{NC})}$$

θ is the Lode's angle; OCR is the overconsolidation ratio; σ_{vi}' is the initial vertical effective stress.

In the present analyses, K_o^{NC} and K_o^{OC} have been assumed to be given by:

$$K_o^{NC} = 1-\sin\varphi' \quad ; \quad K_o^{OC} = K_o^{NC}OCR^{\sin\varphi'} \qquad (6.10)$$

Table 6.3: Soil properties for pre-loaded strip footings

Soil type	φ'	κ	λ	2nd elastic parameter	γ (kN/m^3)	v_1	k (m/sec)
Stiff clay	23°	0.03	0.16	μ=0.2	18	2.84	1 x 10^{-10}
Soft clay	32°	0.02	0.22	G=1700kPa	17	3	5 x 10^{-10}

The stiff clay parameters are based on the behaviour of London Clay. An *OCR* of 6 has been used and the water table has been assumed to be 2.5m below the ground surface. Above this level the clay remains saturated and can sustain tensile pore water pressures. The undrained strength profile is shown in Figure 6.32. Also shown in the figure is field data for London Clay from Carswell *et al.* (1993).

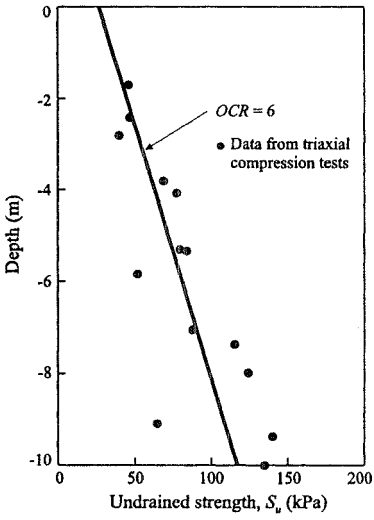

Figure 6.32: Undrained strength profile fitted through London Clay data

The soft clay parameters are based on site investigation and laboratory data from a site in Grimsby, Yorkshire (Mair *et al.* (1992)). At this site the clay is normally consolidated below a depth of approximately 2m, with a stronger crust at the surface. The water table has been assumed to be at a depth of 2m and, as with the stiff clay, the soil above this surface is assumed saturated and able to sustain tensile pore water pressures. To obtain a realistic distribution of undrained strength with depth, the *OCR* has been varied as shown in Figure 6.33. Also shown in this figure is the variation of K_o^{OC}, according to Equation (6.10). The resulting distribution of undrained strength S_u, together with the field data, is show in Figure 6.34. The values of S_u plotted are those appropriate to triaxial compression.

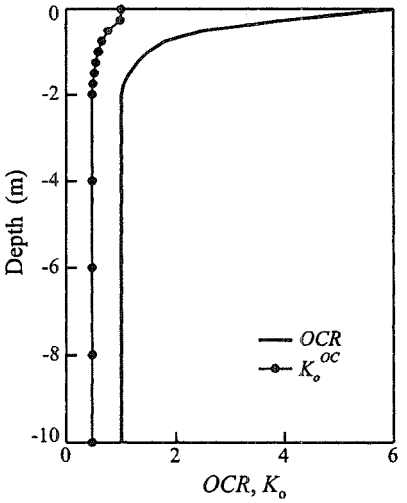

Figure 6.33: OCR and K_o profiles for soft clay

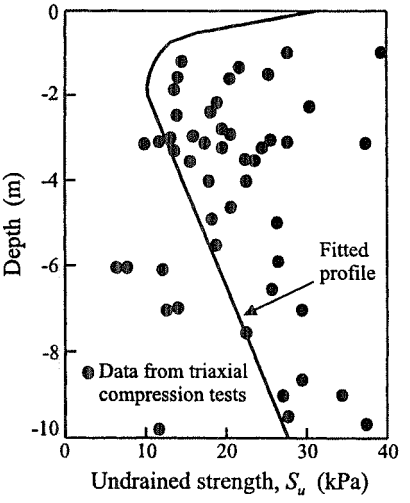

Figure 6.34: Undrained strength profile fitted through soft clay data

6.5.5.3 Geometry and boundary conditions

Analyses have been performed of 2m and 10m wide rigid strip footings. As undrained conditions are required, two alternative types of analysis are available. A fully coupled analysis, combining mechanical deformation and pore water flow could be performed, see Chapter 10 of Volume 1. Alternatively, only the mechanical behaviour could be considered, using a large value for the bulk compressibility of the pore fluid, see Section 3.4 of Volume 1. Although the latter approach is the simplest and probably the best option, the first approach is used here. This is because the analyses are to be further extended to drained conditions in Section 6.5.6 of this chapter.

The finite element mesh for the 2m wide footing is that shown previously in Figure 6.8. Eight noded plane strain isoparametric elements have been used, with the four corner nodes having pore water pressure, as well as displacement, degrees of freedom. The two vertical sides of the mesh have been restrained in the horizontal direction, while the base of the mesh was not allowed to move either in the vertical or horizontal direction. Loading of the footing was modelled by applying increments of equal vertical displacement to nodes located at the soil surface underneath the position of the footing. Both smooth and rough footings have been simulated. For the rough footings the horizontal movement of the nodes immediately below the footing has been restrained.

Throughout the analyses no flow of water has been allowed through the base of the mesh, immediately beneath the footing, across the ground surface adjacent to the footing, nor through the left hand boundary which forms the vertical plane of symmetry through the footing. On the right hand boundary the pore water pressures have been maintained equal to their original values determined by the position of the water table. As the footing was loaded rapidly to failure in 21 days and the permeability of the soil was low (see Table 6.3), undrained conditions prevailed in the soil and therefore the pore pressure boundary conditions on the right hand side of the mesh had little influence on the results. Similar results would have been obtained if it had been assumed to be a no flow boundary, however such a boundary condition was not appropriate for the intended analysis discussed in Section 6.5.6 of this chapter.

For the analyses performed with a 10m wide strip footing, the mesh dimensions have been increased by a factor of 5. The soil properties and initial conditions have, however, been left unchanged.

6.5.5.4 Failure mechanisms

For a smooth strip footing on a clay soil, having a constant undrained shear strength, two classes of failure mechanisms are theoretically possible: the *Hill* (Hill (1950)) and the *Prandtl* (Prandtl (1920)) mechanisms. These are shown graphically in Figure 6.35. For a rough strip footing the Hill mechanism is not appropriate as it implies horizontal soil movements at the soil-footing interface. Consequently, only the Prandtl mechanism is valid for a rough strip footing. Interestingly, for a soil with a constant undrained shear strength, both the Hill and Prandtl solutions

give the same value of the bearing capacity factor N_c (i.e. $N_c=2+\pi$). As the Prandtl solution is valid for both smooth and rough footings, this also implies that in this case the bearing capacity is independent of footing roughness.

While the above is true for a soil with a constant undrained shear strength, S_u, it does not hold if S_u varies spatially (Davis and Booker (1973)). The effects of a spatial variation of S_u on the failure mechanism and bearing capacity can be seen from the results of the present analyses. Vectors of incremental displacement at failure, for a selection of the analyses, are shown in Figure 6.36. The vectors clearly indicate the nature and extent of the failure mechanism for each analysis.

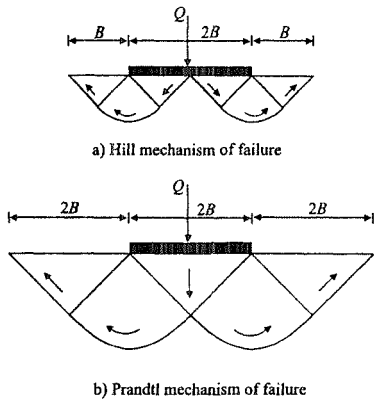

Figure 6.35: Possible mechanisms of footing failure

Results from 2m wide smooth and rough footings on stiff clay are shown in Figures 6.36a and 6.36b respectively. The failure mechanism for the smooth footing is essentially of the Hill type, with soil immediately under the footing having both vertical and horizontal components of displacement. In contrast, the failure mechanism for the rough footing is more like the Prandtl type, with the soil immediately below the footing moving predominantly vertically. Clearly, the failure mechanism for the rough footing penetrates deeper below the footing and involves a considerably larger volume of soil than that for the smooth footing. This occurs because the horizontal restraint imposed at the soil-footing interface causes the failure mechanism to penetrate deeper into the soil for the rough footing case. As the undrained shear strength increases with depth, see Figure 6.32, then it is perhaps not surprising that the bearing capacity for the rough footing is higher than for the smooth footing (note: the bearing capacities are noted on Figure 6.36 as Q_{max}/A).

Because the initial distribution of S_u with depth is linear for the stiff clay, it is possible to obtain an estimate of the bearing capacity using results from Davis and Booker (1973). This gives a value for the smooth footing of Q_{max}/A=145 kPa. To obtain this value interpolation and scaling from the figures supplied in the above paper are necessary. Davis and Booker's figures are based on calculations which involve some finite difference approximations and have been drawn to provide conservative estimates for design purposes. The above result is therefore subject to error. Nevertheless, this value of ultimate bearing capacity is within 5% of the finite element result.

Similar results are also shown in Figures 6.36c and 6.36d, which are from analyses of a 10m wide footing on soft clay. These results imply that the surface crust, see Figure 6.34, does not have a major influence on the failure mechanism. This is not so for the 2m wide footing on soft clay, as can be seen in Figures 6.36e

and 6.36f. In this case a deep Prandtl type mechanism is predicted for both the smooth and rough footing. Here the failure mechanism, the extent of which depends partly on the footing width, is controlled by the 2m deep surface crust which has a strength reducing with depth. The failure mechanisms for both the smooth and rough footings are forced into the weaker soil, as this provides a failure mechanism involving the least resistance. As the failure mechanism is the same for both smooth and rough footings, then the bearing capacity is also the same, which is evident from the results shown on Figures 6.36e and 6.36f.

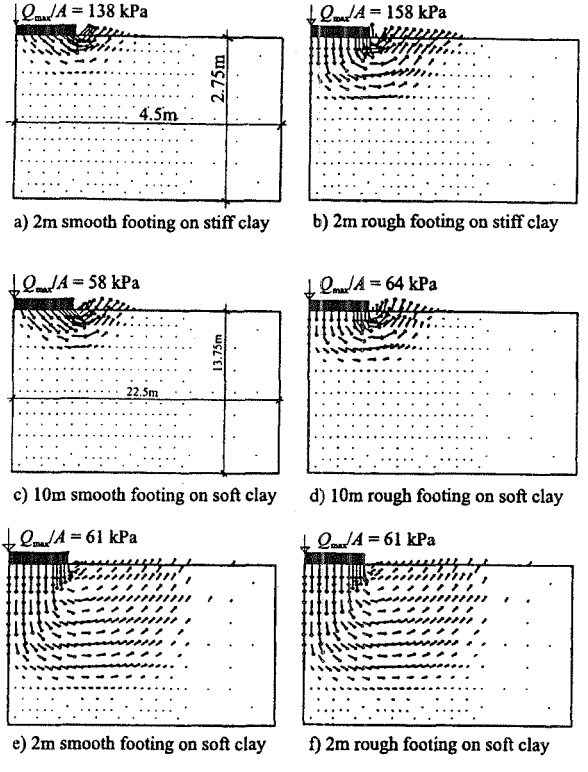

Figure 6.36: Failure mechanisms for smooth and rough footings on stiff and soft clay

6.5.6 Undrained bearing capacity of pre-loaded strip foundations on clay

6.5.6.1 Introduction

The bearing capacity of a soil is essential for the design of near surface foundations. It controls the load which can be supported by the ground and will

influence the size and type of foundation to be used. The problem is well understood for both undrained and drained loading situations, where the soil strength parameters are either constant or vary in a simple manner with depth, and there are several different ways, theoretical and empirical, of determining the bearing capacity (see above). The estimation of the bearing capacity of new foundations is therefore relatively straight forward and in this respect it is the short term (undrained) bearing capacity that usually governs the design of foundations on clay soils.

The situation is not so clear, however, if extra load is to be added to an existing foundation on clay soil, some time after initial construction was completed. This could occur, for example, if new machinery is to be installed, or if additional floors are to be added. It can also occur if old foundations are to be reused for a new building, a situation that is becoming more common as the civil engineering profession is becoming more sensitive to issues related to sustainability. Due to consolidation of the soil after initial loading there is a change in undrained shear strength. The undrained bearing capacity at the time the additional load is applied will therefore differ from that during initial construction. At present, there are no guidelines for determining the magnitude of this change. This is perhaps not surprising as there will be a complex distribution of undrained strength below the foundation, which will render simple analytical solutions almost impossible.

This problem is therefore an ideal candidate for finite element analysis and has been investigated first by Jackson *et al.* (1997) and then by Zdravković *et al.* (2001), who extended the range of soil conditions considered. They performed a series of coupled finite element analyses of strip foundations. A strip footing was first placed on a clay soil, with known initial conditions, and rapidly loaded to failure. This provided the initial short term (undrained) bearing capacity. A series of further analyses were then performed in which the footing was first rapidly loaded (undrained) to a percentage of the original short term bearing capacity. Pre-load values of 20, 40, 60, 80 and 100% were used. The load was then held at this value while all excess pore water pressures in the clay dissipated (i.e. full consolidation). The footing was then subjected to further rapid loading (undrained) to failure, and the new undrained bearing capacity determined.

6.5.6.2 Constitutive model

An important facet of this problem is the change of undrained strength which occurs during consolidation, as this governs the undrained bearing capacity under any subsequent rapid increase in loading. Consequently, it is necessary to employ a constitutive model that can accurately predict such behaviour and therefore the soil was modelled using a form of modified Cam clay. In fact, the same model and soil parameters as described in the previous section were used. The undrained analyses for the stiff clay (OCR=6) and the soft clay described previously, were used to determine the initial undrained bearing capacities. Additional analyses have been performed with the stiff clay properties with OCRs of 1, 2, 4, 9 and 25.

6.5.6.3 Geometry and boundary conditions

Analyses have been performed on 2m and 10m wide rigid strip footings and the finite element mesh for the 2m wide footing is shown in Figure 6.8.

The boundary conditions for the loading stages of the analyses were the same as those described in Section 6.5.5. However, during the consolidation stages of the analyses the nodes located at the soil surface underneath the position of the footing (i.e. those displaced during the undrained loading) were free to displace vertically, but by the same amount, with the total load on the foundation remaining constant. This was achieved by using the tied degrees of freedom concept, see Chapter 3 of Volume 1. The magnitude of the movement that occurred during these consolidation stages of the analysis was therefore not prescribed, but was a result of the analysis.

The same hydraulic boundary conditions (i.e. prescribed flows and pore water pressures), as described in Section 6.5.5, were also maintained throughout the consolidation stages, except that during these stages of the analyses the pore water pressures along the ground surface adjacent to the footing have been set and maintained at the initial values existing prior to footing construction.

Small time steps were used to maintain undrained conditions during the loading stages. For example, the initial loading to failure was achieved in 21 days. Sufficient time was allowed during the consolidation stages for all excess pore water pressures to fully dissipate. Typically this was achieved in 80 years and 30 years for the soft and stiff clay analyses respectively.

6.5.6.4 Results of the analyses

Detailed results from the investigation are given in Zdravković *et al.* (2001). Consequently only the main conclusion concerning the effect of the pre-load will be discussed here.

As an example of the results, the load-displacement curves for the 2m wide smooth footing are shown in Figure 6.37a and 6.37b, for the soft and the stiff (OCR=6) soils respectively. The curve labelled 'initial' corresponds to the situation where the footing is loaded rapidly from the initial conditions and therefore produces the initial short term bearing capacity. These results are from the analysis discussed in Section 6.5.5. The other curves are the results from the analyses in which the footing has been pre-loaded to a percentage of this initial bearing capacity and then allowed to consolidate with no change in load before being subjected to rapid loading to failure. It can be seen that the higher the pre-load, the higher the bearing capacity.

When the footing is initially loaded rapidly, excess pore water pressures are established in the soil. The excess pore water pressures can be considered to consist of two components. The first (positive) being due to an increase in mean total stress, and the second (positive or negative) due to an increase in the deviatoric (shear) stress. The first component will be compressive, with its magnitude dependent on the footing load. The magnitude of the second component will also depend on the footing load, but in addition it will depend on the type of clay and

in particular on its overconsolidation ratio. For a clay with a low *OCR* the second component will also be compressive. However, as the *OCR* increases, the magnitude of this compressive pore water pressure component will decrease, becoming tensile at high *OCR*s. Consequently, the magnitude of the excess pore water pressure that is generated during the initial undrained loading stages of each analysis will depend on the amount of load applied and on the initial *OCR* of the clay.

The changes in the undrained shear strength of the clay during the consolidation stages of the analyses depend directly on the magnitude of the excess pore water pressures and the soil properties. For a given soil, the greater the compressive magnitude of the excess pore pressure, the greater the gain in strength. If the excess pore water pressures are negative, then the undrained strength will reduce as water will be sucked into the soil.

Results from all the rough footing analyses on stiff clay (in which the undrained strength increased linearly with depth) are plotted in Figure 6.38, as undrained bearing capacity after pre-loading normalised by the initial undrained bearing capacity, against amount of pre-load for different *OCR* values. The analyses with *OCR*s less than 6 show an increasing bearing capacity with the amount of pre-load. For the *OCR* = 9 analyses the bearing capacity actually decreases when the pre-load increases above 80%. A similar trend of reducing bearing capacity is also predicted for the *OCR*=25 analyses when the pre-load

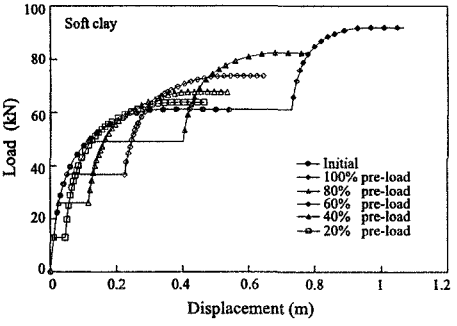

Figure 6.37a: Load-displacement curves for pre-loading on soft clay

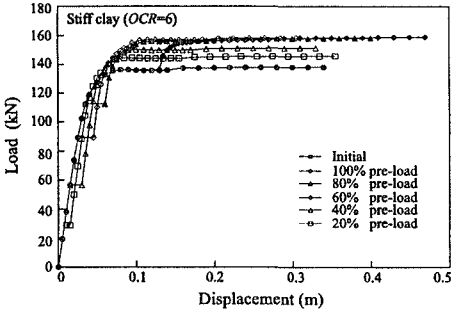

Figure 6.37b: Load-displacement curves for pre-loading on stiff clay

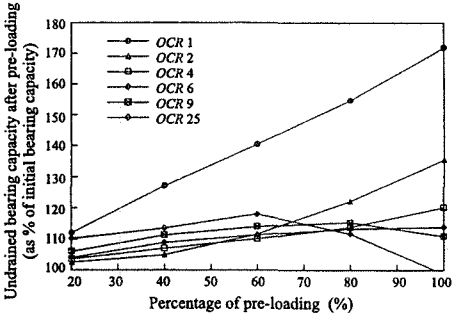

Figure 6.38: Undrained bearing capacity after pre-loading vs. percentage of pre-load

exceeds 60%. In fact for this soil, when an analysis with a 100% pre-load was attempted, the footing failed during the consolidation stage before it could be loaded any further.

This behaviour can be explained by considering the excess pore water pressures developed during pre-loading. As noted above, this consists of two components. For soil with a high *OCR* the relative magnitude of these two components changes with the amount of pre-load. For the *OCR*=9 and *OCR*=25 analyses the component due to a change in total mean stress is compressive, whereas that due to deviatoric shearing is tensile. As the amount of pre-load increases above 80% for the *OCR*=9 and 60% for the *OCR*=25 analyses, the tensile component increases in magnitude relative to the compressive component, and consequently the total magnitude of the excess pore water pressure drops and results in a smaller increase in undrained strength during the consolidation stage. For the *OCR*=25 soil with a 100% pre-load, the tensile deviatoric component of the excess pore water pressure exceeds that component due to the increase in mean stress. This results in tensile excess pore water pressures which on consolidation cause swelling, a drop in undrained strength and therefore a reduction in bearing capacity. Further investigations indicated that for pre-loads in excess of 93%, footings on a stiff *OCR*=25 soil failed during the consolidation stages, before any further load could be added.

To show more clearly the effect of *OCR*, the results presented in Figure 6.38 have been re-plotted in Figure 6.39, as normalised undrained bearing capacity against *OCR* (plotted on a logarithmic scale) for different amounts of pre-load. For pre-load values less than 50% the gain in undrained bearing capacity first reduces with *OCR*, but later recovers slowly as *OCR* is increased still further. This may at first seem to contradict the arguments put forward above, which suggest that as the *OCR* increases then the relative magnitude of the excess pore water pressures which are available to dissipate is likely to reduce and therefore lead to smaller gains in undrained bearing capacity. However, as the *OCR* increases, so does the S_u/σ_v' ratio, see Equation (6.9). Consequently, at the higher *OCR*s there will be a greater increase in S_u for a given change in σ_v'. This effect therefore acts in the opposite sense to that associated with the magnitude of the excess pore water pressure, and explains the behaviour observed in Figure 6.39. For a 100% pre-load the excess pore pressure effect dominates and the gain in bearing capacity falls continuously with increase in *OCR*, see Figure 6.39. In contrast, for the 80% pre-load the gain in bearing capacity first reduces (excess pore water pressure effect dominating), then increases slightly (S_u/σ_v' effect dominating) before reducing again (excess pore water pressure effect dominating) as the *OCR* increases.

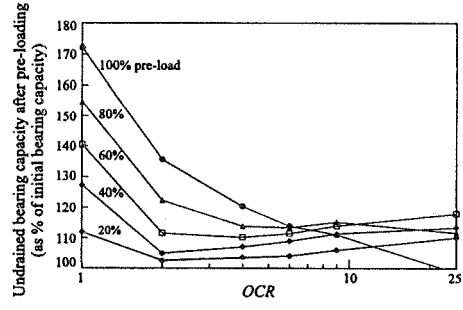

Figure 6.39: Undrained bearing capacity after pre-loading vs. OCR

It is also of interest to note that for the stiff clay analyses, in which the initial undrained shear strength increases linearly with depth, the gain in bearing capacity due to pre-load is independent of footing width. Figures 6.38 and 6.39 are therefore applicable to a footing of any width and may be useful for design purposes.

6.5.6.5 Concluding remarks

The results show that increases of bearing capacity of up to 74% are possible for pre-loaded foundations on normally consolidated clays, whilst for moderately overconsolidated clays the maximum increase is only 15%. In the former case the bearing capacity increases with the amount of pre-load applied. It will also depend on the width of the footing in relation to the depth of any surface crust in the clay. However, for the moderately overconsolidated clays the maximum bearing capacity may occur at pre-loads less than 100%. For heavily overconsolidated clays pre-loading may cause a reduction in undrained bearing capacity.

In practice most foundations will be designed with a factor of safety on load of at least 2. This means that the maximum pre-load is therefore likely to be only 50%. The results of the present investigation indicate that such a pre-load will cause at most an increase in undrained bearing capacity for subsequent loading of 35% for a normally consolidated soil, but only 12% for a soil with an OCR greater than 4. Consequently, for the majority of real situations it is unlikely that pre-loading will give rise to a substantial improvement in undrained bearing capacity.

6.5.7 Effect of anisotropic strength on bearing capacity

6.5.7.1 Introduction

In reality most soils behave in an anisotropic manner. This anisotropic behaviour is often assumed to consist of two components, *inherent* and *induced* anisotropy. Inherent anisotropy is that component which is controlled by the fabric of the soil before it is loaded. Induced anisotropy is that component which arises due to further loading.

In principle, if anisotropic behaviour is to be modelled, the constitutive model should be able to simulate both components. However, if the inherent component dominates behaviour, then a constitutive model that accounts for this component, but not the induced component, might be acceptable. In such a situation a model of the form described in Section 7.10.2 of Volume 1 might be appropriate. Because such models do not represent induced anisotropy, they will not predict any effect of rotating the direction of the principal stresses.

If both components of anisotropy are to be accounted for, then a model which is formulated in terms of all six components of stress and strain, and not in terms of invariants, is required. The MIT models described in Chapter 8 of Volume 1 are such models. MIT-E3 has been used to investigate the influence of anisotropic soil behaviour on the bearing capacity of both strip and circular rough, rigid surface footings, subjected to inclined loading.

6.5.7.2 Soil behaviour

Zdravković (1996) performed an investigation into the anisotropic behaviour of a silt, using the Imperial College large Hollow Cylinder Apparatus (HCA). Results from one of the series of tests (the M-series) are shown in Figure 6.40. In these tests all samples were initially K_o consolidated to point A, with a Lode's angle θ=-30°, (i.e. triaxial compression) and the major principal stress vertical, i.e. α=0°, where α is the angle of inclination of the direction of the major principal stress to the vertical. At Point A the Lode's angle was changed to θ=0°, maintaining the major principal stress in the vertical direction. i.e. α=0°. The test labelled M0 was then sheared undrained to failure, keeping θ=0°, by increasing the major principal stress, again at α=0°. The test labelled M90 was sheared undrained to failure, keeping θ=0°, by reducing the vertical stress so that when failure occurred this was the minor principal stress and hence the major principal stress was now horizontal, i.e. α=90°. Test M15 was initially unloaded to point B15 with θ=0° and α=0°. The major principal stress was then rotated to be inclined to the vertical by 15° (i.e α=15°). This was done maintaining a constant J, p and θ and with the soil undrained. The stress path moved to point C15. The sample was then sheared undrained keeping α=15° and θ=0°. A similar procedure was followed for tests M30, M45 and M70, except that the direction of the major principal stress was rotated to be at 30°, 45° and 70° to the vertical respectively. The details of testing are presented in Zdravković (1996) and Zdravković and Jardine (2000).

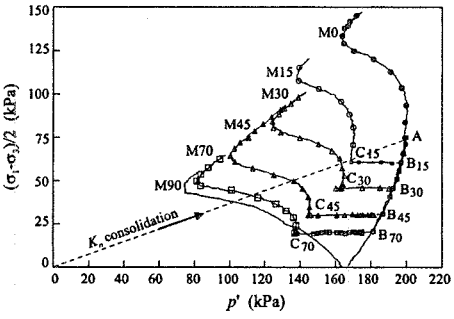

Figure 6.40: Effective stress paths from hollow cylinder tests on silt

The results given in Figure 6.40 therefore indicate the effect of changing the direction of the major principal stress on the behaviour of the soil. Clearly this behaviour is anisotropic, with both the drained angle of shearing resistance and equivalent undrained strength reducing with an increase in the angle of rotation of the direction of the major principal stress.

Parameters were obtained for the MIT-E3 constitutive model, see Table 6.4. Because the model was to be used to simulate both isotropic and anisotropic soils, the effect of the bounding surface plasticity below the state boundary surface had to be switched off. If this was not done, it was impossible to make the model behave in an isotropic manner. Consequently, no values for the parameters γ and h are given in Table 6.4. In any case, as the soils were normally consolidated, the effect of the bounding surface plasticity would not be significant. The model was then used to reproduce the test series given in Figure 6.40. The results are shown in Figure 6.41. Overall, the analyses followed the same steps as imposed in the experiments, except that all samples were unloaded by the same amount, i.e. A to

B. Comparison of Figures 6.40 and 6.41 indicates that the model is able to reproduce the key aspects of the experimental results.

Table 6.4: MIT-E3 material properties

	Parameter description	MIT-E3 value
v_{100}	Specific volume for a K_o normally consolidated sample at p′=100 kPa	1.688
K_o^{nc}	Normally consolidated value of K_o	0.5
φ_{TC}'	Critical state angle of shearing resistance in triaxial compression	35°
φ_{TE}'	Critical state angle of shearing resistance in triaxial extension	30°
c	Ratio of semi-axes of the bounding surface ellipsoid	1.0
Ψ_o	Parameter affecting rotation of bounding surface	100
λ	Slope of the VCL in v-lnp' space	0.014
κ	Initial slope of the swelling line in v-lnp' space	0.0018
μ	Poisson's ratio	0.3
S_l	Parameter affecting strain softening	1.0
C	Parameter affecting the hysteretic elasticity	1.0
n	Parameter affecting the hysteretic elasticity	1.5
ω	Parameter affecting the hysteretic elasticity	0.0

However, it is deficient in one important aspect: while the silt soil showed dilatant behaviour after reaching phase transformation, MIT-E3 indicates ductile failure. This is not a serious deficiency, as the analyses to be described here were intended to model foundations on a soft clay, which shows similar behaviour to the silt up to phase transformation, without dilating at large strains (Porović (1995), Leroueil (1977)).

The undrained triaxial compression strength profile for this soft clay is shown in Figure 6.42. It varies linearly with depth, starting from a finite value at the soil surface, giving S_u/σ_v'=0.36. This would be the profile normally adopted in any analysis using an isotropic soil model. However, MIT-E3 allows the undrained

strength profile to change, depending on the direction of the major principal stress, as shown in Figure 6.42.

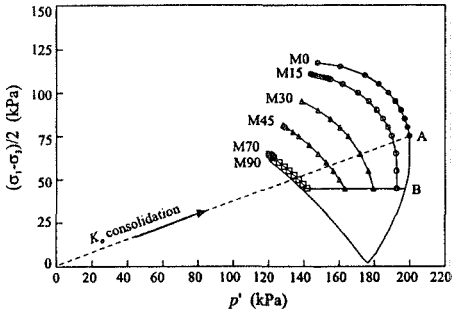

Figure 6.41: Hollow cylinder effective stress paths simulated with MIT model

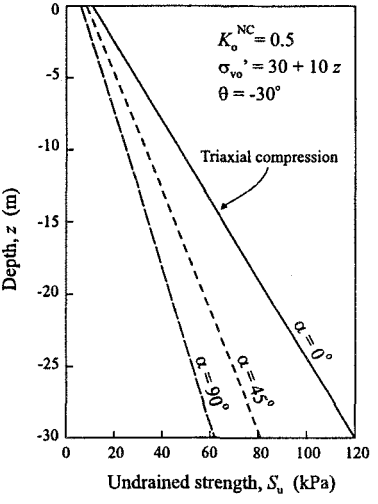

Figure 6.42: Anisotropic undrained strength profiles from MIT model

6.5.7.3 Behaviour of strip footings

Two series of strip footing analyses have been performed, in the first the properties given in Table 6.4 were adopted, whereas in the second the values of φ_{TC}' and φ_{TE}' were reassigned to be $\varphi_{TC}'=35°$ and $\varphi_{TE}'=63°$. This had the effect of making the model isotropic and consequently, when the experimental results given in Figure 6.40 were simulated, each test was predicted to give the same result which was very similar to the M0 test in Figure 6.41. Comparison of the analyses with these different soil properties therefore allows the effects of anisotropy to be quantified.

For each set of material properties five analyses were performed, each having a different inclination of the applied load. This inclination was kept constant in each analysis, and the footing was loaded to failure under load control. To achieve this, components of vertical (V) and horizontal (H) loads were applied as point loads, see Section 3.7.7 of Volume 1, to the node at the centre of the top of the footing. The magnitudes of the load increments were reduced as failure was approached. The finite

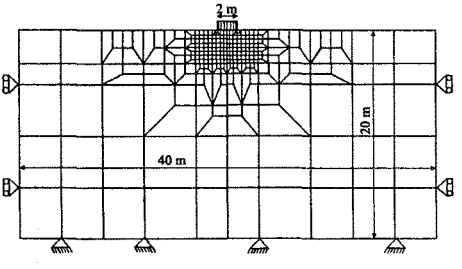

Figure 6.43: Finite element mesh for analysis of strip footing

element mesh is shown in Figure 6.43. As the analyses were performed in load control, the footing itself had to be included in the analysis.

Load-displacement curves from a typical analyses (H/V=0.3) are shown in Figure 6.44. It can be seen that failure is well defined, with both the horizontal and vertical loads reaching limiting values.

The results of both sets of analysis are shown in Figure 6.45 in the form of an interaction diagram showing values of the vertical (V_{ult}) and horizontal (H_{ult}) loads at failure. The results clearly show the adverse effect of the anisotropic behaviour for all inclinations of loading.

It should be noted that for the analyses with horizontal loading only, $H_{ult}=2BS_u$, where S_u is the value of the undrained strength mobilised at the soil surface below the footing. In the present analysis this will be the strength appropriate to plane strain conditions and will therefore be different to the values plotted in Figure 6.42, which are for triaxial compression conditions.

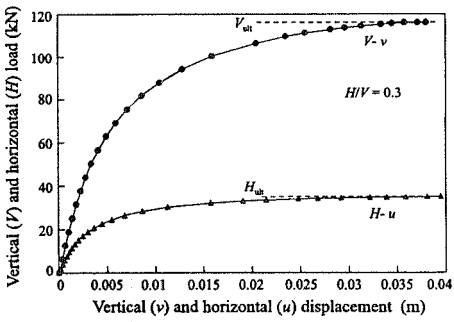

Figure 6.44: Typical load-displacement curves for combined loading analyses

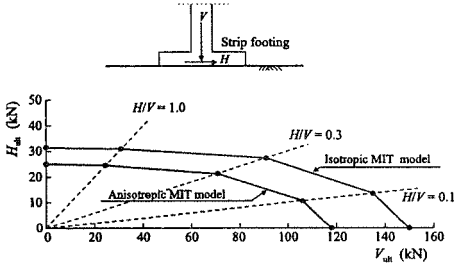

Figure 6.45: Envelopes of ultimate load for strip footing

6.5.7.4 Behaviour of circular footings

The above exercise was repeated for a circular footing. The Fourier series aided finite element approach was adopted using the parallel symmetry option, see Section 12.3.2 of Volume 1. By performing a small parametric study it was found that only 5 harmonic coefficients were required to obtain accurate results. The finite element mesh is shown in Figure 6.46. Vertical and horizontal loading were applied as line loads (in the

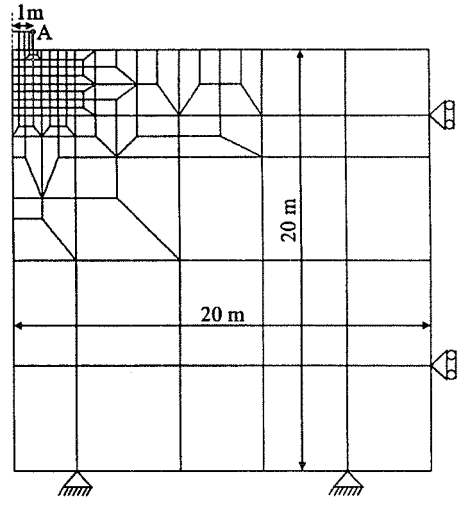

Figure 6.46: Finite element mesh for analysis of circular footing

circumferential direction) at the node representing the top right hand corner of the footing, point A, in Figure 6.46. For the vertical load (V) only the zero harmonic coefficient was specified as non zero (i.e. $\Delta V=\Delta V^0+0...$). To obtain a horizontal load, both radial (H_r) and circumferential (H_θ) line loads were specified. For the radial load only the first cosine harmonic was specified as non zero (i.e. $\Delta H_r=0+\Delta \overline{H}_r^1 \cos\theta+0...$), whereas for the circumferential load the first sine harmonic coefficient was set (i.e. $\Delta H_\theta=0+\Delta \overline{\overline{H}}_\theta^1 \sin\theta+0...$). The latter was of opposite sign but equal magnitude to that set for the radial load, see Figure 12.2 and Appendix XII.2 of Volume 1.

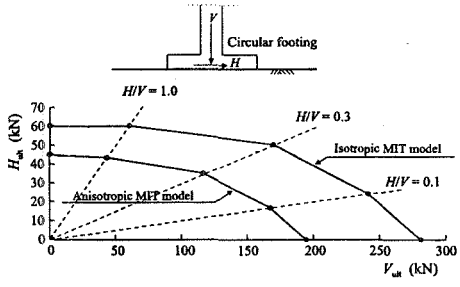

Figure 6.47: Envelopes of ultimate load for circular footing

Again predictions using both sets of soil parameters were obtained. The results are shown as an interaction diagram in Figure 6.47. The adverse effect of the anisotropic behaviour is evident again. Comparison with Figure 6.45 indicates that this effect is larger for the circular footing than for the strip footing.

6.6 Finite element analysis of shallow foundations

6.6.1 Introduction

Most of the comments given above for surface foundations also apply to shallow foundations. However, in this case it is necessary to account for the interface between the soil and the sides of the foundation, see Figure 6.48. It is not usual to model the construction of the foundation itself, but to simply assume it to be 'wished in place'.

6.6.2 Effect of foundation depth on undrained bearing capacity

To account for the depth of a foundation below the ground surface, depth factors are usually introduced into the general bearing capacity equation in a similar way to shape factors. For undrained bearing capacity the general equation becomes:

$$\frac{Q_{max}}{A} = d_c s_c N_c^{strip} S_u + p_o \qquad (6.11)$$

where d_c is the depth factor and p_o is the total overburden stress at foundation level, see Figure 6.49. Exact theoretical solutions are not available to account for foundation depth and therefore the magnitude of the depth factor is often based on semi-empirical correlations. One of the most popular correlations currently in use is that proposed by Skempton (1951) and shown in Figure 6.50. This correlation

is largely based on the results of model footing experiments. It shows that d_c increases with foundation depth until reaching a normalised depth, D/B, of 10, after which it remains constant. It is worth noting that the maximum value of d_c was partly determined by the results from cavity expansion analysis. The curve shown in Figure 6.50 does not distinguish between different footing shapes or different footing roughness. It is therefore commonly applied to all footing types and in this respect B refers to the half width of strip and rectangular footings and the radius of circular footings.

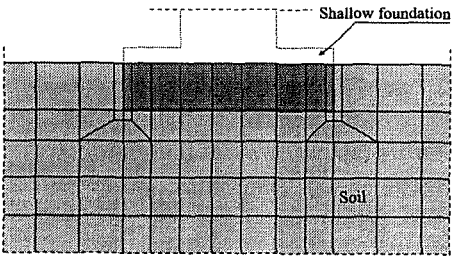

Figure 6.48: General finite element modelling of shallow foundations

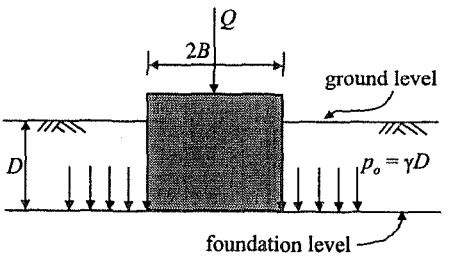

Figure 6.49: General loading scheme for shallow foundations

To investigate the effect of footing depth a series of finite element analyses have been performed with D/B = 0, 2, 4, 6, 8 and 10. Both smooth and rough strip and circular footings have been analysed. A typical finite element mesh, for D/B=8, is shown in Figure 6.51. Due to symmetry only half the geometry is modelled. As with the undrained analyses presented in Section 6.5.4.2, the clay was modelled as an elastic Tresca material with E=100MPa, μ=0.49, S_u=100kPa, K_o=1 and γ_{sat}=20KN/m^3.

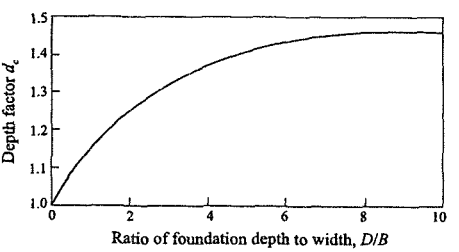

Figure 6.50: Skempton's relationship for depth factor

The foundation itself was not modelled and therefore displacement boundary conditions were applied to that part of the mesh boundary adjacent to the footing, see Figure 6.51. For a smooth footing zero horizontal displacements were applied along 'ab', while increments of downward vertical displacement were applied along 'bc'. For a rough footing zero horizontal displacements and increments of vertical displacement were applied along 'abc'.

If the mesh shown in Figure 6.51 is used to analyse a rough circular footing, then the ultimate footing load is 16500kN. Assuming that the full undrained shear strength of the soil is mobilised in shear along the side of the footing, and noting

that the diameter of the footing is 2m and its depth below the ground surface is 8m, gives a shear force on the side of the footing of 2x8xπx100=5026kN. Taking this value away from the total footing load at failure gives the contribution from the base of the footing as 11474kN. Comparing this with the ultimate load from a similar analysis performed with the footing at the surface implies a depth factor, d_c of 5.6. This value is considerably larger than that given in Figure 6.50.

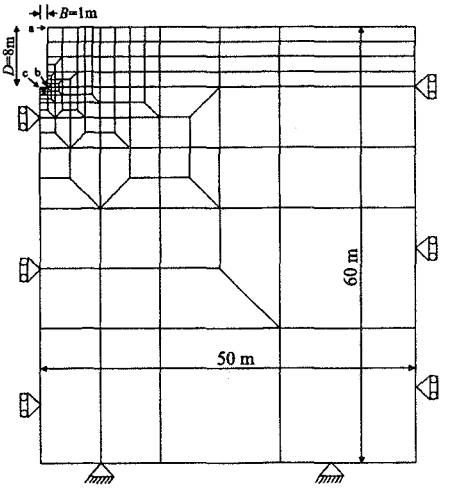

Figure 6.51: Finite element mesh used for analysis of depth factor

Closer inspection of the analysis indicates the shear stress mobilised along the side of the footing is too large. Summing the vertical nodal reactions along the side of the footing gives a force of 12686kN. This is considerably larger than the maximum value of 5026kN calculated above, assuming that the full undrained soil strength is mobilised in shear along the side of the footing.

At first, such a result might indicate some problem with the finite element program. However closer inspection of the analysis shows that at all integration points in the finite element mesh the stresses nowhere exceed the Tresca failure condition. The program is therefore functioning correctly. The problem arises because in the finite element method the stresses are only sampled at integration points. While they may obey the failure condition at these discrete points, the shape functions associated with the elements used might imply a variation of stresses over the element, which is not representative of those occurring in the real problem. In the present case eight noded elements have been used with 2x2 Gauss integration. This implies a linear variation of stresses, whereas in the axi-symmetric circular footing problem the shear stresses are likely to vary exponentially away from the side of the footing.

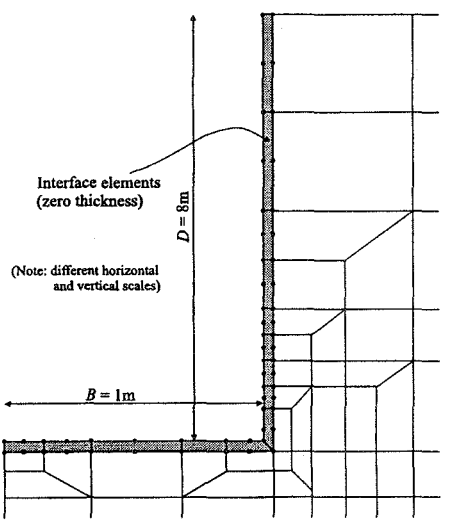

Figure 6.52: Detail of finite element mesh adjacent to footing

To overcome this problem thinner elements could be used to represent the soil immediately adjacent to the side of the footing. Alternatively, interface elements could be used, as shown in Figure 6.52. These are given normal and shear stiffnesses compatible with that of the soil (i.e. $K_n=K_s=10^5$kN/m^3) and a shear strength of 100kPa (i.e. the same as the soil). (Note that the vertical and horizontal scales are different in Figure 6.52 and that, for clarity, the zero thickness interface elements have been drawn with a finite thickness). Repeating the analysis now gives an ultimate footing load of 9307kN. The contribution from the shear stresses on the sides of the footing is 4945kN, which is now less than the maximum possible value of 5026kN and therefore acceptable. (Note that for the maximum possible value to be mobilised, the major principal stress would have to make everywhere an angle of 45° to the vertical sides of the footing). Comparing the contribution from the base of the footing with that from a similar footing located at the ground surface gives a depth factor d_c of 2.2.

The above problem is less severe in the analyses of a rough strip footing and clearly does not occur in the analyses of both smooth strip and circular footings, as the shear stress along the side of the footing is zero.

While the analyses of the rough circular footing with interface elements is an improvement over the original analysis, it is still flawed as tensile horizontal total stresses are predicted between the sides of the footing and the adjacent soil. This is shown in Figure 6.53, which presents the distribution of total horizontal stress down the side of the footing at failure. These stresses are taken from the interface elements. If the soil is unable to sustain such tensile stresses then the analysis is unrealistic. In reality the soil is likely to separate from the footing, leaving a vertical crack.

To overcome this problem, the interface elements positioned down the side of the footing can be given a zero tensile strength. This means that they can sustain compressive normal stresses, but will open when the stress becomes zero, essentially modelling a

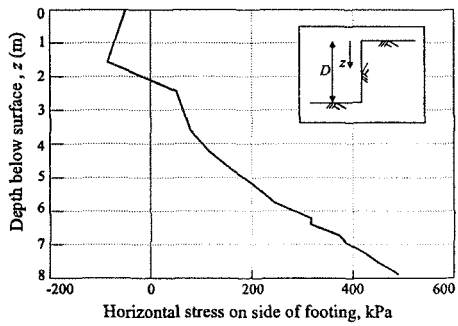

Figure 6.53: Horizontal total stress on side of footing with tension allowed in interface elements

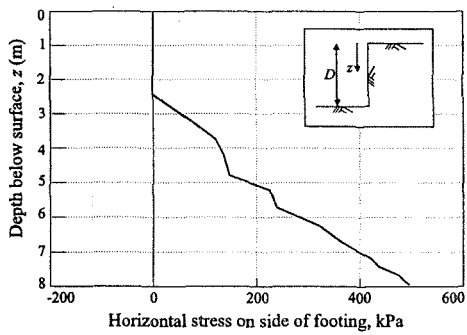

Figure 6.54: Horizontal total stress on side of footing with no tension allowed in interface elements

that the diameter of the footing is 2m and its depth below the ground surface is 8m, gives a shear force on the side of the footing of 2x8xπx100=5026kN. Taking this value away from the total footing load at failure gives the contribution from the base of the footing as 11474kN. Comparing this with the ultimate load from a similar analysis performed with the footing at the surface implies a depth factor, d_c of 5.6. This value is considerably larger than that given in Figure 6.50.

Closer inspection of the analysis indicates the shear stress mobilised along the side of the footing is too large. Summing the vertical nodal reactions along the side of the footing gives a force of 12686kN. This is considerably larger than the maximum value of 5026kN calculated above, assuming that the full undrained soil strength is mobilised in shear along the side of the footing.

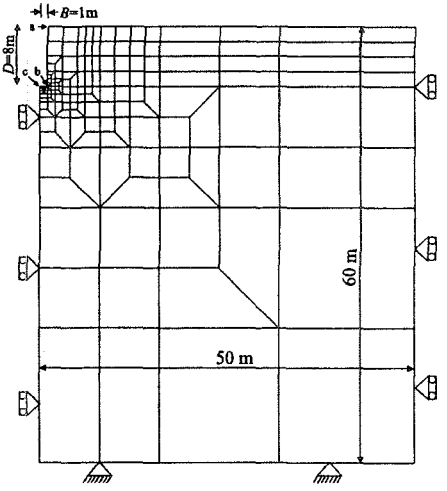

Figure 6.51: Finite element mesh used for analysis of depth factor

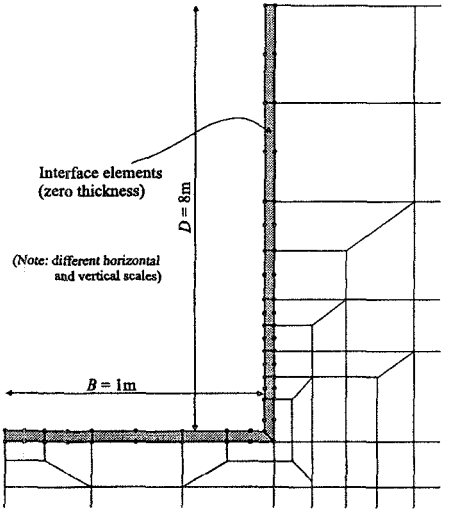

Figure 6.52: Detail of finite element mesh adjacent to footing

At first, such a result might indicate some problem with the finite element program. However closer inspection of the analysis shows that at all integration points in the finite element mesh the stresses nowhere exceed the Tresca failure condition. The program is therefore functioning correctly. The problem arises because in the finite element method the stresses are only sampled at integration points. While they may obey the failure condition at these discrete points, the shape functions associated with the elements used might imply a variation of stresses over the element, which is not representative of those occurring in the real problem. In the present case eight noded elements have been used with 2x2 Gauss integration. This implies a linear variation of stresses, whereas in the axi-symmetric circular footing problem the shear stresses are likely to vary exponentially away from the side of the footing.

To overcome this problem thinner elements could be used to represent the soil immediately adjacent to the side of the footing. Alternatively, interface elements could be used, as shown in Figure 6.52. These are given normal and shear stiffnesses compatible with that of the soil (i.e. $K_n=K_s=10^5$kN/m^3) and a shear strength of 100kPa (i.e. the same as the soil). (Note that the vertical and horizontal scales are different in Figure 6.52 and that, for clarity, the zero thickness interface elements have been drawn with a finite thickness). Repeating the analysis now gives an ultimate footing load of 9307kN. The contribution from the shear stresses on the sides of the footing is 4945kN, which is now less than the maximum possible value of 5026kN and therefore acceptable. (Note that for the maximum possible value to be mobilised, the major principal stress would have to make everywhere an angle of 45° to the vertical sides of the footing). Comparing the contribution from the base of the footing with that from a similar footing located at the ground surface gives a depth factor d_c of 2.2.

The above problem is less severe in the analyses of a rough strip footing and clearly does not occur in the analyses of both smooth strip and circular footings, as the shear stress along the side of the footing is zero.

While the analyses of the rough circular footing with interface elements is an improvement over the original analysis, it is still flawed as tensile horizontal total stresses are predicted between the sides of the footing and the adjacent soil. This is shown in Figure 6.53, which presents the distribution of total horizontal stress down the side of the footing at failure. These stresses are taken from the interface elements. If the soil is unable to sustain such tensile stresses then the analysis is unrealistic. In reality the soil is likely to separate from the footing, leaving a vertical crack.

To overcome this problem, the interface elements positioned down the side of the footing can be given a zero tensile strength. This means that they can sustain compressive normal stresses, but will open when the stress becomes zero, essentially modelling a

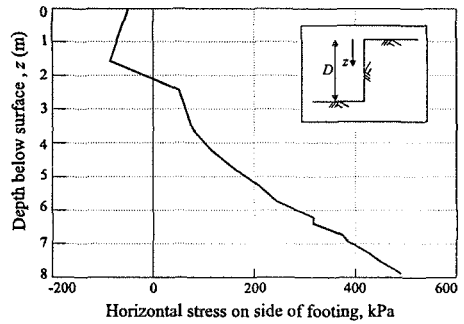

Figure 6.53: Horizontal total stress on side of footing with tension allowed in interface elements

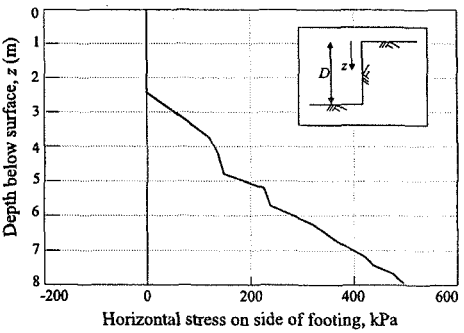

Figure 6.54: Horizontal total stress on side of footing with no tension allowed in interface elements

vertical crack. The distribution of horizontal total stress down the side of the footing at failure, from an analysis performed with such interface elements, is shown in Figure 6.54. Zero tensile stresses are indicated to a depth of 2.5m below the ground surface and consequently separation occurs over this depth. The ultimate footing load from this analysis was 8613kN and the depth factor $d_c = 2.14$.

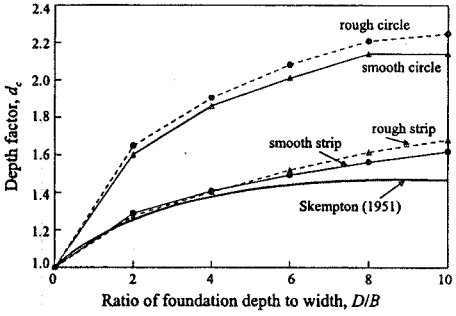

Figure 6.55: Depth factor from FE study compared to Skempton's relationship

Potential separation of soil from the side of the footing also occurs for smooth footings. Analyses for such footings should therefore also include interface elements as shown in Figure 6.52. To model the smooth nature of the interface between the soil and footing, these elements are given very low shear stiffness and strength values (e.g. ideally zero values should be given). To model separation of the soil from the footing these elements are again given a bulk stiffness consistent with that of the soil and a zero tensile stress capacity.

Interface elements were used in all the analyses for the parametric study on the influence of foundation depth. The results of this study in terms of the variation of depth factor, d_c, against normalised foundation depth, D/B, are shown in Figure 6.55. Also shown on this figure for comparison is Skempton's curve. The results for the strip footing are in reasonable agreement with Skempton's curve, while those for the circular footing give higher values of d_c. This agrees with results from pile tests and the recent work of Randolph *et al.* (2000), which indicate higher values than implied by Skempton's curve.

6.6.3 Example: The leaning Tower of Pisa

6.6.3.1 Introduction

In 1989 the civic tower of Pavia, in Italy, collapsed without warning, killing four people. This prompted the Italian Minister of Public Buildings and Works to appoint a Commission to advise on the stability of the Pisa Tower, which was perceived to have a high risk of collapse. The Commission recommended closure of the Tower to the general public and this was instituted at the beginning of 1990. There was an immediate outcry by the Major and citizens of Pisa who, correctly, foresaw the damage that the closure would inflict on the economy of Pisa, heavily dependent on tourism as it is. In March 1990 the Prime Minister of Italy set up a new Commission to develop and implement measures for stabilising the Tower. One of the early decisions of the Commission was to develop a numerical model of the Tower and the underlying ground that could be used to assess the effectiveness of various possible remedial measures. The purpose of this section

is to describe this model, the work that went into its calibration and how it was used to investigate both the temporary lead counterweight solution and some of the various permanent solution options.

The only practical means of calibrating the model was to attempt to get it to match the history of inclination of the Tower during and subsequent to its construction. Therefore, the first part of this section is devoted to a brief description of the history of the Tower. The differences between bearing capacity failure and leaning instability are then discussed before the numerical model is described and some of the results presented. Further details of the analyses can be found in Burland and Potts (1994) and Potts and Burland (2000).

6.6.3.2 Details of the Tower and ground profile

Figure 6.56 shows a cross-section through the Tower. It is nearly 60m high and the foundations are 19.6m in diameter. The weight of the Tower is 14500t. At present the foundations are inclined due south at 5.5° to the horizontal. The average inclination of the axis of the Tower is somewhat less, due its slight curvature. The seventh cornice overhangs the first cornice by about 4.1m.

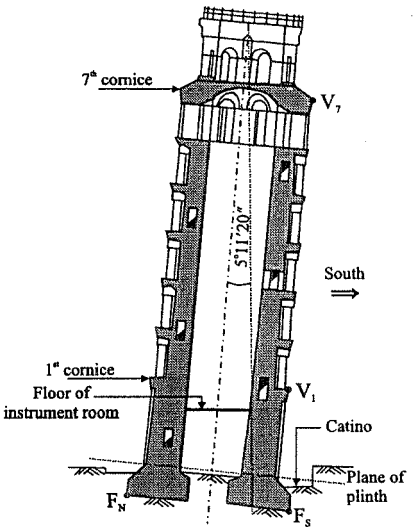

Figure 6.56: Schematic cross-section through Pisa Tower

Construction is in the form of a hollow cylinder. The inner and outer surfaces are faced with marble, and the annulus between these facings is filled with rubble and mortar within which extensive voids have been found. A spiral staircase winds up within the annulus. Figure 6.56 clearly shows that this staircase forms a large opening on the south side, just above the level of the first cornice where the cross section of the masonry reduces. The high stresses within this region are a major cause of concern and could give rise to an instantaneous buckling failure of the masonry without warning. In the summer of 1992 this masonry was stabilised by applying lightly prestressed steel strands around the Tower in the vicinity of the first cornice. At present, the masonry is being consolidated by grouting and the temporary steel strands will soon be reduced in number.

Figure 6.57 shows the ground profile underlying the Tower. It consists of three distinct horizons, the properties of which are described in detail later in this chapter and in AGI (1991). Horizon A is about 10m thick and primarily consists of estuarine deposits laid down under tidal conditions. As a consequence, the soil

types consist of rather variable sandy and clayey silts. At the bottom of Horizon A is a 2m thick medium dense fine sand layer (the upper sand). Based on sample descriptions and piezocone tests the material to the south of the Tower appears to be more silty and clayey than to the north and the sand layer is locally thinner.

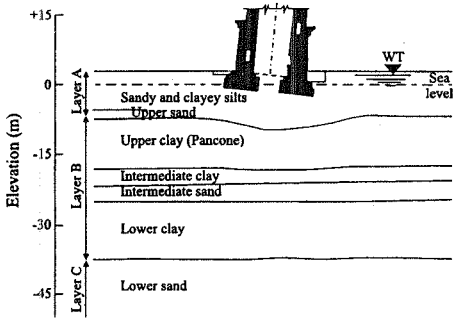

Figure 6.57: Soil profile beneath Pisa Tower

Horizon B consists of marine clay which extends to a depth of about 40m. It is subdivided into four distinct layers. The upper layer is a soft sensitive clay known as the Pancone. It is underlain by a layer of stiffer clay (the intermediate clay), which in turn overlies a sand layer (the intermediate sand). The bottom of Horizon B is a normally consolidated clay known as the lower clay. Horizon B is laterally very uniform in the vicinity of the Tower.

Horizon C is a dense sand which extends to a considerable depth (the lower sand). The water table in Horizon A is between 1m and 2m below the ground surface. Pumping from the lower sand has resulted in downward seepage from Horizon A, with a vertical pore water pressure distribution through Horizon B slightly below hydrostatic.

The many borings beneath and around the Tower show that the surface of the Pancone clay is dished beneath the Tower, from which it can be deduced that the average settlement is approximately 3m.

6.6.3.3 History of construction

The Tower is a campanile for the Cathedral, construction of which began in the latter half of the 11th century. Work on the Tower began on 9th August 1173 by the modern calendar. By about 1178 construction had progressed to about one quarter of the way up the fourth storey when work stopped. The reason for the stoppage is not known, but had it continued much further the foundations would have experienced an undrained bearing capacity failure. The work recommenced in about 1272, after a pause of nearly 100 years, by which time the strength of the ground had increased due to consolidation under the weight of the Tower. By about 1278 construction had reached the 7th cornice, when work again stopped due to military action. Once again there can be no doubt that, had work continued, the Tower would have fallen over. In about 1360 work on the bell chamber was commenced and was completed in about 1370 - nearly 200 years after commencement of the work.

It is known that the Tower must have been tilting to the south when work on the bell chamber began, as it is noticeably more vertical then the remainder of the Tower. Indeed, on the north side there are four steps from the seventh cornice up

to the floor of the bell chamber, while on the south side there are six steps. Another important detail of the history of the Tower is that in 1838 a walk-way was excavated around the foundations. This is known as the catino and its purpose was to expose the column plinths and foundation steps for all to see, as was originally intended. This activity resulted in an inrush of water on the south side, since here the excavation is below the water table, and there is evidence to suggest that the inclination of the Tower increased by as much as a half of a degree as a result.

6.6.3.4 *History of tilting*

As mentioned in the Introduction, the only possible means of calibrating a model of the Tower is to attempt to simulate the history of tilting of the Tower during and subsequent to its construction. Hence it was necessary to learn as much as possible about the history of the tilt of the Tower. The only reliable clues on the history of tilt lie in the adjustments made to the masonry layers during construction and in the shape of the axis of the Tower.

Based on the measured thickness of each masonry layer and a hypothesis on the manner in which the masons corrected for the progressive lean of the Tower, Burland (see Burland and Potts (1994)) deduced the history of inclination of the foundations of the Tower shown in Figure 6.58. In this figure the weight of the Tower is plotted against the deduced inclination. During the first phase of construction to just above the third cornice (1173 to 1178), the Tower inclined slightly to the north. The northward inclination increased slightly during the rest period of nearly 100 years to about 0.2°. When construction recommenced in about 1272, the Tower began to move towards the south and accelerated shortly before construction reached the seventh cornice in about 1278 when work again ceased, at which stage the inclination was about 0.6° towards the south. During the next 90 years the inclination increased to about 1.6°. After the completion of the bell tower in about 1370, the inclination of the Tower increased significantly. In 1817, when Cressy and Taylor made the first recorded measurement with a plumb line, the inclination of the Tower was about 4.9°. The excavation of the catino in 1834 appears to have caused an increase in inclination

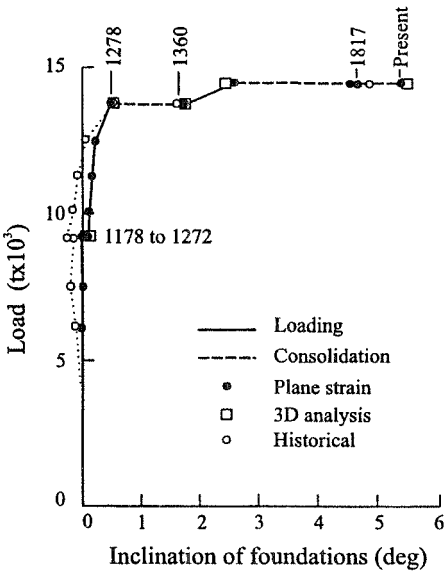

Figure 6.58: Predicted and historical inclination of the Tower during and after construction

of approximately 0.5° and the present day inclination of the foundations is about 5.5°. It can be seen from Figure 6.58 that significant inclination of the Tower only began once the height exceeded the sixth cornice. If the inclination had been due to much more compressible ground beneath one side than the other, it would have developed much earlier. Therefore, another explanation for the rapid onset of inclination is required and will be discussed later. It is the history of inclination depicted in Figure 6.58 which was used to calibrate the numerical models described later in this section.

For most of this century the inclination of the Tower has been increasing. These changes in inclination are extremely small compared with those that occurred during and immediately following construction. The rate of inclination of the Tower in 1990 was about 6 seconds per annum. The cause of the continuing movement is believed to be due to fluctuations of the water table in Horizon A. No attempt has been made to model these small movements.

6.6.3.5 The motion of the Tower foundations

Previously, studies have concentrated on the changes of inclination of the Tower. Little attention has been devoted to the complete motion of the foundations relative to the surrounding ground. The theodolite and precision levelling measurements made in the last century help to clarify this. These observations can be used to define the rigid-body motion of the Tower during steady-state rotation, as shown in Figure 6.59 (see Burland and Potts (1994)).

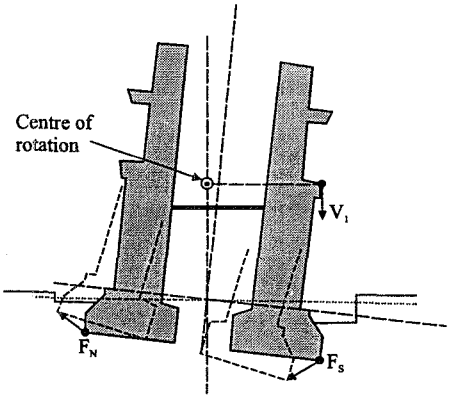

Figure 6.59: Motion of the Tower

It can be seen that the Tower is rotating about a point approximately located level with point V_1 and vertically above the centre of the foundation. The direction of motion of points F_N and F_S are shown by vectors and it is clear that the foundations are moving northwards with F_N rising and F_S sinking. It can therefore be concluded that the seat of the continuing long term tilting of the Tower lies in Horizon A and not within the underlying Pancone clay, as has widely been assumed in the past.

6.6.3.6 Stability of tall towers

Before considering the numerical analysis of the Pisa Tower, it is illuminating to consider the possible mechanisms of failure associated with the stability of the foundations of a tall tower. There are two possible mechanisms that could account for failure of such a tower: (i) bearing capacity failure due to insufficient soil strength, and (ii) leaning instability due to insufficient soil stiffness. Bearing

capacity failure is the more common type of instability and the one covered in most text books and codes of practice. All the analyses presented so far in this chapter showed this type of failure. Leaning instability is not so common and is only relevant to tall structures. It occurs at a critical inclination when the overturning moment, generated by a small increase in inclination, is equal to or greater than, the resisting moment of the foundations generated by the same rotation. In all but the simplest of cases it is difficult, probably impossible, to analyse without using numerical analysis.

These two alternative failure mechanisms are best demonstrated by a simple example. Figure 6.60 shows a simple tower resting on a uniform deposit of undrained clay. The clay is modelled as a linear elastic Tresca material, with an undrained strength S_u=80kPa. The dimensions of the tower are similar to those of the Pisa Tower. To trigger a rotation failure some initial defect (imperfection) must be present. In this example the tower was given an initial tilt of 0.5° (i.e. the initial geometry of the tower had a tilt). The self weight of the tower was then increased gradually in a plane strain large displacement finite element analysis.

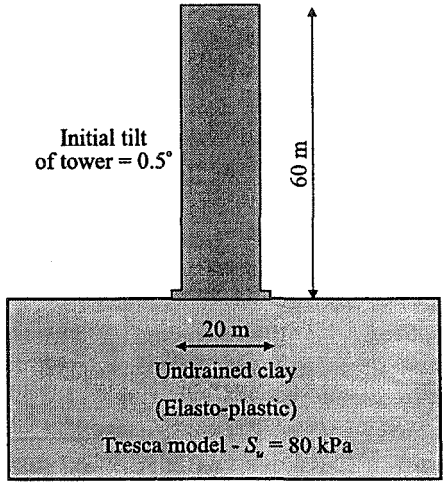

Figure 6.60: Geometry of simple tower

Three analyses were performed, each with a different value of shear stiffness, G, of the soil, and the results are presented in Figure 6.61. Here the increase in rotation of the tower above the initial 0.5° imperfection is plotted against weight of the tower, for analyses with G/S_u values of 10, 100, 1000. Real soils are likely to have properties such that they lie between the two extreme values. It should be noted that in all cases the strength of the soil S_u was 80kPa. The results show that failure occurs very abruptly, with little warning and that the weight of the tower at failure is dependent on the shear stiffness of the soil. The weight at failure for the analysis with the softer soil, G/S_u=10, is about half of that for the analysis with the stiffest soil, G/S_u=1000.

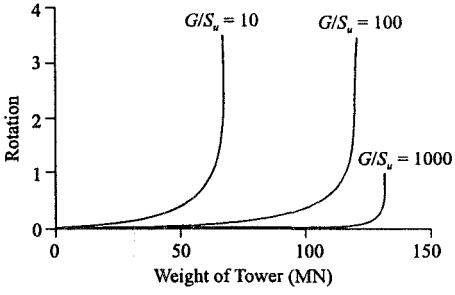

Figure 6.61: Rotation of simple tower for varying soil stiffness

It is of interest to examine the analyses with the two extreme values of G/S_u in more detail. In particular, it is instructive to consider what is happening in the soil at failure. Figure 6.62 shows vectors of incremental displacements for the soft soil. The vectors represent the magnitude and direction of the displacements from the last increment of the analysis. This figure shows that the movements are located in a zone below the foundation and indicate a rotational type of failure. At first sight this looks like a plastic type collapse mechanism. However, examination of the zone in which the soil has gone plastic (also shown on Figure 6.62), indicates that it is very small and not consistent with a plastic failure mechanism. Consequently, this figure indicates a mechanism of failure consistent with a leaning instability.

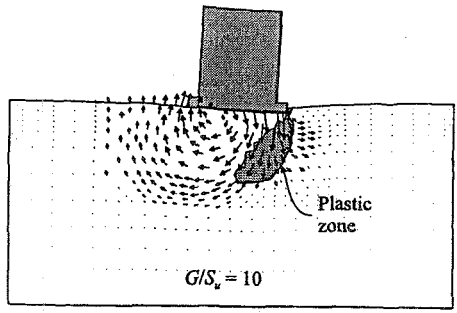

Figure 6.62: Pattern of movement at failure for soil with a low stiffness

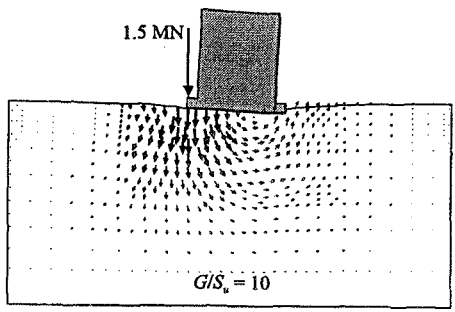

Figure 6.63: Effect of counterweight for soil with a low stiffness

In view of the temporary counterweight scheme, which involved adding lead weights to the north side of the Pisa Tower and which will be discussed in more detail later in this chapter, it is of interest to examine the response of the simple tower in the above example if, at the point of collapse, weight is added to the higher side of the foundation. The effect of a 1.5MN/m load is shown in Figure 6.63. Again vectors of incremental displacement are shown. These indicate the nature of the movements due only to this additional load. It is noted that under this load the sense of movement is reversed and the tower rotates back and collapse is arrested.

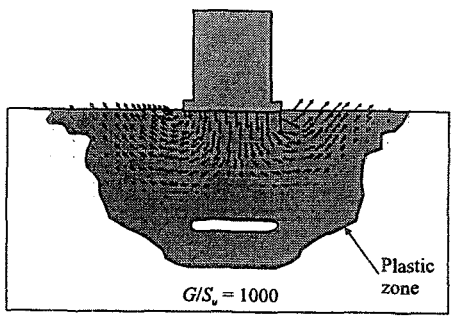

Figure 6.64: Pattern of movement at failure for soil with a high stiffness

Considering the results from the analysis performed with the stiffer

soil, vectors of incremental displacement just before collapse are shown in Figure 6.64. The mechanism of failure indicated by these vectors is very different to the one shown in Figure 6.62 for the softer soil. Instead of the soil rotating as a block with the foundation, the vectors indicate a more traditional bearing capacity type mechanism, with the soil being pushed outwards on both sides. The plastic zone, also indicated on Figure 6.64, is very large and therefore the results clearly indicate a plastic bearing capacity type mechanism of failure.

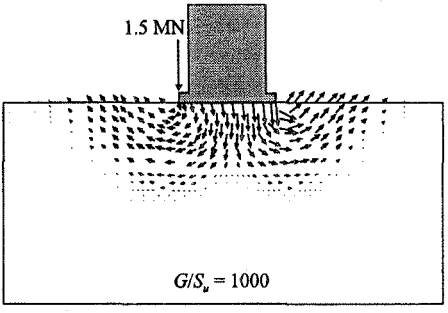

Figure 6.65: Effect of counterweight for soil with a high stiffness

If, as before, load is applied to the higher side of the foundation at the point of collapse, the vectors of incremental displacement given in Figure 6.65 are obtained. These show that, in contrast to the softer soil analysis, the tower continues to increase its inclination. In fact, it was not possible to obtain a converged solution when the weight was added. The addition of the load initiates collapse even though the load acts to reduce the overturning moment.

As well as demonstrating the difference between the two types of instability, these analysis also indicate that a counterweight type scheme will only be beneficial to the Pisa Tower if it is suffering a predominately leaning instability. To complicate matters further, real soils are likely to have stiffness values between the two extremes considered above and therefore both mechanisms of behaviour are likely to be active to some degree. In this respect the motion of the Pisa Tower discussed in Section 6.6.3.5 and shown in Figure 6.59 is more consistent with the movements shown in Figure 6.63 than those shown in Figure 6.65, indicating that the Tower is probably suffering predominately from a leaning instability.

6.6.3.7 Soil properties

The constitutive model chosen for the clay strata was a form of modified Cam clay (Roscoe and Burland (1968)), in which the shapes of the yield and plastic potential surfaces in the deviatoric plane are given by a Mohr-Coulomb hexagon and a circle respectively (see Section 7.9 of Volume1). For the sand layers a Mohr-Coulomb model was used. Fully coupled consolidation for all the soil layers was incorporated into the analyses. In order to implement these models the following soil parameters are required:

- γ_{sat} - saturated unit weight,
- φ_{cs}' - critical state angle of shearing resistance,
- C_c - compression index (note $C_c = 2.3025\lambda$),

C_s - swelling index - taken as $0.1C_c$ (note $C_s = 2.3025\kappa$),
G/p_o' - elastic shear modulus,
e_1 - void ratio on the VCL when p'=1kPa (note $e_1 = v_1 - 1.0$),
k - permeability,
K_o - coefficient of earth pressures at rest,
OCR - overconsolidation ratio,
ν - angle of dilation (sands).

Given the above parameters, the value of the undrained strength S_u can be determined from Equation (6.9). In Horizon A (see below) S_u turned out to be a more reliable parameter than OCR and was therefore specified in its place.

The soil profile at Pisa was characterised in detail by the Polvani Commission (Ministero dei Lavori Pubblici 1971). Horizons A and B were divided into a number of sub-layers, the descriptions of which are as follows:

Horizon A:
MG Top soil and made ground,
A1 Loose to very loose yellow sandy silt to clayey silt without stratification,
A2 Uniform grey sand with interbedded clay layers, broken fossils - Upper sand,

Horizon B:
B1 Highly plastic grey clay with fossils,
B2 Medium plastic grey clay with fossils,
B3 Highly plastic grey clay with fossils,
B4 Dark grey organic clay,
B5 Blue grey to yellow silty clay with calcareous nodules,
B6 Grey, sometimes yellow, sand and silty sand - Intermediate sand,
B7 Medium to highly plastic clay, with fossils and thin sand layers in the upper part,
B8 Grey clay with frequent thin sand lenses,
B9 Blue grey silty clay with yellow zones; calcareous nodules; some dark organic clay at centre,
B10 Grey clay with yellow zones; fossils in the lower part.

Laterally Horizon B is very uniform. However, there is much evidence to show that in Horizon A, layer A1 changes from predominantly silty sands and sandy silts north of the Tower to clayey silts south of the Tower. There is also some evidence from piezocones that the Upper sand layer A2 thins just south of the Tower. A careful study of the detailed sample descriptions given in the Polvani Report suggests that beneath the Tower, in Horizon A, there exists a lense of clayey silt which thins from south to north.

It will become evident that it is the compressibility of the underlying soils which has played the dominant role in the historical behaviour of the Tower (i.e. leaning instability), so that emphasis is placed in this section on these properties. Two major programmes of thin wall sampling and testing have been carried out,

one in 1971 (at the instigation of the Polvani Commission) and another in 1986. The results of these studies have been summarised by Calabresi *et al.* (1993) and Lancellotta and Pepe (1990) respectively. Figures 6.66a, b and c show the experimental values of C_c^*, C_c and OCR respectively, where C_c^* is the compressibility of the reconstituted material - defined by Burland (1990) as the intrinsic compressibility. The values of C_c^* were derived from the correlation with the water content at the liquid limit, w_L, established by Burland. Also shown on Figure 6.66 are the sub-layers established by the Polvani Commission and described above. It can be seen from Figure 6.66a that the values of C_c^* are reasonably well defined for each sub-layer and the average values are shown by the vertical lines. It is of interest to note that sub-layer B7 is made up of two distinct soil types and should perhaps be considered as two separate sub-layers.

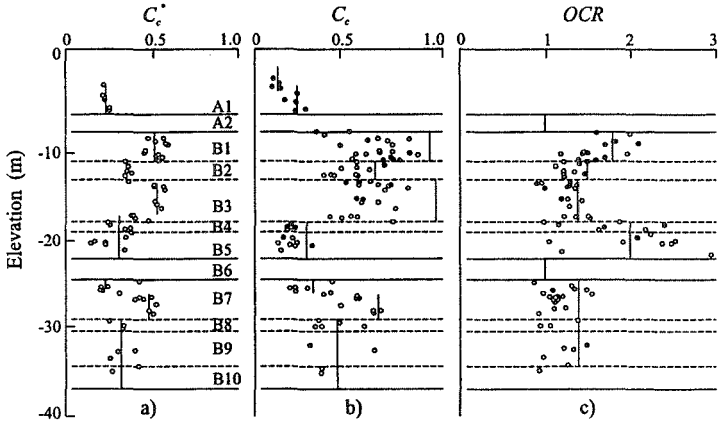

Figure 6.66: Experimental values of C_c^*, C_c and OCR; values used in the analysis are shown as full lines

It can be seen from Figure 6.66b that the experimental values of C_c, determined from high quality samples of the natural clay, show considerable scatter and it is not easy to decide on suitable representative values for analysis. The use of the intrinsic compressibility C_c^* has been particularly useful in this respect (Burland and Potts (1994)). It is well known that measured values of C_c are particularly sensitive to sample disturbance and the scatter in Figure 6.66b is a reflection of this. Nash *et al.* (1992) presented the results of oedometer tests on a sensitive marine clay from the Bothkennar test bed site and showed that the values of C_c obtained from high quality block samples were significantly higher than for other sampling methods including thin wall sampling. Nash's results showed that the measured values of C_c for the best samples were between 1.9 and 2.3 times larger than C_c^*. In Figure 6.66b the vertical lines were obtained by multiplying the average values of C_c^* by a factor depending on the plasticity of the material. For the Pancone clay (B1 to B3) the factor was 2, for the Lower clay (B7 to B10) the

factor was 1.5 and for Horizon A and the Intermediate clay (B4 and B5) the factor was unity. It is these values that have been used in the finite element analyses and it can be seen that they tend to lie at, or a little beyond, the upper limits of the experimental values, as is to be expected.

Figure 6.66c shows experimental values of *OCR*. The vertical lines are the values used in the finite element analyses. Values were chosen near to the upper limit of the experimental values, as the effect of sample disturbance is to reduce the value somewhat.

Table 6.5 gives the values of all the soil parameters that were used in the analyses. The mean values of φ_{cs}' for each sub-layer were obtained from undrained triaxial tests. κ/λ was taken as 0.1 for all the soil layers. The values of permeability were derived from the oedometer tests, taking values in the upper quartile of the range of results for each layer. The values of G/p_o' were chosen on the basis of experience with small strain testing of a wide variety of materials. The choice of values was not important for modelling the history of inclination of the Tower, but proved to be more crucial when predicting its response to small perturbations of load in its present condition. The water table was assumed to be 1m below ground level and in hydrostatic equilibrium - a condition that must have existed at the time of construction.

Table 6.5: Soil parameters used in the analysis

Layer	Elev. (m)	w_L (%)	γ_{sat} kN/m³	φ_{cs}'	ν	K_o	*OCR*	λ	ν_l	G/p_o'	k (m/s)
MG	+3.0	-	18.0	34°	17°	0.44	1.0	-	-	500	10^{-5}
A1″	+0.0	38	19.1	34°	-	1.0	vary	0.06	2.23	400	10^{-5}
A1′	vary	45	19.1	34°	-	1.0	vary	0.11	2.23	400	10^{-9}
A2	-5.2	-	18.2	34°	17°	0.44	1.0	-	-	1000	10^{-5}
B1	-7.4	75	17.3	26°	-	0.56	1.8	0.43	4.53	300	$5x10^{-10}$
B2	-10.9	55	17.8	26°	-	0.56	1.5	0.31	3.93	300	$5x10^{-10}$
B3	-12.9	85	16.7	26°	-	0.56	1.4	0.47	5.10	300	$5x10^{-10}$
B4	-17.8	68	20.0	28°	-	0.56	2.0	0.13	2.48	500	$2x10^{-10}$
B5	-19.0	45	20.0	28°	-	0.74	2.0	0.13	2.48	500	$2x10^{-10}$
B6	-22	-	19.1	34°	17°	0.44	1.0	-	-	1000	37168
B7(a)	-24.4	35	19.6	27°	-	0.55	1.4	0.15	2.67	300	$5x10^{-10}$
B7(b)	-26.0	80	17.8	27°	-	0.55	1.4	0.32	4.17	300	$5x10^{-10}$
B8	-29.0	53	19.1	25°	-	0.58	1.4	0.22	3.11	300	$3x10^{-10}$
B9	-30.4	55	19.1	25°	-	0.58	1.4	0.22	3.11	300	$3x10^{-10}$
B10	-34.4	50	19.1	25°	-	0.58	1.4	0.22	3.11	300	$3x10^{-10}$
C1	-37.0	-	-	-	-	-	-	-	-	-	perm

6.6.3.8 Finite element analysis

Geometry

It must be emphasised that a prime objective of the analysis was to develop an understanding of the mechanisms controlling the behaviour of the Tower. It was felt that until these had been clarified, it would be unhelpful to attempt highly sophisticated and time consuming three dimensional analysis. Accordingly, a plane strain approach was used initially, recognising that the interpretation of the results would require some care. Some of the earlier analyses were carried out using a large strain formulation, but it was found that this introduced time consuming complications in relation to the excavation of the catino and also relative ground water level changes (i.e. settlements exceeded the depth of the original ground water table). The results did not differ significantly from traditional infinitesimal strain analysis, which was therefore adopted for the work described here. Later a limited number of three dimensional analyses were carried out using the Fourier series aided finite element method (see Chapter 12 of Volume 1). The results of both the plane strain and three dimensional analyses are reported here.

The layers of the finite element mesh matched the soil sub-layering discussed above. The lower sand was assumed to be rigid but permeable. The full mesh, for the plane strain analyses, is shown in Figure 6.67 and extends laterally 100m either side of the axis of the Tower. In Horizon B the soil was assumed to be laterally homogeneous. However, a tapered layer of slightly more compressible material was incorporated into the mesh for layer A1 as shown in Figure 6.68, which shows a detail of the mesh in the vicinity of the Tower. The shaded elements beneath and to the south have the properties listed in Table 6.5 for layer A1′, with C_c=0.25 and k=10^{-9}m/s. The remaining elements in layer A1 have the properties listed for layer A1″, with C_c=0.15 and k=10^{-5}m/s. In applied mechanics terms the insertion of this slightly more compressible tapered layer beneath the south side may be considered to be an 'imperfection'.

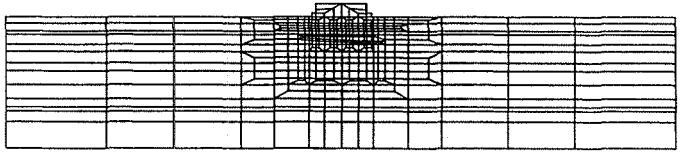

Figure 6.67: Finite element mesh

For the three dimensional Fourier series aided analysis the geometry is assumed to be axi-symmetric. However, the spatial distribution of soil properties and loading can be three dimensional. A mesh similar to that shown in Figure 6.67, but only considering the geometry to the right of the centre line of the Tower, was used. However, no tapered layer was incorporated to provide an 'imperfection'. Instead, the soil properties were assumed to vary linearly beneath the Tower in sub-layer A1. To the north of the Tower the properties were as listed for layer A1″

in Table 6.5, to the south as listed for layer A1′, and beneath the Tower they varied linearly from north to south from those listed for layer A1″ to those listed for layer A1′.

Note that, in modelling the foundation of the Tower, the central hole was neglected for the plane strain analysis, since it only represents a small proportion of the total area of the foundation.

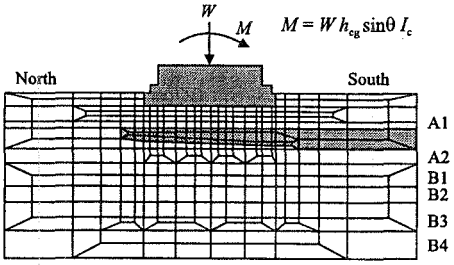

Figure 6.68: Finite element mesh close to Tower foundation

Foundation overturning moment

If any inclination θ of the Tower takes place, the centre of gravity moves horizontally and its weight W generates an overturning moment M. If the height of the centre of gravity above foundation level is h_{cg}, then:

$$M = W h_{cg} (\sin\theta) I_c \qquad (6.12)$$

I_c is a correction factor which takes account of the ratio between the second moments of area of a rectangular and a circular foundation. For a rectangular foundation of width 19.6m and the same area as the foundation of the Pisa Tower, the value of I_c for rotation about the centre is 1.266. For the three dimensional analyses in which the circular shape of the foundation is modelled I_c should theoretically be unity. Equation (6.12) was incorporated into the analysis such that any inclination of the foundations during or subsequent to construction automatically resulted in the application of an appropriate overturning moment to the foundations.

Analyses

All analyses involved coupled consolidation. The calibration analyses were carried out in a series of time increments in which loads were applied to the foundation to simulate the construction history of the Tower together with the rest periods, as summarised Section 6.6.3.4. During a construction period it was assumed that the load was applied at a uniform rate. The excavation of the catino was also simulated in the plane strain analysis.

The only factor that was adjusted to calibrate the model was the factor I_c in Equation (6.12). For the first run, the value of I_c was set equal to unity. At the end of the run the final inclination of the Tower was found to be less than the present value of 5.5°. A number of runs were carried out with successive adjustments being made to the value of I_c until good agreement was obtained between the actual and predicted value of the final inclination. It was found that, for the plane strain analysis with a value of $I_c = 1.27$, the final calculated inclination of the Tower was 5.44°. Any further increase in I_c resulted in instability of the Tower. It is therefore clear from this analysis that the Tower must have been very close to falling over.

The final value of I_c is very close to the theoretical value for rotation about the centroid, but this is probably coincidental.

For the three dimensional analysis a final inclination of 5.48° was obtained with a calibration factor I_c of 1.7. As noted above, theoretically I_c should be unity for these analyses. However, in these three dimensional analyses the excavation of the catino was not simulated.

6.6.3.9 Simulation of the history of inclination

Figure 6.69 shows a plot, from the plane strain analysis, of the predicted changes in inclination and settlement of the Tower with time since the start of construction in 1173. It is important to appreciate that the only point that has been pre-determined on this plot is the final inclination of about 5.5°. All other displacements were generated by the analysis. It can be seen that completion of the Tower up to the seventh cornice (~1278) results in quite small inclinations. It is only when the bell chamber is added in 1360 that the inclinations increase dramatically. Also of considerable interest is the fact that simulation of the excavation of the catino results in a significant increase in inclination of about ¾°. The final settlement of the foundations is seen to be about 3.8m, which is larger than the value deduced from the depression in the surface of the Pancone clay (Figure 6.57). The reason for this is thought to be due to the plane strain analysis. The depth of influence of a circular foundation would be less and would result in a smaller settlement.

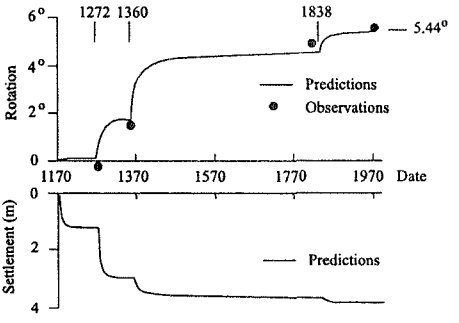

Figure 6.69: Relationship between time, inclination and settlement for plane strain simulation of the history of the Pisa Tower

The results of the analysis are also plotted on Figure 6.58 as a graph of load against inclination and can be compared with the deduced history. Again it must be emphasised that it is only the present inclination that has been fitted. The agreement between the simulated and historical behaviour is remarkable and gives considerable confidence in the reliability of the computer model. A striking difference is that the model does not predict the initial northerly inclination of the Tower. This is not felt to be of importance for the intended application of the model. It was found that, during the early stages of loading, the model did show a small inclination to the north. This was due to the fact that consolidation of the thin northern end of the tapered layer of compressible soil took place more rapidly than the thicker southern end. It should be possible to devise a soil profile in Horizon A that more accurately simulates the early history of inclination of the Tower, but this was outside the scope of the project.

Also shown on Figure 6.58 are the results from the three dimensional analysis.

It can be seen that the agreement between the plane strain and three dimensional analysis is very satisfactory. The final settlement for the three dimensional model is 3.1m, which is much closer to the deduced value than the plane strain model. Figure 6.70 shows zones of fully mobilised strength at the end of the plane strain analysis following complete pore water pressure dissipation after excavation of the catino. As mentioned previously, at this stage the Tower is in a state of unstable equilibrium. Surprisingly, there are no zones of contained failure within the Pancone clay, but there are extensive zones within Horizon A. The lowest zones are in the upper sand layer and result from the lateral extension of this layer. There is a large zone beneath and outside the southern edge of the foundation and a smaller zone underneath the northern side. It is evident from this figure that the impending instability of the Tower foundations is not due to the onset of a bearing capacity failure within the Pancone clay. The cause of the instability can be attributed to the high compressibility of the clay which results in leaning instability.

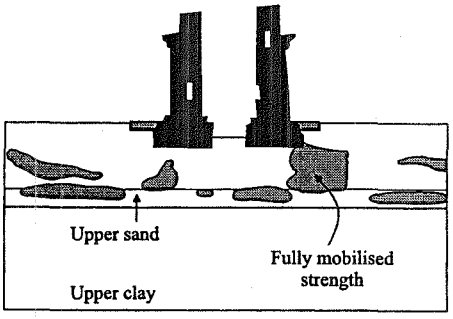

Figure 6.70: Zones of fully mobilised strength at the end of the analysis

Figure 6.71 shows the distribution of vertical effective contact pressure acting on the foundation, corresponding to complete pore water pressure dissipation after excavation of the catino in the plane strain analysis. The distribution is far from linear. Beneath the southern edge of the foundation the effective contact pressure is about 850kPa. At the northern edge the effective contact pressure is zero over approximately the first metre, but further south it increases rapidly.

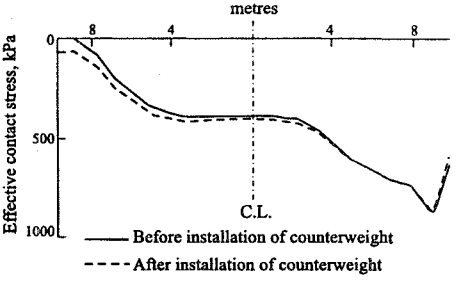

Figure 6.71: Distribution of effective foundation contact stress

In summary, the finite element models described above give remarkable agreement with the deduced historical behaviour of the Tower. It is important to emphasise that the history of foundation inclinations and overturning moments were self generated and were not imposed externally in a pre-determined way. The only parameter that was used to calibrate the model was the present inclination of the Tower. The analyses have demonstrated that the lean of the Tower results from the phenomenon of leaning instability due to the high compressibility of the

Pancone clay. The role of the tapered layer of slightly increased compressibility beneath the south side of the foundations in the plane strain analysis and the linear variation of properties assigned to sub-layer A1 in the three dimensional analysis, is to act as an 'imperfection'. Its principal effect is to determine the direction of lean rather than its magnitude. The model provides important insights into the basic mechanisms of behaviour and has proved valuable in assessing the effectiveness of various proposed stabilisation measures. Its role in evaluating the effectiveness of the temporary counterweight solution will now be described.

6.6.3.10 Temporary counterweight

Fully aware that the selection, design and implementation of permanent stabilisation measures for both the foundations and the masonry of the Tower would take a long time, the Commission took an early resolution to implement short-term temporary and fully reversible measures to increase slightly the stability of these elements (Burland *et al.* (1993)). The use of lightly prestressed steel tendons to stabilise the masonry was described earlier.

The similarity between the motion of the Tower depicted in Figure 6.59 and the movements associated with leaning instability shown in Figure 6.62 suggested a possible temporary means of increasing the stability of the foundation. The observation that the northern side of the foundation had been steadily rising led to the suggestion that application of load to the foundation masonry on the north side could be beneficial in reducing the overturning moment. Clearly, such a solution would not have been considered if it had not been recognised that leaning instability, rather than bearing capacity failure, was controlling the behaviour of the Tower. Before implementing such a solution it was obviously essential that a detailed analysis should be carried out. The purpose of such an analysis was two-fold: firstly to ensure that the proposal was safe and did not lead to any undesirable effects and secondly to provide a class A prediction which could be used to assess the observed response of the Tower as the load was being applied.

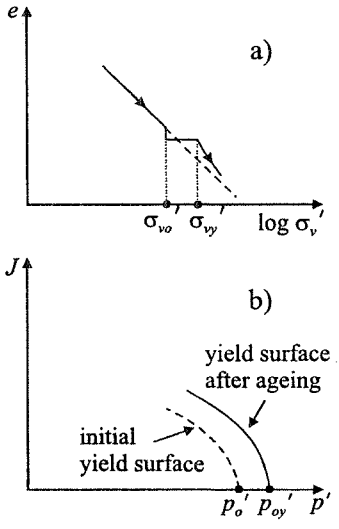

Figure 6.72: a) Increase in yield stress due to aging; b) general shift in the yield surface due to aging

Both the plane strain and three dimensional analyses were therefore extended to simulate the addition of a counterweight to the north side of the Tower. As explained by Potts and Burland (1994), before simulating the addition of the counterweight it was necessary to account for ageing of the clay layers over the past 100 years or so, since the end of construction. There is much evidence to show

that ageing significantly increases the stiffness of clays. For one dimensional compression Leonards and Ramiah (1959) showed that the process of ageing results in an increase in the yield stress σ_{vy}', as illustrated in Figure 6.72a. More generally a shift in the yield surface takes place as illustrated in Figure 6.72b. The parameters p_o' and p_{oy}' are the intersections with the p' axis of the yield surfaces of a 'young' and the 'aged' clay respectively. The ratio p_{oy}'/p_o' is a measure of the degree of ageing and is defined as the yield stress ratio. The effects of ageing can be introduced into the finite element analysis by increasing the current value of p_o' for each integration point to give a prescribed value of the yield stress ratio.

In the laboratory, significant ageing effects have been observed over periods of a few days. Leonards and Ramiah found that the yield stress ratio for a reconstituted clay that was allowed to age for about 90 days was as high as 1.3. In the present analysis the effect of introducing various values of yield stress ratio was studied. The results presented here are for a value of 1.05, which was felt to be conservative. It should be noted that ageing of the Pancone clay increases the stability of the Tower foundations significantly.

The full line in Figure 6.73 shows the predicted response of the Tower due the application of a counterweight to the foundation masonry, at an eccentricity of 6.4m to the north, after allowing ageing of the Pancone and Lower clays to give a yield stress ratio of 1.05. No ageing of Horizon A was assumed. The soil parameters are those given in Table 6.5. At the design load of about 690t the inclination of the Tower is predicted to reduce by about 27.5 seconds of arc with a settlement of 2.4mm. More importantly, the overturning moment is reduced by about 14%. In Figure 6.71 the broken line represents the predicted effective contact pressure beneath the foundation after application of the counterweight.

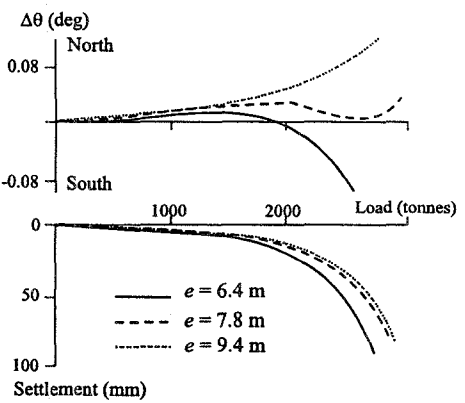

Figure 6.73: Predicted response of the Tower due to application of counterweight

Also shown in Figure 6.73 are the effects of increasing the load above the planned level and the results are of considerable interest. It can be seen from the full lines that, as the load is increased, the rate of increase of inclination to the north reduces, becoming zero at about 1400t. With further increase in load the movement reverses and the Tower begins to move towards the south. The settlement rate also begins to increase once the load exceeds 1400t. Figure 6.73 also shows the results of increasing the eccentricity of the counterweight. At an eccentricity of 9.4m (dotted lines) the Tower continues to rotate northwards as the counterweight is increased. At an intermediate eccentricity of 7.8m (broken lines) a curious response is obtained in which the Tower first moves northwards, then it

reverses and then reverses again. It can be seen that the settlement response is similar for each eccentricity. It would be wise to ensure that (irrespective of the eccentricity) a significant rate of increase of settlement is avoided as this implies the onset of yield.

6.6.3.11 Observed behaviour during application of the counterweight

A description of the counterweight scheme is given by Burland *et al.* (1993). It consists of a temporary prestressed concrete ring cast around the base of the Tower at plinth level. This ring acts as a base for supporting specially cast lead ingots which were placed one at a time at suitable time spans. The movements experienced by the Tower are measured with a highly redundant monitoring system.

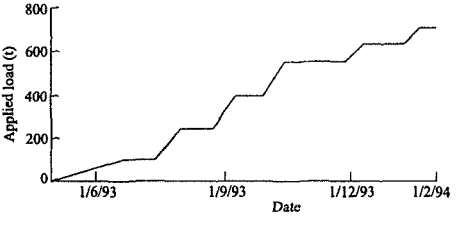

Figure 6.74: History of counterweight loading

Burland *et al.* (1994) describe the response of the Tower to the application of the counterweight. Construction of the concrete ring commenced on 3rd May 1993 and the first lead ingot was placed on 14th July 1993. Figure 6.74 shows the sequence of load application. It can be seen that, after construction of the concrete ring, the load was applied in four phases, with a pause between each phase to give time to observe the response of the Tower. The final phase was split in two either side of the Christmas break. The last ingot was placed on 20th January 1994.

Figure 6.75 shows a comparison of the class A predictions from the plane strain analysis and measurements of (a) the changes in inclination, and (b) the average settlements of the Tower relative to the surrounding ground during the application of the lead ingots. The points in Figure 6.75 represent the measurements at the end of each

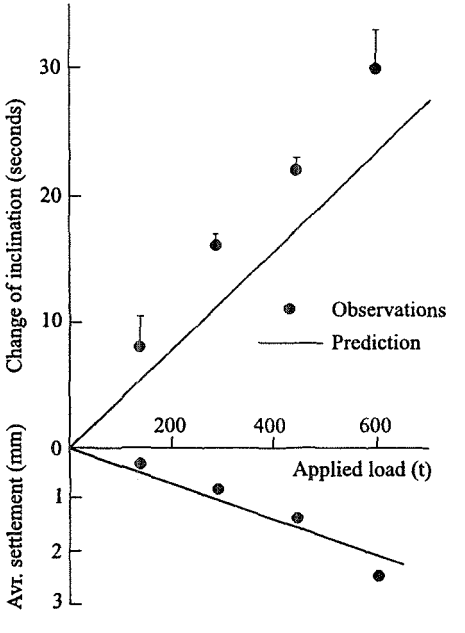

Figure 6.75: Plane strain prediction and observed response due to application of counterweight (class A prediction)

phase of loading and the vertical lines extending from them show the amount of creep movement between each phase. For the final phase the creep after one month is shown. It can be seen that the class A predictions of the computer model give changes in inclination which are about 80% of the measured values. However, the settlements are in excellent agreement with the measurements.

It is perhaps worth emphasising that the purpose of the model was to clarify some of the basic mechanisms of behaviour and it was calibrated against inclinations measured in degrees. The use of the model in studying the effects of the counterweight was to check that undesirable and unexpected responses of the Tower did not occur. In this respect the model has proved to be very useful. It has led to a consideration of the effects of ageing and it has drawn attention to the importance of limiting the magnitude of the load so as to avoid yield in the underlying Pancone clay. Also the beneficial effects of increasing the eccentricity have been highlighted.

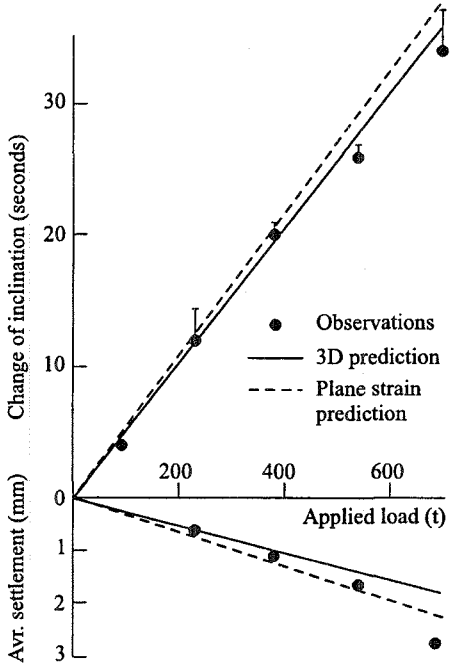

Figure 6.76: Comparison of the 3D and plane strain model for the application of the counterweight (class C prediction)

It is perhaps expecting too much of the model for it to make accurate quantitative predictions of movements which are two to three orders of magnitude less than those against which it was calibrated, and the fact that it has done as well as it has is remarkable. However, the observed movements due to the counterweight may be used to further refine the model. It has been found that the difference between the predicted and measured inclinations are due largely to the values of G/p_o' in Horizon A used in the analysis and given in Table 6.5. Considerably improved agreement can be obtained if the values of G/p_o' in Horizon A are reduced. By trial and error it was found that by reducing these values by a factor of 0.65, the northward rotation due to a counterweight of 6.9MN was increased to 37.5 arc seconds, which corresponds to the observed value one month after the application of the final lead weight. The results are shown in Figure 6.76 and the agreement with the observed rotations is much improved compared with Figure 6.75. It is of interest to note that the reduction in shear modulus in Horizon A only slightly increases the predicted settlement. The re-calibrated model is used in the remainder of this section.

The three dimensional analyses were carried out after the application of the counter-weight and the revised values of G/p_o' were incorporated in it. The predictions of the response of the three dimensional model to the application of the counterweight and comparison with the plane strain model is shown on Figure 6.76. Excellent agreement is achieved for the changes in inclination. The three dimensional model gives slightly smaller average settlements than the plane strain model.

6.6.3.12 Permanent stabilisation of the Tower

Several alternative options for permanent stabilisation of the Tower were considered and some of these were analysed using the numerical models described above. One of these options involved the installation of ten ground anchors on the north side of the Tower. Initially this was suggested as a replacement for the counterweight solution, however, its use as a permanent solution was also considered. Analysis of this option indicated that as the anchor loads increased, the Tower initially rotated towards the north, but that after a relatively small rotation it reverted to rapidly rotating towards the south. The associated settlements also increased rapidly at this point. In light of the results for the counterweight solution presented in Figure 6.73 such a result is perhaps not surprising.

Another permanent solution that was considered was the provision of a north pressing slab. This involved casting a concrete slab on the ground surface to the north of the Tower and loading it with ground anchors extending into the Lower sand. Numerical analysis of this option showed that large loads were required to cause modest rotations of the Tower and that under some loading scenarios the Tower could revert to rotating towards the south.

The numerical analysis therefore showed that neither of the above options were likely to be viable and consequently they were not pursued further. The permanent solution that was finally adopted involved soil extraction from under the north side of the Tower. This was extensively analysed and some of the results are presented below.

6.6.3.13 Soil extraction

Introduction

Under-excavation is the process whereby small quantities of soil are excavated locally by means of a specially designed drill, so as to leave a cavity which closes under the overburden pressure. Closure of the cavity results in localised subsidence of the overlying ground surface. The technique can be used for inducing controlled subsidence of a building.

The Commission considered the use of this method as a means of controlled reduction of the inclination of the Tower and the arrangement is shown schematically in Figure 6.77. There was considerable uncertainty about the response of the Tower to the process of soil extraction from beneath the north side of the foundation, as the Tower is very close to leaning instability. The purpose of

the numerical analyses presented here was to explore the response of the computer model of the Tower to under-excavation and to examine the stress changes that the process induces beneath the foundations and within the soil beneath the south side.

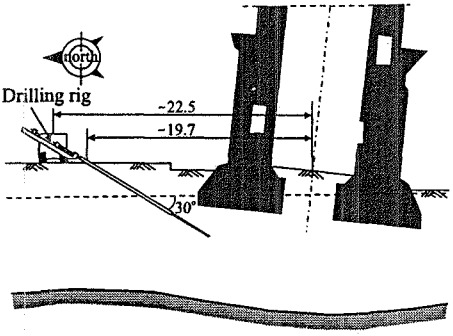

Figure 6.77: Schematic presentation of the soil extraction process

It should be emphasised that the finite element meshes had not been developed with a view to modelling under excavation. The individual elements are rather large for representing regions of extraction. To have repeated the whole analysis using a new finer mesh would have been both expensive and very time consuming. In any case, the purpose of the modelling was to throw light on the mechanisms of behaviour rather than attempt a somewhat illusory 'precise' analysis.

The objective of the simulation of the soil extraction process was to reduce the volume of any chosen element of ground incrementally, so as to achieve a pre-determined reduction in volume of that element. Localised soil extraction was modelled by selecting a chosen element in the finite element mesh, eliminating its stiffness and then progressively reducing its volume by the application of equal and opposite vertical nodal forces to its upper and lower faces so as to compress the element. The nodal forces were increased progressively until the desired volume reduction had taken place. The stiffness of the element was then restored. It is worth commenting on why only the vertical stresses were reduced. The actual operation of soil extraction is from a near horizontal element about 1m long and 0.2m diameter. With such a long thin element the boundary displacements will be primarily vertical. As mentioned above, the finite element mesh was not designed to simulate the process of soil extraction and the length to depth ratios of the elements are much smaller. So as to encourage vertical displacements of the upper and lower faces, only the vertical stresses were reduced. To date only plane strain analyses have been performed to simulate soil extraction.

Critical line

Simple studies carried out on one-g models on sand at Imperial College pointed to the existence of a *Critical line*. Soil extraction from any location north of this Critical line gave rise to a reduction in inclination, whereas extraction from south of the line gave rise to an increase in inclination. The first objective of the numerical analysis was to check whether the concept of a Critical line was valid.

Figure 6.78 shows the finite element mesh in the vicinity of the Tower. Elements numbered 1, 2, 3, 4 and 5 are shown extending southwards from beneath the north edge of the foundations. Five analyses were carried out in which each of the elements was individually excavated to give full cavity closure, and the

response of the Tower computed. For excavation of elements 1, 2 and 3 the inclination of the Tower reduced so that the response was positive. For element 4 the response was approximately neutral with an initial slight reduction in inclination which, with further excavation, was reversed. For element 5 the inclination of the Tower increased as a result of excavation.

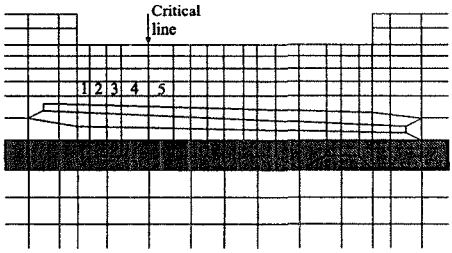

Figure 6.78: Excavated elements used to investigate the existence of the Critical line

The above analyses confirm the concept of a Critical line separating a positive response from a negative one. For the plane strain computer model the location of the Critical line is towards the south end of element 4, which is at a distance of 4.8m beneath the foundation of the Tower, i.e. about one half the radius of the foundations.

It was noted that, as the location of excavation moved further and further south beneath the foundation, the settlement of the south side steadily increased as a proportion of the settlement of the north side. Excavation of elements 1 and 2 gave a proportion of less than one quarter.

It is concluded from this study that, provided soil extraction takes place north of a Critical line the response of the Tower is positive, even though the foundations are close to leaning instability. For the plane strain model the Critical line is located about half the radius of the foundations south of the northern edge of the foundations. It is further concluded that it should be possible to keep the settlements of the south edge of the foundations to less than one quarter of the settlements at the north, provided soil extraction does not extend southwards by more than about 2m beneath the foundations.

Simulation of under-excavation process

Having demonstrated that localised soil extraction gives rise to a positive response, the next stage was to model a complete under-excavation intervention aimed at safely reducing the inclination of the Tower by at least 0.25°. A preliminary study of extraction was carried out, using a shallow inclined drill hole beneath the foundations. Although the response of the Tower was favourable, the stress changes beneath the foundations were large. Consequently, a deeper inclined extraction hole was investigated.

The inset in Figure 6.79 shows the finite element mesh in the vicinity of the foundations on the north side. The elements numbered 6 to 12 were used for carrying out the intervention and are intended to model an inclined drill hole. It should be noted that element 12 lies south of the Critical line established by localised soil extraction as described above. The procedure for simulating the under-excavation intervention was as follows:

a) The stiffness of element 6 was reduced to zero.
b) Equal and opposite vertical nodal forces were applied progressively to the upper and lower faces until the volume of the element had reduced by about 5%. The stiffness of the element was then restored.
c) The same procedure was then applied successively to elements 7, 8, 9, 10 and 11, thereby modelling the progressive insertion of the extraction drill probe. For each step the inclination of the Tower reduced.
d) When element 12 was excavated the inclination of the Tower increased, confirming that excavation south of the Critical line gave a negative response. The analysis was therefore re-started after excavating element 11.
e) The retraction of the drill probe was then modelled by excavating elements 10, 9, 8, 7 and 6 successively. For each step the response of the Tower was positive.
f) The whole process of insertion and extraction of the drill probe was then repeated. Once again excavation of element 12 gave a negative response.

The computed displacements of the Tower are plotted in Figure 6.79. The sequence of excavation of the elements is given on the horizontal axis. The upper diagram shows the change of inclination of the Tower during under-excavation and the lower diagram shows the settlements of the north and south sides of the foundation.

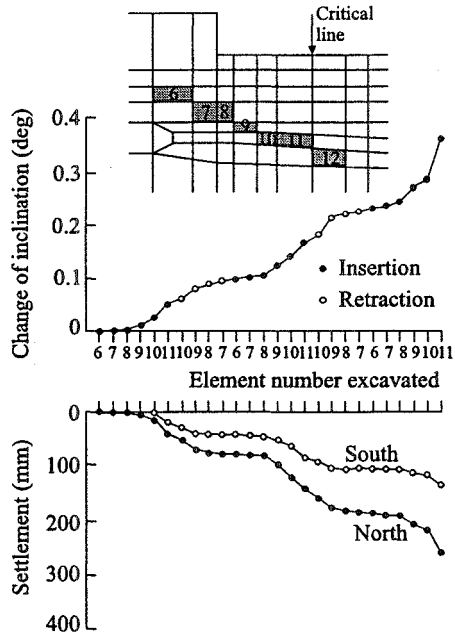

Figure 6.79: Response of Tower to soil extraction

It can be seen that as under-excavation progresses from elements 6 through to 11, the rate of change of northward inclination increases, as do the settlements. As the drill is retracted the rate decreases. At the end of the first cycle of insertion and extraction the inclination of the Tower is decreased by 0.1°. The settlement of the south side is rather more than one half of the north side. For the second cycle of insertion and extraction of the drill a similar response is obtained, but the change of inclination is somewhat larger. After the third insertion of the drill the resultant northward rotation was 0.36°. The corresponding settlements of the north and south sides of the foundation were 260mm and 140mm respectively.

Figure 6.80 shows the contact stress distributions at various stages of the under-excavation intervention. The process results in a small reduction of stress beneath the south side. Beneath the north side fluctuations in contact stress take place as is to be expected, but the stress changes are small.

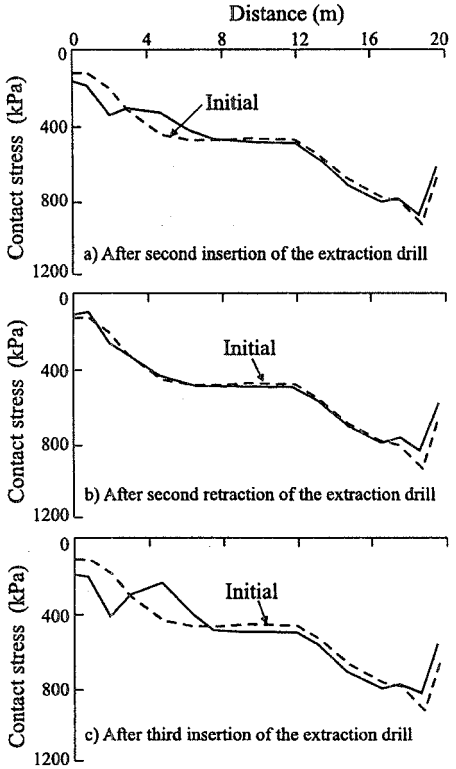

Figure 6.80: Effective contact stress distribution beneath the Tower foundation

6.6.3.14 The response of the Tower to soil extraction

The results of the modelling work were sufficiently encouraging to undertake a large-scale development trial of the drilling equipment. For this purpose a 7m diameter eccentrically loaded instrumented footing was constructed in the Piazza north of the Baptistry. Drilling was carried out using a hollow-stemmed continuous flight auger inside a contra-rotating casing. When the drill was withdrawn to form the cavity, an instrumented probe located in the hollow stem was left in place to monitor its closure. The trials showed that cavities formed in the Horizon A material closed gently and that continued extraction from the same location could

be achieved. The trial footing was successfully rotated by about 0.25° and directional control was maintained even though the ground conditions were somewhat non-uniform. The measured contact stress changes were very small.

In view of the encouraging results from the numerical analysis and the large-scale trial, the decision was taken by the Commission to carry out preliminary soil extraction beneath the north side of the Tower itself, with the objective of observing the response of the Tower to a limited and localised intervention. Preliminary soil extraction was carried out over a width of 6m, using twelve 200mm diameter boreholes. A target of a minimum of 20 arc seconds reduction in inclination was set as being large enough to demonstrate unequivocally the effectiveness of the method.

On 9th February 1999, in an atmosphere of great tension, the first soil extraction took place. For the first week the Tower showed no discernable response, but during the following tense days it began very gradually to rotate northwards. As confidence grew, the rate of soil extraction was increased. At the beginning of June 1999, when the operation ceased, the northward rotation was 90 arc seconds and by mid-September it had increased to 130 arc seconds. At that time three of the 97 lead ingots (weighing about 10t each) were removed and movement ceased.

During preliminary under-excavation soil extraction mainly took place outside the footprint of the foundation and locally only extended beneath the north edge of the foundation by about 1.5m. It is of interest that the southern edge of the foundation was observed to rise by about one tenth of the settlement at the north. This may be contrasted with the numerical model which predicted small settlements at the south. The reason for this difference may be due to the fact that a plane strain model was used, whereas the soil extraction process is highly three dimensional. It is hoped to study this in more detail. Whatever the reason, the uplift at the south is highly beneficial, as the volume of soil to be extracted is reduced and it seems likely that reduction of stress is taking place in this critical region.

Having demonstrated that soil extraction produced a positive response, the Commission formally approved the application of the method for permanent stabilisation. Using 41 extraction tubes, work on the full intervention commenced on 21st February 2000. It is estimated that it will take about eighteen months of careful soil extraction to reduce the inclination of the Tower by about half a degree, which will be barely visible. At the time of writing (July 2000) a reduction of inclination of 800 arc seconds has been achieved and the pattern of uplift at the southern edge has been maintained. There is still a long, tense journey ahead but without the positive results of the numerical analysis it is doubtful that this very sensitive operation on a Tower that is on the point of leaning instability would have been undertaken.

6.6.3.15 Comments

This section describes the development and calibration of two finite element computer models of the Pisa Tower and underlying ground using the modified Cam clay model with coupled consolidation. One of the models is plane strain and

the other is three dimensional. The choice of compressibility parameters turned out to be crucial and the use of the intrinsic compressibility C_c^* has proved useful in interpreting the results of oedometer tests. The main purpose of the model was to aid the understanding of the basic mechanisms of behaviour of the ground-structure interaction. Unlike most other attempts to simulate the behaviour of the Pisa Tower, the model is self consistent in that it generates its own overturning moment in response to any change of inclination.

Calibration of the model was achieved by ensuring that it gave the correct final inclination of the actual Tower. It is shown that the model is in remarkable agreement with the deduced historical inclinations of the Tower during and subsequent to construction. The results of the analysis confirm beyond reasonable doubt that the lean of the Tower is caused by a mechanism known as 'leaning instability', which results from the high compressibility of the underlying clays and is not related to strength. At an inclination of 5.44° the Tower is predicted to be in a state of unstable equilibrium, confirming that the actual Tower is very close to falling over.

The computer model has proved valuable in assessing the effectiveness of the north counterweight solution for temporally increasing the stability of the Tower foundations. Although the model was not developed with a view to making precise predictions of very small movements, nevertheless it predicted the response to the application of the counterweight with remarkable accuracy. The predicted reductions in inclination were about 80% of the observed ones and the settlements were almost exactly as predicted. The observed response of the Tower has been used to slightly refine the model for future use in assessing the effectiveness of various possible permanent solutions.

The technique of soil extraction is currently being used as means of inducing controlled subsidence on the north side of the Tower as a permanent solution. In view of the uncertainty about the response to soil extraction of a Tower close to leaning instability, it was essential to study the mechanisms of behaviour with the numerical model. A method of simulating local soil extraction was developed. Initial studies have demonstrated the existence of a Critical line north of which soil extraction leads to a positive response. The location of this Critical line appears to be about ½ a radius in from the north side.

The process of under excavation by means of an inclined drill was then simulated. A significant reduction in inclination of the model Tower was achieved. Moreover, it was shown that the changes in foundation contact stress distribution were very small. By confining soil extraction to a short distance beneath the north side, settlements beneath the south side can be kept to less than ¼ of those on the north side.

It can be concluded from the numerical studies that the technique of soil extraction offers a very positive method of permanently reducing the inclination of the Tower by as much as a ½°. This encouraging result led to a successful large scale field trial of the soil extraction technique. The technique is now being applied to permanently stabilise the Tower. At present (July 2000) a reduction of 800 arc

seconds has been achieved and the observed behaviour has been consistent with that predicted by the analyses. It is doubtful that this very sensitive operation on a Tower that is on the point of leaning instability would have been undertaken without the positive results of the numerical analysis.

6.7 Summary

1. Shallow foundations can have different shapes in plane. If they are long in one dimension, they are classified as strip foundations and can be analysed assuming plane strain conditions. If they are circular, they can be analysed either assuming axi-symmetric conditions, if the loading is vertical, or using the Fourier series aided finite element method for general loading. For other shapes a full 3D analysis is required.
2. When modelling surface foundations both the soil and the foundation should, in general, be discretised into finite elements. However, if the loading is vertical and the footing is assumed to be either very flexible or very stiff compared to the soil, further approximations can be made in which it is no longer necessary to include the foundation in the mesh.
3. The bearing capacity for a square surface footing is smaller than that of a circular footing.
4. Finite element analyses enable theoretical shape factors to be determined for surface foundations. These differ depending on the roughness of the footing, but in general agree with the empirical formulae used in most design manuals.
5. For drained soils there are three coefficients in the general bearing capacity equation, namely N_c , N_q and N_γ . For strip footings exact theoretical expressions are available for N_c and N_q . Only approximate solutions (e.g. stress fields) exist for N_γ. It has been shown that finite element analyses can recover the theoretical correct values of N_q , but more importantly such analysis provide considerable insight in to the values of N_γ. They have also indicated some surprising differences between the behaviour of strip and circular footings.
6. No design guidance is available for the undrained bearing capacity of pre-loaded strip foundations on clay. It has been shown how finite element analyses can be used to tackle this problem. It was concluded that for the majority of real situations it is unlikely that pre-loading will give rise to a substantial improvement in undrained bearing capacity.
7. Results of finite element analyses using the sophisticated MIT-E3 have been presented to show how the effects of observed anisotropic soil behaviour can be reproduced in finite element analyses. The effect of this anisotropic behaviour on the bearing capacity of both strip and circular surface foundations has been quantified by finite element analysis.
8. For shallow footings founded below the ground surface it is important to correctly model the interface between the sides of the footing and the soil. Interface elements are useful for this purpose, but must be given a zero tensile stress capacity, as well as the appropriate shear strength.

9. Finite element analyses indicate that the depth factors for circular footings are higher than for strip footings.
10. The example of the leaning Tower of Pisa has been used to demonstrate finite element analyses of shallow foundations. The difference between bearing capacity failure and leaning instability has been described. It was shown how finite element analyses were used in the decision making process for the temporary North weighting and permanent under-excavation schemes at Pisa.

7. Deep foundations

7.1 Synopsis

This chapter considers the analysis of deep foundations. It begins by considering axial and lateral loading of a single pile. The pros and cons of using interface elements at the pile shaft are considered, as are the effects of soil dilation. Analysis of pile groups are then discussed. A method of analysis and a design procedure, both based on the analysis of a single pile combined withe the use of superposition, are presented. The chapter finishes by considering the behaviour of bucket foundations subjected to pull-out loads. The effects of geometry, interface strength, anisotropic strength and position of load application are discussed.

7.2 Introduction

In the previous chapter surface and shallow foundations have been considered. While such foundations are usually adequate where the soils below the foundations are both strong and stiff and/or the foundation loading is light, they may not be appropriate in weak soils or in situations where the imposed loads are high. In such situations it is common to extend the foundations deeper into the soil. This has two beneficial effects, firstly soils usually become stronger and stiffer with depth such that bearing capacity increases, and secondly shear and lateral stresses can be mobilised on the sides of the foundation which provide additional resistance to support the applied loads.

Another reason for increasing the depth of a foundation is where pull-out forces have to be resisted. For example, the foundations for some offshore structures often have to resist upwards forces. This can be resisted by the shear and lateral stresses mobilised on the sides of a deep foundation.

The most common form of deep foundation is the pile. This can either be constructed first and then driven into the ground, or a hole can be bored and the pile cast in-situ. Driven piles can be constructed from steel, wood or reinforced concrete and come in many different cross-sectional shapes (e.g. circular, rectangular, H-shaped, etc.). Bored piles on the other hand are usually constructed from reinforced concrete. Sometimes an undersized hole is bored, a pile is then driven and grouted afterwards. There are clearly many other combinations of installation that are possible.

Piles are rarely used in isolation but are installed in groups. They are usually

connected at the soil surface by a pile cap, see Figure 7.1. There are therefore many parameters involved in the design of piled foundations, namely the cross-sectional size and the length of each pile, wether the piles are solid or just a tube, how they are to be installed, the spacing of the piles in the group and the nature of the connection of the piles to the pile cap.

Caissons sometimes offer an alternative to a pile group. They are essentially large hollow piles, see Figure 7.2. They can be precast or constructed in-situ. If they are precast, they are first placed in position on the soil surface. Due to their self weight some penetration occurs. Soil is then excavated from inside the caisson and, as this is continued, the caisson sinks into the ground. If they are built in-situ, the walls are constructed as excavation proceeds. They are often circular in plane, but not always, and usually have a much larger cross sectional area and a lower height to breadth ratio than a pile. Single caissons are often used as a foundation, for example to support bridge piers.

Bucket foundations are similar to caissons and, as their name suggests, they resemble inverted buckets, see Figure 7.3. They are a recent development and are used offshore where the structures they support impose a range of loading conditions including pull-out forces. They are sometimes used solely to resist pull-out forces and, when used for this purpose, are often called suction caissons. Installation into the sea bed usually involves the use of suction forces. For example, the bucket would be prefabricated on land, towed to site and placed on the sea bed. Due to its self weight some embedment would occur. The pressure in the water enclosed inside

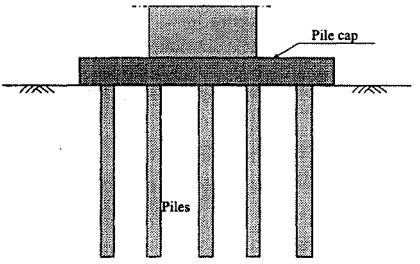

Figure 7.1: Piled foundation

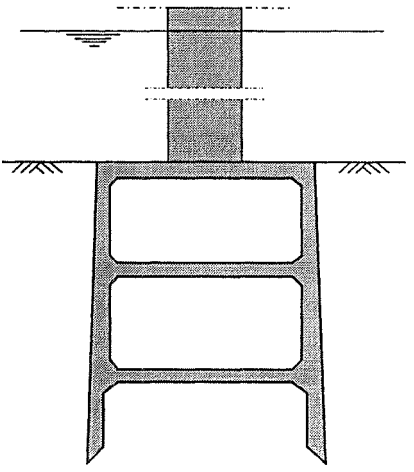

Figure 7.2: Caisson foundation

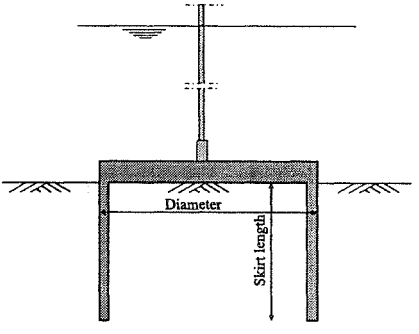

Figure 7.3: Bucket foundation

the bucket is then lowered by pumping, to cause a positive differential water pressure across the top of the bucket which forces the bucket into the soil. This process continues until the required embedment is obtained.

The analysis of single piles will be considered first in this chapter. This will be followed by the analysis of pile groups and then bucket foundations. As the analysis of a caisson has similarities with both that of a single pile and that of a bucket foundation it will not be specifically considered.

All analyses were performed using the Imperial College Finite Element Program (ICFEP). An accelerated modified Newton-Raphson scheme, with a sub-stepping stress point algorithm, was employed to solve the nonlinear finite element equations, see Chapter 9 of Volume 1. For the axi-symmetric and Fourier Series Aided Finite Element analyses (FSAFEM, see Chapter 12 of Volume 1) 8-noded isoparametric elements were used, with reduced (2x2) integration.

7.3 Single piles

7.3.1 Introduction

Although single piles are rarely installed in isolation, it is useful to consider their analysis, as this is similar to, but less complex than, the full analysis of a pile group. As will be discussed subsequently, the latter analyses are currently beyond the capacity of present computing resources for all but some very simple cases.

If the pile is circular in cross section, installed vertically in the ground, which has a horizontal lithology and horizontal water table, then the geometry to be analysed is axi-symmetric. If only vertical loading is applied to the pile then an axi-symmetric analysis is appropriate. However, if either inclined and/or moment loading is applied to the pile then a three dimensional analysis is required. As the geometry is axi-symmetric this can be performed with the computationally efficient FSAFEM. If any of the above conditions are not satisfied, for example the pile is not circular, or is not installed vertically in the ground, or the soil lithology is not horizontal, then a full 3D analysis using three dimensional finite elements must be used even if axial loads are applied to the pile.

For the remainder of this section the geometry will be assumed to be axi-symmetric. Consequently, for vertical loading axi-symmetric analysis, and for lateral loading three dimensional analysis using the FSAFEM, will be considered.

7.3.2 Vertical loading

One of the important issues when analysing a pile subject to vertical loading is the modelling of the interface between the pile and the soil adjacent to the pile shaft. As noted in Section 6.6.2, problems can arise if the elements representing the soil are too large and no interface elements are used. To overcome the problem it is important to either use thin solid elements in the soil adjacent to the pile shaft and/or use interface elements. However, for the pile problem care must be exercised when assigning material properties to the interface elements.

As an example consider the problem of 1m diameter and 20m long pile, installed in clay and loaded vertically under undrained conditions. The pile is assumed to be very stiff and the clay is represented by the Tresca model, with E_u=10^5 kN/m^2, μ=0.49 and S_u=100kN/m^2. The finite element mesh used for the analyses is shown in Figure 7.4 and consists of 1024 eight noded elements. It should be noted that relatively thin (0.05m wide) solid elements, with an aspect ratio of approximately 5 vertically to 1 horizontally, are used adjacent to the pile shaft. The pile itself is modelled with solid elements and behaves linear elastically, with a Young's modulus E=20x10^6 kN/m^2 and a Poisson's ratio μ=0.15. The loading of the pile is modelled by applying increments of vertical displacement to its top. The other boundary conditions consist of restricting both vertical and horizontal movements on the base of the mesh and the horizontal movements on the right hand side of the mesh and along the axis of symmetry (i.e. left hand side of the mesh). Initial stresses in the clay were calculated assuming a saturated bulk unit weight γ_{sat}=18kN/m^3 and coefficient of earth pressure at rest K_o=1.0.

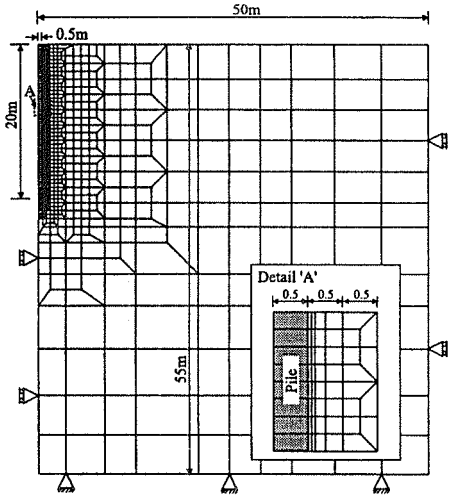

Figure 7.4: Finite element mesh for single pile analysis

In the first analysis no interface elements were used. The pile head load-displacement curve obtained from this analysis is shown in Figure 7.5. This figure also shows the mobilisation of shaft and base capacity with displacement. These capacities have been calculated from the nodal forces arising from the stress changes (from the beginning of the analysis) in the soil elements adjacent to the pile. In agreement with field observations the shaft capacity is mobilised much earlier than the base capacity. The analysis predicts an ultimate shaft capacity of 6345kN, which is not dissimilar to that obtained from the simple calculation in which the undrained strength is multiplied by the shaft area giving 6283kN. It is slightly on the high side due to the inherent problem of only sampling the stresses at integration points, which are not located on the pile-soil

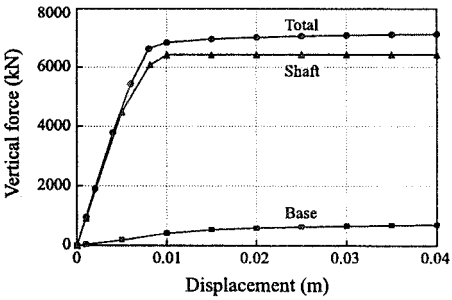

Figure 7.5: Undrained loading of a single pile without interface elements along its shaft

interface. This problem has been discussed in Section 6.6.2. The ultimate base capacity suggests a bearing capacity factor N_c=9.

Three further analyses were then performed, all of which used the finite element mesh shown in Figure 7.4, but with zero thickness interface elements positioned adjacent to the pile shaft and its base. The same soil properties as above were used and the interface elements were assigned an undrained strength S_u=100kN/m^2 (i.e. the same as the soil) and equal shear, K_s, and normal, K_n, stiffnesses. The only difference between the three analyses was the values assigned to K_s and K_n, these being 10^3 kN/m^3, 10^5 kN/m^3 and 10^7 kN/m^3 for each analysis respectively. As noted in Chapter 9 the choice of stiffness values for interface elements is problematic, especially because they have different units (kN/m^3) to those of the soil (kN/m^2).

The resulting total pile head load-displacement curves for the analyses with interface stiffnesses of 10^3kN/m^3 and 10^5kN/m^3 are compared with each other and with that obtained from the analysis with no interface elements in Figure 7.6. The analyses with an interface stiffness of 10^5kN/m^3 and no interface elements agree quite well, the former producing a slightly less stiff response and having a slightly smaller limit load. Closer inspection of the results indicates that the ultimate shaft capacity is now 6279kN, which is near to the value obtained from the simple calculation in which the undrained strength is multiplied by the shaft area (i.e. 6283kN). As the integration points for the interface elements are located on the pile-soil interface, the predicted shaft capacity is likely to be more accurate than that obtained from the analysis with no interface elements.

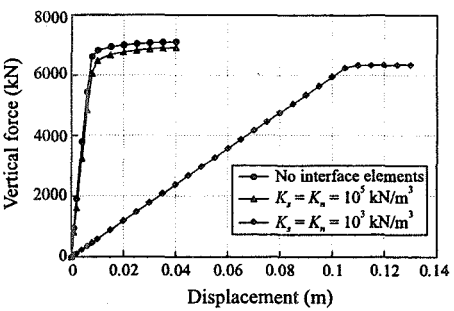

Figure 7.6: Effect of interface element stiffness on pile behaviour

The results from the analysis with an interface stiffness of 10^7 kN/m^3 are not shown on Figure 7.6 for clarity. During the early stages of loading the predicted load-displacement curve is indistinguishable from that of the analysis without interface elements. The ultimate load, however, is slightly smaller than that obtained from the latter analysis, but is in agreement with that from the analysis with an interface stiffness of 10^5 kN/m^3.

The analysis with the softer interface stiffness of 10^3 kN/m^3 predicts a much softer load-displacement curve, see Figure 7.6. It also does not appear to reach the same ultimate load. The reason for this can be seen in Figure 7.7, which shows the separate mobilisation of shaft and base resistance for this analysis. While the shaft resistance is fully mobilised at a displacement of 0.105m, the base resistance is extremely small and requires considerably more displacement before it becomes fully mobilised.

Clearly, the load-displacement behaviour is dominated by the stiffness of the interface elements. As it is difficult to measure interface stiffness, it might be concluded that the most sensible option is to use high stiffness values. However, as noted in Chapter 9, the use of too high a stiffness can lead to numerical ill-conditioning. A better alternative is probably not to use interface elements at all. As the comparison shown in Figure 7.6 indicates, the analyses with no interface elements produces adequate results. While this is acceptable when analysing piles subjected to only vertical loading, it may be necessary to include interface elements for other reasons, when a pile is subjected to lateral or combined loading. This will be discussed further in Section 7.3.3 of this chapter.

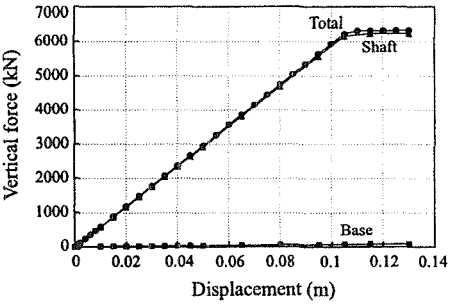

Figure 7.7: Undrained loading of a pile with soft interface elements

Drained analyses of this pile problem have also been performed. For these analyses the soil was modelled using the Moh- Coulomb model with E=10^5 kN/m^2, μ=0.3 and φ'=25°. Initial stresses in the soil were based on γ_{dry}=18kN/m^3 and K_o=1 and on the assumption that the soil was dry.

Load-displacement curves from two analyses, both without interface elements between the pile and the soil, are shown in Figure 7.8. The only difference between these two analyses is that in one the angle of dilation of the soil is v=25°, whereas in the other v=0°. As can be seen from this figure, the analysis with v=25° predicts much higher pile loads for a given displacement than the analyses with v=0°. The results are shown in more detail in Figures 7.9a and 7.9b, where the resistance from the pile shaft and the pile base have been separated. For the analysis with v=25° both the shaft and base components show no sign of reaching a limiting value, see Figure 7.9a. Even if the pile is subject to further displacement, there is no indication of either the shaft or the base resistance reaching a limiting value. In contrast, for the analyses with v=0° the shaft resistance has reached a limiting value at a displacement of 0.01m (δ/D=1%), see Figure 7.9b. The base capacity is, however, still increasing even at a displacement of 0.1m (δ/D=10% which is normally taken as a measure of pile failure in practice) and only reaches a limiting value (not shown in Figure 7.9b) when the pile displacement is 2.0m.

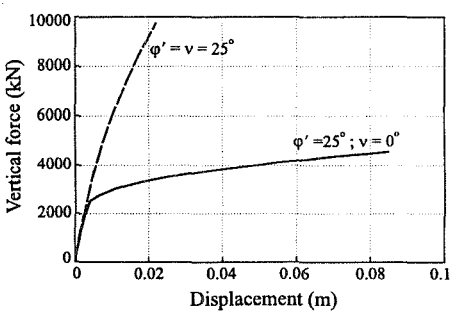

Figure 7.8: Drained loading of a single pile without interface elements along its shaft

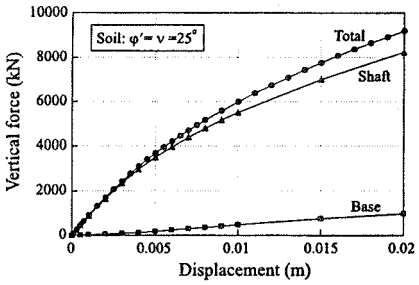

Figure 7.9a: Behaviour of a pile in drained soil with full dilation

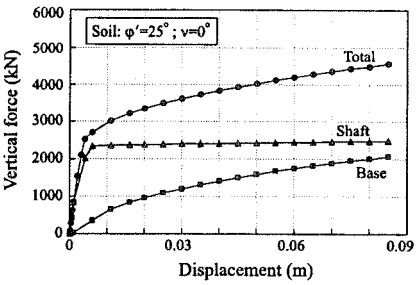

Figure 7.9b: Behaviour of a pile in drained soil with no dilation

The failure of the analysis with ν=25° to predict a limiting pile load is a consequence of the kinematically constrained nature of the problem, combined with the continued plastic dilation predicted by the Mohr-Coulomb model. The problem is not confined to this model but will occur with any constitutive model that predicts finite plastic dilation indefinitely, without reaching a critical state condition. This potential pitfall is discussed in greater detail in Chapter 9.

The use of interface elements between the soil and the pile can, in some respects, suppress the above shortcomings of the constitutive model used to represent the soil. For example, the drained analyses have been repeated with zero thickness interface elements adjacent to the pile. These elements were given a stiffness K_n=K_s=10^5 kN/m^3, an angle of shearing resistance φ'=25° and an angle of dilation ν=0°. The load-displacement curves are shown in Figure 7.10. As with the undrained analysis discussed above, the interface elements dominate the behaviour and the results of the analyses are much closer. Figures 7.11a and 7.11b show the mobilisation of the shaft and base resistance for the two analyses. There are differences in the base resistance. If the pile is subject to further displacement a limiting base resistance is predicted by the analysis with ν=0° in the soil, while no such limiting value is predicted for the analysis with ν=25° in the soil. There are also small differences between the mobilised shaft resistance from the two analyses. This arises due to the different normal stresses mobilised along the pile shaft, especially in the vicinity of the pile base. It can therefore be concluded that while the behaviour, and therefore properties of, the interface elements dominate the mobilisation of pile shaft resistance, they have only a small influence on the base resistance.

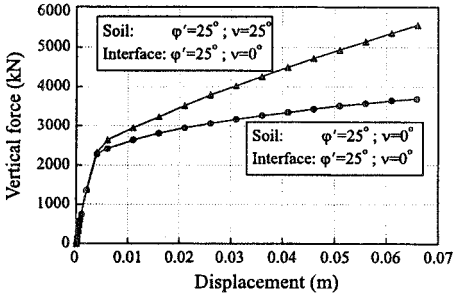

Figure 7.10: Drained loading of a single pile with interface elements along its shaft

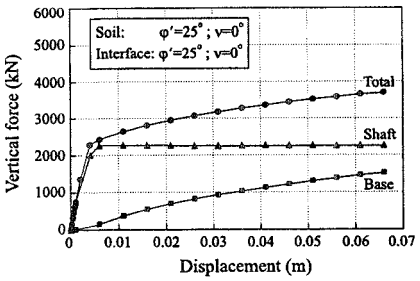

Figure 7.11a: Behaviour of a pile with interface elements - no dilation in a drained soil

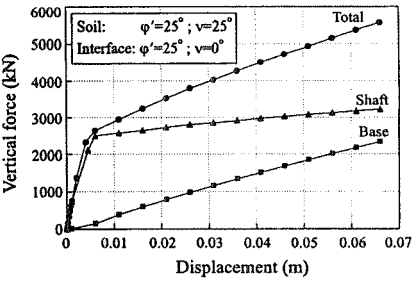

Figure 7.11b: Behaviour of a pile with interface elements - full dilation in a drained soil

7.3.3 Lateral loading

As noted above, if a vertical pile is subjected to lateral and/or moment loading a three dimensional analysis is required. If the geometry is axi-symmetric the FSAFEM can be used. As an example, the pile considered above has been subjected to lateral loading.

The finite element mesh shown in Figure 7.4 was employed. The top of the pile was displaced horizontally by specifying the following incremental radial, Δu_r, and circumferential, Δu_θ, displacements around its out edge:

$$\begin{aligned} \Delta u_r &= \Delta d \cos\theta \\ \Delta u_\theta &= -\Delta d \sin\theta \end{aligned} \tag{7.1}$$

This results in an incremental lateral displacement of the top of the pile of Δd. The remaining boundary conditions consisted of restricting all three components of displacement (i.e. u_r, u_θ and u_z) along the base of the mesh and the radial displacement (u_r) on the right hand side of the mesh. Unlike the vertical analyses described above, no displacements were restricted on the left hand side of the mesh which represents the axis of symmetry of the geometry. Under lateral loading this boundary must be free to move. The analyses were performed using parallel symmetry and ten harmonics, see Chapter 12 of Volume 1.

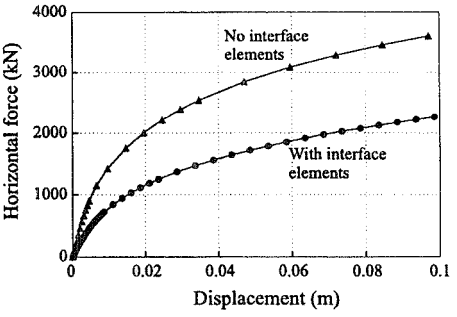

Figure 7.12: Undrained lateral loading of a single pile with and without interface elements along its shaft; constant S_u with depth

Initially the soil was assumed to be undrained with E_u=10^5 kN/m^2, μ=0.49 and S_u=100kN/m^2. The results

of two analyses, one without interface elements and the other with, are shown in Figure 7.12 in the form of pile head lateral load-displacement curves. The lateral load has been determined from the reactions at the nodes at the top of the pile subjected to the prescribed lateral displacement. The interface elements were assigned normal and tangential stiffnesses of $K_n=K_s=10^5$ kN/m^3 and an undrained strength S_u=100kN/m^2. In addition, these elements were unable to sustain tensile normal total stresses. If they experienced such stresses they were allowed to open freely. In such conditions these elements could not transfer shear stress between the soil and the pile shaft.

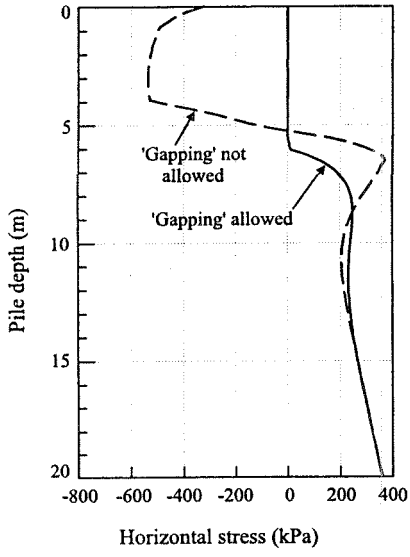

Figure 7.13: Effect of interface elements on horizontal total stress down the back of a pile

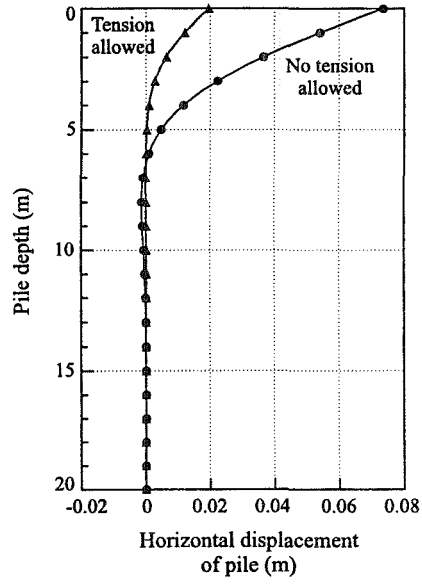

Figure 7.14: Effect of 'gapping' on horizontal displacement along the pile

The horizontal load-displacement curves shown in Figure 7.12 are very different. For a given horizontal load the analysis without interface elements predicts much smaller displacements. The reason for this is apparent from Figure 7.13 which shows the distribution of horizontal total stress acting down the back (i.e. the side opposite to the direction of loading) of the pile shaft at a horizontal pile head displacement of 0.1m. For the analyses performed without interface elements large tensile stresses are predicted over the top 5.5m of the pile. In contrast, because of the no-tension capacity assigned to the interface elements, the analysis with interface elements has zero horizontal stress over this region of the pile shaft. This analysis has therefore modelled a crack forming behind the pile as it moves forward. In practice such behaviour is referred to as 'gapping'. The effect of gapping on the displaced profile of the pile is shown in Figure 7.14, where the

results from the two analysis are compared for a pile head load of 2000kN.

A further analysis was performed in which the soil strength and stiffness increased with depth, S_u=2.7z kN/m^2 (equivalent to S_u=0.3σ_v') and E_u=1350z kN/m^2 (equivalent to E_u=500S_u), where z is the depth below the soil surface. Such an undrained strength distribution with depth is more representative of lightly overconsolidated clay. No interface elements were used adjacent to the pile shaft. The resulting pile head horizontal load- displacement curve is shown in Figure 7.15 and the distribution of horizontal total stress down the back of the pile, at a pile head displacement of 0.1m, in Figure 7.16. For this analysis no tensile horizontal stresses are predicted down the back of the pile and consequently an analysis using interface elements between the soil and the pile would have produced similar results.

It can therefore be concluded that if gapping is likely to occur, then interface elements should be installed along the pile soil interface. Wether or not gapping is likely to occur depends on the soil strength and in particular its distribution with depth.

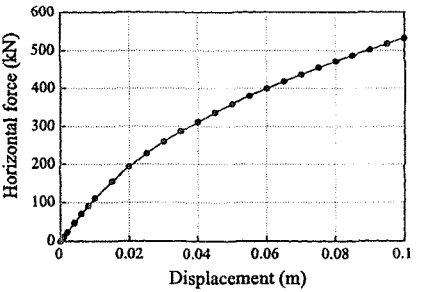

Figure 7.15:Undrained lateral loading of a single pile without interface elements along its shaft - linear variation of S_u with depth

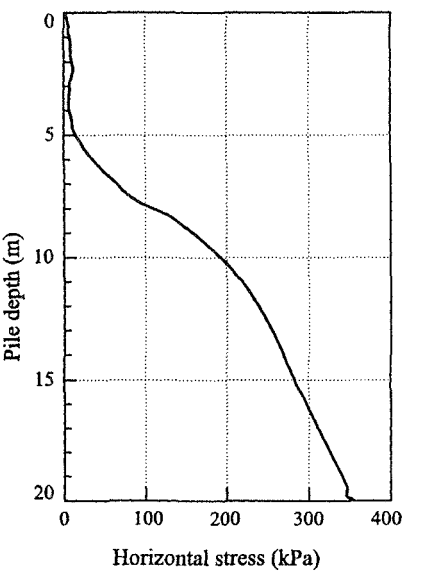

Figure 7.16: Horizontal total stress down the back of a pile for S_u linear with depth

7.4 Pile group behaviour

7.4.1 Introduction

The analysis of a pile group is three dimensional. Consequently current methods of analysis of pile groups subjected to combined axial loads, lateral loads and turning moments are either wholly based on linear elastic soil behaviour (Randolph and Poulos (1982)), or combine nonlinear single pile response with linear elastic forms of interaction (O'Neil *et al.* (1977)). The former methods are too simplistic to give accurate predictions of pile group response. The latter hybrid methods suffer from both the inconsistent nature in which they treat soil response (both linearly and nonlinearly) and the unrealistic assumptions made in obtaining the nonlinear single pile response. These hybrid methods account for nonlinear

single pile behaviour by either using a non-rigorous modified form of elastic response (Poulos and Davis (1968)), or by ignoring the continuum nature of soil behaviour, e.g. the *t-z* method (Coyle and Reese (1966)) and the *p-y* method (Reese (1977)).

While in principle a complete pile group could be analysed by a three dimensional finite element analysis, the number of elements required for an accurate analysis would be excessive and too large for current computer hardware to handle. In the special case where loading on the pile group is vertical (i.e. no horizontal or moment loading), then axes of symmetry can be accounted for and only a segment of the geometry analysed. Some examples are given in Figure 7.17 where it can be seen that this significantly reduces the complexity of the geometry to be analysed. The comments made earlier for the analysis of a single pile to vertical loading also apply to the analysis of such pile groups. In addition, it should be noted that because of the three dimensional nature of the geometry a full three dimensional analysis must be performed.

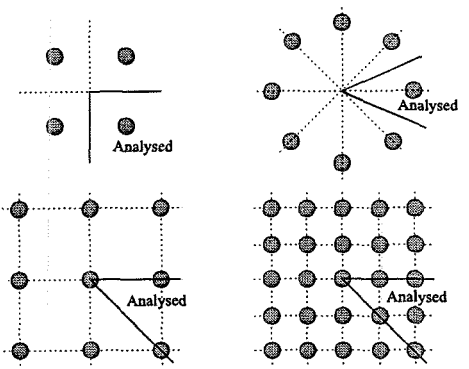

Figure 7.17: Examples of pile group symmetry

If the loading is not vertical and includes a lateral and/or moment component at the pile cap, then there are fewer axes of symmetry and more of the piles must be included in the analysis. Again, full three dimensional finite element analysis must be performed. Because the geometry is no longer axi-symmetric it is not possible to use the Fourier Series Aided Finite Element Method (FSAFEM).

With current computer hardware it is not really a practical proposition to analyse a pile group. Consequently for practical problems simplifications must be made.

A new method for considering pile groups has recently been proposed by Ganendra (1993), Ganendra and Potts (2002a, b). This method is based on results from nonlinear three dimensional analyses of a single pile and superposition techniques which use the same results to account for pile group effects. This method for considering pile groups is thought to be an improvement on the existing methods because:

- A more sophisticated and rigorous method of analysis of single piles is used which is able to incorporate complex soil and pile-soil interaction behaviour.
- A more coherent method for accounting for pile group interaction is used which is based on the results of the single pile analyses.

This new method is divided into two parts, the analysis of a pile group (Ganendra and Potts (2002a)) and the design of a pile group (Ganendra and Potts (2002b)). The proposed method of analysis of a pile group is able to give predictions of pile group rotation, lateral deflection and vertical settlement for a particular applied load, which may consist of any combination of axial load, lateral load and turning moment. This method is essentially an extension of that described by Jardine and Potts (1988), (1992) which was for vertically loaded pile groups only.

The proposed method of design for a pile group provides 'design charts' for any particular pile group such that predictions of pile group rotation, lateral deflection and vertical settlement can be obtained for any combination of axial loads, lateral loads and turning moments. Note, however, that the design method does not give any recommendations regarding the number, size or configuration of piles in a pile group.

As this approach is based on nonlinear finite element analysis of a single pile and as it appears to provide many advantages over current design approaches, it will be described in subsequent sections of this chapter. The application of the proposed analysis and design methods to the foundations of the Magnus oil platform will then be discussed.

7.4.2 Analysis of a pile group

Both the FSAFEM and a full three dimensional finite element analysis are able to analyse the behaviour of a single (vertical and cylindrical) pile subjected to any combination of lateral load, vertical load and turning moment. However, as the FSAFEM is more efficient all the three dimensional analysis referred to in subsequent sections have been performed using this approach. It should be noted however that it is perfectly valid to perform a conventional three dimensional analysis in its place.

To extend the analysis to consider the behaviour of a pile group subjected to such loads two assumptions have to be made:

- The manner in which the loads applied to one of the piles in a group affects the displacement of the other piles.
- The manner in which the loads applied to the group are distributed between the piles in the group.

The proposed method of analysis uses superposition techniques for the first assumption and a rigid pile cap criterion for the second assumption, both of which are described below.

7.4.3 Superposition

The displacements of any pile are affected by the loads imposed on the surrounding piles. This effect is accounted for in the proposed method of analysis

using a superposition technique. As superposition is theoretically invalid for a nonlinear system, approximations must be made and Ganendra and Potts suggested three alternative superposition techniques for the proposed method of analysis:

- Simple superposition;
- Nonlinear superposition;
- Virtual pile.

Of these the simple superposition has been used in this chapter and it is described below. The other techniques are presented in Ganendra (1993).

7.4.3.1 Simple superposition

This method assumes that the additional displacements at any pile head, due to the loads imposed on surrounding piles, can be evaluated from the ground surface movements obtained from a single pile analysis. Consider a pile group with N piles which are labelled from 1 to N. Let the ground surface displacements, u_i^s, at any point due to the loads F_i on the i^{th} pile be given by the function:

$$u_i^s = C_i(r_i, \theta_i) \tag{7.2}$$

where r_i and θ_i are the coordinates expressed in terms of the local cylindrical coordinate system for the i^{th} pile, which has its axis about the centre of the pile, see Figure 7.18. The function $C_i(r_i, \theta_i)$ is obtained from a 3D analysis (i.e. using the FSAFEM) of an isolated pile.

The simple superposition method assumes that the additional displacement u_i^j of the j^{th} pile, induced by the load F_i on the i^{th} pile, is equal to $C_i(r_i^j, \theta_i^j)$. r_i^j and θ_i^j are the coordinates of the j^{th} pile expressed in terms of the local coordinate system for the i^{th} pile. Thus the displacements u_{ss}^j of the j^{th} pile in a pile group can be obtained using simple superposition, by adding the displacement contributions from all the piles in the pile group:

$$u_{ss}^j = \sum_{i=1}^{N} u_i^j = \sum_{i=1}^{N} C_i(r_i^j, \theta_i^j) = u_j^j + u_G^j \tag{7.3}$$

where: $u_j^j = C_j(r_j^j, \theta_j^j)$ is the displacement of the j^{th} pile due to the load on the j^{th} pile;
$(r_j^j, \theta_j^j) = (0, 0)$ are the coordinates for the centre of the j^{th} pile;
u_G^j is the additional displacements induced at the j^{th} pile due to the loads imposed on the other piles in the group.

The vectors of displacements u_{ss}^j and u_i^j are expressed in the pile group global Cartesian coordinate directions x, y and z (where z is the depth from ground surface), see Figure 7.18. The origin for the x and y coordinates is located at the plan view centroid of the pile group and shall be referred to as the group datum. Thus the ground surface displacements (obtained from a FSAFEM analyses) associated with the loads on each pile have to be resolved from the local axi-symmetric coordinate system of the pile into the global pile group Cartesian coordinate system.

Only pile head and ground surface displacements are considered using this superposition technique. Methods of extending these superposition techniques to predict pile displacements with depth are described subsequently. An important feature of this method is that the ultimate load of a pile is unaffected by the loads on the other piles, however the displacements at which this load is mobilised will be different.

This approach is a generalisation of the method used by Jardine and Potts (1988) and is schematically illustrated in Figure 7.19.

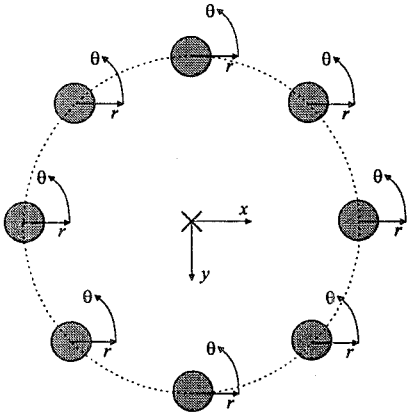

Figure 7.18: Local and global pile group coordinate systems

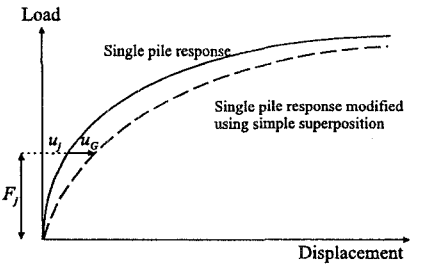

Figure 7.19: Simple superposition

7.4.3.2 Pile displacements with depth

The superposition technique should only be used to give estimates of pile head displacements. If the displacements along the length of the pile are also modified using this technique, the resulting deformed shape of the pile may result in unrealistic stress distributions within the pile. Two options exist for obtaining such displacements from the superposition of pile head displacements and the pile displacements (along the length of the pile) obtained from an isolated single pile FSAFEM analysis:

- The ratio between the superposition pile head displacements and the isolated pile head displacements is used to factor the isolated pile displacements (along the length of the pile). The stresses in the pile associated with these factored displacements would no longer be consistent with the loads applied to the pile.
- The difference between the superposition pile head displacements and the isolated pile head displacements are added to the isolated pile displacements (along the length of the pile). The resulting pile stress distribution is the same as the isolated pile stress distribution and thus is consistent with the

applied pile loads. However, this displacement distribution is considered to be unrealistic, since it predicts significant pile displacements even at great depths.

To obtain reasonable estimates of pile displacements and stresses using the superposition technique, the former option can be used for displacements and the latter option for stresses.

7.4.4 Load distribution within a pile group

The manner in which the loads are distributed between the piles in a pile group depends on the nature of their pile cap connectivity and the stiffness of the pile cap. In the Ganendra and Potts approach a rigid pile cap criterion is used, which assumes that the pile cap is fully rigid and there is full connectivity between piles and pile cap at ground level. In this case the pile head displacement and rotations of any pile can be evaluated from their location within the pile group and the pile group displacements and rotations. These pile group displacements can be expressed as U_x, U_y and U_z, which are the displacement of the pile group datum in the x, y and z (where z is depth) global coordinate directions respectively. The pile group datum and the origin for the global coordinate axes are taken to be the plan view centroid of the pile group at ground level, see Figure 7.18. The group rotations can be expressed as Θ_x and Θ_y, which are the rotations of the group about the x and y axes respectively. As a simplification, torsions applied to the pile group and accordingly rotations about the z axis are not considered. U_x, U_y, U_z, Θ_x and Θ_y are schematically illustrated in Figure 7.20.

Due to the rigid pile cap criterion, the displacements u_x^i, u_y^i and u_z^i (in the x, y and z directions respectively) of any i^{th} pile in a pile group can be related to the pile group displacements via the equations:

$$\begin{aligned} u_x^i &= U_x \\ u_y^i &= U_y \\ u_z^i &= U_z + y^i \tan\Theta_x + x^i \tan\Theta_y \end{aligned} \tag{7.4}$$

where x^i and y^i are the x and y coordinates respectively of the i^{th} pile.

Due to the assumption of full connectivity between pile and pile cap, the pile head rotations Θ_x^i and Θ_y^i (about the x and y axes respectively) of the any i^{th} pile in a pile group should equal the global group rotations:

$$\begin{aligned} \Theta_x^i &= \Theta_x \\ \Theta_y^i &= \Theta_y \end{aligned} \tag{7.5}$$

Note that the global group displacements and rotations (U_x, U_y, U_z, Θ_x and Θ_y) can be evaluated from the pile head displacements, rotations and locations (u_x^i, u_y^i, u_z^i, Θ_x^i, Θ_y^i, x^i and y^i) from any one pile in the pile group.

The loads that are applied to a pile group can be expressed as forces F_x, F_y and F_z and turning moments M_x and M_y. F_x, F_y and F_z are the forces in the x, y and z

directions respectively, and M_x and M_y are the turning moments about the x and y axes respectively. They are schematically illustrated in Figure 7.21. These loads are distributed among the piles in the group in such a way that the rigid pile cap criterion is satisfied, i.e. the same values of global group displacements and rotations (U_x, U_y, U_z, Θ_x and Θ_y) are evaluated from the pile head displacements and rotations (u_x^i, u_y^i, u_z^i, Θ_x^i and Θ_y^i) of each pile in the group. An iterative procedure can be used to evaluate these individual pile loads. The steps in the procedure are:

- Obtain an initial trial division of these applied loads between the piles in the group;
- Evaluate, using a superposition technique, the displacements of each individual pile due to the loads applied to it and the loads applied to its surrounding piles;
- These pile displacements are used to check if the rigid pile cap criterion is satisfied:
  - If it is satisfied (to within a small tolerance) this trial division of loads is assumed correct and the resulting solution for the global group displacements is accepted;
  - If the rigid pile cap criterion is not satisfied, a new trial division of loads is obtained and the procedure repeated until the criterion is satisfied.

A detailed descriptions of these steps is presented below.

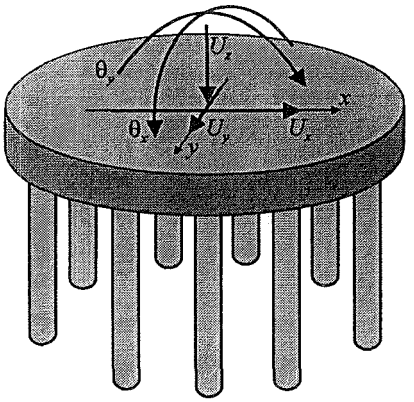

Figure 7.20: Schematic illustration of global pile group displacements

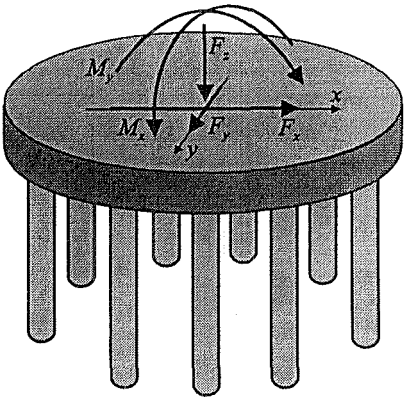

Figure 7.21: Schematic illustration of global pile group loads

7.4.4.1 Obtaining an initial trial division of the applied loads

The initial trial division of the applied forces F_x, F_y and F_z can be obtained by assuming that they are divided equally between all piles in the pile group. Obtaining a trial division of the turning moments M_x and M_y is not so straightforward. The restoring moments from the piles for the applied turning moment M_y can be divided into two parts:

- M_y^{pp}, the push-pull moment, which is the moment resulting from the difference in pile axial loads in the x direction;
- M_y^{hb}, the pile head bending moment, which is the sum of the bending moments about the y axis which are applied to the pile cap from each pile in the pile group.

The division of M_y between M_y^{pp} and M_y^{hb} is illustrated in Figure 7.22. To determine what proportion of M_y is M_y^{pp} and what proportion is M_y^{hb}, estimates are obtained of the push-pull rotational stiffness K_y^{pp} ($=M_y^{pp}/\Theta_y$), and the pile head bending rotational stiffness K_y^{hb} ($=M_y^{hb}/\Theta_y$). A procedure for estimating K_y^{pp} and K_y^{hb} is described in Section 7.4.5.5. Trial values of M_y^{pp} and M_y^{hb} can then be obtained using the following equations:

$$M_y^{pp} = M_y \frac{K_y^{pp}}{K_y^{pp} + K_y^{hb}} \quad \text{and} \quad M_y^{hb} = M_y \frac{K_y^{hb}}{K_y^{pp} + K_y^{hb}} \tag{7.6}$$

To determine the increase/reduction in individual pile axial loads which would yield a push-pull bending moment equal to M_y^{pp}, it is assumed that there is a linear variation of pile axial load with the global x coordinate. The trial division of the moment M_y^{hb} is obtained by assuming it is shared equally between all the piles in the pile group.

The above procedure is repeated for the division of M_x into M_x^{pp} and M_x^{hb} and the division of these into individual pile loads.

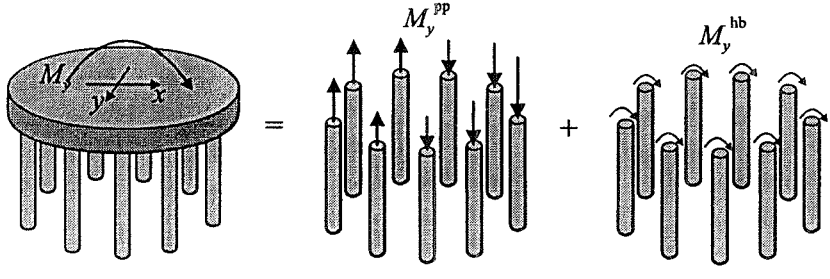

Figure 7.22: Division of M_y into M_y^{pp} and M_y^{hb}

7.4.4.2 Evaluating pile head displacements

The pile head displacement of each pile, due to the loads applied to it and the loads applied to its surrounding piles, is evaluated using FSAFEM analyses of single piles and the superposition technique mentioned above (or an alternative technique). It is of interest to note that the FSAFEM analyses used would in general involve simultaneously loading a pile with lateral loads in both the x and y directions, axial loads, and turning moments about both the x and y axes.

7.4.4.3 Checking the rigid pile cap criterion

The rigid pile criterion can be divided into nine separate conditions. These conditions and the appropriate corrections that should be made if any one of them is not satisfied are described below:

1. Check that the lateral deflections in the x direction for all the piles are the same, if so a value of U_x is obtained. If not, the lateral loads in the x direction of the piles with larger displacements (in the x direction) are reduced and those with smaller displacements are increased. To evaluate these corrective loads, the average displacement of all the piles is calculated and an appropriate tangential value of lateral pile stiffness is evaluated. The corrective load that should be applied to each pile is the product of this stiffness and the difference between the average displacement and the pile displacement. A similar approach can be used for the other conditions discussed below.
2. Check that the lateral deflections in the y direction for all the piles are the same, if so a value of U_y is obtained. If not, the lateral loads in the y direction of the piles with larger displacements (in the y direction) are reduced and those with smaller displacements are increased.
3. Check that the variation of individual pile settlements with x coordinate is linear, if so a value of Θ_y is obtained. If not, the axial loads are reduced for piles with settlements that are too large and are increased for piles with settlements that are too small.
4. Check that the variation of individual pile settlements with y coordinate is linear, if so a value of Θ_x is obtained. If not, the axial loads are reduced for piles with settlements that are too large and are increased for piles with settlements that are too small.
5. If a linear variation of axial displacements exist in both the x and y direction, a value of U_z is obtained.
6. Check that the rotations about the y axis for all the pile heads are the same, if so a value of Θ_y is obtained. If not, the applied pile head moments about the y axis of the piles with larger rotations (about the y axis) are reduced and those with smaller rotations are increased.
7. Check that the rotations about the x axis for all the pile heads are the same, if so a value of Θ_x is obtained. If not, the applied pile head moments about the x axis of the piles with larger rotations (about the x axis) are reduced and those with smaller rotations are increased.

8. Check that the values of Θ_y obtained from checks 3 and 6 are the same. If not, the ratio between M_y^{pp} and M_y^{hb} is adjusted accordingly.
9. Check that the values of Θ_x obtained from checks 4 and 7 are the same. If not, the ratio between M_x^{pp} and M_x^{hb} is adjusted accordingly.

If any one of these conditions is not satisfied to within a prescribed tolerance, the appropriate corrections are made and a new set of pile head displacements is evaluated and all nine checks repeated. If all nine conditions are satisfied concurrently, the solutions for U_x, U_y, U_z, Θ_x and Θ_y are accepted.

The above procedure seems very cumbersome. However, the trial division of loads described in Section 7.4.4.1 should give solutions that satisfy (to within a reasonable tolerance) the majority of the checks described. For most cases it is anticipated that only checks 8 and 9 may not be fulfilled by the trial division and that relatively few iterations would be required to obtain a solution that satisfies all nine conditions. The solutions obtained from this proposed method of analysis only make two basic assumptions:

- Superposition techniques can be used to determine the manner in which the loads applied to one of the piles in a group affect the displacements of the other piles;
- The rigid pile cap criterion can be used to determine the manner in which the loads applied to the group are distributed between the piles in the group.

7.4.5 Pile group design

The design of an offshore platform is a complex interdisciplinary process of which foundation design is a component. The method of analysis of a pile group described in Sections 7.4.2 to 7.4.4 is of limited use in such a procedure, since it is an iterative process for obtaining solutions for a particular set of applied loads and it requires that 3D finite element analyses (i.e. using the FSAFEM) of each pile be undertaken for each iteration. Predictions of this type are more suitable for back analyses than for design. Thus to provide a more flexible tool for the design of an offshore structure a 'design chart' procedure was devised which gives predictions of pile group displacements and rotations for any set of design loadings (without recourse to additional 3D finite element analysis). The manner in which these design charts are obtained and how they should be used is described below. The assumptions that are made in addition to those made for the analysis of a pile group are stated. The procedure used for obtaining these design charts extends the linear elastic procedure described by Randolph and Poulos (1982) to incorporate nonlinear soil behaviour.

7.4.5.1 Matrix formulation of the pile group response

The response of a pile group to a general set of loading conditions can be expressed in matrix form by representing both the pile group displacements and rotations, U_x, U_y, U_z, Θ_x and Θ_y (as defined in Section 7.4.4), and the applied loads

to the pile group, F_x, F_y, F_z, M_x and M_y (also defined in Section 7.4.4), as vectors U and F respectively. These vectors are related via a pile group stiffness matrix K:

$$F = [K]U \tag{7.7}$$

In the linear elastic formulation described by Randolph and Poulos (1982), the components of the matrix $[K]$ are constants. Thus if all the components of $[K]$ were known, displacement U can be calculated for any applied load F by pre-multiplying F with the inverse of $[K]$. Evaluating these values of U for an applied load F is more complex for nonlinear soil behaviour. The components of $[K]$ are no longer constant and vary as a function of the applied loads and displacements.

7.4.5.2 Superposition of loads

To consider the nonlinear problem it is assumed that the loads required to cause displacements U can be obtained by summing the loads required to cause each component of U (superposition of loads). This can be expressed vectorially by dividing the vector of displacements U into sub-vectors U_z, U_{ux}, U_{uy}, $U_{\theta x}$ and $U_{\theta y}$ where:

$$\begin{Bmatrix} U_z \\ U_x \\ \Theta_y \\ U_y \\ \Theta_x \end{Bmatrix} = \begin{Bmatrix} U_z \\ 0 \\ 0 \\ 0 \\ 0 \end{Bmatrix} + \begin{Bmatrix} 0 \\ U_x \\ 0 \\ 0 \\ 0 \end{Bmatrix} + \begin{Bmatrix} 0 \\ 0 \\ \Theta_y \\ 0 \\ 0 \end{Bmatrix} + \begin{Bmatrix} 0 \\ 0 \\ 0 \\ U_y \\ 0 \end{Bmatrix} + \begin{Bmatrix} 0 \\ 0 \\ 0 \\ 0 \\ \Theta_x \end{Bmatrix} \tag{7.8}$$

$$U = U_z + U_{ux} + U_{\theta y} + U_{uy} + U_{\theta x}$$

Let the loads required to cause displacements U_z, U_{ux}, U_{uy}, $U_{\theta x}$ and $U_{\theta y}$ be F_z, F_{ux}, F_{uy}, $F_{\theta x}$ and $F_{\theta y}$ respectively. The assumption of superposition of loads means that the applied load F, required to produce group displacement U, is equal to the sum of the of the loads F_z, F_{ux}, F_{uy}, $F_{\theta x}$ and $F_{\theta y}$:

$$F = F_z + F_{ux} + F_{uy} + F_{\theta x} + F_{\theta y} \tag{7.9}$$

The components of the load vector F_z are given by the reaction forces that have to be applied to the pile group in order that it displaces a distance U_z vertically, while all other components of displacement and rotation are fixed (at zero). The same principle can be used to relate the other load vectors, F_{ux}, F_{uy}, $F_{\theta x}$ and $F_{\theta y}$, with their associated displacements, U_x, U_y, θ_x and θ_y respectively. The manner in which these load vectors can be obtained from single pile FSAFEM analyses is described below.

Evaluating load vector F_z

The load vector F_z consists of five terms: three forces, F_z^z, F_z^x and F_z^y (in the z, x and y directions respectively), and two turning moments, M_z^x and M_z^y (about the x

and y axes respectively). These are the forces and turning moments required for a pure settlement of the pile group. To simplify the procedure it is assumed that F_z^x, F_z^y, M_z^x and M_z^y are zero. F_z^z is obtained from an (axi-symmetric or FSAFEM) analysis of an axially loaded pile and a superposition technique (i.e. the simple superposition method described in Section 7.4.3.1. This is illustrated in Figure 7.23.

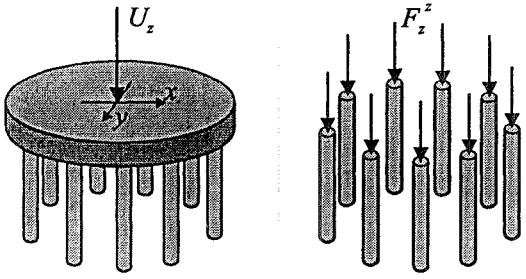

Figure 7.23: Evaluation of load vector F_z

Evaluating load vectors F_{ux} and F_{uy}

The load vector F_{ux} consists of five terms: three forces, F_{ux}^z, F_{ux}^x and F_{ux}^y (in the z, x and y directions respectively), and two turning moments, M_{ux}^x and M_{ux}^y (about the x and y axes respectively). These are the forces and turning moments required for a pure displacement of the pile group in the x direction. To simplify the procedure it is assumed that F_{ux}^z, F_{ux}^y and M_{ux}^x are zero. F_{ux}^x and M_{ux}^y are obtained from a FSAFEM analysis of a fixed head (i.e. not allowed to rotate) laterally loaded pile and a superposition technique. F_{ux}^x is the force required to give lateral displacement U_x and M_{ux}^y is the turning moment required to maintain the fixed head condition. This is illustrated in Figure 7.24.

The components of the load vector F_{uy} are evaluated in a similar manner.

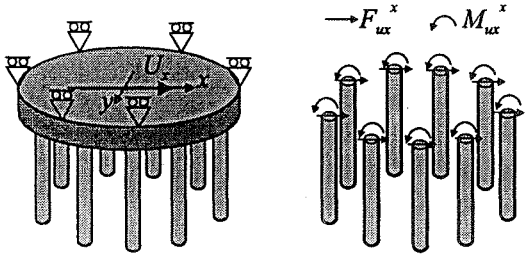

Figure 7.24: Evaluation of load vector F_{ux}

Evaluating load vectors F_{0x} and F_{0y}

The load vector F_{0y} consists of five terms: three forces, F_{0y}^{z}, F_{0y}^{x} and F_{0y}^{y} (in the z, x and y directions respectively), and two turning moments, M_{0y}^{x} and M_{0y}^{y} (about the x and y axes respectively). These are the forces and turning moments required for a pure rotation of the pile group about the y axis. To simplify the procedure it is assumed that F_{0y}^{z}, F_{0y}^{y} and M_{0y}^{x} are zero. M_{0y}^{y} consists of two components (see Figure 7.22):

- $(M_{0y}^{y})^{pp}$, the push-pull component, which is the moment resulting from the differential in pile axial loads in the x direction. $(M_{0y}^{y})^{pp}$ is obtained from an (axi-symmetric or FSAFEM) analysis of an axially loaded pile and a superposition technique. This is illustrated in Figure 7.25.
- $(M_{0y}^{y})^{hb}$, the pile head bending component, which is the sum of the bending moments about the y axis which are applied to the pile cap from each pile in the pile group. $(M_{0y}^{y})^{hb}$ is obtained from a FSAFEM analysis of a pile where the pile head is rotated and lateral deflections are restrained. $(M_{0y}^{y})^{hb}$ is the turning moment required to give rotation Θ_y. F_{0y}^{x} is the lateral force required to prevent lateral deflections of the pile head. This is illustrated in Figure 7.26.

The value of M_{0y}^{y} for a particular Θ_y value is found by performing the above two calculations and then summing the values of $(M_{0y}^{y})^{pp}$ and $(M_{0y}^{y})^{hb}$ obtained.

The components of the load vector F_{0x} are evaluated in a similar manner. Note that these values of $(M_{0y}^{y})^{pp}$ and $(M_{0y}^{y})^{hb}$ can be used to give the estimates of K_y^{pp} and K_y^{hb} required in Section 7.4.4.1:

$$K_y^{pp} = \frac{(M_{0y}^{y})^{pp}}{\Theta_y} \quad \text{and} \quad K_y^{hb} = \frac{(M_{0y}^{y})^{hb}}{\Theta_y} \tag{7.10}$$

Similarly, estimates for K_x^{pp} and K_x^{hb} can be obtained.

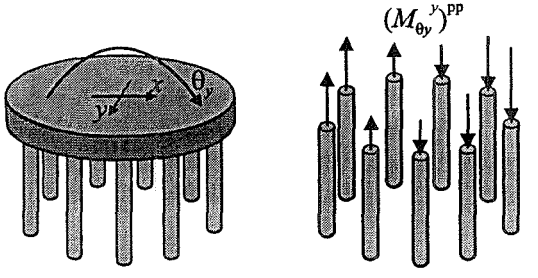

Figure 7.25: Evaluation of $(M_{0y}^{y})^{pp}$

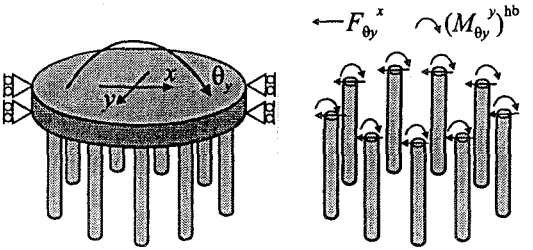

Figure 7.26: Evaluation of $(M_{\theta y}^{\ y})^{hb}$ and $F_{\theta y}^{\ x}$

7.4.5.3 Evaluating the solution displacements and rotations

Vectors K_z, K_{ux}, K_{uy}, $K_{\theta x}$ and $K_{\theta y}$ are obtained by dividing the load vectors F_z, F_{ux}, F_{uy}, $F_{\theta x}$ and $F_{\theta y}$ by their associated scalar displacements U_z, U_x, U_y, Θ_x and Θ_y respectively. These vectors are measures of the secant stiffness of the pile group and can be combined to give the pile group stiffness matrix [K]:

$$[K]=[K_z \ K_{ux} \ K_{\theta y} \ K_{uy} \ K_{\theta x}] \tag{7.11}$$

The various terms in [K] and the method in which each term is derived is depicted in Equation (7.12):

$$\begin{Bmatrix} F_z \\ F_x \\ M_y \\ F_y \\ M_x \end{Bmatrix} = \begin{bmatrix} K_z^z & 0 & 0 & 0 & 0 \\ 0 & K_{ux}^x & K_{\theta y}^x & 0 & 0 \\ 0 & K_{ux}^{my} & K_{\theta y}^{my} & 0 & 0 \\ 0 & 0 & 0 & K_{uy}^y & K_{\theta x}^y \\ 0 & 0 & 0 & K_{uy}^{mx} & K_{\theta x}^{mx} \end{bmatrix} \begin{Bmatrix} U_z \\ U_x \\ \Theta_y \\ U_y \\ \Theta_x \end{Bmatrix} \tag{7.12}$$

where:

- $K_z^{\ z}$ is obtained from the vertical force applied in an axi-symmetric analysis of an axially loaded pile;
- $K_{ux}^{\ x}$ is obtained from the lateral force applied in a FSAFEM analysis of a laterally loaded fixed head pile (in the x direction);
- $K_{ux}^{\ my}$ is obtained from the restoring moment applied in a FSAFEM analysis of a laterally loaded fixed head pile (in the x direction);
- $K_{\theta y}^{\ my}$ is obtained from the moment applied in a FSAFEM analysis of a pile subjected to turning moments and restrained from horizontal deflection (about y axis);
- $K_{\theta y}^{\ x}$ is obtained from the restraining lateral force in a FSAFEM analysis of a pile subjected to turning moments and restrained from horizontal deflection (about the y axis);
- $K_{uy}^{\ y}$ is obtained from the lateral force applied in a FSAFEM analysis of a laterally loaded fixed head pile (in the y direction);
- $K_{uy}^{\ mx}$ is obtained from the restoring moment applied in a FSAFEM analysis of a laterally loaded fixed head pile (in the y direction);

$K_{\theta x}^{mx}$ is obtained from the moment applied in a FSAFEM analysis of a pile subjected to turning moment and restrained from horizontal deflection (about the x axis);

$K_{\theta x}^{y}$ is obtained from the restraining lateral force in a FSAFEM analysis of a pile subjected to turning moments and restrained from horizontal deflection (about the x axis).

Using $[K]$ the displacement U can be calculated for any applied load F. However, the nonlinear nature of soil response means that $[K]$ is not a constant but varies with U. An iterative technique is described below which ensures that the value of U due to an applied load F is evaluated from a $[K]$ which is consistent with U.

The procedures described above allow the variation of F_z, F_{ux}, F_{uy}, $F_{\theta x}$ and $F_{\theta y}$ with respect to their associated scalar displacements U_z, U_x, U_y, Θ_x and Θ_y respectively, to be evaluated. These can be used to relate the vectors of secant stiffness K_z, K_{ux}, K_{uy}, $K_{\theta x}$ and $K_{\theta y}$ with their associated scalar displacements U_z, U_x, U_y, Θ_x and Θ_y respectively. These relationships can be expressed as design charts which can be used to obtain the pile group displacements, U, due to any applied pile group load, F. A simple iterative procedure for obtaining U is as follows:

- A trial value of pile group displacement, U^{tr}, is used to evaluate from the design charts the initial trial values of K_z, K_{ux}, K_{uy}, $K_{\theta x}$ and $K_{\theta y}$;
- These vectors are combined to obtain a trial value of pile group stiffness $[K]$;
- A trial solution for the pile group displacement, U^{sol}, is obtained based on this value of $[K]$ and the applied loads F;
- The validity of this solution is evaluated:
  - If $U^{tr} = U^{sol}$ (to within a specified tolerance) this solution is accepted;
  - Otherwise this value of U^{sol} is used as the new value trial displacement, U^{tr}, and the procedure repeated.

To start the procedure an initial trial displacement has to be obtained; usually a small arbitrary displacement is used.

The solutions obtained from this proposed method of design only make three basic assumptions:

- Superposition techniques can be used to determine the manner in which the loads applied to one of the piles in a group affect the displacements of the other piles;
- The rigid pile cap criterion can be used to determine the manner in which the loads applied to the group are distributed between the piles in the group;
- The loads required to cause displacements U can be obtained by summing the loads required to cause each component of U (superposition of loads).

To assess the validity of the last assumption for any applied load, the solution displacements using this design procedure could be compared with the solution

displacements obtained using the analysis procedure described in Section 7.4.4. This latter solution only makes the first two assumptions above.

7.4.6 Magnus

7.4.6.1 Introduction

The design and analysis procedures for pile groups described above were applied to the foundations of the Magnus platform. Magnus is located in the UK sector of the North Sea and was installed in 186m of water in 1982. The structure is shown in Figure 7.27. When the structure was being designed, in 1979, it was to be the deepest and most northern structure in the North Sea. This resulted in particularly severe environmental design criteria. This, in combination with the very high deck loads, results in the structure being one of the heaviest steel structures installed off-shore (at float out it weighed 340,000 kN). To verify the existing foundation design methods the foundations for one of the legs (A4 in Figure 7.27) were instrumented. Jardine and Potts (1992) studied the vertical response of this foundation using an axi-symmetric finite element analysis. The predictions obtained were in good agreement with the field measurements.

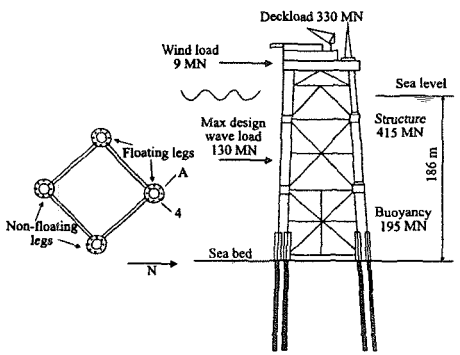

Figure 7.27: Schematic presentation of the Magnus structure

In this section the work carried out by Jardine and Potts (1992) is extended to consider the Magnus foundation response to general loading (axial and lateral forces and turning moments). Design charts of the type described in Section 7.4.5.3 are derived. These design charts and the method of analysis described in Section 7.4.4 are used to analyse the performance of the foundations when subjected to the loads measured from the largest wave of the storm on the 22nd January 1984.

7.4.6.2 Soil properties and initial conditions

Rigden and Semple (1983) summarized the geotechnical surveys performed at Magnus, which identified a thick and relatively consistent sequence of Quartenary soils. Jardine and Potts (1992) divided the soil profile into five main geotechnical units (labelled I to V) which are identified in Figure 7.28. Stratum I may have been deposited as a lodgement till, but strata II-V were considered to be of glaciomarine origin.

The constitutive model adopted for all these strata was a variant of the modified Cam clay model, but different nonlinear expressions were substituted to govern the elastic behaviour and a Hvorslev surface was used on the dry side, see Chapter 7

of Volume 1. The modified Cam clay material properties used for each layer and the depths of each layer are shown in Table 7.1. The shape of the yield surface in the deviatoric plane was assumed to be a Mohr-Coulomb hexagon, and a non-associated flow rule was adopted, with the plastic potential forming a surface of revolution in stress space around the hydrostatic axis. An elliptical form of the plastic potential in J-p' space was used on both the wet and dry side. The critical state angle of shearing resistance, φ', was 30° for all layers. The slope of the Hvorslev surface with respect to the hydrostatic axis at any Lode's angle was 0.75 times the slope of the critical state Mohr-Coulomb hexagon.

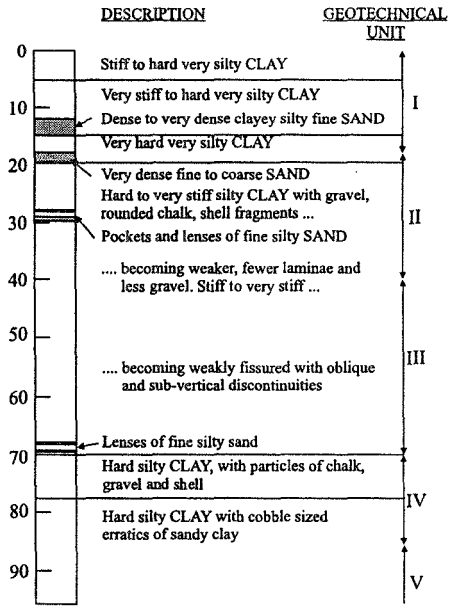

Figure 7.28: Soil profile at Magnus

Table 7.1: Modified Cam clay material properties for Magnus soil profile

Stratum	Depth	v_1	λ	κ
I	0-20m	2.00	0.078	0.0260
II	20-40m	2.10	0.083	0.0110
III	40-70m	2.25	0.100	0.0077
IV	70-82m	2.20	0.091	0.0070
V	82-170m	2.20	0.091	0.0070

Elastic behaviour is governed using the small strain stiffness model described in Section 5.7.5 of Volume 1. Minimum values of E_d and ε_v are specified such that at strains below these values the shear and bulk moduli respectively are assumed to be constant. Similarly, maximum values of E_d and ε_v are specified. The same small strain parameters were used for all the stratum and are shown in Table 7.2.

Table 7.2: Small strain stiffness parameters

Parameters for G	Value	Parameters for K	Value
A	623	R	587
B	643	S	412
C (%)	0.0007	T (%)	0.0007
α	1.349	δ	1.400
γ	0.6385	λ	0.797
$E_{d,\min}$ (%)	0.005	$\varepsilon_{v,\min}$ (%)	0.003
$E_{d,\max}$ (%)	0.433	$\varepsilon_{v,\max}$ (%)	0.2

Interface elements were used to model the pile-soil interface behaviour. A frictional yield surface was specified with an angle of shearing resistance of 22.5° in strata I and II, and of 17.7° in strata III, IV and V. The elastic normal and shear stiffness were both 500MN/m^3. No excess pore pressures were allowed to generate within the interface. A non-associative flow rule was used which allowed for no dilation. The interface elements were allowed to open when the normal effective stress reduced to zero. The amount of separation was recorded and the element would not close until the value of separation reduced back to zero.

The pile was modelled as an elastic solid cylinder of diameter 2.134m. Elastic stiffness parameters were specified such that the bending stiffness of this solid model pile was the same as the bending stiffness of the steel pipe pile used for the Magnus foundations (a Young's modulus of 45.3 GN/m^2 and a Poisson's ratio of 0.3). Note however that there is slight error in the resulting axial stiffness of the pile (if axial stiffnesses were equated, a Young's modulus of 24 GN/m^2 would be required).

The initial stress regime specified was that proposed by Jardine (1985) for the stress state in the soil six months after the installation of the piles. In the far field (greater than 20 radii from the pile) the stress regime was defined by the effective bulk unit weight of the soil (from which vertical effective stress, σ_{zo}', is calculated) and the coefficient of earth pressure, K_o, see Table 7.3. The stresses adjacent to the pile were defined as ratios of σ_{zo}', these ratios are also presented in Table 7.3. A semi-logarithmic variation in stress with radial coordinate was assumed for stresses in the soil less than twenty pile radii away from the pile:

$$\sigma = \sigma_{ap} + \frac{\sigma_{ff} - \sigma_{ap}}{3} \ln \frac{r}{r_o} \tag{7.13}$$

where: σ is any one of the principal stresses in the soil at a radial coordinate r and $r_o < r < 20r_o$;

σ_{ap} is the associated stress adjacent to the pile;
σ_{ff} is the associated stress in the far field;
r_o is the radius of the pile.

A hydrostatic pore water pressure regime was assumed.

The overconsolidation ratios, *OCR*, specified for the soil were such that the same undrained shear strength (in triaxial compression) profile with depth, as shown in Figure 7.29, was obtained from the soil at all radial locations. The resulting *OCR* variation with depth adjacent to the pile and in the far field is plotted in Figure 7.30. To obtain the required undrained shear strength profile, a semi-log variation, similar to that given by Equation (7.13), was used for the *OCR* of the soil less than twenty radii away from the pile. The details of how these soil parameters and the initial stress regime were derived are described fully in Jardine (1985).

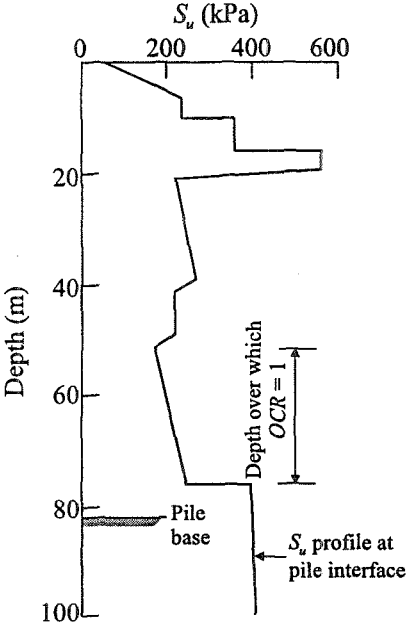

Figure 7.29: Undrained shear strength profile at Magnus

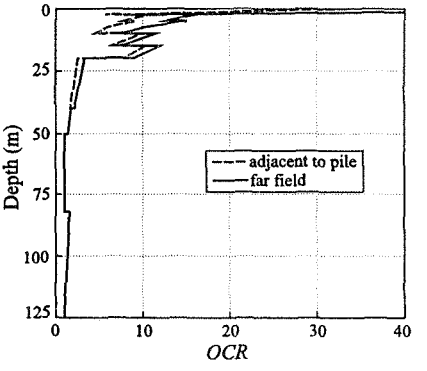

Figure 7.30: Variation of OCR with depth at Magnus

Table 7.3: Specified effective stress regime at pile face and far-field

Stratum	Vertical stress σ_z'/σ_{zo}'	Radial stress σ_r'/σ_{zo}'	Hoop stress $\sigma_\theta'/\sigma_{zo}'$	Far-field K_o	γ' (kN/m^3)
I (0-10m)	1.65	1.4	1.2	1.62	12.0
I (10-20m)	1.15	1.1	1.0	0.95	12.0
II	1.30	0.72	0.6	0.72	11.3
III	1.0	0.5	0.45	0.55	10.7
IV	1.0	0.5	0.45	0.55	11.1
V	1.0	0.55	0.55	0.55	11.1

7.4.6.3 Finite element analyses

The Magnus structure is supported on four pile groups of nine 2.134m outside diameter open ended pipe piles, one pile group for each platform leg. The piles were provided with an externally flush 1400mm long driving shoe having a wall thickness of 80mm. Apart from this shoe the piles have a uniform wall thickness of 63.5mm. This differential in pile thickness is ignored in the finite element presentation. The pitch circle diameter of each group is 13.8m. Details of the design and installation of the Magnus foundations are given by Rigden and Semple (1983).

The finite element mesh used for an isolated pile analysis of a pile in the Magnus pile group is shown in Figure 7.31. To extend the results from such an analysis to consider the behaviour of the pile group, the simple interaction method described in Section 7.4.3.1 was used. The piles are assumed to be uniformly spaced around the pitch circle. To obtain the design charts presented in Section 7.4.5.3 and to perform the analyses of the group as described in Section 7.4.4, the lateral loads are assumed to act in the direction of the x axis (i.e. through the centre of pile 1) and the moments are assumed to act about the y axis, see Figure 7.32.

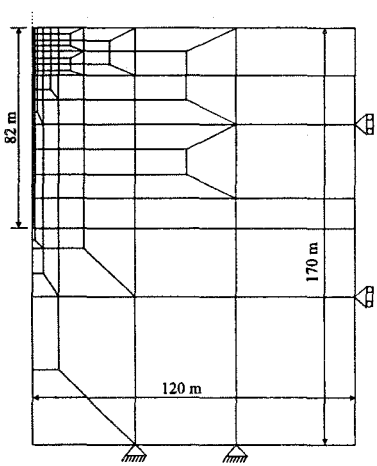

Figure 7.31: Finite element mesh for a single pile

The initial stress regime described in Section 7.4.6.2 is the predicted stress regime after the installation of the pile and just prior

to installation of the top side modules. A number of processes had to be simulated prior to considering the performance of the pile group to environmental loading. The first stage of the finite element analyses was to apply the deadweight associated with the installation of the topside modules. Accordingly, an axial load of 13.5MN was applied to the isolated single pile. This loading was undrained and a pore water bulk modulus of one hundred times the effective bulk modulus of the soil skeleton was specified. After loading, the excess pore water pressures generated were allowed to dissipate to the initial hydrostatic pore water pressures. This is consistent with the load transfer measured from the mudmat (pile cap) to its connecting piles (Sharp (1992)). The rate of this load transfer decayed with time and was found to be negligible after 20 months. After complete dissipation of these pore water pressures the accumulated soil strains were zeroed to retrieve the large initial stiffness obtained at first load from the small strain stiffness model. This stage is taken to be the initial condition from which environmental loads are applied. All subsequent loading was undrained and a pore water bulk modulus of one hundred times the effective bulk modulus of the soil skeleton was again specified. The design charts presented in Section 7.4.5.3 and the analysis of the group presented in Section 7.4.4 consider loads and displacements from this stage. All FSAFEM analyses undertaken assumed parallel symmetry, see Chapter 12 of Volume 1, and used 10 harmonics.

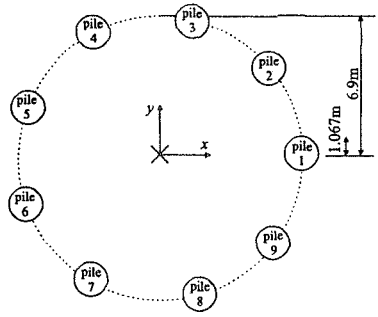

Figure 7.32: Magnus pile layout

7.4.6.4 Design of Magnus foundations

Design charts for the foundations of the Magnus platform are obtained using the method of design described in Section 7.4.5. Figure 7.33 is a plot of the group axial load, F_z^z, versus the group settlement, U_z. These results are obtained from an axi-symmetric analysis of an isolated pile axially loaded (and the simple superposition procedure). Also shown is the group load-displacement curve if the group effects were ignored (no superposition). The effect of superposition is to increase displacements by approximately 20%

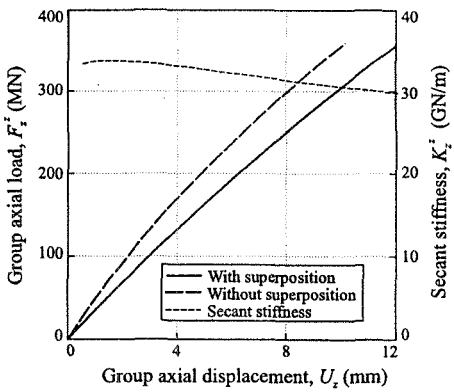

Figure 7.33: Group axial load and stiffness vs. settlement

to 30%. The near linear response of the pile group to axial loading is illustrated by the curve representing secant stiffness, K_z^z, with settlement. For design purposes a constant value of K_z^z equal to 29.8GN/m can be assumed to apply for loads up to 365MN, the ultimate load for design.

The ultimate capacity of the pile group from these analyses is 810MN (not shown in Figure 7.33). This compares favourably with the ultimate capacity of 837MN predicted by Jardine and Potts (1992) for the ten year initial stress regime. This is an indication of how well the ten year stress regime proposed by Jardine and Potts (1992) reproduces the combined effects of the additional loading due to the installation of the top side modules and the subsequent dissipation of the excess pore water pressures generated. However, both these predictions are significantly larger than the conventionally determined ultimate capacity, 549MN, and the ultimate capacity predicted by Jardine and Potts for the six month initial stress regime, 585 MN (which are in agreement with themselves). This difference arises because these latter two analyses do not account for the increase in capacity associated with the dissipation of the excess pore water pressures generated by the installation of the top side modules.

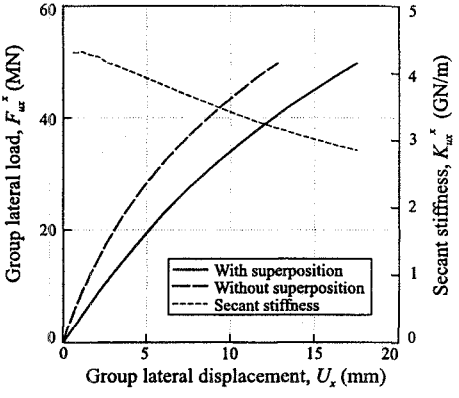

Figure 7.34: Group lateral load and stiffness vs. lateral deflection

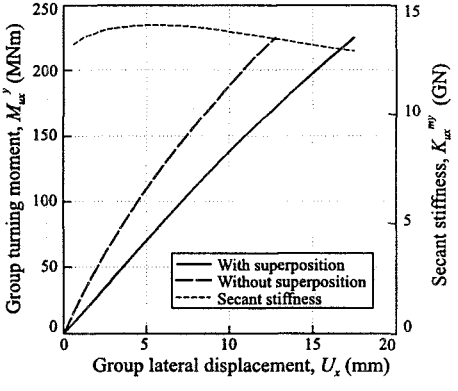

Figure 7.35: Group turning moment and stiffness vs. lateral deflection

The variation of group lateral load, F_{ux}^{x}, with lateral displacement, U_x, is presented in Figure 7.34. These results are obtained by considering the lateral loads and lateral deflections from a FSAFEM analysis of a laterally loaded fixed head pile. The effect of superposition is similar to the effect of superposition in the axial response and there is an increase in displacements of approximately 20% to 30% from the response if group effects were ignored. However, in contrast to the axial response, there is significant nonlinearity in the lateral response. The secant modulus, K_{ux}^{x}, is also plotted and it varies from an initial value of 4.3GN/m to a value of 3.3GN/m at a load of 35MN (the ultimate load for design).

The variation of group turning moments, M_{ux}^{y}, with lateral displacement, U_x, is presented in Figure 7.35. These results are obtained by considering the restraining moments and lateral deflections from the same FSAFEM analysis. There is considerably less nonlinearity in this curve than there is from the curve of F_{ux}^{x} versus U_x. This can be seen from the variation of the secant stiffness, K_{ux}^{my}, also plotted on Figure 7.35. K_{ux}^{my} varies from an initial value of -13.2GN to a value of -13.8 GN at 10.4mm displacement (the displacement corresponding to a lateral load of 35MN). There is also the same increase in displacements due to superposition, as obtained with the lateral loads.

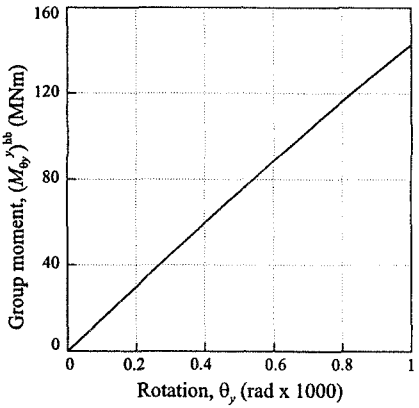

Figure 7.36: Group turning moment due to pile head bending vs. rotation

To obtain the curves based on simple superposition shown in Figures 7.34 and 7.35, it was assumed that the lateral load was equally distributed between all the piles in the pile group. This equal load assumption results in satisfaction of the rigid pile cap criterion to within a reasonable tolerance. To illustrate this, the lateral deflections of all the piles in the pile group are evaluated, on the basis of the equal load assumption, for an applied load equal to the maximum design load (35MN to the group). These results are presented in Figure 7.40, which is a plot of the lateral deflections of the piles against the x-coordinate of their centres. The variation in the magnitudes of these lateral deflections is small and it is inferred that the rigid pile cap criterion is satisfied. Thus for the curves shown in Figures 7.34 and 7.35 (which are for a range of lateral loads), only the displacements of pile 1 are evaluated on the basis of the equal loads assumption and the displacements of the pile group are equated to them. Note that the displacements of pile 1 are the easiest to calculate since the additional displacements due to piles 2 to 5 are equal to the additional displacements due to piles 6 to 9.

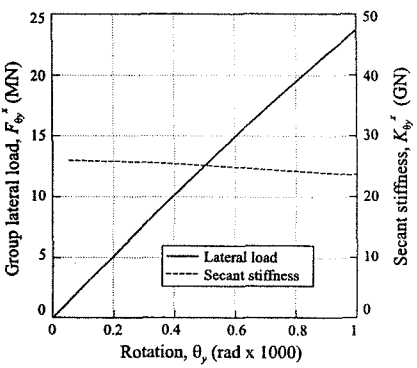

Figure 7.37: Group lateral load due to pile head bending vs. rotation

The variation of group turning moments due to pile head bending, $(M_{\theta y}^{y})^{hb}$, with group rotation, Θ_y, is presented in Figure 7.36. These results are obtained by

considering the turning moments and rotations from a FSAFEM analysis of a pile subjected to rotation and restrained from lateral pile head deflection. No superposition is required in this approach since rotations rather than displacements are applied. The response in moderately linear. The same FSAFEM analysis is used to obtain the plot of lateral load, $F_{\theta y}{}^{x}$, and secant stiffness, $K_{\theta y}{}^{x}$,with group rotation, Θ_y shown in Figure 7.37. The lateral loads are obtained from the restraining loads required in the analysis. This response is very linear and a constant value of $K_{\theta y}{}^{x}$ equal to -23.7GN is assumed for design purposes.

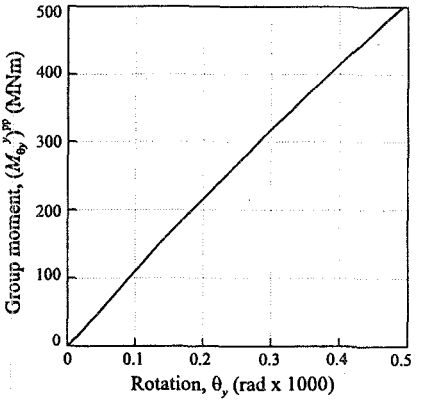

Figure 7.38: Group turning moment due to push-pull effects vs. rotation

The variation of group turning moments due to the push-pull effect , $(M_{\theta y})^{pp}$, with group rotation, Θ_y, is presented in Figure 7.38. The response is nearly linear and is much stiffer than the corresponding pile head bending response, see Figure 7.36. These results are obtained from an axi-symmetric analysis of an axially loaded pile and the simple superposition technique. In addition, a linear variation of axial pile loads with x-coordinate was assumed. This linear load assumption results in satisfaction of the rigid pile cap criterion to within a reasonable tolerance. To illustrate this, the settlements of all the piles in the pile group are evaluated, on the basis of the linear loads assumption, for an applied turning moment equal to the maximum design turning moment. These results are presented in Figure 7.41 which is a plot of the settlements of the piles against the x-coordinate of their centres. A near linear variation in the magnitudes of these settlements with x coordinate is obtained and it is inferred that the rigid pile cap criterion is satisfied. Thus to derive the curve shown in Figure 7.38 only the displacements of pile 1 are evaluated on the basis of the linear load assumption. The rotation of the pile group is evaluated from this displacement and the assumption that the group datum does not displace vertically, see Figure 7.41.

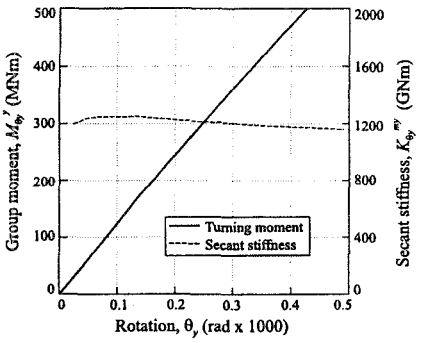

Figure 7.39: Total group turning moment and stiffness vs. rotation

The push pull moments, $(M_{\theta y})^{pp}$, and the pile head bending moments, $(M_{\theta y})^{hb}$, are added to give the variation of the total group turning moment, $M_{\theta y}{}^{y}$, with group

rotation, Θ_y. This is presented in Figure 7.39. Due to the linear nature of its two constituent parts this response is also strongly linear, as can be seen from the variation of secant stiffness, $K_{\theta y}^{my}$, shown in Figure 7.39. $K_{\theta y}^{my}$ is assigned a constant value of 1159GNm for design purposes.

The values of secant stiffnesses K_z^z, K_{ux}^x, K_{ux}^{my}, $K_{\theta y}^x$ and $K_{\theta y}^{my}$ evaluated above can be combined to give the pile group stiffness matrix [K]:

$$\begin{Bmatrix} F_z \\ F_x \\ M_y \end{Bmatrix} = \begin{bmatrix} K_z & 0 & 0 \\ 0 & K_{ux}^x & K_{\theta y}^x \\ 0 & K_{ux}^{my} & K_{\theta y}^{my} \end{bmatrix} \begin{Bmatrix} U_z \\ U_x \\ \Theta_y \end{Bmatrix} = \begin{bmatrix} 29.779 & 0 & 0 \\ 0 & K_{ux}^x & -23.724 \\ 0 & K_{ux}^{my} & 1159 \end{bmatrix} \begin{Bmatrix} U_z \\ U_x \\ \Theta_y \end{Bmatrix} \quad (7.14)$$

where $3.3 < K_{ux}^x < 4.3$ and $-14.1 < K_{ux}^{my} < -13.2$. In the above equation the forces are in terms of GN, displacements in terms of m, and the moments in terms of GNm.

Both K_{ux}^x and K_{ux}^{my} vary with displacement U_x and the iterative procedure suggested in Section 7.4.5.3 should be used in conjunction with Figures 7.34 and 7.35 to find the appropriate value of U_x and hence K_{ux}^x and K_{ux}^{my} for any applied load.

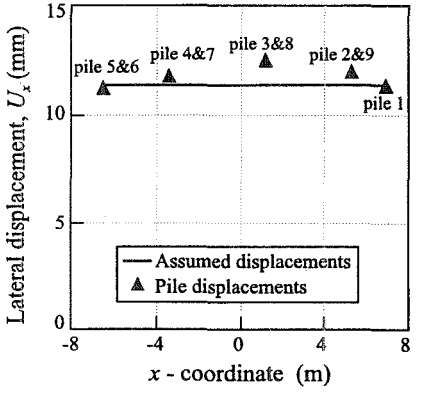

Figure 7.40: Pile head deflection for maximum design lateral load

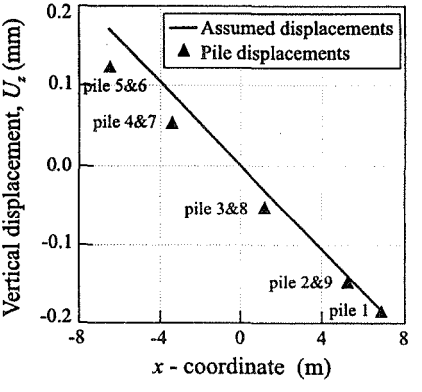

Figure 7.41: Pile head settlement for maximum design turning moment

Horsnell *et al.* (1992) evaluated an average pile group stiffness matrix on the basis of the measured response of the Magnus platform:

$$\begin{Bmatrix} F_z \\ F_x \\ M_y \end{Bmatrix} = \begin{bmatrix} K_z & 0 & 0 \\ 0 & K_{ux}^x & K_{\theta y}^x \\ 0 & K_{ux}^{my} & K_{\theta y}^{my} \end{bmatrix} \begin{Bmatrix} U_z \\ U_x \\ \Theta_y \end{Bmatrix} = \begin{bmatrix} 32 & 0 & 0 \\ 0 & 2.4 & -21 \\ 0 & -21 & 1028 \end{bmatrix} \begin{Bmatrix} U_z \\ U_x \\ \Theta_y \end{Bmatrix} \quad (7.15)$$

The group stiffness matrix derived from the new method of design (Equation (7.14)) compares very well with the stiffness matrix inferred from field measurements. The new design value for K_z^z is only slightly smaller than that measured. Additionally, the measured value falls within the range of secant stiffness shown in Figure 7.33. The new design method moderately overpredicts the values of lateral and rotational stiffness K_{ux}^{x} and $K_{\theta y}^{my}$. Although not explicitly stated by them, the Authors believe that Horsnell *et al.* (1992) assumed that the foundation stiffness matrix was symmetrical. These off diagonal terms in the measured stiffness matrix are in good agreement with the new design value of $K_{\theta y}^{x}$, but are significantly larger than the new design value of K_{ux}^{my}. It is interesting to note that due to the nonlinear approach used to derive the terms in the new design stiffness matrix, the matrix is no longer symmetrical (i.e. $K_{ux}^{my} \neq K_{\theta y}^{x}$).

Horsnell *et al.* (1992) also presented the group stiffness matrix derived from conventional design methods:

$$\begin{Bmatrix} F_z \\ F_x \\ M_y \end{Bmatrix} = \begin{bmatrix} K_z & 0 & 0 \\ 0 & K_{ux}^{x} & K_{\theta y}^{x} \\ 0 & K_{ux}^{my} & K_{\theta y}^{my} \end{bmatrix} \begin{Bmatrix} U_z \\ U_x \\ \Theta_y \end{Bmatrix} = \begin{bmatrix} 7 & 0 & 0 \\ 0 & 1.27 & -9 \\ 0 & -9 & 600 \end{bmatrix} \begin{Bmatrix} U_z \\ U_x \\ \Theta_y \end{Bmatrix} \tag{7.16}$$

This conventional group stiffness matrix is significantly softer than the stiffness matrix inferred from field measurements. The axial stiffness, K_z^z, is over 4.5 times softer than the measured axial stiffness and the other terms in the stiffness matrix are approximately twice as soft as the corresponding measured terms.

7.4.6.5 Environmental loading

The method of design and method of analysis were used to predict the performance of the instrumented pile group (supporting leg A4) on the Magnus platform when subjected to the largest wave of the storm on the 22nd January 1984. Horsnell *et al.* (1992) state that the measured loads on leg A4 for this wave are: an axial load equal to 69.1MN, a lateral load equal to 11.7MN and a turning moment equal to 146.7MNm. It is assumed that these lateral loads act in the x direction and these turning moments act about the y axis. Thus the applied loads can be expressed as a load vector F:

$$F = \begin{Bmatrix} F_z \\ F_x \\ M_y \end{Bmatrix} = \begin{Bmatrix} 69.1 \\ 11.7 \\ 146.7 \end{Bmatrix} \tag{7.17}$$

The predicted displacements due to this imposed load obtained from the new design method, Equation (7.14), and from the conventional design stiffness matrix, Equation (7.16), are presented in Table 7.4. The new design method required four iterations to obtain the solution value of U_x. Also shown on Table 7.4 are the measured displacements of the pile group for this wave (Horsnell *et al.* (1992)). These measurements are based on the readings from accelerometers at the base of

the leg. The new design predictions are in good agreement with the measured displacements, underpredicting lateral displacements and rotations and overpredicting settlements. The conventional design predictions are significantly larger than the measured displacements, with settlements over four and a half times larger and lateral displacements and rotations approximately twice the size of measured lateral displacements and rotations.

Table 7.4: Predicted and measured pile group displacements

Movement	New design	Conventional design	Measured
Vertical settlement, U_z	2.3mm	9.9mm	2mm
Lateral displacement, U_x	3.9mm	12.2mm	5.7mm
Rotation, Θ_y	$1.7\text{x}10^{-4}$ rad	$4.3\text{x}10^{-4}$ rad	$2.5\text{x}10^{-4}$ rad

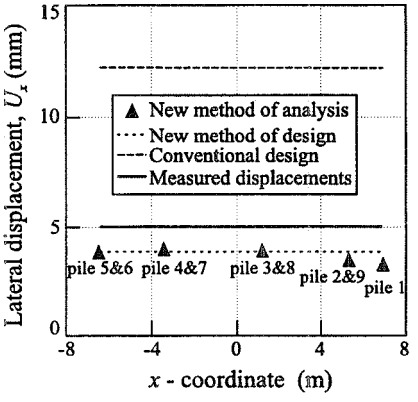

Figure 7.42: Pile head deflection for storm of 22/1/84

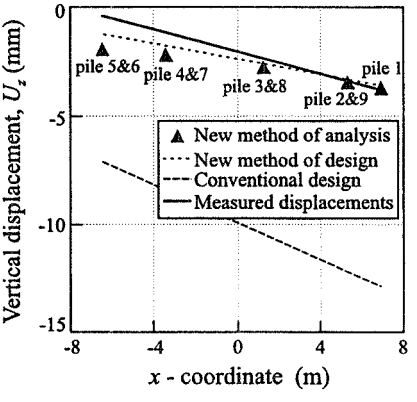

Figure 7.43: Pile head settlement for storm of 22/1/84

The method of analysis described in Section 7.4.4 was also used to give predictions of pile group displacements and rotations. The initial trial division of loads gave predictions that satisfied all but one of the rigid pile cap conditions given in Section 7.4.4.3, the values of Θ_y from pile head bending and push-pull loading were not equal. Five iterations were required to obtain a solution that satisfied all the conditions. Note that additional FSAFEM analyses were required for each iteration. The predictions for lateral displacement of each pile from the method of analysis are plotted against x coordinate in Figure 7.42. Also presented are the measured displacements and the predicted displacements from both the new and conventional design methods. There is good agreement between the new

design and new analysis predictions. This implies that the assumption of superposition of loads described in Section 7.4.5.2 is reasonable.

Figure 7.42 also shows the good agreement of these predictions with the measured displacements, and the large overprediction in displacements obtained from the conventional method. The validity of the assumption of superposition of loads and the accuracy of the predictions from the new methods of design and analysis are also illustrated in Figure 7.43, which is a plot of vertical settlement against x coordinate for the same imposed load.

Kenley and Sharp (1992) provide distributions for bending moment with depth for a pile in the pile group subjected to the above wave loading. Distributions obtained from both conventional design methods and measurements were presented. The measured bending moments were derived from strain gauges at different levels in different piles to give a typical bending moment distribution within a pile. These bending moments are shown in Figure 7.44 with the predicted bending moments from the new method of analysis. The new method of analysis gives a better agreement with the measured bending moments than the conventional method. In particular, the new method does not overpredict the depth of the point at which the maximum bending moment occurs by as much as the conventional method.

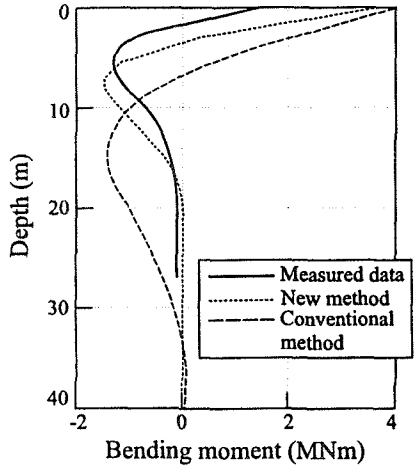

Figure 7.44: Distribution of bending moment with depth

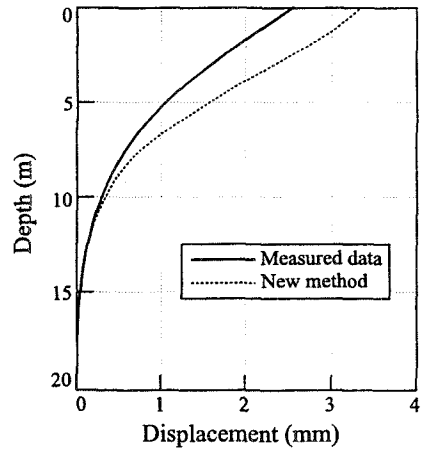

Figure 7.45: Distribution of lateral displacement with depth

Kenley and Sharp (1992) obtained an estimate of the distribution of lateral displacement with depth within a pile by double integrating the bending moment profile shown in Figure 7.44. This is presented in Figure 7.45 with the predictions obtained from the new method of analysis. The predicted displacements have a

similar distribution as the measured displacements, but overpredict them. This is in contrast to the results shown in Figure 7.42, where the measured pile head displacements are greater than the predicted pile head displacements. Horsnell *et al.* (1992) state that the group displacements presented in Figure 7.42, obtained from the accelerometers at the base of the leg, may not necessarily apply directly to the piles at mudline, since the leg-pile connection provided by the grout in the pile sleeve is not necessarily rigid at this depth (thus actual pile displacements may be smaller). The displacement profile provided by Kenley and Sharp (1992) is also subject to inaccuracies due to the approximate manner in which the bending moment distribution is obtained and difficulties associated with the double integration of bending moments. However, the predicted values of displacements from the new method of analysis and the new method of design fall within the range of possible values given by these two measured estimates of pile displacement.

7.5 Bucket foundation

7.5.1 Introduction

Suction caissons (or 'bucket' foundations) are becoming extensively used in the offshore industry as deep water anchors for floating structures or foundations for oil platforms. The caissons are hollow cylindrical structures which have a top cap and a relatively thin wall, the so called skirt. One example of floating tension leg oil platform on bucket foundations is the Snorre platform, illustrated in Figure 7.46, which has a cluster of three buckets connected to each of its four foundation legs (Christophersen *et al.* (1992), Jonsrud and Finnesand (1992)).

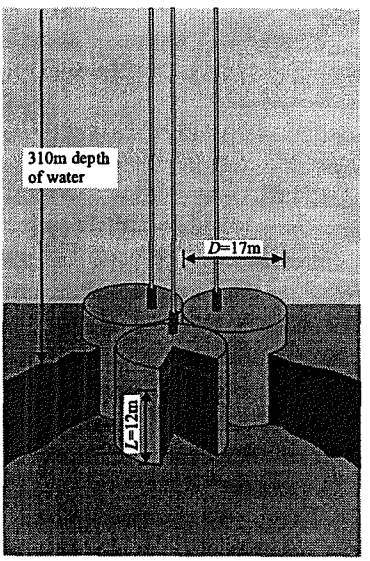

Figure 7.46: Schematic view of Snorre platform foundation template

Installing a bucket foundation involves initial penetration into the sea-bed under self-weight. The pressure in the water trapped inside the bucket, between the soil surface and the top cap, is then lowed by pumping, to cause a positive differential water pressure across the top of the bucket, thus forcing the bucket further into the soil until its final position is reached.

In the case of the Snorre structure, dead weights were added to ensure that compressive loading was acting on the bucket foundations. However, oil exploration is moving more into progressively deeper waters, and there is

considerable interest in utilising the tensile capacity of bucket foundations. Environmental loading produces both vertical and horizontal components of force, such that the resultant force is inclined to the vertical. One of the main design considerations for such foundations becomes the assessment of their pull-out capacity.

Zdravković *et al.* (1998), (2001) present an extensive numerical study of the short-term pull-out capacity of bucket foundations in soft clay. An initial parametric study (Zdravković *et al.* (1998)), involving three dimensional finite element analyses of bucket foundations, in which the diameter, skirt length, soil-structure adhesion and inclination of loading were varied, considered the soil to be an isotropic soft clay, with an undrained shear strength increasing linearly with depth. This study produced a general picture of the influence of each of these parameters on the pull-out capacity of bucket foundations.

Further studies (Zdravković *et al.* (2001)) were then carried out to investigate the effects of soil anisotropy on the pull-out capacity of bucket foundations. For this purpose the soil was modelled using the MIT-E3 model, see Section 8.7 of Volume 1. As bucket foundations are becoming popular as mooring anchors, more recent research at Imperial college has considered the effect of varying the position of the location of the anchor tether down the side of the bucket. Some of the main findings of this research will be discussed below.

7.5.2 Geometry

The reference bucket foundation geometry adopted for the research study is shown in Figure 7.47 and is based on the geometry of the bucket foundations installed at the Snorre platform. A single concrete cylinder is analysed, with a skirt 0.4m thick and a top cap 1.0m thick. The diameter of the cylinder, D, is 17.0m, while the skirt penetrates the sea-bed to a depth L=12.0m, giving a D/L ratio of 1.4. The depth of water is also based on that at Snorre and is assumed to be 310m.

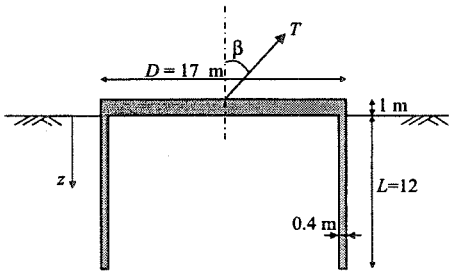

Figure 7.47: Idealised geometry for finite element analysis

Undrained uplift loading is applied at the centre of the top cap, at an inclination β to the vertical, see Figure 7.47. Analyses were performed varying the inclination β from 0° to 90°. The scenario considered is typical of that for a tension leg platform (TLP). Other types of floating structure may apply their loads in different ways.

7.5.3 Finite element analysis

Although the bucket foundation has an axi-symmetric geometry, loading at a general inclination β produces a full three dimensional state of stress and strain in

the bucket and in the soil. This implies that any realistic numerical analysis of this problem must be three dimensional. Only in the special case of vertical loading (i.e. $\beta = 0°$) can the problem be assumed to be axi-symmetric.

The FSAFEM method was used in this study for the analyses of bucket foundations subjected to inclined loading, adopting the finite element mesh presented in Figure 7.48. As indicated in this figure, prescribed displacements were imposed on both the bottom and right hand side mesh boundary. No such displacement restrictions are imposed on the left hand side boundary, because it represents only the geometrical axis of symmetry. The parallel symmetry option was adopted and ten harmonics were used to represent the variation of all quantities in the circumferential direction. A small parametric study, varying the number of harmonics, was performed to ensure that this was adequate. For a vertically loaded foundation (i.e. β=0°) a conventional axi-symmetric finite element analysis was performed, which further reduced the computational effort required.

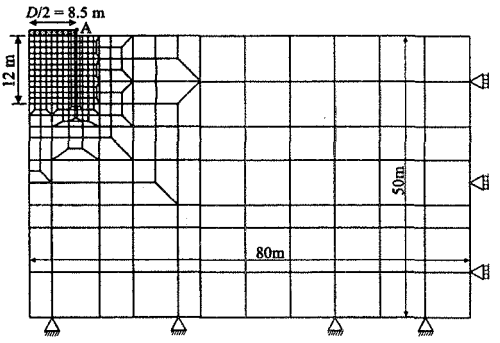

Figure 7.48: Finite element mesh for bucket foundation analysis

The bucket foundation was modelled as concrete material, assuming linear elastic behaviour (with Young's modulus $E = 30*10^6$ kN/m^2 and Poisson's ratio μ=0.15). This implies that the concrete has sufficient strength and reinforcement to sustain the applied loads. The installation of the foundation was not modelled in the analyses, the 'bucket' was assumed to be 'wished in place'.

For the conventional axi-symmetric analyses, when β=0°, the foundation was loaded to failure by applying increments of vertical uplift displacement, v, at the centre of the top cap. The reaction force at this location represents the applied load. For the foundation subjected to inclined loading, when $\beta \neq 0°$, the analyses had to be performed under load control, with increments of vertical and horizontal force being applied as line loads (in the circumferential direction) at the node representing the top right hand corner of the top cap, point A in Figure 7.48. As with the analyses described in Section 6.5.7.4 for circular footings, for the vertical load (V) only the zero harmonic coefficient was specified as non-zero. To obtain the horizontal load, both radial (H_r) and circumferential (H_θ) line loads were specified. For the radial load only the first cosine harmonic was specified as non-zero, whereas for the circumferential load only the first sine harmonic coefficient was set. The latter was of opposite sign but equal in magnitude to that set for the radial load. The magnitudes of these increments were kept in the proportions required to give the desired loading inclinations. As failure was approached, it was necessary to reduce the size of the force increments to obtain an accurate estimate

of the ultimate loads. The resultant load from these boundary conditions acts at the centre of the top cap as desired.

The finite element mesh shown in Figure 7.48 was used for both axi-symmetric and FSAFEM analyses. It consisted of 350 eight noded isoparametric elements. Undrained conditions in the soil were simulated by assigning a high bulk stiffness ($=1000K_{skel}$, where K_{skel} is the effective bulk stiffness of the soil skeleton) to the pore water (see Section 3.4 of Volume 1).

7.5.4 Modelling of the interface between top cap and soil

To model the interface between soil and the top cap, zero thickness interface elements have been used (see section 3.6 of Volume 1). At the outset of this research programme, three different conditions at the interface between the soil and the top cap were identified. These are shown diagrammatically in Figure 7.49. In Case 1 the bucket foundation has been perfectly installed such that there is no water layer between the soil surface and the underside of the top cap. It is assumed that the bucket foundation is water tight. Case 2 represents the other extreme where a water layer exists between the soil surface and the underside of the top cap and the pressure in the water remains equal to that at the sea bed outside the foundation (i.e. there is a hole in the top cap). Case 3 models the intermediate situation in which a water layer exists, but the foundation is water tight.

All three situations were modelled in a conventional axi-symmetric finite element analyses in which the foundation (D=17m, D/L=1.4) was subject to a vertical pull-out load. The isotropic soil properties described in the next section were used for these analyses. Case 1 was modelled by omitting the top cap interface elements and thereby simulating perfect contact between the soil and the underside of the top cap. Case 2 was modelled by letting the interface elements open freely under any vertical loading and Case 3 was modelled by giving the interface elements a very low shear stiffness, but a high normal stiffness. In addition, if the water pressure was to reduce to an absolute value of -100kPa, a facility was provided to reduce the normal stiffness to a very small value, thus simulating cavitation. For all analyses full wall adhesion was assumed between the soil and the skirts of the bucket foundation.

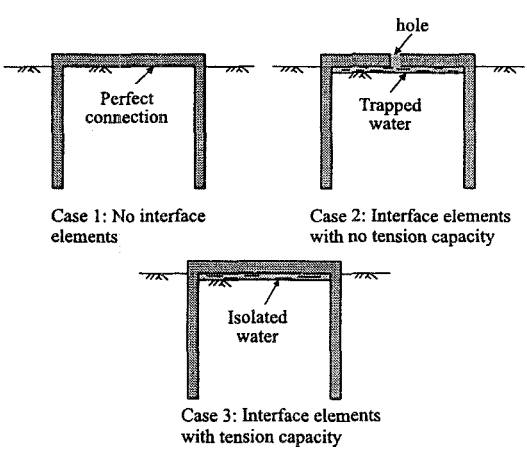

Figure 7.49: Possible scenarios for the interface between the top cap and undersoil

The results of the three analyses are presented in Figure 7.50 in the form of vertical load-displacement curves. As expected, the analysis for Case 2 produces a much lower limit load than for the other two cases. This arises as resistance is only provided by the adhesion between the skirts of the foundation and the soil. In Cases 1 and 3 there is an additional contribution from the soil below the top cap, increasing the ultimate pull out by approximately 180%. The result for Case 3 shows a softer response to that of Case 1. However, both Cases 1 and 3 give the same ultimate load. The differences between Cases 1 and 3 arise because in Case 1 horizontal shear stresses are mobilised between the soil and the top cap, whereas in Case 3 these are zero (i.e. the water layer trapped between the top cap and the soil cannot transfer shear stresses).

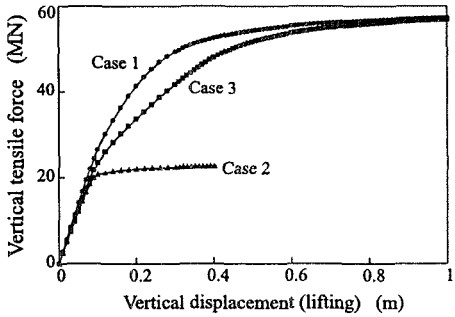

Figure 7.50: Load-displacement curves for different interface cases

As Case 3 was thought to better represent the field situation, all further analyses were performed with this condition. It may be noted that for the Case 3 analysis presented in Figure 7.50 and for all further analyses presented in this chapter, the water trapped between the soil surface and the underside of the top cap did not cavitate. This is, perhaps, not surprising as initially, before loading, this water had a compressive pressure equivalent to 310m head of water.

7.5.5 Isotropic study

7.5.5.1 Soil conditions

As mentioned in the Introduction, the initial study on the pull-out capacity of bucket foundations in soft clay was performed by assuming the soil to be isotropic. A lightly overconsolidated clay (OCR=1.1) was assumed, and a form of the modified Cam clay (MCC) constitutive model was used to simulate its behaviour. The yield and plastic potential surfaces are given by a Mohr-Coulomb hexagon and a circle respectively in the deviatoric plane (see Chapter 7 of Volume 1). The material properties used in the present investigation are summarised in Table 7.5. The triaxial compression undrained shear strength, which can be derived from the basic parameters as indicated in Appendix VII.4 of Volume 1, varies linearly

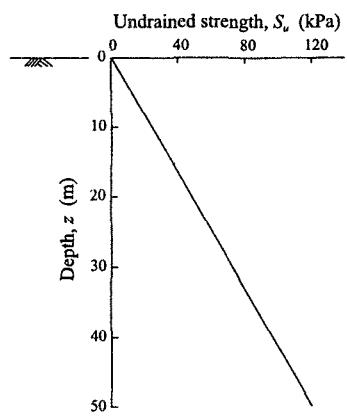

Figure 7.51: Undrained strength for isotropic soil

with depth (see Figure 7.51), giving S_u/σ_v'=0.33, which is typical of soft clays in triaxial compression (Hight *et al.* (1987)).

Table 7.5: Modified Cam clay parameters for soft clay

OCR	γ	K_o	v_1	λ	κ	φ'	μ
1.1	17kN/m^3	0.47	3.1	0.2	0.03	32°	0.3

7.5.5.2 Parametric studies

The reference geometry, identified in Figure 7.47, gives a *D/L* ratio of 1.4. Three parametric studies were performed to investigate the pull-out capacity of bucket foundations:

- To investigate the effect of embedment, the skirt length was varied, keeping the same diameter (D=17.0 m), to L=8.0 m (D/L=2.1), L=12.0 m (D/L=1.4), L=17.0 m (D/L=1.0) and L=24.0 m (D/L=0.7);
- To investigate the effect of the bucket diameter, analyses were performed with similar *D/L* ratios, but with a diameter D=8.5 m;
- Most of the analyses were performed assuming full adhesion, c_w ($=aS_u$), between the soil and the skirt, which means that the full undrained strength is mobilised between the soil and the skirt at failure (i.e. a=1). To investigate the effect of a reduced skirt adhesion, some of the analyses were repeated with a skirt adhesion equal to 50% the undrained shear strength of the adjacent soil.

In each of these studies the inclination, β, of the pull-out force, T, was varied between 0° and 90°.

7.5.5.3 Results

Results from a typical analysis are shown in Figure 7.52. This analysis is for a bucket foundation with D=17.0m and L=12.0m (i.e. D/L =1.4), subjected to a pull-out force, T, inclined at 70° to the vertical (i.e. β=70°). The vertical component, V, of this force is plotted against the vertical displacement and the horizontal component, H, of this force is plotted against the horizontal displacement of the foundation. Figure 7.52 shows that clear limit values are predicted for both the horizontal and vertical load components at failure.

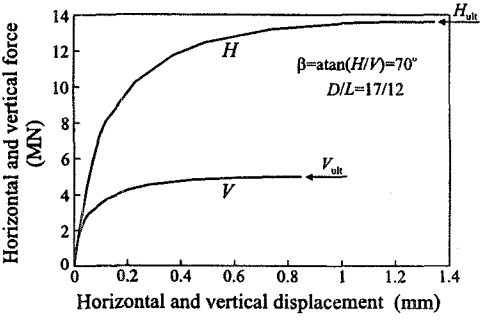

Figure 7.52: Typical load-displacement curves for inclined loading

Figure 7.53 shows, for this particular analysis, the vectors of incremental displacements at failure. While the absolute magnitudes of these vectors are not significant, the directions and relative magnitudes indicate the nature of the failure mechanism.

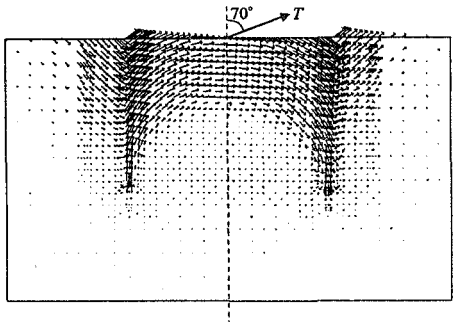

Figure 7.53: Vectors of incremental displacements at the end of an analysis

Full skirt adhesion

The combinations of ultimate vertical, V_{ult}, and horizontal, H_{ult}, loads at which failure is predicted, considering a range of bucket skirt lengths and diameters and full skirt adhesion, are plotted on the interaction diagram in Figure 7.54. As expected, the magnitudes of the ultimate loads are dependent on the diameter and depth of embedment. However, for a particular foundation geometry the finite element predictions indicate that there is an approximately elliptical relationship between the ultimate vertical and horizontal loads, developed under inclined loading with β varying from 0° to 90°. The ellipses fitted to the numerical predictions are plotted in Figure 7.54. The maximum error between these curves and the numerical predictions is ± (0.6 to 1.2)%. Three main conclusions can be derived from this figure:

- For a particular geometry, the largest pull-out capacity occurs under vertical loading and it continually reduces as the inclination of loading increases (i.e. becomes more horizontal);
- The capacities of bucket foundations with constant diameter are nearly directly proportional to their skirt length (e.g. halving the length of the skirt, and hence its contact area with the soil, practically halves the limit loads);
- Changing the bucket diameter, while keeping the same skirt length, has a larger impact than varying the skirt length while keeping the same diameter (e.g. halving the diameter results in a 3.5 times reduction in ultimate loads, while the contact area between the soil and skirt reduces by a factor of 2).

The results plotted in Figure 7.54 are replotted in a normalised form in Figure 7.55. The data from a particular foundation geometry and for a particular load inclination has been normalised by dividing the ultimate horizontal force, H_{ult}, and the ultimate vertical force, V_{ult}, by the maximum vertical force, V_{max}. V_{max} is the maximum vertical load found from the analysis involving purely vertical loading for that particular foundation geometry. The values of H_{ult}/V_{max} and V_{ult}/V_{max} found for all the geometries and pull-out inclinations indicate a unique relationship which can be represented by an ellipse of the following form:

$$\frac{H_{ult}^2}{0.235^2} + V_{ult}^2 = V_{max}^2 \qquad (7.17)$$

All data fit this ellipse with a maximum error of only ± (1.5 to 3.0)%.

Clearly, Equation (7.17) cannot hold for large D/L ratios because in the limit, when the embedment depth L approaches zero, the ultimate horizontal force also becomes zero (i.e. the water interface between the underside of the top cap and the soil cannot sustain shear stress). Further analyses have been performed to determine the limiting value of D/L over which Equation (7.17) does not apply. These analyses indicate that Equation (7.17) is valid for $D/L < 4$.

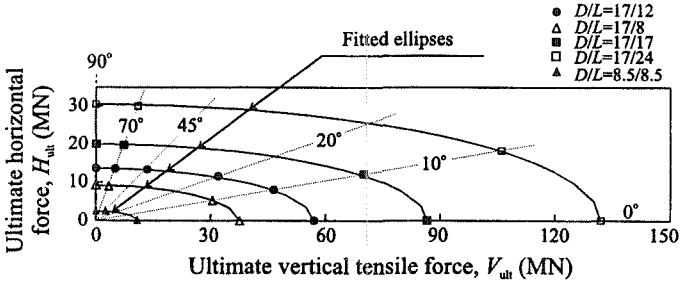

Figure 7.54: Envelopes of ultimate horizontal and vertical load - full skirt adhesion

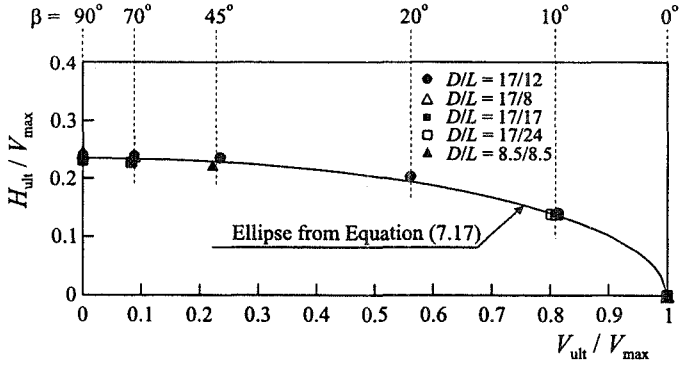

Figure 7.55: Normalised ultimate loads - full skirt adhesion

Reduced skirt adhesion

In the analyses described above, where the full adhesion between the foundation skirt and the adjacent soil was assumed, there was no need to incorporate interface elements in this locality. However, zero thickness interface elements were introduced between the skirt and the soil for the set of analyses in which the skirt adhesion was assumed to be 50% of the undrained strength of the adjacent soil (i.e. $c_w=0.5S_u$). These elements were assigned normal and shear stiffnesses of $100G$ and

$10G$ respectively, where G is the elastic shear modulus of the adjacent soil which varies with depth.

Two sets of analyses were repeated with the reduced skirt adhesion, considering D/L=17/12 and D/L=17/24. The resulting interaction diagram is presented in Figure 7.56. It can be noted that:

- The finite element predictions for a particular geometry can be fitted with an elliptical curve, similar to the analyses performed with full skirt adhesion, shown as full lines in Figure 7.56.
- The ultimate loads obtained for 50% reduced skirt adhesion are approximately 10 to 15% smaller than those for the full skirt adhesion (marked as dashed lines in Figure 7.56), indicating that the reduction in ultimate loads is not directly proportional to the reduction in skirt adhesion.

The results are also plotted in normalised form in Figure 7.57, together with the ellipse from Equation (7.17). They agree with this curve with a maximum error of 6%.

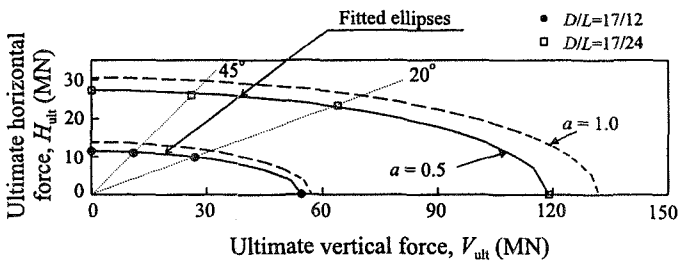

Figure 7.56: Envelopes of ultimate horizontal and vertical load - reduced skirt adhesion

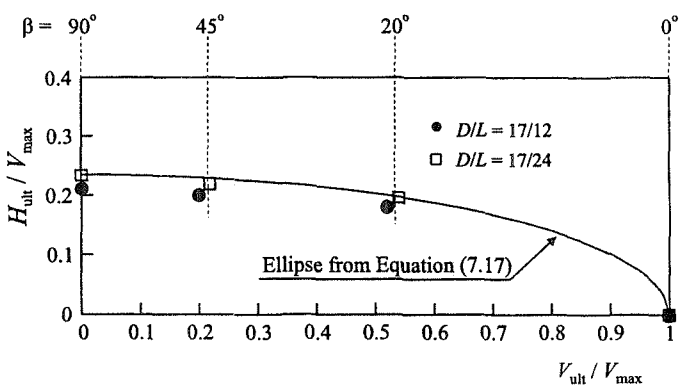

Figure 7.57: Normalised ultimate loads - reduced skirt adhesion

7.5.6 Anisotropic study

7.5.6.1 Introduction

To model the anisotropic behaviour of the soil the MIT-E3 model has been used. Selection of appropriate parameters for a soft sea bed clay have been discussed in some detail in Section 6.5.7. The parameters are listed in Table 6.4 and these have been adopted for the analyses presented here.

The undrained triaxial compression strength profile for this soft clay is shown in Figure 6.42. It varies linearly with depth, starting from a finite value at the soil surface, giving S_u/σ_v'=0.36. This triaxial compression profile differs slightly from that used in the previous isotropic analyses, but is a consequence of trying to model the anisotropy experienced in the Hollow Cylinder Apparatus (see Section 6.4.1). The difference has no bearing on the conclusions that come.

7.5.6.2 Results

In order to quantify the effect of soil anisotropy on the pull-out capacity of bucket foundations two sets of analyses were performed, assuming the foundation to have a reference geometry (D/L=17/12) and full skirt adhesion:

- Analyses where the bucket foundation was loaded with a tensile force whose inclination, β, varied from 0° to 90° and in which the soil was assumed to be anisotropic, i.e. to possess the variation of undrained strength presented in Figures 6.41 and 6.42.
- Analyses where the bucket foundation was loaded in the same way, but the soil was assumed to be isotropic. The soil properties for the MIT-E3 model were chosen such that, for any inclination α of the major principal stress, the undrained strength was the same as that obtained from the anisotropic soil when sheared with α=0°, see Section 6.5.7.3. This means that the effective stress paths for any α match the effective stress path for test M0 in Figure 6.41.

Again, an interaction diagram of ultimate vertical and horizontal forces for each particular inclination of loading is produced, as shown in Figure 7.58. The upper envelope represents the results from the isotropic analyses, while the lower envelope is for the anisotropic analyses. Similar to the previous analyses, both isotropic and anisotropic numerical predictions can be fitted with a simple elliptical curve, with a maximum error of ± (0.6 to 1.2)%. However, the main conclusion from these analyses is that taking account of soil anisotropy reduces the pull-out capacity of the bucket foundation. For this particular soil the anisotropic analyses lead to capacities that are about 22% lower than those for isotropic cases. Clearly, the reduction of pull-out capacity due to anisotropic soil behaviour will depend on the amount of strength anisotropy that each particular soil possesses.

The resulting normalised interaction diagram is presented in Figure 7.59, together with the ellipse from Equation (7.17). The analytical data points conform to the curve with a maximum error of 6%.

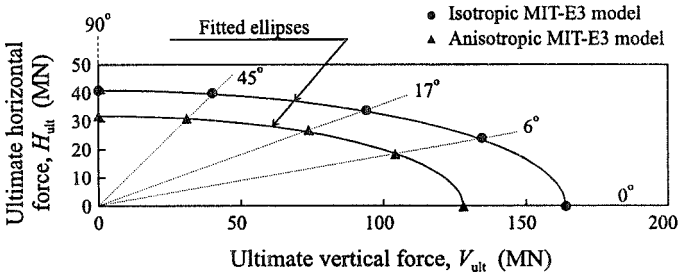

Figure 7.58: Envelopes of ultimate horizontal and vertical load from isotropic and anisotropic analyses using the MIT-E3 model

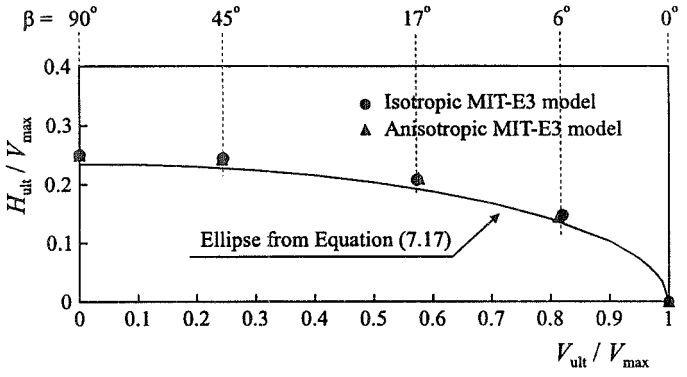

Figure 7.59: Normalised ultimate loads from isotropic and anisotropic analyses using the MIT-E3 model

7.5.7 Suction anchors

7.5.7.1 Introduction

In the previous sections the behaviour of bucket foundations loaded at the centre of the top cap has been considered. Such a loading situation is typical of that of a tension leg platform, but may not mobilise the maximum possible capacity of the anchor. Recent results from large scale field test have shown that by lowering the attachment point of the loading tether from the top to half way down the skirt, the load capacity increases (Anderson (1998)). To illustrate this effect the results of some numerical analysis in which the position of the loading tether is varied will now be described.

7.5.7.2 Geometry

The bucket is now assumed to be made of steel and have a diameter of D=3m and a skirt length of L=9m, see Figure 7.60. The loading tether is assumed to be attached to a point some distance l down the skirt.

The finite element mesh is shown in Figure 7.61. As the software that was used did not have the facility to use shell elements in Fourier Series Finite Element Analyses, the steel bucket was modelled using solid elements. In reality the steel of the bucket is likely to be approximately 10mm thick, however if this had been modelled in the analyses then a large number of elements would have to be used to avoid elements with large aspect ratios. Consequently the steel was modelled as 100m thick, but its Young's modulus, E, was reduced from 210×10^6 kN/m^2 to 30×10^6 kN/m^2 to compensate. The Poisson's ratio μ=0.15. The clay was assumed to be isotropic and was therefore modelled using the modified Cam clay model and the parameters given in Table 7.5.

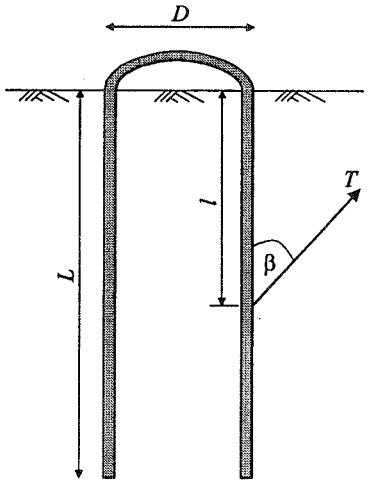

Figure 7.60: Geometry of the suction anchor used in analysis

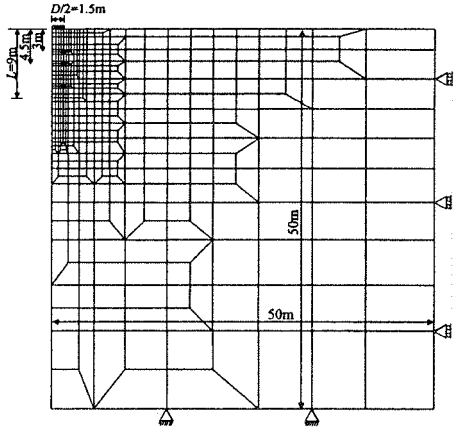

Figure 7.61: Finite element mesh for suction anchor analysis

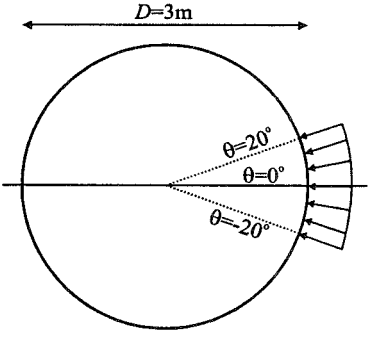

Figure 7.62: Anchor loading modelled in FSAFEM

As the attachment point of the loading tether is positioned on one side of the bucket and at some distance down the skirt, care must be exercised when specifying the loading conditions. In the present analysis a single line load was applied at the node on the outside of the bucket at the required depth down the skirt. In addition a *local axis* (see Section 3.7.2 of Volume 1) was specified at this node so that one of the axis aligned in the direction of loading (i.e. β to the vertical). The line load was then oriented in this direction, but its magnitude varied

in the circumferential direction as shown in Figure 7.62, which shows the line load distribution for an increment of the analysis. The load has an intensity of 100kN/m over a 40° sector of the skirt and is zero over the remaining part. This gives a resultant load in the direction of the tether of 100kN per increment.

This loading condition was specified using the fitted method described in Appendix XII.7 of Volume 1. In this approach a series a line load intensities and the values of θ at which they act are input.

7.5.7.3 Results

Analysis have been performed with the attachment point at four positions, namely at the top of the skirt, one third of the way down the skirt, half way down the skirt and at the bottom of the skirt. For each attachment point analyses have been performed with the direction of loading β equal to 0° (i.e. vertical), 45°, 70° and 90° (i.e. horizontal), see Figure 7.60.

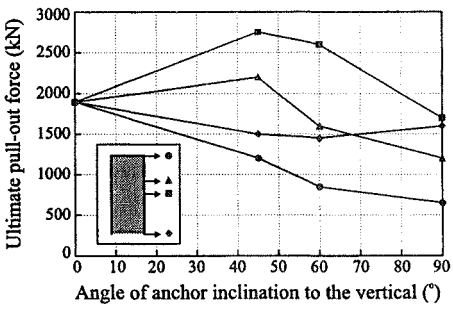

Figure 7.63: Ultimate anchor pull-out force for different anchoring points

The ultimate capacities predicted by these analyses are summarised in Figure 7.63. Interestingly all the analysis with vertical loading predict approximately the same load capacity, independent of the depth of attachment of the tether. However, this is not so if the loading is inclined, where the analyses indicate that the greatest capacity is predicted for the analysis with the attachment point located half way down the skirt. The analyses are therefore in agreement with the field observations.

7.6 Summary

1. When analysing a single pile subject to axial loading either thin solid elements or special interface elements should be placed adjacent to the pile shaft. If solid elements are used and they are not sufficiently thin, the analysis will over estimate the pile shaft capacity.
2. If interface elements are positioned adjacent to the pile shaft care should be taken when selecting their normal and shear stiffness. These values, if not sufficiently large, can dominate pile behaviour. However, if the values are too large numerical ill conditioning can occur.
3. Soil dilation can have a dominant effect on pile behaviour and consequently care must be exercised when selecting an appropriate constitutive model and its parameters.
4. When analysing axially loaded piles using an effective stress constitutive model it is unwise to use a model which predicts finite plastic dilation

indefinitely, without reaching a critical state condition (e.g. the Mohr-Coulomb model with $\nu>0°$). Such analyses will not predict an ultimate pile capacity.

5. When analysing a single pile subject to lateral loading the possibility of a crack forming down the back of the pile (i.e. gapping) should be considered. If this is likely to occur interface elements should be installed along the pile soil interface, which cannot sustain tensile normal stresses. Wether or not gapping is likely to occur depends on the soil strength and in particular its distribution with depth.
6. A new method of design and analysis for pile groups is proposed. This method is thought to be an improvement on the existing methods because:
   - A more sophisticated and rigorous method of analysis of single piles is used which is able to incorporate complex soil and pile-soil interaction behaviour;
   - A more coherent method for accounting for pile group interaction is used which is based on the results of single pile analyses.
7. The proposed method of analysis predicts pile group rotations and displacements for any applied load. The method is an iterative procedure that requires FSAFEM analyses be carried out for each iteration. The basic assumptions in this method are:
   - Superposition techniques can be used to determine the manner in which the loads applied to one of the piles in a group affects the displacement of the other piles;
   - The rigid pile cap criterion can be used to determine the manner in which the loads applied to the group are distributed between the piles in the group.
8. The design method produces design charts from which the pile group displacements and rotations can be evaluated without recourse to additional FSAFEM analysis. The basic assumption made by this method, in addition to the two method of analysis assumptions, is that the loads required to cause displacements $\boldsymbol{U}$ can be obtained by summing the loads required to cause each component of $\boldsymbol{U}$ (superposition of loads).
9. The proposed analysis and design methods for a pile group were applied to the foundations for the Magnus platform. The pile group stiffness obtained from the new method of design was in good agreement with the measured foundation stiffness.
10. The methods of design and analysis were used to predict the pile group displacements and rotations for the loads imposed by the largest wave of a storm on the 22nd January 1984. The predictions obtained were shown to be in good agreement with each other and with the measured displacements and rotations. The predictions from the new methods are shown to be much more accurate than the predictions from conventional methods.

11. A parametric finite element study has quantified the effects on the pull-out capacity of 'bucket' foundations loaded at their top of (i) foundation geometry, (ii) skirt adhesion and (iii) load inclination. The main conclusions are as follows:
    - The largest pull-out capacity occurs under vertical loading;
    - Pull-out capacity continually reduces as the inclination of loading rotates from the vertical;
    - Foundation diameter affects pull-out capacity more significantly than embedment depth;
    - Ultimate pull-out capacity is not directly proportional to the value of skirt adhesion.
12. Finite element analyses using the MIT-E3 model have shown how account may be taken of the anisotropic soil strength observed in the laboratory. Anisotropy in S_u was seen to reduce the pull-out capacity by approximately 22%, compared to equivalent analyses assuming isotropic behaviour.
13. It has also been shown that normalising the ultimate horizontal and vertical pull-out forces with respect to the ultimate vertical force, obtained from an analysis involving only vertical pull-out, results in a unique interaction curve, at least for the soil profiles considered and for $D/L < 4$, that specifies a non-dimensional failure envelope that is independent of the foundation dimensions, skirt adhesion or soil anisotropy. This curve is of a simple elliptical form with ratio of minor to major axis of 0.235, and once the vertical pull-out capacity has been evaluated, designers may use such a curve to determine the capacity under any inclined loading conditions, without performing additional complex three dimensional analyses.
14. It should be noted that the above conclusions are valid for tension leg platform type bucket foundations that are loaded at the centre of the top cap. If such foundations are used as suction anchors, for mooring other vessel types, the load is often applied at a point someway down the skirt. In such cases it has been shown that the maximum capacity is obtained when the point of load application is approximately half way down the skirt and the load is inclined at 45° to the vertical.

8. Benchmarking

8.1 Synopsis

This chapter discusses the benchmarking of finite elements programs, but the comments made are equally applicable to the testing of other computer software. The aim of this chapter is to demonstrate that problems can arise when undertaking finite element analysis, which, unless they are detected, can have serious implications.

A number of geotechnically orientated benchmark problems are presented and discussed, together with the results of a benchmarking exercise carried out to assess the reliability of a number of finite element programs.

8.2 Definitions

Throughout this chapter the following terms are used:

Benchmark: A problem formulated to check the performance of a computer program.

Benchmarking: The processes of testing, validating, verifying or checking the performance or operation of software.

Closed form solution: An exact and unique theoretical solution to a well defined problem, which usually involves the analytical solution of a series of equations without the use of iterative techniques.

Computer Hardware: Physical components of a computer, such as hard discs, floppy discs, disc drives, printers, processors, etc.

Computer Software: The computer code that provides the computer with the instructions necessary to perform a set of calculations. This includes the operating system used by the computer (e.g. Windows® 98, Windows® NT, Unix, etc), a compiler and any manuals that explain how the software operates and the method of calculation.

Developer(s): The person(s) or organisation(s) responsible for writing and developing the computer software.

User: The person or organisation who simply uses the developer's software, but does not produce code or modify the operation of the software in any way.

Validation: Ratifying or confirming that a particular operation is being performed correctly. The process of evaluating software at the end of the

software development process to ensure compliance with software requirements.

Verification: Establishing the truth or correctness by examination or demonstration. The process of determining whether or not the products of a given phase of the software development cycle fulfil the requirements established during the previous phase.

When applied to the testing of computer software, and its operation, the terms 'validation' and 'verification' are often confused, since to most people they have a very similar meaning. Although in some technical literature a distinction is made between the two, in this chapter they are taken to mean the process of testing computer software to evaluate its performance, assessing its accuracy and correct operation by an individual and on specified hardware.

8.3 Introduction

Computers have for many years been available to engineers to aid design. In recent years engineers have had the possibility to routinely use advanced numerical methods (finite element analysis, boundary element analysis and finite difference techniques) in design. The possibility to do so is largely due to the increased availability of such programs, combined with the rapid pace of hardware development. It is apparent that the use of these methods is becoming more widespread, as more engineers appreciate the benefit of using such techniques to examine complex problems and the sensitivity of these problems to various influences.

When undertaking any calculation, an engineer has a responsibility to check that the calculation is appropriate and numerically correct. A check should therefore be made to ensure that the tools used are working correctly and that the results obtained are reliable. It is important to remember that computers and computer programs do not have a mind of their own, they simply execute a series of pre-defined instructions. The question is, do these instructions correctly follow the desired method of analysis and produce the intended result, and/or does the user understand what the result is.

There is a number of reasons why errors may occur in calculations performed using computer programs. These include errors or bugs in the software through mistakes in coding or interpretation of the method of analysis, the use of the software, or, in exceptional circumstances, there may be hardware problems. A technique for checking the computer program and the use of it is known as benchmarking. Essentially, it is a technique which forms part of the validation or verification process.

This chapter starts by discussing, in general terms, the issue of verification and validation of computer software and then goes on to discuss the benchmarking of finite element programs, with particular reference to geotechnical engineering. Most of the principles and techniques are equally applicable to the finite element analysis of other problems (structural, thermal, hydraulic, etc.) and to the use of computer programs in general.

The principles of benchmarking (what is benchmarking, why is it necessary and what is to be gained from it) are outlined and some examples of benchmarking exercises of geotechnical problems are discussed.

8.4 Causes of errors in computer calculations

Problems may arise with computer calculations for a number of reasons. The most common causes are as follows:

- An error in the interpretation of the underlying theory by the developer. The analytical technique or theory has not been understood correctly by the programmer and therefore has not been coded correctly.
- There are errors, mistakes or 'bugs' in the code, which mean that the program does the wrong calculation and not the calculation that the developer or user believe the program is doing (refer to the problems associated with the Aston Park multi-storey car park, Section 8.5). These 'bugs' may extend to the operating system or compiler, which cause problems to occur even when a previously tested version of a program is run. Such problems are not uncommon even now.
- The numerical techniques used are not appropriate or are prone to error. There may be some numerical instability which results in mis-leading answers. In finite element analyses nonlinear problems are solved using iterative methods. Under certain circumstances convergence may be difficult to attain and may require several attempts using different increment sizes (refer to Chapter 9 of Volume 1).
- Interface conflicts between software and hardware or between software and software. The same program gives different answers when run on different types of computer, or under a different operating system.
- The user does not understand the theory or the method of calculation used by the program, and therefore cannot formulate the problem in the correct way.
- The program is not being used in an appropriate way, i.e. using it to analyse a problem for which it was not designed.
- Mistakes in manuals or the method used to input data (pre-processing) that mislead the user and mean that data is not input correctly. Likewise, there may be errors in the post-processing such that, although the calculations are correct and accurate, incorrect results are presented to the user.
- Faults in the hardware. When Pentium processors were first introduced there was a flaw which gave inaccurate results in division calculations which lead to a 'reduction in precision'. This obviously had serious implications for many users who had to undertake comparative calculations using other hardware (NCE (1994)).

The computer programs and hardware need to be checked before they are used, in order to ensure that none of these problems exist. As the three examples of failures resulting from errors demonstrate (see Section 8.5), the consequences of

an error being made could be severe and could have extremely serious implications. It is obviously important that any of the potential problems with the computer program, or the use of it, are identified and dealt with.

8.5 Consequences of errors

The consequences of errors occurring in any calculation can vary enormously. There may be small errors which, in practical terms, are of little significance for most situations, but under certain conditions they become much more critical. This may result in the reduction of a factor of safety, or, in exceptional circumstances, a structure may fail. Alternatively, the error may lead to over design, incurring unnecessary construction costs, or it may falsely highlight an apparent problem which has to be resolved incurring additional cost or economic loss. In the Authors' experience the latter is not uncommon. For example, tunnel linings have incorrectly been shown to be overstressed and movements of structures have been erroneously overestimated. These erroneous results have thrown into question the viability of quite significant schemes, or delayed construction while the problems have been resolved.

If failure occurs, the consequences may not be just economic, but lives may be put at risk. Failures that were attributed to errors in computer programs, and their use, include the following cases:

- The Aston Park multi-storey car park (constructed circa 1983). After construction cracks were noticed in the slabs of the reinforced concrete structure on the upper two levels. Eventually, cracks spread to the lower floors and it became clear that there was a serious problem. Apparently faulty programming resulted in reinforcement being placed 90° out of orientation. Essentially, 'the slabs were light of steel in the direction of span in which they should have been heavy'. The report on the failure concluded that an 'off the shelf' computer program was to blame (it was subsequently acknowledged by the developer that there was a bug in the program) and went on to severely criticise the designers, claiming that there was no evidence of any checks being carried out. To make matters worse, the program indicated that there was a problem with the computation but, due to a failure of understanding between the users and the developers, the full implication of the fault was not appreciated. The designer apparently mistakenly believed that he fully understood the output and the significance of the warning signal was missed (NCE (1983), (1984a) and (1984b)). This failure caused some alarm at the time, since the program was commonly used by engineers to design structures of this form.
- Trial wind turbine (circa 1990). The failure of a blade on an advanced wind turbine was caused by a wrongly written computer program. The tension side of the blade split and progressive failure caused the other half to break off. The finite element program used for the analysis had apparently been adapted to suit

the project (NCE (1991)). At the time concerns were raised about the safety of other turbine blades produced by the same manufacturer.

- Sleipner offshore platform (1993). In August 1993 the concrete gravity base of the Sleipner A platform sank during ballasting trials. An explosion was heard and 15 minutes later the final 10m of the structure disappeared below the water surface and the structure was lost. Twenty two people were on or around the structure at the time and fortunately all were evacuated safely. The cost of the structure was approximately $180m, but the economic loss was about $700m. Problems arose when one of the buoyancy cells imploded under load. In the design of the structure extensive use was made of finite element analysis, but for whatever reason, problems with the use of the software or problems associated with interpretation of the results, a critical design condition was not identified.

In all three cases the consequences for the Client and the designers were serious, although potentially in two of the cases matters could have been far worse. At the time all three cases received unwanted publicity and were an unpleasant reminder to all engineers that computer programs and calculations need to be checked. Had adequate checks on the software been undertaken, before they were used for design, errors in the computer code, or problems with the use of it, could have been detected and the failures avoided.

8.6 Developers and users

8.6.1 Developers

Traditionally, developers of software have tended to be either organisations or academics who program specific analytical and/or numerical techniques. The software they produce may be made available to users commercially by selling or leasing it.

Some software developers expend enormous resources on checking their programs and ensuring that they are robust. Limitations may even be placed on the use of the program, to prevent misuse, by introducing default values for certain control features. They may submit their software for independent assessment or type approval (fitness for purpose), which is undertaken by certain organisations (e.g. Lloyds Register). This is a check on the 'product' rather than the procedures used for development. Other developers carry out relatively little testing beyond fairly basic checks on the code and its operation. They tend to adopt the principle of 'user beware'. Such effort, or lack of it, is usually reflected in the cost. Obviously, cheaper programs are likely to be less robust than more expensive programs, which are likely to have been subjected to more testing. A potential user should take this into account when considering the purchase of any program.

Although the developer may be responsible for the code, and should carry out sufficient checks to ensure that the program is working correctly and that the relevant theory has been correctly applied, the developer cannot be responsible for the way the program is used, or the interpretation of the user on the way it is used.

Further, the developer cannot trace all the bugs in a program, which may consist of many thousands of lines of code, and some of these bugs may only become apparent if the program is used in a certain way. Therefore, the user has to be aware that such problems may exist.

In the past the user was rarely given the opportunity to modify code. If changes had to be made this was usually done by the developer. However, in recent times the situation has become more complicated. Some computer programs that are sold commercially allow the introduction of 'User Defined Subroutines' (UDS) to allow special features to be added, or new constitutive models to be introduced into the program. Under these circumstances the traditional user or purchaser assumes the role of the developer. Not only must the person writing these features ensure that the subroutine is working correctly, but the interface with the rest of the program needs to be checked. The subroutine may function perfectly adequately by itself, but it may cause errors in other parts of the program which were otherwise functioning correctly. This requires a very extensive checking procedure, particularly with the more complex codes. The UDS will have to include all the error control routines, which further complicates the issue. There are obviously still further complications if there is limited access to the source code. Essentially, if changes are made the program has to be re-validated (consider the example of the wind turbine that failed).

8.6.2 Users

Users should expect that developers have carried out sufficient checks to ensure that the program is working correctly, but this cannot, and should not, be taken for granted. A number of issues arise: does the user or engineer have a responsibility to carry out sufficient validation of any computer applications used in design; if so, what procedures have to be adopted; is the implication of this that if the engineer does not adopt such procedures, then there has been a breach of professional responsibility?

Some people are of the opinion that users should be given greater access to computer source codes. This would allow users to better understand how the program was operating and might, under certain circumstances, allow them to customise it. This is obviously desirable when testing the program by benchmarking or other means because, if problems occur, it might be possible to identify the source of any errors.

There is, however, a number of drawbacks. In the case of finite element programs, and other programs based on advanced numerical methods, there are very few people capable of interpreting the code and even fewer with sufficient knowledge to successfully customise it. Even after a relatively minor modification a sufficiently rigorous testing programme needs to be initiated to ensure that no unforeseen errors have been introduced, or interface problems have developed with other sections of the code.

Does the fact that the user has access to the source code, and has had the opportunity to inspect it, shift the onus of responsibility for checking the program

further away from the developer onto the user? Is there even more need for the user to comprehensively test or benchmark the program? If problems did arise, even in an unmodified code, would the developer be able to use the fact that the user could have identified these problems if it had been correctly tested, or benchmarked, to minimise or even evade any responsibility?

The professional responsibility of an engineer to adequately check computer programs has long been recognised by the Institution of Civil Engineers. The following question was for sometime included in the list of essay questions forming part of their professional examination (Q.24, The place of the engineer in the community and management topics; questions applicable to Section B of the Essay for the 1981 April and October Professional Examination):

"Discuss the impact of increasing computer applications on the civil engineer's design responsibilities and the procedures that must be adopted to ensure the proper use of such applications."

In the early 1980's there were numerous articles in New Civil Engineer, the Institution of Civil Engineers' weekly journal, discussing these issues. Much was made of a comparative study undertaken by the Construction Industry Research and Information Association (CIRIA). The exercise compared the results obtained from seven different programs that were based on code of practice for the design of reinforced concrete beams. No two programs gave the same answers.

In 1990 the UK's National Economic Development Office warned the users of computer hardware and software that, under current UK legislation, they were very unlikely to be able to sue suppliers or developers if faults were found in hardware or software. Commenting on this statement, the Association of Consulting Engineers reminded engineers that, irrespective of any legal redress, they had a responsibility to ensure that calculations were accurate, whether or not they were done using a computer.

Identifying that there was potentially a problem with the use of computer programs, in 1994 the Association of Geoenvironmental and Geotechnical specialists (AGS (1994)) published a guide for the validation and use of geotechnical software. This document was not aimed specifically at users of advanced numerical methods, but it did draw on the work of NAFEMS (National Agency for Finite Element Methods and Standards) for setting out strategies for testing software. When published, the guide stimulated a number of debates as to how these issues should be dealt with. A number of suggestions were put forward, including formation of an industry sponsored testing organisation for software. However, to date this has not materialised.

In recent times many engineers work in an environment where quality assurance (QA) procedures are applied. Although at times these procedures may appear to be unnecessarily bureaucratic, they lay down management principles which are measured against a standard, most commonly ISO 9000. There is a requirement to ensure that the 'tools' being used to produce the product (i.e. design) are of an adequate quality and that checks are made to ensure that this

quality is maintained. Obviously, the results of computer analyses could have a major impact on a design, or a product, and therefore sufficient checks need to be made on the program and the results obtained to ensure their adequacy.

8.7 Techniques used to check computer calculations

There are several techniques that may be used by the developer or user to check programs. These include the following approaches:

- A check carried out on the code by reading it, to check if there are no inadvertent errors.
- Sample calculations of specific algorithms.
- Checks against closed form solutions.
- Checks against other calculations made by either another program, another technique or an earlier version of the program, if that version has been tested and found to be correct.
- Checks made by running the same problem with the same computer program on different hardware, to ensure there are no interface problems between different software packages and the hardware or operating system.

In most instances, because of the complexity of the code or because there is limited access to it, the checker is not in a position to check the code line by line. Therefore the checker must rely on checking the program against other calculations. This technique is known as benchmarking.

The process of benchmarking can be used to establish not only whether or not the program in question is working correctly, but also to establish how accurate the program is. Under some circumstances specific techniques may need to be applied to improve accuracy.

8.8 Benchmarking

8.8.1 General

There may be a number of reasons for wanting to undertake a benchmarking exercise. These include:

- Testing the fundamental operation of the software. As many of the features of the program as possible, both as individual components and in combination with each other, should be tested. Therefore problems need to be formulated that adequately check these features. Obviously, the more complex programs require a greater range of test problems. Ideally checks against closed form theoretical solutions should be made. However, the results of one analysis might be compared with the results obtained from an analysis using another software package, but there is potentially a problem. What if both codes are in error? If both codes use the same solution strategy and this is not accurate, is this a fair test (this will be illustrated by one of the examples of benchmark problems which will be presented later)?

- Checking that there are no hardware-software interface problems, or no interface problems when the operating system is changed. Then, apart from checking against closed form solutions, it may be acceptable to compare results of the same version of the program run in a different environment. The Authors have had some experience of this problem. When upgrading an operating system from one version to another (this was not a change in the operating system), a problem occurred with a program that was in daily use. Meshes that could be generated with the program when using the earlier version of the operating system could not be generated when the same program was used with the newer operating system. It was fortunate that the error was so obvious since it was quickly found and rectified, but it involved a series of rather tortuous and time wasting discussions with the supplier of the operating system.
- To familiarise a user with the software or an updated version of it, or to test the competence of a user to use a program. The benchmarking process therefore becomes a test of the user and not just a test of the software. To illustrate the importance of such an approach two benchmarking exercises, the INTERCLAY II project (EUR 15285 (1993)) and a project initiated by the German Society for Geotechnics, are discussed in Sections 8.10 and 8.11.

Depending on the structure and/or complexity of the program the benchmarking exercise may be, of necessity, a time consuming and extensive task. Standard benchmarks do exist but other tests, non-standard benchmarks, may need to be developed, particularly for geotechnical software.

8.8.2 Standard benchmarks

NAFEMS is an organisation based in the U.K., which was formed by users and software developers, the majority of whom are associated with the aeronautical industry or process engineering. Over a number of years NAFEMS has published a number of standard benchmarks for finite element programs. The background to the development of these benchmarks is explained in the publication "The standard NAFEMS benchmarks" (NAFEMS (1990)), from which the following extract is taken:

"In 1986 NAFEMS attempted to produce the first set of independent 'standard' tests which could be applied to any finite element system. The tests were intended for the use of code developers, users and others who were interested in the performance of their specific codes. They were designed to be a little more searching than those publicised or quoted by the software developers, since these were naturally intended to demonstrate the favourable performance of a system, rather than the deficiencies".

These benchmarks are actually quite demanding in the way the problem is formulated. The specification for the problem is quite detailed and very rigid. Not only are the essential features, such as geometry, loading, boundary conditions and material properties defined, but so are the element types and the dimensions of each element.

The 1990 NAFEMS publication provided standard benchmarks, covering structural problems (plates and shells), heat transfer and vibration problems. More recently some other topics have been covered, but as yet not geotechnical engineering.

The INTERCLAY II project, sponsored by the European Commission, was a coordinated benchmark exercise on the rheology of clays. The report on the project (EUR 15285 (1993)) provides four examples of problems which might be used for benchmarking purposes. This exercise will be discussed in some detail subsequently (refer also to Jefferies and Knowles (1994)).

8.8.3 Non-standard benchmarks

For the reasons NAFEMS explained, the geotechnical engineer cannot rely on those problems produced by the developer to properly check the program. However, these may be useful when first installing the program, as they allow any obvious problems with the hardware and operating system to be identified at an early stage. The user of a geotechnical software package therefore has a serious problem, since standard geotechnical benchmarks do not exist.

Users therefore need to develop sufficient and exacting benchmarks to adequately test the software. Problems need to be formulated which have a known solution that can be compared with the results of the program being tested.

8.9 The INTERCLAY II project

The INTERCLAY II project was sponsored by the European Commission within the 'European Atomic Energy Community 4th Research and Development Programme'. This was a collaborative exercise involving 10 organisations, although not all organisations participated in every aspect of the project (see EUR 15285 (1993) for full details). Two of the objectives of the project were to:

"assess the usability and capability of the (finite element) codes available within Europe, with respect to the geomechanical behaviour of clay" and to *"assess the accuracy and reliability of the numerical predictions of geomechanical behaviour"*.

A number of test problems were specified by a steering group which were analysed by the participants and then individual's results were compared with each other.

When considering the results of the INTERCLAY II exercise, it is important to remember that all the participants were very experienced analysts, some of whom were using finite element codes that they had developed and which had been in use for some years. Others used commercially available codes, although these were very highly developed programs. If it were possible to categorise such programs, those used for this exercise would most certainly fall towards the upper end of the market in terms of their development and the effort put into testing them. As such, they are costly to purchase, lease or acquire the use of.

There were three stages to the project. The first stage involved the solution of hypothetical problems with a defined geometry (not element type or size as for the NAFEMS standard benchmarks), loading conditions and material properties. Stage 2 involved the back-analysis of two laboratory tests to predict results for a third experiment. The third stage involved the analysis of in-situ tests at the Mol (Belgium) underground facility. In the context of benchmarking only the first stage of the project is of interest.

The results of the analyses undertaken during Stage 1 are discussed in Section 8.10 of this chapter, in which the Stage 1 INTERCLAY II problems are used as examples of benchmarking problems. However, when assessing the results of the project as a whole Jefferies and Knowles (1994) commented as follows:

"*The project highlights the need to recognise, more formally, the opportunity for human error and to devise a means of controlling it. The experience from this exercise is that in most cases 'errors' were not discovered until the results were compared with the experimental results and those of other participants. Errors were primarily due to misinterpretations of the benchmark specification as a result of either incomplete definition of the required parameters or misinterpretation of their meaning*".

Despite these comments some participants did discover that there were fundamental problems with their software, or that it was not ideally suited to the analysis of some problems. The exercise proved to be a beneficial experience for all concerned and highlighted the need for caution when using computer programs of any form.

8.10 Examples of benchmark problems - Part I

8.10.1 General

In this section examples of benchmarking problems are presented and discussed. They do not form a complete suite of test problems since they do not cover all the boundary conditions and load cases that a general purpose geotechnical based finite element or finite difference package might be expected to cover. The problems described by Schweiger (1998) could be added to this list if more details of the comparisons made could be obtained for reference.

In Chapter 9 of Volume 1 four simple problems were discussed to demonstrate the accuracy of different solution techniques. These were an idealised triaxial test, a footing problem, an excavation problem and a pile problem. Any one of these problems would be ideal for benchmarking a program, but the first of these, the idealised triaxial test, is perhaps better than the others, because there is an analytical solution to the problem. This is the first of the 5 examples reviewed.

The other four examples of benchmarking problems that are presented are taken from the INTERCLAY II project. Selected results are presented, purely to illustrate certain features of each problem. A full set of results and specifications for the problems can be obtained by reference to the INTERCLAY II report (EUR 15285

(1993)), although specifications for these problems are provided in Appendices VIII.1 to VIII.5. The specifications are less detailed than the NAFEMS standard benchmarks, because there are no restrictions on the mesh details or the solution technique. However, they are no less demanding.

Example 1 Analyses of an idealised triaxial test: two analyses, one drained and one undrained, of a triaxial sample, isotropically normally consolidated and subjected to compression.

Example 2 Analysis of a thick cylinder: a thick cylinder of clay subjected to a differential pressure between the inner and outer surfaces. This problem has a closed form solution.

Example 3 Analysis of an advancing tunnel heading: simulation of the progressive excavation and construction of a cylindrical tunnel.

Example 4 Analysis of a shallow waste disposal: analysis of construction of a shallow repository and emplacement of waste and capping material.

Example 5 A one dimensional problem based on Example 4.

8.10.2 Example 1: Analyses of an idealised triaxial test

Definition of the problem

The geometry of the problem is not specified, but as there are no 'end effects' a single element could be used. Constant increments of axial strain, up to 20%, under undrained and drained conditions, are applied to represent compression of the sample, see Appendix VIII.1.

Results

Analytical solutions for ideal (no end effects) drained and undrained triaxial tests on modified Cam clay are given in Chapter 9 of Volume 1. Figure 8.1 shows the results for the drained triaxial test, using the modified Newton-Ralphson technique with a substepping stress point algorithm for solving the nonlinear finite element equations, while Figure 8.2 shows similar results for the same test performed using the tangent stiffness approach. In each figure results from 3 finite element analyses are given. These differ in the size of the increment of axial strain applied, i.e. 0.5%, 1.0% and 2.0%.

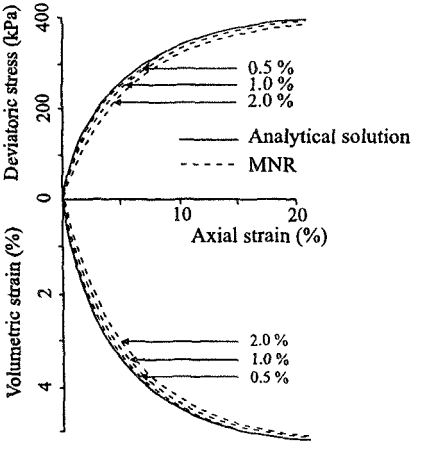

Figure 8.1: Modified Newton-Raphson prediction of drained triaxial test

Comment

There is an analytical solution available which can be used for comparison with

the results obtained from any numerical analysis, but if such a solution was not available then there is potentially a problem. What if an analyst was using a code that used one of the two apparently less robust solution techniques (e.g. tangent stiffness or visco-plasticity, see Chapter 9 of Volume 1) and chose to compare it with the results from a different code using a similar approach?

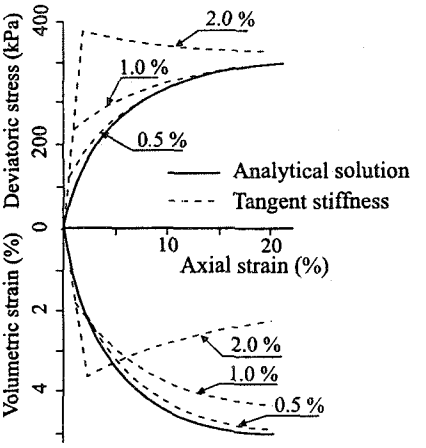

Figure 8.2: Tangent stiffness prediction of drained triaxial test

It is apparent from the discussion in Chapter 9 of Volume 1 that there is potentially a problem with software that uses certain approaches for the solution of the nonlinear governing equations. If an analysis was run using the tangent stiffness approach, then, even if there were no errors in the code or other problems with the use of the program, the results obtained might not be particularly accurate. Simply comparing these results with a program using a similar approach and similar loading increments would not be a sufficiently exacting test. Equally inaccurate results could be obtained.

From this problem the user is able to gauge the accuracy of the software and the measures necessary to obtain sufficiently accurate results.

8.10.3 Example 2: Analysis of a thick cylinder

Definition of the problem

Using a total stress analysis a pressure, σ_i, was applied to the internal boundary of a thick cylinder (see Figure 8.3), so as to unload it. The analysis started with an initial internal pressure within the cylinder of 5000kPa. This pressure was then reduced in stages to give a final pressure of 1500kPa at the end of the analysis, see Appendix VIII.2.

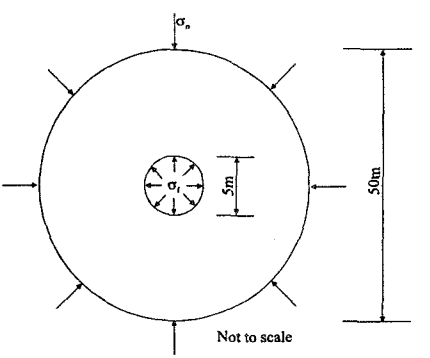

Figure 8.3: Geometry of a thick cylinder

Results

Figure 8.4 shows the pressure-deformation behaviour and Figure 8.5 shows the position of the elastic-plastic interface.

Comment

Like Example 1, this is an ideal benchmark because there is an analytical solution available which can be used to compare with the results.

The results obtained from the INTERCLAY II exercise all showed apparently good agreement between all participants and the analytical solution. All of the participants were aware of the analytical solution when undertaking their analyses and could have made adjustments to the increments of loading to obtain sufficiently accurate results. However, given that all of the participants were very experienced in the use of their own software, it was reasonable to assume that they were able to use these programs well enough to obtain accurate results. The same may not be true if an inexperienced user or a user of some less robust software was to analyse the problem.

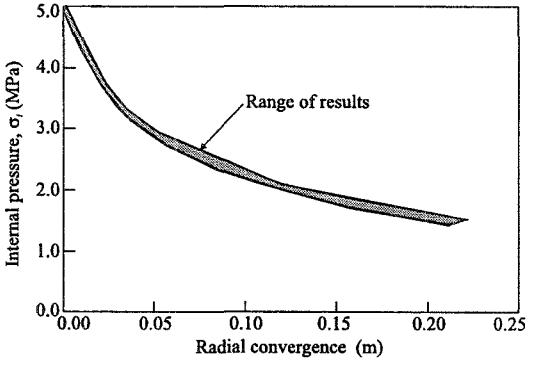

Figure 8.4: Pressure-deformation behaviour

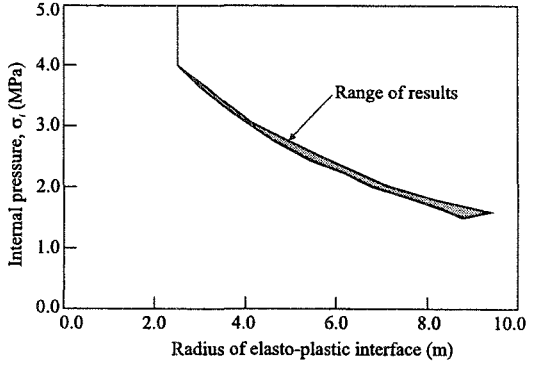

Figure 8.5: Position of elasto-plastic interface vs. pressure

8.10.4 Example 3: Analyses of an advancing tunnel heading

Definition of the problem

Figure 8.6 shows the geometry of the problem which was axi-symmetric. The analyses modelled progressive tunnel construction by advancing the tunnel face and then inserting a rigid lining to provide support, see Appendix VIII.3.

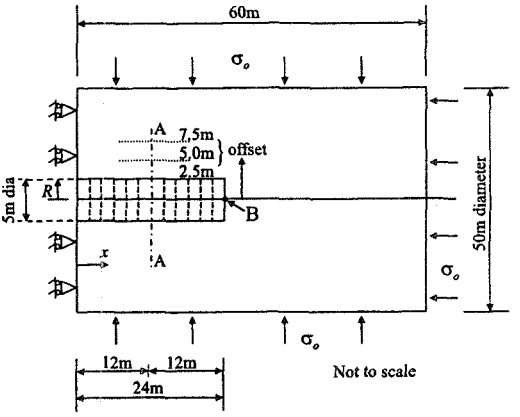

Figure 8.6: Geometry for analysis of advancing tunnel heading

Results

Figure 8.7 shows the range of predicted radial displacements towards the tunnel, using the total stress approach, at three offsets from the tunnel along section A-A (refer to Figure 8.6), while Figure 8.8 shows comparable data for the effective stress approach (the effective and total stress parameters are not compatible and so comparisons between the magnitude of the displacements from the two analyses should not be made). Shown on Figure 8.9 are the displacements of point B (refer to Figure 8.6) versus increasing length of excavation, for both total and effective stress approaches.

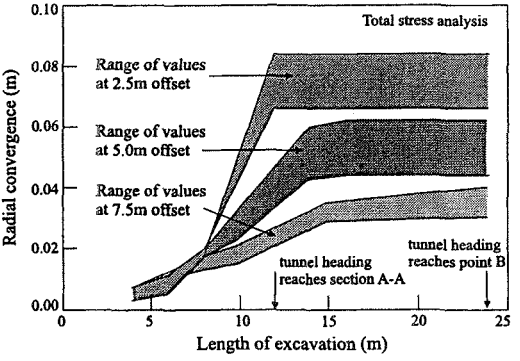

Figure 8.7: Radial convergence with progression of excavation (total stress analysis)

The report on this work (EUR 15285 (1993)) has a series of plots which show stresses at three specified offsets from the tunnel at different stages in the analyses. Figure 8.10 summarises some of these results for the radial stress at the end of excavation.

Figure 8.11 shows the distribution of the radial total stress on the tunnel's periphery (2.5m offset) along the first 12m of the tunnel (from the start of the tunnel up to section A-A, refer to Figure 8.6), when the tunnel has reached point B. Both this and the previous figure relate to the total stress analysis.

Comment

This is not an ideal benchmark. Unlike the previous two examples, there is no closed form solution available. Unlike the standard NAFEMS problems, no restrictions were placed on the geometry of the finite element mesh.

There was significantly more scatter in the results obtained from the analysis of this problem by the INTERCLAY II participants. The plots of displacement (Figures 8.7 and Figure 8.8) show more scatter close to the tunnel than remote from it. For the total stress approach there is a difference of almost 20mm between participant's results for a point on the edge of the tunnel, 2.5m offset. This is probably a consequence of an ill-conditioned problem, because of the boundary condition applied to the sides of the excavation to represent the tunnel lining (zero radial displacement), rather than the accuracy of individual codes. It is important therefore, when formulating benchmarks, that care is taken to ensure that the boundary conditions are reasonable and realistic.

However, close to the tunnel all the participants obtained some oscillations in radial stresses, as illustrated by Figure 8.11. There was considerable scatter, not only between participants, but some of the predictions showed considerable fluctuation along the length of the tunnel for the 2.5m offset (along the boundary of the

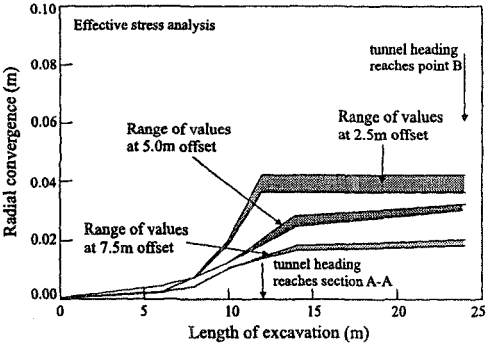

Figure 8.8: Radial convergence with progression of excavation (effective stress analysis)

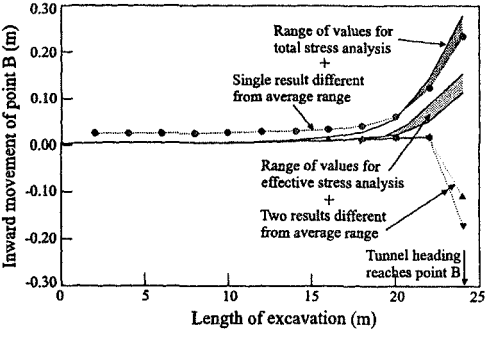

Figure 8.9: Displacement of B vs. length of excavation

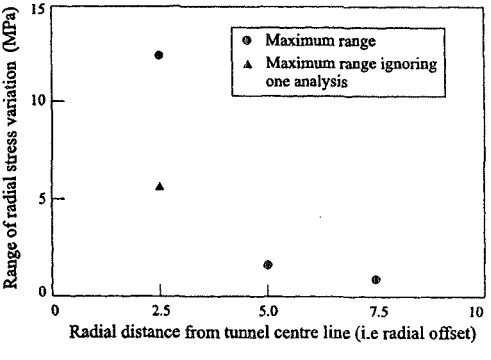

Figure 8.10: Range of radial stress variation at different offsets

excavation). The variation of radial stress was much less along the profiles offset 5.0m and 7.5m from the centre line of the tunnel.

In discussions following completion of this example it was considered that the problem of oscillation of stresses, and the differences in the predicted displacements, were caused by the high stress gradients close to the lining and a singularity at the advancing face, although there may have been some mesh dependancy which influenced results close to the edge of the tunnel (if results are influenced by the mesh, then this problem is just as much a test of the user's ability to formulate the analysis, as it is a test of the software). However, as two participants demonstrated, much smoother results could be obtained by looking at stresses along an offset 0.5m from the edge of the tunnel, rather than along the edge of the tunnel itself, see Figure 8.11. For purposes of future comparisons these results are probably more useful. On profiles further away from the tunnel agreement was much better.

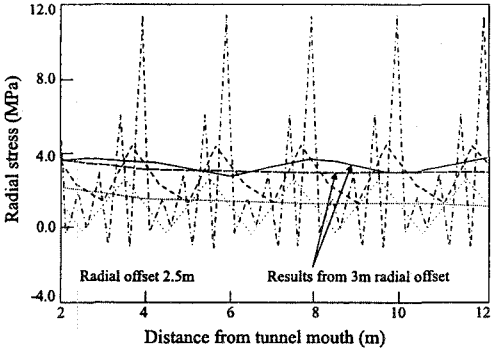

Figure 8.11: Radial stress along tunnel boundary

Despite the apparent problems close to the tunnel, it was generally considered that it had been a worthwhile exercise, since it posed a more demanding test than the previous two problems described. It is a two dimensional problem unlike the previous examples which were essentially one dimensional.

8.10.5 Example 4: Analysis of a shallow waste disposal

Definition of the problem

This was a complex problem which was intended to model the construction of a shallow nuclear waste disposal. The geometry is shown in Figures 8.12 and 8.13.

After setting the initial stress conditions the analyses modelled the excavation for the disposal and construction of the cell walls and base slab. Pumping beneath the base slab was then activated (i.e. zero pore water pressure under the base slab). Filling with the waste material followed and then construction of the capping layers. Long term pore water pressure conditions were then established and collapse of the waste was modelled (see Appendix VIII.4).

There was some discussion about how the collapse of the waste should be modelled. The method adopted may not have been particularly realistic, but for the purposes of this exercise it was considered to be sufficient, since all participants adopted the same procedure.

Results

Again the INTERCLAY II report gives detailed results (EUR 15285 (1993)). Figures 8.14 to 8.18 show vertical displacements along the underside of the base slab, at each of the five stages in the analyses (see Appendix VIII.4). Figure 8.19 compares displacements of point B (refer to Figure 8.12), which is on the centre line at the base of the sand capping layer.

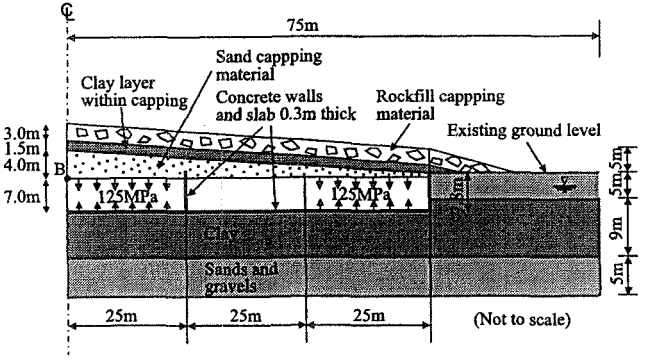

Figure 8.12: Geometry of shallow waste disposal

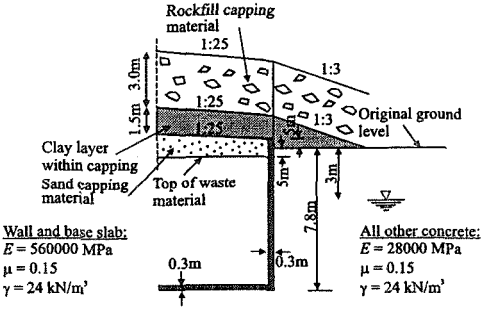

Figure 8.13: Detail of perimeter wall and base slab

Comment

This is the most demanding of the five examples and, like Example 3, there is no analytical solution available and therefore there is no direct check on the results. With this problem some of the deficiencies with some of the codes used by INTERCLAY II participants became apparent. There were also some problems with interpretation of the specification.

With the exception of two participants, similar results for the displacements of the underside of the base slab were obtained for the first stage of the analysis (Figure 8.14). For stages 2, 3 and 4 there was some scatter in the results, although

4 or 5 of the participants obtained reasonable agreement with each other (Figures 8.15 to 8.17). The final stage of the analysis modelled the collapse of the waste. There were obviously some problems with the original specification, since all but one participant did not interpret it correctly.

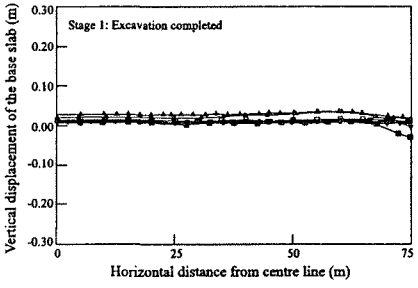

Figure 8.14: Stage 1: Excavation completed

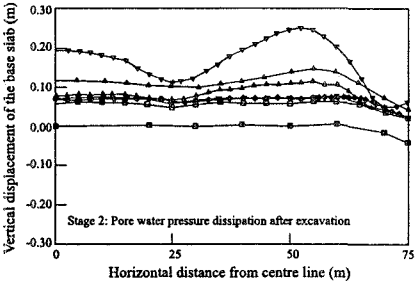

Figure 8.15: Stage 2: Pore pressure dissipation

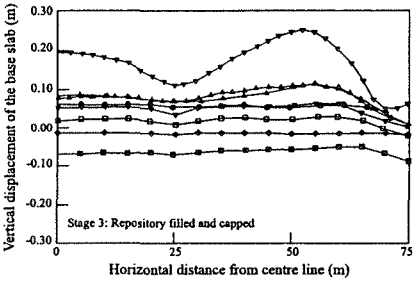

Figure 8.16: Stage 3: Repository filled and capped

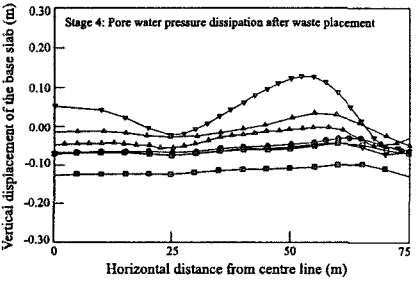

Figure 8.17: Stage 4: Pore pressure dissipation

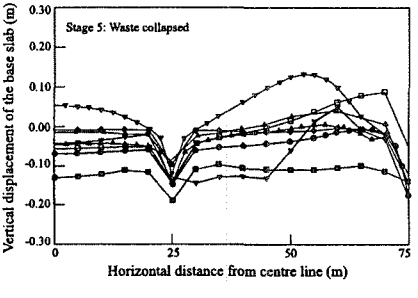

Figure 8.18: Stage 5: Waste collapsed

The analysis of this problem was considered to be a fairly exacting test of any program. It involved the analysis of a two dimensional problem with construction, excavation, prescribed displacements and drainage.

Drainage was tackled in slightly different ways (coupled and non-coupled analyses) and later work identified this as a potential source of minor differences between codes. Further differences were attributable to the method of modelling the walls and base slab. Some participants chose to model these components with zero thickness elements (e.g. beam elements) to which they gave appropriate properties, whereas others used solid elements.

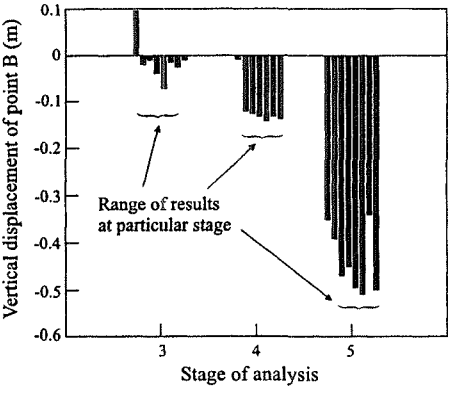

Figure 8.19: Vertical displacement of point B on centre line

Discussions following completion of this work did expose some problems with some of the codes, which had not been identified before undertaking this exercise. This reinforced the point made by NAFEMS concerning the nature of 'supplied' problems for benchmarking. It also reinforced the need for very clear and exact specifications to be drawn up before undertaking any analysis.

In the discussions between participants following completion of this exercise it was apparent that there had been some subtle differences in the way some of the participants had approached the problem. It was therefore resolved that a much simpler analysis should be undertaken, that could be more clearly defined and therefore less ambiguous. This is the fifth example of benchmarking problems that is presented.

8.10.6 Example 5: Simplified analysis of a shallow waste disposal

Definition of the problem

Example 4 raised certain issues regarding the interpretation of the specification for the problem and the boundary conditions applied. Therefore, to remove any ambiguity regarding these difficulties, two further problems were analysed. Both problems (5a and 5b) were intended to reproduce the main features of Example 4.

In case 5a the boundary conditions were explicitly defined (see Appendix VIII.5), whereas in the second case (5b) participants were asked to use the boundary conditions they had used for the main analysis (Example 4), if these differed from those used for 5a.

Figure 8.20 shows the geometry used for the analyses. When the analyses started, none of the soil above existing ground level was present. With the

exception of construction of the cell walls and the collapse of the waste, the sequence used for the analyses followed the sequence used for Example 4.

The report (EUR 15285 (1993)) presents results for both cases analysed. However, the second case (5b) was intended merely to highlight any inconsistences in the interpretation of the specification for Example 4. As such it cannot be regarded as a benchmark, whereas the first case, in which all the boundary conditions were explicitly defined, is an excellent example of a benchmark. Although there is not a theoretical solution to this particular problem, the results can be checked by a series of fairly simple hand calculations.

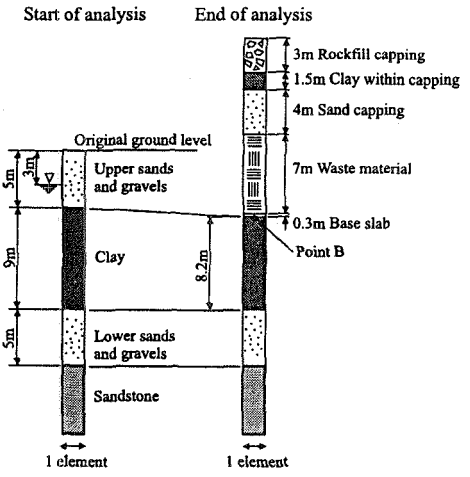

Figure 8.20: Simplified geometry for waste disposal analysis

Results

Figure 8.21 shows the displacement of a point B at base slab level at different stages in the analysis, for case 5a. Similarly Figure 8.22 shows the vertical total stress beneath the base slab.

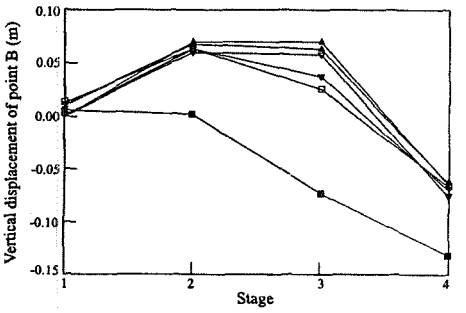

Figure 8.21: Vertical displacement at point B

Comment

Figure 8.21 shows that, with the exception of one of the codes, there was quite good agreement between those who chose to study this problem. The agreement might have been even better, but at least one of the participants was using fully coupled consolidation to model an undrained event. The time steps used may not have been sufficiently short and some drainage may have occurred during this stage, resulting in some settlement. However, the final displacement obtained from this

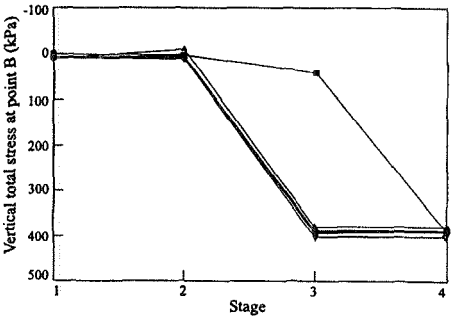

Figure 8.22: Vertical total stress at point B

analysis was very close to that obtained from the other analyses. Again, with the exception of one participant, the predicted total stresses beneath the base slab were very close to each other (Figure 8.22).

Careful examination of the results of the analyses of this example (5a) and the additional analysis (5b) of the same problem, using alternative methodologies, allows conclusions to be drawn as to which analyses of Example 4 were the most reliable (the INTERCLAY II report provides these comparisons, but the figures presented in this chapter are not sufficient to do so).

This is another useful example of a benchmark problem, the specification is very clear and the problem is simple, but it involves the use of a number of different features of a program.

8.11 Examples of benchmark problems - Part II (German Society for Geotechnics benchmarking exercise)

8.11.1 Background

Schweiger (1998) (see also Carter *et al.* (2000)) describes a benchmarking exercise sponsored by a working group of the German Society for Geotechnics. The aim of the exercise was to develop a series of problems which could serve the following functions:

- Provide a check on commercial codes (and presumably on bespoke software).
- Provide a learning aid for young geotechnical engineers to become familiar with numerical analysis.
- Provide verification examples for proving competence in numerical analysis of geotechnical problems.

The aims of this project were therefore broadly similar to the aims of the INTERCLAY II project. This study aimed to use actual practical problems, simplified in such a way that the solution could be obtained with reasonable computation effort.

Two examples are given by Schweiger (1998). For the first example (Example 6) construction of a tunnel was modelled, and for the second example (Example 7) the formation of a deep excavation was modelled. Both are problems that are commonly analysed by geotechnical engineers.

These problems were analysed by a number of participants and the results compared. It should be noted that for both these problem no closed form solution exists and so some reliance has to be placed on a consensus being obtained (this was also true for the more complex INTERCLAY II problems).

8.11.2 Example 6: Construction of a tunnel

Definition of the problem

The first of the two examples involved the construction of a non-circular tunnel,

as shown in Figure 8.23. Two analyses were requested for the exercise: a single-step excavation and a two-step excavation, both assuming an elastic-perfectly plastic Mohr-Coulomb type soil. Material parameters are given in Appendix VIII.6, while a detailed specification is provided by Schweiger (1998).

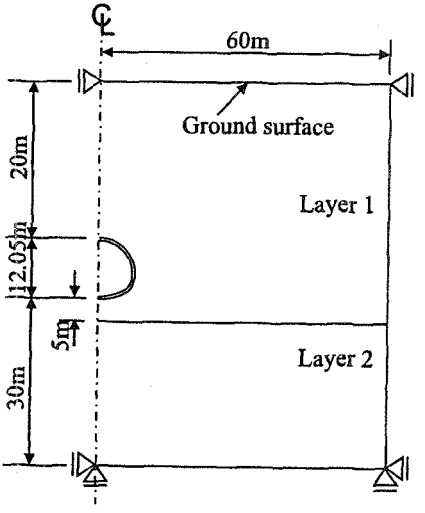

Figure 8.23: Geometry for tunnel excavation

Results

Figure 8.24 shows the predicted surface settlements for one step tunnel excavation, from 10 groups that undertook the exercise, while Figure 8.25 summarises the predicted bending moments and forces in the tunnel lining.

Comment

Although half of the predictions gave maximum surface settlements between 52mm to 55mm, overall there were significant differences in the predicted settlements. Two groups used a different method of tunnel construction to that specified, because of restrictions of their codes. It was difficult to match the different approaches. This probably accounts for the differences in the results.

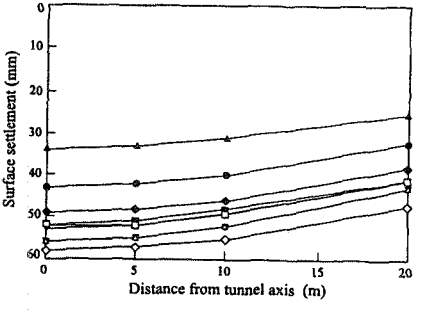

Figure 8.24: Surface settlement profiles

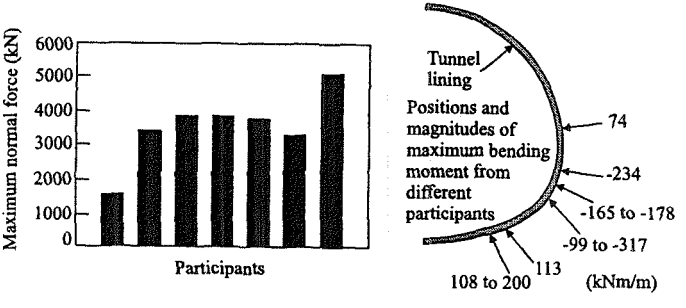

Figure 8.25: Maximum normal forces and bending moments in lining

There were also discrepancies in the predicted bending moments and forces in the tunnel lining and the positions of the maximum bending moment, as shown on Figure 8.25. Even if the results of the groups that did not follow the specification are discounted, there are still significant differences in the predicted magnitudes and positions of maximum bending moment.

8.11.3 Example 7: Deep excavation

Definition of the problem

Figure 8.26 shows the geometry of the problem. The analysis was intended to model a staged excavation 12m deep and 30m wide, assuming a Mohr-Coulomb soil. At two intermediate stages struts were installed, but there was no strut at the top of the wall. Therefore, before the first prop was installed 3m below ground level the wall acted as a cantilever. Material properties and construction stages are listed in Appendix VIII.7. Schweiger (1998) provides further details.

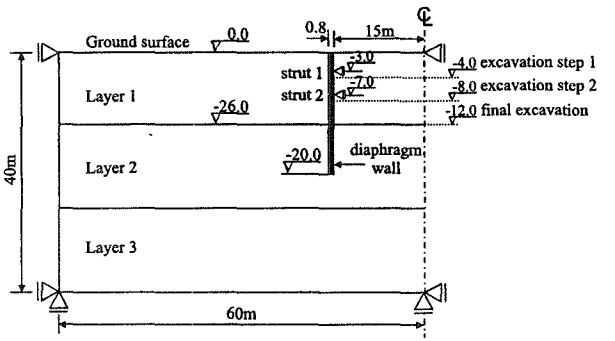

Figure 8.26: Geometry for deep excavation

Results

Figure 8.27 shows the predicted vertical surface displacements behind the wall for the first stage of construction. Horizontal displacements at the top of the wall at the same stage in construction are shown on Figure 8.28. Figure 8.29 shows the vertical displacements behind the wall upon completion of the excavation (construction stage 3).

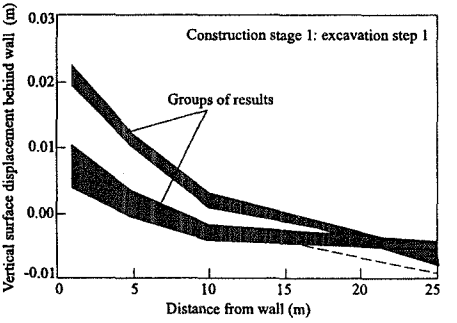

Figure 8.27: Surface settlement behind the wall - stage 1

Comment

A wide scatter of the results is apparent, even at the first stage in construction when the wall acted as a cantilever (see Figures 8.27 and 8.28). Some participants used beam elements to model the diaphragm wall, others used solid elements, and some groups used interface elements between the ground and the wall. These differences in modelling technique might explain some of the variations in the results, but they do not account for all of them. As far as horizontal wall displacements are concerned at this stage, only half the participants show positive displacements of the top of the cantilever wall, i.e. movements towards the excavation. Curiously, the remaining groups showed movements away from the excavation (negative) at this stage. At the final stage in the construction process there is significant variation in the results, with the maximum surface settlements predicted being between 10mm and 50mm.

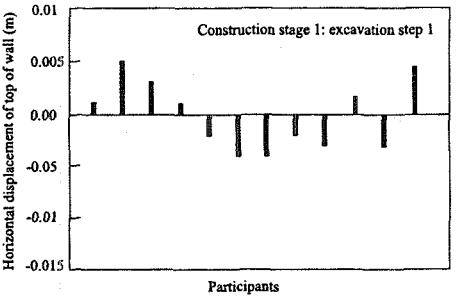

Figure 8.28: Horizontal displacement of the top of the wall - stage 1

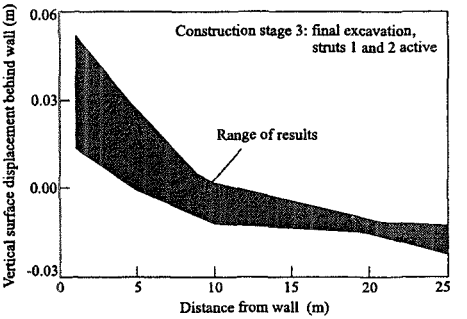

Figure 8.29: Surface settlement behind the wall - stage 3

8.11.4 General comments

Although, quite rightly, Schweiger questions the suitability of the linear elastic perfectly plastic constitutive models to analyse these problems, all the calculations have been done on the same basis and should be reasonably consistent. There were some differences in the approaches which may go someway to explaining the discrepancies in the results. For the tunnelling problem there were differences in the method of tunnel construction and for the deep excavation different methods of modelling the diaphragm wall were used. However, differences such as the horizontal movement of the cantilever wall are hard to explain.

It is worth mentioning that 5 of the 12 participants used the same computer program. In this case some consistency between users of the same program would be expected, even if the results obtained were unrealistic. The comments made by Jefferies and Knowles (1994), referred to in Section 8.9, may be relevant. As Schweiger recognised, interpretation of the specification may have been a factor

that led to some of the differences that were observed. It is however surprising that experienced analysts would have submitted results with obvious errors, such as a cantilever wall moving backwards into the ground, without comment.

8.12 Summary

1. This chapter has reviewed the role of benchmarks in the validation and verification of computer software and discussed the responsibilities of the developers and users of a code in this respect. Before a computer program is used, it should be checked by both the developer and user to ensure that it is accurate, it is working as intended and it is being used correctly. Any checks made by a user should be independent of the developer, it is not sufficient simply to use supplied problems.
2. Despite the developer having tested the program before releasing it for use, it is unlikely that all the potential 'bugs' will have been identified. Even if this programme of testing is rigorous, it is difficult to anticipate some of the ways the program may be used and there may be interface problems with hardware or operating systems. In commercial terms, the degree of testing by the developer is likely to be reflected in the cost of the program. Users must be aware that potentially problems may occur and must take sufficient measures to ensure that these problems do not affect any analysis that may be undertaken. The program has to be benchmarked.
3. Ideally a program should be checked against a closed form solution, or an independent means of calculation, to validate it. A series of simple hand calculations checking stages of an analysis may be sufficient.
4. Benchmark problems of this form tend to be fairly simple and may not be sufficiently demanding to expose any potential problems. It may therefore be necessary to devise more demanding problems which can be checked against the results of the same analysis being run using at least one other program. For most users this is not a very satisfactory or practical situation, since they may not have access to more than one code. There is therefore a need to devise and publish 'standard' benchmarks for geotechnical problems.
5. The consequences of errors or 'bugs' in computer programs can be serious and can result in significant economic loss.
6. A series of examples of benchmark problems have been reviewed. The INTERCLAY II exercise has not only provided a number of valuable examples of benchmark problems that could be used to validate geotechnical software, but it also demonstrated the need for programs to be thoroughly tested. During the course of the exercise potential problems with some of the codes were exposed. The exercise also highlighted the need for detailed and unambiguous specifications to be produced before any analysis is run.

Appendix VIII.1: Specification for Example 1: Analyses of an idealised triaxial test

VIII.1.1 Geometry

Not specific, single element may be used.

VIII.1.2 Material properties and initial stress conditions

Modified Cam clay model for triaxial sample.

Table VIII.1: Modified Cam clay parameters

OCR	v_1	λ	κ	M	G/p_o'
1.0	1.788	0.066	0.0077	1.2	100

Initial stress conditions: Vertical effective stress, σ_v': 200 kPa
Horizontal effective stress, σ_h': 200 kPa
Pore water pressure, p_f: 0 kPa

VIII.1.3 Loading conditions

Unspecified, but constant, increments of compressive vertical strain up to 20% under undrained and drained conditions. No change in horizontal total stress.

Appendix VIII.2: Specification for Example 2: Analysis of a thick cylinder

VIII.2.1 Geometry

The geometry is shown in Figure 8.3.

VIII.2.2 Material properties

Total stress analysis using a Tresca soil model.

Table VIII.2: Tresca parameters

E_u (MPa)	μ	S_u (MPa)
240	0.499	1.0

Initial stress conditions: Vertical effective stress, σ_v': 5000 kPa
Horizontal effective stress, σ_h': 5000 kPa

VIII.2.3 Loading conditions

Using a total stress analysis a pressure was applied to the internal boundary so as to unload it. The maximum pressure applied was 3500kPa, giving a residual pressure of 1500kPa. Incremental load steps were not specified.

Appendix VIII.3: Specification for Example 3: Analysis of an advancing tunnel heading

VIII.3.1 Geometry

The geometry is shown on Figure 8.6 and the analysis was run as an axi-symmetric problem.

VIII.3.2 Material properties

A) Total stress analysis using a Tresca soil model.

Table VIII.3: Tresca parameters

E_u (MPa)	μ	S_u (MPa)
240	0.499	1.0

B) Effective stress analysis using a Mohr-Coulomb failure criteria with a fully associated flow rule.

Table VIII.4: Mohr-Coulomb parameters

E' (MPa)	μ	c' (MPa)	K_f (MPa)	φ'
200.13	0.25	0	3000	23°

Note: A porosity of 0.4 and permeability of 4.0×10^{-12} m/s were required for some codes.

Initial stress conditions:

Vertical effective stress, σ_v':	2500 kPa
Horizontal effective stress, σ_h':	2500 kPa
Pore water pressure, p_f:	2500 kPa

VIII.3.3 Loading conditions

The total stress analysis used stages 1 to 3 only, the effective stress analysis used all stages:

1. Advance tunnel face instantaneously by 2m, assuming that the internal pressure on the excavated face is zero.
2. Insert rigid lining to provide radial support.

3. Repeat stages 1 and 2 until tunnel heading has reached its full length (i.e. 24m).
4. Allow excess pore water pressures to dissipate with the tunnel lining and face fully permeable and rigid (around the outer boundary pore water pressure p_f=2.5 MPa, around the boundary of the tunnel p_f=0 and no longitudinal displacement of the face).

Appendix VIII.4 Specification for Example 4: Analysis of a shallow waste disposal

VIII.4.1 Geometry

The geometry is shown in Figures 8.12 and 8.13.

VIII.4.2 Material properties

The Mohr-Coulomb parameters for the different materials involved in this analysis are shown in Table VIII.5.

Table VIII.5: Mohr-Coulomb parameters for shallow waste disposal

	Sand and gravels		Clay	Concrete	Sand capping	Clay capping	Waste	Rockfill capping
	Upper	Lower						
E' (MPa)	25	100	15	28000	25	5	2500	10
μ'	0.2	0.2	0.3	0.15	0.2	0.2	0 & 0.2	0.2
c' (kPa)	0	0	0	N/A	0	0	N/A	0
φ' (°)	35	35	28	N/A	35	25	N/A	40
v (°)	17.5	17.5	7	N/A	17.5	0	N/A	20
γ (kN/m^3)	20	20	20	24	20	20	30	20
K_o (initial)	0.5	1.0	1.0	N/A	0.5	0.8	N/A	0.5
p_f (kPa)	Initially hydrostatic from GWL			N/A	0	0	0	0

For the waste material a constant value of Poissons ratio of 0.2 was specified for stages 1 to 4 in the analysis, but in stage 5 this was set to zero. All the materials were drained, apart from the clay. Initially pore water pressures below ground water level (GWL) were hydrostatic. Above GWL pore water pressures were zero.

VIII.4.3 Loading conditions

Stages of analysis:

1.* Construct perimeter wall (wished in place), excavate repository, place drainage layer (zero thickness), construct repository base slab and construct partition wall.
2. Allow pore water pressures to dissipate to a steady state condition assuming that pore water pressures in the drainage layer under the base slab are zero and that the Upper and Lower sands and gravels are fully recharged.
3.* Fill with waste and place capping layers.
4. Allow excess pore water pressures to dissipate to the same conditions as 2.
5.* Reduce Poisson's ratio of waste to zero. Apply a vertical stress of 125MPa to upper and lower boundaries of waste to model collapse.

(* No drainage)

Appendix VIII.5: Specification for Example 5: Simplified analysis of a shallow waste disposal

VIII.5.1 Geometry

The geometry is shown on Figure 8.20.

VIII.5.2 Material properties

The material properties and initial stresses are the same as for Example 4. The initial stresses are as shown on Figure VIII.1.

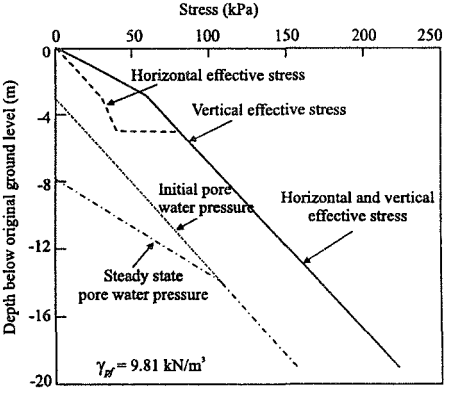

Figure VIII.1: Initial stresses

VIII.5.3 Loading conditions

Stages of analysis:

1.* Excavate to 7.8m below existing ground level and construct 0.3m thick concrete slab.
2. Allow pore water pressures to dissipate to the steady state.
3.* Place the waste material to 0.5m below original ground level and then place 4.0m of sand capping, 1.5m of clay capping and 3m of rockfill capping.

4. Allow excess pore water pressures to dissipate as in Stage 2.

   (* No drainage in clays)

VIII.5.4 Additional boundary conditions

1. All vertical boundaries are to have zero horizontal displacement.
2. The base of the mesh (the interface between the sandstone and the Lower sand and gravel layer) is to have zero vertical and horizontal displacement.
3. All vertical boundaries to have no drainage.
4. The base of the concrete slab is to be undrained in Stages 1& 3 and drained in Stages 2 & 4.
5. The base of the mesh is to be drained.

Appendix VIII.6: Specification for Example 6: Construction of a tunnel

VIII.6.1 Geometry

The geometry of the problem is specified in Figure 8.23.

VIII.6.2 Material properties

The Properties for the soil and shotcrete are listed in Table VIII.6.

Table VIII.6: Material parameters for tunnel construction

	E (kPa)	μ	φ' (°)	c' (kPa)	K_o	γ (kN/m^3)
Layer 1	50000	0.3	28	20	0.5	21
Layer 2	200000	0.25	40	50	0.6	23
Shotcrete*	5x10^6	0.15	-	-	-	-

* Shotcrete thickness is 25cm

Appendix VIII.7: Specification of Example 7: Deep excavation

VIII.7.1 Geometry

The geometry of the problem is given in Figure 8.26.

VIII.7.2 Material properties

The properties of materials used in this example are given in Table VIII.7.

Table VIII.7: Material parameters for deep excavation analysis

	E (kPa)	μ	φ' (°)	c' (kPa)	K_o	γ (kN/m^3)
Layer 1	20000	0.3	35	2	0.5	21
Layer 2	12000	0.4	26	10	0.65	19
Layer 3	80000	0.4	26	10	0.65	19
Wall*	21×10^6	0.15	-	-	-	22

*Diaphragm wall thickness is 80cm

VIII.7.3 Construction stages

The following construction stages are specified:

1. Excavation step 1 (to level -4.0m).
2. Excavation step 2 (to level -8.0m), with strut 1 (at -3.0m) active.
3. Full excavation (to level -12.0m), struts 1 and 2 (at -3.0m and -7.0m respectively) active.

9. Restrictions and pitfalls

9.1. Synopsis

This chapter considers some of the common pitfalls that can arise when performing finite element analysis of geotechnical problems. Some of the restrictions that may occur when using this method are also discussed. Most of these arise when trying to model what is clearly a three dimensional component of a problem in a two dimensional plane strain analysis. For example, modelling ground anchors to tie back a retaining wall. Problems associated with the use of the Mohr-Coulomb model for undrained analysis are also discussed. In particular, it is shown that it is possible to obtain a failure condition only if the angle of dilation is set to zero. As noted in Chapter 7 of Volume 1 of this book, the shape of the plastic potential in the deviatoric plane controls the stress conditions at failure in plane strain analyses. The implications of this are examined by considering boundary value problems involving modified Cam clay. Some of the pitfalls in using critical state constitutive models for undrained analyses, as well as problems associated with modelling underdrainage and the use of zero thickness interface elements are also discussed.

9.2. Introduction

From the preceding chapters, both in Volume 1 and this volume of the book, it is clear that the finite element method, when applied to geotechnical problems, can be extremely complex. While in principal the method can be used to provide a solution to most of the problems that we may wish to analyse, there are approximations which can lead to errors. These approximations can be classified into two groups. Firstly, there are approximations in the finite element method itself and secondly, there are approximations arising from the idealisations made by the user when reducing the real problem to a form which can be analysed.

The two main sources of error involved in the finite element method itself are associated with the integration of the constitutive equation and the discretisation of the problem geometry into finite elements. The errors associated with the integration of the constitutive equations have already been considered in Chapter 9 of Volume 1 of this book, where it has been shown that the errors can be minimised to an acceptable level by the use of an appropriate solution strategy. However, the errors due to discretisation have not yet been considered and

consequently, in the first section of this chapter, the likely magnitude of these errors is investigated by using an example of the surface footing problem. Some of the problems associated with the use of zero thickness interface elements are also discussed.

The rest of the chapter then concentrates on errors that can arise due to the manner in which the user idealises the real problem. First of all, some of the approximations that may arise in plane strain analyses are considered. Although the dominant feature of a geotechnical problem (e.g. a long excavation) may render itself suitable to a plane strain idealisation, some of the smaller components of the problem (e.g. ground anchors, piles, etc.) do not. Consequently, some restrictions are imposed on any plane strain analysis of the problem. Some of these restrictions are discussed and comments are made on how they may be accounted for in an approximate manner.

Another potential source of error can be associated with a users lack of 'in depth' understanding of the constitutive model employed to represent soil behaviour. This is a common source of error, due to the complexities of many of the constitutive models currently available. Two examples are considered in the chapter. The first example involves the use of the Mohr-Coulomb model in undrained analysis. It is shown that if the model is asigned any plastic dilation, no failure can be predicted. The second example considers the effect of the shape of the plastic potential on soil strength. This is demonstrated by using the modified Cam clay model to show that what seems like sensible input parameters can result in unrealistic predictions. Our experience indicates that this is a very common pitfall that many users unknowingly fall into, with the result that their analyses predict erroneous collapse loads which are usually unconservative.

As the undrained strength is not one of the input parameters to the conventional critical state constitutive models, use of such models to analyse undrained problems can be problematic. This is particularly so if the site investigation has been designed towards obtaining undrained strength values. This problem is considered in some detail in this chapter, where it is shown that realistic undrained strength profiles can be obtained by a suitable selection of the model input parameters and initial stress conditions. However, such conditions can only be achieved if the finite element program has flexible input facilities. The chapter concludes by discussing some of the problems associated with the simulation of construction and underdrainage.

9.3 Discretisation errors

Errors arising from the discretisation of the problem geometry into finite elements is demonstrated by considering the behaviour of smooth rigid strip and circular surface foundations under vertical loading, see Figure 9.1. The soil is assumed to be linear elastic perfectly plastic, with a Tresca yield surface (see Chapter 7, Volume 1), having a Young's modulus E=10000 kPa, Poisson's ratio μ=0.45 and undrained strength S_u=100 kPa.

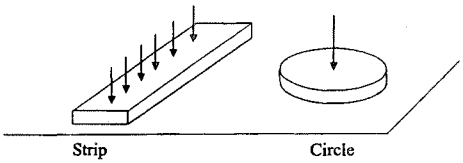

Figure 9.1: Strip and circular surface foundations under vertical loading

Two alternative finite element meshes are shown in Figures 9.2a and 9.2b. The mesh shown in Figure 9.2a has 110 eight noded isoparametric elements, whereas the mesh shown in Figure 9.2b has only 35 elements. Both meshes have been used to perform plane strain (for strip footing) and axi-symmetric (for circular footing) analyses, in which the foundation is displaced vertically downward to obtain the complete load-displacement curve. From a cursory glance at the two meshes, most users would probably conclude that the 110 element mesh was likely to produce the more accurate predictions due its larger number of elements and their more even spatial distribution.

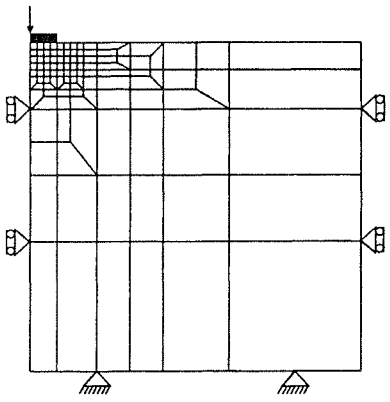

Figure 9.2a: Smooth footing - 110 element mesh

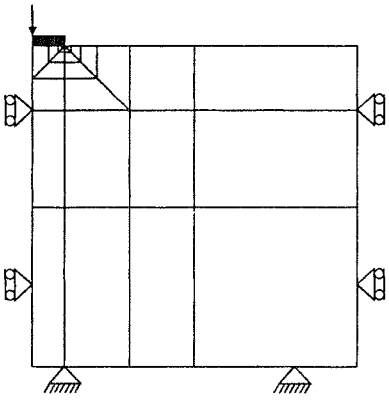

Figure 9.2b: Smooth footing - 35 element mesh

Although there is no analytical solution for the complete load displacement curve for either the strip or circular surface footings, there is an analytical solution for the ultimate load, Q, for the strip footing which gives $Q_{max} = 2BN_cS_u$ per metre length, where $N_c = (2+\pi)$ and $2B$ is the width of the footing. Often text books quote an equivalent analytical solution for the circular footing of $Q = N_c S_u \pi R^2$, where $N_c = 5.69$ and R is the radius of the footing. However, this solution is not strictly an analytical solution, as it involves the numerical integration of some stress field equations. It is however thought to be reasonably accurate.

Results from finite element analysis using the meshes shown in Figures 9.2a and 9.2b are presented in Figure 9.3. Also marked on this figure are the theoretical limit loads discussed above. Assuming that the theoretical limit loads are correct, then the analyses with the 110 element mesh overestimate the collapse loads by

3.8% for the strip footing (i.e. N_c=5.33) and 8.8% for the circular footing (i.e. N_c=6.19) . However, the errors are much smaller, 0.5% for the strip (N_c=5.17) and 2% for the circular (N_c=5.8) footing, for the analyses performed using the 35 element mesh. The reason for the relatively bad performance of the 110 element mesh can be seen from Figure 9.4, which shows vectors of incremental nodal displacements for the last increment of the 110 element strip footing analysis. Each vector indicates the magnitude (by its length) and the direction (by its orientation) of the associated incremental nodal displacement. While the absolute magnitudes of the incremental displacements are not important, the relative magnitude of each of the vectors and their orientation clearly indicate the mechanism of failure. Attention should, however, be focussed on the corner of the footing, where a rapid change in the direction of the incremental vectors is indicated. The direction changes by approximately 120° between the vector immediately below the corner of the footing and the adjacent node on the soil surface. Such behaviour clearly indicates that under the corner of the footing there are large stress and strain gradients. In the 110 element mesh the elements in the vicinity of this corner are too large and of insufficient number to accurately reproduce this concentration of behaviour. In comparison, the 35 element mesh, which has smaller elements and a graded mesh under the corner of the footing, see Figure 9.5, can accommodate this behaviour more easily and therefore produces more accurate solutions.

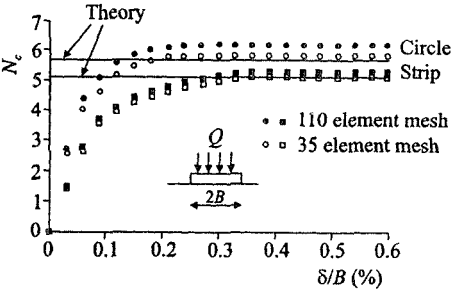

Figure 9.3: Load-displacement curves for smooth footing

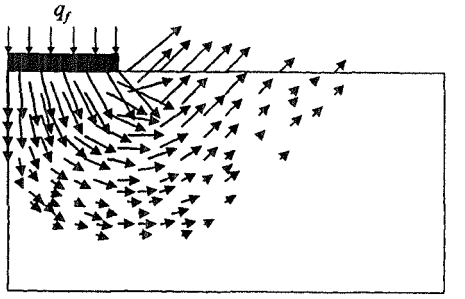

Figure 9.4: Vectors of incremental displacements at failure (110 element mesh)

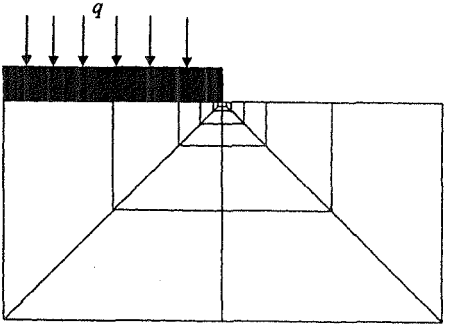

Figure 9.5: Detail from 35 element mesh

Clearly it is important that smaller and therefore more elements are placed where there are rapid changes in stresses and strains and therefore directions of movement. Some computer programs will automatically re-generate the finite element mesh to improve the accuracy of the solution. They work by first performing a solution with a relatively even mesh. Based on the results of this analysis a new mesh is generated with more elements in the zones of greatest stress and strain changes. The analysis is then repeated. In principal, this process of refinement could be repeated until the results were unaffected by further mesh refinement.

9.4 Numerical stability of zero thickness interface elements

9.4.1 Introduction

As noted in Section 3.6 of Volume1, there are several different methods available to model the behaviour at soil-structure interfaces. Of these alternatives, the use of zero thickness elements is probably the most popular and consequently details of their finite element implementation were given in Volume 1. Examples of their use in finite element analyses of boundary value problems have been discussed in earlier chapters of this volume.

While these elements are extremely useful, they have limitations. For example, numerical problems, such as ill-conditioning, poor convergence of the solution and unstable integration point stresses, have been experienced by several authors in the past (Wilson (1977), Desai *et al.* (1984), Day and Potts (1994)). Some of these pitfalls/restrictions will be discussed in this section.

9.4.2 Basic theory

Although a detailed description of the theory behind zero thickness interface elements is given in Section 3.6.2 of Volume 1, it is instructive to restate here the main equations for 2D analyses.

The interface stress consists of a normal and a shear component. The normal stress, σ, and the shear stress ,τ, are related by the constitutive model to the normal and tangential element 'strains', ε and γ:

$$\begin{Bmatrix} \Delta\tau \\ \Delta\sigma \end{Bmatrix} = [\boldsymbol{D}] \begin{Bmatrix} \Delta\gamma \\ \Delta\varepsilon \end{Bmatrix} \tag{9.1}$$

The interface element 'strain' is defined as the relative displacement of the top and bottom of the interface element:

$$\gamma = \Delta u_l = u_l^{\text{bot}} - u_l^{\text{top}} \tag{9.2}$$

$$\varepsilon = \Delta v_l = v_l^{\text{bot}} - v_l^{\text{top}} \tag{9.3}$$

where:

$$\begin{aligned} u_l &= v\sin\alpha + u\cos\alpha \\ v_l &= v\cos\alpha - u\sin\alpha \end{aligned} \tag{9.4}$$

and u and v are the global displacements in the x_G and y_G directions respectively. Hence:

$$\begin{aligned} \gamma &= (v^{bot} - v^{top})\sin\alpha + (u^{bot} - u^{top})\cos\alpha \\ \varepsilon &= (v^{bot} - v^{top})\cos\alpha - (u^{bot} - u^{top})\sin\alpha \end{aligned} \tag{9.5}$$

It is important to note that the element 'strains' are *not dimensionless*, but have the same *dimensions* as the displacements (i.e. length).

The elastic constitutive matrix $[\boldsymbol{D}]$ takes the form:

$$[\boldsymbol{D}] = \begin{bmatrix} K_s & 0 \\ 0 & K_n \end{bmatrix} \tag{9.6}$$

where K_s and K_n are the elastic shear stiffness and normal stiffness respectively. Noting that these stiffnesses relate stresses (in units of force/(length)^2) to strains (in units of length) via Equation (9.1), implies that they must have units of force/(length)^3). They therefore have different units to the Young's modulus, E, of the soil and/or structure adjacent to them (i.e. E has the same units as stress - force/(length)^2). As it is difficult to undertake laboratory tests to determine K_n and K_s, selecting appropriate values for an analysis is therefore difficult.

If a pore fluid exists in the interface, undrained behaviour can be modelled by including the effective bulk stiffness of the pore fluid (again in force/(length)^3) in the stiffness matrix, in the same manner as described for solid elements in Section 3.4 of Volume1. It is also possible to allow the interface elements to consolidate by implementing one dimensional consolidation along their length.

The interface stresses can also be limited by imposing a failure criterion. This is conveniently achieved by using an elasto-plastic constitutive model. For example, the Mohr-Coulomb failure criterion can be used to define the yield surface, F:

$$F = |\tau| + \sigma' \tan\varphi' - c' \tag{9.7}$$

along with the gradient of the plastic potential function, P:

$$\frac{\partial P}{\partial \sigma'} = \tan\nu \quad ; \quad \frac{\partial P}{\partial \gamma} = \pm 1 \tag{9.8}$$

where φ' is the maximum angle of shearing resistance, c' is the cohesion (see Figure 9.6) and ν is the dilation angle. If the interface moves such that the maximum normal tensile strength is exceeded ($c'/\tan\varphi'$), the interface is allowed to subsequently open and close and in a finite element analysis the residual tensile stress is redistributed via the nonlinear solution algorithm. When the interface is open, the normal stress remains equal to $c'/\tan\varphi'$ and the shear stress remains equal

to zero. The amount of opening of the interface is recorded. When the interface re-closes and reforms contact, the constitutive model again defines the interface behaviour.

The facility for opening and closing of the interface element is particularly useful when analysing problems where tensile cracks may form, for example behind a laterally loaded pile (see Section 7.3.3) or behind a retaining wall.

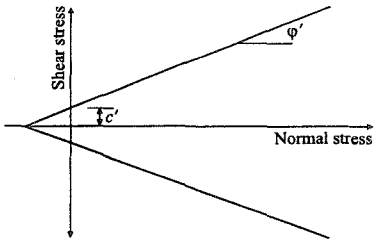

Figure 9.6: Mohr-Coulomb yield function

The formulation for 3D interface elements is similar to that described above, except that there are three interface stresses (a normal stress, σ, and two mutually perpendicular shear stresses, τ_a and τ_b) and strains (ε, γ_a and γ_b), and three displacements (u_l, v_l and w_l).

9.4.3 Ill-conditioning

Ill-conditioning of the global stiffness matrix can occur if the element stiffness matrices of adjacent elements vary in magnitude by a significant amount. This results in large off-diagonal terms in the global stiffness matrix and, consequently, loss of accuracy. The analysis of the overturning of an elastic block will be used to illustrate problems associated with ill-conditioning (Wilson (1997), Day and Potts (1994)). Some of the results of Day and Potts (1994) will be presented here.

This problem is crudely representative of a gravity wall. It consists of an elastic block, Young's modulus E=10^6 kPa and Poisson's ratio μ=0, separated from a rigid foundation along the base AB by interface elements, see Figure 9.7. For clarity, the interface elements are shown artificially expanded in Figure 9.7. Ten 6 noded interface elements and fifty 8 noded 2D solid elements were used to model the problem. A downwards vertical stress of 200kPa and a shear stress of 50kPa in the positive x direction were applied to the top boundary CD. A large number of analyses were undertaken and in these the interface elements were assumed to be elastic, with stiffnesses varying from K_s and K_n =10^6 to K_s and K_n =10^{10} kN/m^3. Note that in general K_s was not equal to K_n.

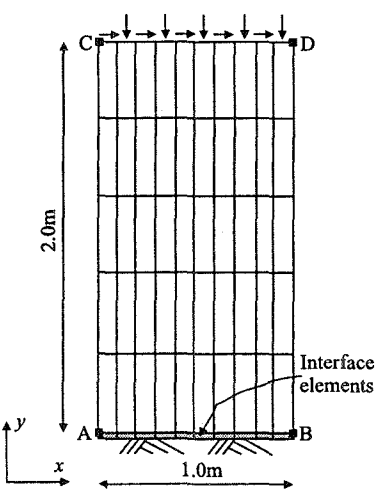

Figure 9.7: Overturning of elastic block

The integration point stresses in the interface elements for the analysis with K_s=K_n=10^7 kN/m^3 are plotted in Figure 9.8. The linear normal and shear stress

distributions shown in this figure are the theoretical distributions for a rigid block on elastic springs. Since the vertical faces of the block are stress free, the shear stress *within* the base of the block must reduce to zero at the corners (A and B), however the shear stress *applied* by the interface element to the base does not. To satisfy continuum theory a singularity therefore occurs in the shear stress and the vertical stress distributions at the corners within the block. The theoretical shear stress distribution is parabolic (Figure 9.8) for a long flexible block on a rigid foundation (Young (1989)). The shear stress distribution in the interface elements lies between these two theoretical extremes. Results from analyses with 2 (reduced) and 3 (full) point Gaussian integration gave similar results. These results are well conditioned and do not suffer from the effects of ill-conditioning of the stiffness matrix.

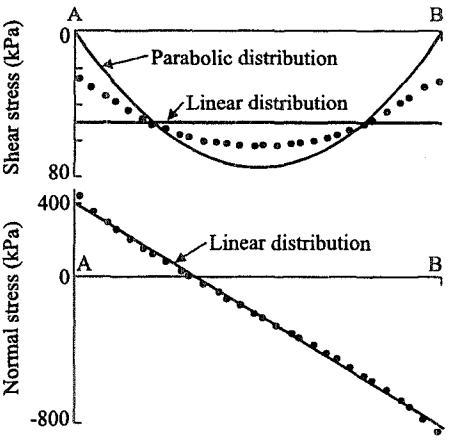

Figure 9.8: Integration point stresses in interface elements

Ill-conditioning of the stiffness matrix, which causes fluctuating stresses in the interface elements, occurred when the interface element stiffness was large with respect to the stiffness of the 2D elements. For example, the results of the analysis with $K_s=K_n=10^9$ kN/m^3, using 3 point Gaussian integration, are shown in Figure 9.9. Fluctuations in the normal stress at the edges of the block and of the shear stress across the whole base of the block are clearly evident. The use of reduced integration (i.e. 2 point) does not prevent the fluctuation in interface stress which is observed in Figure 9.9. The results of the study by Day and Potts (1994), which included variations of both the stiffness of the elastic block and of the interface elements, showed that the effect of ill-conditioning was noticeable if either K_s or K_n was greater than $100E$. However, it should be noted that, because of the difference in the

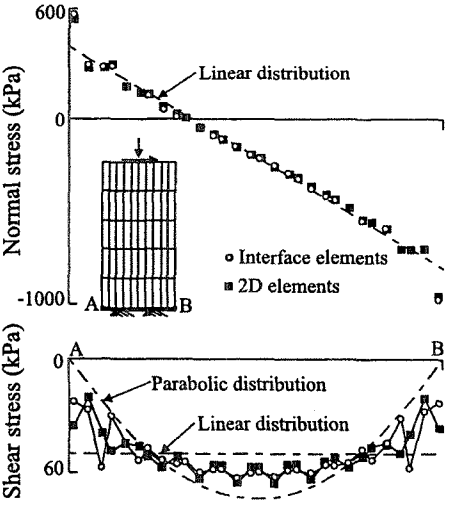

Figure 9.9: Effect of ill-conditioning on interface element stresses (full integration)

dimensions of K_s and K_n with those of E, this simple relationship depends on the units used. It is also likely to be problem dependent.

An analysis with a thin layer of 2D elements in place of the interface elements was also performed by Day and Potts (1994). The elastic properties of the thin layer are E_i and μ_i and the thickness is t. The equivalent normal and shear stiffnesses of the thin layer are:

$$K_{in} = \frac{E_i}{t(1-\mu_i^2)} \quad ; \quad K_{is} = \frac{E_i}{2t(1+\mu_i)} \tag{9.9}$$

It is noted that when $K_{in}=K_{is}$ then $(1-\mu_i^2)=2(1+\mu_i)$. The solution of this equation gives $\mu_i=-1$, in which case the stifnesses, K_{in} and K_{is} are infinite. To avoid this paradox and to be consistent with the overlying elements, the Poisson's ratio was chosen to be zero ($\mu_i=0$). With the thickness chosen to be 0.02m and $E_i=2\text{x}10^7$ kPa, the normal stiffness of the thin elements is equivalent to that of the interface elements (i.e. $K_{in}=10^9$ kN/m^3) and the shear stiffness is half that of the interface elements (i.e. $K_{is}=5*10^8$ kN/m^3). The analyses was also performed with full (3x3point) Gaussian integration and the integration point stresses along the centre line of the thin 2D elements is also shown in Figure 9.9. These show fluctuations similar to those from the analysis using interface elements. This demonstrates that the fluctuations are not due to the formulation of the interface elements, but due to a difference in stiffness between the elements in the elastic block and those forming the interface.

Reducing the size of the 2D elements in the elastic block adjacent to the interface elements reduced the effect of ill-conditioning, even though the total number of elements remained the same. This is illustrated in Figure 9.10, where the analysis presented in Figure 9.9 has been repeated with a different finite element mesh, see inserts in Figures 9.9 and 9.10. In this case the contribution to the global stiffness matrix from the 2D elements is increased in the locations concerning the interface element degrees of freedom. This arises as the stiffness contribution of the 2D elements, given by (Equation (2.28) of Volume 1):

$$[K_E] = \int_{-1}^{1}\int_{-1}^{1} t[B]^T[D][B]|J|\,dS\,dT \tag{9.10}$$

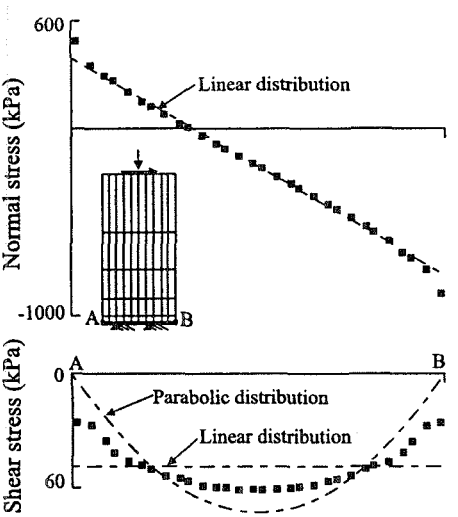

Figure 9.10: Reduced ill-conditioning with smaller elements (full integration)

depends on the [D] and [B] matrices and the determinant of the Jacobian matrix $|J|$ (note: t=1 for a plane strain analysis). As the constitutive matrix [D] is elastic, it is independent of the size of the element. However, the strain matrix [B] is proportional to the inverse of $|J|$ (see Equations (2.11) and (2.15) of Volume1). Consequently, the stiffness contribution given by Equation (9.10) is also proportional to the inverse of $|J|$ and, as $|J|$ reduces as the element size reduces (see Equation (2.16) of Volume1), the contribution to the global stiffness increases. The contributions from the interface elements remain unchanged. Thus there is less difference between the stiffness of the interface elements and the stiffness of the 2D elements and hence less ill-conditioning. This example clearly demonstrates the need to carefully proportion the size of the elements within the finite element mesh.

9.4.4 Steep stress gradients

Another problem where stress fluctuations can occur is in the simple pull out test. In view of the potential applications to soil reinforcement and pile analysis, this example demonstrates the interface element in a problem controlled by the sliding mode of deformation. The problem consists of a thin strip of 2D elements, representing a reinforcing membrane, on a rigid base, see Figure 9.11. The contact between the membrane and the base is modelled by interface elements. Five 8 noded 2D elements and five 6 noded interface elements were used to model the test. Initially a uniformly distributed load of 10kPa was applied to the top of the membrane. End A of the membrane was then moved horizontally by the amount δ, in the direction shown, under displacement control. This problem involves a sliding front that moves progressively from the point of load application towards the other end of the membrane.

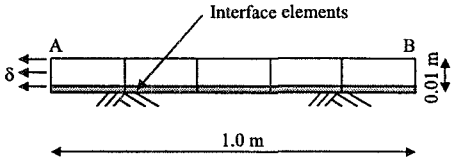

Figure 9.11: Finite element mesh for pull-out test

To demonstrate this behaviour, an example where stress fluctuations did not occur will be considered initially. The membrane was assumed elastic, with Young's modulus E=10^6 kPa and Poisson's ratio μ=0, while the elasto-plastic Mohr-Coulomb model was used to describe the behaviour of the interface, with properties K_s=K_n=10^6 kN/m^3, φ'=30°, c'=0 and v=0°. The membrane was withdrawn in displacement increments of 0.3mm. Figure 9.12 shows the shear stress distribution along the interface and the distribution of axial force in the membrane at different stages of the test. It can be seen that a sliding front moves from the left to the right as the membrane is pulled out. The maximum calculated force needed to withdraw the membrane is 5.7736 kN, which agrees with the theoretical value of 5.7735 kN.

Two further analyses were then performed in which the Young's modulus of the membrane was reduced to $E=10^5$kPa and $E=10^4$ kPa, all other parameters remaining unchanged. Figure 9.13 compares the shear stress distributions in the interface elements from all three analyses when the displacement, δ, of point A (see Figure 9.11) is 0.12mm. As the stiffness of the membrane reduces, the integration point stresses oscillate widely near the sliding front.

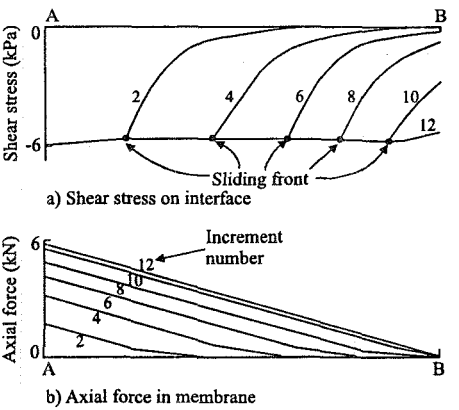

Figure 9.12: Results of pull-out test analysis

Gens *et al.* (1989) also found such behaviour and concluded that the cause of the large stress oscillations near the sliding front was due to the use of Gaussian integration (note the above results were obtained using 3 point Gaussian integration). They reported that if the Newton-Cotes integration scheme was adopted, the results were satisfactory. The analyses presented above were therefore repeated with this integration scheme (again 3 point integration was used) and the results are also shown on Figure 9.13.

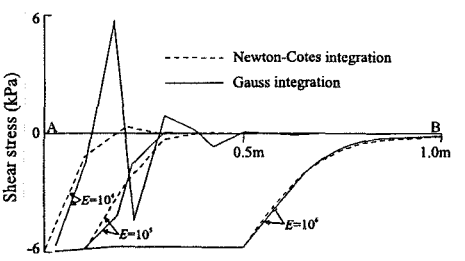

Figure 9.13: Shear stress in interface elements

The difference between Gaussian and Newton-Cotes integration is the location of the integration points and their corresponding weights (Zienkiewicz (1977)). The integration points for the 3 point Newton-Cotes method correspond to the positions of the three nodal pairs (i.e. at each end and the midpoint) of each interface element. The stress in the element, at each integration point, is then given by the relative displacement between the pair of nodes at the integration point. The displacement of the other nodes in the element has no influence. The element is therefore essentially a linkage element (Frank *et al.* (1982), Hermann (1978)). Three point Newton-Cotes integration is equivalent to Simpson's rule for integration. For Gaussian integration the integration points are located between the end and the midpoint of the element, and at the midpoint of the element. The relative displacement of all nodes affects the stress at each integration point.

On first inspection of the results given in Figure 9.13 it appears that the Newton-Cotes integration scheme greatly improves the behaviour of the interface elements, as the oscillation of the stresses given by the analyses using Gaussian

integration have been suppressed. However, further investigation of the pull-out test with E=10^{4}kPa shows that the stress distribution given by the Newton-Cotes integration scheme is actually a poor approximation to the correct solution.

Figure 9.13 indicates that, as the stiffness of the membrane reduces, the gradient of the shear stress distribution on the interface becomes steeper. When E=10^6 kPa, the stress reduces from the maximum value of 5.8kPa to nearly zero over a distance of 0.4m. This reduction therefore occurs over two elements, or six integration points. When E=10^5 kPa the stress reduces over a distance of 0.2m, which is the size of a single element. When E=10^4 kPa the same stress change probably occurs over a distance less than that represented by one element. This is likely to cause the stress oscillation seen in Figure 9.13. Smaller elements (less than 0.2m) are clearly necessary for the analysis of this problem if E<10^5 kPa.

Further analyses were performed with E=10^{4}kPa, but with smaller elements at end A of the membrane and interface. Elements with lengths of 0.05m and 0.025m were placed at the end of the membrane and interface. Figure 9.14 shows the results of these analyses when δ=0.12mm and also the results taken from Figure 9.13 where the element size is 0.2m.

At end A of the interface the shear stress is greater than the expected value of 5.77kPa (10tan30°) and the distribution of shear stress in the first 0.05m is rather surprising. The membrane is experiencing a shear stress acting on its underside only. Being thin, the bending stiffness of the membrane is very small. The shear stress acting on the side of the membrane causes end A of the membrane to bend downwards, increasing the normal stress in the interface. Thus the maximum permissible shear stress is increased.

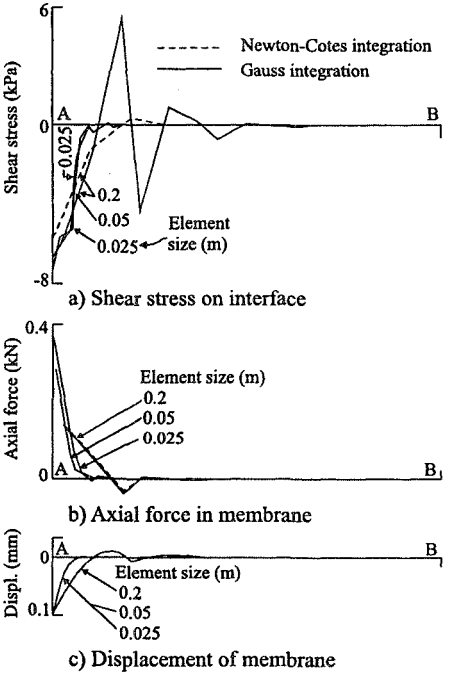

Figure 9.14: Effect of element size on pull-out results

At a short distance from the end of the membrane the curvature of the membrane causes a reduction in normal stress in the interface element, resulting in a complex distribution of shear stress. When the membrane was constrained so that it could not bend, the maximum normal stress in the interface element remained at 10kPa and the maximum shear stress at 5.77kPa. This confirms that bending of the membrane causes the unusual distribution of shear stress, shown in Figure 9.14.

The problem of oscillating stress is due to the use of elements too large to model adequately the steep stress gradient that occurs in this problem. Stress oscillation does not occur when small elements are used. The numerical problems encountered here are not due to poor performance of the interface element, but are due to inadequate modelling of the problem at hand. Only high-order elements that allow for a complex distribution of stress across the element will be able to accurately model the sliding front with the use of larger elements. Newton-Cotes integration is unnecessary and perhaps undesirable, as it has the effect of 'glossing over' or 'smoothing out' the steep stress gradient, thus hiding the real solution. When sufficiently small elements are used to describe adequately the stress gradient, Newton-Cotes and Gaussian integration give similar results.

9.5 Modelling of structural members in plane strain analysis

With many geotechnical problems, while the main feature might be adequately represented by a plane strain idealisation, other, smaller components of the same problem, might not be. For example, a typical urban excavation problem, as shown in Figure 9.15, is considered. Here an embedded retaining wall is supported by ground anchors and a foundation slab is tied down by tension piles. This could represent a cross section of an excavation for a road. The structural members are now considered in turn below.

9.5.1 Walls

If the wall is of the concrete diaphragm type, then it is best modelled using solid finite elements with the appropriate geometry and material properties. There are no serious modelling problems here as the wall satisfies the plane strain assumption. However, if the wall is made from secant or contiguous concrete piles, steel sheet piles, or some combination of steel columns and sheeting, then the properties and geometry of the wall will vary in the out of plane direction and therefore will not satisfy the requirements of plane strain (see Section 1.6 in Volume 1). Modelling of these components in a plane strain analysis will therefore involve some approximations. Usually it is possible to estimate the average axial (EA) and bending stiffness (EI) per metre length of wall. If beam elements are used to model the wall, then these parameters can be input directly as the material properties, see Section

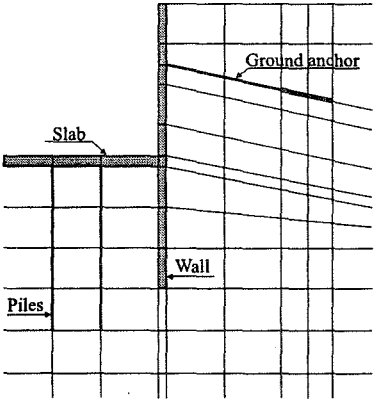

Figure 9.15: Typical urban excavation

3.5 in Volume 1. However, if solid elements are to be used, then the average axial and bending stiffness must be converted into an equivalent thickness t of the solid elements and an equivalent Young's modulus, E_{eq}. This is done by solving the following two simultaneous equations:

Axial stiffness: $$t E_{eq} = E A \tag{9.11}$$

Bending stiffness: $$\frac{E_{eq} t^3}{12} = E I \tag{9.12}$$

where E is the Young's modulus of the wall and A and I are cross sectional area and moment of inertia per metre length, respectively. It may also be necessary to calculate some form of average strength, but this will depend on the constitutive model employed to represent the wall. Clearly, the above procedure only treats the wall in an approximate manner and it will not be possible to accurately estimate the details of the stress distribution within the separate components of the wall.

9.5.2 Piles

Modelling the piles below the base slab involves additional assumptions as the piles are not continuous in the out of plane direction, but are separated by relatively large expanses of soil. While it is again possible to estimate average axial and bending stiffnesses per unit length in the out of plane direction and calculate equivalent parameters, as was shown for the wall above, modelling the piles with solid or beam elements implies that the soil is not able to freely move between the piles, as the piles are essentially modelled as a wall in the out of plane direction, see Figure 9.16. As a consequence, the lateral movements of the soil below the excavation will be restricted. It may therefore be more realistic to neglect the bending stiffness of the piles so that they provide no resistance to lateral soil movement. A spring or a series of membrane elements (see Chapter 3 in Volume 1) can then be used to represent the piles.

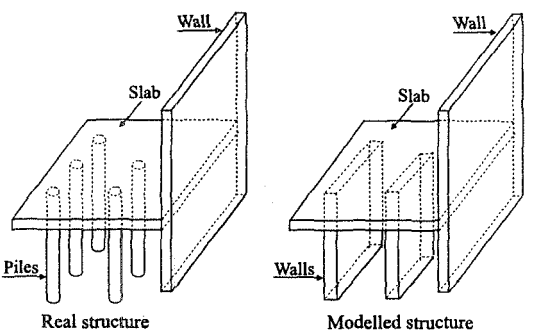

Figure 9.16: Comparison between real and simulated conditions for piles

If a linear spring is used to represent the pile, only elastic behaviour of the pile can be represented. In addition, if the spring is connected between a node on the concrete slab and a node in the soil (e.g. nodes A and B in Figure 9.17), only forces at these two nodes will be accounted for (i.e. the pile and soil are not connected between A and B). It will then not be possible to account for shaft friction nor set a limit to the end bearing resistance of the pile (i.e. at node B).

If a series of membrane (or beam) elements are used to model the pile, see Figure 9.18, then the pile will be connected to the soil along its shaft and consequently mobilisation of shaft resistance will be simulated to some limited extent. However, the zero thickness of the elements in the plane of analysis implies that base resistance will be mobilised through a single node and it is therefore difficult to impose a limit to the end bearing resistance.

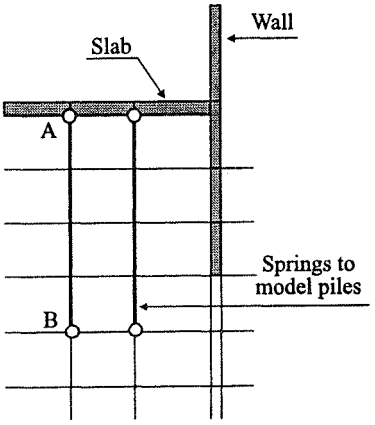

Figure 9.17: Springs used to model piles

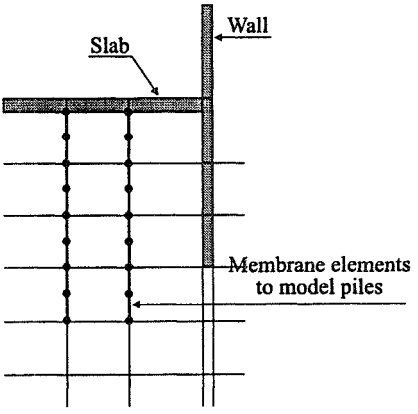

Figure 9.18: Membrane elements used to model piles

9.5.3 Ground anchors

The ground anchors located behind the wall can be conveniently divided into two parts: the *fixed* and *free* anchor lengths, as shown in Figure 9.19. As with the piles, equivalent axial and bending stiffnesses per unit length in the out of plane direction can be calculated for both components of a row of anchors. Account must be taken of the spacing of the anchors in the out of plane direction when calculating these equivalent values. Again, it is probably best to ignore the bending

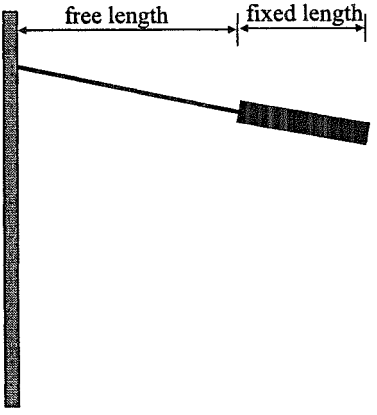

Figure 9.19: Ground anchor

stiffness and model the two anchor components with either springs, membrane elements or a combination of both, see Figure 9.20. The situation shown in Figure 9.20c, where a spring is used to model the free anchor length, and a series of membrane elements the fixed length, is probably the more realistic approach. It is usual to neglect any shear stresses mobilised between the soil and the free anchor length, consequently the springs are connected to the wall at one end (point A in Figure 9.20c) and the soil (and fixed anchor length) at the other end (point B). As with the piles, modelling the anchors in this way is rather crude as it is not possible to accurately account for the limiting end and shaft capacity of the fixed anchor length.

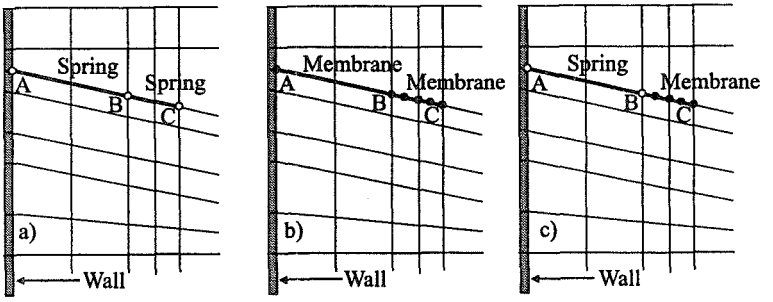

Figure 9.20: Modelling ground anchors using a) springs, b) membrane elements and c) a combination of spring and membrane elements

An alternative way of modelling the fixed anchor length is shown in Figure 9.21 and involves the use of solid and interface elements. It is now possible to simulate the mobilisation of both shaft and end bearing resistance and to apply limits to these quantities. However it is necessary to assign equivalent properties to the solid and interface elements to take account of the spacing of the anchors in the out of plane direction. This is often not straight forward. By assigning an equivalent Young's modulus to the solid elements, the fixed anchor length will have bending stiffness. This will limit soil movements perpendicular to the anchor. In the real problem the soil will be able to deform between the anchors.

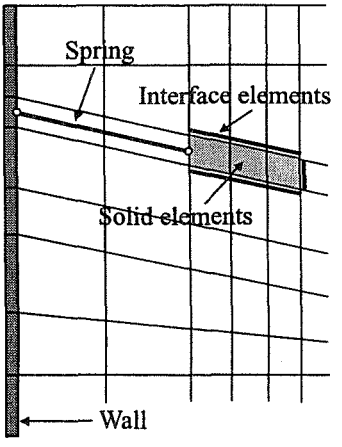

Figure 9.21: Modelling a ground anchor with solid elements

The above discussion indicates that while it is possible to approximate the wall behaviour in a realistic manner, much greater approximations

are involved with the modelling of both the piles and ground anchors. This arises because these structural elements are not continuous in the out of plane direction.

9.5.4 Structural members in coupled analyses

A further pitfall can occur when using membrane or beam elements to model structural members in coupled consolidation analyses. The problem is best explained by considering the example of the retaining wall shown in Figure 9.22. The wall is modelled using beam elements and therefore shares a common set of nodes with both the elements in front of and behind it, see Figure 9.22b. As the solid elements on either side of the wall have common nodes at the wall, the wall will be implicitly assumed to be permeable in a consolidation analysis. Water will therefore flow freely through the wall. This may not be the desired outcome. If the wall is to be assumed impermeable, this can be achieved by placing interface elements along one side of the wall as shown in Figure 9.22c. If these elements are non consolidating, they will provide an impermeable break between the solid elements on either side of the wall.

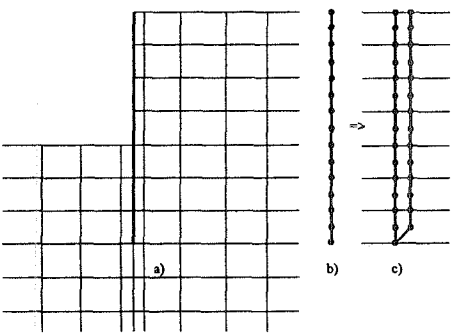

Figure 9.22: Dealing with impermeable line elements in consolidation problems (use of interface elements)

9.5.5 Structural connections

Potential problems can arise when modelling connections between different structural components. As an example, the connection between a prop and a retaining wall is considered. Such a connection can be modelled as either a *simple*, *pin-joined* or *full moment* connection. These conditions and the possible alternative ways that can be used to model them in plane strain analyses are shown in Figures 9.23, 9.24 and 9.25. It is often all to easy to use the options given in Figure 9.25 when in reality the connection is pin-jointed.

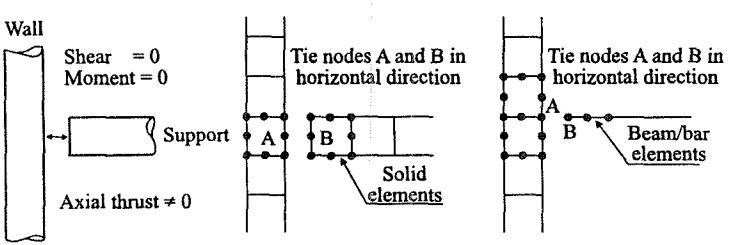

Figure 9.23: Simple connection between wall and prop

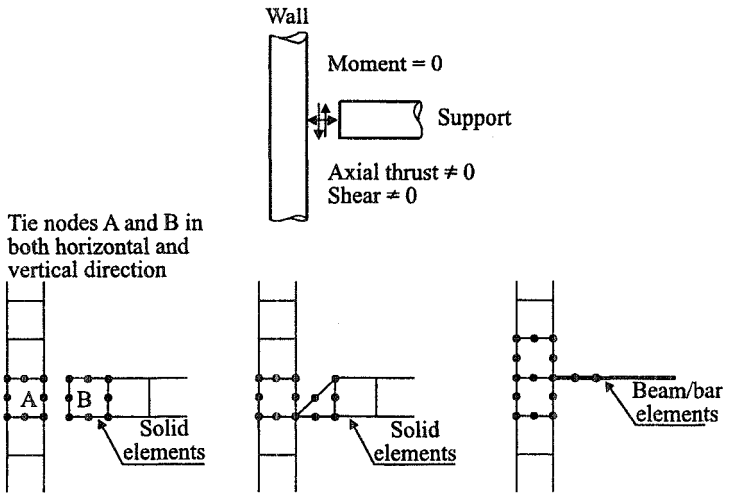

Figure 9.24: Pin-jointed connection between wall and prop

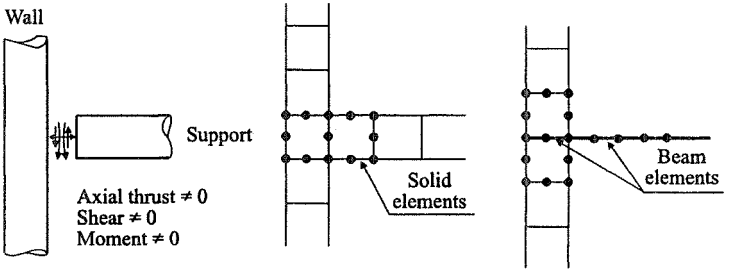

Figure 9.25: Full connection between wall and prop

9.5.6 Segmental tunnel linings

Many tunnel linings are constructed from segments. Usually between 8 and 12 segments are required to form a complete circular ring, see Figure 9.26a. Sometimes the segments are bolted to each other, whereas sometimes they are not. In either event there is little bending resistance between the segments. It is often convenient to model the lining using beam or solid elements. However, if these elements are placed as a sequential ring, see Figure 9.26b, a full moment connection between the segments will be implied. If this is not what is required, then an alternative approach must be used. At Imperial we have developed special beam elements which represent the interface between the segments (see Chapter 2). Each segment is modelled as a group of beam elements and these are then joined together by these small special beam elements, see Figure 9.26c.

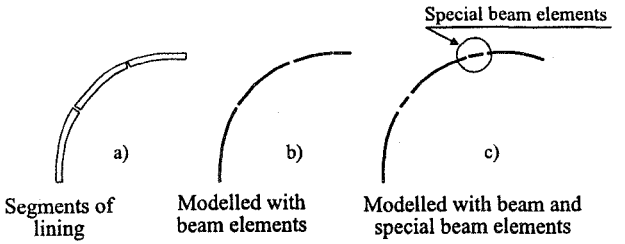

Figure 9.26: Modelling tunnel lining

9.6 Use of the Mohr-Coulomb model for undrained analysis

As noted in Chapter 7 of Volume1 of this book, the Mohr-Coulomb model can be used with a dilation angle ranging from $v = 0°$ to $v = \varphi'$. This parameter controls the magnitude of the plastic dilation (plastic volume expansion) and remains constant once the soil is on the yield surface. This implies that the soil will continue to dilate indefinitely if shearing continues. Clearly such behaviour is not realistic as most soils will eventually reach a critical state condition, after which they will deform at constant volume if sheared any further. While such unrealistic behaviour does not have a great influence on boundary value problems which are unrestrained (e.g. the drained surface footing problem), it can have a major effect on problems which are constrained (e.g. drained cavity expansion, drained axial pile loading), due to the restrictions on volume change imposed by the boundary conditions. In particular, unexpected results can be obtained in undrained analysis in which there is a severe constraint imposed by the zero total volume change restriction associated with undrained soil behaviour. To illustrate this problem two examples are presented here.

The first example considers ideal (no end effects) undrained triaxial compression ($\Delta\sigma_v > 0$, $\Delta\sigma_h = 0$) tests on a linear elastic Mohr-Coulomb plastic soil, with parameters E'=10000 kPa, μ=0.3, c'=0, φ'=24°. As there are no end effects, a single finite element is used to model the triaxial test with the appropriate boundary conditions. The samples were assumed to be initially isotopically consolidated with p'=200kPa and zero pore water pressure. A series of finite element analyses were then performed, each with a different angle of dilation, v, in which the samples were sheared undrained. Undrained conditions were enforced by setting the bulk modulus of the pore water to be 1000 times larger than the effective elastic bulk modulus of the soil skeleton, K', see Chapter 3 of Volume 1. The results are shown in Figure 9.27a and 9.27b in the form of J-p' and J-ε_z plots. It can be seen that in terms of J-p' all analyses follow the same stress path. However, the rate at which the stress state moves up the Mohr-Coulomb failure line differs for each analysis. This can be seen from Figure 9.27b. The analysis with zero plastic dilation, v=0°, remains at a constant J and p' when it reaches the

failure line. However, all other analysis move up the failure line, those with the larger dilation moving up more rapidly. They continue to move up this failure line indefinitely with continued shearing. Consequently, the only analysis that indicates failure (i.e a limiting value of J) is the analysis performed with zero plastic dilation.

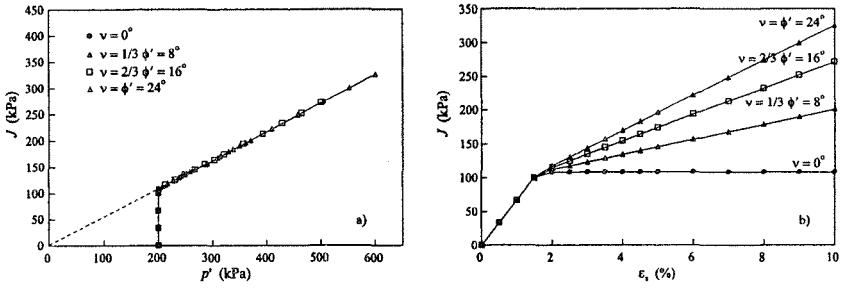

Figure 9.27: Prediction of a) stress paths and b) stress-strain curves in undrained triaxial compression using the Mohr-Coulomb model with different angles of dilation

The second example considers the undrained loading of a smooth rigid strip footing. The soil was assumed to have the same parameters as that used for the triaxial tests above. The initial stresses in the soil were calculated on the basis of a saturated bulk unit weight of 20 kN/m^3, a ground water table at the soil surface and a K_o=1−sinφ'. The footing was loaded by applying increments of vertical displacement and undrained conditions were again enforced by setting the bulk modulus of the pore water to be 1000 times K'. The results of two analyses, one with $\nu = 0°$ and the other with $\nu = \varphi'$, are shown in Figure 9.28. The difference is quite staggering: while the analysis with $\nu = 0°$ reaches a limit load, the analysis with $\nu = \varphi'$ shows a continuing increase in load with displacement. As with the triaxial tests, a limit load is only obtained if $\nu = 0°$.

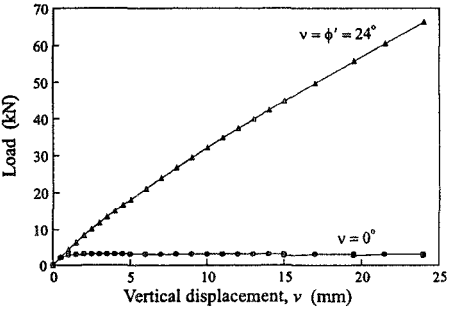

Figure 9.28: Load-displacement curves for a strip footing, using the Mohr-Coulomb model with different angles of dilation

It can be concluded from these two examples that a limit load will only be obtained if $\nu = 0°$. Consequently, great care must be exercised when using the Mohr-Coulomb model in undrained analysis. It could be argued that the model should not be used with $\nu > 0°$ for such analysis. However, reality is not that simple and often a finite element analysis involves both an undrained and a drained phase (e.g. undrained excavation followed by drained dissipation). Consequently, it may

be necessary to adjust the value of v between the two phases of the analysis. Alternatively, a more complex constitutive model which better represents soil behaviour may have to be employed. However, similar problems will occur with any constitutive model which does not reproduce critical state conditions. Consequently, great care must be exercised when selecting the model to use.

9.7 Influence of the shape of the yield and plastic potential surfaces in the deviatoric plane

As noted in Section 7.9 of Volume 1, the shape of the plastic potential in the deviatoric plane can affect the Lode's angle θ at failure in plane strain analyses. This implies that it will affect the value of the soil strength that can be mobilised. In many commercial software packages, the user has little control over the shape of the plastic potential and it is therefore important that its implications are understood. This phenomenon is investigated here by considering the modified Cam clay constitutive model.

Many software packages assume that both the yield and plastic potential surfaces plot as circles in the deviatoric plane. This is defined by specifying a constant value of the parameter M_J. Such an assumption implies that the angle of shearing resistance, φ', varies with the Lode's angle, θ. By equating M_J to the expression for $g(\theta)$ given by Equation (7.41) in Volume 1 and re-arranging, gives the following expression for φ' in terms of M_J and θ:

$$\varphi' = \sin^{-1}\left(\frac{M_J \cos\theta}{1 - \dfrac{M_J \sin\theta}{\sqrt{3}}}\right) \tag{9.13}$$

From this equation it is possible to express M_J in terms of the angle of shearing resistance, φ_{TC}', in triaxial compression, $\theta = -30°$, see Equation (7.26), Volume 1:

$$M_J(\varphi_{TC}') = \frac{2\sqrt{3}\sin\varphi_{TC}'}{3 - \sin\varphi_{TC}'} \tag{9.14}$$

Figure 9.29 shows the variations of φ' with θ, given by Equation (9.13), for three values of M_J. The values of M_J have been determined from Equation (9.14) using $\varphi_{TC}' = 20°$, 25° and 30°. If the plastic potential is circular in the deviatoric plane, it can be shown, see Chapter 7 in Volume 1, that plane strain failure occurs when the Lode's angle $\theta = 0°$. Figure 9.29 indicates that for all values of M_J there is a large change in φ' with θ. For example, if M_J is set to give $\varphi_{TC}' = 25°$, then under plane strain conditions the mobilised φ' value is $\varphi_{PS}' = 34.6°$. This difference is considerable and much larger than indicated by laboratory testing. The difference between φ_{TC}' and φ_{PS}' becomes greater the larger the value of M_J.

The effect of θ on undrained strength, S_u, for the constant M_J formulation is shown in Figure 9.30. The variation has been calculated using Equation (7.50) (in Volume 1) with:

$$OCR = 1$$
$$g(\theta) = M_J$$
$$K_o = 1 - \sin\varphi'_{TC}$$
$$\kappa / \lambda = 0.1$$

The equivalent variation based on the formulation which assumes a constant φ', instead of a constant M_J, is given in Figure 9.31. This is also based on Equation (7.50) in Volume 1 and the above parameters, except that $g(\theta)$ is now given by Equation (7.41) in Volume 1. The variation shown in this figure is in much better agreement with the available experimental data than the trends shown in Figure 9.30.

To investigate the effect of the plastic potential in a boundary value problem, two analyses of a rough rigid strip footing, 2m wide, have been performed. The finite element mesh is shown in Figure 9.32. The modified Cam clay model was used to represent the soil which had the following material parameters:

$$OCR = 6$$
$$v_l = 2.848$$
$$\lambda = 0.161$$
$$\kappa = 0.0322$$
$$\mu = 0.2$$

In one analysis the yield and plastic potential surfaces were assumed to be circular in the deviatoric plane. A value of M_J=0.5187 was used for this analysis, which is equivalent to φ_{TC}'=23°. In the second analysis a constant value of φ'=23° was used, giving a Mohr-Coulomb

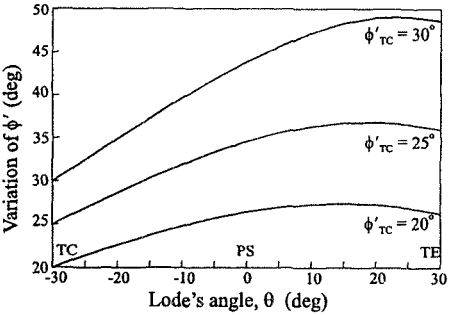

Figure 9.29: Variation of ϕ' with θ for constant M_J

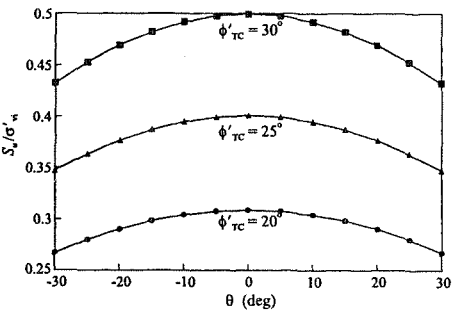

Figure 9.30: Effect of θ on S_u for the constant M_J formulation

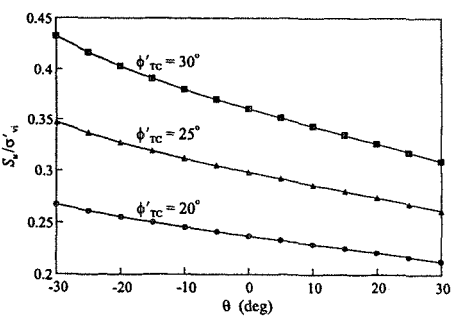

Figure 9.31: Effect of θ on S_u for the constant ϕ' formulation

hexagon for the yield surface in the deviatoric plane. However, the plastic potential still gave a circle in the deviatoric plane and therefore plane strain failure occurred at $\theta = 0°$, as for the first analysis. In both analyses the initial stress conditions in the soil were based on a saturated bulk unit weight of 18kN/m^3, a ground water table at a depth of 2.5m and a K_o=1.227. Above the ground water table the soil was assumed to be saturated and able to sustain pore water suctions. Coupled consolidation analyses were performed, but the permeability and time steps were chosen such that undrained conditions existed. Loading of the footing was simulated by imposing increments of vertical displacement.

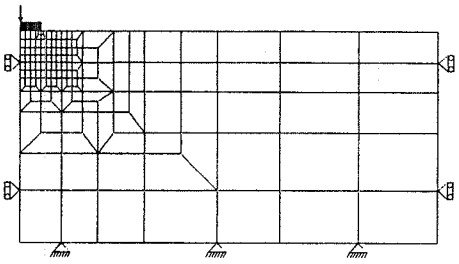

Figure 9.32: Finite element mesh for footing analysis

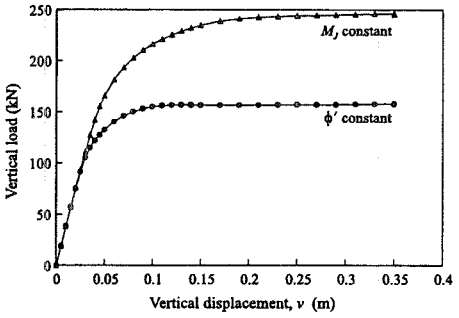

Figure 9.33: Load-displacement curves

In summary, the input to both analysis is identical, accept that in the first the strength parameter M_J is specified, whereas in the second φ' is input. In both analyses $\varphi_{TC}' = 23°$ and therefore any analysis in triaxial compression would give identical results. However, the strip footing problem is plane strain and therefore differences are expected. The resulting load displacement curves are given in Figure 9.33. The analysis with a constant M_J gave a collapse load some 58% larger than the analysis with a constant φ'. The implications for practice are clear, if a user is not aware of the plastic potential problem and/or is not fully conversant with the constitutive model implemented in the software being used, he/she could easily base the input on $\varphi_{TC}' = 23°$. If the model uses a constant M_J formulation, this would then imply a $\varphi_{PS}' = 31.2°$, which in turn leads to a large error in the prediction of any collapse load.

9.8 Using critical state models in undrained analysis

The input parameters to most critical state models are based on drained soil behaviour and do not involve the undrained shear strength, S_u. Consequently, undrained analyses can be problematic. For example, if constructing an embankment or foundation on soft clay, short term undrained conditions are likely to be critical from a stability point of view. It is therefore important for any analysis to accurately reproduce the undrained strength that is available. It is also

likely that establishing the undrained strength profile would be a priority of any site investigation.

Although the undrained strength is not one of the input parameters to the constitutive model, it can be calculated from the input parameters and the initial state of stress in the ground, as shown in Appendix VII.4 in Volume 1 for the Cam clay and modified Cam clay models. Consequently, if the undrained strength profile is known, it is possible to use Equations (7.49) or (7.50) in Volume 1 (for Cam clay or modified Cam clay respectively) to back calculate one of either *OCR*, K_o^{OC} or κ/λ. For example, if the undrained strength profile at a site resembles that shown in Figure 9.34b, which is typical of a soft clay deposit, it is possible to set all parameters, except the *OCR*, and then to use either Equation (7.49) or (7.50) to calculate the distribution of *OCR* which is consistent with the required S_u profile. Such a distribution of *OCR*, based on Equation (7.50) (modified Cam clay) is given in Figure 9.34a. Clearly it will be necessary for the finite element software to be flexible enough to allow the user to input such a variation of *OCR*.

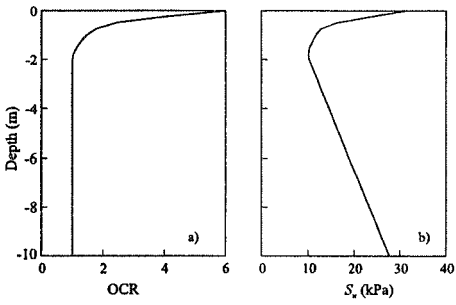

Figure 9.34: Variation with depth of a) overconsolidation ratio and b) undrained strength

It should be noted that for both Cam clay and modified Cam clay the undrained strength, S_u, is linearly related to the vertical effective stress, σ_{vi}'. Consequently, if $\sigma_{vi}' = 0$, then so will the undrained strength. This explains why it is necessary for the *OCR* to increase rapidly near to the ground surface in Figure 9.34a. However, even if $\sigma_{vi}' = 0$ at the ground surface (i.e. no pore water suctions present) it is still possible to perform a finite element analysis which simulates a finite undrained strength at the surface. This is possible because the constitutive model is only evaluated at the integration points which lie at a finite distance below the ground surface.

9.9 Construction problems

The procedure that is usually followed when constructing material in a finite element analysis is described in Chapter 3 in Volume 1. During construction the elements representing the new material are given a constitutive model which is consistent with its behaviour during construction. In practice this is usually achieved by assuming the material is linear elastic with a very low stiffness. Once constructed, the constitutive model is changed to represent the behaviour of the material once in place. This usually involves an elasto-plastic constitutive model. Clearly problems can arise if the stress states in the elements immediately after

construction are inconsistent with the new constitutive model.

When constructing material in a finite element analysis, problems can arise if the elements are constructed to the side of existing material. For example, consider the situation shown in Figure 9.35 where material is to be backfilled behind a retaining wall. Typically each row of elements in the backfill would be constructed sequentially. During construction of row 1, element A immediately adjacent to the retaining wall will be restrained by the stiffness of the wall. This could result in the element *hanging* from the wall and the calculation of tensile direct stresses at the integration points adjacent to the wall. If the constitutive model to be used after construction cannot tolerate these tensile stresses, then an incompatibility arises. A similar pattern of events could occur when constructing the remaining rows of backfilled elements. There are several options to overcome this problem, including:

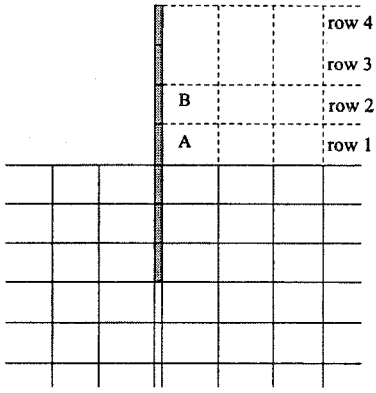

Figure 9.35: Construction of material adjacent to existing material

- Adjust the stresses after construction such that they are consistent with the new constitutive model. Clearly, there is no obvious way in which this should be performed and therefore this process involves and ad-hoc approach. The accumulated right hand side vector of the finite element equations must also be adjusted to account for the changed stresses so that equilibrium is maintained.
- Construct a new mesh with more rows of shorter elements behind the wall and try again.
- Use frictionless interface elements between the wall and soil during construction. Once constructed, the adjacent interface element should be reset to sustain friction.
- Use the same constitutive model to represent the soil during and after construction. Unfortunately, many of the current constitutive models are unable to cope with the conditions arising during construction.

9.10 Removal of prescribed degrees of freedom

During a finite element analysis it is sometimes necessary to change the boundary conditions so that a degree of freedom at a particular node changes from being prescribed to being not prescribed. For example, consider the problem of undrained loading followed by consolidation under constant load of a smooth rigid surface strip footing. During the undrained stage the loading of the footing could be simulated by applying increments of vertical displacement to the nodes on the ground surface immediately below the footing (i.e. along AB in Figure 9.36).

During the subsequent consolidation stage the load on the footing is required to remain constant but the footing is free to move vertically if it wishes. This could be modelled in the finite element analysis by replacing the prescribed displacements along AB with tied freedom boundary conditions which tie the subsequent incremental vertical displacements of the nodes along AB.

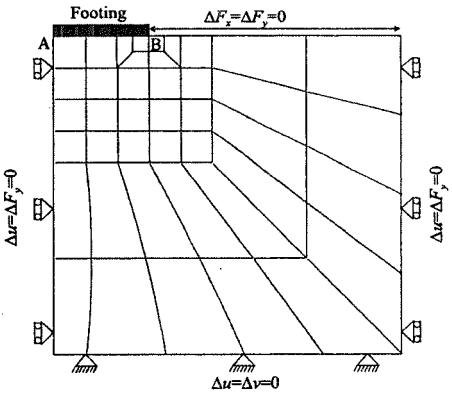

Figure 9.36: Boundary conditions for footing problem

What happens when the prescribed displacement boundary condition for the nodes along AB is removed is crucial. In the above discussion it has been assumed that the reactions associated with the prescribed displacements, and which represent the load on the footing, remain for further increments of the analysis. This is the preferred manner in which the software should deal with the situation. However, it involves a considerable amount of book keeping and it is much simpler for the software to automatically remove the reactions on the increment at which the prescribed displacement condition is removed. This is not desirable and software which works in this manner should be used with caution. Of course, there are situations where the user may wish to remove some or all of the reactions created by previous prescribed displacements. For example, at some stage after or during consolidation it may be necessary to unload the strip footing in the example quoted above. This is best simulated by having a facility in the software for removing a proportion of the reactions. If this is not available then the analysis must be stopped so that the reactions can be evaluated and then restarted with stress or point load boundary conditions which impose nodal forces in the opposite direction and of the required magnitude to cancel all, or part of, the reactions.

9.11 Modelling underdrainage

It is not uncommon, especially in urban areas, to find that the pore water pressure distribution in the ground is controlled, in part, by underdrainage. For example, in London, the situation shown in Figure 9.37 is not uncommon. Due to extraction of water from the chalk aquifer during the Industrial Revolution in the early part of the 19th century, the pore water pressures in the chalk and in the overlying Lamberth Group were depressed. They have remained depressed and currently, if extrapolated upwards, indicate a phreatic surface (zero pore water pressure) some distance into the London Clay. To complicate matters, a perched water table has remained in the permeable Thames Gravel which lies on top of the London Clay. The distribution of pore water pressure in the less permeable London Clay is

therefore controlled by these two hydraulic boundary conditions. This has resulted in the complex distribution of pore water pressure shown in Figure 9.37.

If the London Clay had a constant permeability which did not change with depth and if sufficient time for full consolidation had passed, then the pore water pressure distribution should theoretically vary linearly with depth, from the value at the bottom of the Thames Gravel to that at the top of the Lambeth Group, as shown by the dotted line in Figure 9.37. The fact that it does not can be explained by one of, or the combination of, two scenarios. Firstly, the permeability of the clay is so low that full equilisation of excess pore water pressures has not occurred and therefore consolidation is not complete, or secondly, the permeability of the clay varies with depth. Calculations based on measured values of permeability indicate that it is likely that full consolidation is more or less complete and therefore that it is a variation of permeability with depth that causes the nonlinear distribution of pore water pressure that is observed in the field. There is also considerable evidence from laboratory and field tests that permeability varies with voids ratio. As voids ratio decreases with depth, so will permeability.

A similar situation occurs in the soils below Bangkok, as discussed in Chapter 4 and shown in Figure 4.5, which is repeated here as Figure 9.38. A perched water table exists in the more permeable weathered surface crust and the pore water pressures have been reduced to zero at the top of the deep sand layer. This results in a nonlinear distribution of pore water pressure with depth throughout the soft and stiff clay layers.

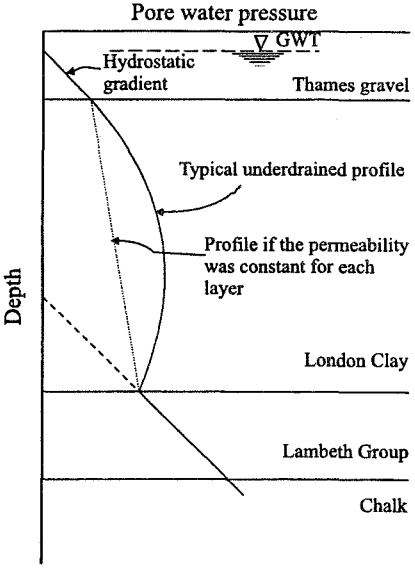

Figure 9.37: Typical underdrained pore water pressure profile in London Clay

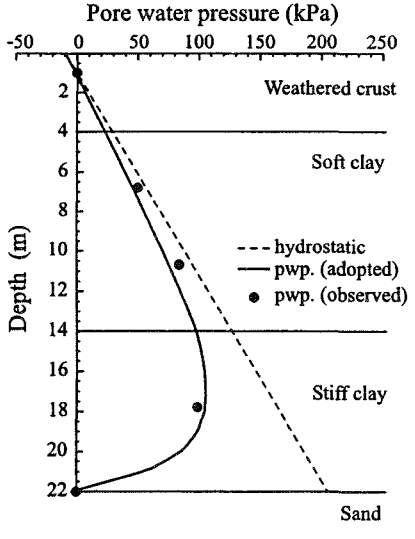

Figure 9.38: Underdrained pore water pressure profile in Bangkok Clay

As noted on many occasions throughout this book, it is essential to establish or input realistic and accurate distributions of the initial stresses and pore water pressure in the ground prior to the analysis of any loading and unloading due to construction or excavation. For example, if a tunnel was to be excavated in either the lower levels of the London Clay or in the stiff clay below Bangkok, then it is important to accurately model the initial pore water pressure conditions, as these would influence the initial effectives stresses which in turn would control the undrained strength of the clay.

It is desirable, and in principle acceptable, to input the stresses and pore water pressures directly as initial conditions into a finite element analysis. In this way it is quite easy to input the nonlinear distribution of pore water pressure. However, if the analysis involves coupled consolidation, this must be done with great care because the distribution of pore water pressure must be consistent with the distribution of permeability that is input in the form of soil properties.

As an illustration of the problems that can arise, the Bangkok situation shown in Figure 9.38 will be considered. The soil profile is modelled by the simple column of elements shown in Figure 9.39, which is constrained vertically at the bottom and horizontally along the vertical sides. The soil properties are discussed in detail in Chapter 4 and are listed in Tables 4.2, 4.3 and 4.4. Note that the standard critical state formulation of the elastic component of the model was used here. The initial distributions of overconsolidation ratio (*OCR*) and K_o are shown in Figures 4.10 and 4.11.

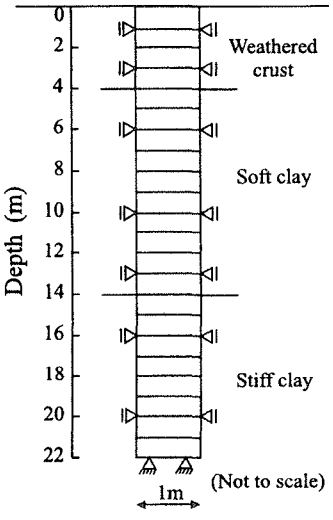

Figure 9.39: Finite element mesh for column analysis

The initial effective stress distribution based on the bulk unit weight of the soil, the K_o distribution and the initial pore water pressure distribution shown in Figure 9.38, were input as initial values.

Two coupled consolidation analyses were then performed. In both analyses the pore water pressures at the soil surface and at the bottom of the stiff clay layer were maintained at their initial values and only time increments were imposed. The two analyses differed in that in the first constant values of permeability (independent of depth) were specified for the clay layers. A value of k=8x10^{-10}m/s was used for the weathered crust, whereas values of k of 5.5x10^{-10}m/s and 1x10^{-10}m/s were used for the soft and stiff clays respectively, see Figure 9.40. In the second analysis the permeability was assumed to vary according to Equation (4.4), as given in Figure 4.13 and repeated in Figure 9.40. Ideally the permeability should vary with voids ratio, however in practice there is seldom sufficient data available and, as an

expedient, an expression in terms of mean effective stress is often employed, see Chapter 10 of Volume 1.

In both analyses sufficient time steps were imposed to allow steady state conditions to be reached. Of course, if the permeability distribution is consistent with the initial pore water pressure distribution, steady state conditions should exist from the beginning of the analysis. In addition, no movements or stress changes within the soil should occur. The results of the two analysis are presented in Figures 9.41, 9.42 and 9.43.

Figure 9.41 compares the predicted steady state pore water pressures with the initial values. While the analysis using a permeability based Equation (4.4) indicates that the steady state values are identical to the initial values, this is not so for the analysis with constant permeabilities, where a linear distribution of pore water pressure is predicted within the soft and stiff clay layers. The distribution of vertical movements within the soil is shown in Figure 9.42. While there are negligible movements from the analyses using Equation (4.4), significant movements are predicted for the analysis with constant permeabilities. Figure 9.43 shows the predicted changes in undrained strength. Again significant changes are predicted by the analysis with constant permeabilities.

The analysis based on permeabilities given by Equation (4.4) indicates compatibility between the distributions of initial permeability and pore water pressure. This is not so for the analysis based on constant permeabilities. The implications for finite element analyses are clear. For example, if a tunnel was to be excavated in the stiff clay, then if permeabilities inconsistent with the initial pore water pressure profile were used the analysis would be in error. If sufficient

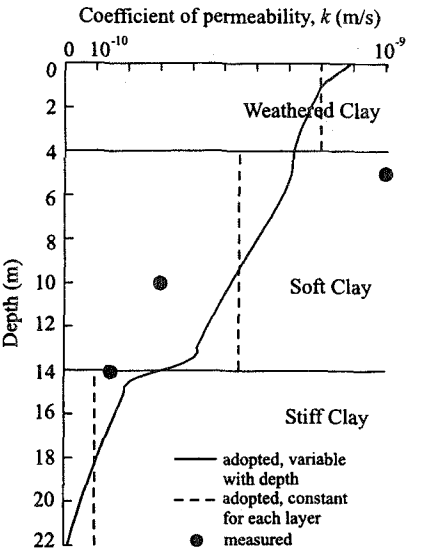

Figure 9.40: Permeability profiles adopted for two column analyses

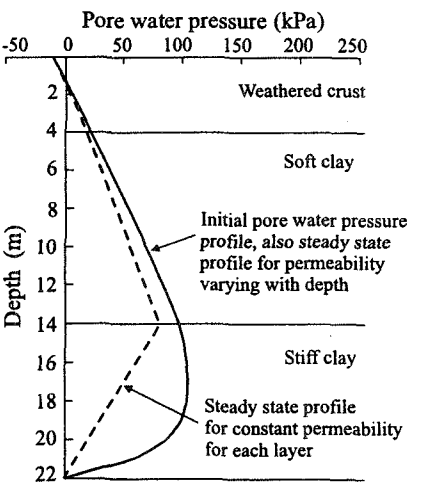

Figure 9.41: Comparison of initial and steady state pore water pressure profiles from two column analyses

time was allowed for equilisation of pore water pressures before excavating the tunnel, then the analyses would essentially not be simulating construction in soil with the assumed initial conditions. Alternatively, if sufficient time was not allowed for initial equilisation, the predicted movements and stress changes would be a combination of those arising from tunnel excavation and equilisation due to the initial incompatibility between permeabilities and initial pore water pressures.

Clearly, an incompatibility between the initial distributions of pore water pressure and permeability is a potential pitfall when performing analyses. In this respect it should be noted that it is not the absolute values of permeability that dictate the shapes of the pore water pressure distribution, but their relative changes with depth. The shape is also dependent on the hydraulic boundary conditions. If these conditions are such that the initial pore water pressure profile is hydrostatic, then this condition is not affected by the distribution of permeability, as such a profile is independent of both the magnitude and distribution of permeability.

As noted in Chapter 4, the parameters defining the permeability variation given by Equation (4.4) were chosen to be compatible with the initial pore water profile. It is for this reason that the analysis based on this permeability distribution was correct. In practice information on the pore water pressure profile is often available, but there is little information on the distribution of permeability. It is therefore useful to perform the simple column analysis described above to experiment with

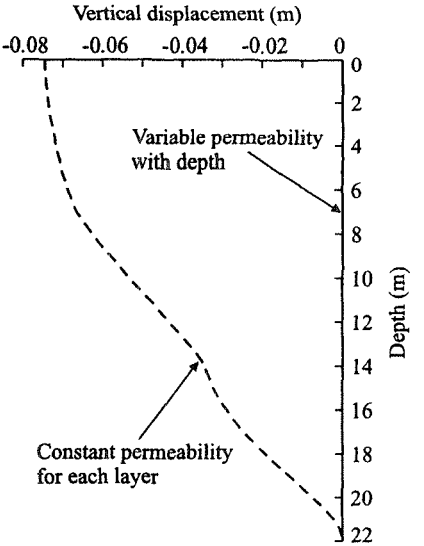

Figure 9.42: Comparison of vertical displacements at steady state from two column analyses

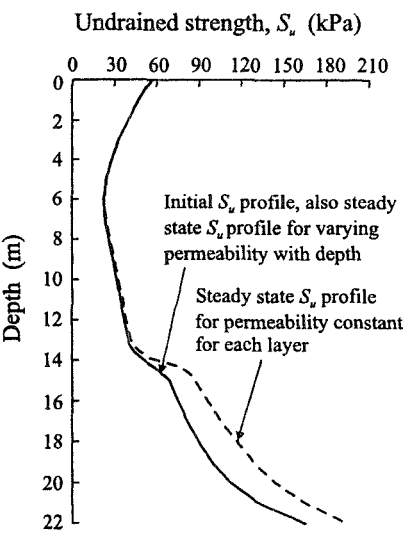

Figure 9.43: Comparison of initial and steady state undrained strength profiles from two column analyses

different distributions. Even if permeabilty data is available, it is still sensible to perform the column analysis to ensure compatibility between the initial permeability and pore water pressure distributions.

While in the above example the correct behaviour was obtained using a permeability varying with mean effective stress, see Equation (4.4), initial compatibility could have been obtained by allowing the permeability simply to change with depth. In such a case the distribution shown in Figure 4.13 would have to be adopted.

9.12 Summary

1. The two main sources of error involved in the finite element method itself are associated with the integration of the constitutive equations and with the discretisation of the geometry into finite elements. The magnitude of the errors involved in the former have been discussed in Chapter 9 of Volume1, where it was shown how they could be minimised by the use of a robust stress point algorithm. In this chapter the magnitude of the discretisation error has been investigated. This can be significant, but can be reduced by a suitable choice of finite element mesh. In particular, small elements need to be placed where there are rapid changes in stresses and strains.
2. The zero thickness interface element is useful for modelling relative slip and opening and closing on a pre-defined surface. Numerical problems can however occur through ill-conditioning of the stiffness matrix and high stress gradients in the interface elements. In many situations stress gradients are likely to be high and are increased with increased interface stiffness. The problem can therefore easily be confused with ill-conditioning.
3. Ill-conditioning was noticed in the problems analysed when the stiffness of the interface element was greater then approximately 100 times the Young's modulus of the surrounding soil. This however depends on the units used in the problem and the size of the surrounding elements.
4. The normal and shear stiffness of zero thickness interface elements have dimensions of force/(length)^3. They are therefore different to the bulk and shear stiffness of solid elements which have dimensions of force/(length)^2.
5. Newton-Cotes integration tends to improve the numerical behaviour of interface elements at, possibly, the expense of hiding the true solution. When sufficiently small elements are used to model the interface behaviour, Newton-Cotes and Gaussian integration give similar results.
6. The modelling of structural components in plane strain analysis can be problematic. While the major component of the problem may render itself to a plane strain idealisation, many of the structural components may not satisfy such requirements. Approximations must then be made. This usually involves some averaging of material properties and is likely to impose some restrictions on the analysis.
7. Particular attention must be made where structural elements are modelled using beam or membrane elements in coupled consolidation analyses. It is

very easy to make a mistake and model what are supposed to be impermeable structural components as permeable in such situations.

8. Care must also be exercised when modelling the connections between structural members.
9. When using the Mohr-Coulomb model for undrained analysis, it must be recognised that failure is unlikely to be predicted, unless the angle of dilation is set to zero.
10. The shape of the plastic potential in the deviatoric plane can have a major effect on the strengths mobilised in plane strain analysis. Particular care must be exercised when using critical state models, as many finite element programs assume that both the yield and plastic potential surfaces are circular in the deviatoric plane. This can lead to unrealistic angles of shearing resistance and/or undrained strengths being mobilised. It is more realistic to use a model which assumes a Mohr-Coulomb hexagon for the shape of the yield surface in the deviatoric plane, in conjunction with a plastic potential which produces a circle.
11. Although the undrained strength, S_u, is not an input parameter to most critical state models, it can be evaluated from the input data and initial stress conditions. It is therefore possible to adjust one or some of these values to give the desired undrained strength profile. One alternative is to keep all parameters fixed, except the *OCR*, which is varied with depth to obtain the desired S_u profile.
12. Problems can occur when constructing material in finite element analyses. This arises due to an incompatibility between the stresses calculated during construction and the constitutive model that is then assigned after construction. Several alternatives are available for dealing with this problem.
13. There is a potential problem associated with changing the boundary condition for a particular degree of freedom from prescribed to not prescribed during an analysis. It is important the user knows how the software being used will treat such a change.
14. If the initial pore water pressure distribution at the beginning of an analysis is influenced by underdrainage and a coupled finite element analysis is to be undertaken, then care must be exercised to ensure compatibility between this profile and the distribution of permeability. Otherwise, significant errors will be introduced into the analysis. In such cases a simple 1D column analysis is recommended before undertaking the main analysis.

References

Abbo A.J. & Sloan S.W. (1996), "An automatic load stepping algorithm with error control", Int. Jnl. Num. Meth. Engng, Vol. 39, pp 1737-1759

Addenbrooke T. I. (1996), "Numerical analysis of tunnelling in stiff clay", PhD thesis, Imperial College, University of London

Addenbrooke T.I & Potts D.M. (2001), "Twin tunnel interaction - surface and subsurface effects", accepted for publication in the Int. Jnl. Geomech

Addenbrooke T.I., Potts D.M. & Puzrin A.M. (1997), "The influence of pre-failure soil stiffness on numerical analysis of tunnel construction", Geotechnique, Vol. 47, No. 3, pp 693-712

A.G.I. (1991), "The leaning Tower of Pisa: present situation", Proc. 10th Eur. Conf. Soil Mech. & Found. Eng., Florence

A.G.S (1994), "Validation and use of geotechnical software", Association of Geotechnical Specialists, London

Anderson K.H. (1998), "Skirted anchors - case histories in cost effectiveness", NR.199, Norwegian Geotechnical Institute

Apted J.P. (1977), "Effects of weathering on some geotechnical properties of London Clay", PhD thesis, Imperial College, University of London

Arthur J.R.F. & Menzies B.K. (1972), "Inherent anisotropy in a sand", Geotechnique, Vol. 22, No. 1, pp 115-128

Barton M.E., Cooper M.R. & Palmer S.N. (1988), "Diagenetic alteration and micro-structural characteristics of sands: neglected factors in the interpretation of penetration tests", Proc. Conf. Penetration Testing in the UK, I.C.E., Birmingham

Bernat S. (1996), "Modelisation du creusement d'un tunnel en terrain meuble", Qualification sur chantier experimental, PhD thesis, Ecole Central de Lyon

Binnie G.M. (1978), "The collapse of the Dale Dyke dam in retrospect", Q.J. Engng.Geol.,Vol. 11, pp 305-324

Bishop A.W. (1955), "The use of the slip circle in the stability analysis of slopes", Geotechnique, Vol. 5, No.1, pp 7-17

Bishop A.W. & Bjerrum L. (1960), "The relevance of the triaxial test to the solution of stability problems", ASCE Research Conf. Shear Strength of Cohesive Soils, Boulder, Colorado, pp 437-451

Bishop A.W & Henkel D.J. (1962) "Test measurement of soil properties in the

triaxial test", Arnold, London

Bishop A.W. & Wesley L.D. (1975), "A hydraulic triaxial apparatus for controlled stress path testing", Geotechnique, Vol. 25, No. 4, pp 657-670

Bolton M.D. (1986), "The strength and dilatancy of sands", Geotechnique, Vol. 36, No. 1, pp 65-78

Bolton M.D. & Lau C.K. (1993), "Vertical bearing capacity factors for circular and strip footings on Mohr-Coulomb soil", Can. Geotech. Jnl., Vol. 30, pp 1024-1033

Boscardin M.D. & Cording E.J. (1989), "Building response to excavation induced settlement", Jnl. Geotechnical Eng, ASCE, Vol. 115, No. 1, pp 1-21

Burland J.B. (1969), Discussion. Proc. Conf. Insitu Investigations in Soil & Rock, I.C.E., pp 62

Burland J.B. (1990), "On the compressibility and shear strength of natural clays", Geotechnique, Vol. 40, No. 3, pp 327-378

Burland J.B. (1995), "Assessment of risk of damage to buildings due to tunnelling and excavation", Proc. 1st Int. Conf. Earthquake Geotechnical Eng, IS-Tokyo

Burland J. B. & Hancock, R. J. R. (1977)," Underground car park at the House of Commons, London: Geotechnical aspects", The Structural Engineer, Vol. 55, No. 2, pp 87-100

Burland J.B., Jamiolkowski M., Lancellotta,R., Leonards G.A. & Viggiani C. (1993), " Leaning Tower of Pisa - what is going on", ISSMFE News, 20, 2

Burland J.B., Jamiolkowski M., Lancellotta R., Leonards G.A. & Viggiani C. (1994), "Pisa update - behaviour during counterweight application", ISSMFE News, 21, 2

Burland J. B. & Kalra J.C. (1986), "Queen Elizabeth II Conference Centre: Geotechnical Aspects", Proc. Inst. Civ. Eng, Part I, Vol. 80, pp 1479-1503

Burland J.B., Longworth T.I. &Moore, J.F.A. (1977), "A study of ground movement and progressive failure caused by a deep excavation in Oxford Clay", Geotechnique, Vol. 27, No. 4, pp 557-591

Burland J.B. & Maswoswe J. (1982). Discussion on "In-situ measurement of horizontal stress in overconsolidated clay using push-in spade-shaped pressure cells" by P. Tedd & J.A. Charles, Geotechnique, Vol. 32, No. 3, pp 285-286

Burland J.B & Potts D.M. (1994), "Development and application of a numerical model for the leaning tower of Pisa", Pre-failure Deformation of Geomaterials, Edt. Shibuya, Mitachi & Miure, Balkema, Rotterdam, pp 715-737

Burland J.B., & Wroth C.P. (1974), "Settlement of buildings and associated damage", BGS conference 'Settlement of Structures', Cambridge, pp 611-651

BS8002 (1994), "Code of practice for earth retaining structures", BSI publications,

British Standards Institution, London

BS8006 (1995), "Code of practice for strengthened/reinforced soils and other fills", BSI publications, British Standards Institution, London

Calabresi G., Rampello S. & Callisto L. (1993), "The Leaning Tower of Pisa - Geotechnical characterisation of the Tower's subsoil within the framework of the Critical State Theory", Studi e Ricerche, Dipartimento di Ingegneria Strutturale e Geotechnica, Universita di Roma 2 La Sapienza

Carter J.P., Desai C.S., Potts D.M., Schweiger H.F. & Sloan S.W. (2000), "Computing and computer modelling in geotechnical engineering", GeoEng 2000, Melbourne, Technomic, Lancaster, Vol. 1, pp 1157-1252

Caswell I., Carder D.R. & Gent A.J.C. (1993), "Behaviour during construction of a propped contiguous bored pile wall in stiff clay at Walthamstow", TRRL Project Report 10 (E468A/BG), Transport and Road Research Laboratory

Chandler R.J. (1974), "Lias Clay:The long-term stability of cutting slopes", Geotechnique, Vol. 24, No. 1, pp 24-38

Chandler R.J. (1984a), "Recent European experience of landslides in over-consolidated clays and soft rocks", Proc. 4th Int. Symp. Landslides, Toronto, Vol. 1, pp 61-81

Chandler R.J. (1984b), "Delayed failure and observed strengths of first-time slides in stiff clay", Proc. 4th Int. Symp. Landslides, Toronto, Vol. 2, pp 19-25

Chandler R.J. & Skempton, A.W. (1974), "The design of permanent cutting slopes in stiff fissured clays", Geotechnique, Vol. 24, No. 4, pp 457-464

Charles J.A. (1976), "The use of one-dimensional compression tests and elastic theory in predicting deformations of rockfill embankments", Can. Geotech. J., Vol. 13, No. 3, pp 189-200

Charles J.A. & Watts K.S. (1985), "Report on testing of rockfill for Roadford Reservoir", Job No.W84/203, Building Research Establishment, UK

Christophersen H.P., Bysveen S. & Stove O.J. (1992), "Innovative foundation systems selected for the Snorre field development", Behaviour of offshore structures (BOSS), Vol. 1, pp 81-94

Clough G. W. & Leca E. (1989), "Whit focus on use of finite element methods for soft ground tunnelling", Tunnels et micro-tunnels en terrain Meuble du chantier a la theome (Proc. Int. Conf. on tunnelling and micro-tunnelling in soft ground, from field to theory). Presses de l'ecole national des pot et chaussees, Paris, Vol. 1, pp 531-573

Coyle H.M. & Reese L.C. (1966), "Load transfer for axially loaded piles in clay", Jnl. Soil. Mech. Found. Div., ASCE, Vol. 92, SM2, pp 1-26

Crabb G.I. & Atkinson J.H. (1991), "Determination of soil strength parameters for the analysis of highway slope failures", Proc. Int. Conf. Slope Stability Engineering, Inst. Civ. Eng., London, pp 13-18

Davies R.V. & Henkel D.J. (1982), "Geotechnical problems associated with the construction of Chater Station", The Arup Journal 17, No. 1, pp 4-10

Davis E.H. (1968), "Theories of plasticity and the failure of soil masses", Soil Mechanics - Selected Topics, Edt. I.K. Lee, Butterworths, London, pp 341-380

Davis E.H. & Booker J.R. (1973), "The effect of increasing strength with depth on the bearing capacity of clays", Geotechnique, Vol. 23, No. 4, pp 551-565

Day R.A. & Potts D.M. (1994), "Zero thickness interface elements - numerical stability and application", Int. Jnl. Num. Anal. Geomech., Vol. 18, pp 698-708

Day R.A & Potts D.M. (1998), "The effect of interface properties on retaining wall behaviour", Int. Jnl. Num. Anal. Meth. Geomech., Vol. 22, pp 1021-1033

Day R.A. & Potts D.M. (2000), Discussion on "Observations on the computation of the bearing capacity factor N_γ by finite elements" by Woodward & Griffiths, Geotechnique, Vol. 50, No. 3, pp301-303

De Moor E.K. (1994), "An analysis of bored pile/diaphragm wall installation effects", Geotechnique, Vol. 44, No. 2, pp 341-347

Desai C.S., Zaman M.M, Lightner J.G. & Siriwardane H.J. (1984), "Thin-layer element for interfaces and joints", Int. Jnl. Num. Anal. Meth. Geomech., Vol. 8, pp 19-43

Dounias G.T. (1987), "Progressive failure in embankment dams", PhD thesis, Imperial College, University of London

Dounias G.T., Potts D.M. & Vaughan P.R. (1996), "Analysis of progressive failure and cracking in old British dams", Geotechnique, Vol. 46, No. 4, pp 621-640

Dounias G.T., Potts D.M. & Vaughan, P.R. (1989), "Numerical stress analysis of progressive failure and cracking in embankment dams", Report to the Department of the Environment, Contract No.PECD 7/7/222, Building Research Establishment

Duncan J.M. (1992), "Static stability and deformation analysis", Proc. Spec. Conf. Stability and Performance of Slopes and Embankments - II, Geot. Eng. Div., ASCE, Vol. 1, (Edt. Seed and Boulanger), pp 222-266

Duncan J.M. (1994), "The role of advanced constitutive relations in practical applications", Proc. 13th Int. Conf. Soil Mechs. Found. Eng., New Delhi, Vol. 5, pp 31-48

Duncan J.M., Byrne P.M., Wang K.S. & Mabry, P. (1980), "Strength, stress-strain and bulk modulus parameters for finite element analyses of stresses and movements in soil masses", Geotechnical Engineering Research Report No. UCB/GT/80-01, University of California, Berkeley

Duncan J.M. & Seed R.B. (1986), "Compaction induced earth pressures under K_o conditions", Jnl. Geotech. Eng., ASCE, Vol. 112, No. 1, pp 1-21

EUR 15285 (1993), "INTERCLAY II project: A co-ordinated benchmark exercise on the rheology of clays"", The European Commission, Brussels

Fernie R., Kingston P., St John H.D., Higgins K.G. & Potts D.M. (1996), "Case history of a deep 'stepped box' excavation in soft ground at the seafront - Langney Point, Eastbourne", Geotechnical Aspects of Underground

Construction in Soft Clay, Edt. R.J. Mair & R. N. Taylor, Balkema, Rotterdam, pp 123-130

Finno R.J., Harahap I.S. & Sabatini P.J. (1991), "Analysis of braced excavations with coupled finite element formulations", Computers & Geotechnics, Vol. 12, pp 91-114

Frank R., Guenot A. & Humbert P. (1982), " Numerical analysis of contacts in geomechanics", Proc. 4th Int. Conf. Num. Met. Geomech., Rotterdam, pp 37-42

Ganendra D. (1993), "Finite element analysis of laterally loaded piles", PhD thesis, Imperial College, University of London

Ganendra D. & Potts D.M. (2002a), "A new approach to the analysis and design of pile groups - Theory", In preparation

Ganendra D. & Potts D.M. (2002b), "A new approach to the analysis and design of pile groups - Application", In preparation

Garga V.K. (1970), "Residual strength under large strains and the effect of sample size on the consolidation of fissure clay", PhD thesis, Imperial College, University of London

Gens A., Carol I. & Alonso E.E. (1989), "An interface element formulation for the analysis of soil-reinforcement interaction", Comput. Geotech. Vol. 7 (1,2), pp 133-151

Gens A. & Potts D.M. (1988), "Critical state models in computational geomechanics", Engineering and Mechanics, Vol. 15, pp178-197

Geotechnical Consulting Group (1993), "Finite element parametric study on long term settlement caused by tunnelling", Report to 'Crossrail', May 1993.

Germaine J.T. (1982), "Development of the Directional Shear Cell for measuring cross anisotropic clay properties", DSc thesis, MIT, USA

Gourvenic S. (1998), "Three dimensional effects of diaphragm wall installation and stagged construction sequences", PhD thesis, University of Southampton

Gun M.J., Satkunananthan A. & Clayton C.R.I. (1993), "Finite element modelling of installation effects", Retaining Structures, Edt. C.R.I. Clayton, Thomas Telford, London, pp 46-55

Griffiths D.V. & Lane P.A. (1999), "Slope stability analysis by finite elements", Geotechnique, Vol. 49, No. 3, pp 387-403

Hamza M.M.A.F. (1976), "The analysis of embankment dams by nonlinear finite element method", PhD thesis, Imperial College, London University

Hansen J.B. (1970), "A revised and extended formula for bearing capacity", Bulletin No. 28, Danish Geotechnical Institute, Copenhagen

Harris D.I., Potts D.M., Brady K.C., Hight D.W. & Higgins K.C. (1993), "Finite element analysis of anchored earth retaining walls", Retaining Structures, Edt. C.R.I. Clayton, Thomas Telford, London, pp 599-608

Head K.H. (1994), "Manual of soil laboratory testing", Vol. 2, Wiley, New York

Hermann L.R. (1978), "Finite element analysis of contact problems", Proc. ASCE, Vol. 104, EM5, pp1043-1057

Hight D.W. (1993), "A review of sampling effects in clays and sands", Offshore site investigation and foundation behaviour, Society for Underwater Technology, Vol. 28, pp 115-146

Hight D.W. & Higgins K.G. (1994), "An approach to the prediction of ground movements in engineering practice: background and application", Pre-failure Deformation of Geomaterials, Edt. Shibuya, Mitachi & Miura, Balkema, Rotterdam, pp 909-945

Hight D. W., Higgins K. G., Jardine R. J., Potts D. M., Pickles A. R., DeMoor E. K., & Nyirende, Z. M. (1992), "Predicted and measured tunnel distortions associated with construction of Waterloo International Terminal", Predictive Soil Mechanics, Proc. Wroth Memorial Symp., pp 317-338

Hight D.W., Jardine R.J. & Gens A. (1987), "The behaviour of soft clays", Embankments on soft clays, Bulletin of the Public Works Research Centre, Athens, pp 33-158

Higgins K.G. (1983), "Diaphragm walling, associated ground movements and analysis of construction", MSc thesis, Imperial College, London University

Higgins K.G., Fernie R., Potts D.M. & Houston C. (1999), " The use of numerical methods for the design of base propped retaining walls in a stiff fissured clay", Geotechnical Aspects of Underground Construction in Soft Ground, Edt. Kusakabe et al, Balkema, Rotterdam, pp 511-516

Higgins K. G., Potts D. M., and Mai, R. J. (1996), "Numerical modelling of the influence of the Westminster Station excavation and tunnelling on Big Ben Clock Tower", Geotechnical Aspects of Underground Construction in Soft Clay, Edt. R.J. Mair & R. N. Taylor, Balkema, Rotterdam, pp 525-530

Higgins K.G., Potts D.M. & Symonds I.F. (1993), "The use of laboratory derived soil parameters for the prediction of retaining wall behaviour", Retaining Structures, Edt. C.R.I. Clayton, Thomas Telford, London, pp 92-101

Hill R. (1950), "The mathematical theory of plasticity", Clarendon Press, Oxford

Hird C.C., Pyrah I.C. & Russell D. (1990), "Finite element analysis of the collapse of reinforced embankments on soft ground", Geotechnique, Vol. 40, No. 4, pp 633-640

Horsnell M.R., Norris V.A. & Ims B. (1992), "Mudmat interaction and foundation analysis", Proc Int. Conf. Recent Large Scale Fully Instrumented Pile tests in Clay, Thomas Telford, London

Huder J. (1972), "Stability of bentonite slurry trenches with some experience of Swiss practice", Proc 5th European Conf. Soil Mech. & Found. Eng, Madrid, pp 517-522

Jackson C., Zdravkovic L. & Potts D.M. (1997), "Bearing capacity of pre-loaded surface foundations on clay", Computer Methods & Advances in Geomechanics, Edt. J.X. Yuan, Balkema, Rotterdam, Vol. 1, pp 745-750

Jamiolkowski M, Lancellotta R., & Lo Presti D.C.F. (1994), "Remarks on the stiffness at small strains of six Italian clays", Pre-Failure Deformation of

Geomaterials, Edt. S. Shibuya, T. Mitachi & S. Miura, Balkema, Rotterdam, pp817-836

Jardine R.J. (1985), "Investigation of pile-soil behaviour with special reference to the foundations of offshore structures", PhD thesis, Imperial College, London University

Jardine R.J. (1992), "Non-linear stiffness parameters from undrained pressuremeter tests", Canadian Geotechnical Journal, Vol. 29, pp 436-447

Jardine R.J. (1994), "One perspective of the pre-failure deformation characteristics of some geomaterials", Pre-failure Deformation of Geomaterials, Edt. Shibuya, Mitachi & Miura, Balkema, Rotterdam, pp 855-885

Jardine R.J. & Chow F.C., "New design methods for offshore piles", MTD Publication 96/103

Jardine R.J & Potts D.M. (1988), "Hutton tension leg platform foundations: predictions of driven pile behaviour", Geotechnique, Vol. 38, No. 2, pp231-252

Jardine R.J & Potts D.M. (1992), "Magnus foundations: soil properties and predictions of field behaviour", Proc. Int. Conf. Recent Large Scale Fully Instrumented Pile tests in Clay, Thomas Telford, London

Jardine R. J., Potts D. M., Fourie A. B. & Burland J. B. (1986), "Studies of the influence of nonlinear stress-strain characteristics in soil-structure interaction", Geotechnique, Vol. 36, No. 3, pp 377-396

Jefferies R.M. & Knowles N.C. (1994), "Finite element benchmarks for clay - the INTERCLAY project", Proc. 3rd Eur. Conf. Num. Meth. Geotech. Eng., Edt. I.M. Smith, Balkema, Rotterdam, pp 165-170

Jonsrud R & Finnesand G. (1992), "Instrumentation for monitoring the installation and performance of the concrete foundation templates for the Snorre tension leg platform", Behaviour of offshore structures (BOSS), Vol. 1, pp 690-703

Jovičić V. & Coop M.R. (1998), "The measurement of stiffness anisotropy in clays with bender element tests in the triaxial apparatus" Geotechnical Testing Journal, ASTM, Vol. 21, No. 1, pp 3-10

Kimmance J.P, Lawrence S., Hassan O., Purchase N.J. & Tollinger G. (1996), "Observations of deformations created in existing tunnels by adjacent and cross cutting excavations", Geotechnical Aspects of Underground Construction in Soft Ground, Edt. R.J. Mair & R. N. Taylor, Balkema, Rotterdam, pp 707-712

Kovačević N. (1994), "Numerical analyses of rockfill dams, cut slopes and road embankments", PhD thesis, Imperial College, University of London

Kovačević N., Potts D.M., Vaughan P.R., Charles J.A. & Tedd P. (1997), "Assessing the safety of old embankment dams by observing and analysisng movement during reservoir operation", Proc. 19th Int. Cong. Large Dams (ICOLD), Florence, pp 551-566

Kenley R.M. & Sharp D.E. (1992), "Magnus foundation monitoring project - instrumentation, data processing and measured results", Proc Int. Conf.

Recent Large Scale Fully Instrumented Pile tests in Clay, Thomas Telford, London

Kuwano R. (1999), "The stiffness and yielding anisotropy of sand", PhD thesis, Imperial College, University of London

Kuzuno T., Takasaki H., Tanaka M. & Tamai, T. (1996), "Driving control and ground behaviour of triple circular face shield machine", Geotechnical Aspects of Underground Construction in Soft Ground, Edt. R.J. Mair & R. N. Taylor, Balkema, Rotterdam, pp 283-288

La Rochelle P., Trak B., Tavenas F.A. & Roy M. (1974), "Failure of a test embankment on a sensitive Champlain clay deposit"; Canadian Geotechnical Journal, Vol. 11, pp 142-164.

Lade P.V. (1977), "Elasto-plastic stress-strain theory for cohesionless soil with curved yield surfaces", Int. J. Solids Structures, Vol. 13, pp 1019-1035

Lade P.V. & Kim M.K. (1988), "Single hardening constitutive model for frictional materials, III. Comparison with experimental data", Computers and Geotechnics, Vol. 6, pp 13-29

Lambe T.W. (1973), "Predictions in soil engineering", Geotechnique, Vol. 23, No. 2, pp 149-202

Lancellotta R. & Pepe C. (1990), "Pisa Tower - A preliminary report", Politecnico di Turino, Dipartimento Ingegnaria Strutturale, Rapporto di Ricerca, No 2.1

Leonards G.A. & Ramiah B.K. (1959), " Time effects in the consolidation of clay", ASTM, STP 254, pp 116-130

Leroueil S. (1977) Quelques considerations sur le comportement des argiles sensibles; PhD thesis, University of Laval, Quebec, Canada

Lo Presti D.C.F., Pallara O., Lancellotta R., Armandi M. & Maniscalco R. (1993), "Monotonic and cyclic loading behaviour of two sands at small strains", Geotechnical Testing Journal, Vol. 16, No. 4, pp 409-424

Lunne T. & Kleven A. (1981), "Role of CPT in North Sea foundation engineering", Cone penetration testing, ASCE

Lupini J.F., Skinner A.E. & Vaughan P.R. (1981), "The drained residual strength of cohesive soils", Geotechnique, Vol. 31, No. 2, pp 181-213

Mair R.J., Hight D.W. & Potts D.M. (1992), "Finite element analyses of settlements above a tunnel in soft ground", Contractor Report 265, Transport and Road Research Laboratory

Mair R.J. & Wood D.M. (1987), "Pressuremeter testing: Methods and interpretation", CIRIA Ground Eng. Report: In-situ testing, CIRIA & Butterworths, London & Sevenoaks

Marsland A. & Eason B.J. (1973), "Measurements of displacements in ground below loaded plates in boreholes", Proc. Conf. Filed Instrumentation, Butterworths, pp 304-317

Marsland A. & Quaterman R.S. (1982), "Factors affecting the measurements and interpretation of quasi-static penetration tests in clays", Proc. 2nd Eur. Sym. Penetration Testing, Amsterdam

Ministero dei Lavori Pubblici (1971), "Ricerche e studi sulla Torre di Pisa ed i fenomeni connessi alle condizione di ambiente, Vol. 3, I.G.M., Florence

Mori R.T. & Pinto N.L.deS. (1988), "Analysis of deformations in concrete face rockfill dams to improve face movement prediction", Proc. 16th Int. Cong. Large Dams (ICOLD), San Francisco, Vol. 2, pp 27-34

NAFEMS (1990), "The standard NAFEMS benchmarks", Publication P18, NAFEMS

Nash D.F.T., Sills G.C. & Davison L.R. (1992), "One -dimensional consolidation testing of soft clay from Bothkennar", Geotechnique, Vol. 42, No. 2, pp 241-256

Naylor D.J. (1975). "Numerical models for clay core dams, Proc. Int. Symp. Criteria and Assumptions for Num. Analysis of Dams, Swansea, Edt. Naylor, Stagg & Zienkiewicz, pp 489-514

Naylor D.J. (1991a), "Stress-strain laws and parameter values", Advances in Rockfill Structures, Edt. Maranha das Neves, pp 269-290

Naylor D.J. (1991b), "Finite element methods for fills and embankment dams", Advances in Rockfill Structures, Edt. Maranha das Neves, pp 291-340

Naylor D.J., Tong S.L. & Shahkarami A.A. (1989), "Numerical modelling of saturation shrinkage", Numerical Models in Geomechanics NUMOG III, Edt. Pietruszczak and Pande, pp 636-648

Naylor D.J. (1999), "On the use of the FEM for assessing the stability of cuts and fills", Numerical Models in Geomechanics, NUMOG VII, Edt. Pietruszczak & Pande, Balkema, Rotterdam, pp 553-560

NCE (1983), New Civil Engineer, October Issue, Emap, London

NCE (1984a), New Civil Engineer, January Issue, Emap, London

NCE (1984b), New Civil Engineer, February Issue, Emap, London

NCE (1991), New Civil Engineer, March Issue, Emap, London

NCE (1994), New Civil Engineer, December Issue, Emap, London

Ng C.W.W. (1992), "An evaluation of soil-structure interaction associated with a multi-propped excavation", PhD thesis, University of Bristol

Nyren R. (1998), "Field measurements above twin tunnels in London Clay", PhD thesis, Imperial College, University of London

Ong J.C.W. (1997), "Compensation grouting for bored tunnelling in soft clay", MSc dissertation, Imperial College, University of London

Ong H. L. (1996), "Numerical analysis for tunnelling and grouting in soft ground", MSc dissertation, Imperial College, University of London

O'Neil M.W., Ghazzaly O.I. & Ha H.B. (1977), "Analysis of three dimensional pile groups with non-linear soil response and pile-soil-pile interaction", Offshore Technology Conf., Paper 2838, pp 245-256

Padfield C.J. & Mair R.J. (1984), " Design of retaining walls embedded in stiff clay", CIRIA Report 104

Pagano L. (1998), "Interpretation of mechanical behaviour of earth dams by numerical analysis", Proc. Symp. Prediction and Performance in Geotechnical Engineering, Hevelius Edizioni, Napoli, pp 89-150

Panet M. & Guenot A. (1982), "Analysis of convergence behind the face of a tunnel", Proc. Tunnelling '82, London, The Institution of Mining & Metalluragy, pp 197-204

Peck R.B. (1969), " Deep excavations and tunnelling in soft ground", Proc. 7th Int. Conf. Soil Mech. & Found. Eng., Mexico, pp 225-290

Penman A.D.M., Burland J.B. & Charles J.A. (1971), "Observed and predicted deformations in a large embankment dam during construction", Proc. Instn. Civ. Eng., London, Vol. 49, pp 1-49

Penman A.D.M. & Charles J.A. (1985), "Behaviour of rockfill dam with asphaltic membrane", Proc. 11th Int. Conf. Soil Mechs. Found. Eng., San Francisco, Vol. 4, pp 2011-2014

Perry J. (1989), "A survey of slope condition on motorway earthworks in England and Wales", Transport and Road Research Laboratory, Research Report No.199, pp 49

Porović E. (1995), "Investigations of soil behaviour using a resonant column torsional shear hollow cylinder apparatus", PhD thesis, Imperial College, University of London

Potts D.M. & Addenbrooke T.I. (1997), "A structure's influence on tunnelling-induced ground movements", Proc. Inst. Civ. Eng. Geotech. Eng., Vol. 125, pp 109-125

Potts D.M., Addenbrooke T.I. & Day. R.A. (1993), "The use of soil berms for temporary support of retaining walls", Retaining Structures, Edt. C.R.I. Clayton, Thomas Telford, London, pp 440-447

Potts D.M. & Burland J.B. (2000), "Development and application of a numerical model for simulating the stabilisation of the Leaning Tower of Pisa", Developments in Theoretical Geomechanics, Booker Memorial Symp., Edt. D.W. Smith & J.P. Carter, Balkema, Rotterdam, pp 737-758

Potts D.M. & Day R.A. (1990), "The use of sheet pile retaining walls for deep excavations in stiff clay", Proc. Inst. Civ. Engineers, Part 1, Vol. 88, pp 899-927

Potts D.M., Dounias G.T. & Vaughan P.R. (1987), "Finite element analysis of the direct shear box test", Geotechnique, Vol. 37, No. 1, pp 11-23

Potts D.M., Dounias G.T. & Vaughan P.R. (1990), "Finite element analysis of progressive failure of Carsington embankment", Geotechnique, Vol. 40, No. 1, pp 79-101.

Potts D.M. & Fourie A.B. (1986), "A numerical study of the effects of wall deformation on earth pressures", Int. Jnl. Num. Anal. Geomech., Vol. 10, No. 4, pp 383-405

Potts D.M. & Knights M.C. (1985), "Finite element techniques for the preliminary assessment of a cut and cover tunnel", Tunnelling '85, Edt. M.J. Jones, The Institution of Mining & Metallurgy, pp 83-92

Potts D.M., Kovačević N. & Vaughan P.R. (1997), "Delayed collapse of cut slopes in stiff clay", Geotechnique, Vol. 47, No. 5, pp 953-982.

Potts D.M. & Zdravković L. (1999) "Finite element analysis in geotechnical

engineering: Theory", Thomas Telford, London
Poulos H.G. & Davis E.H. (1968), "Pile foundation analysis and design", Wiley
Prandtl L. (1920), "Uber die Harte Plastischer Korper", Nachrichten von der Koniglichen Gesellschaft der Wissenschaften,. Gottingen, Math. Phys., Klasse, pp 74-85
Puzrin A, & Burland J.B (1998), "Non-linear model of small-strain behaviour of soils", Geotechnique, Vol. 48, No. 2, pp 217-233
Randolph M.F. & Poulos H.G. (1982), "Estimating the flexibility of offshore pile groups", Proc. 2nd Int. Conf. Num. Meths, Offshore Piling, Austin Texas, pp 313-328
Randolph M.F., Martin C.M. & Hu Y., "Limiting resistance of a spherical penetrometer in cohesive material", Geotechnique, Vol. 50, No. 5, pp 573-582
Reese L.C. (1977), "Laterally loaded piles: program documentation", Jnl. Geot. Eng. Div., ASCE, Vol. 103, No GT4, pp 287-305
Rigden W.J. & Semple R.M. (1983), "Design and installation of the Magnus foundations; Predictions of pile behaviour", Conf. on design and construction of offshore structures, Thomas Telford, London, pp 29-52
Robertson P.K. & Campanella R.G. (1983), "Interpretation of cone penetration tests. Parts 1 & 2", Canadian Geotechnical Journal, Vol. 20, pp 718-745
Roscoe K.H. & Burland J.B. (1968), "On the generalised stress-strain behaviour of 'wet' clay", Eng. plasticity, Cambridge Univ. Press, pp 535-609
Rowe R. K., Lo K. Y. & Kack G. J. (1983), "A method of estimating surface settlement above tunnel constructed in soft ground", Canadian Geotechnical Journal, Vol. 20, pp 11-22
Rowe P.W. (1971), "Theoretical meaning and observed values of deformation parameters for soil; Stress-Strain Behaviour of Soils", Proc. Roscoe Memorial Symp., Cambridge University, Foulis, pp 143-194
Rowe R. K., Booker J. R. & Balaam N. P. (1978), "Application of the initial stress method to soil - structure interaction", Int. Jnl. for Num. Meth. Eng., Vol. 12, pp 873-880
Sandroni S.S. (1977), "The strength of London Clay in total and effective stress terms", PhD thesis, Imperial College, University of London
Sarrailh J. & Tavenas F.A. (1972), "Etude geotechnique preliminarie du site de Saint-Alban", Internal report GCN-72-09-02 (MS-N2), University of Laval, Quebec, Canada
Schultheiss P.J. (1981), "Simultaneous measurement of P & S wave velocities during conventional laboratory soil testing procedures", Marine Geotechnology, Vol. 4, No. 4, pp 343-367
Schweiger H.F. (1998), "Results from two geotechnical benchmark problems", Proc. 4th European Conf. Num. Meth. Geotech. Eng., Edt A. Cividini, pp645-654
Schweiger H.F. & Freiseder M. (1994), "Three dimensional finite element analysis of diaphragm wall construction", Computer Methods and Advances in

Geomechanics", Edt. H.J. Siriwardane & M.M. Zaman, Balkema, Rotterdam, pp 2493-2498

Sharp D.E. (1992), "Magnus foundation monitoring - an overview", Proc Int. Conf. Recent Large Scale Fully Instrumented Pile tests in Clay, Thomas Telford, London

Shibuya S. (1999), Personal communication

Shin J.H. (2000), "Numerical analysis of tunnelling in decomposed granite soil", PhD thesis, Imperial College, University of London

Shin D.M. & Potts D.M. (2001), "Time-based two dimensional modelling of tunnelling", in preparation

Sieffert J.G. & Bay-Gress Ch. (2000), "Comparison of European bearing capacity calculation methods for shallow foundations", Proc. Inst. Civ. Eng. Geotech. Eng., Vol. 143, pp 65-74

Simpson B., Atkinson J. H. & Jovičić, V. (1996), "The influence of anisotropy on calculations of ground settlements above tunnels", Geotechnical Aspects of Underground Construction in Soft Ground, Edt. R.J. Mair & R. N. Taylor, Balkema, Rotterdam, pp 51 -514

Skempton A.W. (1951), "The bearing capacity of clays", Proc. Build. Res. Congress, Vol. 1, pp 180-189

Skempton A.W. (1964), "Long term stability of clay slopes", Geotechnique, Vol. 14, No. 2, pp 77-101

Skempton A.W. (1977), "Slope stability of cuttings in brown London Clay", Proc. 9th Int. Conf. Soil Mechs. Found. Eng., Tokyo, Vol. 3, pp 261-270

Skempton A.W. (1985), "Geotechnical aspects of the Carsington dam failure", Proc. 16th Int. Conf. Soil Mech. Found. Eng., San Francisco, Vol. 5, pp 2581-2591

Skempton A.W. (1986), "Standard penetration test procedures and the effects in sands of overburden pressure, relative density, particle size, ageing and overconsolidation", Geotechnique, Vol. 36, No. 2, pp 425-447

Skempton A.W. & Chrimes M.M. (1994), "Thames tunnel: geology, site investigation and geotechnical problems", Geotechnique, Vol. 44, No. 2, pp 191-216

Skempton A.W. & Henkel D.J. (1957), "Tests on London Clay from deep borings at Paddington, Victoria and South Bank", Proc. 4th Int. Conf. Soil Mechs. Found. Eng., London, Vol. 1, pp 100-106

Skinner A.E. (1975), "The effect of high pore water pressures on the mechanical behaviour of sediments", PhD thesis, Imperial College, University of London

Standing J.R., Farina M. & Potts D.M. (1998), "The prediction of tunnelling induced building settlements - a case study",Tunnels & Metropolises, Edt. A. Negro &A.A. Ferreira, Balkema, Rotterdam, pp 1053-1058

St John H.D. (1975), "Field and theoretical studies of behaviour of ground around deep excavations in London Clay", PhD thesis, University of Cambridge

St John H.D., Harris D.I., Potts D.M. & Fernie R. (1993), "Design study for a

List of symbols

This list contains definitions of symbols and an indication of the section in the book where they first appear. Because of the large number of parameters that are used, some symbols represent more than one quantity. To minimise any confusion this may cause, all symbols are defined in the text, when they are first used. If some symbols are missing from the list below, they are in the List of symbols in Volume 1.

a	constant for the log permeability law	(2.5.4)
a	horizontal extent of reduced K_o zone	(2.6.3)
b	relative magnitude of the intermediate principal stress	(1.3.3)
c'	cohesion	(2.7.2)
c_p'	peak value of cohesion	(4.3.2)
c_r'	residual value of cohesion	(4.3.2)
c_w	interface cohesion	(5.5.6)
e	void ratio	(1.3.2)
e	eccentricity of building axis relative to tunnel axis	(2.4.1)
f_s	sleeve resistance	(1.4.3)
$g(\theta)$	gradient of the yield function in J-p' plane, as a function of Lode's angle	(6.5.5)
k	coefficient of permeability	(2.5.4)
k_o	coefficient of permeability at zero effective stress	(2.5.4)
k_v	coefficient of permeability in vertical direction	(1.3.2)
k_x, k_y	permeability in x and y direction	(2.7.2)
m_v	volume compressibility	(2.5.4)
n'	ratio of E_v' to E_h'	(2.6.3)
m'	ratio of G_{vh}' to E_v'	(2.6.3)
p_a	atmospheric pressure	(5.3.3)
p'	mean effective stress	(1.3.2)
p_i	inner cell pressure	(1.3.8)
p_o	outer cell pressure	(1.3.8)

p_o	total overburden pressure	(1.4.5)
p_f	pore fluid pressure	(1.3.3)
p_{fb}	pore fluid pressure on boundary	(4.3.2)
p_k'	in-situ mean effective stress	(1.3.3)
q	deviator stress in triaxial plane	(1.3.3)
q_c	cone resistance	(1.4.3)
q_{ult}	ultimate load	(1.4.2)
r_u^*	pore pressure ratio	(4.3.2)
s	$(\sigma_a'+\sigma_a')/2$	(1.3.3)
s_c, s_q, s_γ	bearing capacity shape factors	(6.5)
t	$(\sigma_a'-\sigma_a')/2$	(1.3.3)
t	element thickness	(9.4.3)
u	horizontal displacement	(1.3.5)
v	vertical displacement	(1.3.5)
v	specific volume	(1.3.2)
v_1	specific volume at unit mean effective stress	(5.5.3)
A	area	(3.4.5)
A_s	pore water pressure parameter	(1.3.3)
B	diameter of plate	(1.4.5)
B	building width	(2.4.1)
B	half width of the footing	(6.5.4)
C_c	compression index	(1.3.2)
C_s	swelling index	(1.3.2)
D	tunnel diameter	(2.4.1)
D_l	final tunnel diameter	(2.4.4)
D_m	initial tunnel diameter	(2.4.4)
D_r	relative density	(1.4.2)
DR_{hog}	hogging deflection ratio	(2.7.1)
DR_{sag}	sagging deflection ratio	(2.7.1)
E	Young's modulus	(1.3.2)
E'	effective Young's modulus	(1.3.3)
E_u	undrained Young's modulus	(1.3.3)
E_c	constrained modulus	(1.3.2)
E_r	hammer energy in SPT	(1.4.2)
E_x	free-fall energy in SPT	(1.4.2)
E_s	secant Young's modulus	(1.3.3)
E_t	tangent Young's modulus	(1.3.3)
E'_{max}	small strain Young's modulus	(1.3.3)
E_v'	vertical effective Young's modulus	(2.6.3)
E_h'	horizontal effective Young's modulus	(2.6.3)
EI	bending stiffness	(2.7.1)
EA	axial stiffness	(2.7.1)
ER_r	rod energy ratio in SPT	(1.4.2)
F_a	axial force	(1.3.3)

F_V, F_H	vertical and horizontal force	(1.3.5)
F_x, F_y, F_z	forces on pile group in x, y and z direction	(7.4.5)
G	shear modulus	(1.3.3)
G_{hh}	shear modulus in horizontal plane	(1.3.10)
G_{hv}	shear modulus in horizontal-vertical plane	(1.3.10)
G_{vh}	shear modulus in vertical-horizontal plane	(1.3.10)
H	building half-width	(2.7.1)
J	deviatoric stress invariant	(1.3.3)
J_f	value of J at failure	(A.III.1)
$\boldsymbol{K}$	pile group stiffness matrix	(7.4.5)
K	bulk modulus	(1.3.3)
K_f	bulk modulus of pore fluid	(3.4.3)
K_{skel}	bulk modulus of soil skeleton	(7.5.3)
K_o	coefficient of earth pressure at rest	(1.3.2)
K_o^{NC}	K_o normally consolidated	(1.3.2)
K_o^{OC}	K_o overconsolidated	(1.3.2)
K_p	passive coefficient of earth pressure	(4.5.4)
K_t	tangent bulk modulus	(5.4.3)
K_s	shear stiffness of interface element	(5.5.6)
K_n	normal stiffness of interface element	(5.5.6)
M	bending moment	(2.4.5)
M_e	limiting moment on joint extrados	(2.4.5)
M_i	limiting moment on joint intrados	(2.4.5)
M_T	torque load	(1.3.8)
M_x, M_y	moments on pile group about x and y axes	(7.4.5)
N	SPT blowcount	(1.4.2)
N_{60}	normalised SPT blowcount	(1.4.2)
N_k	cone factor	(1.4.3)
N_c, N_q, N_γ	bearing capacity factors	(6.5)
OCR	overconsolidation ratio	(1.3.2)
P	cavity pressure	(1.4.4)
P_L	limiting cavity pressure	(1.4.4)
Q	load on the footing	(6.5.4)
Q_{max}	maximum load on footing	(6.5.4)
R	residual factor	(4.5.4)
R	principal stress ratio	(5.3.2)
S_{max}	maximum shear force	(2.4.5)
S_u	undrained strength	(1.3.8)
S	stress level	(A.III.1)
T	pull-out force of suction anchor	(7.5.2)
U_x, U_y, U_z	pile group displacement in x, y, and z direction	(7.4.4)
V	volume of cavity	(1.4.4)
V, H	vertical and horizontal load	(6.5.7)

V_e	excavated tunnel volume	(2.4.4)
V_L	volume loss	(2.4.4)
V_S	volume of settlement trough	(2.4.4)
V_t	final tunnel volume	(2.4.4)
W	vertical load	(1.3.8)
W	water content	(4.5.4)
W_L	water content at liquid limit	(4.5.4)
W_p	water content at plastic limit	(4.5.4)
α	inclination of the major principal stress to the vertical	(1.3.8)
α^*	relative axial stiffness	(2.7.1)
β	soil stiffness reduction factor	(2.4.4)
γ	bulk unit weight	(2.7.2)
γ'	effective bulk unit weight	(6.5.4)
γ_{dry}	dry bulk unit weight	(7.3.2)
γ_{sat}	saturated bulk unit weight	(5.5.3)
γ_{xy}	shear strain in x-y plane	(1.3.5)
γ_{rz}	shear strain in r-z plane	(1.3.8)
$\gamma_{r\theta}$	shear strain in r-θ plane	(1.3.8)
$\gamma_{z\theta}$	shear strain in z-θ plane	(1.3.8)
γ_w	unit weight of water	(5.3.5)
δ	interface friction angle	(1.3.5)
δ	relative displacement	(4.4.4)
δ	vertical displacement of footing	(6.5.4)
δ_h	horizontal displacement at mid-slope	(4.3.2)
ε_a	axial strain	(1.3.2)
ε_r	radial strain	(1.3.2)
ε_θ	circumferential strain	(1.3.8)
ε_v	volumetric strain	(1.3.2)
ε_c	cavity strain	(1.4.4)
ε_{hc}	compressive horizontal strain	(2.7.1)
ε_{ht}	tensile horizontal strain	(2.7.1)
ε_h	horizontal strain	(2.7.1)
θ	Lode's angle	(1.3.3)
κ	inclination of swelling line in v-lnp' plane	(1.3.2)
λ	inclination of VCL in v-lnp' plane	(1.3.2)
λ	convergence-confinement parameter	(2.4.4)
λ_d	value of λ at which lining is installed	(2.4.4)
μ	Poisson's ratio	(1.3.3)
μ	coefficient of friction	(4.4.4)
μ_{ar}'	Poisson's ratio for straining in the radial direction due to changes in axial stress	(1.3.3)
μ_{vh}'	Poisson's ratio for straining in the horizontal	

	direction due to changes in vertical stress	(1.3.8)
μ_{hv}'	Poisson's ratio for straining in the vertical direction due to changes in horizontal stress	(1.3.8)
μ_{hh}'	Poisson's ratio for straining in the horizontal direction due to changes in horizontal stress	(1.3.8)
ν	angle of dilation	(1.3.5)
ν_w	angle of interface dilation	(5.5.6)
ρ	material density	(1.3.10)
ρ	settlement	(1.4.2)
ρ^*	relative bending stiffness	(2.7.1)
$\sigma_1, \sigma_2, \sigma_3$	major, intermediate and minor principal stress	(1.3.4)
$\sigma_x, \sigma_y, \sigma_z$	direct stresses in x, y and z direction	(1.3.5)
σ_a	axial total stress	(1.3.2)
σ_a'	axial effective stress	(1.3.2)
$(\sigma_a')_b$	pre-consolidation pressure	(1.3.2)
σ_c	cell pressure	(1.3.3)
σ_r	radial total stress	(1.3.3)
σ_r'	radial effective stress	(1.3.3)
σ_z	vertical total stress	(1.3.8)
σ_θ	circumferential total stress	(1.3.8)
σ_n	normal stress	(1.3.6)
σ_{ho}	in-situ horizontal stress	(1.4.4)
σ_{vo}	total overburden pressure	(1.4.3)
σ_f	maxim permissible compressive stress across interface	(2.4.5)
τ	shear stress	(1.3.5)
τ_p	peak shear stress	(1.3.5)
τ_r	residual shear stress	(1.3.5)
τ_{mob}	mobilised shear stress	(5.4.4)
τ_{xy}	shear stress in x-y plane	(1.3.5)
$\tau_{z\theta}$	shear stress in z-θ plane	(1.3.8)
τ_{zr}	shear stress in z-r plane	(1.3.8)
$\tau_{r\theta}$	shear stress in r-θ plane	(1.3.8)
φ'	angle of shearing resistance	(1.3.2)
φ_{cs}'	critical state angle of shearing resistance	(1.4.2)
φ_p'	peak angle of shearing resistance	(1.3.3)
E_d	invariant deviatoric strain	(1.3.3)
Θ_x, Θ_y	pile group rotations about x and y axes	(7.4.4)

Index